Runoff Analysis using Satellite Data for Flood Reginal Assessment:
Spatial and Time-series Bias Correction of Satellite Data

Kwanchai Pakoksung

A dissertation submitted to
Kochi University of Technology
in partial fulfillment of the requirements
for the degree of

Doctor of Engineering

Graduate School of Engineering

Kochi University of Technology

Kochi, Japan

September 2016

Abstract

Floods are one of all the major natural disasters, affecting to human lives and economic loss. Understanding floods behavior using simulation modelling, of magnitude and flow direction, is the challenges of hydrological community faces. Most of the floods behaviors are depended on mechanism of rainfall and surface data sets (topography and land cover) that are specific for some area on a ground observation data. Remote sensing datasets possess the potential for flood prediction systems on a spatially on datasets. However, the datasets are confined to the limitation of space-time resolution and accuracy, and the best apply of these data over hydrological model can be revealed on the uncertainties for the best flood modelling. Furthermore, it is important to recommend effective of data collecting to simulate flood phenomena. For modelling nearby the real situation of the floods mechanism with different data sources, the difficult task can be solved by using distributed hydrological models to simulate spatial flow based on grid systems. Therefore, the objective of this dissertation is to contribute the correction and evaluation of remote sensing sources for flood prediction through basin scales, and application of the model to demonstrate the approach of flood risk estimation method on small area. It also aims to present and create general bias methodology for runoff analysis using the remote sensing data sources to model the flood simulation. The geographical point of this study is the Yoshino river basin in Japan and the Upper part of Nan river basin in Thailand.

Firstly, the modification and implementation of distributed hydrological modeling as the RRI model are included by VOXEL model for convenient on input and output and the GPU coding for speedup. The VOXEL model was used to integrate the input data the watershed data (DEM and Land cover) and rainfall data (spatial and temporal) and the output data runoff and inundation depth (spatial and temporal). The GPU on NVIDIA CUDA was setup for speedup about 2.6x on the complex terrain.

The accuracy assessment, bias correction method evaluation, and impact of flood analysis validation were shown in the second part based on three components of flood mechanism, DEM, satellite land cover, and satellite based rainfall. The six DEM sources (GSI-DEM, ASTER GDEM, SRTM, GMTED2010, HydroSHEDS, and GTOPO30) evaluated by the referent elevation points (GCP) that are used to estimate bias correct coefficient based on spatial linear transformation, and then the data are driven by the distributed hydrologic model (RRI) to reveal the impact of the topography sources. The GSI-DEM was a high accuracy among the five DEMs and the correction algorithm could improve the accuracy responding with the coarse resolution DEMs (HydroSHEDS and GTOPO30), while the high resolution (GSI-DEM, ASTER GDEM, SRTM, and GMTED2010) had a small sensitivity. In the Shikoku Island, ASTER DEM was suitable for runoff simulation, have estimated from stereo matching. SRTM presented a performance for runoff and inundation simulation in the Nan river basin, have explored from radar laser scan with Shuttle. MODIS product outperformed

AVHRR products that Manning's coefficient of MODIS also showed higher performance. The MODIS roughness also presented higher performance evaluated from the hydrological modeling results.

The rain gauges were interpolated into grid system with five algorithms, Inverse Distance Weight (IDW), Thiessen Polygon (TSP), Simple Kriging (SKG), Ordinary Kriging (OKG), and Surface Polynomial (SPL). The IDW outperformed as high performance algorithm in the Shikoku area that represented with the dense rain gauge network area, while the sparse rain gauge network area was the Nan river basin that the SKG was suitable algorithm. GSMaP and GPV showed the high accuracy for the Shikoku in Japan, while CMORPH outperformed among other sources in the Nan area in Thailand, on the international sources. GPV and GSMaP in Japan and GPM in Thailand as the high resolution showed the highest performance on runoff simulation, while low resolution was TRMM. The five algorithms (Mean ratio, Geometrics transformation, Linear transformation, Data assimilation, and Quantile mapping) and two schemes (Temporal and Spatial) were evaluated only GPM and TRMM in the Nan river basin, Thailand. The three algorithms (Linear, Geometrics, Data assimilation) on the spatial scheme showed the high performance, resulting from runoff validation.

Finally, the application of the remote sensing data sets on flood forecasting and flood risk assessment was demonstrated. The first approach, the river basin scale simulation was used to define as the boundary condition of small area to simulate a high resolution of flood map. The second approach based on small area results, the flood risk assessment was consisted by hazard and vulnerability data. In this task, the streamflow for estimating the flood risk map was the main point for proposing.

Acknowledgments

Table of Content (continued)

List of figures

List of figures (continued)

List of figures (continued)

List of tables

List of tables (continued)

Chapter 1 Introduction

1.1 Motivation

1.1.1 Flood disaster

Floods are one kinds of disaster around the world, affecting to human lives and make economic losses. Approximately about 66% of water related disasters (see **Figure 1-1**) in the world are floods (WWC, 2000). Nowadays, impacts of floods have been increased because of population growth, decreasing of floods plain, and climate change. Flood mitigations have two guidelines, structural and nonstructural, are selected by social and also investment. The major tools firstly used for planning and developing structural and non-structural flood mitigation and management approaches, which is hydrologic and hydraulic modeling used for flood simulation on decision and design. Understanding floods behavior used for simulation modelling as shown in **Figure 1-2**, of magnitude and flow direction, is the challenges of hydrological community. For actual of flood behavior in magnitude, the best input dataset are ground truth observation data, rain gauge, topographical and land cover data. The flow direction of the actual flood mechanism is spatial heterogeneity to represent on quadrate grid system. The flood modeling to conform to real situation has two components, input dataset and flow distribution algorithm. This mechanism of flow distribution can be modeled by using distributed hydrological modelling, to require the spatial input data. The ground truth dataset, rainfall, elevation and land use, is normally observed based on point data, are specific in some convenient area.
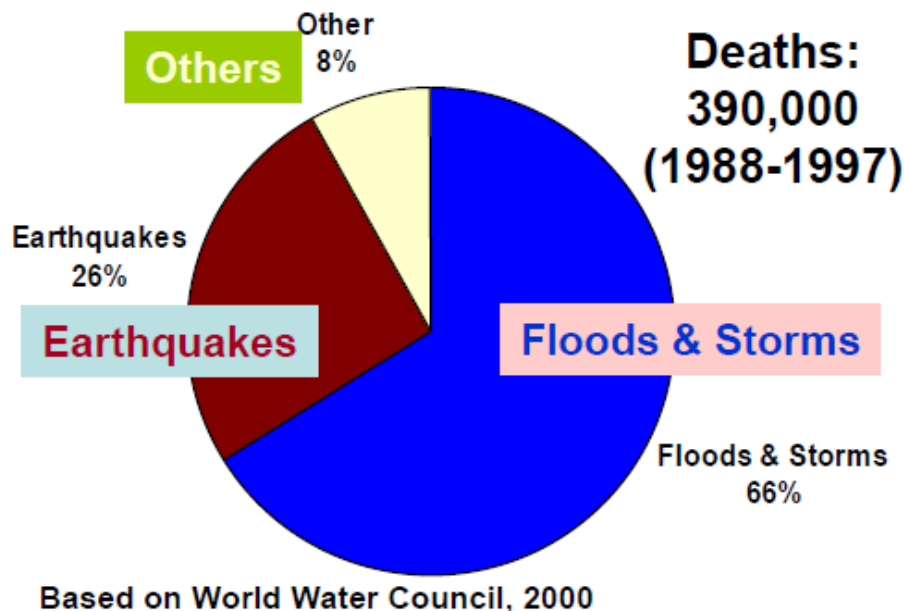
Figure 1-1 Water related disasters in the world

Floods modeling have been gotten on some problems for ground observation data because of non-spatially of data sets, rainfall and ground surface, all of which can be solved by remote sensing data. Nowadays satellite remote sensing have several types of sensor for exploring the natural resources as exampled in **Figure 1-3**. The remote sensing datasets possess the potential for flood prediction systems on a spatially on datasets. However, the datasets, satellite base rainfall, digital elevation model (DEM) and global land cover, are confined to the limitation of space-time resolution and accuracy. The best application of these data over hydrological model for the flood prediction can be revealed on the uncertainties for the best flood modeling. Furthermore, it is important to recommend effective of data collecting to simulate flood phenomena. For modeling nearby the real situation of the floods mechanism with different data sources, the difficult task can be solved by using distributed hydrological models to simulate spatial flow based on grid systems.
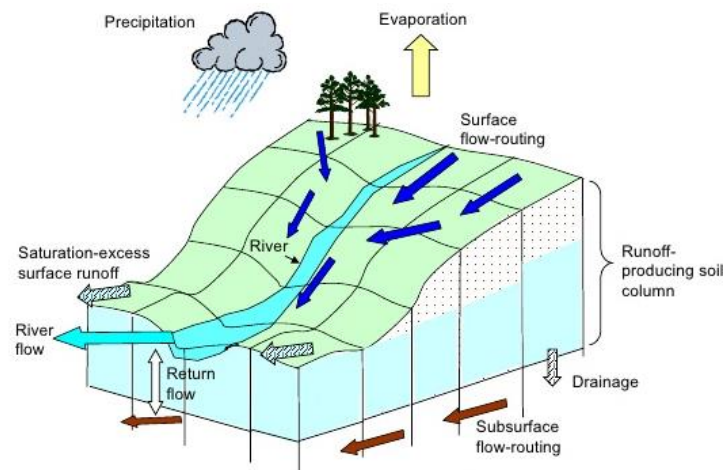
Sources: https://www.meted.ucar.edu/training_module.php?id=491

Figure 1-2 Components of hydrologic processes for flood mechanism
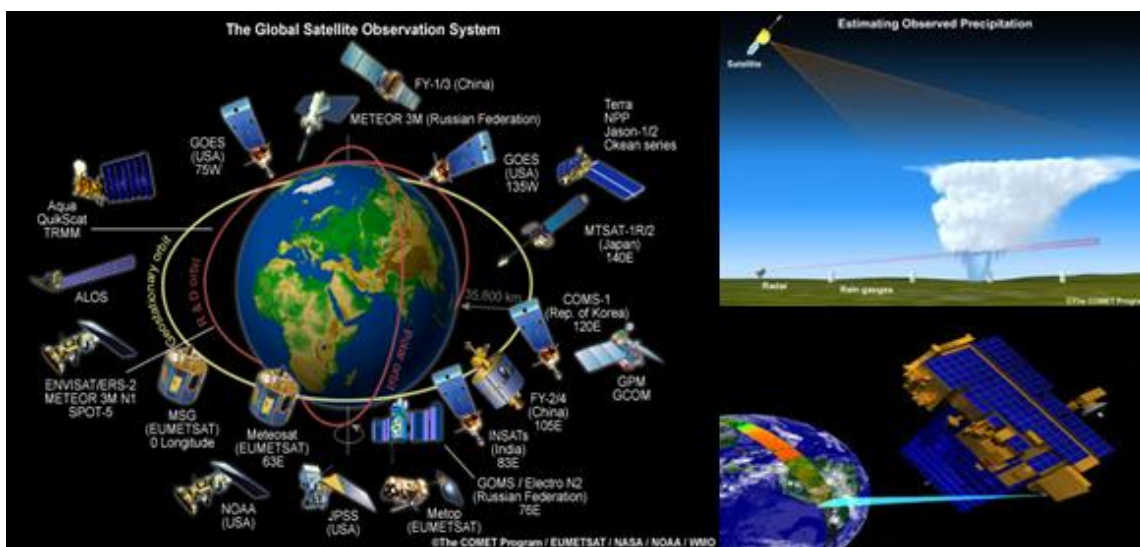
Sources: http://www.goes-r.gov/users/comet/tropical/textbook_2nd_edition/print_2.htm

Figure 1-3 Satellite remote sensing datasets

1.1.2 Historical of hydrological modeling

The hydrological models have developed to start in the 60s (see **Figure 1-4**) and challenged by the advance of high-speed computers that its demand was proposed by advanced water engineering topics. Lumped models were firstly implemented to depend on limitations of computer and spatial information. Spatial variability of the landscape characterization, hydro-meteorological data, or initial conditions was not clearly accounted for in this formulation type. The weaknesses were overcome that effective parameters were calibrated based on the hydrograph at the outlet of the basin. The parameter calibration certain as good fit and a exact on a mass balance but did not agreement based on physical processes correction. Generally, the lumped model is the Sacramento Soil Moisture Accounting Model (Burnash et al, 1973), which is the key model applied for flood forecasting by the National Weather Service River Forecast Centers across the United States.

	Theory(physics)	Hydrological models
1800	Chezy formula, 1749 Dalton eqn., 1802	
	Darcy, 1856 Saint-Venant, 1871	Rational model, Mulvany 1850
1900	Manning, 1891	
	Green-Amp, 1911 Richards, 1931	Unit hydrograph, Sherman 1932
1650	Horton, 1933	
1960	Philip, 1954	Linear & cascade reservoir, Nash & Dooge
1970		Tank model Lumped conceptual
1980		Time-series modeling
1990		Physically-based, distributed model

Figure 1-4 Historical of hydrologic on theoretical and modeling

1.1.3 Applications of remote sensing for flood prediction

Remote sensing data sets provide information for estimating the local, regional, and global water resources modeling (Schultz, 1996; Bindlish et al., 2009; Conesa-Garcia et al., 2010). The data sets can potentially be implemented to forecast floods, while some limitations are occurred by the coarse resolution of the information in spatial and temporal scale, the sampling interval, and reparation uncertainties (Lakshmi, 2004). It needs to know the information content of each data set and define the best approach to apply the data sets specifically to flood modeling. Its information such as digital elevation model and precipitation is directly implemented in the flood simulation model, in some studies. By the contrast cases, the satellite remote sensing data is used to drive for land surface modeling that implement water and energy flux investigation (Lohmann et al., 2004). The outcomes of these investigations are potentially suitable for flood simulation such as soil and surface moisture, vegetation interception, and evaporation. These models are capable to correct anomalies in relationships of soil moisture and runoff conditions as well as involved in uncertainties (Xia et al., 2012). Several floods studies research were shown in the **Table 1-1** that classify as three class, Global, Regional, River Basin, and Local.

Table 1-1 Literature review of remote sensing data applied for flood study

Title	River basin	Area, sq.km	Data sets/ resolution	Evaluation data	Evaluation indexes	Reference
Global flood risk under climate change	Global		Topo: topo 15 min Rain: IPCC 20km 1d	Return period	PPCC	Hirabayashi et al., 2013
Real-time Global Flood Estimation using 1 Satellite-based Precipitation and a Coupled Land 2 Surface and Routing Model	Mississippi upstream sub-basin , USA	1,772,548	Topo: HydS 1.0 km Rain: 3B42V7 0.25d 3h	Runoff obs.	POD FAR CSI NSC	Huan et al., 2014
Flood Forecasting for Bangladesh with Satellite Data	Brahmaputra and Meghna, Bangladesh	907,000	Topo: HydS 1.0 km L/C : SWAT 1km Rain: 3B42RT 0.25d 3h	Runoff obs.	R RMSE MAE maxME	Akhtar, 2006
Influence of human activities on the BTOPMC runoff simulations in large-scale	Mekong	795,000	Topo: GTOPO30 3 min Rain: RG 1.0d 1.0d	Runoff obs.		Nawarathna et al., 2000

Table 1-1 Literature review of remote sensing data applied for flood study (continuous)

Title	River basin	Area, sq.km	Data sets/ resolution	Evaluation data	Evaluation indexes	Reference
Hydrological modeling of large-scale ungauged basin case study: Ayeyarwady (Irrawaddy) basin, Myanmar	Ayeyarwady (Irrawaddy), Myanmar	411,000	Topo: GTOPO30 1.0 km L/C : IGBT 5.0 km Rain: GPCP 1.0d 3h	Runoff obs.	comparison	Chavoshian et al., 2007
An emergency response-type rainfall-runoff-inundation simulation for 2011 Thailand floods	Chao phraya river, Thailand	160,000	Topo: HydS 1.0 km L/C : - 1km Rain: 3B42RT 0.25d 3h	Runoff obs.	FIT	Sayama et al., 2015
Rainfall-Runoff Modeling of the Trans-Boundary Kabul River Basin Using Integrated Flood Analysis System (IFAS)	Kabul, Pakistan	92,605	Rain: GSMaP_NRT 0.1d 1h	Runoff obs.	Ew Ev Ep	Aziz, A., 2014
Rainfall–runoff–inundation analysis of the 2010 Pakistan flood in the Kabul River basin	Kabul, Pakistan	92,605	Topo: HydS 1.0 km L/C : - 1km Rain: GSMaP_NRT 0.1d 1h	MODIS UNOSAT	FIT	Sayama et al., 2012
Satellite Remote Sensing and Hydrologic Modeling for Flood Inundation Mapping in Lake Victoria Basin: Implications for Hydrologic Prediction in Ungauged Basins	Nzoia, Kenya	12,900	Topo: SRTM 1.0 km L/C : MODIS 1km Rain: 3B42RT 0.25d 3h	MODIS 250m (flood area)	POD FAR CSI	Khan et al., 2011
Development of a large basin rainfall-runoff modeling system using the object-oriented hydrologic modeling system	Geum, Korea	3,994	Topo: SRTM 250 km Rain: RG 12km 1h	Runoff obs.	PDR NSC	Lee et al., 2011

Table 1-1 Literature review of remote sensing data applied for flood study (continuous)

Title	River basin	Area, sq.km	Data sets/ resolution	Evaluation data	Evaluation indexes	Reference
Satellite-based Flood Modeling Using TRMM-based Rainfall Products	Cumberland, USA	970	Topo: HydS 1.0 km Rain: 3B41RT 0.25d 1h	Runoff obs.	Peak flow Total volume Time to peak	Harris et al., 2007
Distributed hydrologic simulations to analyze the impacts of land use changes on flood characteristics in the Yasu River basin in Japan	Yasu, Japan	377.1	Rain: obs. 500m 3h	Runoff obs.	Difference of peak flow	Kimaro et al., 2005
Modeling large-scale inundation of Amazonian seasonally flooded wetlands	Solimoes, Brazil	240 km	Topo: SRTM 270m	Runoff obs.	F	Wilson et al., 2007
Improving models of river flood inundation using remote sensing	Seven river, UK	10 km	Topo: LiDAR 6km	Runoff obs.		Mason, 2007
Predicting floodplain inundation: raster-based modelling versus the finite-element approach	Thames river, UH	4 km	DEM 50m	Scenario test		Horritt and Bates, 2011

1.2 Overview of the thesis

1.2.1 Research problem

The objective of this research is to contribute the correction and evaluation of remote sensing sources for flood prediction through basin scales, and application of the model to demonstrate the approach of flood loss estimation method on small area. This research mainly motives to explore uncertainties in flood simulation caused by limitations of data, accuracy or resolution of source. It will similarly to present and create general methodology for runoff analysis using the remote sensing data sources to model the flood simulation. Therefore, the remote sensing datasets can be used to simulate floods with an acceptable level of accuracy, and the specific goal of this work is to reveal the remote sensing data for basin area of flood simulation as closely as possible. In order to achieve the goal, this study is to follow research question:

1. How does flood simulation based on hydrological modeling, using satellite remote sensing datasets? (**Chapter 2**)
2. What are the effects of DEM sources on flood estimation? (**Chapter 3**)
3. What are the impacts of surface roughness based on different land cover sources on flood simulation results? (**Chapter 4**)
4. What are the results from different rainfall sources driven by the Distributed Hydrological Modeling? (**Chapter 5**)
5. What are the applications of flood modeling approaches for estimating floods to map flood hazard to analyze flood damage? (**Chapter 6**)

In order to receive the answers of research question based on the main objective. Specific objective as following:

1. To apply the distributed hydrological model as the Rainfall-Runoff-Inundation model that is a combination of rainfall-runoff processes and flood modeling. (**Chapter 2**)
2. To explore the accuracy, bias correction of DEM data set and to evaluate flood simulation results from different topography sources. (**Chapter 3**)
3. To explore the accuracy of both approaches, satellite land cover data sources and surface roughness coefficient, and to evaluate flood modeling results from different surface roughness data sets. (**Chapter 4**)
4. To explore the accuracy of rainfall sources, rain gauge spatial, satellite, and simulated products, to investigate bias correction of the satellite rainfall product as a demonstration, and to evaluate runoff simulation results from different rainfall sources. (**Chapter 5**)
5. To apply of flood simulation model for water resource management in flood hazard mapping for flood damage cost estimation. (**Chapter 6**)

1.2.2 Scope of the thesis

The geographical points of this study are the Yoshino river basin in Japan and the Upper part of Nan river basin in Thailand which are representative of flood disaster area. First, Yoshino river basin is rich in high resolution of temporal and spatial data in hydrologic information. Second, Nan river basin has low resolution datasets. This datasets all of both areas will be used to evaluate accuracy of remote sensing data and to verify flood simulation. In this study, it proposes an implementation of the remote sensing datasets to input to distributed hydrological model including inundation processes, Rainfall-Runoff-Inundation (RRI) Model, to obtain analytical result of flood characteristic in the river basin and local area. The satellite base rainfall is the spatial and up-to-date data, have explored more ten years ago.

The six rainfall products were used in this study, of which three are high resolution dataset and three are low resolution dataset. The accuracy of each product was assessed at time scale by comparing with the rain gauges. Using the six products as input to the RRI model, their outputs have performed an accuracy assessment with observation discharge at runoff station on the five performance statistical coefficients.

Global Precipitation Measurement (GPM) is a high resolution on temporal scale, which is moderately significant for effective uses such as flash flood warning systems. Tropical Rainfall Measuring Mission (TRMM), which is one type of the satellite base rainfall, has been observed since 1998. CPC Morphing Technique (CMORPH) is a global precipitation analyses for real-time monitoring of global scale developed by NOAA's Climate Prediction Center [CPC]. The CMORPH resolution of 0.25 degree spatial and 3-h temporal product is implemented. Precipitation Estimation from Remotely Sensed Information using Artificial Neural Networks (PERSIANN) is a satellite-based precipitation product that are implemented by using the artificial neural networks (ANN) to estimate rainfall intensity based on merged infrared product of brightness temperature from geostationary satellite. Grid Point Value (GPV) data provided from Japan Meteorological Agency (JMA) calculated with Global Spectral Model (GSM) and MesoScale Model (MSM).

Six open source DEMs are represented by the different contained accuracy and coverage were invested for this study. The 10m-mesh DEM have been provided from the Geographical Survey Institute (GSI) of Japan (GSI-DEM), with scales between 1:5,000 and 1:25,000. The Advanced Space Borne Thermal Emission and Reflection Radiometer-Global Digital Elevation Model (ASTER GDEM) was established from two international agencies, the METI (Ministry of Economy, Trade, and Industry) of Japan and the NASA (National Aeronautics and Space Administration). The topography represented by digital elevation model (DEM) is Shuttle Radar Topography Mission (SRTM) in the year 2000, which is a useful produce for application fields. The SRTM DEM has the

resolution about 90 meters, is a source of surface data for flood modelling. The Global Multi-resolution Terrain Elevation Data 2010 (GMTED2010) has been published by the U.S. Geological Survey (USGS) and the National Geospatial-Intelligence Agency (NGA). GMTED2010 was firstly provided on 2010 that GTOPO30 at 30 arc-seconds data (GTOPO30) was reconstructed for a new digital global elevation model. Hydrological data and maps based on Shuttle Elevation Derivatives at multiple Scales (HydroSHEDS) is provided as reconstructed from elevation data of the Shuttle Radar Topography Mission (SRTM) based on the 3 arc-second resolution that hydrologically conditioned is a main procedure to apply void-filling, filtering, stream burning, and upscaling techniques. Global 30Arc-Second Elevation (GTOPO30) is published from U.S. Geological Survey for free available on 1993 to represent a global digital elevation model (DEM).

In this study, two land cover data sources (MODIS and AVHRR) are selected to evaluate the flood modeling. Moderate Resolution Imaging Spectroradiometer (MODIS) data have spatial resolution from 250 m to 1 km and offer the possibility for time series coverage at moderate resolution. MCD12Q1 is one of global MODIS land cover product, which data product is generated at annually over ten years using a supervised classification. The Advanced Very High Resolution Radiometer (AVHRR) is presented for land cover data, provided in 2008. The AVHRR based on 1 kilometer of resolution is NDVI composites, this data set is used in the land cover characterization.

1.3 Outline of the thesis

The dissertation comprises of 7 chapters are outline in **Figure 1-5** that in **Chapter 1**, the motivation and research problem is presented, the research objectives are also started in this chapter.

Chapter 2 is the modification and implementation of distributed hydrological modeling (RRI model) that are included by VOXEL model for convenient on input and output and the GPU coding for speedup. The VOXEL model as a 3D array was used to integrate the data sets in two groups, watershed data (DEM and land cover) and rainfall data (spatial and temporal), for the input data, and the output data were runoff and inundation depth in spatial and temporal scales. The GPU on NVIDIA CUDA was setup for speedup about 2.6x on the complex terrain.

Chapter 3 presents the accuracy of the six DEM sources evaluated by the referent elevation points (GCP) that are used to estimate bias correct coefficient based on the spatial linear transformation, and then the data are driven by the distributed hydrologic model (RRI) to reveal the impact of the topography sources. On the statistical approach, the six candidate DEMs (GSI-DEM, ASTER GDEM, SRTM, GMTED2010, HydroSHEDS, and GTOPO30) were evaluated that the GSI-DEM was a high accuracy among the five DEMs. The correction algorithm could improve the accuracy responding with the coarse resolution DEMs (HydroSHEDS and GTOPO30), while the high resolution (GSI-

DEM, ASTER GDEM, SRTM, and GMTED2010) had a small sensitivity. Based on the DEM data and simulation results, Shikoku is the mountain complex terrain to contain with a steep slope, while Nan river basin is the mountain area where represent with the mild slope. In the Shikoku Island, ASTER DEM is suitable to apply for runoff simulation using distributed hydrologic modeling, have estimated from stereo matching. SRTM presented a performance for runoff and inundation simulation in the Nan river basin, have explored from radar laser scan with Shuttle.

Chapter 4 shows the performance of land cover data sets to estimate the surface roughness on the Manning's coefficient that area used to drive in the RRI model for presenting an uncertainty. MODIS with MCD12Q1 outperformed the AVHRR products on the both study sites. The Manning's coefficient produced from the MODIS data also showed higher performance than the AVHRR roughness products. Manning's *n* coefficient based on the MODIS presented higher performance than the AVHRR that was evaluated by using runoff data estimated from the hydrological modeling.

Chapter 5 has three topics as evaluation of rain gauges spatial distribution algorithms, remote sensing data sets, and bias correction methods, based on the RRI model results (runoff data). The rain gauge data sets as a point data were interpolated into grid data sets with five algorithms, Inverse Distance Weight (IDW), Thiessen Polygon (TSP), Simple Kriging (SKG), Ordinary Kriging (OKG), and Surface Polynomial (SPL). The IDW outperformed as high performance algorithm in the Shikoku area that represented with the dense rain gauge network area, while the sparse rain gauge network area was the Nan river basin that the SKG was suitable algorithm. Evaluating the accuracy of satellite based products using the rain gauges data sets as point data was investigated. For the high resolution data, GSMaP showed the high accuracy for the Shikoku in Japan, while CMORPH outperformed among other sources in the Nan area in Thailand, on the international sources. According to specify in the Shikoku area, the GPV outperformed among the five remote sensing data. For their runoff products, GPV and GSMaP in Japan and GPM in Thailand as the high resolution data showed the highest performance to simulate runoff, while low resolution of satellite rainfall was TRMM. The bias correction method evaluated with five algorithms (Mean ratio, Geometrics transformation, Linear transformation, Data assimilation, and Quantile mapping) and two schemes (Temporal and Spatial), only GPM and TRMM in the Nan river basin, Thailand as the demonstration. The three algorithms (Linear, Geometrics, Data assimilation) on the spatial scheme showed the high performance among ten candidate algorithms, resulting in runoff products.

Chapter 6 is the application of the remote sensing data sets on flood forecasting and flood risk assessment. The first approach, the river basin scale simulation was used to define as the boundary condition of small area to simulate a high resolution of flood map. The second approach based on small area results, the flood risk assessment was consisted by hazard and

vulnerability data. In this task, the streamflow for estimating the flood risk map was the main point for proposing.

Chapter 7, the main contributions are summarized. In the chapter, the conclusions and recommendations are explained.
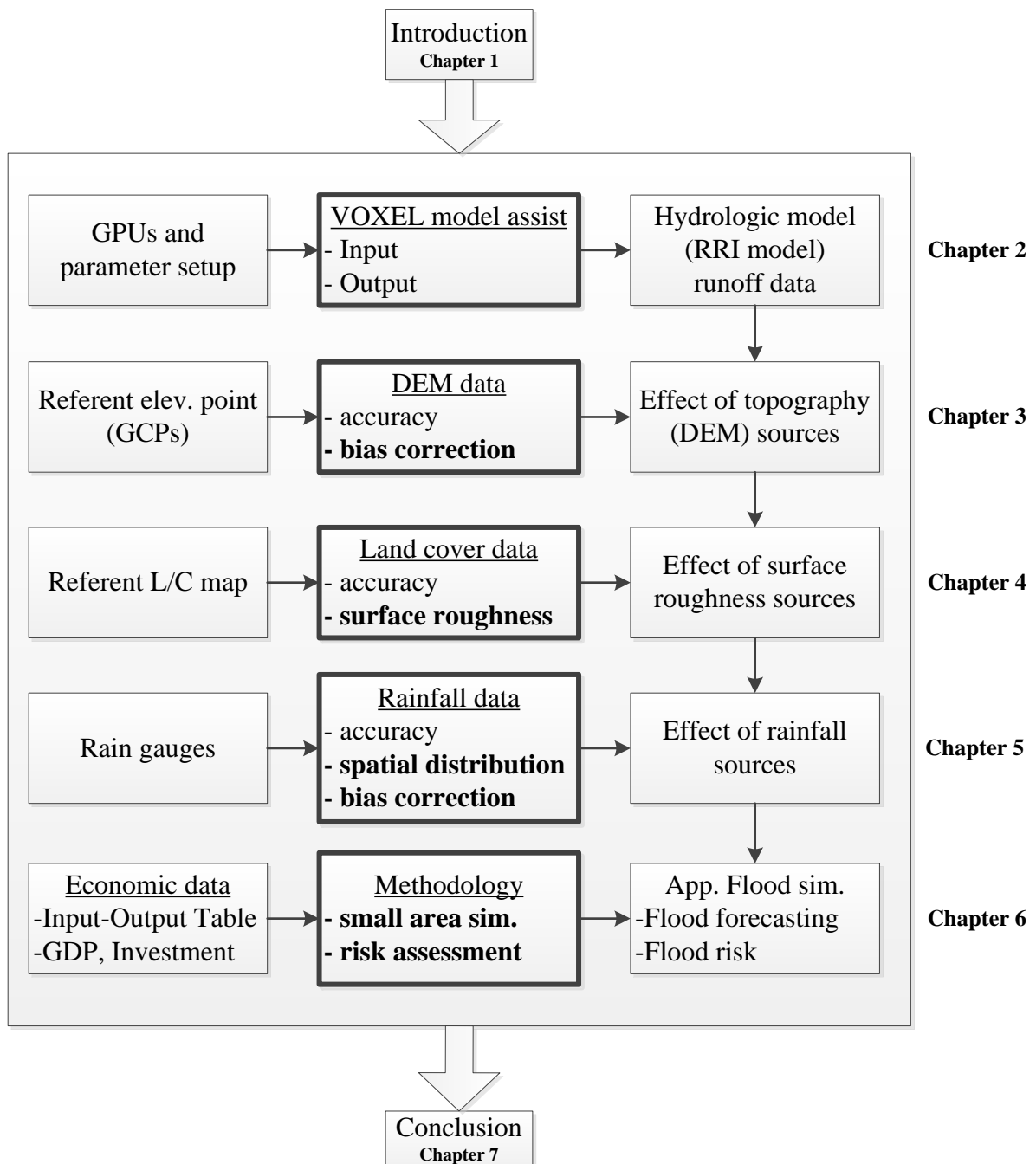
Figure 1-5 Outline of the dissertation

1.4 Study area

The dissertation based on the five objectives to present the impact of satellite remote sensing data on accuracy, bias correction, and runoff estimation is implemented to basin with different physical characteristics (catchment and climate).

1.4.1 Shikoku Island, Japan

Shikoku in Japan is selected as validation area. The Shikoku (**Figure 1-6**) is the 4th largest island of Japan located in the western territory within a bounding rectangle defined by the geographic coordinates 32°N to 35°N and 132°E to 135°E. This area is represented by a remote and mountainous condition to make the area extremely in the need of validation, covering an area about 18,800 square kilometers. The elevation ranges from approximately 0–1,982 m.MSL, and the average slope, computed from SRTM DEM, is 8-30°. The predominant land cover type with forests occupy in mountain slopes.

The mountains along the east side to west side divide the Island into Northern and Southern. The average annual rainfall of the southern part is about 3,500 mm, while the northern is about 850 mm, due to the orographic rain. The land covers consist of 80% forest, 1% grasslands, 12% cropland, 6% urban, and 1% water. The Yoshino River is major river in Shikoku. It is 196 km from Mount Ishizuchi, flowing west to east across the northern of Kochi and Tokushima Prefectures, and reaching the sea at the Tokushima city.

The Shikoku accounts for 5% of the total land area of Japan and its population is about 3.9 million. This Island is comprised of four prefectures, Tokushima, Kagawa, Ehime and Kochi and the combined gross domestic product of four prefectures is about 12,730 billion Yens.
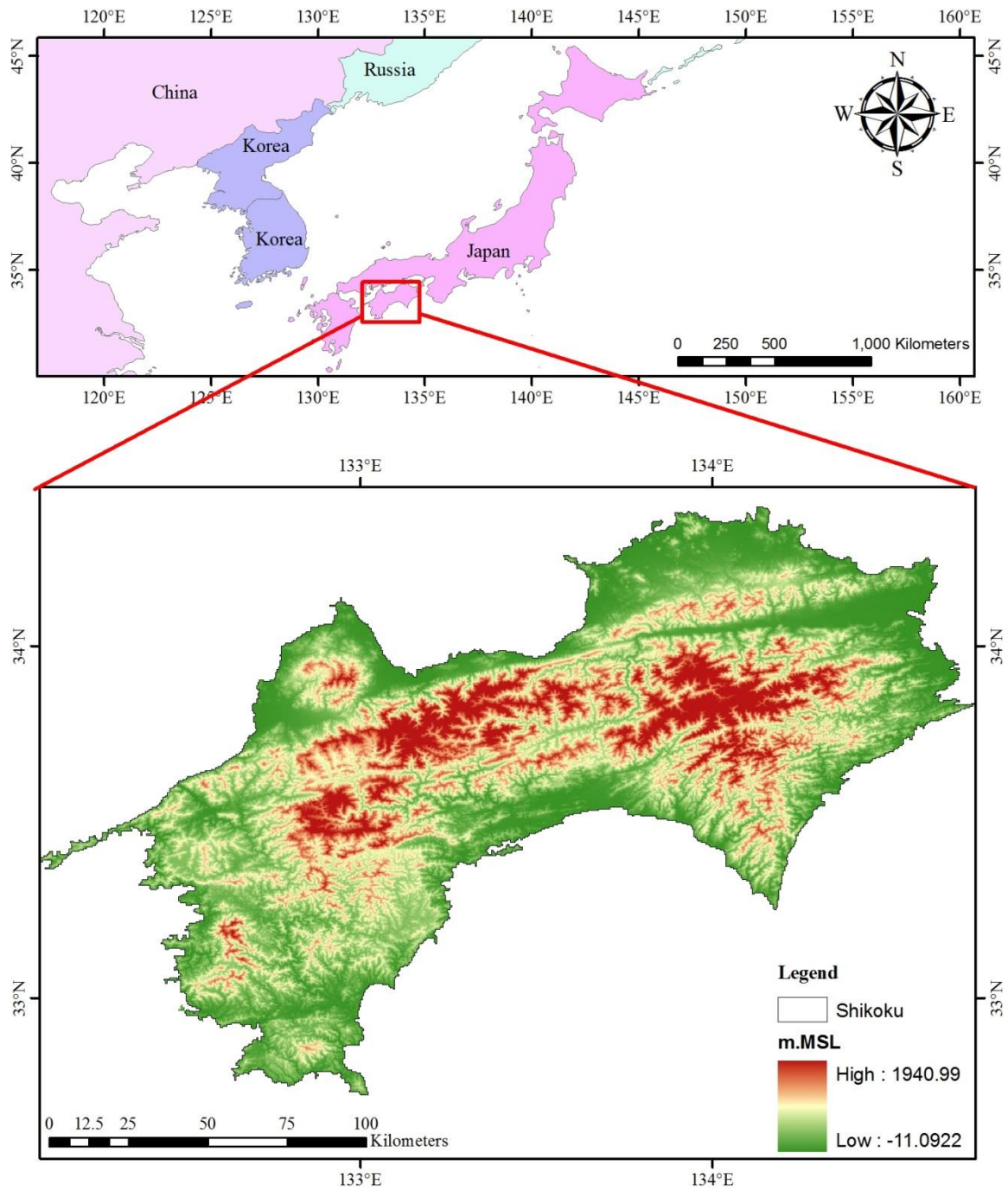
Figure 1-6 Location of the Shikoku Island, Japan

1.4.2 Nan river basin, Thailand

Upper part of Nan River Basin or upper part of Sirikit dam is important area because release of the SIRIKIT dam have been supplied for the central plain of Thailand, including Bangkok area capital city. **Figure 1-7** show the upper part of Nan river basin locates in the northern region of Thailand with the total catchment area of 13,000 square kilometers. The river originates from Bor Klua District, Nan Province, is situated between latitude 17° 42' 12" N to latitude 19° 37' 48" N and longitude 100° 06' 30" E to longitude 101° 21' 48" E. In this river basin, the mountain area accounts large area and residents inhabit in the middle of watershed that detail consist of 70% forest, 2% deforestation, 10% grasslands, 15% cropland, 1% urban, and 2% water.. From the Sirikit dam identified as river outlet of modelling to the upstream 150 km, the river bed slop is steep about 1/1,500. Upstream of this part, the slop is flat (1/10,000) and next is very steep (1/600). The elevation mention to the mean sea level ranges from 70 m to 1,200 m. The mean annual rainfall is 1,380 mm. There are some important tributary such as the Wa River, Nam Pua River and Nam Yao River. Flooding in this area, over flow from river bank have occurred in some vulnerable area, Tawang Pha, Muang Nan and Wiang Sa district.
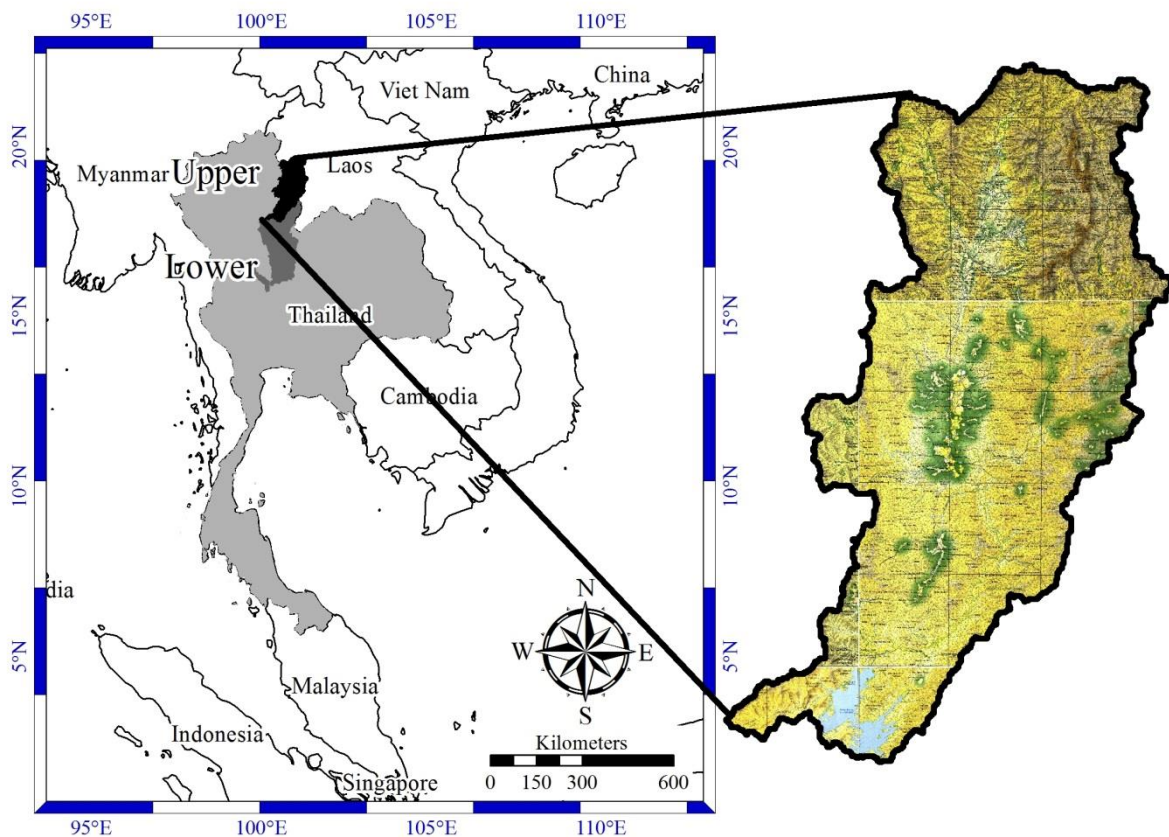
source: based on RID and LDD Thailand

Figure 1-7 Location of the Nan river basin, Thailand

Chapter 2 Hydrological Modeling[.]

2.1 Introduction

Floods are one kinds of disaster around the world, affecting to human lives and make economic losses. Flood mitigations have two guidelines, structural and nonstructural, which are selected by social and also investment. To minimize resistance from stakeholder of flood mitigation project, the nonstructural is the essential for decreasing flood damage using flood forecasting which use flood simulation for decision and design. The flood modelling to conform to real situation has two components, input dataset and flow distribution algorithm. For actual of flood behavior in magnitude, the best input dataset are ground truth observation data, rain gauge, topographical and land cover data. The flow direction of the actual flood mechanism is spatial heterogeneity to represent on quadrate grid system. This mechanism can be modeled by using distributed hydrological modelling, to require the spatial input data.

Mathematics model of flood based on hydrological processes (see **Figure 2-1**) have been used for more than thirty years ago and it is a powerful tool for water resources management (Crawford and Linslay 1966; Liang and Smith 2015). The model is developed on accuracy with a complexity of the hydrological mechanism on the computational using a governing equation with continuity and momentum (Zhang and Cundy 1989; Tayfur et al. 1993; Lamb et al. 2009; Kalyanapu et al. 2011). It has 2 tasks in a traditional for flood simulation, Rainfall-Runoff model on a terrain and flow routing model in a river channel. Most of the modern mathematics model of Rainfall-Runoff model is based on a physical-based of hydrological processes represented by using the spatial heterogeneity on a continuous grid cell system. The Rainfall-Runoff model simulates a streamflow discharge from a rainfall using either a kinematic or diffusive wave scheme between upstream to downstream to solve with the finite difference scheme. The river flow routing model is driven by the Saint-Venant equation and also solved by the finite difference method, using upstream hydrograph from the Rainfall-Runoff model. Therefore, Rainfall-Runoff-Inundation (RRI) model has integrated the two tasks for convenience use and included flood inundation model in a difference. The flood inundation model is

---

used for estimating the flood flow spreading on flood plains area with inflow and computing interaction flow between terrain slope with the Rainfall-Runoff model and river channel.

RRI model is the important tool for analysis in the hydrologic study. The modelling has a difference component such as topography data, land cover, soil type, and precipitation data. The component of the modelling is represented in varies format and pattern. This study presents the hydrological modelling components that are integrated into the VOXEL model for convenient to use in the flood model on the RRI model. The application of VOXEL model is followed as two topics. First, to integrate the component of the hydrological modeling for flood simulation in the VOXEL model such as the topography represented by DEM, land cover data and rainfall data, based on the 3D array as a 4D dimension. Second, to demonstrate the application of flood modelling represented by the RRI model using the VOXEL model datasets and presented its results in VOXEL model pattern.
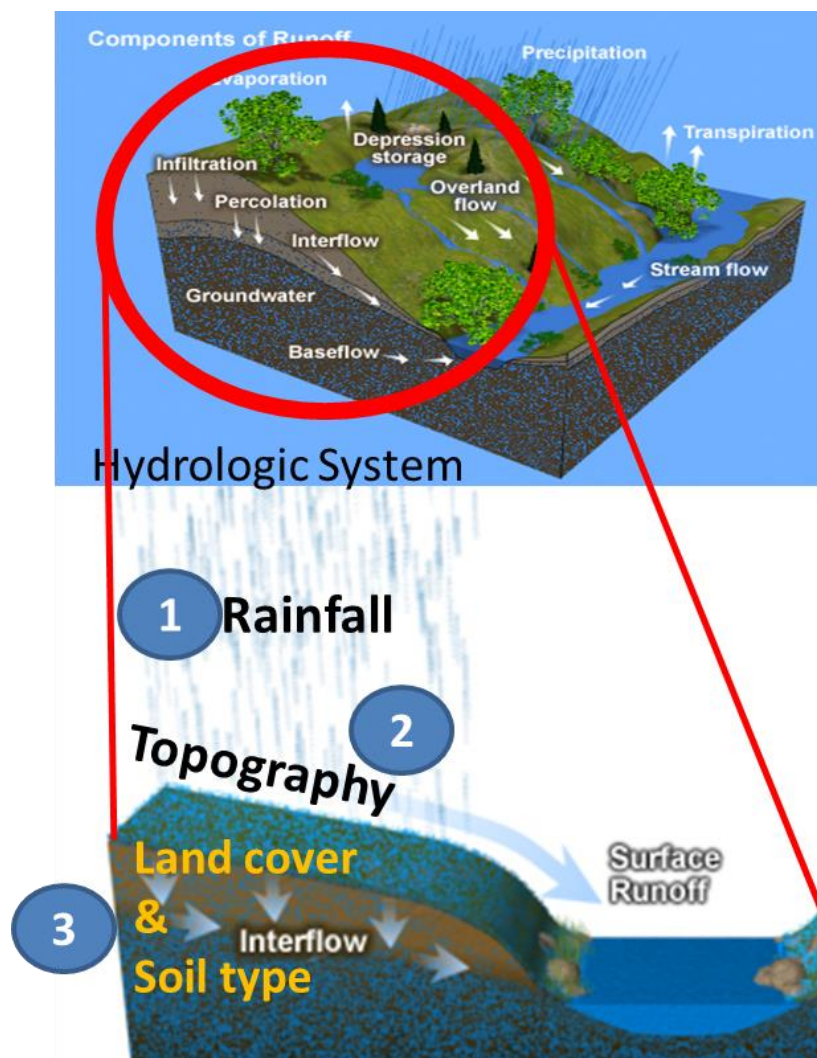
Source: MetEd, 2015

Figure 2-1 Hydrological processes

RRI model has already applied for flood studies in a several areas based on river basin scale. At first, the Kabul river basin was simulated on the 2010 Pakistan flood by using the RRI model. The resolution of topography data is about 761m x 924m based on the HydroSHEDS DEM. The flood model of this area has a potential for a good relationship to evaluate its inundation area with satellite data such as MODIS data (Sayama et al. 2012). On the 2011 Thailand flood, this model was used to simulate the flood on the Chao Phraya river basin for emergency responses during the disaster. The outcome of the prediction is overestimation about 40% on the river discharge and 2 m for the inundation water level with upscaling of the topography resolution from the HydroSHEDS 30 arc-seconds to 60 arc-seconds (Sayama et al. 2015). The RRI model on the Yom river basin based on the 2011 flood in Thailand was applied to estimate the flood losses and its simulation result has closed to the observation data based on 30 arc-seconds topography resolution (Anurak et al. 2013). On uncertainty of a precipitation data sources, the RRI model on 15 arc-seconds resolution of topography data was simulated on the Nan river basin on the Norther part of Thailand to compare the runoff from rain gauge observation data and 3B42RT produced by TRMM satellite. The evaluation concluded that the rain gauge runoff overestimated on the observation runoff while the TRMM runoff is underestimation (Pakoksung and Takagi, 2015). All of applications of the RRI model have done on the coarse resolution, while requiring a high resolution of terrain for accuracy of an inundation forecasting is limited by the capability of computer machine to run the existing RRI model.

Flood forecasting on high resolution of the existing RRI model is related with a computational cost, and the RRI code is accelerated on parallelizing of central processing units (CPUs) by using OpenMP (Open Multi-Processing) (Sayama et al. 2012). In a recent year, the parallel programming has been enabled through graphic processing units (GPUs) that have been applied in the different area of scientific and engineering computing. GPUs application has a limitation to apply in modeling of computation fluid dynamic and flood. A dynamic analysis on a real-time visualization modeling has a speedup about 25x on a NVIDIA® GeForce 4 using GPUs comparing to the CPU computation (Harris et al. 2002). Shallow water wave simulation implementation on GPU has reported on speedup approximately 15x to 30x to compare with CPU (Hagen et al. 2005). Flood model based on diffusive wave scheme can be speeded by using GPU as 112x comparing with a CPU modeling (Lamb et al. 2009). GPUs coding into flood simulation remain in different study of scientific research (Neal et al. 2009; Liang et al. 2015; Kalyanapu et al. 2011). The implementing of traditional graphics machine has a limitation to transform an algorithm in a graphics procedure sets. The NVIDIA ® Corporation develops the Compute Unified Data Architecture (CUDA) to addresses the limitation. CUDA aims to convenience parallelization programming for engineering and scientific implementation.

This chapter is done by three objectives, to descript the detail of the RRI model as the Hydrologic model, to implement the VOXEL model for assisting the RRI model on input and output method, and

to present the model setup of the RRI model as parameter and GPU setup. The specific objective of the GPU setup is to show the acceleration of GPU performance on simple and complex terrain.

2.2 Hydrological model by Rainfall-Runoff-Inundation model

2.2.1 Rainfall-Runoff-Inundation model

Rainfall-runoff-inundation (RRI) model, which is a new developed model in a two dimension, was used for simulation in this study. **Figure 2-2** shows that the model is dealt with slopes and river channels separately. The river channel is located on the grid cell while the model assumes that both slope and river are positioned within the same grid cell. A channel is discretized as a single vector along its centerline of the overlying slope grid cell. The channel represents an extra flow path between grid cells lying over the actual river course. Lateral flows are simulated on slope cells on a two dimensional basis. Slope grid cells on the river channel have two water depths: one for the channel and the other for the slope (or floodplain). The inflow-outflow interaction between the slope and river is calculated based on different overflowing formulae depending on water-level and levee-height conditions. The flow rate equation in governing equation of the RRI model is mass balance equation based on continuity equation as equation (1). For unsteady flow, the momentum equation is included in the governing equation of the RRI model in x as equation (2) and y as equation (3) directions.

$$\frac{\partial h}{\partial t} + \frac{\delta q_x}{\delta x} + \frac{\partial q_y}{\partial y} = r - f \tag{1}$$

$$\frac{\partial q_x}{\partial t} + \frac{\partial u q_x}{\partial x} + \frac{\partial v q_x}{\partial y} = -gh\frac{\partial H}{\partial x} - \frac{\tau_x}{\rho_w} \tag{2}$$

$$\frac{\partial q_y}{\partial t} + \frac{\partial u q_y}{\partial x} + \frac{\partial v q_y}{\partial y} = -gh\frac{\partial H}{\partial y} - \frac{\tau_y}{\rho_w} \tag{3}$$

where h is the water height in local surface, t is the time step , q_x and q_y are discharge per unit width in x and y directions, r is rainfall intensity or lateral inflow, f is infiltration, H is the height of water from a datum, u and v are flow velocities in x and y directions, ρ_w is the density of water, g is gravitational acceleration, and τ_x and τ_y are shear stress in x and y directions. On the right hand side of Eq. (1) and (2), a second term is computed by using Manning's equation. The RRI model is used to apply diffusive wave routing for solving the two-dimensional equation by using the fifth-order Runge-Kutta method in numerical scheme. The water surface slope is estimated by using difference of water height from cell 1 to cell 2 based on combination between water depth and ground elevation as shown in **Figure 2-2**. The water surface slope of this model that show in **Figure 2-2**, is estimated by using difference of water height from cell 1 to cell 2 based on combination between water depth and ground elevation.
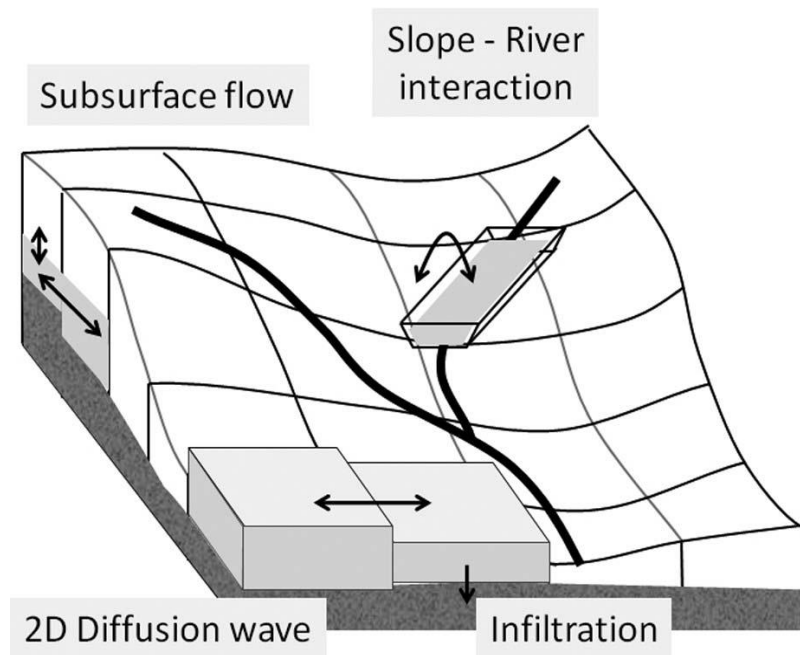
source: Sayama et al., 2012

Figure 2-2 RRI model schematic

2.2.2 Components of the RRI model programming

RRI model code on the FORTRAN based have contained with six modules, which, respectively, represent pre-processing, river routing, slope routing, interaction between river and slope, infiltration and output as indicated in **Figure 2-3**. The pre-processing including initial condition, rainfall, topography, land cover information and value of those hydrological parameters is firstly read into the machine memory. Then the water depth and forces are calculated that is distributed by the forces to downstream cell along the river line. After the river routing, the water depth and forces on the terrain is calculated by using the rainfall, which flow distribution on the terrain is based on the neighbor cell with eight directions (0d, 45d, 90d, 135d, 180d, 225d, 270d and 315d) (Jenson and Domangue 1988; Martz and Jong 1988; O'Callaghan and Mark 1984). The flow routing of both modules is implemented by using the Saint Venant equation based on the equation (1), (2) and (3). Next, the interaction of cell between river and terrain indicated that the water depth is recalculated for balancing the mass of water. After the flow have calculated on the terrain and river, infiltration processes is used to update the water depth by using the Green-Ampt parameter of soil based on the land cover types. Finally, the water depth, flow and infiltration data is written into the files on the hard drive, which this processes is run until the end of simulation time.

Based on the six components of the RRI model, that has counted a calling time as shown into **Figure 2-3** based on the percentage. The results of the RRI model profiling indicated that the most calling is the Slope subroutine, followed by the pre-processing, River, Infiltration, Output and River-Slope interaction. From the aim of this study, the RRI could reduce the simulation as possible. The results of

model profiling have indicated the slope subroutine that is called as 82.74% on the simulation because of many numbers of terrain pixels. Hence, reducing the simulation time of the RRI model is done by accelerating a computing time of the slope subroutine.

Input data sets are collected for containing to the RRI model and evaluating the simulation result which are four data types; rainfall data, topography, land cover/soil type and validation data by observation. **Figure 2-4** shows a methodology stream line of the collected data to RRI model and digital topography on pixel-based has be used for estimation of river cross section, using flow accumulate that is generated by flow direction.
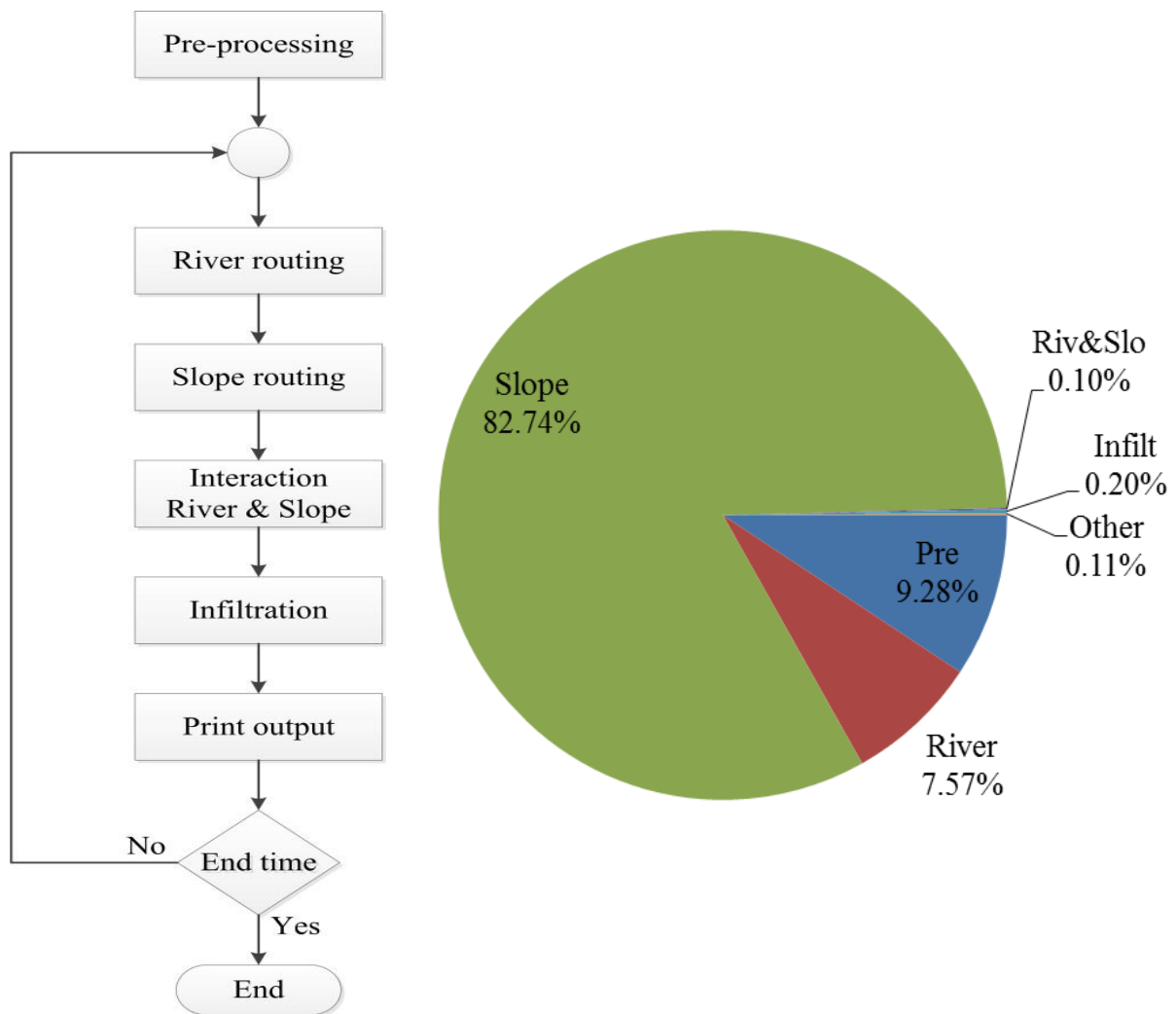
Figure 2-3 Component of the RRI coding
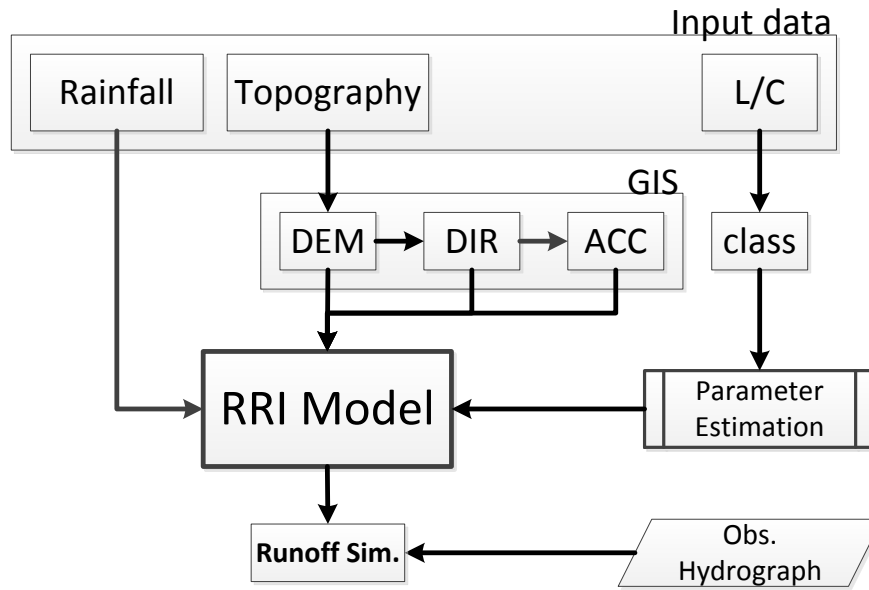
Figure 2-4 Input and output on the RRI model

2.3 VOXEL model assisted RRI model

2.3.1 VOXEL model

VOXEL is the word contracted with VOX (volume) and EL (element). The VOXEL model is based on the three dimensions space on the regular cell represented a value. For scientific analysis and visualization, this model is established on a 3D structure as shown in **Figure 2-5**. The coordinate of the cell is referred with a corner of first cell and resolution of a cell. On this study, the VOXEL model is applied to collect the data as integrating the data based on the layer for the watershed data. Rainfall data is the four dimensions data, for it established on the VOXEL model with the 3D structures each cell value is the precipitation data of the spatial and time series.
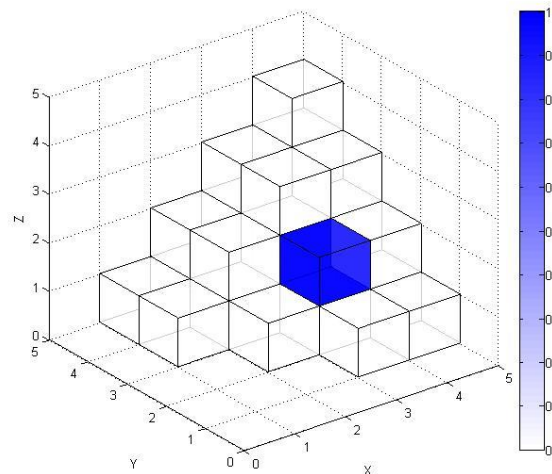
Figure 2-5 VOXEL model conceptual

2.3.2 Application for the RRI model

Hydrological modelling for flood simulation has three important components as topography data, land cover and precipitation based on the RRI model. The components are included in the VOXEL model that is the objective of this study. Methodology as shown in **Figure 2-6** is to collect the component of the RRI model. Next, the collected data are projected and resampled as same as information of geometric. After the data is reprocessed, the VOXEL model is applied to store the dataset. The dataset have two VOXEL models set, watershed and precipitation. The VOXEL modelling of watershed are included by five layers, digital terrain, flow direction, flow accumulation, land cover, and soil type, covering the river basin area. The precipitation has 2 characteristics, spatial and temporal, as same as 4 dimensions valuable which is represented by the VOXEL model to apply in the RRI model. The both datasets is input to the RRI model, the model results two datasets such as runoff and inundation depth in each temporal scale. The modeled results as conceptual (**Figure 2-7**) are also included in the VOXEL model due to it convenient to use for presenting and analyzing.
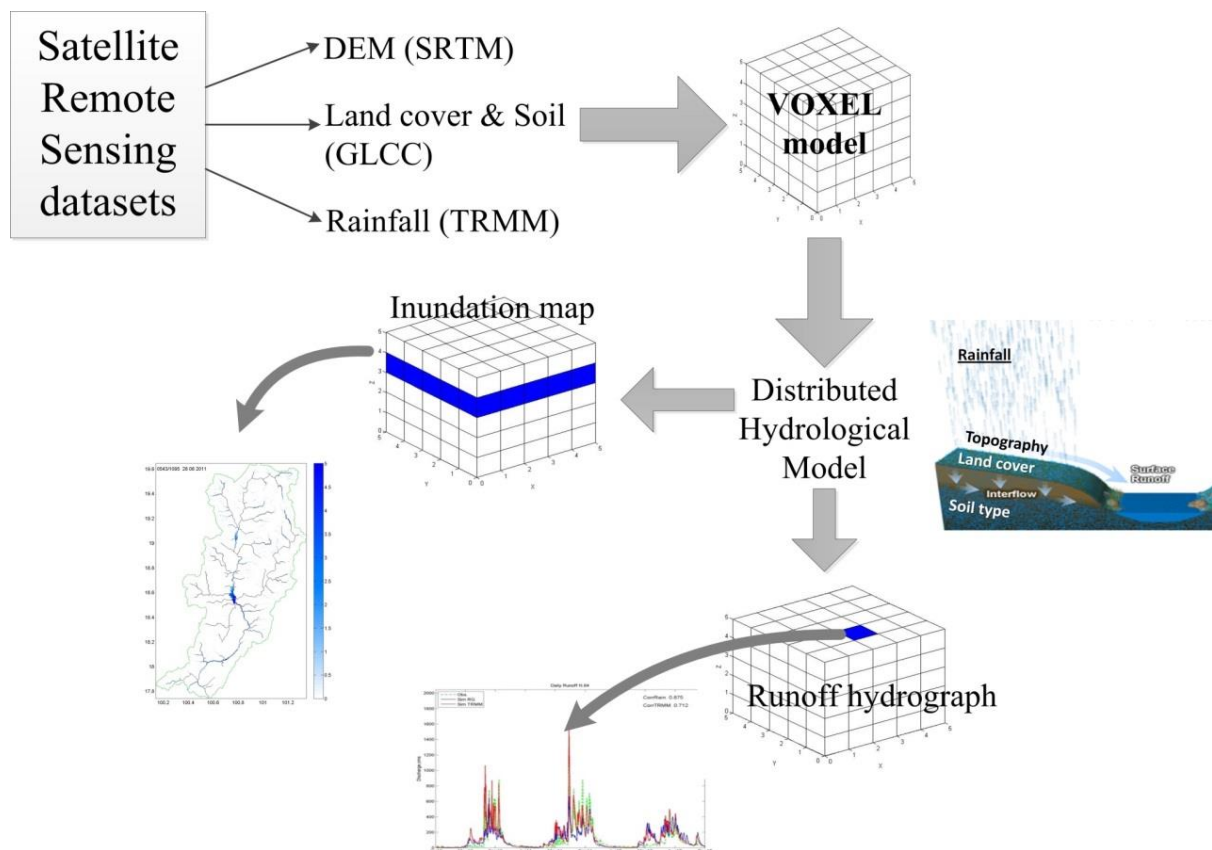
Figure 2-6 Stream line concept of this study
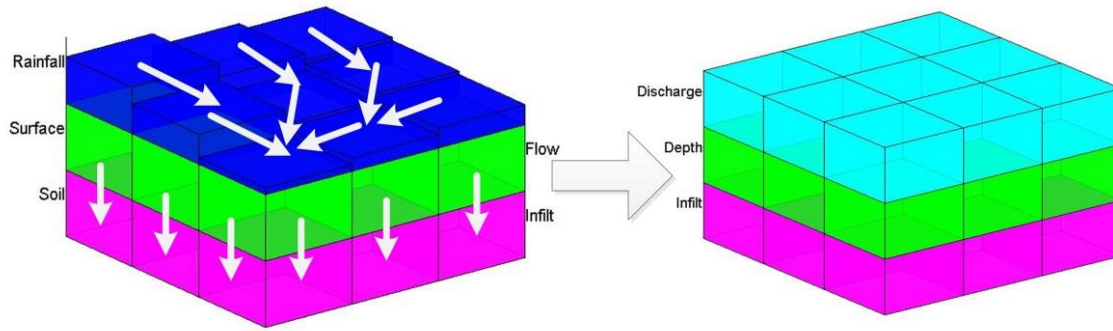
Figure 2-7 Flow modeling based on VOXEL model in the RRI model

2.4 Model setup

2.4.1 Setup model

Input data sets of the RRI model are four data types; rainfall data, topography (see **Figure 2-8a**), land cover (see **Figure 2-8c)** and soil type (see **Figure 2-8d**). On the definition of the distributed hydrologic model with the RRI model, the used hydrologic parameters in this study are recommended by previous study such as Chow et al, 1964, Sayama et al, 2010, Anurak et al, 2013, and Pakosung and Takagi, 2015. Those parameters have been based on calibration in previous RRI modeling studies. According to the mathematics modeling of the RRI model, flow routing is based on the Manning's roughness that correlates with the land cover type. **Table 2-1** show the Manning's roughness of the land covers type. According to the hydrological soil type parameters represented by the Green-Amp parameter of soil is shown in **Table 2-2**. The hydrologic parameters as shown in the tables were utilized to simulate on the RRI model for different scenario.

For the characteristic of river channel, the resampled DEM was used for generating a flow direction to identify with 8 directions (0d, 45d, 90d, 135d, 180d, 225d, 270d and 315d) depended on a differential of the downstream elevation pixel. The flow direction was used for counting numbers of the upstream pixels to identify a flow accumulate value to a specific pixel. In this study, the flow accumulation was used for estimation width and depth of the river channel followed as equation (4) and (5) by Sayama et al., 2012.

$$W = 16.93 \cdot A_{ba\sin}^{0.186} \tag{4}$$

$$D = 16.93 \cdot A_{ba\sin}^{0.120} \tag{5}$$

where W is the channel width in meter, $A_{ba\sin}$ is the catchment area in square kilometer, and D is the channel depth in meter.

The June 2011 storm events were implemented that are used to run the RRI model over the basin as a demonstration. In addition to Tropical storm and Thunderstorm, causing of a huge rainfall obtains from the storm that are originates from Pacific Ocean to travel westward cross this area in June to August. From 24th to 30th June 2011, tropical storm the Haima hit the northern part Thailand to bring precipitation as 200 mm in the upstream of study area over two days. The rainfall on the 2011 is implemented over the basin with the temporal scale. The ground rainfall observation product was collected from the Royal Irrigation Department (RID), Thailand. There are 28 stations as shown in **Figure 2-8b**, of which 17 stations are located in the watershed while 11 stations are located on the west side. The 28 stations were used to construct the rainfall spatial distribution by using kriging algorithms. The semi-variogram model of the kriging method is based on the spherical semi-variogram equation, that the geostatistical theoretical can be referred to the previous studies (Chiles and Definer, 1999; Webster and Oliver, 2007; Ly et al., 2011). The parameter of the spherical semi-variogram, the nugget variance (C_0) is 0.425, the partial sill (C) is 1.404 and the range (a) is 0.545 degree, are analyzed from the observed rain gauges and applied for interpolating to grid spatial rainfall.

Table 2-1 Land cover parameter represented by the n manning coefficient

Land cover type	n manning
Forest	0.50
Deforestation	0.40
Grasslands	0.30
Cropland	0.35
Urban and Build-up	0.05
Water bodies	0.04

Table 2-2 Soil type parameter represented by the Green-Amp coefficient

Soil textural	Soil depth, m	Saturated hydraulic conductivity (ka), cm/h	Green-Ampt parameter		
			Ksv, cm/h	Porosity	Capillary head, cm
Clay	1.0	0.462	0.06	0.475	31.63
Clay loam	1.0	0.882	0.20	0.464	20.88
Loam	1.0	2.500	1.32	0.463	8.89
Sandy clay	2.0	0.781	0.12	0.430	23.90
Sandy clay loam	1.5	2.272	0.30	0.398	21.85
Sandy loam	1.5	12.443	2.18	0.453	11.01
Silty clay	1.0	0.366	0.10	0.430	29.22
Silty loam	1.0	2.591	0.68	0.501	16.68
Stone	1.5	-	-	-	-

2.4.2 Performance statistical

The estimation results were evaluated to analysis bias of volume (V_{bias}), bias of peak (P_{bias}), root mean square error ($RMSE$), square of the Pearson correlation coefficient (R^2), and mean error (ME). The following formulas (see **Table 2-3**) were applied to evaluate simulation performance. The volume bias and peak bias estimate the systematic bias of simulated runoff in percentage (%). The correlation index is quantification in correlation of two data sets, simulated and observed runoff, which 0 is no correlation while 1 is perfect correlation. The RMSE is a different measure of difference magnitude between two datasets, while the ME is the bias from two data sets.

Table 2-3 Description of performance statistical

Statistical index	Description
Volume bias (%)	$V_{bias} = \dfrac{|Q_{vo} - Q_{vs}|}{Q_{vo}} \times 100$
Peak bias (%)	$P_{bias} = \dfrac{|Q_{po} - Q_{ps}|}{Q_{po}} \times 100$
Root mean square	$RMSE = \sqrt{\dfrac{\sum_{i=1}^{n}(Q_{o(i)} - Q_{s(i)})^2}{n}}$
Correlation	$R^2 = \dfrac{\sum_{i=1}^{n}((Q_{o(i)} - \overline{Q_o}) \cdot (Q_{s(i)} - \overline{Q_s}))}{\sqrt{\sum_{i=1}^{n}(Q_{o(i)} - \overline{Q_o})^2 \cdot \sum_{i=1}^{n}(Q_{s(i)} - \overline{Q_s})^2}}$
Mean bias	$ME = \dfrac{\sum_{i=1}^{n}(Q_{o(i)} - Q_{s(i)})}{n}$

where

Q_{vo} is observation volume

Q_{vs} is simulation volume

Q_{po} is observation peak

Q_{ps} is simulation peak

Q_o is observation data

Q_s is simulation data

n is total number of sample

a) Topography

b) Rain gauge and Runoff sta.

c) Land cover type

d) Soil textural

Figure 2-8 Watershed datasets in the study area

2.4.3 GPU applied on the RRI model

RRI model is encoded as following the CPU approach in FORTRAN programming language on the GPU framework using NVIDIA's CUDA. **Figure 2-9** presents the stream flow in the GPU framework with their implementation (Ruetsch and Fatica, 2011). CUDA programming is proposed that processing control system have initialized from the CPU. The input processing control coding and datasets are transferred to the GPU though the RAM on the CPU. In the GPU environment, the data sets and coding is located on the global memory of the graphic card. Kernels on CUDA function are called that generate a large amount of threads for parallelism computation. The domain data set is divided into the block groups of grid that are sets of computational elements. The computation of GPU cores is controlled by the blocks that assigns to threads. For computation and storage in each block, the data sets are allocated by using a shared memory.

The water depth and discharge values are computed by the Saint-Venant equation, (1), (2) and (3), on the terrain using the slope subroutine of the RRI model implemented by the GPU. **Figure 2-10** indicates the slope subroutine of RRI model on CUDA code contained by five components. The components are represented by input, neighbor cell searching, water depth and flow estimating, check error and output. First, the input data containing initial condition, values of those hydrological parameters, rainfall, topography, and land cover information is read and transferred though the RAM (host memory) onto the memory of the GPU device (global memory). Then, blocks and threads are setup by using the cell domain index of the terrain, which the water depth and flow of terrain call index are calculated by groups of GPU cores as parallel computation. Next, the computed data are transferred back to the RAM (host memory), and the error of computation are evaluated on the CPU. The data is written onto the files, when the error is smaller than an allowable value.

In this study, GPUs are done by solving the continuity and momentum equation with the CUDA coding. The multi-core simulation of GPU-RRI model compared with the CPU based to reveal its performance. The implementation of the GPU-RRI model tests on the NVIDIA graphics cards, GeForce 780 Ti. The former, a low-end card, consider the impact of GPUs on the model performance. **Table 2-4** presents the characteristics of the GPU application; the computer uses the Window7 64-bit operating system with PGI workstation for the simulation.

Table 2-4 configuration of the machine

Info	Computation machine
CPU Frequency	2.67 GHz
RAM	4 GB
NVIDIA Graphics Card	GeForce GTX 780 Ti
GPU Frequency	875 MHz
GPU Ram	3 GB
CUDA Cores	512

The computational of RRI model accelerated by using GPU comparing with CPU is investigated for two cases. First, the speedup of GPU from CPU is considered on a simple terrain that contains a single value of land cover type and uniform rainfall. Resampling from a high to low resolution of terrain and vary a temporal scale is implemented in this case. Second, the complex terrain as a natural topography is investigated on the model speedup with a different spatial resolution, 500 m and 1000 m, at the same temporal condition. The model speedup is estimated as the ratio of simulation times from CPU and GPU. The equation is written as:

$$SpeedUp = \frac{CPU\ time}{GPU\ time} \tag{6}$$
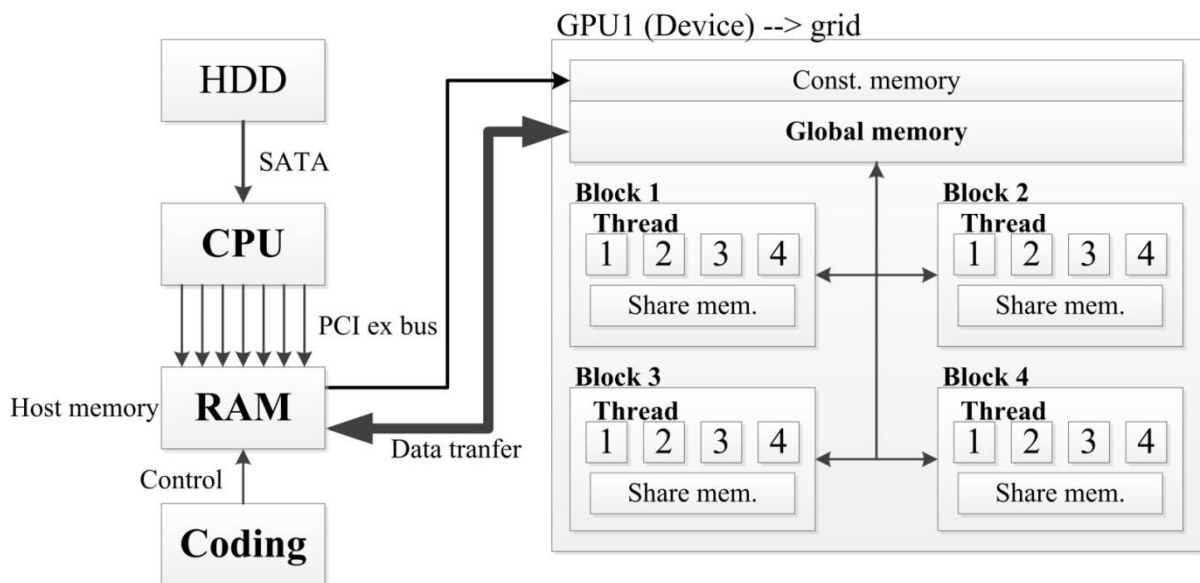
Figure 2-9 Data transfer between CPU and GPU
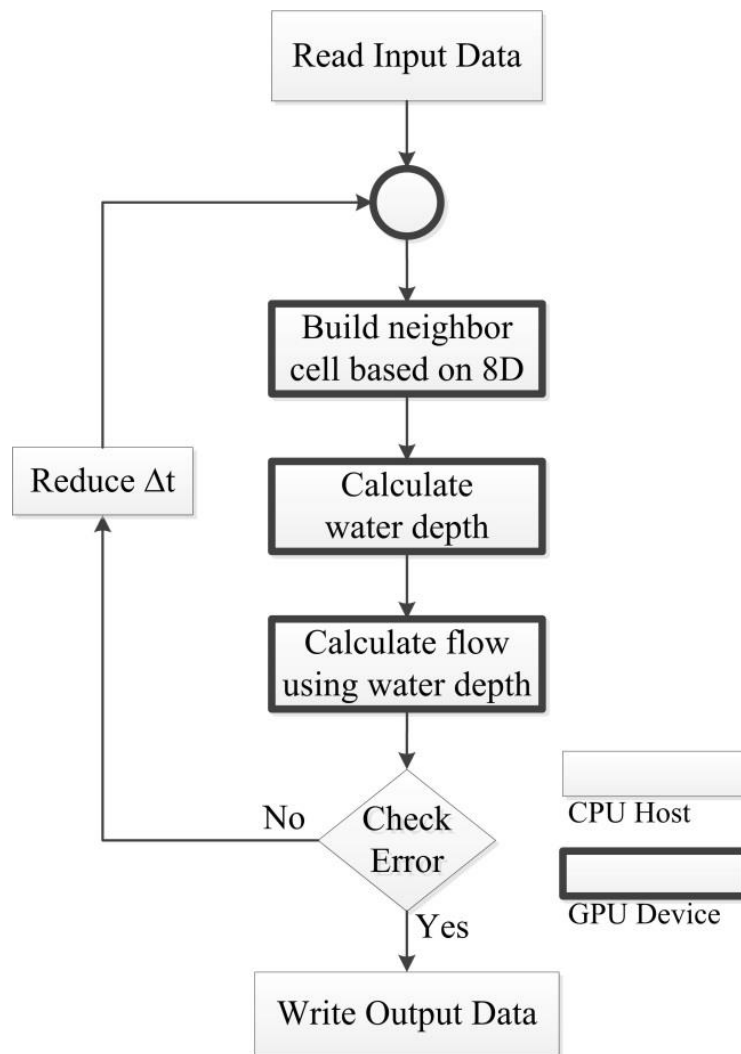
Figure 2-10 RRI model on the slope routing conceptual

2.5 Simulation results

2.5.1 VOXEL model of watershed and rainfall data for the RRI model

VOXEL model was applied on integrating of input data, watershed and rainfall, for the RRI model to simulate flood investigation, and also its results on a runoff and inundation depth. The VOXEL model of watershed is presented in **Figure 2-11** that was combined with five layer, DEM, flow direction, flow accumulation, land cover and soil type. The spatial and temporal of rainfall were input on the VOXEL model as shown in **Figure 2-12**.
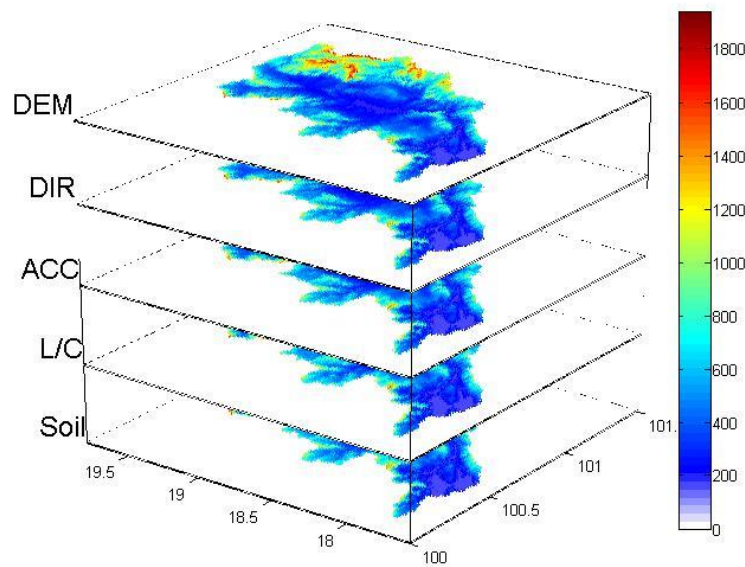
Figure 2-11 VOXEL model of the watershed area
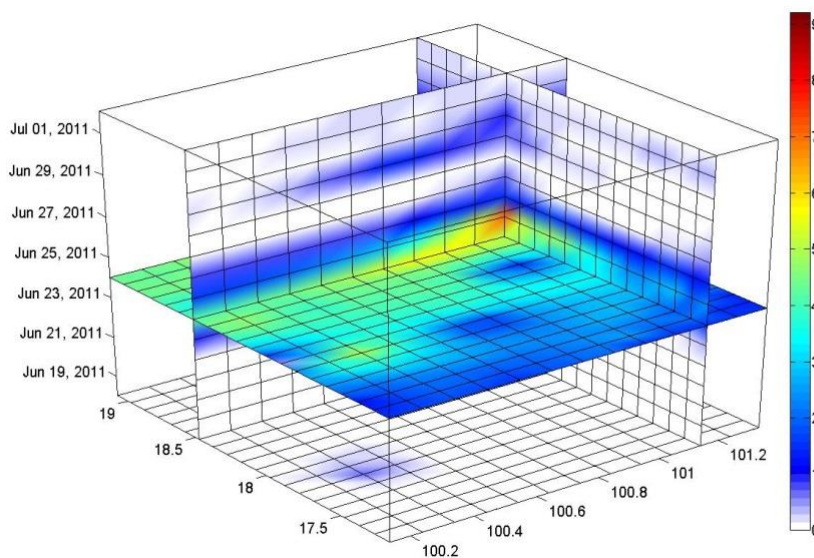
Figure 2-12 VOXEL model of the rainfall data

2.5.2 Simulated runoff and inundation

Input dataset were simulated by the RRI model that the results of the flood simulation were analyzed as spatial runoff and inundation depth every temporal scale. **Figure 2-13** have shown the VOXEL model of the daily runoff. Accuracy of the RRI model on was assessed on simulating in the Nan river basin. The model was driven for 2011 rainfall events that scenario case was estimated at daily on a temporal scale to match the Royal Irrigation Department Thailand observed streamflow data. Three runoff stations were selected in the Nan river basin (see **Figure 2-8b**), the first one belonging to the upstream sub-catchment (N.64), the second one belonging to the middle area (N.1) and the third one belonging to the downstream area (N.13A), to show the daily hydrograph that results from the different scenario. **Figure 2-14** present the hydrographs for storm event of respectively runoff station N64, N.1 and N.13A.
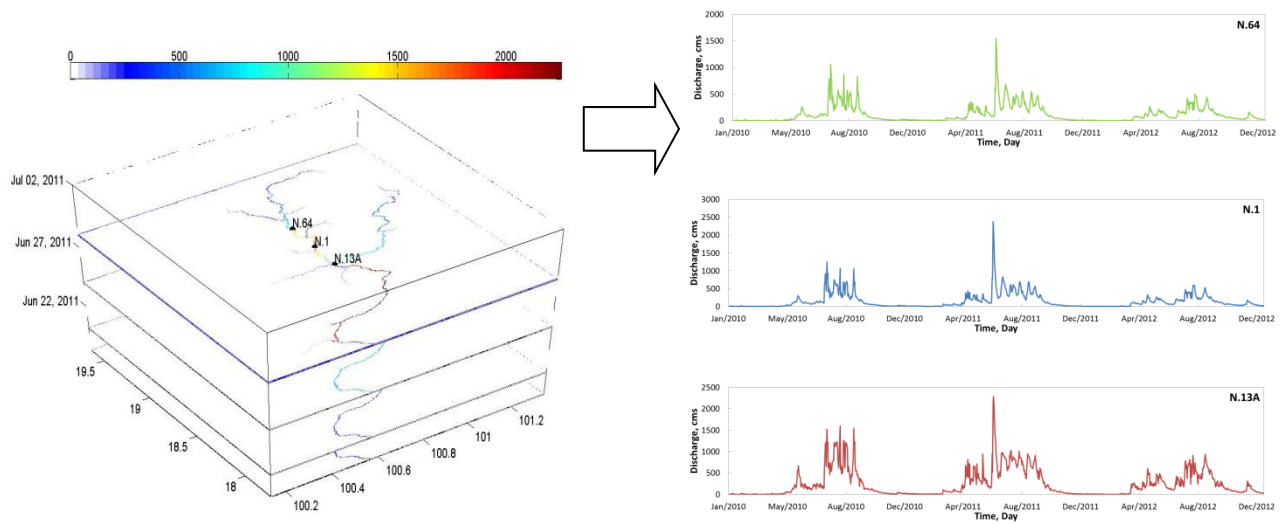
Figure 2-13 VOXEL model of the modeled time series runoff

Over all of the runoff station, the simulation captured the peak at the same time with the observation. The three runoff station on the daily hydrograph were analyzed and calculated for evaluation by the performance statistical. The results are given in **Table 2-5** that is concluded by five indexes. The N.64 simulated discharge best matched the observed runoff with the highest R^2 of 0.906 and lowest RMSE of 67.07 cms. This simulated runoff overestimated the runoff volume, peak flow and mean runoff by 3.09%, 8.16% and 4.46 cms, respectively. The N.1 simulated runoff was lowest R^2 and low RMSE, however, its simulated runoff was the lowest difference of Volume bias of 2.13% and Mean bias of -4.09%. The peak flow of N.1 overestimated about 39.3%. The N.13A significantly underestimated the runoff volume about -30%, peak and mean runoff (-35% and -131 cms), with high RMSE and low correlation value (288 cms and 0.87).

The N.13A had more error in RMSE which responded to a residual between observed and simulated data, because 3 branches junction (Wa River, Sa River and Nan River) are located around this station. For up scaling of a pixel size, the rough resolution about 1 km was used for modelling, so the 3 tributary junctions were grouped into the pixel of the N.13A. This problem can be solved by a high resolution of geography represented by DEMs data, will be applied in a future work.

The VOXEL model of inundation depth based on the spatial and temporal were illustrated in **Figure 2-15**. The simulated inundation map was presented in **Figure 2-16** that modeling was a good performance to compare with the observed inundation map from the satellite (MODIS).

Table 2-5 performance statistical measurements of the GPU RRI model

Runoff station	$\%V_{bias}$	$\%P_{bias}$	RMSE, cms	Correlation	ME, cms
N.64	3.09	8.16	67.07	0.906	4.46
N.1	-2.13	39.14	123.05	0.854	-4.09
N.13A	-29.96	-35.84	288.31	0.874	-131.04

a) N.64

b) N.1

c) N.13A
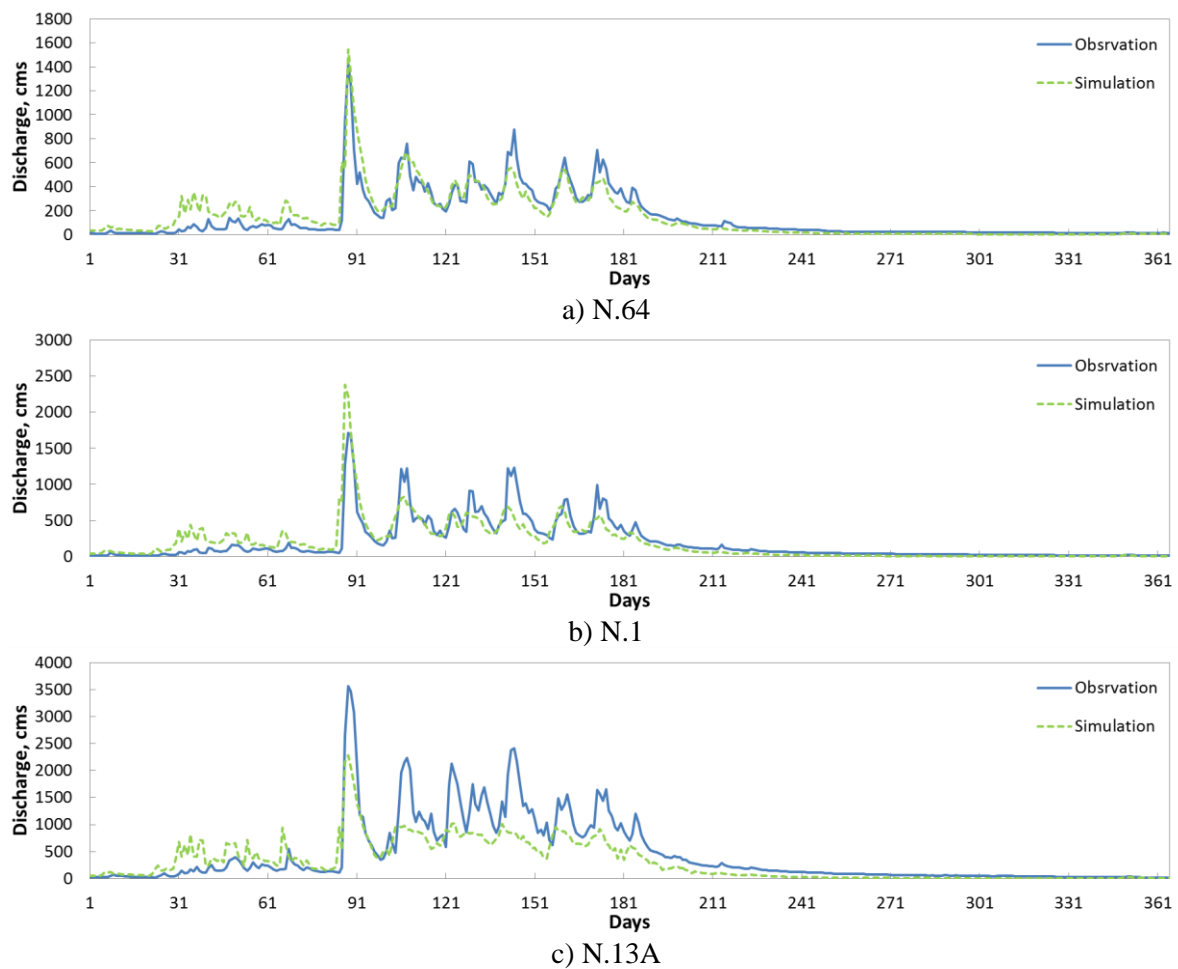
Figure 2-14 Observation and simulation of daily runoff
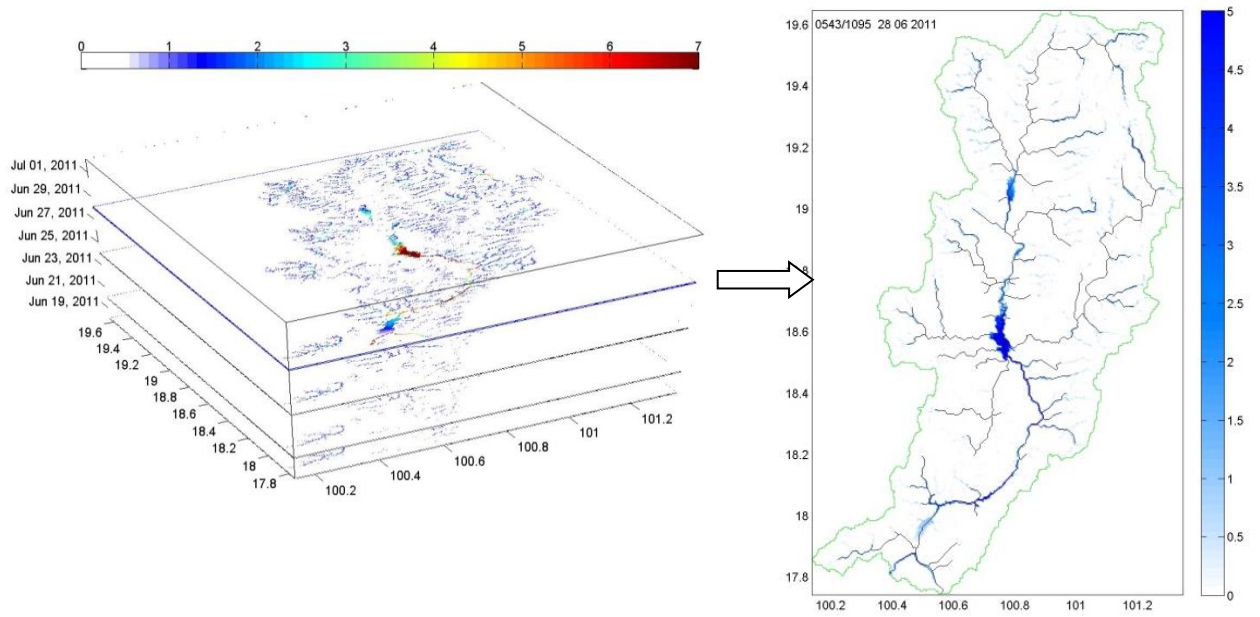
Figure 2-15 VOXEL model of the simulated time series inundation map

a) Satellite flood map (MODIS)   b) Simulated flood map
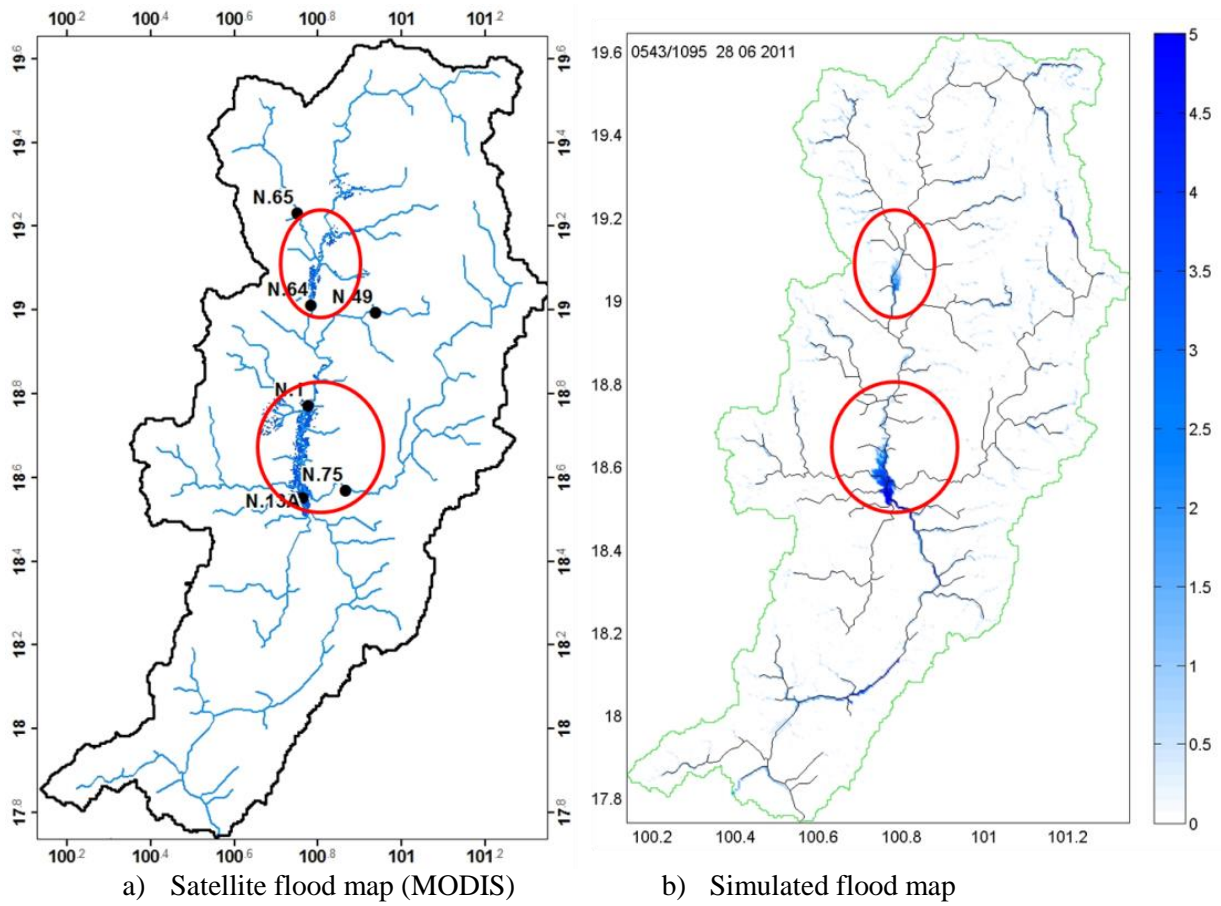
Figure 2-16 Comparison between Simulated and Observed inundation map

2.5.3 Speedup of the GPU-RRI model

Simple terrain is used to present a performance of GPU machine based on the single slope, uniform distribution of rainfall and one land cover types. In this case, we want to reveal the performance of the GPU based on the effect of resolution on the terrain and temporal scale at the same environment condition. The terrain in different spatial resolution is shown in **Table 2-6** that is contained with single slope of 0.0005 m/m. The different resolution (from 30 m to 1000 m) is a rectangular area about 12 x 12 km. During all of simple terrain case, a constant value of the Manning's coefficient ($n = 0.05$) and uniform rainfall (10 mm/day) is assumes for the whole simulation. The simulation time assessment is presented in **Table 2-7** that different temporal scale has varied from 15 days to 365 days. The computer configuration on the **Table 2-4** is used to investigate the GPU performance on 49 cases of the simple terrain.

Table 2-6 Simple terrain information for simulation

Resolution size, m	Pixel Number	Dimension, pixel x pixel
30	129,600	360 x 360
60	32,400	180 x 180
90	14,400	120 x 120
125	8,100	90 x 90
250	2,304	48 x 48
500	576	24 x 24
1000	144	12 x 12

Table 2-7 Simulation time for assessment a GPU performance

Temporal scale		Time step
Days	hour	
15	360	2,160
30	720	4,320
60	1,440	8,640
90	2,160	12,960
180	4,320	25,920
270	6,840	38,880
365	8,760	52,560

Simple terrain was driven on the RRI model by using two options of computational machine, CPU and GPU. The simple terrain is the rectangular area of 12 x 12 km that contained the single value of terrain slope and the Manning's coefficient. The rainfall on temporal scale was generated on the uniform pattern. This case used the different of spatial and time scale to reveal effect of the GPU application. The different spatial was that the rectangular area was divided by using size of pixel. The size of pixel was varied from 30 m to 1,000 m represented by number of pixel about 129,600 to 144 pixels. The time scale was a varying of 2,160 to 52,560 time steps, which was about 600 seconds on iteration of simulation.

CPU simulated tests was the firstly base run, which the RRI model was driven on the machine on the **Table 2-4** without the GPU. **Figure 2-17** indicated the CPU runtime on the simple terrain. The computed time of CPU with 144 pixels was minimum, while 129,600 pixels was maximum, evaluating on the spatial scale. On the iteration scale, the 2,160 time steps was minimum and the 52,560 time steps was maximum for CPU computed time. Overall on the 49 summations of the simple terrain case, maximum time used to run was presented by the 129,600 pixels with 52,560 time steps about 41,783 seconds (11.6 h). The minimum simulation runtime of all was presented by the 144 pixels with 2,160 time steps about 12.1 seconds.

GPU application based on the NVIDIA's CUDA coding was programmed on the RRI model. The case of the simple terrain was run by the RRI-GPU model at the same environment of computer machine. **Figure 2-18** presented that GPU runtime was presented on the different of the spatial and iteration scale. On the pixel number scale, the minimum was the 144 pixels with 29.6 seconds of run time that was greater than the CPU testing. By contrast, the maximum run time on this scale was 357.6 seconds with the 129,600 pixels, but its run time was little than the CPU testing. The maximum and minimum on the iteration scale of the GPU test was similar to the CPU testing, but it had the difference on run time as same as the spatial scale evaluation. Overall on the 49 summations of the simple terrain case on this GPU testing, maximum time used to run was presented by the 129,600 pixels with 52,560 time steps about 9,504.8 seconds (2.64 h) that was smaller than the CPU testing. By contrast, the minimum simulation runtime of all was presented by the 144 pixels with 2,160 time steps about 29.6 seconds to be greater than the CPU case.

Speedup times represented by the GPU performance was analyzed by using the equation (6), of which the CPU time was based on the **Figure 2-17** and the GPU time was based on the **Figure 2-18**. **Figure 2-19** revealed the speedup of the GPU performance from the 49 simulation cases. The performance ratio varied from 0.4 to 4.4 on the overall results. On the spatial evaluation, amount of pixel at 144 pixels presented the minimum ratio and at 129,600 pixels showed the maximum ratio. The number of pixel had effect with the performance of the GPU, which during range 144 to 2,340 pixels the ratio was little than 1.0 and range 2,304 to 129,600 pixels the ratio was greater than 1.0. By the contrast on the iteration scale, the ratio value stilled with constant number in each spatial case on the difference of the iteration time steps. According to the ratio value was little than 1.0, which the CPU had a performance better than the GPU. However, the value greater than 1.0 revealed that the GPU had performance greater than the CPU. **Figure 2-20** presented the performance zone between the CPU and GPU. Based on the speedup ratio, that affected with only the number of pixel, which optimum boundary between the CPU and GPU divided by value about 2,304 pixels. Then, the implementation of CPU have limited at the number of pixel little than the 2,304 pixels, while GPU was recommended on a better performance with higher of the 2,304 pixels.
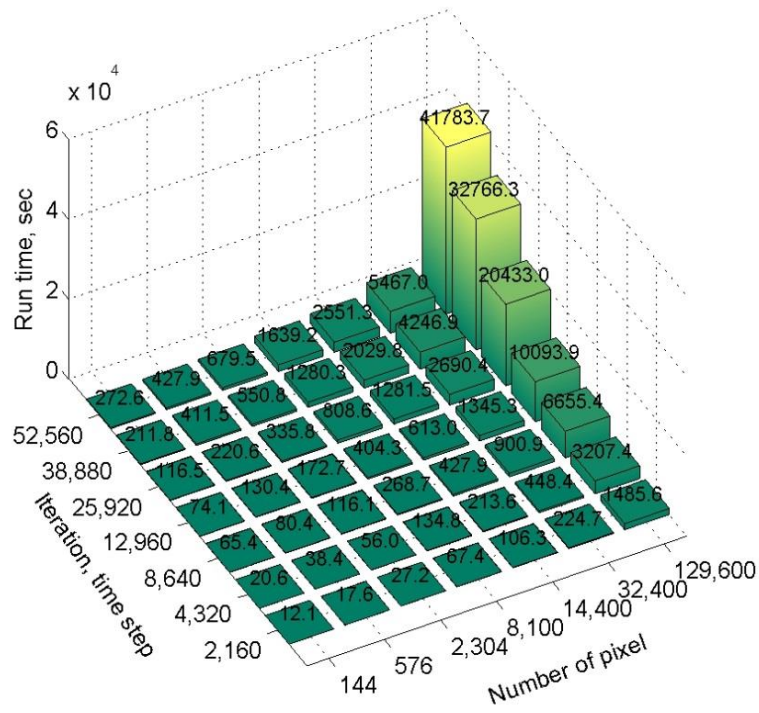
Figure 2-17 CPU runtime
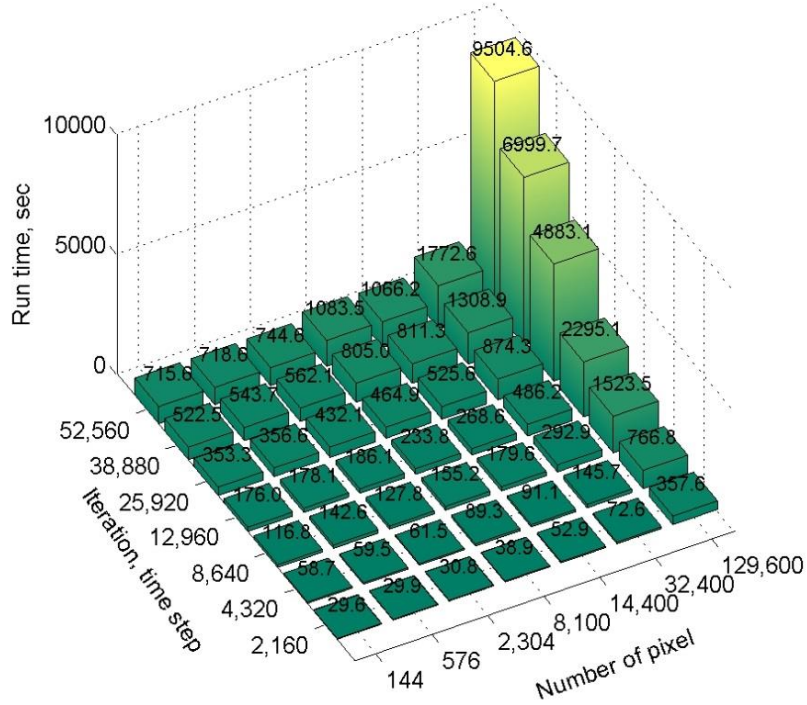
Figure 2-18 GPU runtime
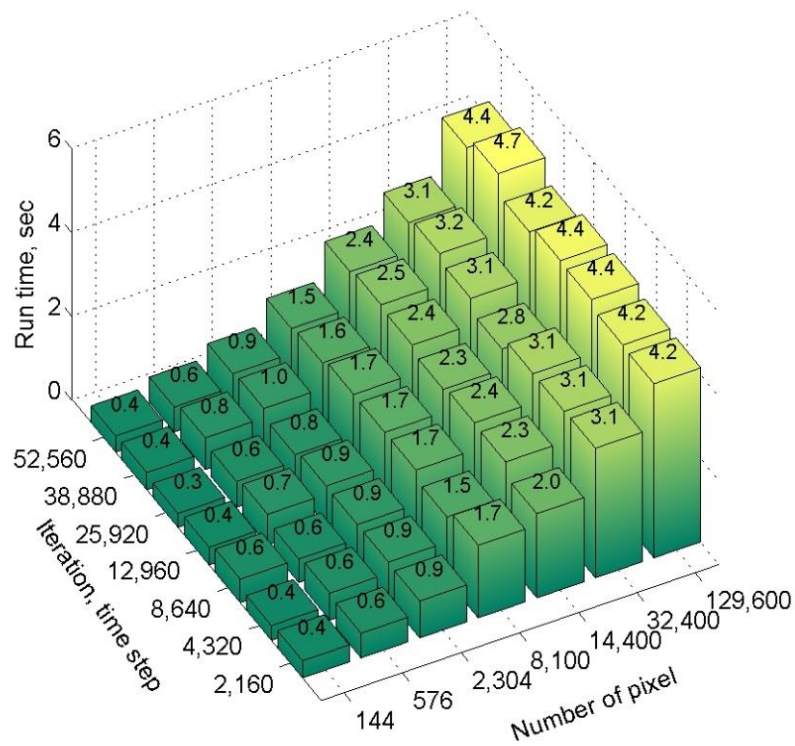
Figure 2-19 Speedup of the GPU machine
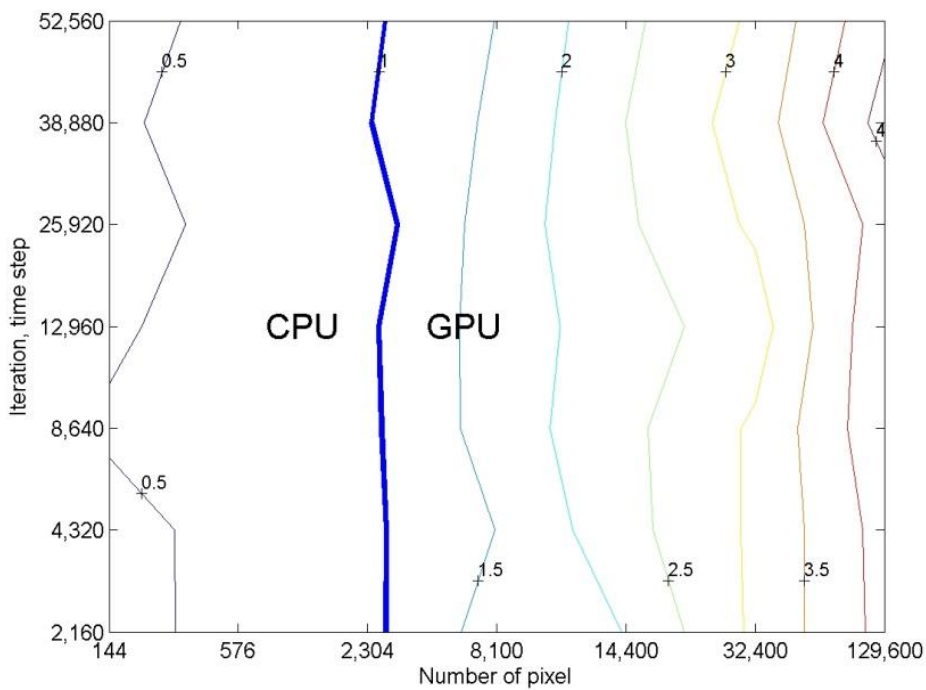
Figure2-20 Identification optimization zone between CPU and GPU

Topography of the Nan river basin in Thailand used in simulation on above, that was represented on complex terrain. GPU was evaluated on this terrain by using two scenarios that was divided on the pixel size. The pixel size was about 500 m, containing 64,998 pixels, while 1,000 m contained pixel about 16,275 cells. The both scenarios were firstly run by using the CPU machine for the base case. Then, the GPU machine was driven on the both scenarios for assessing the speedup on the complex terrain.

Table 2-8 presented the performance of RRI-GPU model based on the complex terrain as natural topography on the watershed area. The RRI-GPU model performed a speedup about 2.6x to compare with the CPU machine as same as environmental parameter. For pixel size about 1,000 m, the CPU run time was about 1.04 h and the GPU time was 22.7 minutes. The run time of the 500 m case (64,998 pixels) was greater than the first about 650% at the similar speedup of GPU machine.

Table 2-9 presents the difference between GPU speedup from CPU and the other implementation reported in the recent studies. The results are only relative as model scheme, while the other components are different such as hardware, flood events, input data, and computational domains. The potential acceleration of parallelization approach is presented for the flood models. Their results have provided the excellent speedup. This is suggestion of GPU implementation to be a necessary tool for mathematics model speedup. The GPU implementation will be developed by the new technology such as a new hardware and high-level programming.

The speedup results of this study have contrasted with other studies because of the limitation of RRI model. The model has contained with two main components as Rainfall-Runoff processes and a Runoff-Inundation process that is not only flood processes. On the GPU implementation, the 2D array of fourteen variables is transferred from RAM to Global memory of GPU and the GPU card is the low-end hardware contained by the low capacity of RAM card. This is the reason of the RRI-GPU model that has gotten the low speed up on the GPU implementation.

Table 2-8 Simulation time of CPU and GPU on a study area

Number of pixel	Simulation time, sec		Speed up
	CPU	GPU	
16,275	3,766.195	1,365.804	2.75x
64,998	23,880.120	9,340.920	2.55x
Speed up	6.34x	6.83x	

Table 2-9 Comparative summary of recent model speeds in the literature

Processor info	Processor cores	Model name	Approximation	Parallelization method	Domain size (pixels)	Max speeds	Reference
NVIDIA GeForce 8800GTX	122	JFLOW	2D Diffusive wave	DirectX 9	96k	114x	Lamb et al., 2009
NVIDIA GeForce 8400GS	16	Flood2D	2D Dynamic wave	CUDA	1.05M	3.5x	Kalyanapu et al., 2011
NVIDIA Tesla C1060	240	Flood2D	2D Dynamic wave	CUDA	1.05M	88x	Kalyanapu et al., 2011
NVIDIA GeForce GTX780Ti	512	RRI	2D Diffusive wave	CUDA	130k	4.4x	This study (Simple topo.)
NVIDIA GeForce GTX780Ti	512	RRI	2D Diffusive wave	CUDA	65k	2.6x	This study (Complex topo.)

2.6 Conclusion

In this chapter, the hydrologic modeling was introduced for flood event that used the RRI model for simulating the runoff. For integrating component of flood model based on its mechanism with topography, rainfall, and land cover, the VOXEL model was used to collect the data set. In acceleration of the RRI model, GPUs was applied on the CUDA coding that implemented on the natural and simple terrain, including comparison with other researches.

On the first, simulation results compared to observed discharge. The VOXEL model of the daily runoff was implemented into the RRI model results. Accuracy of the RRI model on was assessed on simulating in the Nan river basin. The model was driven for 2011 rainfall events that case was estimated at daily on a temporal scale to match the observed streamflow data. Three runoff stations were selected in the Nan river basin. Over all of the runoff station, the simulation captured the peak at the same time with the observation. The three runoff station on the daily hydrograph were analyzed and calculated for evaluation by the performance statistical by five indexes. The N.64 and N.1 simulated discharge the best matched the observed runoff; its runoff overestimated the runoff volume, peak flow and mean runoff. The N.13A significantly underestimated the runoff volume, peak and mean runoff, with high RMSE and low correlation value. This part has presented a task for application of VOXEL model on the RRI model. The VOXEL model application has convenient to present and input to the numerical model.

RRI model applied by the GPU used NVIDIA's CUDA coding is presented as introduction. The RRI-GPU model is simulated and validated by using a simple terrain and natural terrain model in Thailand.

The computational have the advantage to use the GPU that outperform the CPU. This is presented in the two different scenarios. The RRI-GPU model is done by using the complex terrain to represent the implementation of natural effect. The natural river basin (the Nan river basin, Thailand) has tested on the two scenarios based on the resolution size (500 m and 1,000 m). The GPU speedup is about 2.6x, with high accuracy of the simulated runoff.

Second, the RRI model accelerated of using the parallel programming technology is shown with analysis speedups ranging between 1.5x to 4.4x compared to a CPU model computing the same mathematical scheme. For the simple terrain scenario, the RRI-GPU model executed on the NVIDIA GeForce GTX 780 Ti is done by simulating amount cell ranging between 144 to 129,600 pixels and iteration times between 2,160 to 52,560 time steps, contained with single slope, soil type and uniform rainfall. The GPU model have only affected with the spatial resolution scale, which the 2,304 pixels is a responding value of GPU performance.

Overall, the RRI-GPU model offer faster hydrological simulation on flood event results that are obtained from parallelization method implementing the diffusive wave routing. The next generation of GPU implementation in hydrological modeling has more potential development in high level computer language and new hardware technology.

Chapter 3 Bias correction of DEM sources and their effect on flood estimation.

3.1 Introduction

Digital Elevation Model (DEM) is regularly defined as being the key representing the terrain of the Earth to provided fundamental data of raised-relief map (Guth, 2006). DEM is an essential parameter to assess in any procedure using topography analysis, including its derived features (slope, curvature, roughness, drainage area and network, etc.). It has been used in scientific applications such as hydrological, geological, geomorphological, development, urban planning, and surveying (Pakoksung and Takagi, 2015; Lee et al., 2009; Weibel and Heller, 1990; Fraser et al., 2002). The accuracy of DEM affect to the result of the models.

DEM is established by using various techniques, for example, stereoscopic photogrammetry using air-borne or satellite-borne, interferometry of RADAR or SAR, laser scanning using airborne, conventional surveys. Each technique has a limitation depended on price, accuracy, sampling density, and preprocessing requirements. DEM generated procedure is normally about four steps such as data acquisition, grid spacing resampling, height interpolation, repeating, and accuracy assessment (Li et al., 2006). DEM's error is related by the resampling methods to grid spacing and interpolating techniques (Fisher and Tate, 2006). Errors on a spatial of DEM have been classified by gross errors based on data collection, systematic errors on stereo image with setting an elevation height values, and random errors from unknown error. There errors varying on a terrain are depended on topography conditions (Hebeler and Purves, 2009).

DEM's quality is affected by any factors such as sensor types, algorithm, terrain type, grid spacing, and characteristics, which is widely investigated on causes and consequences of errors. The free provided DEM, including GSI-DEM produced by the Geographical Survey Institute (GSI) of Japan (10 m only Japan), ASTER GDEM from METI of Japan and NASA of USA (30 m), SRTM provided by NIMA and NASA of USA (1 arc-seconds for USA and 3 arc-seconds for the other country),

---

. This chapter is based on:

1. K. Pakoksung, M. Takagi, 2015, DIGITAL ELEVATION MODELS ON ACCURACY VALIDATION AND BIAS CORRECTION IN VERTICAL: Modeling Earth Systems and Environment, 2(1), 1-13. DOI :10.1007/s40808-015-0069-3
2. K. Pakoksung, M. Takagi, 2016, Assessment and Comparison of Digital Elevation Model (DEM) Products in Varying Topographic, Land Cover Region and Its Attribute: *Journal of the Indian Society of Remote Sensing* (**submitted**).
3. K. Pakoksung, M. Takagi, 2015, Vertical Accuracy Validation of Digital Elevation Models (DEMs) in Shikoku Island, Japan, Asian Association on Remote Sensing 2015, Oct 2015, Manila, Philippines.
4. K. Pakoksung, M. Takagi, 2016, Effect of DEM sources on Distributed Hydrological Model outputs of Runoff and Inundation Area: (in **preparing**).

GMTED based on GTOPO30 (7.5 arc-seconds, 15 arc-seconds, and 30 arc-seconds), HydroSHEDS developed from the SRTM (3 arc-seconds, 15 arc-seconds, 30 arc-seconds, and 5 minutes), and GTOPO30 (30 arc-seconds) is the model of the terrain of the Earth in worldwide. For application modeling in global and local scale, the vertical accuracy of DEM on specific location is necessary requirement. Approach of DEM accuracy investigation on a specific location is assessed by using the reference point to examine the vertical accuracy that the field measurements use high precision equipment such as Global Positioning System (GPS) (Gonga-Saholiariliva et al., 2011; Jarvis et al., 2004; Kolecka and Kozak, 2013; Forkuor and Maathuis, 2012; Pakoksung and Takagi, 2015; Nikolakopoulos et al., 2006). This is also investigation of DEM accuracy in Japan especially in the Shikoku Island has a different terrain type.

Topography data is an important variable in analyzing runoff in physical hydrological modeling. DEM can be used to estimate morphologic attribute of river basin such as slope, drainage area, and river network that are also physical parameter in the distributed hydrological model (Pakoksung, K. and Takagi, M., 2015). Several studies have used DEM products in the distributed hydrologic modeling to generate runoff. Sayama et al. (2012) demonstrated that HydoSHEDS DEM performed a good agreement simulated by using the Rainfall-Runoff-Inundation (RRI) model to compare with an inundation map produced by MODIS satellite for large-scale area flood. Pakoksung and Takagi (2015) concluded that SRTM product was used to simulated runoff in the upper part of Nan river basin, Thailand. For flood simulated on the 2011 event in Sukothai province Thailand, the SRTM and HydroSHEDS DEM was used and its results was done for estimating damage cost (Anurak et al., 2013). Chintalapudi et al. (2014) used ASTER DEM to drive the distributed hydrologic simulation over the Guadalupe watershed in USA.

The main objective of this study evaluates the influence of using different DEM sources and resolution in distributed hydrological modeling (RRI model). Results of the analyses are the guideline of used in hydrologic modeling, and enhancement the accuracy of the water resources application data input. The specific aims of the present study are to assess six DEM products; and to assess how the DEM products effect to the runoff and inundation area. The study area is the Upper part of Nan river basin in Thailand.

The main objectives of this chapter are to assess accuracy of DEM data using observed referent elevation point, to investigate bias correction using transformation method, and to evaluate effect of DEM sources on runoff estimation using hydrologic model. The specific objective of accuracy assessment is done by revealing accuracy based on topography morphology and land cover classification, and presenting in overall, based on the statistical approach. For the bias correction, the geometrics linear transformation is implemented. From six candidate DEMs, GSI-DEM, ASTER

GDEM, SRTM, GMTED2010, HydroSHEDS, and GTOPO30, were used to present and evaluate the uncertainty of runoff estimation on the RRI model to simulate on flood event.

3.2 Data and Methodology

3.2.1 Digital Elevation Model sources and Reference elevation points

Open source DEMs are represented by the different contained accuracy and coverage were invested for this study as presented in **Table 3-1**, the 10 m-mesh DEM produced by the Geographical Survey Institute (GSI) of Japan (GSI-DEM), Advanced Spaceborne Thermal Emission and Reflection Radiometer-Global Digital Elevation Model version 2 (ASTER GDEM), the Consultative Group for International Agriculture Research Consortium for Spatial Information Shuttle Radar Topographic Mission version 4.1 (SRTM), Global Multi-resolution Terrain Elevation Data 2010 (GMTED2010), Hydrological data and maps based on Shuttle Elevation Derivatives at multiple Scales (HydroSHEDS) and Global 30Arc-Second Elevation (GTOPO30). **Figure 3-1** presented the DEM in the Shikoku Island Japan, and **Figure 3-2** showed the DEM in the Nan river basin Thailand.

The 10m-mesh DEM have been provided from GSI the Geographical Survey Institute (GSI) of Japan (GSI-DEM), with scales between 1:5,000 and 1:25,000 (Tachikawa et al., 2011). The GSI-DEM is based on digitized topographic maps and published for freely available only Japan region on 2008. The resolution of GSI-DEM is about 10 m that have a geography projection on Japan Geodetic Datum 2000 (JGD2000). This DEM contain absolute vertical accuracy about 5 m, and its data sets are in the Geographical Survey Institute of Japan, from 393 indexes were downloaded for the Shikoku Island.

The Advanced Space Borne Thermal Emission and Reflection Radiometer-Global Digital Elevation Model (ASTER GDEM) was established from two international agencies, the METI (Ministry of Economy, Trade, and Industry) of Japan and the NASA (National Aeronautics and Space Administration). The ASTER GDEM (ASTER, 2013) has firstly published on 29 June 2009 (ASTER GDEM Validation Team, 2012). This DEM is one arc-second resolution (approximately 30 m) with the World Geodetic System 1984 (WGS84). The DEM contains an absolute vertical accuracy about 20 m at 95% confidence level. The Data Pool at the NASA Land Processes Distributed Active Archive Center (LP DAAC) is one of the ASTER GDEM providers (ASTER GDEM2, 2013). For the Shikoku Island on the LP DAAC, an index number N32E132, N32E133, N33E132, N33E133, N33E134, N34E132, N34E133 and N34E134 were downloaded. The downloaded indexes for the Nan river basin are N17E100, N17E101, N18E100, N18E101, N19E100, and N18E101.

Shuttle Radar Topography Mission (SRTM) has freely provided by the U.S. Geological Survey (USGS), SRTM was originated from two international agencies, the National Imagery and Mapping Agency (NIMA) and the National Aeronautics and Space Administration (NASA). The SRTM is

established by using radar interferometry that the digital terrain is done by two radar images from a different point observed by the shuttle. The Endeavour shuttle observed the terrain of the Earth based on 3D during February 2000, using radar interferometry. Radar instrument observed from two components, dual Space Borne Imaging Radar (SIR-C) and dual X-band Synthetic Aperture Radar (X-SAR). The shuttle had observed the terrain data about 80% of the Earth, covering latitude 60 degrees north to 56 degrees south. The observed data established the digital elevation model (DEM) on 3 arc-seconds (about 90 m) that have provided for all location around the Earth. The provided DEM have contained a vertical accuracy about 16 m at 90% confidences and a horizontal accuracy about 20 m at 90% confidences (Jarvis et al., 2012). The SRTM product can be downloaded through the Consultative Group for International Agriculture Research Consortium for Spatial Information (CGIAR-CSI) database. For the Shikoku Island, an index number 6306 was collected. The index number 5709 was downloaded for the Nan river basin.

The Global Multi-resolution Terrain Elevation Data 2010 (GMTED2010) has been published by the U.S. Geological Survey (USGS) and the National Geospatial-Intelligence Agency (NGA). GMTED2010 was firstly provided on 2010 (Danielson and Gesch, 2011) that GTOPO30 at 30 arc-seconds data (GTOPO30) was reconstructed for a new digital global elevation model. The GMTED2010 was established 11 rasters by using the DEMs fusion technique. The product is divided as three different resolutions, 30 arc-seconds, 15 arc-seconds, and 7.5 arc-seconds to contain absolute vertical accuracy about 26-29 m represented by RMSE (Carabajal et al., 2011). For the Shikoku Island, an index number 30N120E of the GMTED2010 was downloaded. The index number of GMTED for the Nan river basin is N10E90.

Hydrological data and maps based on Shuttle Elevation Derivatives at multiple Scales (HydroSHEDS) is provided by the Conservation Science Program of World Wildlife Fund (WWF), in cooperating with the U.S. Geological Survey (USGS), the International Centre for Tropical Agriculture (CIAT), The Nature Conservancy (TNC), and the Center for Environmental Systems Research (CESR) of the University of Kassel, Germany. For this project, WWF by JohnsonDiversey, Inc provided the main funding. HydroSHEDS have provided hydrographical information in global-scale applications and offered a study of geo-referenced data with drainage directions, flow accumulations, distances, and river topology information. The HydroSHEDS is reconstructed from elevation data of the Shuttle Radar Topography Mission (SRTM) based on the 3 arc-second resolution that hydrologically conditioned is a main procedure to apply void-filling, filtering, stream burning, and upscaling techniques (USGS, 2008; Lehner, 2013). The objective of HydroSHEDS is to generate key data feature to assist regional and global watershed analyses. This product has available resolutions range from 3 arc-seconds (approx. 90 meters at the equator) to 5 minutes (approx. 10 km

at the equator). Its resolution about 15 arc-seconds (approx. 500 m) covering Asia region was downloaded for the Shikoku Island used to evaluate in this study.

Global 30Arc-Second Elevation (GTOPO30) is published from U.S. Geological Survey for free available on 1993 to represent a global digital elevation model (DEM) (USGS, 2008; Nawarathna et al., 2001). GTOPO30 are regularly resolution about 30 arc-seconds (approximately 1 kilometer). The GTOPO30 covers latitude 90 degrees south to 90 degrees north, and longitude from 180 degrees west to 180 degrees east. At the 30-arc seconds (0.008333 degrees), the GTOPO30 whole in the Earth results the dimensions of 21,600 rows and 43,200 columns. Its projection coordinate system is a WGS84 in latitude and longitude as decimal degrees. Its elevation vertical unit is based on meters above the mean sea level that range varies from -407 to 8,752 meters. Index number E100N40 was collected for the Shikoku Island and the Nan river basin.

The GPS-VRS have accuracy less than 2cm on observation. **Figure 3-3** presented the observed GCP data that are freely provided by the TAKAGI laboratory in Kochi University of Technology. These points are about 562 GCPs in the Shikoku Island, JAPAN. The attribute of the observed points is included by the information such as 3D coordinates (x, y, z), projection name, latitude and longitude with the geodetic datum, observed date, observation pictures and satellite images as ALOS PRISM/AVNIR2 (Uda and Takagi, 2010). These data can be downloaded at URL: http://www.infra.kochi-tech.ac.jp/takalab/Information/research/GCPDB/GCPDB.html.

Table 3-1 Information of the DEMs

DEMs	Data source	Generator and distribution	Release year	Resolution, m	Accuracy (stdev.), m	Coverage area
GSI-DEM	Topo- map	GSI	2008-	10	5	Japan
ASTER	ASTER	METI/NASA	2009-	30	7-14	83dN-83dS
SRTM	Space shuttle radar	NASA/USGS	2003-	90	10	60dN-60dS
GMTED2010	GTOPO30	USGS	2010-	225	29	60dN-60dS
HydroSHEDS	SRTM	WWF/USGS	2009-	500	None	60dN-60dS
GTOPO30	Org. of the world	USGS	1993-	1000	30	90dN-90dS
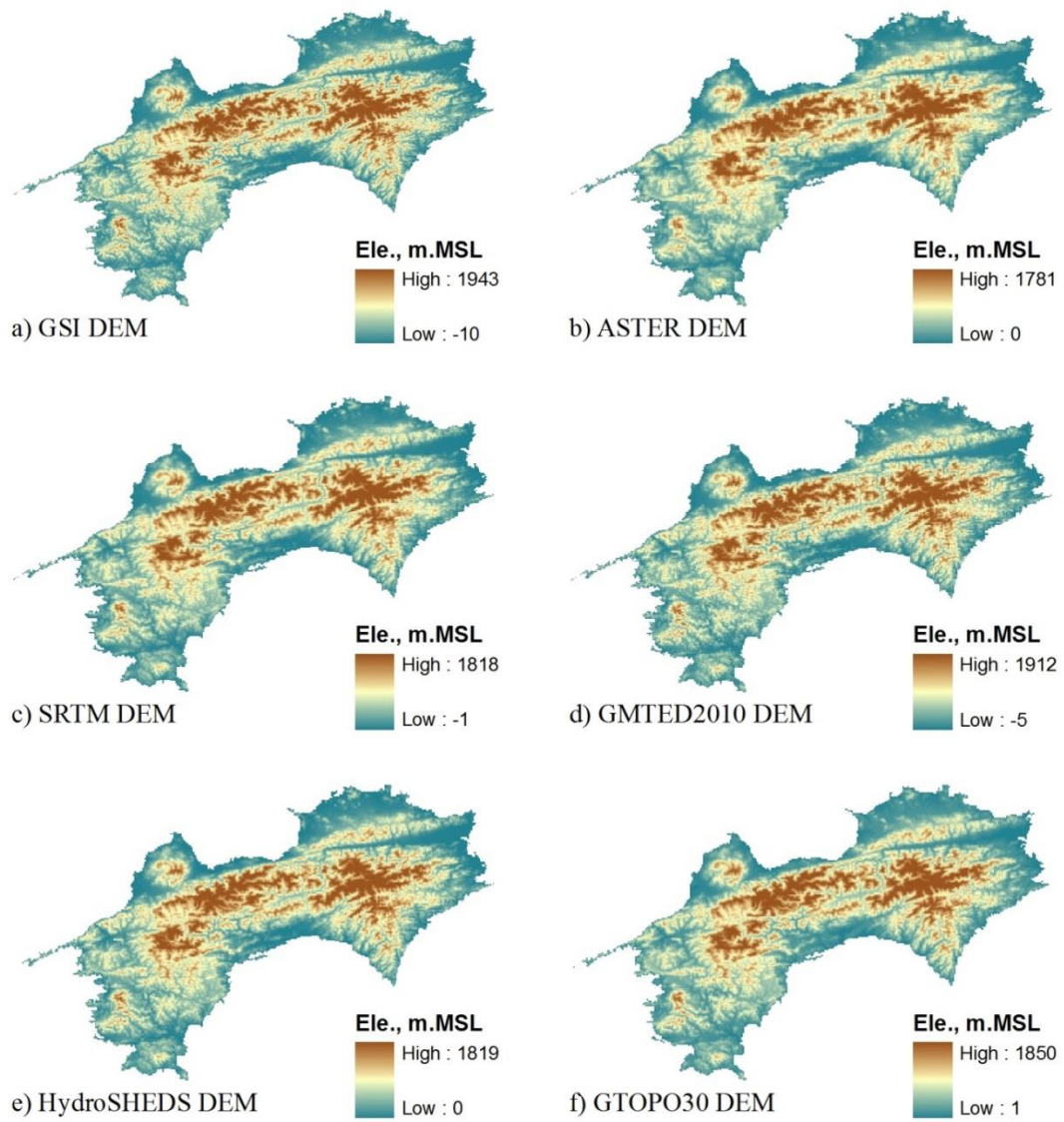
Figure 3-1 DEMs in the Shikoku Island Japan
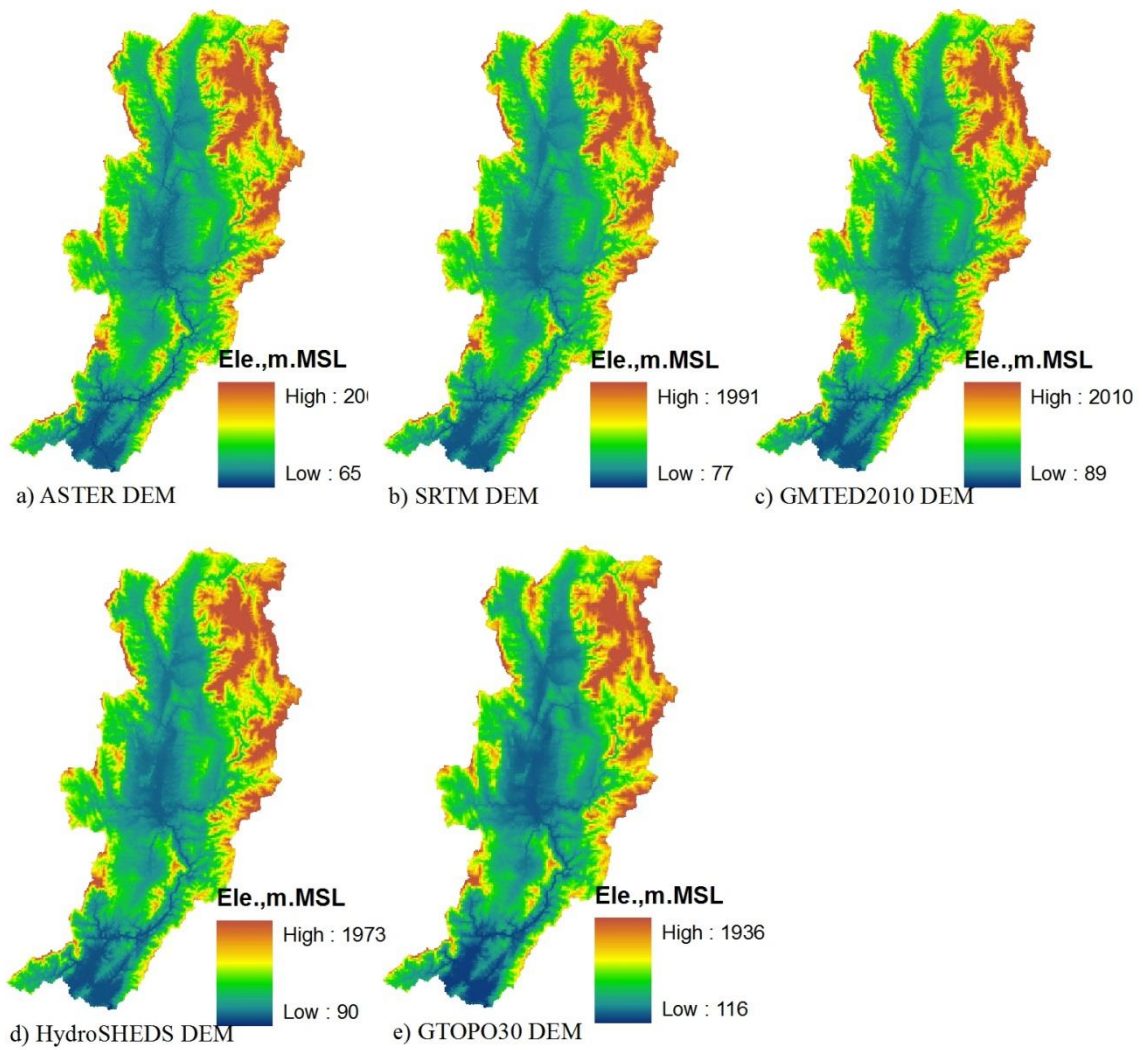
Figure 3-2 DEMs in the Nan river basin Thailand
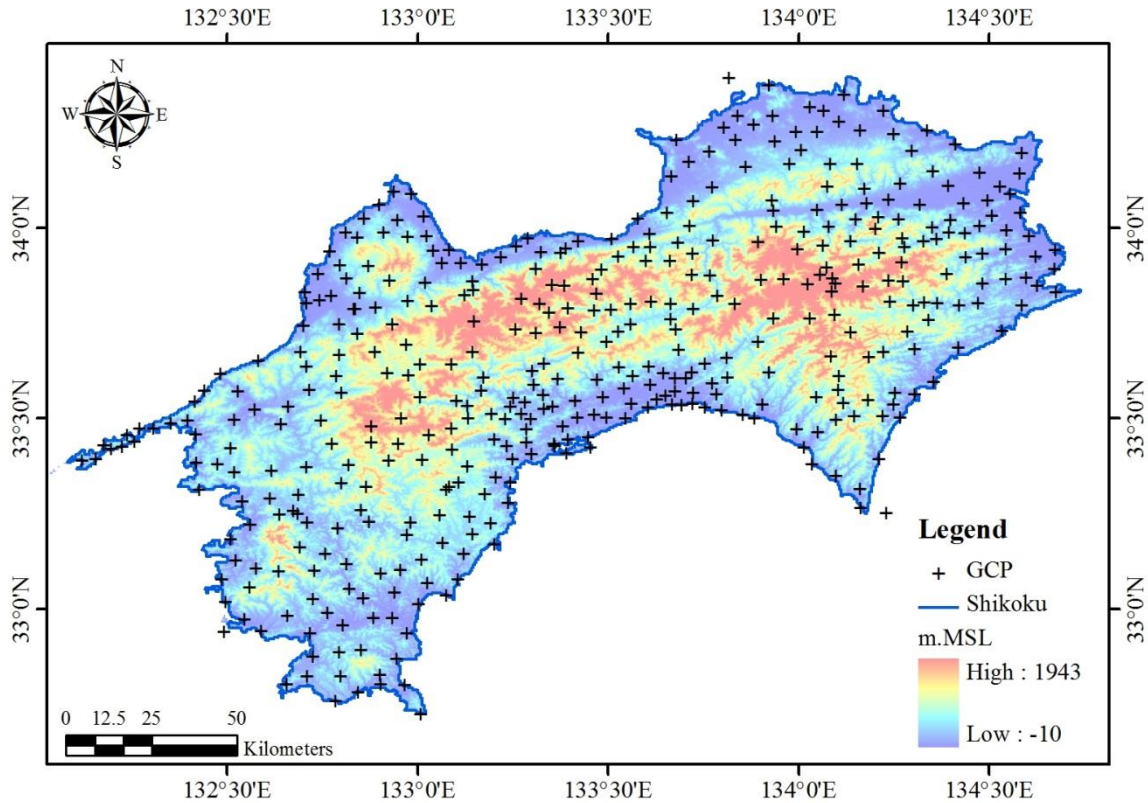
Figure 3-3 The GCP location in the Shikoku Island

3.2.2 Accuracy assessment

The vertical accuracy of the six DEMs was calculated from the differences corresponding between the value of the DEM pixel and the GPS point only in the Shikoku Island Japan. Elevation error was estimated which positive differences denote the locations of the DEM elevation exceeded the GPS point elevation while negative errors ensue at the locations of the DEM elevation was under the GPS elevation. After the elevation error estimated, a statistical, maximum error (Max), minimum error (Min), Mean Error (ME), Standard Deviation Error (STD), and Root Mean Square Error (RMSE), were estimated. STD and RMSE are revealing of surface quality and offer perception into the distribution of deviations on the side of the mean value. The agreement level between derived elevation values of six DEMs and linear regression with correlation is used to evaluate in terms with GPS data.

A normality test is used to describe and compare the error distributions in each DEM. A Quantile-Quantile plots (Q–Q plots) based on the normal distribution are created for visual examination. The Q-Q plot is shown by using a scatter plot that quantile of the observation are located on the horizontal and the predicted normal values are set on the vertical axis. The best-fit in the linear relationship showed that the observed values were normally distributed (Zandbergen, 2008). This test is also used

in statistical evaluation to investigate whether data estimate from a normal distribution (Höhle and Höhle, 2009).

DEMs were collected from provider as the original resolution, and reference elevation point represented by GCPs that was collected from GPS. The DEMs on a grid spatial resolution were captured by using the GCPs as same as their location, and these data have assessed a performance statistical based on the whole area based on statistical in **Table 3-2**. The captured DEMs and the GCPs were categorized by an altitude of the GCPs represented with **Figure 3-4a**, and statistical of error on each DEM products were estimated on each altitude. The GCPs and the captured DEMs were grouped by the land cover types based on **Figure 3-4b**, and the error assessment of the both dataset was calculated. An important attribute of the DEM used as a river network was analyzed by using an 8-direction algorithm that its accuracy was evaluated by an observation river line.

The basic of generating river network is to identify flow direction of all pixels in the DEMs. The commonly implemented method is the D8 algorithm as shown in **Figure 3-5** (Jenson and Domangue, 1988; Martz and Jong, 1988). This algorithm determines the maximum prop from eight neighbor's pixel (O'Callaghan and Mark, 1984). The D8 algorithm results a good product in high vertical slope while low steep region it produces direction in parallel line (Chang, 2006). This problem has been improved by using geomorphological operation to reconstruct the DEM for generating the flow direction in the flat area (Garcia and Camarasa, 1999). Then flow accumulation is estimated by sum of upstream pixel on each pixel. River network can be estimated by the flow accumulation.

The river network generation is implemented on each evaluated DEMs. The estimated river line revealed accuracy based on the comparison to the observed river line. The accuracy assessment is done by distance measurement between referenced river line and estimated river line. The distant is represented by buffer of the referenced line as shown in **Figure 3-6** on the example. The buffer line is established on ranging from 10 m to 200 m. Then the river network accuracy is based on the buffer zone in percentage of capturing in each zone.
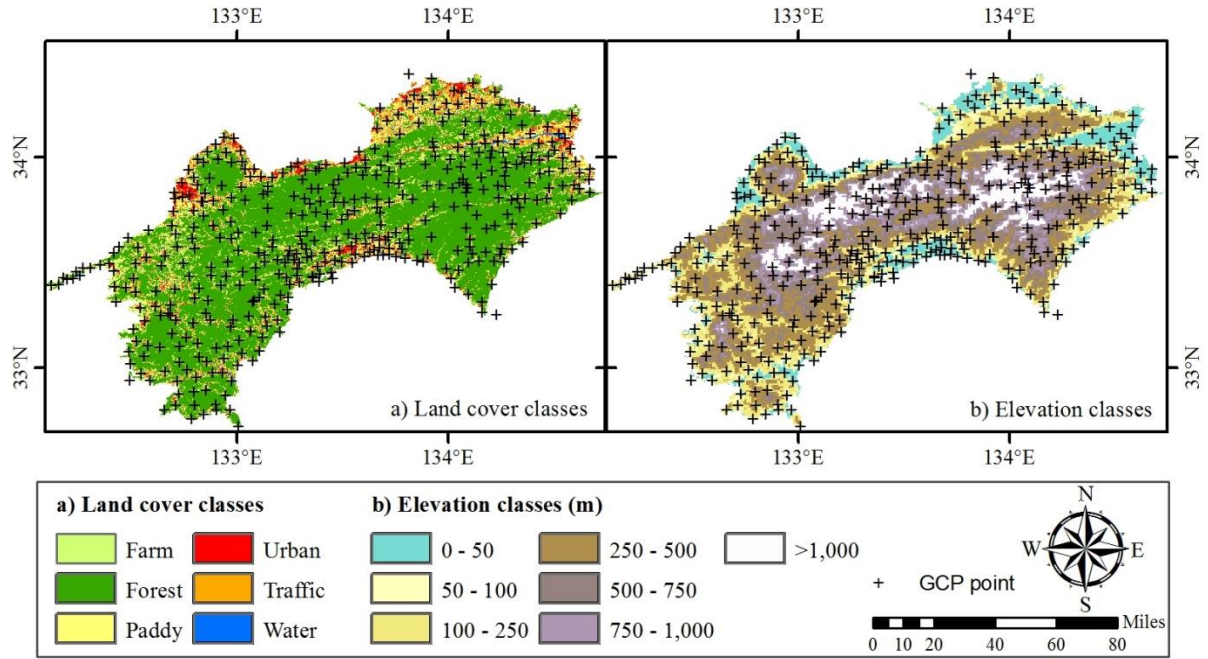
Figure 3-4 (a) Land covers type and (b) Attitude category of the study area

Table 3-2 Description of statistical assessment

Statistical	Description
Elevation error	$Z_{dif} = Z_{DEM} - Z_{GCP}$
Mean error	$ME = \dfrac{\sum_{i=1}^{n} Z_{dif(i)}}{n}$
Standard deviation error	$STD_{err} = \sqrt{\dfrac{\sum_{i=1}^{n}(Z_{dif(i)} - ME)^2}{n-1}}$
Nash-Sutcliffe (NSE)	$NSE = 1 - \left[\dfrac{\sum_{i=1}^{n}\left(Z_i^{GCP} - Z_i^{DEM}\right)^2}{\sum_{i=1}^{n}\left(Z_i^{GCP} - \bar{Z}^{GCP}\right)^2}\right]$
Pearson Correlation Coefficient (PCC)	$PCC = \dfrac{\sum_{i=1}^{n}\left(Z_i^{GCP} - \bar{Z}^{GCP}\right) \cdot \left(Z_i^{DEM} - \bar{Z}^{DEM}\right)}{\sqrt{\sum_{i=1}^{n}\left(Z_i^{GCP} - \bar{Z}^{GCP}\right)^2} \cdot \sqrt{\sum_{i=1}^{n}\left(Z_i^{DEM} - Z^{DEM}\right)^2}}$
Root Mean Square Error (RMSE)	$RMSE = \sqrt{\dfrac{\sum_{i=1}^{n}\left(Z_i^{GCP} - Z_i^{DEM}\right)^2}{n}}$
Percent Bias (PBIAS)	$PBIAS = \left[\dfrac{\sum_{i=1}^{n}\left(Z_i^{DEM} - Z_i^{GCP}\right)}{\sum_{i=1}^{n}\left(Z_i^{GCP}\right)}\right] \times 100$
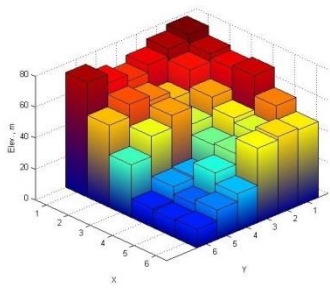
a) 3D and DEM
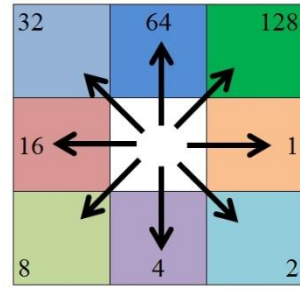
b) 8-direction modeling
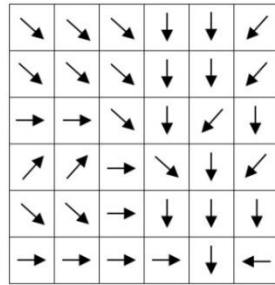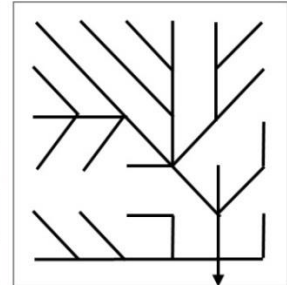
c) Numeracal and visualization of flow direction

d) Flow accumulation and river line

Figure 3-5 The 8-Direction algorithm conceptual to analysis river network
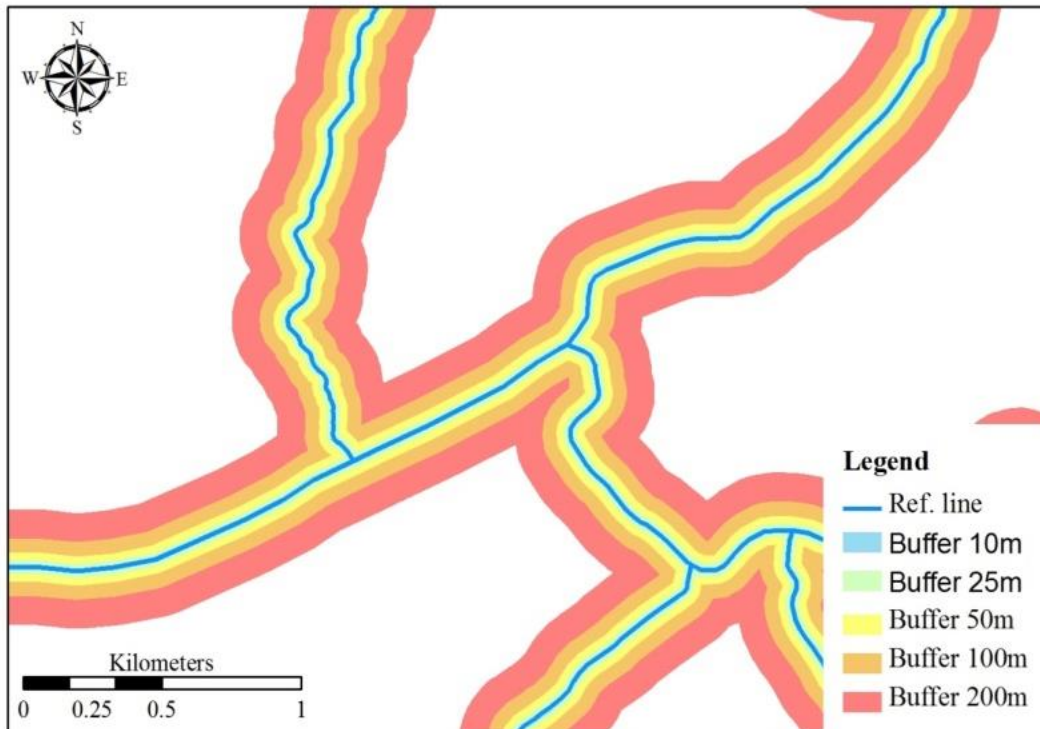
Figure 3-6 The comparisons conceptual of simulation and observation dataset

3.2.4 Bias correction for DEM

Comparison with reference point measurements will be shown the most accurate DEMs product. However, two DEMs were different with reference data that may be reduced. It obtained a bias correction equation to achieve a close fit between the six DEMs source and ground reference points. To accommodate for the finding that relative bias varied with total, a linear transformation function will be used to derive bias corrected of the DEMs elevation as follows in equation (1) on conceptual and equation (2) on application (Zhang and Zhang, 2011; Kuriakose and Viswas, 2013).

$$Z = f(u, v, w) \qquad (1)$$

$$Z = a.u + b.v + c.w + Z_0 \qquad (2)$$

where Z is observation data, u, v are coordinate of estimation, w is estimation data, and $a, b, c,$ and Z_0 are transformation parameter. Observation data at the first point until n point are shown in equation (3) to (7) to summarize in equation (8).

$$Z_1 = a.u_1 + b.v_1 + c.w_1 + Z_0 \qquad (3)$$

$$Z_2 = a.u_2 + b.v_2 + c.w_2 + Z_0 \qquad (4)$$

$$Z_3 = a.u_3 + b.v_3 + c.w_3 + Z_0 \qquad (5)$$

$$\vdots$$

$$Z_{n-1} = a.u_{n-1} + b.v_{n-1} + c.w_{n-1} + Z_0 \qquad (6)$$

$$Z_n = a.u_n + b.v_n + c.w_n + Z_0 \qquad (7)$$

Summarize equation from the equation (3) to (7) as follows:

$$\sum_{i=1}^{n} Z_i = \sum_{i=1}^{n} (a.u_i + b.v_i + c.w_i + Z_0) \qquad (8)$$

Least square methods of equation (8) based on sum square error (E) are presented in equation (9).

$$E = \sum_{i=1}^{n} (a.u_i + b.v_i + c.w_i + Z_0 - Z_i)^2 \qquad (9)$$

To minimize sum square error by ordinary least square methods as follows:

$$\frac{\partial E}{\partial a} = 0, \frac{\partial E}{\partial b} = 0, \frac{\partial E}{\partial w} = 0 \text{ and } \frac{\partial E}{\partial Z_0} = 0 \qquad (10)$$

To represent in a matrix form are shown in equation (11).

$$
\begin{bmatrix}
\sum\limits_{i=1}^{n} u_i.u_i & \sum\limits_{i=1}^{n} u_i.v_i & \sum\limits_{i=1}^{n} u_i.w_i & \sum\limits_{i=1}^{n} u_i \\[2ex]
\sum\limits_{i=1}^{n} u_i.v_i & \sum\limits_{i=1}^{n} v_i.v_i & \sum\limits_{i=1}^{n} v_i.w_i & \sum\limits_{i=1}^{n} v_i \\[2ex]
\sum\limits_{i=1}^{n} u_i.w_i & \sum\limits_{i=1}^{n} v_i.w_i & \sum\limits_{i=1}^{n} w_i.w_i & \sum\limits_{i=1}^{n} w_i \\[2ex]
\sum\limits_{i=1}^{n} u_i & \sum\limits_{i=1}^{n} v_i & \sum\limits_{i=1}^{n} w_i & n
\end{bmatrix}
\cdot
\begin{bmatrix} a \\ b \\ c \\ Z_0 \end{bmatrix}
=
\begin{bmatrix}
\sum\limits_{i=1}^{n} Z_i.u_i \\[2ex]
\sum\limits_{i=1}^{n} Z_i.v_i \\[2ex]
\sum\limits_{i=1}^{n} Z_i.w_i \\[2ex]
\sum\limits_{i=1}^{n} Z_i
\end{bmatrix}
\tag{11}
$$

The parameters a, b, c, and Z_0 were derived by minimizing between bias corrected value and ground observed point above the study area. The inverse matrix algorithm was used to obtain an optimized value of a, b, c, and Z_0 (Ishida and Takagi, 2010).

3.2.5 Hydrological simulation

Input data sets of the RRI model are four data types; rainfall product, topography, land cover and soil type. On the definition of the distributed hydrologic model with the RRI model, the used hydrologic parameters were mentioned in the **Chapter 2** such as Manning's roughness of land cover type and Green-Amp parameter of soil type. The spatially pixel of DEM is about 30 m, 90m, 225m and 1000m, but in this study it has been scaled to 500 m of pixel size (about 15 x 15 arc-second). Addition to the numbers of pixel, row and column numbers are 457 and 292 respectively to present the watershed area as 13,000 km^2 for the Nan river basin. For the Shikoku Island, row and column numbers are 401 and 650 respectively for the area about 18,000 km^2. The estimation of width and depth were recommended in the equation (4) and (5) in the **Chapter 2**. Rainfall data was collected from the rain gauges, covering the study area. For the Nan river basin, June 2011 storm event is implemented to evaluate different DEM products that are used to run the RRI model over the basin. The rainy season during July to October in 2014 is used to evaluate the runoff in different DEM source for the Shikoku Island.

The estimated results driven by the different topography sources were evaluated to analysis bias of volume (V_{bias}), bias of peak (P_{bias}), Root Mean Square Error ($RMSE$), square of the Pearson correlation coefficient (R^2), and Mean Error (ME). The following formulas in **Table 2-3** were applied to evaluate simulation performance. The volume bias and peak bias estimate the systematic bias of modeled runoff in percentage (%). The correlation index is quantification in correlation of two data sets, simulated and observed runoff, which 0 is no correlation while 1 is perfect correlation. The $RMSE$ is a different measure of difference magnitude between two datasets, while the ME is the bias between the two datasets.

The RRI model simulated inundation spatial extents were evaluated with the satellite inundation map. The several performance verification statistics measure the correspondence between the simulated and observed, were implemented in this research (see **Figure 3-7**): probability of detection (POD), false-alarm ratio (FAR), critical success index (CSI), and accuracy (ACC). POD presents the fraction of observed marks to analysis an exact data (hit rate). FAR measures the value of data that were not observed. CSI provides the total exact event. ACC give the overall correction of simulation data. Perfect values for the statistical are POD = 1, FAR = 0, CSI = 1, and ACC = 1.

$$POD = \frac{Hit}{Hit + Miss}$$

$$FAR = \frac{False}{Hit + False}$$

$$CSI = \frac{Hit}{Hit + Miss + False}$$

$$ACC = \frac{Hit + Corr.}{Hit + False + Miss + Corr.}$$
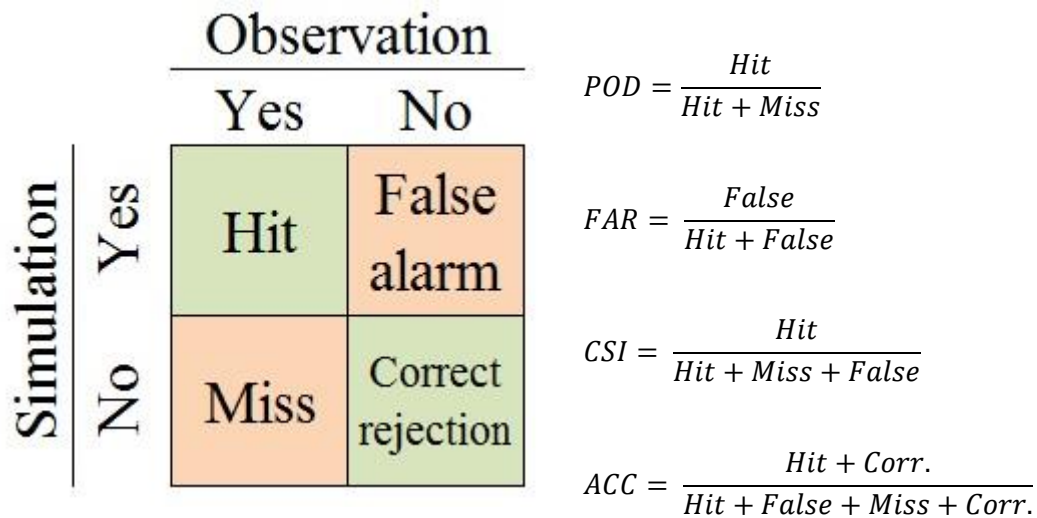
Figure 3-7 Detection analysis for inundation data

3.3 Results and Discussion

3.3.1 Geomorphological property of DEMs

The six DEMs at original resolution were presented in **Figure 3-2** on different information of elevation for the Shikoku Island in Japan. The GSI-DEM is revealed as the highest resolution in this study and provided only in Japan. This data contained a pixel size about 10 m and elevation range from -10 to 1,943 m.MSL. The ASTER DEM used the stereo-correlation to produce a digital terrain from the imagery data. The elevation range of ASTER DEM is 0 – 1,781 m.MSL, with the pixel size about 30 m. The SRTM DEM is investigated by the shuttle space and used the radar interferometry to collect the terrain elevation. With the 90 m pixel size at original of SRTM that have elevation range from -1 to 1,818 m.MSL for the study area. The GMTED2010 is the reconstruction to base on the GTOPO30 as the mainly source that provide resolution have produced in different sizes. In the Shikoku Island, elevation range of this DEM is -5 – 1,912 m.MSL to contain a pixel size about 225 m. The HydroSHEDS DEM is developed from the SRTM DEM using several tools from matching with hydrological condition on a global scale. In this study, this DEM resolution at 500 m is used and it contains an elevation range of 0 – 1,819 m.MSL. The GTOPO30 DEM is firstly provided that have

collected data from satellite and elevation spots. This DEM provides digital terrain only 1,000 m resolution and have elevation range from 1 – 1,850 m.MSL in this study area. All of DEM products, the average elevation is in the range 500 – 1,000 m.MSL with about 45% of the total area and followed with the range about 250-500 m.MSL, 1,000 – 1,500 m.MSL. For the Shikoku Island, **Figure 3-8** presents Areal distribution of DEM products in each altitude zone and **Figure 3-9** shows Slope distribution of DEM products in each slope zone. For slope of the terrain distribution, ones important attribute for runoff estimation, all products have maximum range with 15 – 30 degree about 45% of total area, followed by 10-15 degree, and 5-10 degree. Thus, the Shikoku has been represented by the high steep slope with the mountain area on the complex terrain based on the information as above.

Nan river basin was presented by the five DEM sources, ASTER, SRTM, GMTED2010, HydroSHEDS, and GTOPO30. The elevation range of ASTER DEM is 65 – 2,060 m.MSL, while the SRTM DEM is range from 89 to 1,991 m.MSL. The GMTED2010 is 89 – 2,010 m.MSL presented by the medium resolution about 225 m. The HydroSHEDS DEM is range of 90 – 1,973 m.MSL and the GTOPO30 DEM identified as the course resolution is range from 116 – 1,936 m.MSL. **Figure 3-10** presents areal distribution of DEM products in each altitude zone and **Figure 3-11** shows Slope distribution of DEM products in each slope zone, for the Nan river basin. The range about 500 – 1,000 m.MSL all of DEM products is the average elevation with about 45% of the total area and followed with the range about 250-500 m.MSL, 1,000 – 1,500 m.MSL. Slope of the terrain is average in range about 5 – 30 degree with 25% of total area. Thus, the Nan has been represented by the mild slope area with the mountain area on the rolling terrain type based on the information as above.
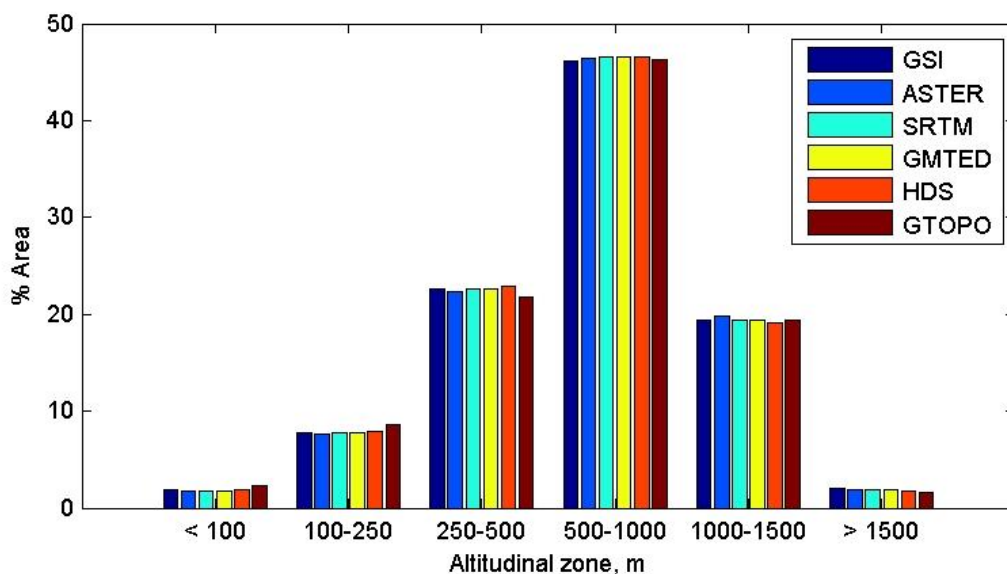
Figure 3-8 Areal distribution of DEM products in each altitude zone of the Shikoku Island Japan
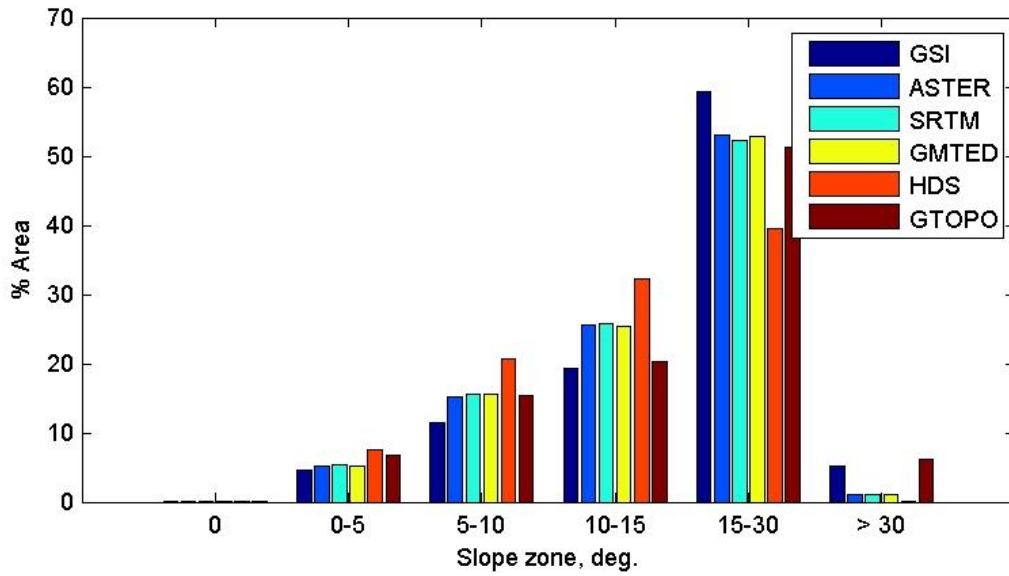
Figure 3-9 Slope distribution of DEM products in each slope zone of the Shikoku Island Japan
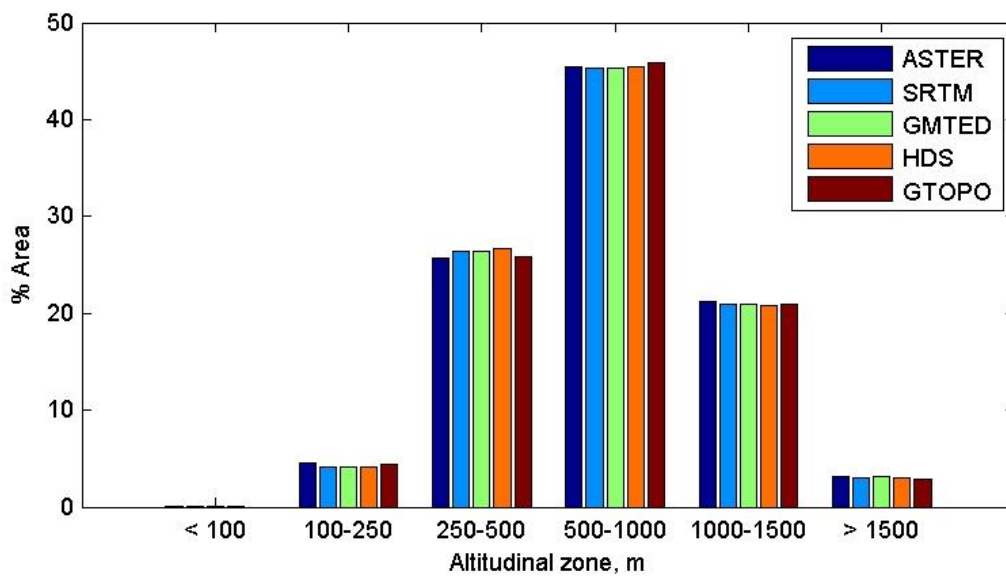
Figure 3-10 Areal distribution of DEM products in each altitude zone of the Nan river basin Thailand
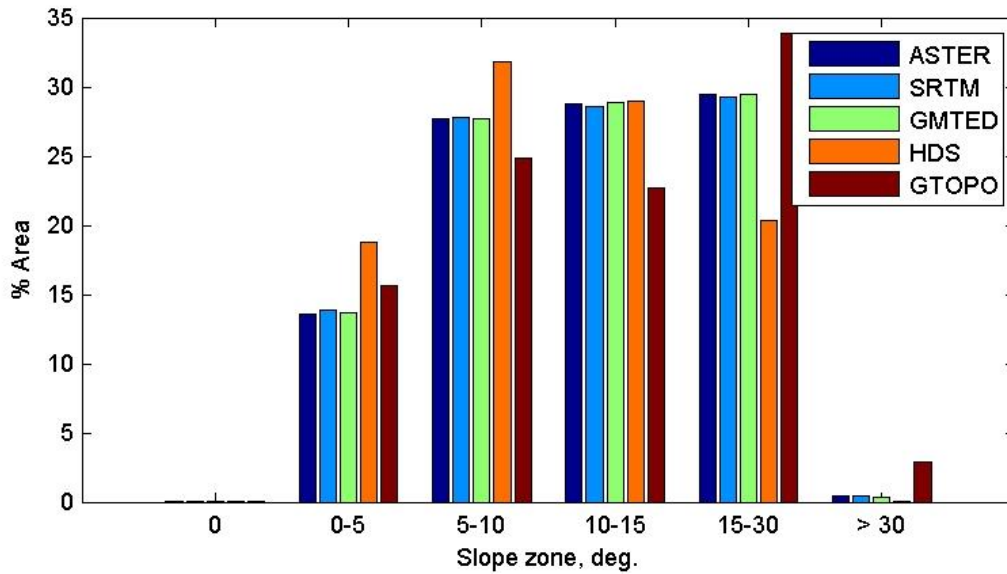
Figure 3-11 Slope distribution of DEM products in each slope zone of the Nan river basin Thailand

3.3.2 Accuracy assessment of DEMs

Accuracy of the six DEMs was evaluated by using the reference points that was investigated from the GPS. First, the accuracy was presented on scatter plot between the observed and modeled data to reveal the correlation. Second, the difference elevation was plotted on a histogram and fitted to a normal distribution to show an average and variation of bias. Third, overall performance in each DEM was estimated on performance statistical that had compared with the other region. Finally, the accuracy was presented on a spatial map by using the RMSE.

Figure 3-12 presented the correlation between observed and estimated data on the scatter plot. The observed points was selected from the database about 418 points, covering the study area. Overall DEMs, the comparison between both data revealed the relation that fitted to the conformation line (1:1 line). The six results showed the strong correlation about 0.9. The high and middle definition the variation was a little to close along the conformation line, while low definition (HydroSHEDS and GTOPO30) presented the contrast.

Figure 3-13 presented the elevation difference between observed and estimated data on a histogram plot and the difference was fitted by the normal distribution. The results revealed that evaluation of the mean bias and variation was validated. The best accuracy was the GSI DEM on the small overestimation of the mean error, with standard deviation about 5.9 m. According to the best was followed by the ASTER GDEM, SRTM, and GMTED2010 that were presented on underestimation. The ASTER GDEM and SRTM contained the standard deviation about 9.4 m, while the GMTED was

16.7 m. By the contrast, the lowest accuracy was the HydroSHEDS and GTOPO30 with underestimation of the mean error to contain he standard deviation about 56.6 m and 46.48 m, respectively.

Table 3-3 showed the statistical performance values of the candidate DEM, including the NSE, PCC, mean, RMSE, and PBIAS. The statistical value of the GSI-DEM was presented on small overestimation by the PBIAS of 0.04%, with the strong of NSE and PCC, and the lowest RMSE. The ASTER GDEM offered the underestimation about -1.6% and good correlation on NSE and PCC, with the RMSE value about 9.93 m. The results were agreed with the previous studies that have been reported by Hirt et al. (Hirt et al, 2010) on the underestimation on the ASTER GDEM to validate with the observed points. The statistical performance value of SRTM was also underestimation about 1.8%, with good correlation on NSE and PCC. Its RMSE was about 10 m. The results of SRTM were underestimated elevation that was insisted by previous studies (Li et al., 2013 and Zhao et al, 2010). GMTED2010 presented the PBIAS about 3.4% to reveal the underestimation. The RMSE was about 18.2 m and good correlation of NSE and PCC abut 0.995 and 0.998, respectively. The GMTED2010 was correspondingly underestimation that was reported by C.C. Carabajal et al. (2010). By the contrast, the HydroSHEDS and GTOPO30 presented the high underestimation of PBIAS about 19.9% and 20.6%, respectively. The RMSE of HydroSHEDS was the highest value about 69.4 m and good correlation of NSE and PCC. The NSE and PCC of GTOPO30 was a good correlation, with high RMSE value about 61.8 m.

The assessment accuracy from the five international DEMs presented that the ASTER GDEM outperformed the four DEMs. By the contrast, the SRTM has better accuracy than ASTER GDEM that previous studies have been mention as shown in **Table 3-4**. The results of this study was similar to the recommendation of Mukherjee et al. (Mukherjee et al., 2013), which ASTER GDEM presented better accuracy. However, the large differences in global scale the height precision are found in the studied DEMs literature. It demonstrates that the DEMs accuracy is depended on accuracy of reference point, terrain characteristics, and surface properties. Hence, the recommendation achieves to the study of those features. In addition to the **Table 3-4**, the RMSE value on this study about 10.08 m of SRTM closed to the described by Mukherjee et al. (2013). The RMSE of ASTER GDEM presented about 9.93 m to close with Djamel and Achour (2014). According to the DEMs provided in global scale, this study recommended that the ASTER GDEM was higher accuracy to compare with SRTM and GMTED2010 for high definition while a coarse resolution GTOPO30 (30 arc-second) was higher accuracy than HydroSHEDS product (15 arc-second).

Figure 3-14 presents the Q-Q plots of elevation errors in six data sources. A reference line at 95% confidence intervals is along with upper and lower. The Q-Q plots for six DEMs indicate that the data were not conforming to normal distributed, representing a sigmoid-type function with a significant

deviation from the fit line. The most observations present a strong deviation with the 95% confidence boundary. GSI-DEM has 93.2% of acceptable in the 95% confidence intervals (370 points from 418 points). ASTER has an acceptable data with 382 points of 418 points (95%) while the SRTM can capture with 90% of 418 points (361 points). The conformable point with the 95% confidence intervals of GMTED2010 is 347 points (85.9%) of total GCP data. HydroSHEDS and GTOPO30 have an acceptable point of 385 points and 381 points, respectively. All of the investigations reveal a deviation based on the 95% confidence intervals boundary.

An evaluation of the RMSE index spatially on the study area is presented in the **Figure 3-15**. The GSI DEM outperformed on the five DEMs, with range about 0 – 10 m of RMSE. Some area on the eastern part about 5 spots was high RMSE value about 10 – 25 m where the high error spots were located in the mountain area. The ASTER GDEM and SRTM had also presented the high accuracy in the low elevation zone with low value of the RMSE. The low accuracy of both DEMs was also located in the mountain area in the eastern and middle part. The GMTED2010 and HydroSHEDS presented the low RMSE value as border area of the study area, while the higher value located in the middle part. By the contrast, the GTOPO30 had the RMSE value ranging about 0 – 150 m that the high accuracy value was located on the flat area. Based on the **Figure 3-15**, the results summarized that the terrain morphology have affected with the accuracy of the DEM. The effect of terrain morphology has been reported from the literature that was examined by using the ASTER GDEM and SRTM (Mukherjee et al., 2013).

Table 3-3 Difference statistical between before and after bias correction (Units in meters)

DEMs	Min	Max	ME	S.D.	RMSE	NSE	PCC	PBIAS
GSI	-34.19	23.04	0.08	5.98	5.97	0.9995	0.9997	0.0400
ASTER	-52.09	22.61	-3.12	9.44	9.93	0.9986	0.9994	-1.5859
SRTM	-44.91	23.24	-3.71	9.38	10.08	0.9986	0.9994	-1.8798
GMTED	-97.77	45.93	-6.68	16.74	18.01	0.9953	0.9980	-3.3909
HydroSHEDS	-394.86	126.42	-39.04	56.57	68.67	0.9321	0.9789	-19.9491
GTOPO	-258.42	173.59	-40.90	46.47	61.86	0.9460	0.9850	-20.6739

Table 3-4 Varying reports height accuracies represented by RMSE for the ASTER GDEM2 and SRTM v4.1 DEMs

Study Areas	ASTER GDEM2	SRTM v4.1	Remark
Karian dam, Indonesia	5.68	3.25	Suwandana et al., 2012
Bare areas, Australia	8.05	3.43	Rexer and Hirt, 2014
Southern Sardinia, Italy	12.95	n/a	Pulighe and Fava, 2013
Tibetan Plateau, China	14.10	8.60	Li et al., 2013
Shiwalik Himalaya, India	6.08	9.2	Mukherjee et al., 2013
Anaguid, Tunisia	5.30	3.60	Djamel and Achour, 2014
Tebessa, Algeria	9.80	8.30	
Shikoku Island, Japan	9.93	10.08	This study; Pakoksung and Takagi, 2015
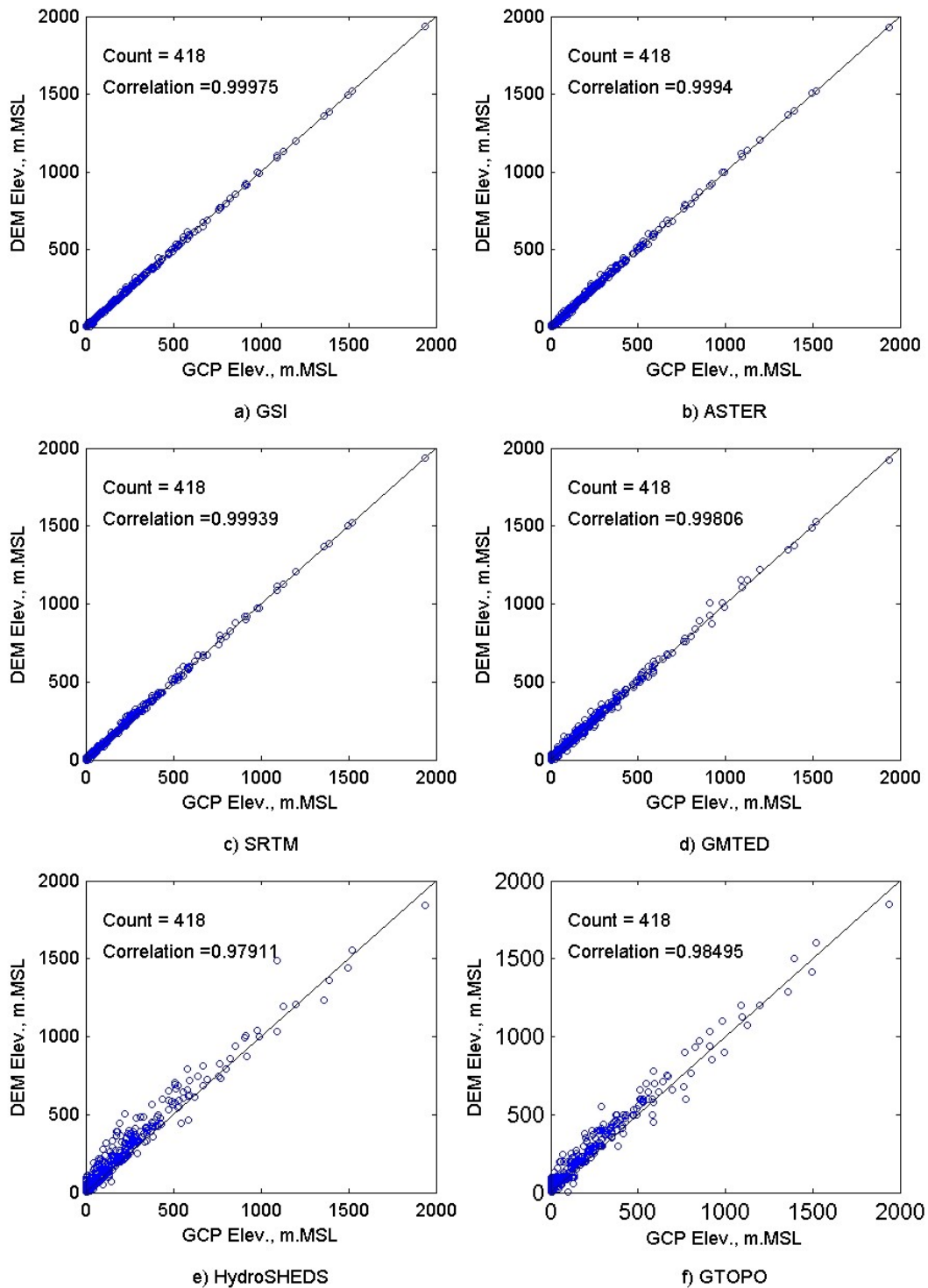
Figure 3-12 Scatter plots between GCPs and a) GSI-DEM; b) ASTER; c) SRTM; d) GMTED2010; e) HydroSHEDS; f) GTOPO30. The perfect fit is represented by the black line
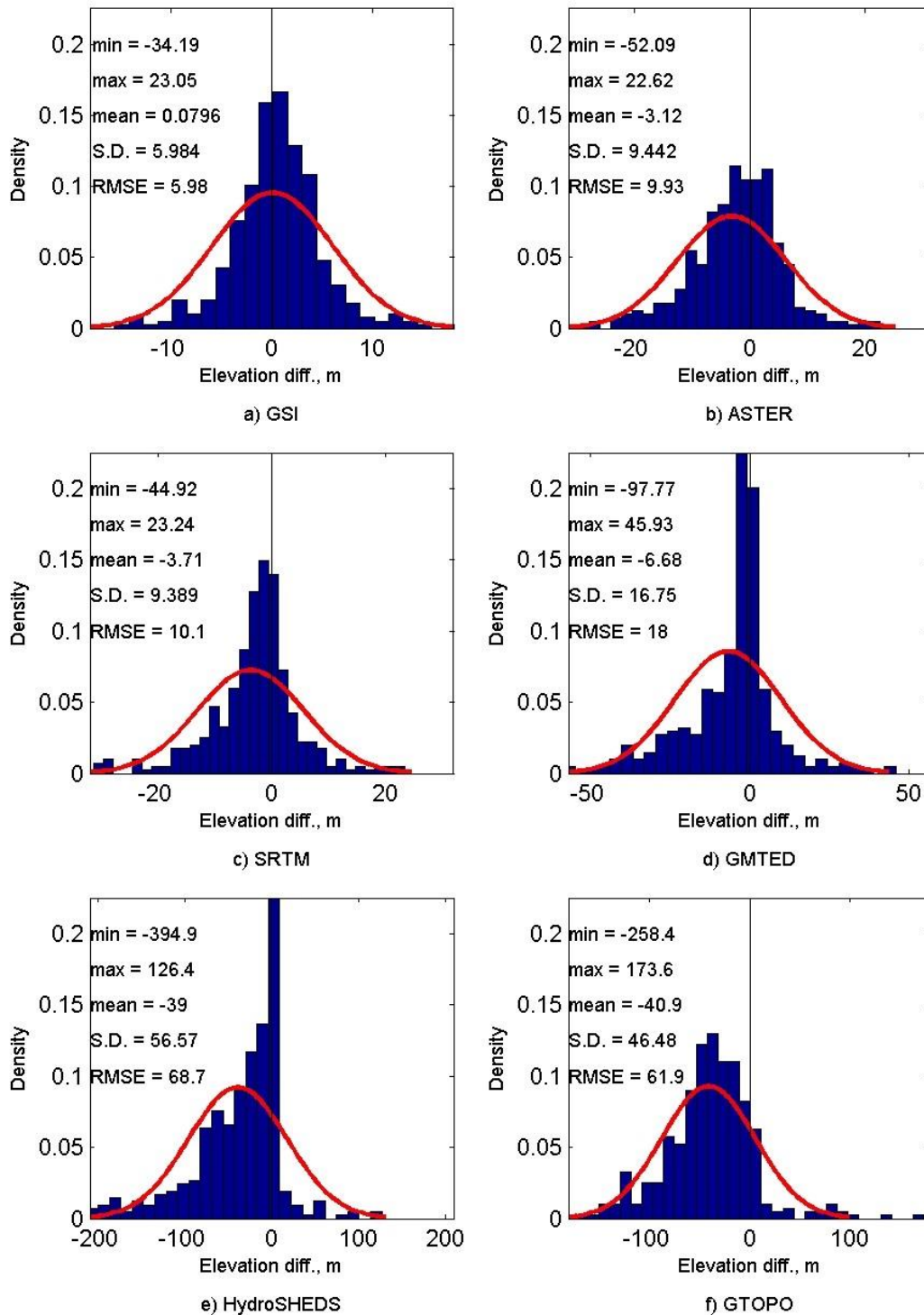
Figure 3-13 Histograms of elevation error and estimated basic statistical. a) GSI-DEM; b) ASTER; c) SRTM; d) GMTED2010; e) HydroSHEDS; f) GTOPO30. The continuous red line reveals the fit curve based on normal distribution
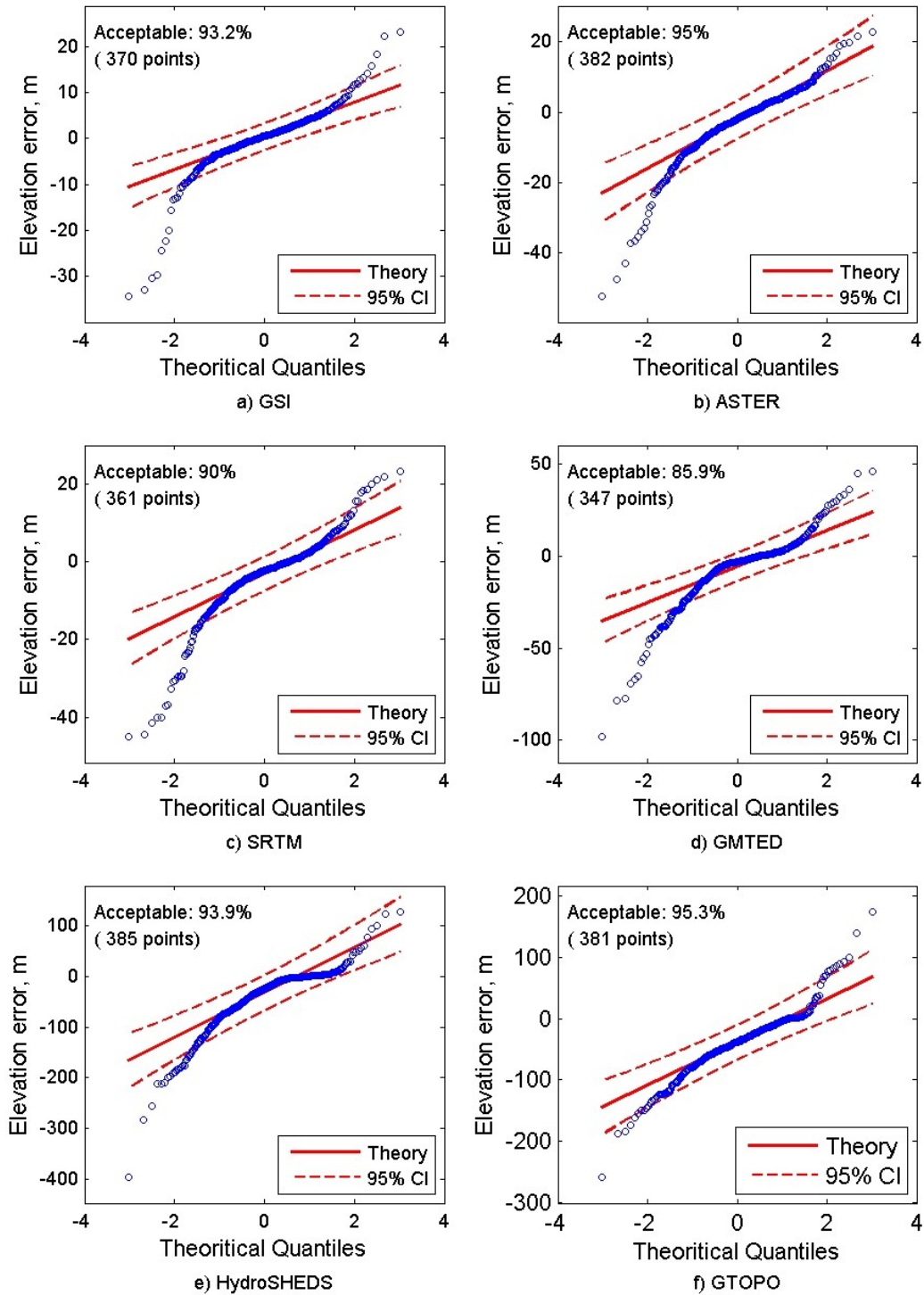
Figure 3-14 Quantile-Quantile plots to show the error distribution for a) GSI-DEM; b) ASTER; c) SRTM; d) GMTED2010; e) HydroSHEDS; f) GTOPO30
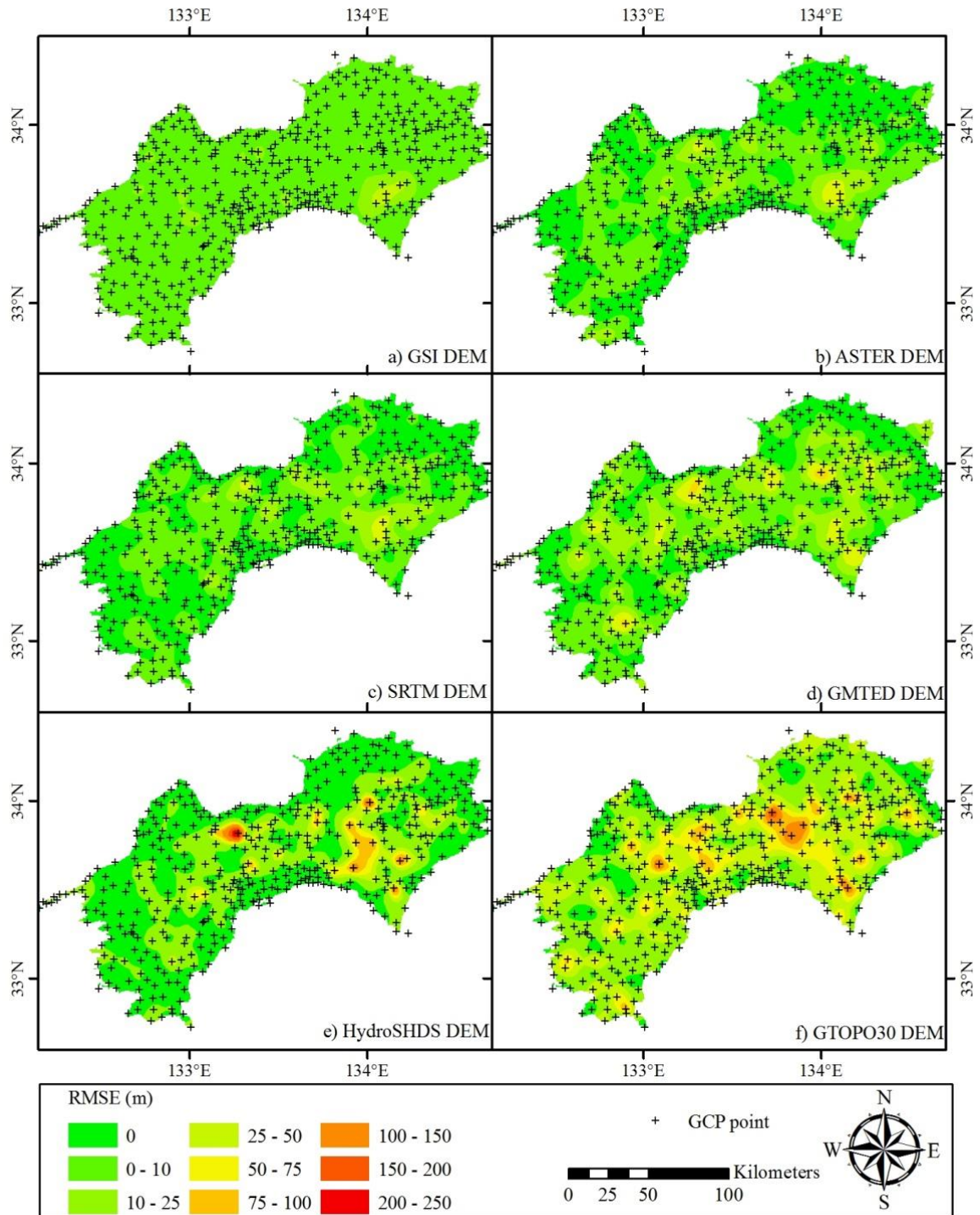
Figure 3-15 RMSE spatial distribution of the DEM products; a) GSI-DEM; b) ASTER; c) SRTM; d) GMTED2010; e) HydroSHEDS; f) GTOPO30

3.3.3 Effect of terrain morphology in the DEMs accuracy

Terrain morphology have affected to the vertical accuracy of DEM as mention in above and previous research (Mukherjee et al., 2013). In order to estimate this effect, the elevation is divided into 7 altitudinal classes (0 – 50 m, 50 – 100 m, 100 – 250 m, 250 – 500 m, 500 – 750 m, 750 – 1,000 m, and >1,000 m). The first zone ranges about 0 – 50 m that the referent point was located on the highest, while zone >1,000 was lowest. The performances statistical were shown in **Table 3-5** for each altitudinal zone and different DEM source. The NSE, PCC and PBIAS was the highest correlation in the highest elevation zone, and lowest in the lowest elevation zone. The correlation between RMSE and elevation zone was presented in **Figure 3-16** that the error of the validated DEMs was shown the impact of terrain morphology. The DEMs was more error until high elevation zone about 500 – 750 m, and the error was drop to higher accuracy in the higher zones. The first result in **Figure 3-16** is agreed with the previous researches (Holmes et al., 2009; Mukherjee et al., 2013), while the second was the contrast. The fine resolution provided more accuracy compared to coarse resolution that was the impact of grid size. The GSI DEM was the highest accuracy, followed by ASTER GDEM and SRTM. The ASTER GDEM and SRTM was quite the same that had different value in range 50 – 100 m and 750 – 1,000 m. The GMTED2010 was the lowest accuracy among the fine resolution DEM. On the coarse resolution DEM, the GTOPO30 as lowest resolution showed more accuracy than the HydroSHEDS.

The slope effect on the vertical accuracy is estimated and the slope zone is divided into 7 zones. The performances statistical were shown in **Table 3-6** for each slope zone and different DEM source. The NSE, PCC and PBIAS was the highest correlation in the highest slope zone, and lowest in the lowest slope zone as same as the terrain effect. The RMSE of vertical value of each DEM source and in each slope zone was estimated to show in **Figure 3-17**. The effect of slope on the vertical accuracy affected to the RMSE value that the DEM was more error in the high steep slope to reveal in the fine resolution DEM. The GSI DEM was also the highest accuracy, followed by the ASTER GDEM and SRTM. The ASTER GDEM provided more accuracy compared to the SRTM, and the GMTED2010 was the lowest accuracy among the fine resolution DEM. The coarse resolution DEM showed the slope effect on the range from 0 – 15 degree as same as the effect on fine resolution. By the contrast on the steep slope, the accuracy was higher than the first zone. On the coarse resolution, the HydroSHEDS provided more accuracy compared to GTOPO30 at first range until 15 degree, while the high steep zone GTOPO30 was more accuracy.

Table 3-5 Statistical summaries of the DEM products analyzed on the elevation- based classification

DEM Product/Classification		NSE	PCC	RMSE	PBIAS
0 – 50 m	GSI	0.9121	0.9552	4.156	-0.39
	ASTER	0.8695	0.9380	5.058	9.31
	SRTM	0.8768	0.9459	4.914	7.40
	GMTED	0.5689	0.8790	9.230	19.99
	HydroSHEDS	-3.5676	0.6005	29.962	103.53
	GTOPO	-9.3324	0.6514	45.160	231.92
50 – 100 m	GSI	0.9396	0.9741	3.347	-1.02
	ASTER	0.5040	0.8298	9.589	-1.76
	SRTM	0.8021	0.9301	6.056	4.05
	GMTED	-0.7858	0.7066	18.194	11.22
	HydroSHEDS	-19.8281	0.4725	62.137	57.78
	GTOPO	-13.3398	0.1360	51.558	48.00
100 – 250 m	GSI	0.9799	0.9907	6.326	-0.32
	ASTER	0.9373	0.9768	11.186	2.31
	SRTM	0.9349	0.9780	11.396	3.07
	GMTED	0.7958	0.9262	20.186	4.45
	HydroSHEDS	-2.5344	0.6688	83.985	31.71
	GTOPO	-1.0017	0.7810	63.204	26.28
250 – 500 m	GSI	0.9854	0.9928	7.976	0.24
	ASTER	0.9591	0.9848	13.374	1.98
	SRTM	0.9551	0.9845	14.007	2.31
	GMTED	0.8980	0.9619	21.118	3.01
	HydroSHEDS	-0.4132	0.8267	78.591	18.14
	GTOPO	-0.2371	0.7714	73.530	16.45
500 – 750 m	GSI	0.9615	0.9808	10.746	0.05
	ASTER	0.9199	0.9696	15.494	1.23
	SRTM	0.9006	0.9535	17.259	0.87
	GMTED	0.8379	0.9315	22.037	1.40
	HydroSHEDS	-3.0632	0.4156	110.347	12.25
	GTOPO	-1.7432	0.4593	90.668	9.48
750 – 1,000 m	GSI	0.9946	0.9981	5.918	0.16
	ASTER	0.9832	0.9957	10.452	0.84
	SRTM	0.9638	0.9819	15.334	-0.09
	GMTED	0.7838	0.9242	37.483	1.36
	HydroSHEDS	0.4972	0.8898	57.160	3.23
	GTOPO	-0.7299	0.6805	106.028	1.95
>1,000 m	GSI	0.9997	0.9999	4.756	-0.08
	ASTER	0.9985	0.9997	9.882	0.37
	SRTM	0.9988	0.9996	8.937	0.30
	GMTED	0.9898	0.9974	26.131	0.71
	HydroSHEDS	0.6769	0.8269	147.110	1.18
	GTOPO	0.9120	0.9557	76.791	0.35

Table 3-6 Statistical summaries of the DEM products based on the slope zones

DEM Product/Classification		NSE	PCC	RMSE	PBIAS
0 d	GSI	0.9954	0.9981	9.237	2.81
	ASTER	0.9540	0.9890	25.407	15.01
	SRTM	0.9039	0.9872	49.774	32.79
	GMTED	0.9998	0.9999	2.957	-0.04
	HydroSHEDS	0.9994	0.9998	5.541	0.98
	GTOPO	0.9970	0.9990	9.582	3.22
0 – 2 d	GSI	0.9917	0.9977	14.977	5.28
	ASTER	0.9185	0.9846	60.528	23.76
	SRTM	0.8493	0.9745	81.471	27.65
	GMTED	0.9994	0.9997	5.290	0.52
	HydroSHEDS	0.9986	0.9994	8.724	1.01
	GTOPO	0.9979	0.9993	12.017	2.74
2 – 5 d	GSI	0.9921	0.9981	25.793	7.31
	ASTER	0.9234	0.9891	77.592	23.79
	SRTM	0.8888	0.9658	117.899	14.24
	GMTED	0.9996	0.9998	5.813	-0.59
	HydroSHEDS	0.9987	0.9994	11.159	1.49
	GTOPO	0.9986	0.9994	13.659	1.40
5 – 10 d	GSI	0.9913	0.9971	30.952	5.27
	ASTER	0.8225	0.9719	146.311	28.84
	SRTM	0.8686	0.9553	119.138	6.98
	GMTED	0.9992	0.9996	8.839	0.01
	HydroSHEDS	0.9980	0.9993	14.543	2.09
	GTOPO	0.9987	0.9993	14.883	0.32
10 – 15 d	GSI	0.9940	0.9972	28.314	0.57
	ASTER	0.8998	0.9734	152.063	11.82
	SRTM	0.9782	0.9958	61.838	-3.10
	GMTED	0.9994	0.9997	11.076	0.33
	HydroSHEDS	0.9958	0.9986	15.837	2.01
	GTOPO	0.9979	0.9991	13.040	2.17
15 – 30 d	GSI	0.9831	0.9922	62.730	1.00
	ASTER	0.6258	0.9348	29.111	-10.12
	SRTM	0.2040	0.6459	34.343	48.47
	GMTED	0.9954	0.9981	9.237	2.81
	HydroSHEDS	0.9540	0.9890	25.407	15.01
	GTOPO	0.9039	0.9872	49.774	32.79
>30 d	GSI	0.9998	0.9999	2.957	-0.04
	ASTER	0.9994	0.9998	5.541	0.98
	SRTM	0.9970	0.9990	9.582	3.22
	GMTED	0.9917	0.9977	14.977	5.28
	HydroSHEDS	0.9185	0.9846	60.528	23.76
	GTOPO	0.8493	0.9745	81.471	27.65
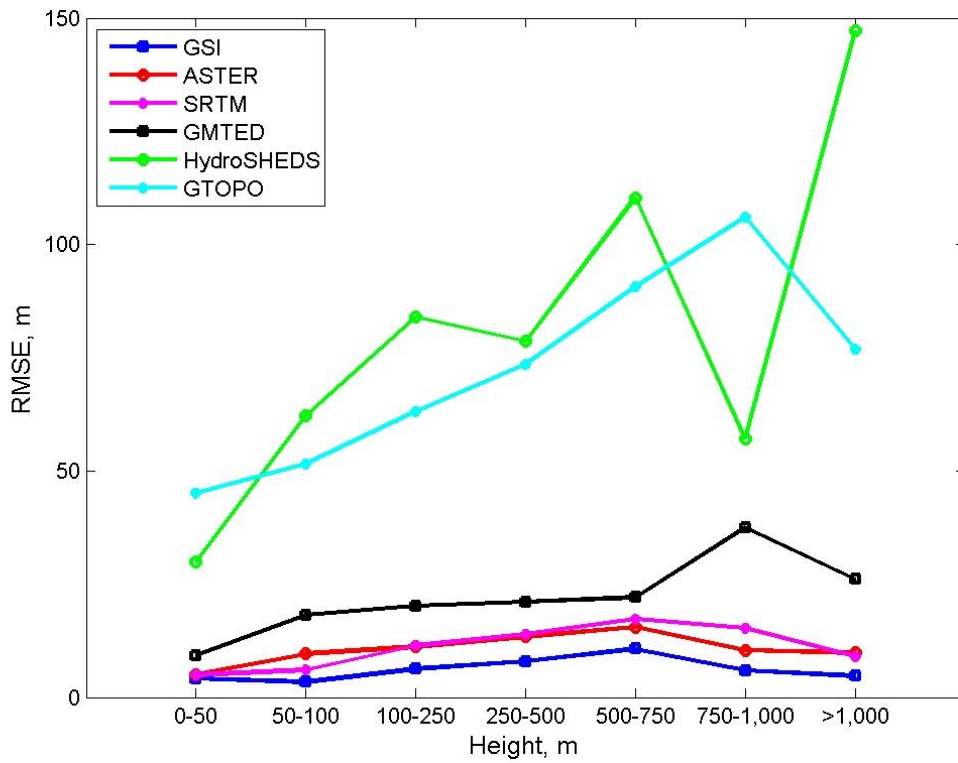
Figure 3-16 Vertical accuracy represented by RMSE of the DEMs relate to the terrain morphology
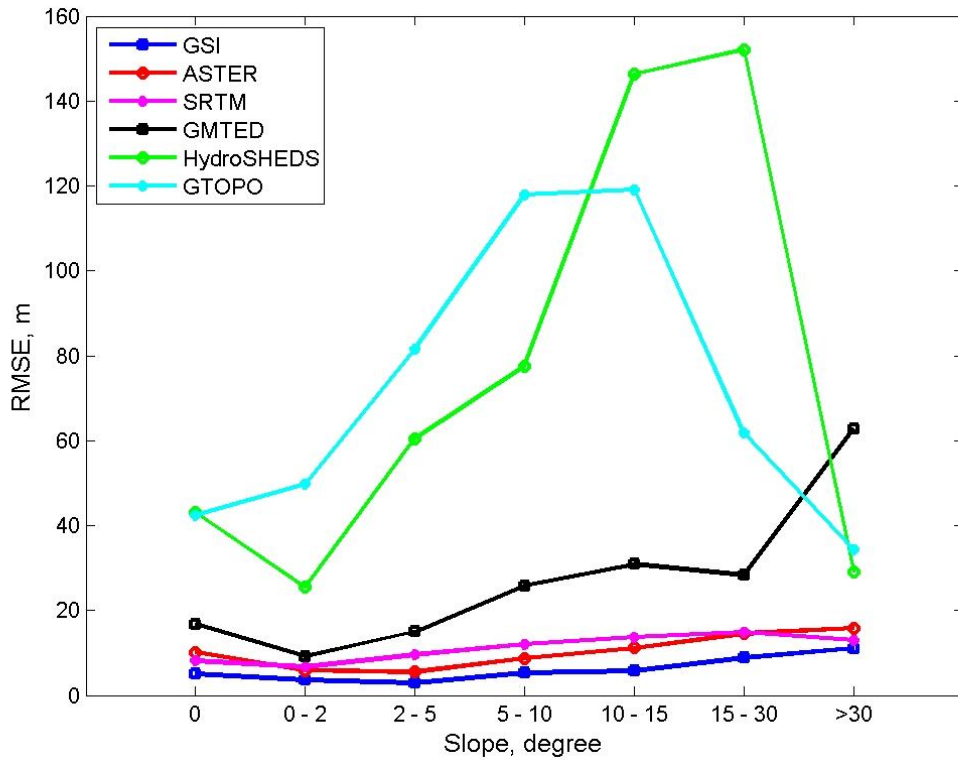
Figure 3-17 Vertical accuracy represented by RMSE of the DEMs relate to the terrain's slope

3.3.4 Effect of land cover in the DEM accuracy

The land cover effect on the vertical accuracy is estimated into 6 classification types for each DEM. The performances statistical were shown in **Table 3-7** for each land cover type and different DEM source. The NSE, PCC and PBIAS was the highest correlation in traffic type, and lowest in forest type. Interestingly, GTOPO30 provided more accuracy than HydroSHEDS on farm and water type because of the stream burning process on the HydroSHEDS (Lehner, 2013). The RMSE of vertical value of each DEM source and in each the land cover type was estimated to show in **Figure 3-18**. The effect of land cover on the vertical accuracy affected to the RMSE value that all the DEM data were the highest error in the forest area. The highest error occurred in the forest area because it normally located in the mountain area represented by complex terrain. The top of canopy have normally affected to the sensor (Jason and Edward, 2006; Lees et al, 2008; Athmania and Achour, 2014). The highest accuracy was the traffic type for the fine resolution, while the coarse resolution was the urban area.

The GSI DEM and ASTER GDEM provided the highest accuracy on the traffic type, followed by paddy, water, farm, urban, and forest. For the SRTM, the urban type outperformed the farm type, while the urban type of GMTED2010 performed better than other four types (paddy, water, farm, and forest). On the coarse resolution, the GTOPO30 provided more accuracy compared to HydroSHEDS, but in the urban and paddy the HydroSHEDS was still higher.
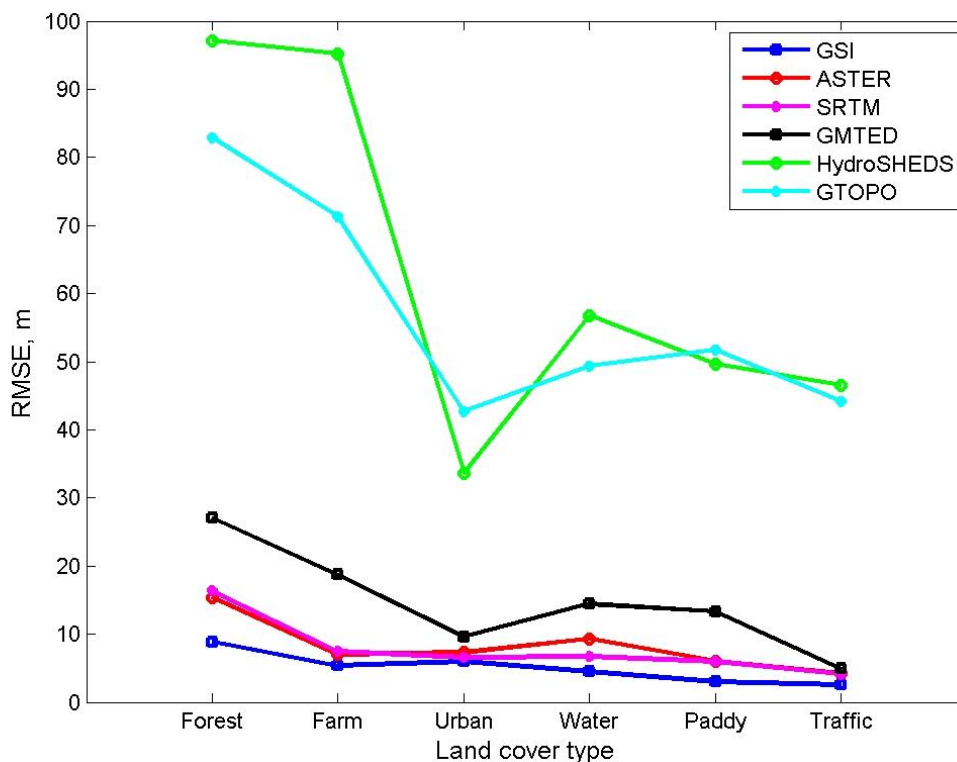
Figure 3-18 Vertical accuracy represented by RMSE of the DEMs relate to the land cover type

Table 3-7 Statistical summaries of the DEM products analyzed on the land cover- based classification

DEM Product/Classification		NSE	PCC	RMSE	PBIAS
Forest	GSI	0.9994	0.9997	8.9535	0.1938
	ASTER	0.9981	0.9994	15.5133	2.2879
	SRTM	0.9978	0.9992	16.7109	2.0361
	GMTED	0.9942	0.9975	26.9229	2.6413
	HydroSHEDS	0.9234	0.9775	97.6392	15.7057
	GTOPO	0.9424	0.9798	84.6737	11.7012
Farm	GSI	0.9994	0.9997	5.5293	-0.4732
	ASTER	0.9990	0.9995	7.3220	0.7663
	SRTM	0.9990	0.9996	7.2629	1.5411
	GMTED	0.9927	0.9972	20.1260	4.3839
	HydroSHEDS	0.8540	0.9595	89.7383	28.5335
	GTOPO	0.9190	0.9801	66.8484	24.3474
Urban	GSI	0.9977	0.9989	6.1304	0.1821
	ASTER	0.9962	0.9982	7.7319	1.7601
	SRTM	0.9968	0.9987	7.1051	2.1080
	GMTED	0.9894	0.9960	13.1341	5.4786
	HydroSHEDS	0.8722	0.9777	45.3762	26.3714
	GTOPO	0.8749	0.9809	44.7584	35.1865
Water	GSI	0.9996	0.9998	4.4070	-1.4315
	ASTER	0.9982	0.9992	9.2579	1.8936
	SRTM	0.9991	0.9996	6.6596	-1.0894
	GMTED	0.9968	0.9985	12.1854	1.2264
	HydroSHEDS	0.9296	0.9821	57.5585	26.4054
	GTOPO	0.9484	0.9854	49.2942	22.4215
Paddy	GSI	0.9995	0.9998	2.8777	-0.0643
	ASTER	0.9980	0.9990	5.9011	-0.0902
	SRTM	0.9982	0.9994	5.5937	2.5465
	GMTED	0.9910	0.9965	12.6808	4.7696
	HydroSHEDS	0.8619	0.9620	49.6138	24.3767
	GTOPO	0.8506	0.9812	51.6635	36.7302
Traffic	GSI	1.0000	1.0000	1.8297	-0.3446
	ASTER	0.9998	1.0000	5.3136	1.6208
	SRTM	0.9999	1.0000	4.3842	1.4892
	GMTED	0.9993	0.9997	12.1355	2.2773
	HydroSHEDS	0.9858	0.9954	51.5535	3.1975
	GTOPO	0.9881	0.9952	45.6667	10.0445

3.3.5 Evaluation of the river network

The river network generated from the six DEMs that the 8D algorithm was used in the generating. The generated river network lines were compared with the observed river line for evaluating the best fit on stream line model. After flow direction was estimated on the D8 algorithm, flow accumulate was generated by the upstream pixels. The river network line used the flow accumulate value to identify the stream line. The threshold watershed area used to draw the stream line was about 0.03 km^2 that have reported from the literature review (Mukherjee et al., 2013). **Figure 3-19** presented a comparison between estimated river line from the candidate DEM and observed river line. The comparison results showed that the fine resolution delineated river lines were seen as smoother than the stream lines come from the coarse resolution DEM.

In order to measure the length between referenced river line and each estimated river line, the buffer around the referenced line was created on 5 zones (0-10m, 10-50m, 50-100m, 100-200m, and >200m) in this study. The 0-10m zone revealed the highest accuracy, while the lowest accuracy was the >200m zone. **Table 3-8** presented the accuracy of estimated river network come from the different DEM. The GSI DEM was the highest accuracy with 44.7% in the 0-10m zone, followed by ASTER GDEM, SRTM, GMTED2010, HydroSHEDS and GTOPO30. The ASTER GDEM, SRTM and GMTED2010 were still in the 10-50m zone with the maximum percentage, while the HydroSHEDS and GTOPO30 were still in the >200m zone.

Table 3-8 the comparisons table of simulation and observation river network dataset

DEM	0 - 10m	10 - 50m	50 - 100m	100 - 200m	> 200m
GSI-DEM	44.7%	29.5%	18.2%	5.6%	2.0%
ASTER	16.5%	49.7%	17.3%	8.0%	8.5%
SRTM	11.0%	39.9%	28.0%	8.7%	12.4%
GMTED2010	10.4%	36.4%	26.6%	13.3%	13.3%
HydroSHEDS	4.6%	17.1%	22.8%	23.9%	31.5%
GTOPO30	4.0%	15.7%	8.3%	36.4%	35.6%
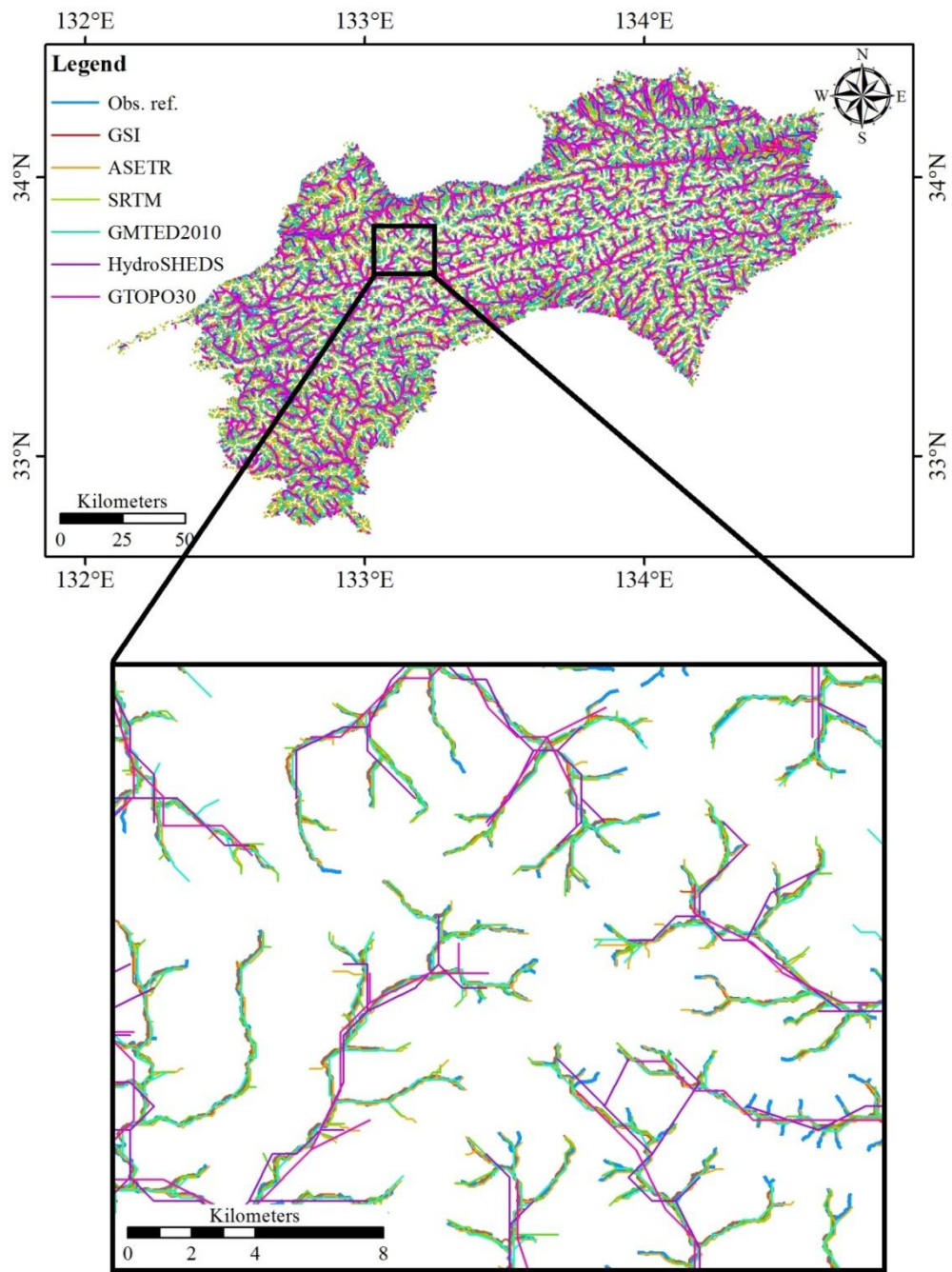
Figure 3-19 Comparison of the river network generated from the DEMs with actual river line

3.3.6 DEMs bias correction

A Linear transformation approach was applied in this study and it used to correct for shifting the bias between DEM and GCP. The inverse matrix algorithm (Marsh, 2015) was used to obtain an optimized value (see **Table 3-9**) for $a, b, c,$ and Z_0 of each DEM for bias correction. The a parameter of GMTED is a positive value while five DEMs is a negative value between -0.07 and -10.91. All of the DEM sources b parameter is a positive value in the range 0.34 to 23.84, and c parameter is also the positive values are close to 1. The Z_0 is the positive value on GSI-DEM, ASTER, and HydroSHEDS, while this parameter of SRTM, GMTED2010 and GTOPO30 is the negative value. According to the value of the parameter from this transformation, the coordinate of the pixel has a relationship with the elevation based on the variation of parameter a and b. Elevation all pixels in each DEM was recalculated by using the bias correction parameter.

After re-computation with transformation parameter, the comparison of the accuracy of all DEMs was recalculated (see **Table 3-10**) and **Figure 3-20** presented the reconstructed DEMs. **Figure 3-21** shows a histogram of the modified DEM as six datasets that transformed to return a better accuracy than existing data set. The modified DEMs present a mean error close to zero, indicating that these data sets are unbiased. **Figure 3-22** reveal the difference between existing and modified DEM based on MAE. **Figure 3-23** presents the difference between existing and modified DEM based on RMSE. The transformation approach greatly increased the accuracy of all DEM. The RMSE value is improved by 0.099 m for GSI-DEM (-1.66%), 0.85 m for ASTER (-8.55%) and 0.77 m for SRTM (-7.66%). The RMSE measured for differences of GMTED2010 is 1.48 m (-8.21%), while this value for HydroSHEDS is 15.31 m (-22.29%) and 15.93 m (-25.74%) for GTOPO30. The GSI-DEM is more accuracy than five DEMs model for all validation sources, but it is published only in Japan region. For the international source, the ASTER shows the best accuracy, while GTOPO30 is more accuracy than HydroSHEDS to compare with coarse resolution.

The assessment of vertical accuracy of the five international DEMs exposes that the ASTER data displays a better vertical accuracy than the four DEM. The accuracy of ASTER is better than SRTM, which has been marked in previous studies. ASTER gives better accuracy and those results were concluded (see **Table 3-4**) that were mentioned by Mukherjee et al. (2013). On the other hand, the large variations in global height precision are found in the examined DEMs literature. It shows that the DEMs on vertical precision depend on location, errors of reference point, terrain characteristics, and surface properties. Hence, this recommendation performs to an investigation about those factors. In addition, **Table 3-10** exposes that the RMSE value of 9.3 m for SRTM are very similar to those described by Mukherjee et al. (2013). The ASTER GDEM presents the RMSE value about 9.08 m to close with Athmania and Achour (2014). According to the international DEMs, this study reports that

the SRTM is lower accuracy to compare with ASTER and GMTED2010 for a fine resolution while a coarse resolution GTOPO30 is higher accuracy than HydroSHEDS pixel size of 15 arc-second.

Table 3-9 Parameter of affine transformation based on multiple linear regressions for bias correction

DEMs	a	b	c	Z_0
GSI	-1.830	3.523	0.999	125.963
ASTER	-3.188	3.629	0.993	301.737
SRTM	-0.187	1.304	0.996	-21.741
GMTED	0.467	0.341	0.991	-78.566
HydroSHEDS	-10.911	23.842	0.936	628.969
GTOPO	-0.074	7.467	0.976	-276.667

Table 3-10 Difference statistical between before and after bias correction (Units in meters)

DEMs	DEM Bias correction				
	Min	Max	ME	S.D.	RMSE
GSI	-32.69	23.22	-2.96E-10	5.88	5.87
ASTER	-45.66	26.82	-2.16E-09	9.09	9.08
SRTM	-40.72	28.92	-8.80E-10	9.32	9.31
GMTED	-83.74	57.69	1.14E-09	16.55	16.53
HydroSHEDS	-282.13	237.37	1.24E-09	53.43	53.37
GTOPO	-212.03	222.19	-1.60E-11	45.99	45.94
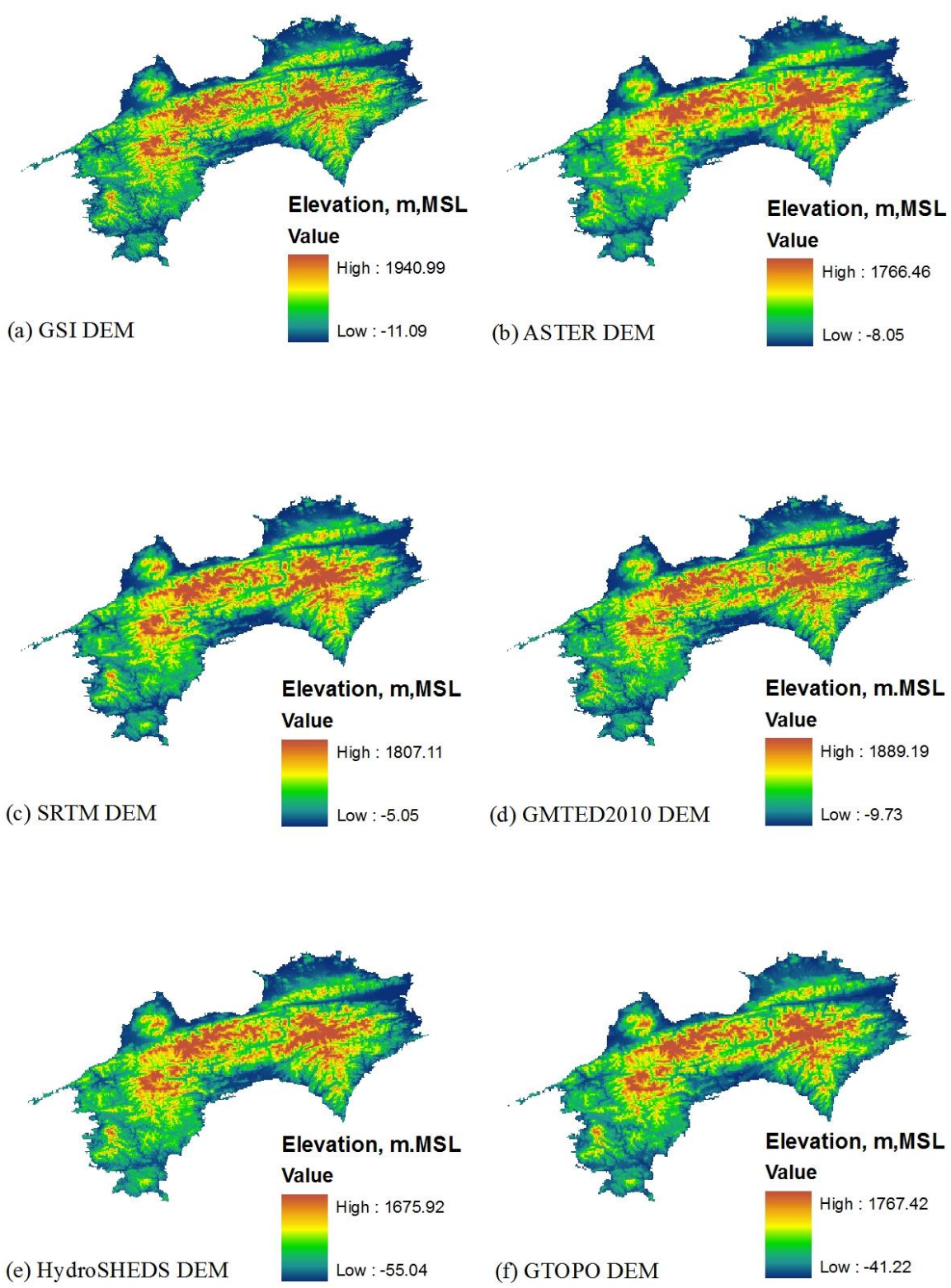
Figure 3-20 The reconstructed DEM based on the liner transformation, a) GSI-DEM; b) ASTER; c) SRTM; d) GMTED2010; e) HydroSHEDS; f) GTOPO30
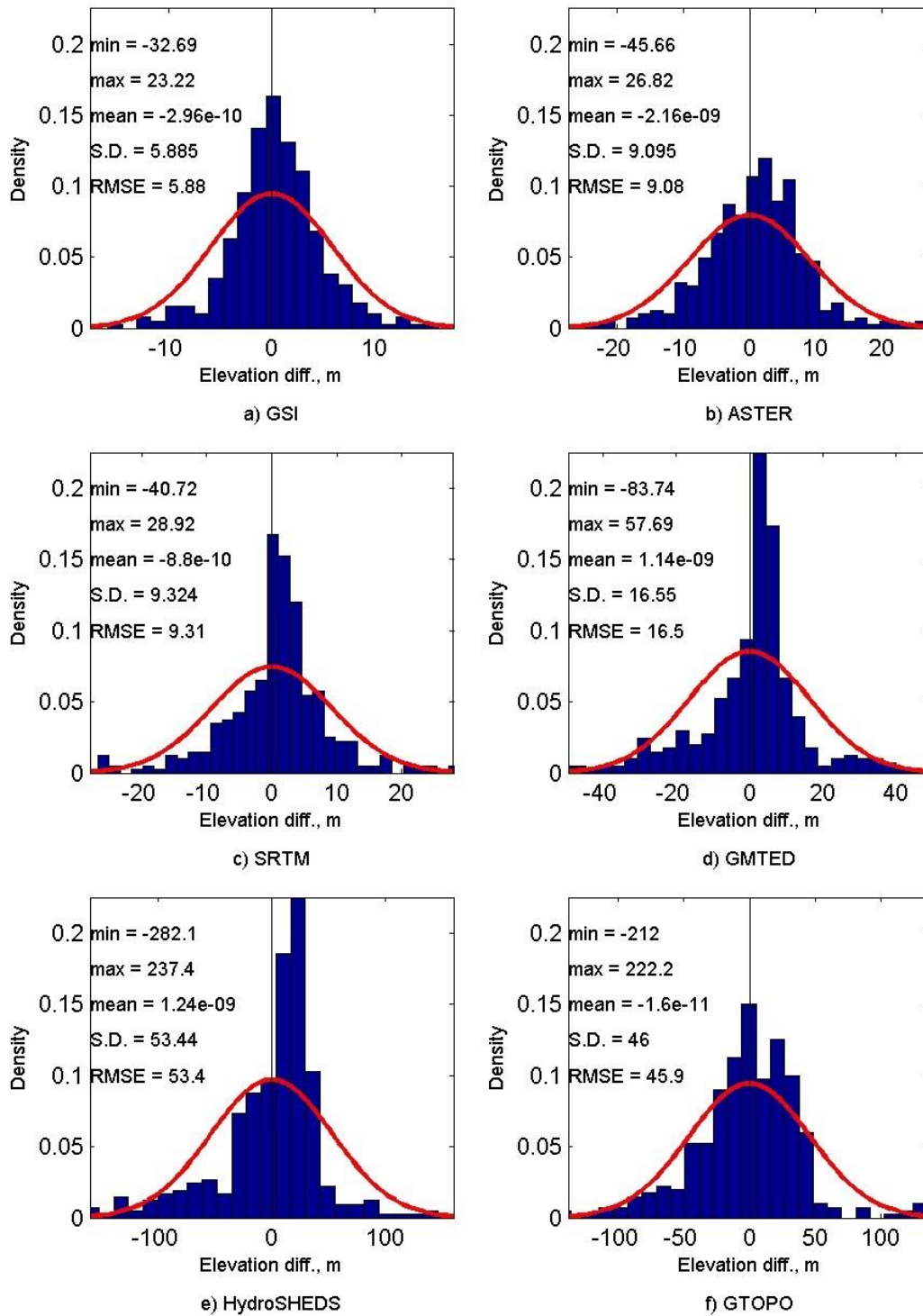
Figure 3-21 Histogram of elevation error and estimated basic statistical after bias correction; a) GSI-DEM; b) ASTER; c) SRTM; d) GMTED2010; e) HydroSHEDS; f) GTOPO30
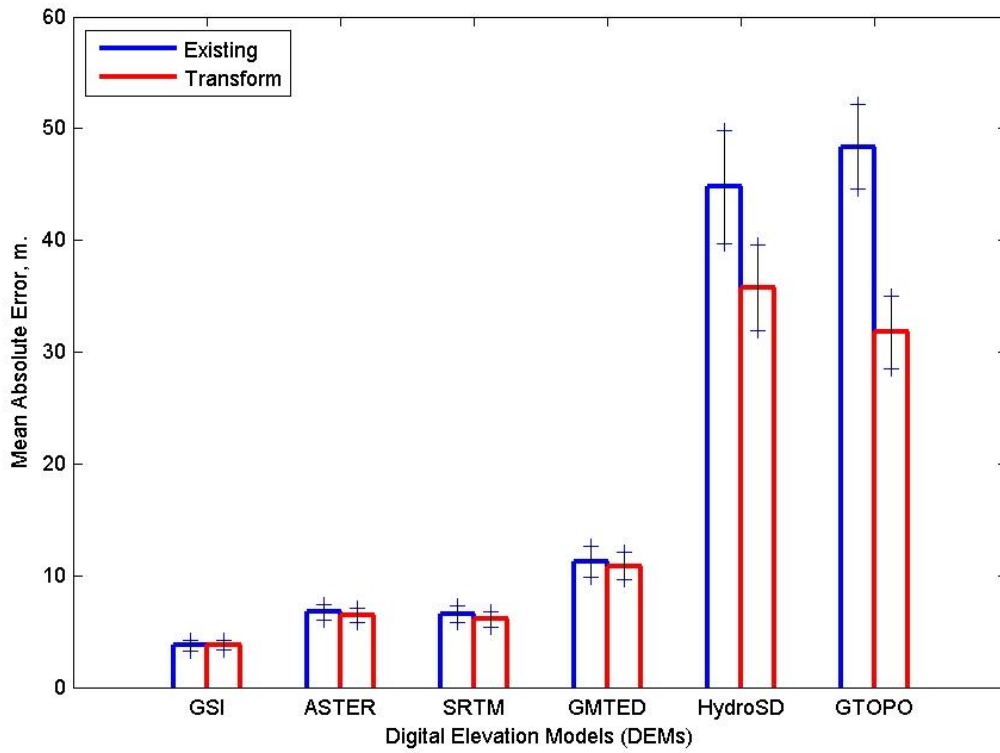
Figure 3-22 Comparison of MAE between before and after bias correction
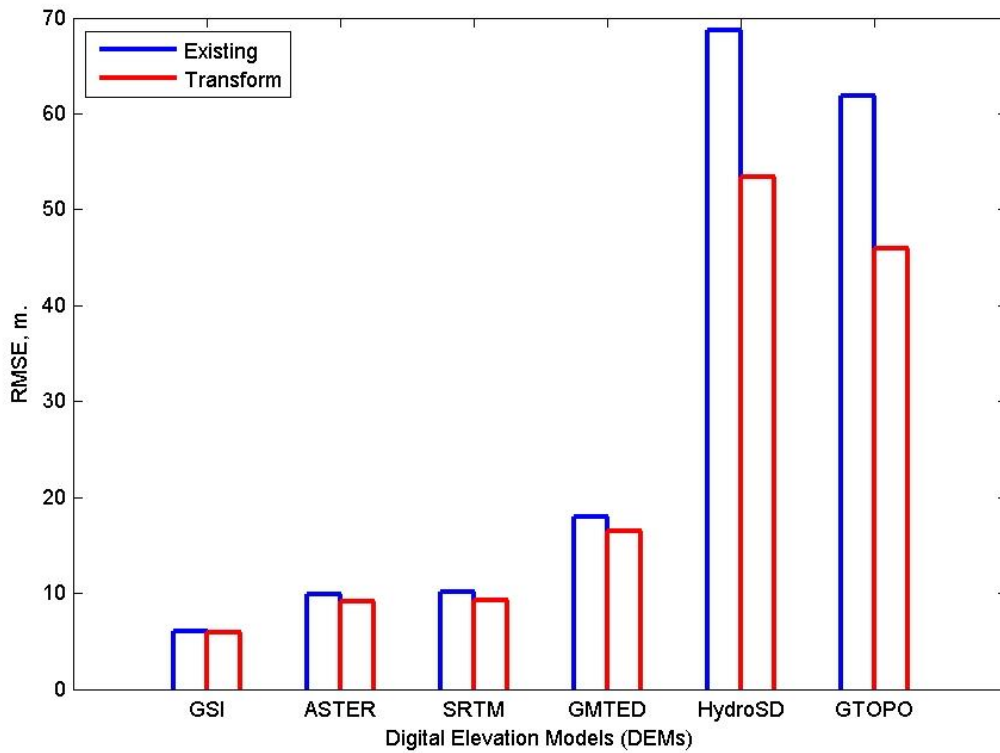
Figure 3-23 Comparison of RMSE between before and after bias correction

3.3.7 Runoff simulation in the Shikoku Island Japan

The hydrological model (RRI model) was driven for flood events in 2014 for Shikoku Island in Japan. The six topography products were simulated at hourly on a temporal scale to match the observed streamflow data. Seven runoff stations were selected in the Shikoku Island (see **Figure 3-24**), the first (Ikeda dam) and second (Chuobashi) belong to the Yoshino River. The third (Furushou) is in the Naka River and the fourth (Fukabuchi) in the downstream area of the Monobe River. The fifth is located in the Ino, belonging to the Noyodo River; the sixth located in the Shimanto River is the Gudoudaini station. The seventh station is the Deai located in the Shigenobu River. All of stations showed in the hourly hydrograph that results from the different topography source. **Figure 3-25** presents the hydrographs for all sources with the seven runoff stations.

All simulated runoff driven by different products was provided as the temporal data similar to the observed hydrograph for the flood event. Over view of all the runoff station, all products symmetrically captured the peak at the same time with the observation, and it systematically underestimated observed runoff. For the third and fourth station, their simulated runoffs were the highest underestimation to compare with the observed hydrograph.

All of seven runoff station on the hourly hydrograph were analysed and calculated for evaluation by the performance statistical. The results are given in **Table 3-11** that is concluded by five indexes. GSI DEM simulated discharge was the best matched by observed runoff with a high Correlation of 0.942 and lowest RMSE of 307.59 cms. This simulated runoff underestimated the runoff volume, peak flow and mean runoff by 2.55%, 31.41% and 7.26 cms, respectively. ASTER DEM simulated runoff was the highest Correlation (0.943) and low RMSE, and its simulated runoff was underestimation in Volume bias of 3.36% and Mean bias of 9.58%. The peak flow of the ASTER DEM underestimated about 33.99%. SRTM DEM simulated runoff was low RMSE value of 312.46 cms with strong correlation value of 0.942, this simulated results underestimated the runoff volume, and mean runoff by 3.74%, 10.67 cms, respectively. The peak flow of the SRTM DEM underestimated about 34.54%. The three products (GMTED2010, HydroSHEDS and GTOPO30) significantly underestimated the runoff volume, mean runoff, and peak flow, with high RMSE and low correlation value.

In summary performance on estimating the streamflow, the best of the DEM products was GSI DEM that statistical presented the best value. The GSI DEM was represented only Japan, while ASTER product was the best performance among the international products.
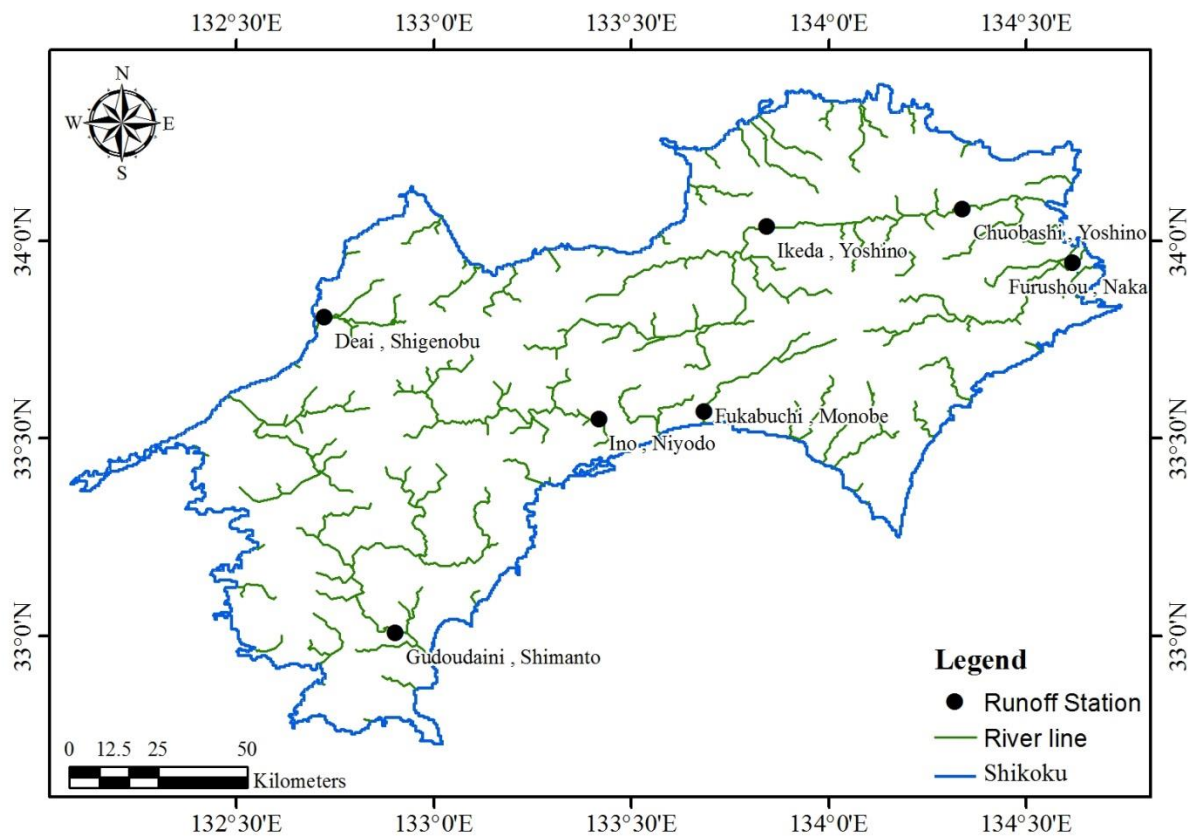
Figure 3-24 Runoff station in the Shikoku Island Japan

Table 3-11 Performance statistical of runoff from the rainfall spatial prediction products

Rainfall products	Volume bias, %	Peak bias, %	RMSE, cms	Correlation	Mean bias, cms
GSI	**-2.55**	**-31.41**	**307.59**	0.942	**-7.26**
ASTER	-3.36	-33.99	310.41	**0.943**	-9.58
SRTM	-3.74	-34.54	312.46	0.942	-10.67
GMTED2010	-4.82	-35.77	320.95	0.938	-9.05
HydroSHEDS	-4.26	-34.22	326.37	0.935	-9.45
GTOPO30	-9.23	-35.32	359.57	0.942	-26.48
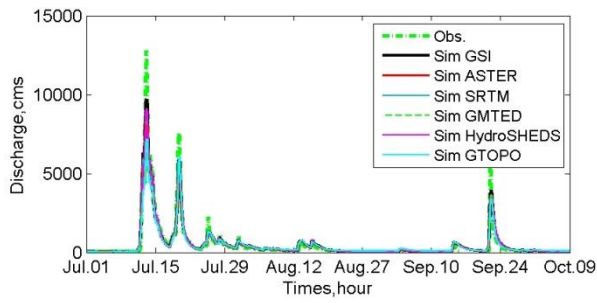
a) Ikeda, Yoshino river
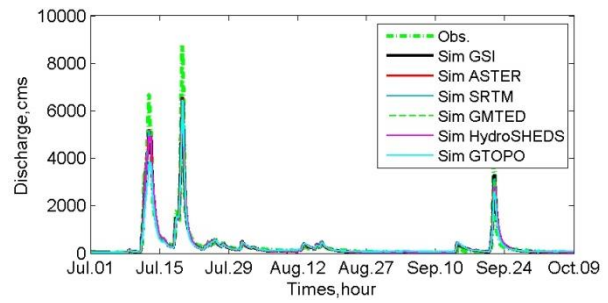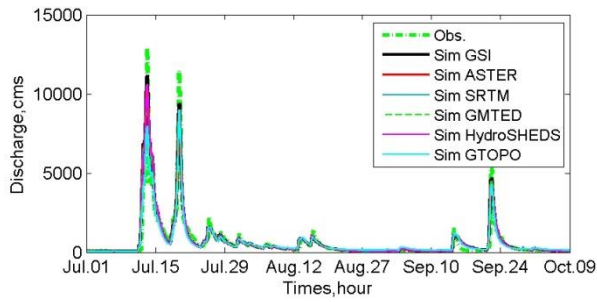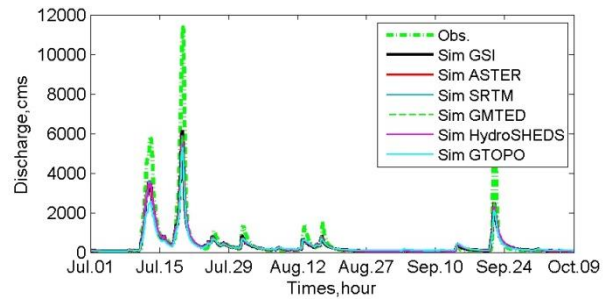
b) Chuobashi, Yoshino river

c) Furushou, Naka river

d) Fukabuchi, Monobe river

e) Ino, Niyodo river

f) Gudoudaini, Shimanto river
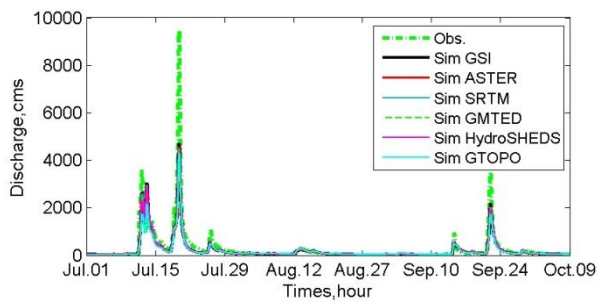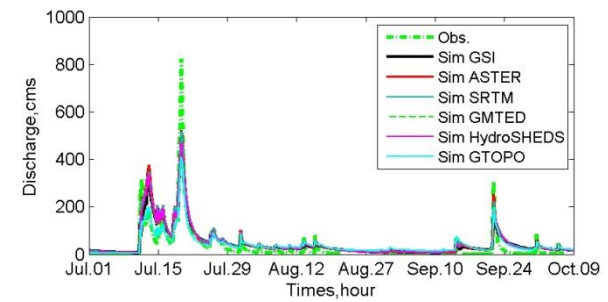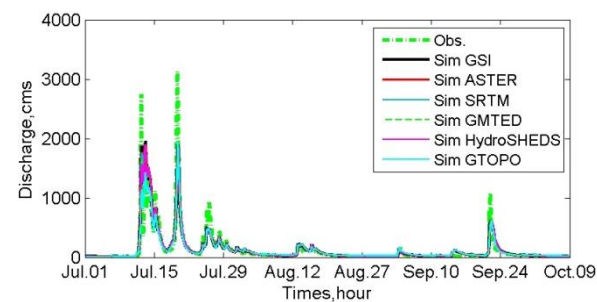
g) Deai, Shigenobu river

Figure 3-25 Hourly discharge hydrograph at runoff observation station of flood event based on different DEM product in the Shikoku Island Japan

3.3.8 Runoff simulation in the Nan river basin

The hydrological model (RRI model) was driven for flood events in 2011 for Nan river basin in Thailand. The five DEM products were simulated at daily on a temporal scale to match the Royal Irrigation Department Thailand observed streamflow data. Three runoff stations were selected in the Nan river basin (see **Figure 3-26**), the first one belonging to the upstream sub-catchment (N.64), the second one belonging to the middle area (N.1) and the third one belonging to the downstream area (N.13A), to show the daily hydrograph that results from the different interpolation scenario. **Figure 3-27** presents the hydrographs for all rainfall products with the three runoff station, N64, N.1 and N.13A.

All simulated runoff driven by different products was to provide the temporal pattern similar to the observed hydrograph for the flood event. Over view of all the runoff station, their results symmetrically captured the peak at the same time with the observation. At peak, ASTER, SRTM and HydroSHEDS DEM systematically overestimated observed runoff, while the other two products (GMTED2010 and GTOPO30 DEM) were underestimation. For N.13A, all patterns of rainfall products were underestimation to compare with the observed hydrograph.

All of three runoff station on the daily hydrograph were analysed and calculated for evaluation by the performance statistical. The results are given in **Table 3-12** that is concluded by five statistical. GMTED2010 DEM simulated discharge was the best matched by observed runoff with a highest Correlation of 0.885 and lowest RMSE of 381.75 cms. This simulated runoff underestimated the runoff volume, peak flow and mean runoff by 4.85%, 2.05% and 35.03 cms, respectively. SRTM DEM simulated runoff was high Correlation (0.882) and low RMSE (382.04 cms), however, its simulated runoff was overestimation of peak flow of 15.06%. Volume bias about 13.27% and Mean bias about 55.84%, both of the SRTM DEM were underestimation. ASTER DEM simulated runoff was low RMSE value of 405.29 cms with strong correlation value of 0.862, this simulated results overestimated the runoff volume, and mean runoff by 6.44%, 46.51 cms, respectively. The peak flow of the ASTER DEM overestimated about 17.72%. The two products (HydroSHEDS and GTOPO30) significantly underestimated the runoff volume, and mean runoff with high RMSE and low correlation value, but the peak of HydroSHEDS was overestimation.

In summary performance on estimating the streamflow, the best of the DEM products was GMTED2010 that statistical presented the best statistic value. The GMTED2010 product was represented on the highest performance products, while SRTM product was the second highest performance among the five products.
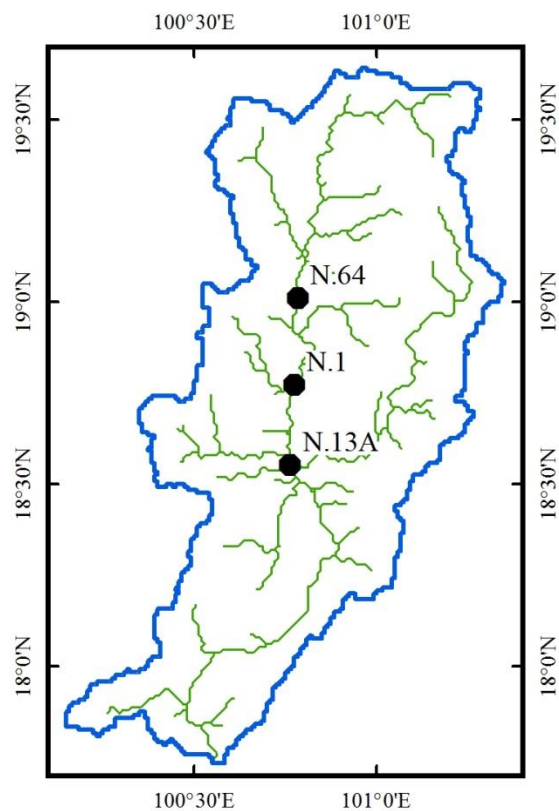
Figure 3-26 Runoff station in the Nan river basin Thailand

Table 3-12 Performance statistical of runoff from the rainfall spatial prediction products

Rainfall products	Volume bias, %	Peak bias, %	RMSE, cms	Correlation	Mean bias, cms
ASTER	-6.44	17.72	405.29	0.862	-46.51
SRTM	<u>-5.36</u>	<u>15.06</u>	<u>382.04</u>	<u>0.882</u>	<u>-38.72</u>
GMTED2010	**-4.85**	**-2.05**	**381.75**	**0.885**	**-35.03**
HydroSHEDS	-10.08	27.62	473.48	0.800	-72.73
GTOPO30	-22.18	-18.47	577.87	0.741	-160.11
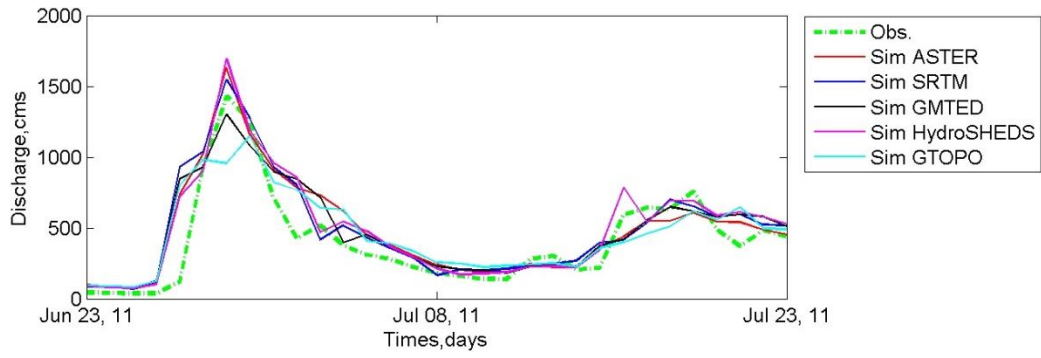
a) N.64
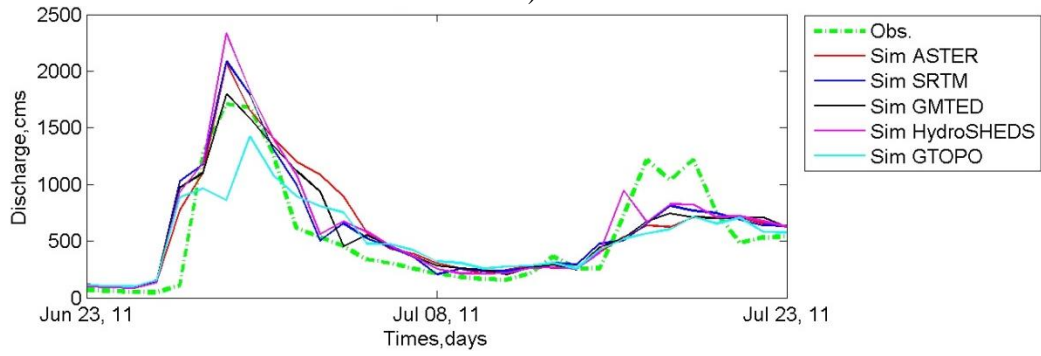
b) N.1
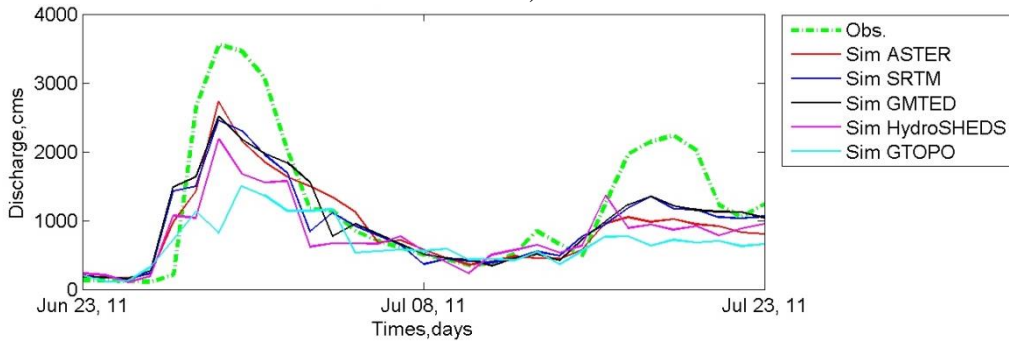
c) N.13A

Figure 3-27 Daily discharge hydrograph at runoff observation station of flood event based on satellite base rainfall products

3.3.9 Inundation map from the different DEM sources

The RRI model was run in 2011 for Nan river basin in Thailand. The five DEM products were implemented for inundation map estimation at daily scale. MODIS satellite data were selected at June 27 in 2011 to evaluate the inundation results. **Figure 3-28** presents the MODIS data that inundation area was selected between 2 stations, N.1 and N.13A. The referent inundation map form MODIS is about 62.25 km^2. **Figure 3-29** presented the inundation resulted from the different DEM source. **Table 3-13** summarized a value of the simulated inundation area. The close value of inundation area was SRTM DEM that had a different about 10% and followed by GMTED2010, ASTER, GTOPO30, and HydroSHEDS.

In the detail to find the best DEM source, the accuracy of simulated inundations were measured by using POD, FAR, CSI, and ACC. **Table 3-14** showed detection inundation on pixel to pixel between referred map (MODIS) and simulated map. The detection parameters were Hit, Miss, False, and Reject that were used to estimate an accuracy of the simulation. Based on the **Table 3-14,** that presented accuracy assessment of the simulated inundation map for each DEM sources. SRTM DEM showed the highest performance among the four DEMs with high value of POD and CSI, and its FAR was the lowest. ACC of the SRTM DEM was about 0.846 to identify as the highest precision.
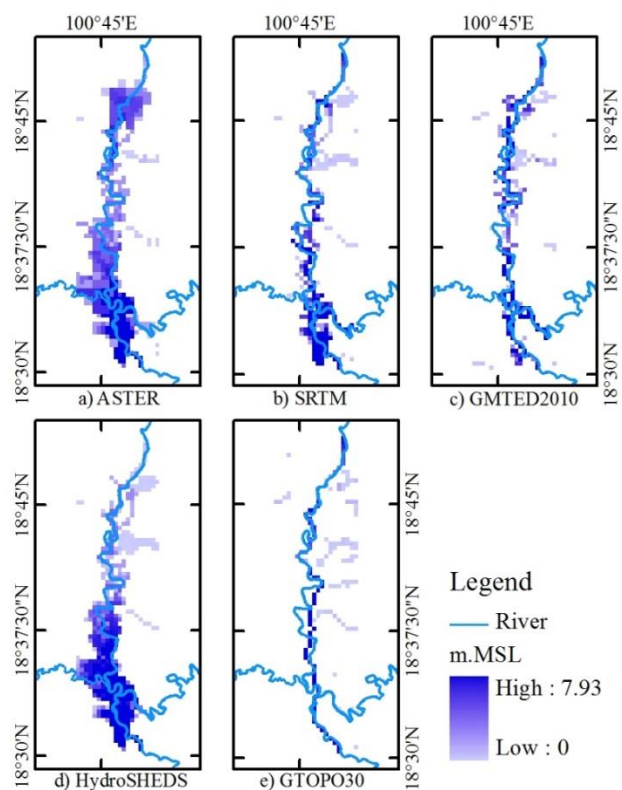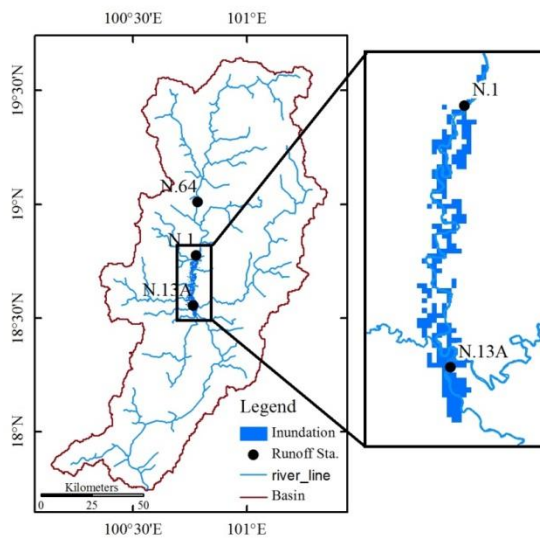
Figure 3-28 Reference inundation map based on MODIS on June 27, 2011   **Figure 3-29** Inundation area in each DEM products

Table 3-13 Total inundation area within each DEM products

Data product	Inundation area, km^2
MODIS	**62.25**
ASTER	81.25
SRTM	**55.50**
GMTED2010	49.25
HydroSHEDS	96.75
GTOPO30	37.75

Table 3-14 Detected Inundation on pixel by pixel between satellite and simulation data, and accuracy assessment of inundation map based on each DEM products

DEM	Hit	Miss	False	Reject	POD	FAR	CSI	ACC
ASTER	138	111	181	976	0.554	0.567	0.321	0.817
SRTM	127	122	94	1,063	0.510	0.425	0.370	**0.846**
GMTED2010	100	149	97	1,060	0.402	0.492	0.289	0.825
HydroSHEDS	185	64	196	961	0.743	0.514	0.416	0.815
GTOPO30	41	208	50	1,107	0.165	0.549	0.137	0.792

3.4 Conclusion

This chapter assessed the vertical accuracy of six DEMs (GSI DEM, ASTER GDEM, SRTM, GMTED2010, HydroSHEDS, and GTOPO30) on the Shikoku Island in Japan, all of which are open source data. The validation was operated by the GCPs with matching coordinate to compare the elevation value. The impacts of terrain morphology and land cover properties were analyzed. The river networks estimated from six DEMs were evaluated.

First, the DEMs characteristics were described on basically. Then, the six DEMs were presented with vertical accuracy estimated from the difference elevation. Finally, DEM accuracy was analyzed on the statistical approach. For the accuracy assessment, the statistical approach was based on the four performance parameters, scatter plot, and histogram of error that were investigated. The investigation revealed that the GSI DEM provided the highest accuracy, followed by ASTER GDEM, SRTM, GMTED2010, GTOPO30, and HydroSHEDS, in overall. Interestingly, the GTOPO30 provided higher accuracy than the HydroSHEDS, with lower definition.

Effect of terrain morphology in the vertical accuracy of the DEMs was assessed by using altitudinal range and slope range. The altitudinal have affect to the vertical accuracy presented by the RMSE value. The DEM was more error until altitudinal zone in range about 500 – 750 m, after that the error was drop down among the fine resolution. For the coarse resolution, the HydroSHED have error drop down at range about 700 – 1,000 m, while the GTOPO30 presented the drop down of error at the highest range. The slope effect was revealed by the relationship between RMSE value and slope range. The fine resolution DEMs was more error in the higher slope range. By the contrast, the coarse resolution provided the slope effect on the 0 – 15 degree, after that the error was drop down in the steepest slope.

In this study, land cover was divided into 6 types and the DEMs in each type were evaluated on the vertical accuracy. All the DEM data had the lowest accuracy in the forest area because of the top of canopy affected to the sensor (Athmania and Achour, 2014). The highest accuracy was the traffic type for the fine resolution, while the coarse resolution was the urban area. Due to the upscaling processes, the fine resolution and coarse resolution got the difference on the highest accuracy (Li et al., 2006).

In conclusion, this study presented the key of validation DEM on the statistical approach. It also described the spatial information of DEM accuracy for various terrain morphology and land cover. Further study might be implemented to correct the vertical accuracy of provided free DEM and to find the methodology for making a high accuracy on river stream line.

In the second objective of this study, that examined the quality of six digital elevation models GSI-DEM, ASTER, SRTM, GMTED2010, HydroSHEDS and GTOPO30 over the Shikoku Island in Japan, all of which are available free published data. From the first, the basic characteristics of the DEMs were described. Then, comparisons of the six DEMs were presented with vertical accuracy that was estimated by using GPS reference data (GCPs). On the bias correction, DEM differences were discussed from the statistical assessment. For the evaluation of the accuracy, statistical approaches based on histograms and Q-Q plots were presented and the error characteristics in six sources of DEM were investigated. After bias correction using a geometrics linear transformation, the validation statistics were recomputed for each DEM. The results for RMSE of terrain elevation are 5.87 m for GSI-DEM with GCPs on high definition resolution. For the fine resolution, the RMSE is 9.08 m for the ASTER, 9.31 for the SRTM and 16.53 m for GMTED2010. The RMSE of coarse resolution DEM is 53.37 m for HydroSHEDS and 45.94 m for GTOPO30. For all DEM sources, the transformed results suggest to unbias altitudes based on the mean error value. This transformation could increase more accuracy responding in the coarse resolution, while the high resolution was a little impact.

The evaluation of six DEM products (GSI, ASTER, SRTM, GMTED2010, HydroSHEDS and GTOPO30) was input to the physical-based hydrological model (RRI model) over the Shikoku Island

Japan and the Nan river basin Thailand. According to the aim of this study used the flood event for estimating the streamflow to evaluate the performance of each product. The simulation of the streamflow was done by using without a calibration of the hydrologic parameter to specific product. The streamflow were simulated and reported at hourly to match with the MLIT observed runoff and daily to match with the RID observed runoff.

For the Shikoku Island, GSI DEM demonstrated to be the best product to model a streamflow for flood event on 2014. The simulated runoff of ASTER also closed to the observed dataset; however, it underestimated the runoff volume, mean runoff, and peak flow. The four DEM (SRTM, GMTED2010, HydroSHEDS and GTOPO30 also underestimation the runoff volumes, mean runoff, and peak flow. In conclusion, the GSI DEM simulation was the best performance DEM product for hydrological modeling to estimate the runoff, representing with the high resolution products. However, the ASTER was the best among the international products.

The Nan river basin in Thailand used only the international DEM sources for evaluation on runoff simulation in 2011. GMTED2010 DEM demonstrated to be the best product to model a streamflow for flood event with underestimation on the runoff volume and mean runoff. The simulated runoff of SRTM also closed to the observed dataset; however, it overestimated the peak flow. The three DEM (ASTER, HydroSHEDS and GTOPO30 also underestimation the runoff volumes and mean runoff. In conclusion, the GMTED2010 DEM simulation was the best performance DEM product for hydrological modeling to estimate the runoff on the river basin scale. However, the SRTM was the second performance among the international products. For the simulated inundation map comparison, the SRTM presented the highest accuracy among the five DEM products. The evaluation accuracy of inundation map used the MODIS data for referent data.

Based on the DEM data and simulation results, Shikoku is the mountain complex terrain to contain with a steep slope, while Nan river basin is the mountain area where represent with the mild slope. In the Shikoku Island, ASTER DEM is suitable to apply for runoff simulation using distributed hydrologic modeling, have estimated from stereo matching. SRTM presented a performance for runoff and inundation simulation in the Nan river basin, have explored from radar laser scan with Shuttle.

Chapter 4 Estimation of surface roughness based on land cover datasets and their effect on

Distributed Rainfall-Runoff simulation.

4.1 Introduction

Floods are one kind of natural disasters causing human life and economic losses. Approximately 66% of water related disasters in the world are floods (WWC, 2000). Nowadays, impacts of floods have been increased because of population growth, decreasing of floods plain, and climate change. Mitigation impacts of floods are implementation of structural and non-structural scheme (Bedient et al., 2008; USEOP, 1994). The major tools firstly used for planning and developing structural and non-structural flood mitigation and management approaches are Hydrologic and hydraulic models (Jin and Fread, 1997; Hokr et al., 2003). Mathematic models of floods have been established from peak flow estimation schemes with multi dimension, multi-scale distributed simulations able of demonstrating the spatial and temporal variation of floods runoff over a river basin surface (Singh and Woolhiser, 2002). According to the floods model in historical, hydraulic roughness is a main parameter for analysis floods (Kidson et al., 2006; Sellin et al., 2003; Marcus et al., 1992). The Manning equation has been implemented in several models to relate surface roughness to flow rate that the Manning's roughness coefficient (n) is used for hydraulic roughness of the models. Manning coefficient (n) is empirical parameter normally used for gravity, uniform flow in open channel flow analysis (Gioia and Bombardelli, 2002). The resistance of surface flow uses the land surface for modeling in most of the used hydrologic and hydraulic models such as HEC (HMS and RAS) (Feldman, 1981; HEC, 1981, 2000), SHE (Abbott et al., 1986), EPA SWMM (Metcalf and Eddy et al., 1971; Huber and Dickinson, 1988; Huber, 1995), LISFLOOD (De Roo et al., 2000), and RRI model (Sayama et al., 2012).

The performance of hydrologic models is improved by the estimation accuracy of Manning's coefficient (Wu et al., 1999; Jain et al., 2004). However, the influence of physical characteristics and types of surface materials such as hydraulic conductivity, moisture content, and surface density that quantification is difficult because of its natural processes of empirical. In the indirect definition, the Manning's coefficient is related to surface friction resistance, surface form, and wave resistances of unsteady flow (Manning, 1891; Kalyanapu, 2009). Moreover, Manning's coefficient approximation is subjective as the roughness of surface is depended on the granular characteristic of surface in multifaceted interactions because of the elevation change, surface irregularity, flow depth, vegetation density, scale, and obstructions (Arcement and Schneider, 1990, Vieux, 2001, Jain et al., 2004). However, because of its natural processes of empirical and estimate approximation methods, the exact approximation of Manning's coefficient is unreasonable (Kidson et al., 2006).

. This chapter is based on:

1. K. Pakoksung, M. Takagi, 2016, Effect of Land Cover-based Surface roughness on Distributed Rainfall-Runoff Model Results: (in **preparing**).

The selecting values of Manning coefficient is difficult to identify as simplification processes but numerous scientific consideration practiced in a standard data (Arcement and Schneider, 1990; Wu et al. 1999; Tsihrintzis, 2001; Jain et al., 2004). Estimating Manning's coefficient is a state of the art on experiment and consideration (Limerinos, 1970; Philips and Tadayon, 2006). The state of the art on estimating is improved from several such as experiment, field, and numerical approaches to present for determining the Manning's coefficient (Urquhart, 1975; Stevens et al., 1983; Ugarte and Madrid, 1994; Das, 2004; Abood et al., 2006). One differential among methods is that it is proposed for implementation in river, flood plain, or basin surfaces. Several interest of Manning's coefficient estimation has been specified on river channels, even though some studies have been focused on flood plain and basin surfaces. Geographic Information System (GIS) and Remote Sensing (RS) approach can be used to categorize for estimation methods (Arcement and Schneider, 1990 and Sellin et al., 2003). The approach (GIS and RS) is widely used that have begun to define Manning's coefficient powerfully for the large scale using look-up table and extrapolation with a numerical relationships (Finn et al., 2002). The GIS and RS method is presently the recommendation method for the large area application in rapidly (Hornberger and Boyer, 1995; Paniconi et al., 1999). Hydrologic modeling at currently state is practically with distributed hydrologic modeling based on spatial grid approach that is done by acquiring a digital land cover data sets (such as satellite based data) and assigning Manning's coefficient values in a GIS using Manning's coefficient values obtainable in the literature based on a look-up table (Vieux, 2001; Burian et al., 2002). One of the normally used satellite based land cover data sets is Moderate Resolution Imaging Spectroradiometer (MODIS) and Advanced Very High Resolution Radiometer (AVHRR).

The objective of the chapter presented in this dissertation is to assess the error presented into hydrologic modeling results when using the satellite based land cover data sets for estimating Manning's coefficient for surface roughness in the river basin scale. The impact of generating a Manning's coefficient map from the satellite sources are presented from comparison to the referent land cover map that is lack of the study to archive from the literature. This study presented a comparison of Manning's coefficient maps to estimate the uncertainty created in distributed hydrologic modeling simulation.

4.2 Data and Methodology

4.2.1 Land cover referent map and land cover based satellite data sources

In this study, two data sources (MODIS and AVHRR) are selected to evaluate Manning's coefficient with a look-up table. The study is performed on 18,000 km^2 area of the Shikoku Island in the southern of Japan and 13,000 km^2 catchment of the Nan river basin in the northern part of Thailand.

Figure 4-1 present the Shikoku area with its land cover distribution. The area is mostly mountain area with relatively steep slopes. The land cover types (12 categorizes) in the area as shown in **Table 4-1** are paddy, agricultural, forest, bare land, urban, water and grass. Topography causes surface runoff to flow from the central area towards downstream in a border area of Island. More than 79% of the Island is the forest area, 11% is the agricultural area (paddy and farm), and 10% is developed and open area (build-up land, transportation area, grass, water and bare land). The 18,000 sq.km area is selected to provide a numerous of land covers.

Land cover distribution in **Figure 4-2** is presented for the Nan river basin. The area is mostly mountain area with relatively mild slopes. The land cover types (15 categorizes) in the watershed as shown in **Table 4-2** are farm, paddy, agricultural, perennial, orchard, horticulture, swidden cultivation, pasture, aquaculture land, forest, deforestation, miscellaneous land, swamp, urban and water. Topography causes surface runoff to flow from the northern area towards southern area where downstream is the SIRIKIT reservoir. More than 70% of the watershed is the forest area, 25% is the agricultural area, and 5% is developed and open area (Build-up land, deforestation, miscellaneous and water). The 13,000 sq.km area is selected to provide a numerous of land covers.

The two satellite based land cover products were used in this study. **Table 4-3** shows the information of the satellite based land cover. The accuracy of each product was assessed as area based value and pixel by pixel based to evaluate with the referent land cover map. Using the three products (referent, MODIS and AVHRR) as input to the RRI model, their outputs have performed an accuracy assessment with observation discharge at runoff station on the five performance statistical coefficients
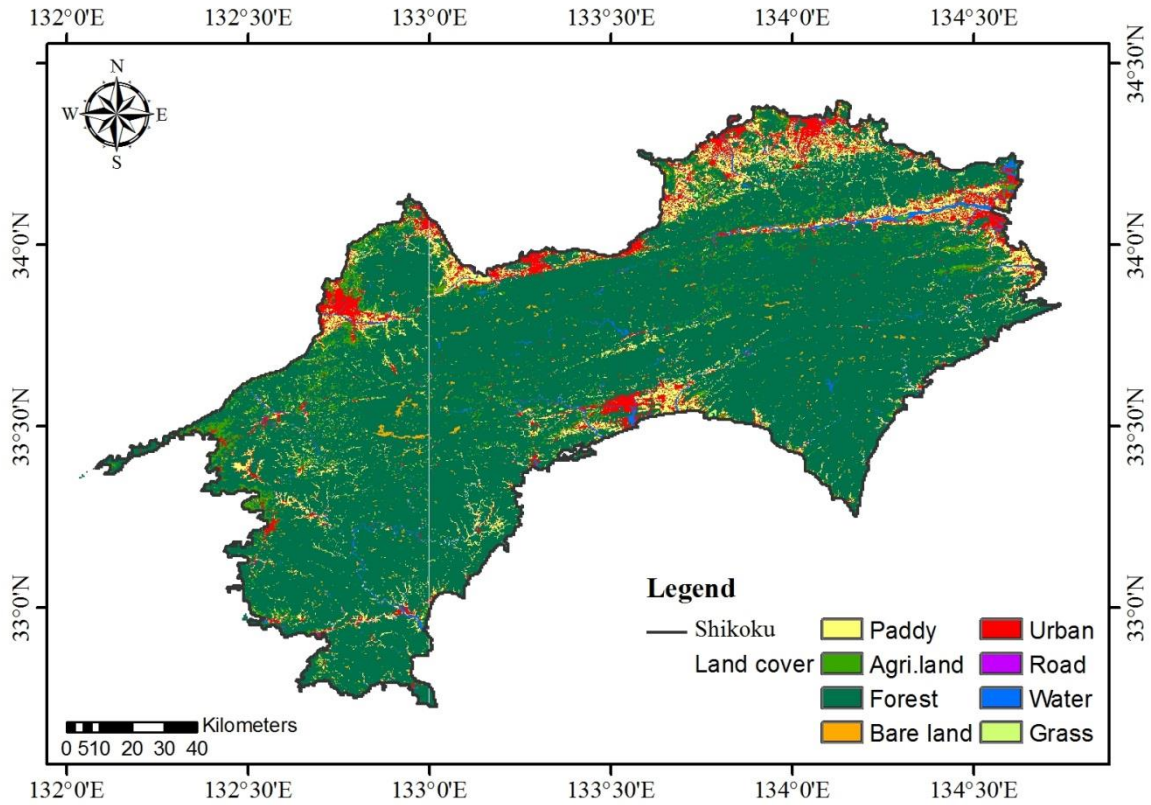
source: MLIT Japan

Figure 4-1 Land cover map base in the Shikoku Island, Japan

Table 4-1 Land cover type area in the Shikoku Island, Japan

No	Code	Land cover name	Pixel	Area, km^2	Percentage
1	100	Paddy	180,343	1,349.37	7.03%
2	200	Agricultural	118,966	890.13	4.64%
3	500	Forest	2,033,243	15,213.23	79.26%
4	600	Bare land	23,337	174.61	0.91%
5	700	Build-up land	137,922	1,031.97	5.38%
6	901	Road	2,280	17.06	0.09%
7	902	Rail road	283	2.12	0.01%
8	1000	Build-up land	14,181	106.11	0.55%
9	1100	Water	43,832	327.96	1.71%
10	1400	Beach	176	1.32	0.01%
11	1500	Sea water	5,307	39.71	0.21%
12	1600	Grass	5,269	39.42	0.21%
		Total	2,565,139	19,193.01	100.00%
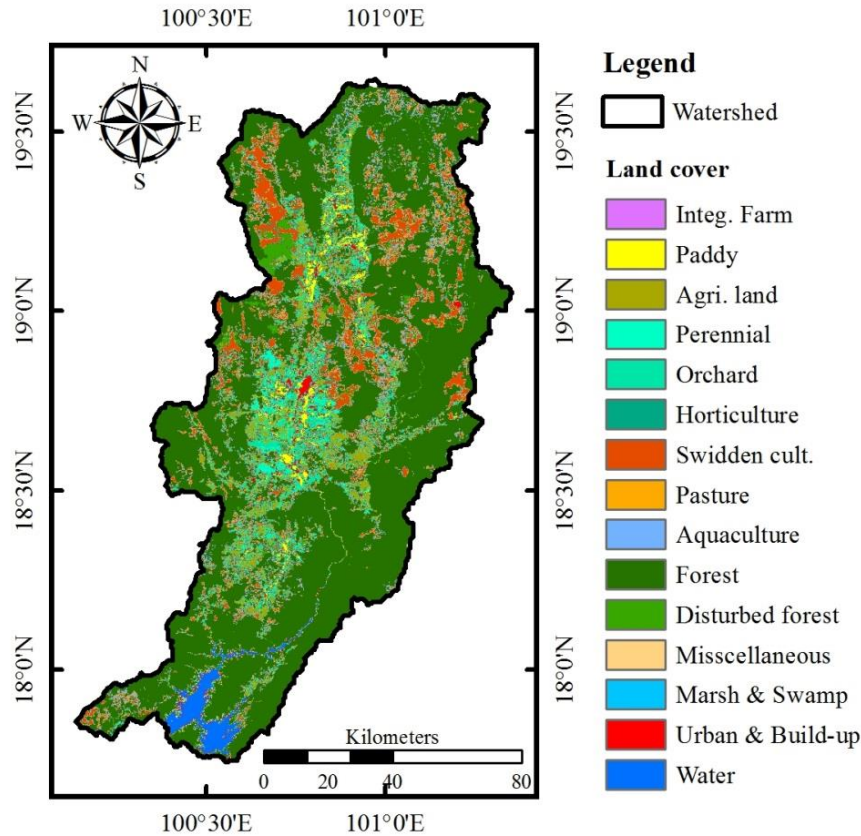
source: LDD Thailand

Figure 4-2 Land cover map based on areal data base in the Nan river basin, Thailand

Table 4-2 Land cover type area in the Nan river basin area, Thailand

No	Code	Land cover name	Pixel	Area, km2	Percentage
1	A0	Integrated farm	11	0.03	0.0002%
2	A1	Paddy	143,123	357.81	2.7846%
3	A2	Agricultural	348,229	870.57	6.7751%
4	A3	Perennial	86,871	217.18	1.6902%
5	A4	Orchard	141,175	352.94	2.7467%
6	A5	Horticulture	39	0.10	0.0008%
7	A6	Swidden cultivation	546,243	1,365.61	10.6276%
8	A7	Pasture and farm house	302	0.76	0.0059%
9	A9	Aquacultural land	21	0.05	0.0004%
10	F	Forest	3,529,820	8,824.55	68.6757%
11	F0	Disturbed forest land	107,806	269.52	2.0975%
12	M	Miscellaneous land	26,541	66.35	0.5164%
13	M2	Marsh and Swamp	70	0.18	0.0014%
14	U	Build-up land	81,127	202.82	1.5784%
15	W	Water	128,458	321.15	2.4993%
		Total	5,139,836	12,849.59	100.00%

.

Moderate Resolution Imaging Spectroradiometer (MODIS) data have spatial resolution from 250 m to 1 km and offer the possibility for time series coverage at moderate resolution. A numerous from MODIS data in global products are land cover, primary production, and leaf area index (Justice et al., 2002). MODIS land cover products is mainly of available set of global MODIS products. The product is established from various MODIS provided input such as surface reflectance, vegetation index, surface temperature and texture, and generated data is provided as global product according to the global IGBP (International Geosphere–Biosphere Programme) classification system (Friedl et al., 2002). Global MODIS land cover product is suitable for global and region scale, however, MODIS surface reflectance has provided at 250 and 500 m can also be used to map regional land cover at higher resolution according to a user-specified classification system. Empirical analyses demonstrated that higher resolutions than 1 km are highly desirable for mapping a land cover (Townshend and Justice,1988), and the MODIS instrument was designed to deliver 250 and 500 m resolution data (Justice et al., 2002; Townshend & Justice, 2002). MCD12Q1 is one of global MODIS land cover product, which data product is generated at annually over ten years (2001-2012, Friedl et al., 2010). A supervised classification samples for each mapping class is collected from 2,000 training sites in worldwide that are done for training by the decision tree classifier. In this study, the MCD12Q1 product of MODIS is categorized in 12 classes with the global accuracy about 74.8% (Freund and Schapire, 1997).

Advanced Very High Resolution Radiometer (AVHRR) data were provided by the U.S. Geological Survey National Center for Earth Resources Observation and Science, the University of Nebraska-Lincoln, and the European Commission's Joint Research Centre, on a continent with continent basis. All continental databases are based on two different map projections, Interrupted Goode Homolosine and Lambert Azimuthal Equal Area, on a 1-km spatial resolution. AVHRR is one kilometer 10-day NDVI (Normalized Difference Vegetation Index) composites. These are core data set to use in a land cover characterization, spanning April 1992 through March 1993 for source imagery data. In the database, the classifications were included by 7 categories (global ecosystem, IGBP land cover classification, U.S. geological survey land use/land cover system, simple biosphere model, simple biosphere 2 model, biosphere atmosphere transfer scheme, and vegetation lifeform). All of the classifications based on raster images were identified by class number values for a pixel, corresponding to the appropriate classification scheme legend. In this study, the AVHRR is categorized in 13 classes with the global accuracy about 71.9% (Gervin et al., 1985).

Table 4-3 Information of rainfall products

No.	Name	Generator/ distribution	Spatial resolution	Covering	Release	Global accuracy	Reference
1	MCD12Q1	USGS/ NASA	500m	Global	2012	74.8%	Freund and Schapire, 1997
2	AVHRR	NOAA/ NASA	1,000m	Global	1994	71.9%	Gervin et al. 1985

4.2.2 Manning's coefficient estimation and comparison

A land cover maps represent a natural surface features based on pixel grid that is interpreted from the aerial photograph for referent map and satellite for candidate data. The map is presented on the raster and digital format. The land cover maps contain the surface feature is identified in the pixel grid and a corresponding Manning's coefficient value is allocated to that wherever cell based on the proposed values for land surface. Numerical of Manning's coefficient presented in **Table 4-4** are typical values obtained from the previous studies (Dickinson et al., 1993; Lull, 1964; Zinke, 1967; Rowe, 1983; Chow, 1964; Haan, 1982; Yen, 1992; Ferguson, 1998). These numerical values are normally correspondence exists between reality and mathematical model of flow over a plan.

The raster and digital format of ESRI grid format also applied in the satellite data sources; each land cover code has a definition as a description of surface texture. The Manning's coefficient is assigned in each pixel based on the code and **Table 4-4** that assignment of coefficient has a limitation from spatial resolution and seasonal variation of vegetation. Manning's coefficient as empirical values is directly investigated from field measurements that its values assigned to each land cover types are not physically based. The misinterpretation may be occurred in some data sets. This methodology also has weakness to capture a small pixel that is menaced by the large portion pixel. Such as a small pixel is urban area and a large portion of the pixel is covered by the forest area that the interpreted pixel is the forest area.

The next step of the analysis is the comparison of the two Manning's coefficient maps (aerial and satellite base) based on pixel by pixel and overall. Aerial based Manning's coefficient maps is considered as the referent observed map, although in real situation it is not a true data. Satellite based Manning's coefficient maps is generated by look-up table as a supervised classification method. Therefore, the difference between Manning's coefficient values measured by aerial and satellite will be important that is the highlight.

Table 4-4 Default parameter charaterrizing Land cover classes

No	Land cover	Manning's n coefficient
1	Evergreen Needle leaf forest	0.40
2	Evergreen Broadleaf forest	0.60
3	Deciduous Needle leaf forest	0.40
4	Deciduous Broadleaf forest	0.80
5	Mixed forest	0.55
6	Closed Shrub lands	0.40
7	Open Shrub lands	0.40
8	Woody savannah	0.50
9	Savannahs	0.40
10	Grasslands	0.30
11	Permanent wetlands	0.50
12	Croplands	0.35
13	Urban and build-up	0.05
14	Natural vegetation	0.35
15	Snow and ice	0.05
16	Barren or sparsely vegetation	0.10
17	Water bodies	0.05

4.2.3 Hydrological simulation

The comparison of the different in runoff results when using the three Manning's coefficient map in distributed hydrologic model as RRI model is involved in this step. The distributed hydrologic model incorporate the spatial variation of input based on the raster format. Input data sets of the RRI model are four data types; rainfall product, topography, land cover and soil type. On the definition of the distributed hydrologic model with the RRI model, the used hydrologic parameters were mentioned in the **Chapter 2** such as Green-Amp parameter of soil type. The three Manning's coefficient maps candidate input are referent observed, MODIS and AVHRR. In this study, the input data has been scaled to 500 m of pixel size (about 15 x 15 arc-second). Addition to the numbers of pixel, row and column numbers are 457 and 292 respectively to present the watershed area as 13,000 km^2 for the Nan river basin. For the Shikoku Island, row and column numbers are 401 and 650 respectively for the area about 18,000 km^2. The estimation of width and depth were recommended in the equation (4) and (5) in the **Chapter 2**. Rainfall data was collected from the rain gauges, covering the study area. For the Nan river basin, June 2011 storm event is implemented to evaluate different DEM products that are used to run the RRI model over the basin. The rainy season during July to October in 2014 is used to evaluate the runoff in different DEM source for the Shikoku Island.

The estimated results driven by the different topography sources were evaluated to analysis bias of volume (V_{bias}), bias of peak (P_{bias}), Root Mean Square Error ($RMSE$), square of the Pearson correlation coefficient (R^2), and Mean Error (ME).

4.2.4 Performance statistics

Satellite based land cover and Manning's coefficient map spatial extents were evaluated with the referent observed map. The performance verification statistic measure the correspondence between the simulated and observed, was implemented in this research (see **Figure 4-3**): accuracy (ACC). ACC give the overall correction of simulation data and its perfect values for the statistical as 1.

$$ACC = \frac{Hit + Corr.}{Hit + False + Miss + Corr.}$$
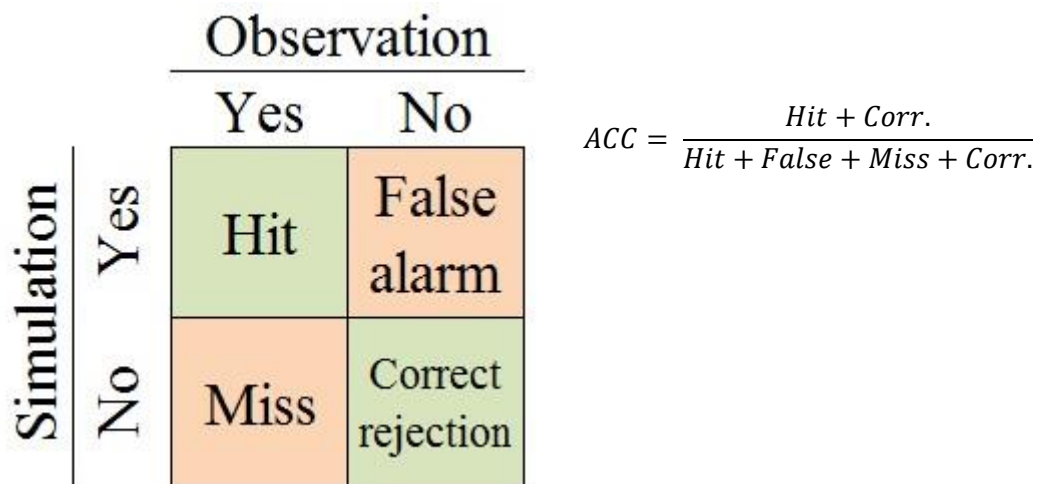
Figure 4-3 Detection analysis for inundation data

The estimation results driven by the several methods based on the hourly and daily data were evaluated to analysis bias of volume (V_{bias}), bias of peak (P_{bias}), root mean square error ($RMSE$), square of the Pearson correlation coefficient (R^2), and mean error (ME). The following formulas (see **Table 4-5**) were applied to evaluate simulation performance. The volume bias and peak bias estimate the systematic bias of modelled runoff in percentage (%). The correlation index is quantification in correlation of two data sets, simulated and observed runoff, which 0 is no correlation while 1 is perfect correlation. The RMSE is a different measure of difference magnitude between two data sets, while the ME is the bias from two data sets.

Table 4-5 Description of performance statistical

Statistical index	Description
Volume bias (%)	$V_{bias} = \dfrac{|Q_{vo} - Q_{vs}|}{Q_{vo}} \times 100$
Peak bias (%)	$P_{bias} = \dfrac{|Q_{po} - Q_{ps}|}{Q_{po}} \times 100$
Root mean square error	$RMSE = \sqrt{\dfrac{\sum_{i=1}^{n}(Q_{o(i)} - Q_{s(i)})^2}{n}}$
Correlation	$R^2 = \dfrac{\sum_{i=1}^{n}((Q_{o(i)} - \overline{Q_o}) \cdot (Q_{s(i)} - \overline{Q_s}))}{\sqrt{\sum_{i=1}^{n}(Q_{o(i)} - \overline{Q_o})^2 \cdot \sum_{i=1}^{n}(Q_{s(i)} - \overline{Q_s})^2}}$
Mean bias	$ME = \dfrac{\sum_{i=1}^{n}(Q_{o(i)} - Q_{s(i)})}{n}$

where

Q_{vo} is observation volume

Q_{vs} is simulation volume

Q_{po} is observation peak

Q_{ps} is simulation peak

Q_o is observation data

Q_s is simulation data

n is total number of sample

4.3 Results and Discussion

4.3.1 Accuracy assessment of MODIS land cover data

MODIS land cover data represented using MCD12Q1 product was used in this study at 500 m resolution. MCD12Q1 was selected and evaluated for two study area (Shikoku and Nan). The MCD12Q1 contained with 12 classes of land cover type was grouped into 6 classes (forest, shrub, grass, agriculture, urban, water) for matching with aerial based land cover as the referent observed data set for the overall area based. For the pixel to pixel based the land cover type was reconstructed at 7 types (forest, shrub, grass, paddy, agriculture, urban, water), dividing the paddy from the agriculture to make more detail of validation. The reconstructed MCD12Q1 product was considered in an accuracy assessment based on the area and pixel based. Finally, the accuracy of both areas was compared with the other area in the world.

MCD12Q product of MODIS land cover data set is shown in **Figure 4-4** to present the Shikoku Island in Japan with its land cover distribution. The Island area is mostly forest area that located in the central part of the Island, and urban area is located along border area. Agriculture area is near to the urban area and water area in the plain area. **Table 4-6** reveals value and percentage of land cover in each class. More than 70% of the Island was evergreen forest area (Evergreen Needle leaf tree and Evergreen Broad leaf tree), 17% was deciduous forest (Deciduous Needle leaf tree and Deciduous Broad leaf tree), and 8% was agriculture area (Cereal and Broad-leaf crops). For the urban area, it was about 3% and open area (Shrub, Grass, Snow, Water, and Bare land) was about 2% of the total area.

Figure 4-5 present MCD12Q product of MODIS land cover data set and its distribution in the Nan river basin Thailand. The basin area is mostly forest area that located along a border area and in the central part is the urban area with a small area. Agriculture area is near to the urban area and floods plain area, while the large water body is located in the southern part as the SIRIKIT reservoir, main water supply of the central part of Thailand. **Table 4-7** shows value and percentage of land cover in each class. More than 63% of the basin was evergreen forest area (Evergreen Broad leaf tree), 19% was open area (Shrub, Grass, Snow, and Bare land), and 14% was deciduous forest (Deciduous Broad leaf tree). For the urban area, it was about 0.2% and agriculture (Cereal and Broad-leaf crops) was about 3.8% of the total area.

MCD12Q1 of MODIS product contained with 12 classes of land cover type was grouped into 6 classes (Forest, Shrub, Grass, Agriculture, Urban, Water) for matching with aerial based land cover as the referent observed data set. The grouping of the MODIS products (MCD12Q1) is followed as Evergreen Needle leaf tree, Evergreen Broad leaf tree, Deciduous Needle leaf tree, and Deciduous Broad leaf tree were became to the forest class. Cereal and Broad-leaf crops were grouped as the agriculture type, and grass land class was consisted by Grass and Snow. Shrub was a combination between Shrub and Bare land. Water body and Urban were stilled.

Table 4-6 Land cover data of MODIS product in the Shikoku area

No	Description	code	Area, km^2	Percentage
1	Water	0	124.72	0.65%
2	Evergreen Needle leaf tree	1	6,410.09	33.40%
3	Evergreen Broadleaf tree	2	6,968.13	36.31%
4	Deciduous Needle leaf tree	3	4.33	0.02%
5	Deciduous Broadleaf tree	4	3,149.18	16.41%
6	Shrub	5	110.35	0.57%
7	Grass	6	286.70	1.49%
8	Cereal crops	7	1,074.89	5.60%
9	Broad-leaf crops	8	480.24	2.50%
10	Urban and build-up	9	581.24	3.03%
11	Snow	10	1.68	0.01%
12	Bare or sparse vegetable	11	1.46	0.01%
	Total		19,193.01	100.00%
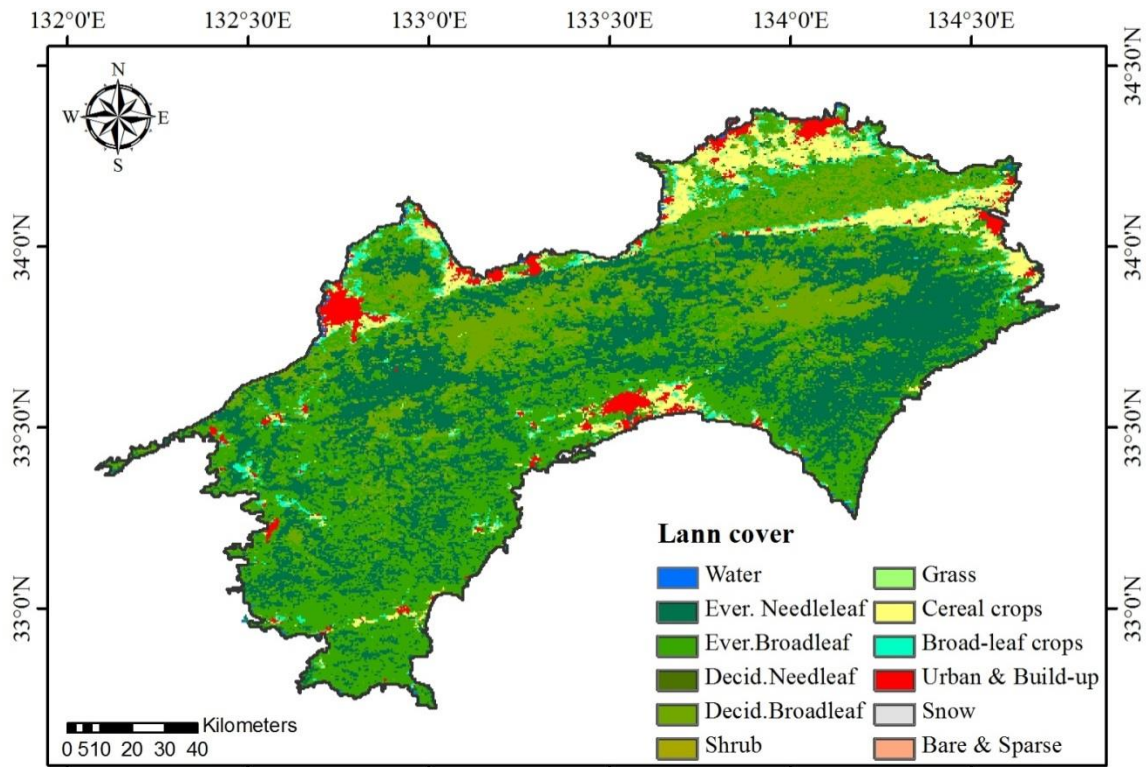
Figure 4-4 MODIS Satellite land cover product in the Shikoku Island
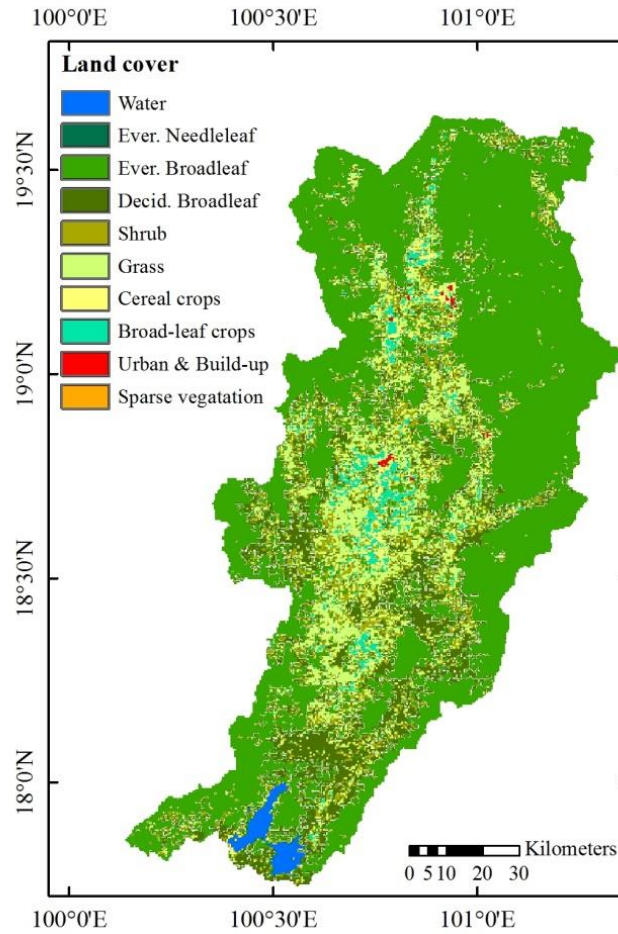
Figure 4-5 MODIS Satellite land cover product in the Nan river basin

Table 4-7 Land cover data of MODIS product in the Nan river basin

No	Description	code	Area, km^2	Percentage
1	Water	0	138.82	1.08%
2	Evergreen Needle leaf tree	1	5.72	0.04%
3	Evergreen Broadleaf tree	2	8,095.02	63.00%
4	Deciduous Needle leaf tree	3	-	-
5	Deciduous Broadleaf tree	4	1,785.58	13.90%
6	Shrub	5	880.73	6.85%
7	Grass	6	1,377.75	10.72%
8	Cereal crops	7	132.58	1.03%
9	Broad-leaf crops	8	413.05	3.21%
10	Urban and build-up	9	20.16	0.16%
11	Snow	10	-	-
12	Bare or sparse vegetable	11	0.20	0.002%
	Total		12,849.59	100%

The aerial based land cover data of the Shikoku Island is grouped as following Paddy and Agriculture was combined into the agriculture land class. Build-up land, Road, and Rail road were grouped into the urban area type, and Bare land and Beach were became to shrub land type. Forest, Water, and Grass were stilled. In the Nan river basin, the 15 land cover types is grouped as Integrated farm, Paddy, Agriculture, Perennial, Orchard, Horticulture, and Pasture were grouped as the agriculture land type. Water type was combination of three classes (Aquaculture, Swamp, and Water), and Forest and Disturbed forest became to the forest land class. Swidden cultivation, Miscellaneous, and Build-up land were stilled as shrub, grass, and urban, respectively.

The regrouping of the MODIS land cover product represented by 500 m resolution was resampled as same as the pixel of the aerial based land cover of the two study areas. The Shikoku Island has pixel size about 100 m, and the Nan river basin represents a pixel size with 50 m. The resampled MODIS data was evaluate in the accuracy assessment based on two schemes, overall area and pixel to pixel based. **Table 4-8** shows the comparison between referent observed and MODIS product on the area based in the Shikoku and Nan area. All of both area, forest type was the best accuracy, and grass land was the lowest accuracy, representing with the overestimation. Underestimation was occurred in other four classes (shrub, agriculture, urban, and water). For the Shikoku on underestimation, the lowest was shrub type, while the highest was water body. The lowest underestimation in the Nan was also the shrub, but the highest was contrast as the urban. This evaluation based on the overall in area was the primary comparison validation that the detail validation with pixel based was described in below.

The deep detail of validation on the pixel to pixel based was a comparison between observed and satellite based data set for two study areas with the 7 classes as mention in above. **Table 4-9** presents an accuracy assessment of the MODIS data on the pixel to pixel based of the Shikoku area. The overall accuracy was about 82.07% with the hit pixel at 2,105,302 pixels of a total pixel about 2,565,139 pixels. The forest area outperformed among the six land cover types with highest accuracy and followed by paddy (2.67%), and urban (1.76%), while the shrub showed as the lowest accuracy at 0.01%. For the Nan river basin, **Table 4-10** presents an accuracy assessment of the MODIS data the area. The overall accuracy was about 75.79% with the hit pixel at 3,895,311 pixels of a total pixel about 5,139,836 pixels. The forest area outperformed among the six land cover types with highest accuracy and followed by agriculture (6.09%), and shrub (1.41%), while the grass showed as the lowest accuracy at 0.02%.

The assessment accuracy from the MODIS product presented that the Shikoku Island outperformed the Nan river basin. **Figure 4-6** shows the large differences in global scale the height precision are found in the studied of MODIS land cover in literature (Freund and Schapire, 1997; Blanco et al., 2013; Clark et al., 2010; Klein et al., 2012; Shao and Lunetta, 2012; Sulla-Menashe et al., 2011). It demonstrates that the MODIS accuracy is depended on accuracy of reference point, terrain

characteristics, and surface properties. Hence, the recommendation achieves to the study of those features. In addition to the **Figure 4-6**, the accuracy value on this study about 82% of the Shikoku area closed to the mean value of overall. The Nan accuracy presented about 75% to close with low boundary as mean – standard deviation value. According to the MCD12Q1 products of MODIS, it recommended that the product was high accuracy to compare with other area based on the value of the mean ± standard deviation.

Table 4-8 Comparison between reference and MODIS satellite products

No	Description	Shikoku Island			Nan river basin		
		Ref. Obs	MODIS	% error	Ref. Obs	MODIS	% error
1	Forest	79.26%	86.13%	8.7%	70.77%	76.94%	8.7%
2	Shrub	0.91%	0.58%	-35.8%	10.63%	6.86%	-35.5%
3	Grass	0.21%	1.50%	>100.0%	0.52%	10.72%	>100.0%
4	Agricultural	11.67%	8.10%	-30.6%	14.00%	4.25%	-69.7%
5	Urban	6.04%	3.03%	-49.8%	1.58%	0.16%	-90.1%
6	Water	1.92%	0.65%	-66.1%	2.50%	1.08%	-56.8%

Table 4-9 Accuracy assessment of MODIS land cover product between pixel to pixel in the Shikoku

		Reference data						
		Forest	Shrub	Grass	Agriculture	Paddy	Urban	Water
MODIS	Forest	**1,979,323**	20,255	2,345	84,966	66,915	30,505	25,151
	Shrub	5,973	**154**	113	1,827	2,074	3,553	1,249
	Grass	7,668	680	**545**	3,908	8,014	14,830	2,897
	Agriculture	16,214	1,231	1,676	**10,853**	20,244	11,553	2,413
	Paddy	8,904	754	332	9,956	**68,412**	44,670	10,630
	Urban	8,230	214	226	4,773	13,160	**45,148**	5,932
	Water	6,931	49	32	2,683	1,524	4,583	**867**
		77.16%	0.01%	0.02%	0.42%	2.67%	1.76%	0.03%

Table 4-10 Accuracy assessment of MODIS land cover product between pixel to pixel in the Nan

		Reference data						
		Forest	Shrub	Grass	Agriculture	Paddy	Urban	Water
MODIS	Forest	**3,389,137**	459,554	12,752	189,273	41,460	31,632	57,345
	Shrub	220,634	**72,240**	7,913	1,202	33,231	-	7,105
	Grass	4,643	2,046	**1,205**	11,750	20,178	8,033	5,258
	Agriculture	218	28	276	**313,044**	2,675	3,510	156
	Paddy	22,510	12,364	4,697	61,053	**45,579**	20,702	1,798
	Urban	-	-	-	-	-	**17,219**	-
	Water	484	11	-	3	-	31	**56,887**
		65.94%	1.41%	0.02%	6.09%	0.89%	0.34%	1.11%
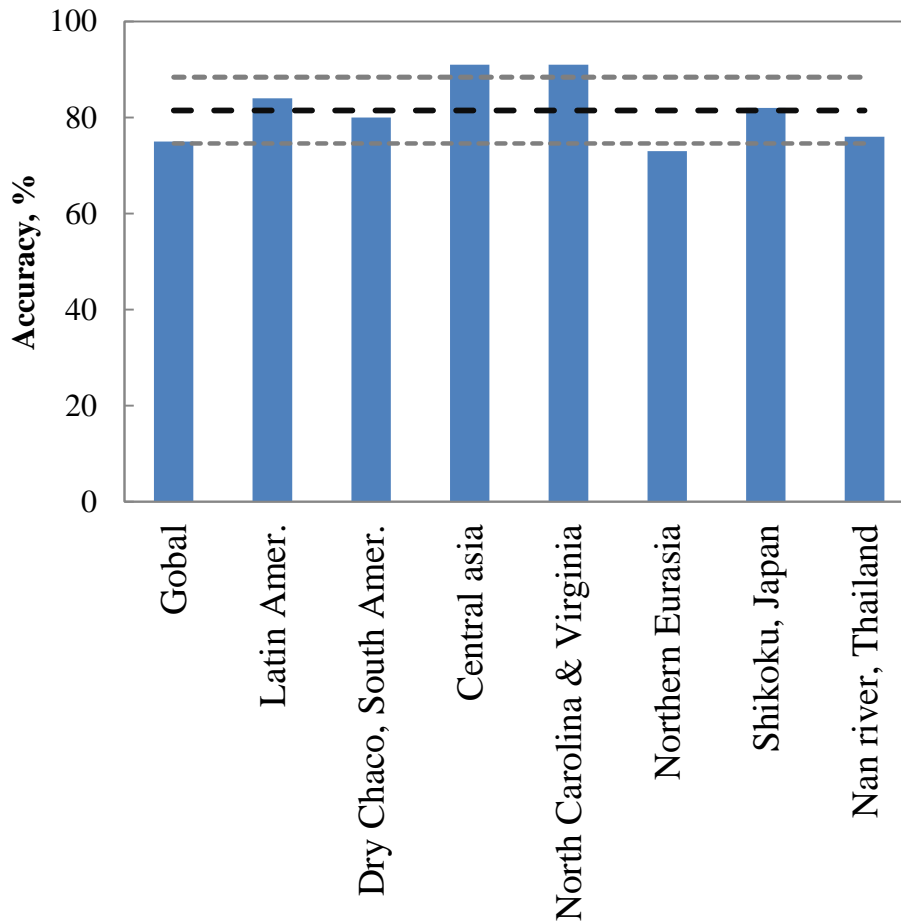
Figure 4-6 Accuracy of the MODIS land cover product camparing with other region

4.3.2 Accuracy assessment of AVHRR land cover data

AVHRR land cover data product was used in this study at 1,000 m resolution. The AVHRR was selected and evaluated for two study area (Shikoku and Nan). The product contained with 13 classes of land cover type was grouped into 6 classes for matching with the referent observed data set, as mention on above. The reconstructed product was considered in an accuracy assessment based on the area and pixel based.

Land cover data set of AVHRR is shown in **Figure 4-7** to present the Shikoku Island in Japan with its land cover distribution. The Island area is mostly forest area that located in the central part of the Island, and urban area is located along border area. Agriculture area is near to the urban area and water area in the plain area. **Table 4-11** reveals value and percentage of land cover in each class. More than 51% of the Island was evergreen forest area (Evergreen Needle leaf tree), 28% was forest (Mixed forest and Wooded land), and 18% was grass land (Wooded grassland, Grassland and Cropland). For the urban area, it was about 0.7% and open area (Shrub and Water) was about 2.3% of the total area.

Figure 4-8 present AVHRR land cover data set and its distribution in the Nan river basin Thailand. The basin area is mostly forest area that located along a border area and in the central part is the urban area with a small area. Agriculture area is near to the urban area and floods plain area, while the large water body is located in the southern part as the SIRIKIT reservoir, main water supply of the central part of Thailand. **Table 4-12** shows value and percentage of land cover in each class. More than 53% of the basin was wooded forest area (Wooded land), 24% was forest (Evergreen and Deciduous), and 20% was grassland (Wooded grassland, grassland and grassland). For the urban area, it was about 0.03% and open area (Shrub and Water) was about 2.97% of the total area.

The reclassification of the AVHRR land cover product represented by 1000 m resolution was resampled as same as the pixel of the aerial based land cover of the two study areas. For the Shikoku Island, pixel size is about 100 m, and the Nan river basin, pixel size is 50 m. The resampled AVHRR data was evaluate in the accuracy assessment based on two schemes, overall area and pixel to pixel based. **Table 4-13** shows the comparison between referent observed and AVHRR product on the area based in the Shikoku and Nan area. All of both area, water body was the best accuracy, and grass land was the lowest accuracy, representing with the overestimation, but the grassland of Nan was underestimation. Underestimation was occurred in other three classes (shrub, agriculture, urban, and water) in the Shikoku. For the Shikoku on underestimation, the lowest was urban type, while the highest was forest. The lowest underestimation in the Nan was also the urban, but the highest was contrast as the grass. This evaluation based on the overall in area was the primary comparison validation that the detail validation with pixel based was described in below.
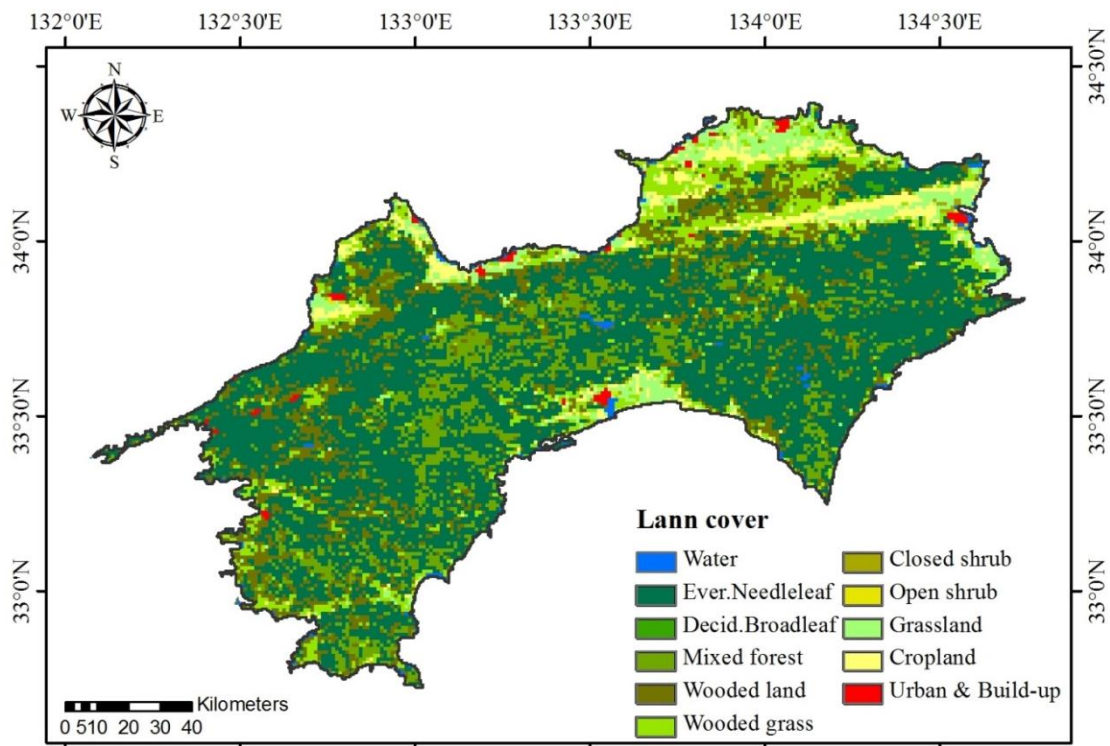
Figure 4-7 AVHRR Satellite land cover product in the Shikoku Island

Table 4-11 Land cover data of AVHRR product in the Shikoku area

No	Description	code	Area, km2	Percentage
1	Water	0	374.91	1.95%
2	Evergreen Needle leaf tree	1	9,727.79	50.68%
3	Evergreen Broadleaf tree	2	-	-
4	Deciduous Needle leaf tree	3	-	-
5	Deciduous Broadleaf tree	4	41.14	0.21%
6	Mixed forest	5	2,226.04	11.60%
7	Wooded land	6	3,042.04	15.85%
8	Wooded grassland	7	1,902.68	9.91%
9	Closed shrub land	8	31.67	0.17%
10	Open shrub land	9	11.65	0.06%
11	Grassland	10	907.30	4.73%
12	Cropland	11	799.15	4.16%
13	Urban and build-up	12	128.66	0.67%
	Total		19,193.01	100.00%
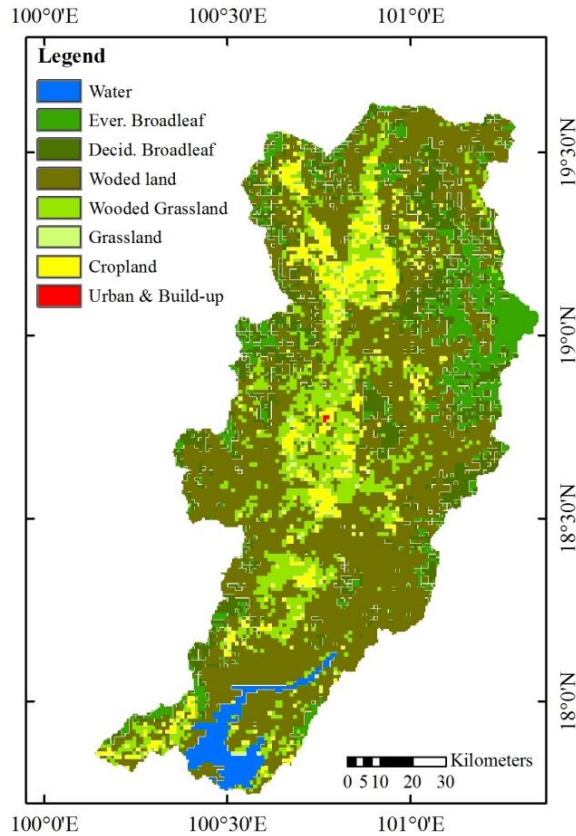
Figure 4-8 AVHRR Satellite land cover product in the Nan river basin

Table 4-12 Land cover data of AVHRR product in the Nan river basin

No	Description	code	Area, km2	Percentage
1	Water	0	343.67	2.67%
2	Evergreen Needle leaf tree	1	-	-
3	Evergreen Broadleaf tree	2	1,301.37	10.13%
4	Deciduous Needle leaf tree	3	-	-
5	Deciduous Broadleaf tree	4	1,759.33	13.69%
6	Mixed forest	5	-	-
7	Wooded land	6	6,785.40	52.81%
8	Wooded grassland	7	1,722.24	13.40%
9	Closed shrub land	8	-	-
10	Open shrub land	9	-	-
11	Grassland	10	30.32	0.24%
12	Cropland	11	903.80	7.03%
13	Urban and build-up	12	3.47	0.03%
	Total		12,849.59	100.00%

The deep detail of validation on the pixel to pixel based was a comparison between observed and satellite based data set for two study areas with the 6 classes as mention in above. **Table 4-14** presents an accuracy assessment of the AVHRR data on the pixel to pixel based of the Shikoku area. The overall accuracy was about 75.35% with the hit pixel at 1,932,953 pixels of a total pixel about 2,565,139 pixels. The forest area (70.47%) outperformed among the five land cover types with highest accuracy and followed by agriculture (4.21%), and urban (0.45%), while the shrub showed as the lowest accuracy at 0.001%. For the Nan river basin, **Table 4-15** presents an accuracy assessment of the AVHRR data the area. The overall accuracy was about 73.45% with the hit pixel at 3,775,048 pixels of a total pixel about 5,139,836 pixels. The forest area outperformed among the five land cover types with highest accuracy (61.37%) and followed by agriculture (8.22%), and shrub (2.09%), while the grass showed as the lowest accuracy at 0.001%.

Table 4-13 Comparison between reference and AVHRR satellite products

No	Description	Shikoku Island			Nan river basin		
		Ref. Obs	AVHRR	% error	Ref. Obs	AVHRR	% error
1	Forest	79.26%	78.35%	-1.2%	70.77%	76.63%	8.3%
2	Shrub	0.91%	0.23%	-75.2%	10.63%	-	-
3	Grass	0.21%	4.73%	>100.0%	0.52%	0.24%	-54.8%
4	Agricultural	11.67%	14.08%	20.6%	14.00%	20.44%	46.0%
5	Urban	6.04%	0.67%	-88.9%	1.58%	0.03%	-98.3%
6	Water	1.92%	1.95%	2.0%	2.50%	2.67%	6.9%

Table 4-14 Accuracy assessment of AVHRR land cover product between pixel to pixel in the Shikoku

		Reference data					
		Forest	Shrub	Grass	Agriculture	Urban	Water
AVHRR	Forest	**1,807,725**	18,734	1,744	134,791	29,403	17,293
	Shrub	55	**1**	24	826	3,913	971
	Grass	22,000	1,000	**335**	44,594	42,997	10,334
	Agriculture	178,778	3,206	2,592	**108,084**	53,969	14,469
	Urban	3,121	44	43	1,513	**11,605**	869
	Water	21,564	352	531	9,501	12,955	**5,203**
	Percentage, %	70.47%	0.00%	0.01%	4.21%	0.45%	0.20%

Table 4-15 Accuracy assessment of AVHRR land cover product between pixel to pixel in the Nan

		Reference data					
		Forest	Shrub	Grass	Agriculture	Urban	Water
AVHRR	Forest	**3,154,389**	38,254	7,580	291,897	22,726	23,592
	Shrub	-	**107,212**	-	-	-	-
	Grass	5,107	443	**142**	4,722	501	1,212
	Agriculture	431,824	-	19,100	**422,256**	56,226	13,798
	Urban	-	-	-	147	**1,171**	69
	Water	46,306	334	21	426	503	**89,878**
	Percentage, %	61.37%	2.09%	0.00%	8.22%	0.02%	1.75%

4.3.3 Manning's coefficient analysis in the Shikoku Island

Manning's coefficient map is estimated and presented in **Figure 4-9** for the referent observed data and **Figure 4-10** for the satellite based data (MODIS and AVHRR). The comparison tries to illustrate map as the same legend to both map. For MODIS, it is shown that the MODIS source generated higher Manning's coefficient vales that the based referent maps. Based on the 2,565,139 pixels in the Shikoku, their based referent map values about 36% pixels were greater than MODIS map values and their MODIS map values about 59% pixels were greater than those of based referent map values, on the same value was about 5%. By the contrast in AVHRR, it is presented that the AVHRR source generated lower Manning's coefficient vales that the based referent map. Their pixels of the based referent map values about 60% pixels greater that AVHRR map values and their AVHRR map values about 14% pixels greater than those of based referent map values. The similar Manning's coefficient vale was about 26%.

The different in percentage between the satellite sources generated and based referent Manning's coefficient value is estimated and showed in **Figure 4-11** for MODIS and AVHRR. These map are reclassified into five ranges depended on the percentage of difference between satellite and based referent map. The first range contains pixels whose Manning's coefficient values derived from satellite sources map are less than 25% of their matching values from the based referent map. The meaning of this range is that the Manning's coefficient values of the based referent map are higher than the satellite based, revealing to values of smoother roughness resistance. The second range contains pixels whose Manning's coefficient values derived from satellite sources map are within -10% to -25% of their matching values from the based referent map. The third range contains pixels whose Manning's coefficient values derived from satellite sources map are within - or +10% of their matching values from the based referent map. The meaning of this range is that the Manning's coefficient values of the based referent map and the satellite based are the close value. The fourth range contains pixels whose Manning's coefficient values derived from satellite sources map are within 10% to 25% of their matching values from the based referent map. The fifth range contains

pixels whose Manning's coefficient values derived from satellite sources map are more than 25% of their matching values from the based referent map.

Based on the 2,565,139 pixels to represent the Shikoku area, MODIS data only 943,287 pixels about 37% are within the third range (-10% to +10%). To combine both ranges, second and fourth, number of pixel about 47,977 pixels about 2% still in these ranges, while the 1,573,875 pixels about 61% are within the significant different magnitude (>25%). For AVHRR source, only 828,583 pixels about 32% are within the third range (-10% to +10%). To combine both ranges, second and fourth, number of pixel about 135,885 pixels about 5% still in these ranges, while the 1,600,671 pixels about 62% are within >25% difference that is the significant different magnitude
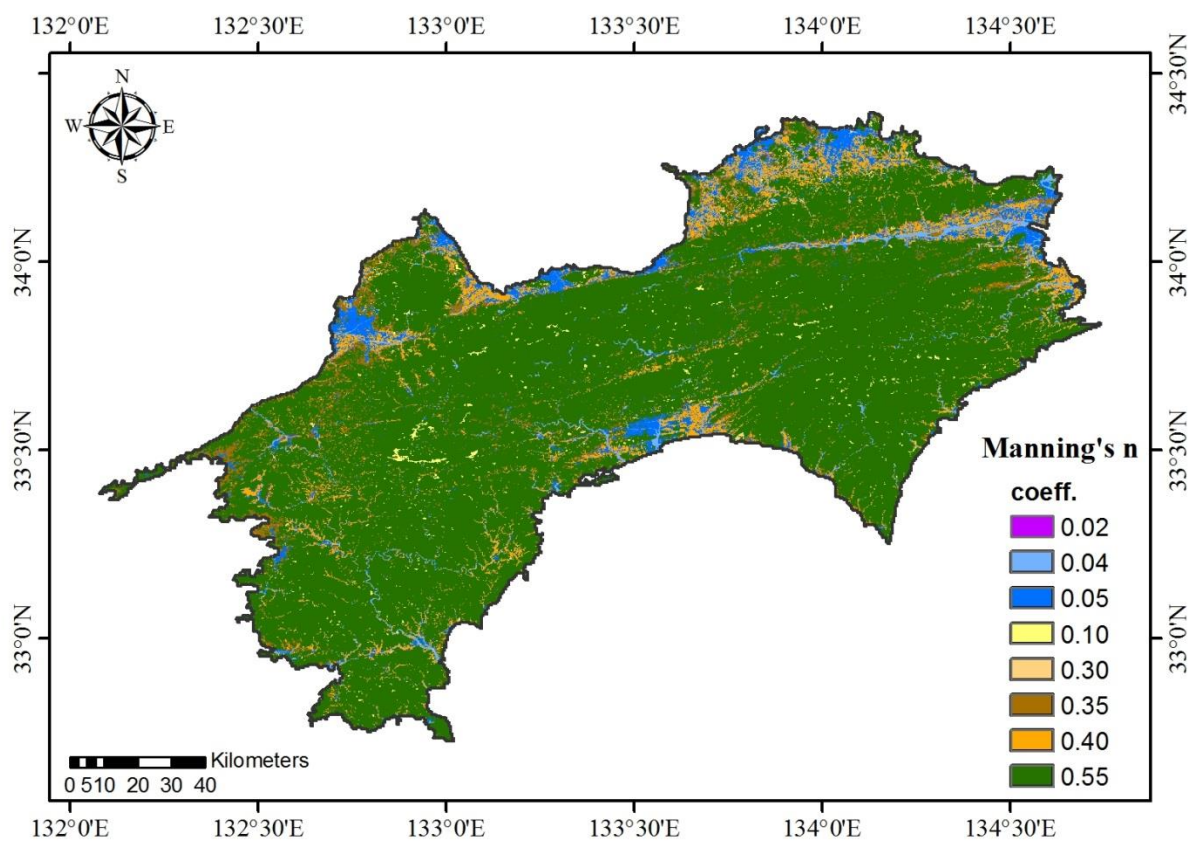
Figure 4-9 Manning's n map in the Shikoku Island
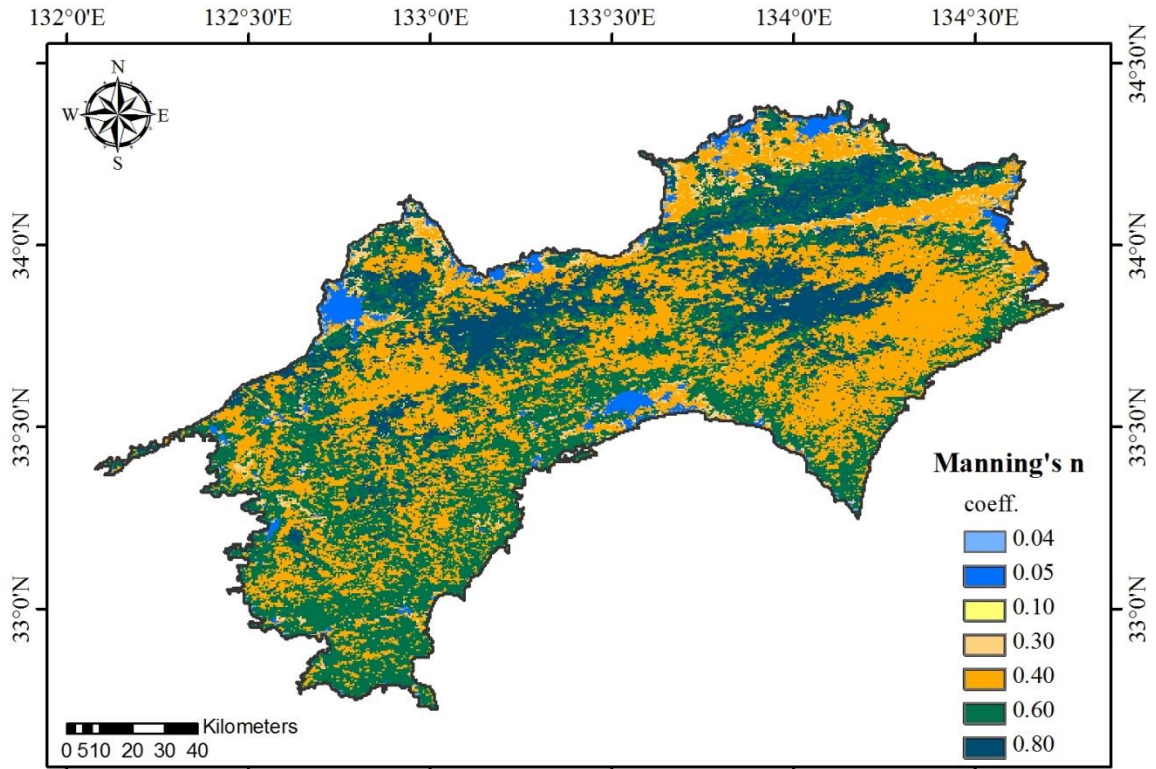
a) MODIS
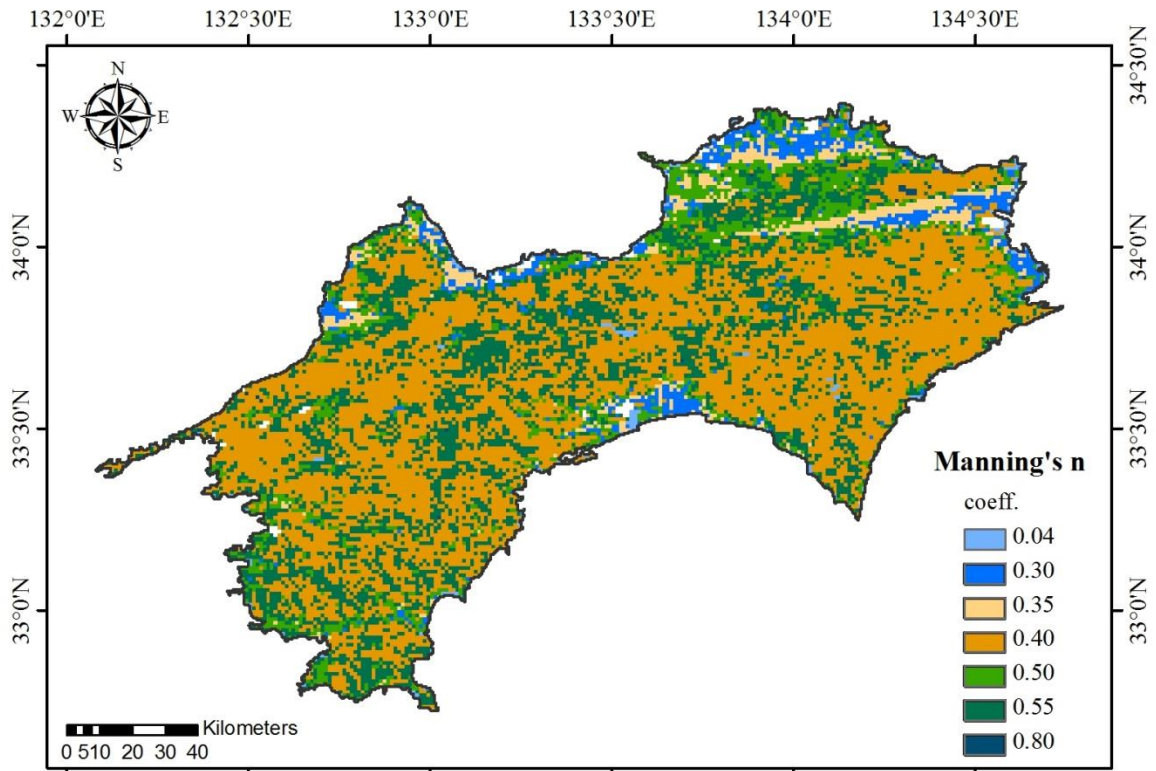
b) AVHRR

Figure 4-10 Manning's n map of the satellite products, MODIS and AVHRR
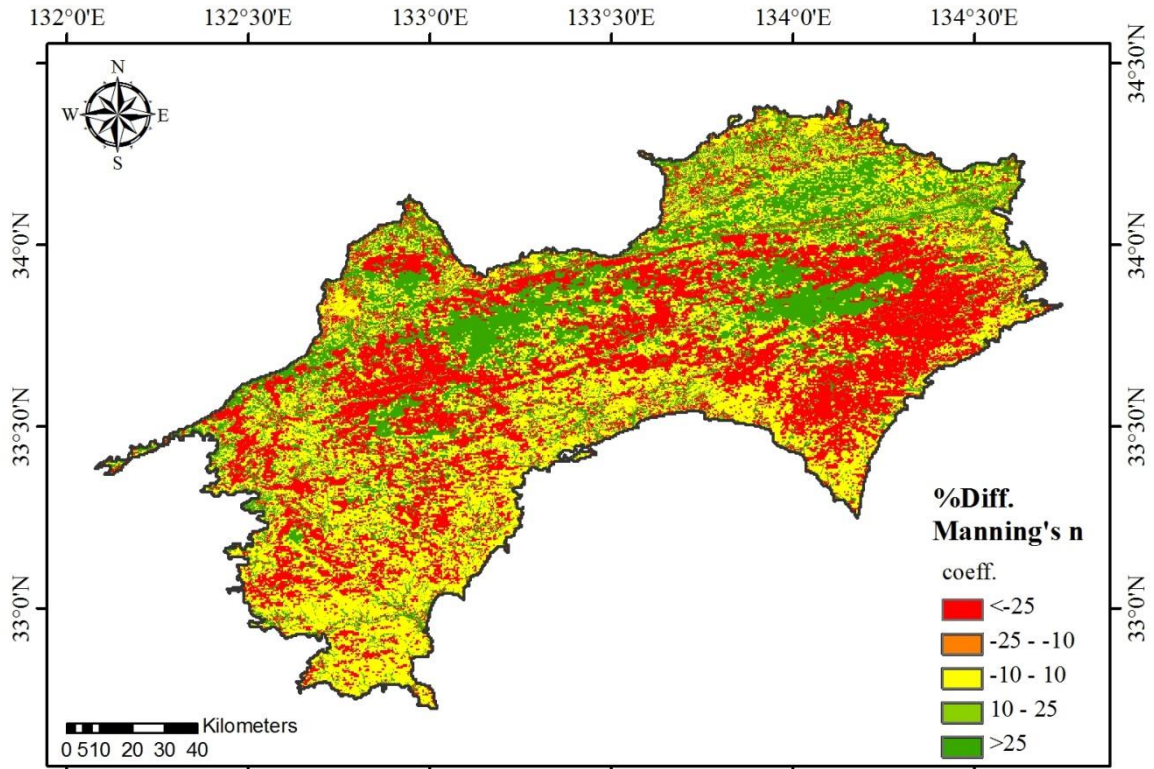
a) MODIS
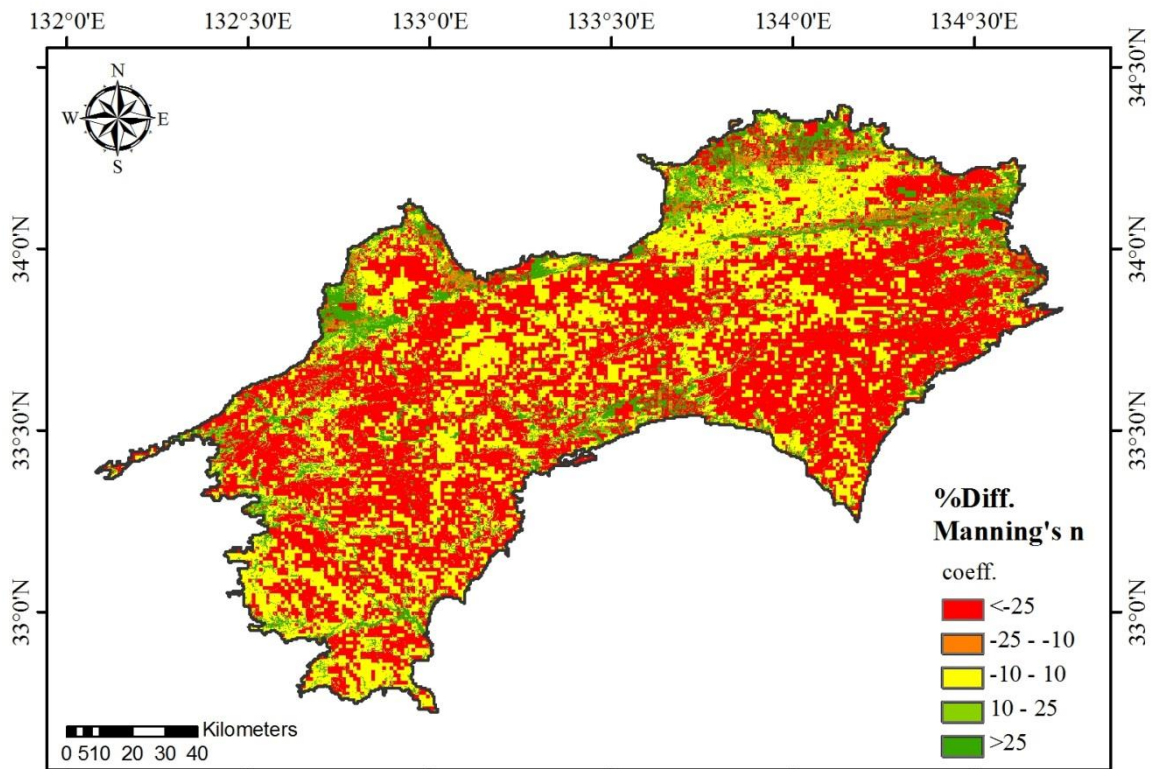
b) AVHRR

Figure 4-11 Deviation of manning's n map of the satellite products, MODIS and AVHRR

Overall quantify a difference between satellite referent observed land cover map, the both satellite based is over laid onto the based referent map. Within each satellite land cover type the average Manning's coefficient values based on the satellite land cover map and the based referent map are calculated. The averages for all the land cover types in the Shikoku area and the calculated percent differences are presented in **Table 4-16** for MODIS and **Table 4-17** for AVHRR. For the example on the MODIS source, the Grass land cover type, its average Manning's coefficient of all the MODIS pixels within this land cover type is 0.30 and the average Manning's coefficient of the corresponding based referent map pixels is 0.255, a difference of 0.045 about 17.6 % difference. The differences of percentage were weighted by the ratio of the pixel number of the land cover type within the tested area to the total pixel number in the tested area to create a weighted percentage difference as presented in **Table 4-16** for MODIS and **Table 4-17** for AVHRR. The weighting helps to focus the significance of the differences in the land cover classification to influence the overall difference for the tested area and for affecting hydrologic model outputs.

Table 4-16 Performance statistics of Manning's n in each MODIS land cover type

MODIS Description	No. pixels	Avr. MODIS, n	Avr. Ref., n	Diff. (MODIS-Ref.)	% Rel. Err.	Weighted % Rel. Err
Water	16,669	0.04	0.338	-0.298	-88.2%	-0.57%
Evergreen Needleleaf tree	856,706	0.40	0.524	-0.124	-23.7%	-7.92%
Evergreen Broadleaf tree	931,288	0.60	0.516	0.084	16.4%	5.94%
Deciduous Needleleaf tree	579	0.40	0.274	0.126	45.9%	0.01%
Deciduous Broadleaf tree	420,887	0.80	0.525	0.275	52.5%	8.62%
Shrub	14,748	0.40	0.340	0.060	17.6%	0.10%
Grass	38,317	0.30	0.255	0.045	17.6%	0.26%
Cereal crops	143,658	0.40	0.268	0.132	49.0%	2.74%
Broad-leaf crops	64,184	0.30	0.344	-0.044	-12.9%	-0.32%
Urban and build-up	77,683	0.05	0.181	-0.131	-72.3%	-2.19%
Snow	225	0.05	0.420	-0.370	-88.1%	-0.01%
Bare or sparse vegetable	195	0.10	0.051	0.049	95.8%	0.01%

Table 4-17 Performance statistics of Manning's n in each AVHRR land cover type

AVHRR Description	No. pixels	Avr. MODIS, n	Avr. Ref., n	Diff. (AVHRR-Ref.)	% Rel. Err.	Weighted % Rel. Err
Water	50,106	0.04	0.328	-0.288	-87.8%	-1.72%
Evergreen Needleleaf tree	1,300,115	0.40	0.525	-0.125	-23.9%	-12.09%
Evergreen Broadleaf tree	-	0.60	-	-	-	-
Deciduous Needleleaf tree	-	0.40	-	-	-	-
Deciduous Broadleaf tree	5,498	0.80	0.489	0.311	63.6%	0.14%
Mixed forest	297,510	0.55	0.537	0.013	2.4%	0.28%
Wooded land	406,567	0.55	0.501	0.049	9.7%	1.54%
Wooded grassland	254,292	0.50	0.434	0.066	15.3%	1.52%
Closed shrubland	4,233	0.40	0.114	0.286	>100.0%	0.42%
Open shrubland	1,557	0.40	0.075	0.325	>100.0%	0.27%
Grassland	121,260	0.30	0.266	0.034	12.6%	0.60%
Cropland	106,806	0.35	0.317	0.033	10.4%	0.43%
Urban and build-up	17,195	0.05	0.169	-0.119	-70.5%	-0.47%

4.3.4 Manning's coefficient analysis in the Nan river basin

Manning's coefficient map of the Nan is estimated and presented in **Figure 4-12** for the referent observed data and **Figure 4-13** for the satellite based data (MODIS and AVHRR). The comparison tries to illustrate map as the same legend to both map. For MODIS, it is shown that the MODIS source generated higher Manning's coefficient vales that the based referent map. Based on the 5,139,836 pixels in the Nan, their based referent map values about 15% pixels were greater than MODIS map values and their MODIS map values about 81% pixels were greater than those of based referent map values, on the same value was about 4%. By the contrast in AVHRR, it is presented that the AVHRR source generated lower Manning's coefficient vales that the based referent map. Their pixels of the based referent map values about 11% pixels greater that AVHRR map values and their AVHRR map values about 44% pixels greater than those of based referent map values. The similar Manning's coefficient vale was about 44%.

The different in percentage between the satellite sources generated and based referent Manning's coefficient value is estimated and showed in **Figure 4-11** for MODIS and AVHRR. These map are reclassified into five ranges depended on the percentage of difference between satellite and based referent map. The five range are mentioned on above as a description of each range. Based on the 5,139,836 pixels to represent the Shikoku area, MODIS data only 2,858,880 pixels about 56% are within the third range (-10% to +10%). To combine both ranges, second and fourth, number of pixel about 337,070 pixels about 6% still in these ranges, while the 1,943,886 pixels about 38% are within the significant different magnitude (>25%). For AVHRR source, only 3,103,750 pixels about 60% are within the third range (-10% to +10%). To combine both ranges, second and fourth, number of pixel

about 165,591 pixels about 3% still in these ranges, while the 1,871,495 pixels about 36% are within >25% difference that is the significant different magnitude
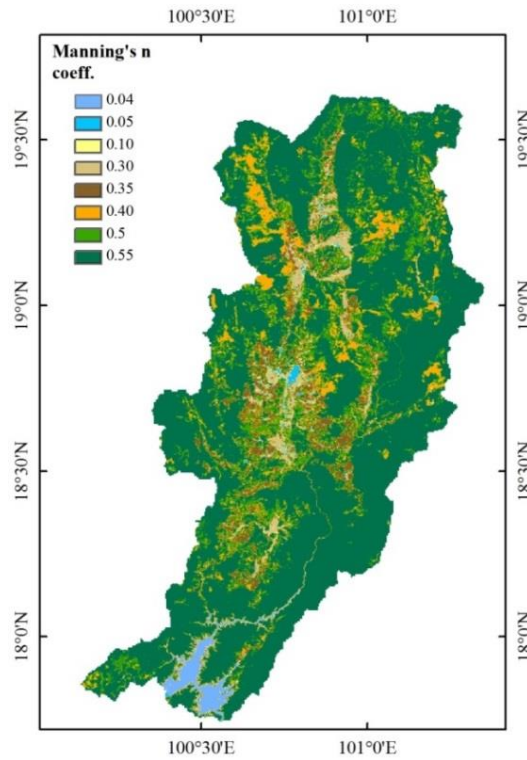
Figure 4-12 Manning's n map in the Nan river basin
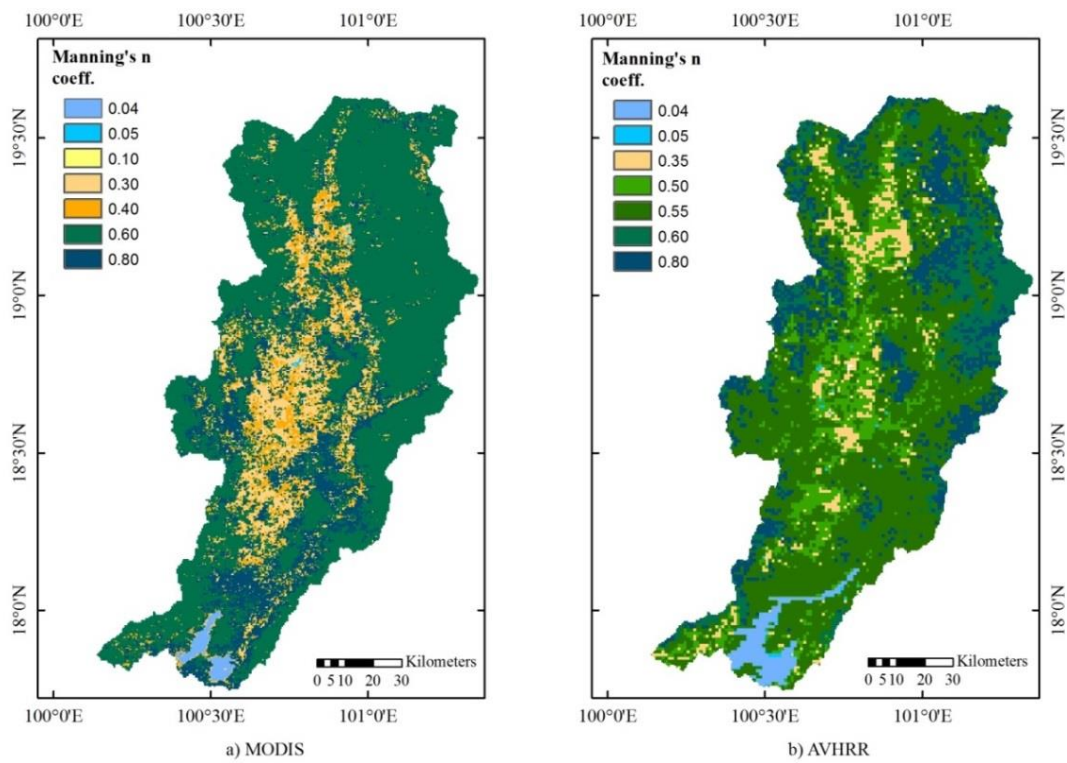
Figure 4-13 Manning's n map of the satellite products, MODIS and AVHRR
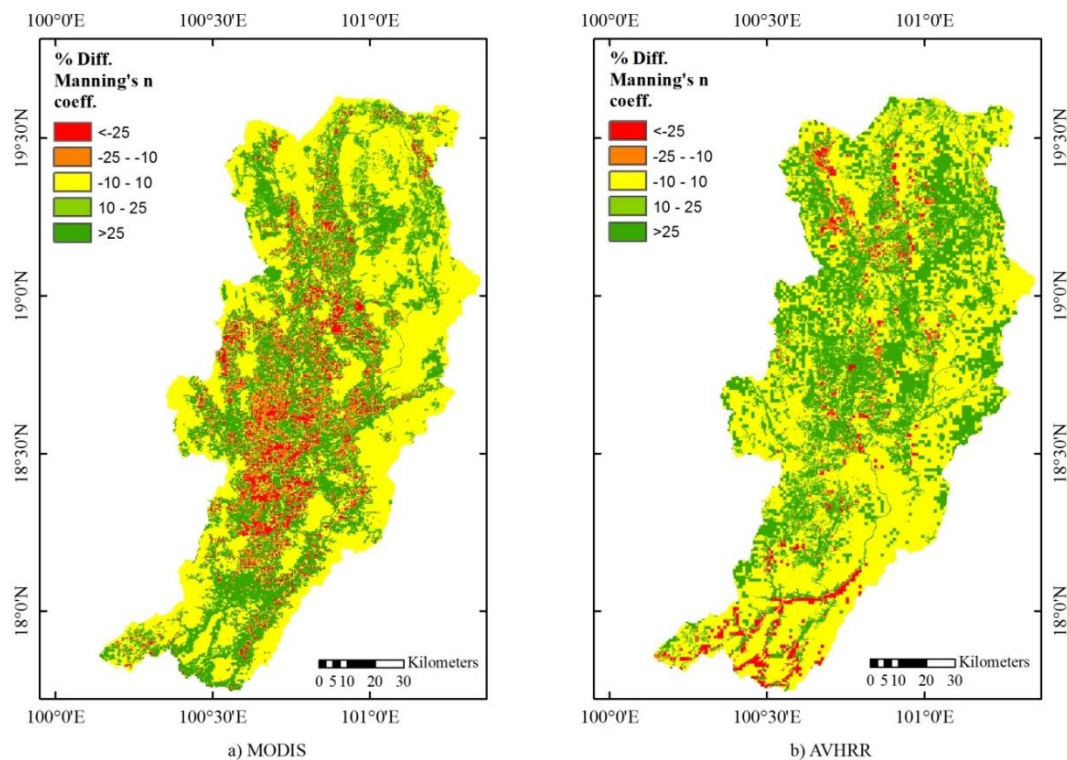
Figure 4-14 Deviation of manning's n map of the satellite products, MODIS and AVHRR

Overall quantify a difference between satellite referent observed land cover map, the both satellite based is over laid onto the based referent map. Within each satellite land cover type the average Manning's coefficient values based on the satellite land cover map and the based referent map are calculated. The averages for all the land cover types in the Shikoku area and the calculated percent differences are presented in **Table 4-18** for MODIS and **Table 4-19** for AVHRR. The differences of percentage were weighted by the ratio of the pixel number of the land cover type within the tested area to the total pixel number in the tested area to create a weighted percentage difference as presented in **Table 4-18** for MODIS and **Table 4-19** for AVHRR. The weighting helps to focus the significance of the differences in the land cover classification to influence the overall difference for the tested area and for affecting hydrologic model outputs.

On hypothesis of this study, the Manning's coefficient differences from the different sources are different. The differences are suspected to be major impact for distributed hydrologic modeling. The question is how the differences in Manning's coefficient vales affect in the distributed hydrologic model results.

Table 4-18 Performance statistics of Manning's n in each MODIS land cover type

MODIS Description	No. pixels	Avr. MODIS, n	Avr. Ref., n	Diff. (MODIS-Ref.)	% Rel. Err.	Weighted % Rel. Err
Water	55,526	0.04	0.054	-0.014	-25.3%	-0.274%
Evergreen Needleleaf tree	2,286	0.40	0.158	0.242	>100.0%	0.068%
Evergreen Broadleaf tree	3,238,006	0.60	0.518	0.082	15.9%	10.029%
Deciduous Needleleaf tree	-	0.40	-	-	-	-
Deciduous Broadleaf tree	714,230	0.80	0.498	0.302	60.8%	8.447%
Shrub	352,292	0.40	0.440	-0.040	-9.1%	-0.625%
Grass	551,098	0.30	0.426	-0.126	-29.6%	-3.169%
Cereal crops	53,032	0.40	0.286	0.114	39.9%	0.411%
Broad-leaf crops	165,220	0.30	0.345	-0.045	-13.1%	-0.420%
Urban and build-up	8,065	0.05	0.201	-0.151	-75.1%	-0.118%
Snow	-	0.05	-	-	-	-
Bare or sparse vegetable	81	0.10	0.062	0.038	60.4%	0.001%

Table 4-19 Performance statistics of Manning's n in each AVHRR land cover type

AVHRR Description	No. pixels	Avr. AVHRR, n	Avr. Ref., n	Diff. (MODIS-Ref.)	% Rel. Err.	Weighted % Rel. Err
Water	137,468	0.04	0.220	-0.180	-81.8%	-2.19%
Evergreen Needleleaf tree	-	0.40	-	-	-	-
Evergreen Broadleaf tree	520,548	0.60	0.535	0.065	12.2%	1.24%
Deciduous Needleleaf tree	-	0.40	-	-	-	-
Deciduous Broadleaf tree	703,731	0.80	0.529	0.271	51.2%	7.01%
Mixed forest	-	0.55	-	-	-	-
Wooded land	2,714,159	0.55	0.505	0.045	9.0%	4.75%
Wooded grassland	688,897	0.50	0.431	0.069	16.1%	2.16%
Closed shrubland	-	0.40	-	-	-	-
Open shrubland	-	0.40	-	-	-	-
Grassland	12,127	0.30	0.400	-0.100	-24.9%	-0.06%
Cropland	361,519	0.35	0.404	-0.054	-13.3%	-0.94%
Urban and build-up	1,387	0.05	0.083	-0.033	-39.9%	-0.01%

4.3.5 Runoff simulation in the Shikoku Island

The hydrological model (RRI model) was driven for flood events in 2014 for Shikoku Island in Japan. The three land cover products were simulated at hourly on a temporal scale to match the observed streamflow data. Seven runoff stations were selected in the Shikoku Island as mention in **Figure 3-24**, the first (Ikeda dam) and second (Chuobashi) belong to the Yoshino River. The third (Furushou) is in the Naka River and the fourth (Fukabuchi) in the downstream area of the Monobe River. The fifth is located in the Ino, belonging to the Niyodo River; the sixth located in the Shimanto River is the Gudoudaini station. The seventh station is the Deai located in the Shigenobu River. All of stations showed in the hourly hydrograph that results from the different topography source. **Figure 4-15** presents the hydrographs for all sources with the seven runoff stations.

All simulated runoff driven by different products was provided as the temporal data similar to the observed hydrograph for the flood event. Overview of all the runoff station, all products symmetrically captured the peak at the same time with the observation, and it systematically underestimated observed runoff. For the third until seventh station, their simulated runoffs showed the high underestimation to compare with the observed hydrograph.

All of seven runoff station on the hourly hydrograph were analysed and calculated for evaluation by the performance statistical in a summary. The results are given in **Table 4-20** that is concluded by five indexes. Manning's coefficient value of based referent map simulated discharge was the best matched by observed runoff with a high Correlation of 0.942 and lowest RMSE of 307.59 cms. This simulated runoff underestimated the runoff volume, peak flow and mean runoff by 2.55%, 31.41% and 7.26 cms, respectively. MODIS product simulated runoff was the high Correlation (0.941) and low RMSE, and its simulated runoff was underestimation in Volume bias of 2.65% and Mean bias of 7.57%. The peak flow of the MODIS underestimated about 32.79%. AVHRR product simulated runoff was low RMSE value of 310.21 cms with strong correlation value of 0.942, this simulated results underestimated the runoff volume, and mean runoff by 2.68%, 7.65 cms, respectively. The peak flow of the AVHRR underestimated about 32.5%.

In summary performance on estimating the streamflow, the best land cover products was based referent map that statistical presented the best value. AVHRR product was the best performance among the satellite source products with a small difference evaluated value. Based on the **Table 4-20**, it shows the statistics for the three simulations and contributes the claim that there is no significant impact on the runoff hydrograph at the observed station when using difference in spatial Manning's coefficient map.

a) Ikeda, Yoshino river

b) Chuobashi, Yoshino river

c) Furushou, Naka river

d) Fukabuchi, Monobe river

e) Ino, Niyodo river

f) Gudoudaini, Shimanto river

g) Deai, Shigenobu river
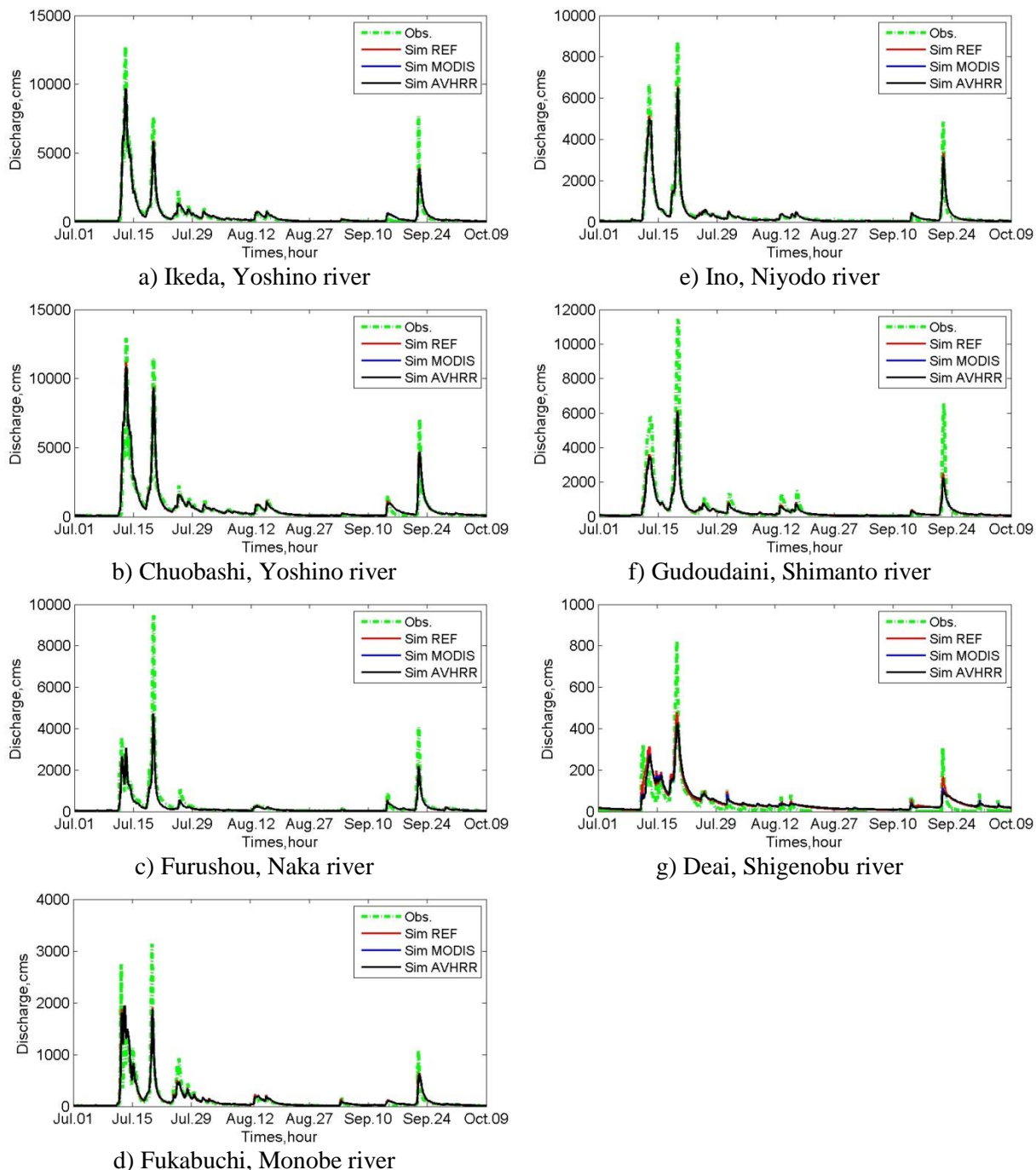
Figure 4-15 Hourly discharge hydrograph at runoff observation station of flood event based on different satellite products in the Shikoku Island Japan

Table 4-20 Performance statistical between observed and simulated data in flood 2014

Rainfall products	Volume bias, %	Peak bias, %	RMSE, cms	Correlation	Mean bias, cms
REF.	-2.54	-31.40	307.59	0.942	-7.26
MODIS	**-2.65**	-32.79	312.05	0.941	**-7.57**
AVHRR	-2.68	**-32.50**	**310.21**	**0.942**	-7.65
MODIS- REF.	-0.11	-2.02	36.54	0.9989	-1.10
AVHRR- REF.	-0.14	-1.60	23.82	0.9995	-1.41
MODIS-AVHRR	0.03	-0.42	16.28	0.9997	0.31

118

4.3.6 Runoff simulation in the Nan river basin

The hydrological model (RRI model) was driven for July 2011 and August 2014 storm events, using the similar hydrologic parameters set. The three different land cover data were estimated at daily on a temporal scale to match the Royal Irrigation Department Thailand observed streamflow data. Three runoff stations were selected in the Nan river basin as mention in **Figure 3-26**, the first one belonging to the upstream sub-catchment (N.64), the second one belonging to the middle area (N.1) and the third one belonging to the downstream area (N.13A), to show the daily hydrograph that results from the different interpolation scenario. **Figure 4-16** and **4-17** present the hydrographs for all rainfall interpolation scenarios and storm event of respectively runoff station N64, N.1 and N.13A.

All the modeled runoff driven by different interpolation methods was to provide the temporal pattern similar to the observed hydrograph for the June 2011 event. Overview all the runoff station, the three land cover data sets symmetrically captured the peak at the same time with the observation. For N.13A, all of interpolation products were underestimation to compare with the observed hydrograph. AVHRR was significantly overestimated of peak in a small value, while volume and mean were significantly underestimation. The simulated streamflow in the August 2014 provided the similar temporal pattern with observed hydrograph. With the first peak, all data sources were overestimation with observed hydrograph, while the second peak was underestimation. All of products on this peak at N.13A were underestimation.

All of three runoff station on the daily hydrograph were analyzed and calculated for evaluation by the performance statistical in a summary. The results are given in **Table 4-21** that is concluded by five statistical. The based referent map simulated discharge best matched the observed runoff with the highest Correlation and low RMSE for the first event (June 2011). This simulated runoff underestimated the runoff volume, peak flow and mean runoff. The MODIS simulated runoff was high Correlation and lowest RMSE, however, its simulated runoff was overestimation in volume bias, mean bias and peak flow. The AVHRR significantly overestimated the runoff volume, mean runoff and peak flow.

For the August 2014 storm event as shown in **Table 4-22**, the based referent map simulated flow also matched perfectly with overestimation based on the volume bias, RMSE and mean bias and highest correlation, with underestimation of peak flow. The MODIS runoff overestimated with high runoff volume and mean runoff value, on the lowest bias of the peak. Its result presented the lowest RMSE and good correlation value. The AVHRR results showed the overestimation of runoff volume and mean runoff, however, their peak flow were underestimation.

In summary performance on estimating the streamflow, the best land cover products was based referent map that statistical presented the best value. The based referent map based on the aerial data

source, while AVHRR product was the best performance among the satellite source products with a small difference evaluated value. Based on the **Table 4-22**, it shows the statistics for the three simulations and contributes the claim that there is significant in a small impact on the runoff hydrograph at the observed station when using difference in spatial Manning's coefficient map.
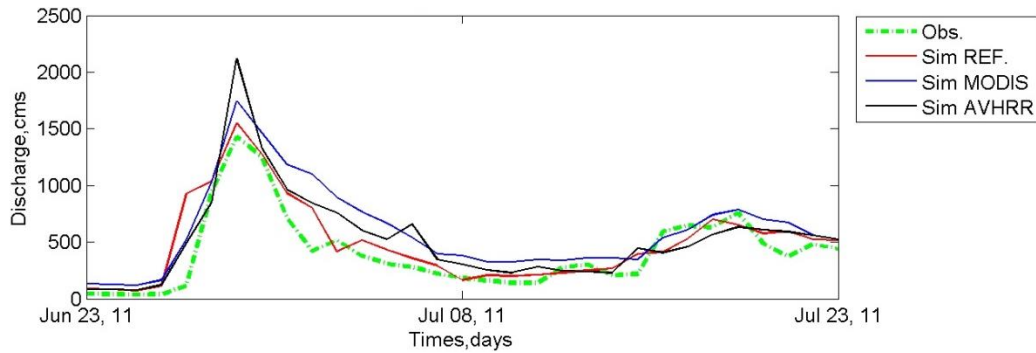
d) N.64
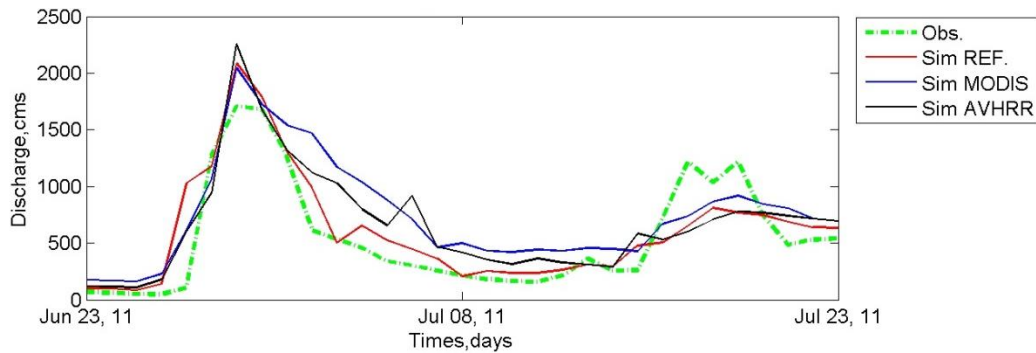
e) N.1
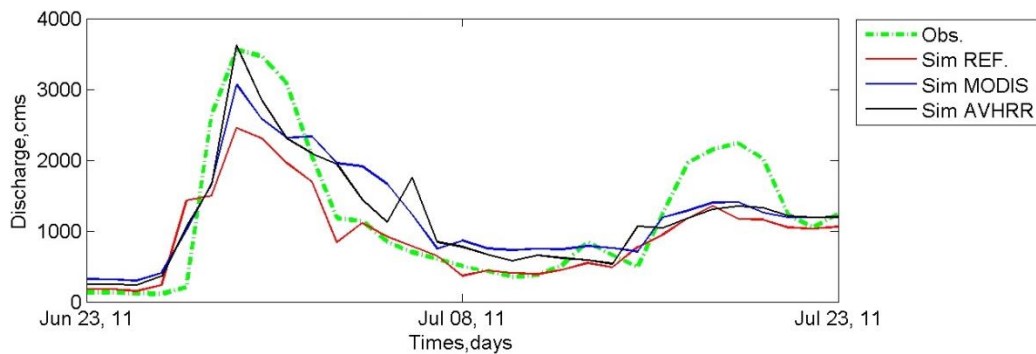
f) N.13A

Figure 4-16 Daily discharge hydrograph at runoff observation station of 2011 storm event

Table 4-21 Performance statistical between observed and simulated data in 2011 storm event

Rainfall products	Volume bias, %	Peak bias, %	RMSE, cms	Correlation	Mean bias, cms
REF.	-5.36	-9.11	382.04	0.882	-38.72
MODIS	19.26	**2.22**	387.63	**0.881**	139.04
AVHRR	**10.66**	19.40	**366.31**	0.879	**76.95**
MODIS- REF.	26.02	12.47	284.95	0.925	177.76
AVHRR- REF.	16.93	31.38	270.76	0.927	115.67
MODIS-AVHRR	7.77	-14.39	172.92	0.967	62.08
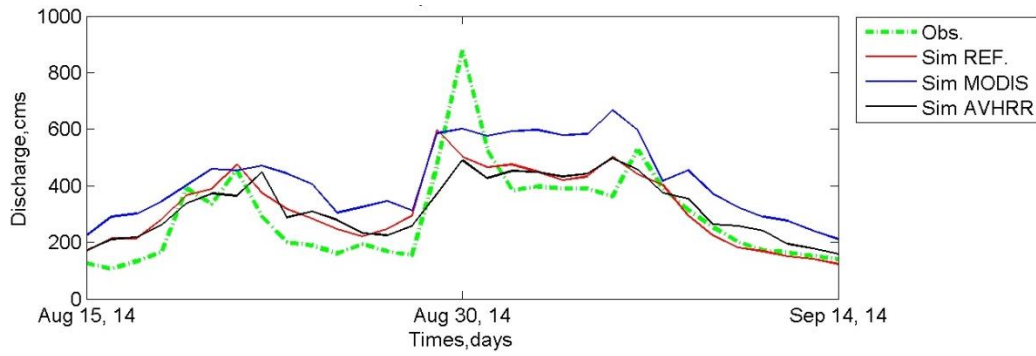
a)   N.64
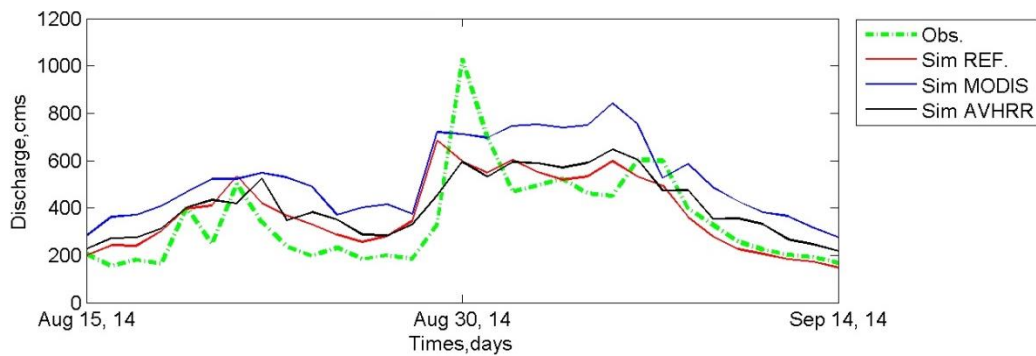
b) N.1
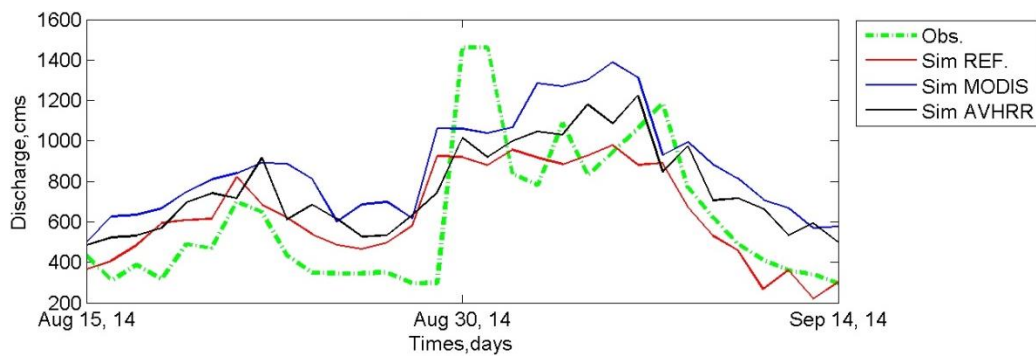
c)   N.13A

Figure 4-17 Daily discharge hydrograph at runoff observation station of 2014 storm event

Table 4-22 Performance statistical between observed and simulated data in 2014 storm event

Rainfall products	Volume bias, %	Peak bias, %	RMSE, cms	Correlation	Mean bias, cms
REF.	6.40	-34.59	163.88	0.821	26.94
MODIS	43.40	**-14.15**	253.67	0.797	182.71
AVHRR	**18.30**	-32.28	**180.23**	**0.818**	**77.04**
MODIS- REF.	34.78	31.26	186.25	0.931	155.77
AVHRR- REF.	11.19	3.54	116.75	0.902	50.11
MODIS-AVHRR	21.22	26.77	124.85	0.971	105.66

121

4.4 Conclusion

This study addresses the uncertainty affected in approximating the Manning's coefficients of surface roughness and the effect it has on distributed hydrologic modeling outputs. A land cover based approach to approximate Manning's coefficient on a satellite based was compared to referent observed land cover (aerial based) for two study areas, the Shikoku Island Japan and the Nan river basin Thailand. The two satellite sources Manning's coefficient maps produced by the look-up table method were compared and significant differences in the aerial based Manning's coefficient values were observed. The relationship between land cover classes and Manning's coefficient values were collected from the previous as a literature review. The based referent map generated "smoother" surfaces than the MODIS, while the AVHRR generated "rougher" surfaces than those the based referent map, in the Shikoku Island, Japan. For the Nan river basin, Thailand, The based referent map generated "smoother" surfaces than the MODIS, while the AVHRR also generated "smoother" surfaces than those the based referent map. These variations are attributed to the unsupervised classification algorithm used in the development of both satellite data sources (MODIS and AVHRR). It is also observed that the significant variation of Manning's coefficient between the three sources does not translate into significant runoff response differences on both hydrograph magnitude and shape, for the distributed hydrological model (RRI model). This is confirmed by three storm events on two study areas, although small differences in runoff response were observed at the observed runoff station. This observation suggests the use of MODIS, AVHRR or other Manning's coefficient estimation approaches for large watersheds provide a reasonable estimate of Manning's coefficient for simulating runoff hydrographs. Further studies are needed to confirm this observation for different watersheds and different method for estimating Manning's coefficient.

Chapter 5 Evaluation of different bias correction methods of satellite rainfall sources and their impact on distributed hydrological modeling results[.]

5.1 Introduction

Rainfall is regularly defined as being the key variable for considering the runoff based on the hydrological processes. Consequently, the spatial of rainfall is directly impacts the hydrological system on a distributed hydrological model, several researches have focused on the outcome on discharge. Goodrich et al. (1995) reported that uniform rainfall can be applied for modeling the runoff on small catchments although the rainfall spatial has significant impact to discharge. Schuurmans and Bierkens (2007) point out a single rain gauge has carried a false prediction if it located outside the watersheds, and rainfall spatial is essentially for runoff modeling. They conclusion is summarized by using the eight rainfall scenario based on spatial either distribution or uniform resulting from the distributed hydrological model of small catchment. Tsntikidis et al. (2002) and Chintalapudin et al. (2012) noted that watersheds contain with the sparse distribution of rain gauges, it cannot capture a spatial of rainfall for runoff modeling. Rainfall variable is direct to essential discharge for frequent events proposed by Arnaud et al. (2002). This study is done by using four artificial catchments of 20-1500 sq.km and 3 different hydrological models. Bell and Moore (2000) present the use of high spatial of rainfall that has specially utilized in the convective rainfall event case.

Several have utilized rainfall-runoff modeling of hydrological processes to generate runoff, such as the Rainfall-Runoff-Inundation (RRI) model. Sayama et al. (2012) demonstrated that RRI model performed a good agreement simulated by an inundation map produced to compare with MODIS satellite for large-scale area flood. Pakoksung and Takagi (2015) showed a good performance of the RRI model to simulate runoff in the Nan River, Thailand. The RRI model was simulated on the 2011

[.] This chapter is based on:

1. K. Pakoksung, M. Takagi, 2016, Effect of Spatial Distribution of Ground Rainfall Products on River Basin Responses of a Distributed Hydrological Model: *Journal of Spatial Hydrology* (**submitted**).

2. K. Pakoksung, M. Takagi, 2016, Effect of Satellite Based Rainfall Products on River Basin Responses of Runoff Simulation on Flood Event: Modeling Earth Systems and Environment, 2(143), 1-14. DOI :10.1007/s40808-016-0200-0.

3. K. Pakoksung, M. Takagi, 2016, Modeling the Distribution of Rainfall Intensity using Daily Data: *Engineering Journal* (**submitted**).

4. K. Pakoksung, M. Takagi, 2016, Effect of Bias Correction Algorithm of Satellite Base Rainfall on Runoff Estimation: (in **preparing**).

flood in Sukothai province, Thailand. The simulation, has closed by observation data, was used for estimating damage cost (Anurak et al., 2013).

A promising approach to capture the rainfall spatial is satellite based data. Near real time satellite products are now conveniently obtainable in the world, especially in developing countries. The uses of earth observation satellites have been about 30 years ago however these data have contained error from estimating rainfall dataset. In a recent year, the rainfalls produced by satellite have been increasing to application on basin scale of distributed hydrological model. The accuracy of satellite based precipitation products have been increased as GPM data that is the new open source satellite product generated by using several new techniques such as merge different satellite.

Several have utilized different satellite based rainfall products in modeling of hydrological processes to generate runoff, such as Global Satellite Mapping of Precipitation (GSMaP), Tropical Rainfall Measuring Mission (TRMM), CPC MOPGHing technique (CMORPH), and Precipitation Estimation from Remotely Sensed Information using Artificial Neural Networks (PERSIANN). Sayama et al. (2012) demonstrated that GSMaP data performed a good agreement simulated by using the Rainfall-Runoff-Inundation model to compare with an inundation map produced by MODIS satellite for large-scale area flood. Pakoksung and Takagi (2015) concluded that TRMM precipitation data was the best precipitation data to simulated runoff in the upper part of Nan river basin, Thailand, whereas Tan et al. (2015) showed that TRMM estimated a good rainfall rates that CMORPH and PERSIANN rainfall product over Malaysia. Jiang et al. (2010) used CMORPH product to simulate runoff that its result were better correlation than TRMM applied over the Laohahe river basin in norther part China. Chintalapudi et al. (2014) recommended that PERSIANN represented by coarse resolution data have produced better discharge results than higher resolution data such as TRMM over the Guadalupe watershed in USA.

The several studies present that it is important to decrease the error in the satellite rainfall products before the data are implemented in hydrological application. Bias correction methods are established for radar rainfall application (Seo and Breidenbach, 2002; Seo and Breidenbach, 1999; Zhang et al., 2009) and adapted to satellite remote sensing approach. The bias correction have implemented on monthly data (Huffman, 2007), downscale of daily data to hourly data (Boushaki, 2009), and assimilation observation and satellite rainfall data with a non-parametric kernel smoother (Li and Shao, 2010). Manz et al. (2016) evaluated five merging methods: linear modeling, residual inverse distance weighting, ordinary kriging, residual ordinary kriging, and kriging with external drift method. The study indicated that the inverse distance method was similar to the geostatistical method that outperformed the other methods. Muller and Thompson (2013) used the stochastic modeling to adjust the satellite rainfall, and concluded that the bias correction based on frequency domain outperformed the other approaches. Vernimmen et al. (2012) proposed the power transformation algorithm to bias

the satellite rainfall data in spatial and temporal scale on monthly-based. The biased products can apply to real-time drought monitoring. Comparison of five assimilation scheme, additive bias correction, ratio bias correction, gauge-to-satellite monthly correction factors, and a combined scheme, indicate that the combined scheme presented the highest performant (Vila et al., 2009). Other reports, Hong et al. (2006), Chiang et al. (2007), Tobin and Bennett (2010), and Tian et al. (2010), mentioned to bias correction of satellite rainfall. The conclusion of these studies is that selection of bias correction method must depend on accuracy requirement and characteristics of rainfall in spatial and temporal scale. Though, the data requirements, computational analysis, and, more essentially, the hydrological model are used for the biased data. Generally, products of satellite rainfall bias correction are estimated to better match rain gauges compared to satellite only even of the data set in complex terrain (Krahaner et al., 2013) and intrinsically adjustment must develop hydrological model by developed rainfall pattern. However, outcome of hydrological modeling are inconsistent and need further assessment.

Satellite rainfall data in negative bias resulted a pool performance driven by rainfall-runoff modeling that model requires recalibration when *in-situ* rainfall data is replaced to the satellite rainfall data (Artan et al, 2007). The satellite rainfall data outperforms rain gauge data to evaluate in a hydrological modeling that a parameter values is unreasonable due to the model compensate the error in the rainfall input (Zeweldi et al, 2011). Bias correction products of satellite rainfall data can result a runoff to capture pattern and magnitude on temporal scale at six hourly and monthly (Behrangi et al., 2011). Satellite rainfall products were corrected by rain gauge that the results are improvement in performance of runoff estimation (Yong et al., 2010). By the contrast, the satellite product as TRMM 3B42RT outperforms the satellite bias correction product as TRMM 3B42 to evaluate with hydrological modeling (Bitew and Gebremichael, 2011). The poor results could be identified due to sparse rain gauges that spatial and intensity of the rain gauges was used for the bias correction method.

The chapter is consisted by three objectives. Firstly, evaluation effect of spatial interpolation method of rain gauges on runoff estimation is considered. Secondly, evaluation effect of satellite rainfall is investigated on runoff simulation using hydrological modeling. Thirdly, effect of satellite rainfall bias correction is evaluated in five algorithms and two schemes. Their specific objectives of the three main are to assess accuracy of rainfall products from the rain gauge data using the statistical approach, and to evaluate the rainfall products on runoff estimation using hydrologic model.

5.2 Data and Methodology

5.2.1 Rain gauge and satellite rainfall data sets

Ground observed rainfall station for the Shikoku Island Japan was collected from the WIS in the MLIT data base on the website. There are 126 stations distributed in the area, which temporal data is hourly datasets during 35 years (1980-pressent). **Figure 5-1** presents a location of the 126 stations.

The ground rainfall observation product in the Nan river basin Thailand and neighbor basin was collected from the Royal Irrigation Department (RID), Thailand. There are 28 stations as shown in **Figure 5-2**, of which 17 stations are located in the watershed while 11 stations are located on the west side. The rain gauge temporal data is daily datasets during 28 years (1987-pressent).
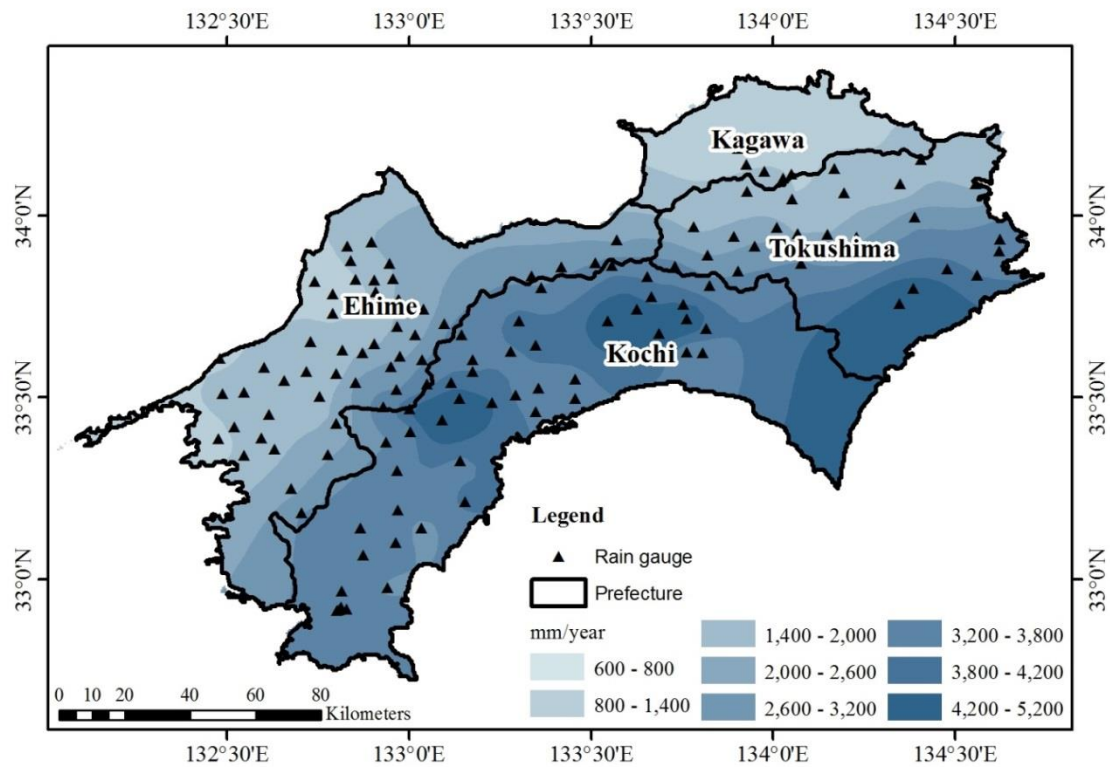
source: MLIT Japan

Figure 5-1 Rain gauges distribution and average annual rainfall in the Shikoku Island Japan
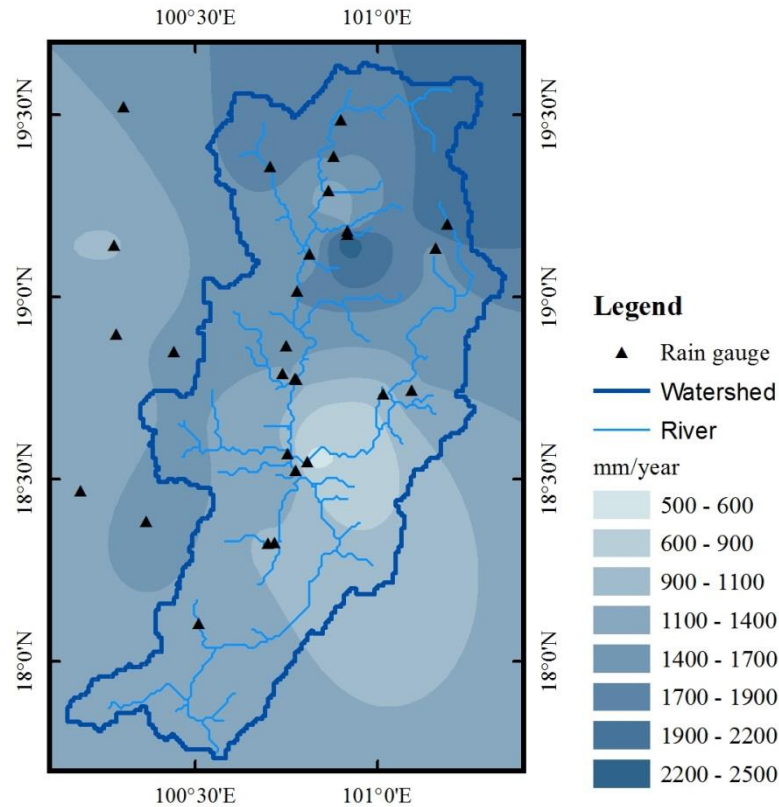
source: RID and TMD Thailand

Figure 5-2 Rain gauges distribution and average annual rainfall in the Nan river basin Thailand

The five satellite based rainfall products were used in this study, of which two are high resolution dataset and three are low resolution dataset. **Table 5-1** shows the information of rain gauge and satellite rainfall. The accuracy of each product was assessed at time scale by comparing with the rain gauges. Using the five products as input to the RRI model, their outputs have performed an accuracy assessment with observation discharge at runoff station on the five performance statistical coefficients.

Global Precipitation Measurement (GPM) project is originated generally by the United States and Japan, and then it is actively supported in Europe, France, India, and China with international cooperation. In this project, the microwave radiometers investigating microwave emission from precipitation will be measured on many low-orbit satellites, to downscale the interval to 3 hours in exploration time for each location on the earth (Kubota et al., 2014). However, the sampling error problem occurs when the global precipitation estimates are smaller than three hours. Therefore, it is essential to apply a gap-filling algorithm to establish precipitation maps with high resolution on temporal scale, which is moderately significant for effective uses such as flash flood warning systems.

The Global Satellite Mapping of Precipitation (GSMaP) project is supported and developed by JST-CREST and the JAXA Precipitation Measuring Mission (PMM) Science Team respectively (Okamoto et al., 2005). GSMaP, which have applied the Kalman filter algorithm to estimate the current surface

rainfall intensity at 0.1° pixel of the infrared brightness temperature by using the GEO-IR satellites, is implemented for this study. The detail of the algorithm can be referred in the literature (Aonashi and Liu, 2000 and Ushio et al., 2009). The GSMaP contained by the highest temporal and spatial resolution, can capture a precipitation event with real situation as observed rainfall, however, the precipitation quantity mostly has been underestimated (Fukami, 2010; Kubota et al., 2009; Makino, 2012; Seto et al., 2009; Shrestha et al., 2011). The GSMaP presents a good correlation on monthly and daily data using data in Japan (Seto et al., 2009), which appear to be enough for flood early warning.

Tropical Rainfall Measuring Mission (TRMM) with 3B42V7 number of collected product is the satellite based rainfall that locates in the tropical zone in the present day, which is a joint mission between NASA of USA and JAXA of Japan under the cooperation project in monitoring and exploration of space (Huffman et al., 2007). TRMM is the first satellite for monitoring variables, dynamic of precipitation, and latent heat of the precipitation process. The precipitation in the tropical zone is two-third of the total precipitation in the world, which plays an important role of the weather cycle. TRMM measurement is the combination between visible infrared and microwave sensor with high frequency for monitoring and recording data both space and time. The satellite operation has been built for measuring the occurrence of precipitation both in the earth and the equatorial since 1997. The satellite is consisted by five main type sensor of Precipitation Radar (PR), TRMM microwave Image (TMI), Visible Infrared Scanner (VIRS), Clouds and the Earth's Radiant Energy System (CERES) and Lighting Imaging Sensor (LIS). It has a circular and non-sun-synchronous orbit. The satellite observes from 305 km above the ground and 35 degree of orbit angle to equator, and it moves around the earth in 90 minutes or 16 times a day.

CPC Morphing Technique (CMORPH) is a global precipitation analyses for real-time monitoring of global scale developed by NOAA's Climate Prediction Center [CPC]. CMORPH has provided the high resolution with 8 km spatial and 30 minute temporal scale. In the CMORPH technique, geostationary satellite IR temperature data and polar orbiting passive microwave (PMW) sensors are implemented. The morphing algorithm is used to estimate the precipitation by the PMW and interpolate temporal weight in linearly (Joyce et al., 2004). In this study, the CMORPH resolution of 0.25 degree spatial and 3-h temporal product is implemented for comparing with other satellite rainfall; this product can be download from National Centers for Environmental Prediction (NCEP) CMORPH website.

Precipitation Estimation from Remotely Sensed Information using Artificial Neural Networks (PERSIANN) is a satellite-based precipitation products that are implemented by using the artificial

neural networks (ANN) to estimate rainfall intensity based on merged infrared product of brightness temperature from geostationary satellite (Hong et al., 2004). The detailed procedure of developing PERSIANN products are explained in the study of Sorooshian et al., (2014). This study implemented to use the PERSIANN of 0.25 degree spatial resolution and three hours temporal resolution products to compare with the other satellite products, that the dataset can be downloaded from the PERSIANN website.

The Grid Point Value (GPV) from the Meso Scale Model is the weather forecast data among other weather variable. The GPV-MSM data provides precipitation data at high resolution that have spatial pixel size about 0.0625 degree on longitude and 0.05 degree on latitude for surface data sets, every 1.0 hour. This data have been provided from Japan Meteorological Agency (JMA) and it can be collected from the Kyoto University site: http://database.rish.kyoto-u.ac.jp/arch/jmadata/data/. The forecasting method of GPV-MSM rainfall has calculated with Global Spectral Model (GSM) and Meso Scale Model (MSM) that data have provided only in Japan.

Table 5-1 Information of rainfall products

No.	Name	Spatial/ temporal resolution	Covering	Period	Reference
1	Rain gauges	Point data	Shikoku, Japan	1980-present	MLIT, Japan
2	Rain gauges	Point data	Nan, Thaialand	1987-present	RID, Thailand
3	GPM	0.10d/0.5h	Global/(90dN-S)	2014-present	Kubota et al., 2014
4	GSMaP	0.10d/1.0h	Global/(60dN-S)	2006-present	Okamoto et al., 2005
5	TRMM	0.25d/3.0h	Global/(50dN-S)	2000-Jun,2015	Huffman et al., 2007
6	CMORPH	0.25d/3.0h	Global/(50dN-S)	2002-present	Joyce et al., 2004
7	PERSIANN	0.25d/3.0h	Global/(60dN-S)	2000-present	Sorooshian et al. 2014
8	GPV	0.05d/1.0h	Japan	2003-present	Saito et al., 2006

5.2.2 Spatial interpolation methodology of rain gauges

Rainfall spatial distribution was used in this study to analysis from five input scenarios, of which three are deterministic spatial method and two are geostatistical spatial method. Using the five scenarios as input to the RRI model, their outputs have performed an accuracy assessment with observation discharge at runoff station, using five performance statistical coefficients.

In this study, deterministic methods (Inverse distance weighting, Thiessen polygon and Surface Polynomial), geostatistical (Simple kriging and Ordinary kriging) were developed by using Python to product the rainfall grid spatial. The performance of these methods was evaluated by the five statistics that the **Table 5-2** descripts detail of the statistics.

In generally, a spatial interpolation of sampling points value is estimated by a weight observed point values. The sampling points refer to the center of regular grid covering the watershed area. The formula of spatial interpolation is as follows:

$$R_e = \sum_{i=1}^{n} w_i \cdot R_i \tag{1}$$

where R_e is the estimated value of point e; R_i is the observed value of point i; n is the number of observed points as rain gauge in this study; w is the weight of observation point for interpolation. Coordinates of observed point is x_i and y_i in two dimensional space, and R_i is depended on x_i and y_i. The equation (1) can be used to estimate R_e at any coordinate x_e and y_e (Tabios and Salas, 1985).

i) Inverse Distance Weight (IDW)

Inverse Distance Weight (IDW) method estimates the sampling point's values using average weight of observed surrounding point's values. The weight of this method is represented by function of distance reverse, which increases as the distance decreases (Teegavarapu and Chandramouli, 2005). The weight can be estimated by:

$$w_i = \frac{\frac{1}{D_i^k}}{\sum_{i=1}^{n} \frac{1}{D_i^k}} \tag{2}$$

where D_i is the distance between observed point and sampling point; and k is friction distance that is usually used as 2 and also in this study (following Goovaert, 2000; Lloyd, 2005; Pakoksung and Takagi, 2015). Hence, the friction distance value of 2 is known as the Inverse Distance Square method.

ii) Thiessen polygon (TSP)

Thiessen polygon (TSP) method is called as the nearest neighbor (NN) method (Tabios and Salas, 1985; Nalder and Wein, 1998), which a value of unknown point such as center of each rainfall grid is estimated by using taking an observed value of a closest point. The weight based on the nearest distance can be estimated by:

$$D_{ei} = \sqrt{(x_e - x_i)^2 + (y_e - y_i)^2} \tag{3}$$

for $D_j = min(D_{e1}, \ldots, D_{en})$ and then $w_i = 0$ for $i \neq j$ while $w_i = 1$ for $i = j$.

This method is the simple algorithm, but it is unsuitable for mountain area due to the orographic effect of the rain (Ly et al., 2013).

iii) Surface Polynomial (SPL)

Surface Polynomial (SPL) is the trend surface method, which a global function is fitted to the study area of interest using either an algebraic or trigonometric polynomial function (Tabios and Salas, 1985). The general function is followed as:

$$R_e(x, y) = \sum_{k1=0}^{m} \sum_{k2=0}^{m} a_{k1,k2} \cdot x^{k1} \cdot y^{k2} \tag{4}$$

where $a_{k1,k2}$ is the $k1$ and $k2$ th polynomial coefficient; x and y are the coordinate of interpolated point; and m is total number of polynomial function fitted degree. Based on the study of Tabios and Salas in 1985, the weight value of each observed points is estimated by using Least-Squares method. The equation form is written as:

$$w_i = \sum_{k1=0}^{m} \sum_{k2=0}^{m} a_{k1,k2,i} \cdot x^{k1} \cdot y^{k2} \tag{5}$$

The polynomial coefficient for interpolating over an area is estimated by using the inverse matrix algorithm (Tabios and Salas, 1985; Pakoksung and Takagi, 2015). In this study, the total number of polynomial function fitted degree is used as 3 that is known as the Cubic Spline method.

iv) Semi-variogram model

Semi-variogram is a core tool of geostatistical methods to represent the spatial correlation in the experimental network at interest area. The geostatistical theoretical can be referred to Cressie (1991), Goovaerts (1997), Chiles and Definer (1999), Webster and Oliver (2007), and Ly et al. (2011). The semi-variogram can be analyzed by using the variance in distance between all pairs of sampled points. Its equation is followed as:

$$\hat{\gamma}(h) = \frac{1}{2N(h)} \sum_{i=1}^{N(h)} (R_i - R(U_i + h))^2 \tag{6}$$

where $N(h)$ is the number of pairs divided by lag h; U is vector of spatial coordinates. In this study, the semi-variogram was estimated from 28 rain gauges with daily rainfall of the both events. The estimated semi-variogram on a pooled semi-variogram was fitted by using spherical semi-variogram model. The semi-variogram model function is written as:

$$\gamma(h) = \begin{cases} C_0 + C(\frac{3h}{2a} - \frac{1}{2}\left(\frac{h}{a}\right)^3), & 0 < h \leq a \\ C_0 + C, & h > a \\ 0, & h = 0 \end{cases} \tag{7}$$

The spherical variogram model, the nugget variance (C_0) is 0.425, the partial sill (C) is 1.404 and the range (a) is 0.545 degree. The coefficients of the spherical model were used to estimate the weight though equation (1) with two different kriging methods, simple kriging and ordinary kriging.

a) Simple kriging (SKG)

Simple kriging uses mean of sampling data set and semi-variogram model to estimate the weight in each observed points. The weight equation of the SKG is followed as:

$$w_i = \gamma_i \left[C - \gamma(h_{ij}) \right]^{-1} \cdot (C - \gamma(h_{ip})) \tag{8}$$

where $\gamma(h_{ij})$ is the semi-variogram of R between point i and j; h_{ip} is the semi-variogram distance of observed and interpolated point.

b) Ordinary kriging (OKG)

Ordinary kriging is a linear system of geostatistical method. Its weights are achieved from minimized variance and unbiased estimation. The weight system of the OKG is written as:

$$w_i = \gamma(h_{ij})^{-1} \cdot \gamma(h_{ip}) \; ; \sum_{i=1}^{n} w_i = 1 \tag{9}$$

where $\gamma(h_{ij})$ is the semi-variogram of R between point i and j; h_{ip} is the semi-variogram distance of observed and interpolated point. With the unbiased estimation, constraint of the function, sum of the weight is equal to one.

5.2.3 Bias correction methodology of satellite rainfall products

The bias correction with five methods and two schemes were used in this study to produce improvement products. The accuracy of each product was assessed at time scale by comparing with the rain gauges. Using the biased products as input to the RRI model, their outputs have performed an accuracy assessment with observation discharge at runoff station on the five performance statistical coefficients.

i) Bias correction methods

Five bias correction techniques were used to compare bias corrected satellite rainfall data to respect with rain gauge rainfall data. Description of the bias correction techniques is presented in following sections. Main variable of the bias correction is R and S, observation and satellite rainfall.

a) Mean ratio

The corrected data was firstly adjusted by finding the mean ratio between rain gauge and satellite (Ines and Hansen, 2006; Acharya et al., 2013; Aws et al., 2015). As shown in equation (10).

$$R_i = \frac{\bar{R}}{\bar{S}} \cdot S_i \tag{10}$$

The ratio vale is calculated in the cross validation method. The advantage of this technique is that the bias value is removed from mean, while its disadvantage is to fail in correction of rainfall intensity.

b) Geomatics transformation

This technique bases on assumption as the elevation and coordinate have effect to rainfall intensity (Mohamed, 2015). Then, the relationship between observation and satellite rainfall is functioned by the geometrics data, latitude, longitude, and altitude that can be formed in the multiple linear regressions (Zhang and Zhang, 2011; Kurakose and Viswan, 2013).

$$R_i = a \cdot X_i + b \cdot Y_i + c \cdot Z_i + d \cdot S_i + R_0 \tag{11}$$

where a, b, c, d and R_0: coefficient and constant of the multiple linear regression. Inverse matric method is used to estimate the coefficient and constant in this study (Ishida and Takagi, 2010; Pakoksung and Takagi, 2015).

c) Linear transformation on normal distribution

This technique follows with the linear equation as shown in equation (12). The technique is a simple mean based, but it may not capture change in frequency distribution (Achaya et al., 2013; Aws et al., 2015).

$$R_i = a + b \cdot S_i \tag{12}$$

where a, b are a constant and coefficient of the linear equation. The constant and coefficient of the linear regression can be estimated by the least square method as follows (Krishnamurti et al., 2000; Kharin and Zwiers, 2002).

$$b = Cov(R, S)/Var(S) \tag{13}$$

$$a = R - b.S \tag{14}$$

where $Cov()$ is the covariance for rain gauge and satellite rainfall, $Var()$ is variance for rain gauge and satellite rainfall.

d) Data assimilation on normal distribution

This technique is the 1DVAR of the variational data assimilation methods that consider a model scalar variable with error variance and an observation uncertainty (Reichle, 2008). The variance of both follows as equation (15) and merged data ($\hat{S}$) is described in equation (16).

$$Var = \sqrt{(Var_R^{-2} + Var_S^{-2})^{-1}} \tag{15}$$

$$\hat{S} = Var^2 \cdot (Var_S^{-2} \cdot S + Var_R^{-2} \cdot R) \tag{16}$$

where $Var()$ is variance for rain gauge and satellite rainfall.

e) Quantile mapping

This technique is one of the most common in statistical bias correction approach that the technique has been widely applied in the model forecasting (Wood et al., 2002, 2004; Ines and Hansen, 2006; Piani et al., 2010; Acharya et al., 2013). Transformation function of this technique is directly

estimated form the observed and modeled data. The transformation of both data sets is fitted to a probability distribution function (PDF) of continuous statistical. For this study, empirical PDF is used that are based on the Kaplan-Meier method (Picad et al., 2013; Cai and Rouss, 1998). The quantile mapping technique follow two steps: estimate the cumulative distribution function (CDF), and use the transfer function to generate a correction data (Ines and Hansen, 2006).

$$\hat{S} = CDF_S^{-1}(CDF_R \times R) \tag{17}$$

where CDF_R and CDF_S are the cumulative distribution function of observation and satellite rainfall.

ii) Bias correction schemes

In the current study, two schemes are tested for bias correction, point to point and grid to grid. The point to point is identified as temporal bias correction, while spatial bias correction is grid to grid scheme.

a) Point to point bias scenario

This scheme is analysis the bias correction at point of the data sets between rain gauge and satellite data. **Figure 5-3** presents the stream line of this scheme. Firstly, the satellite data in grid data sets is captured to point data sets by using the coordinate of the rain gauges. Secondly, the captured satellite data set as point data are corrected by using the rain gauge data set with the five bias correction techniques. Finally, the corrected products is interpolated to grid by the best spatial algorithm that are descried in section 5.3, and the five bias grid products are evaluated the best for runoff estimation in section 5.5.
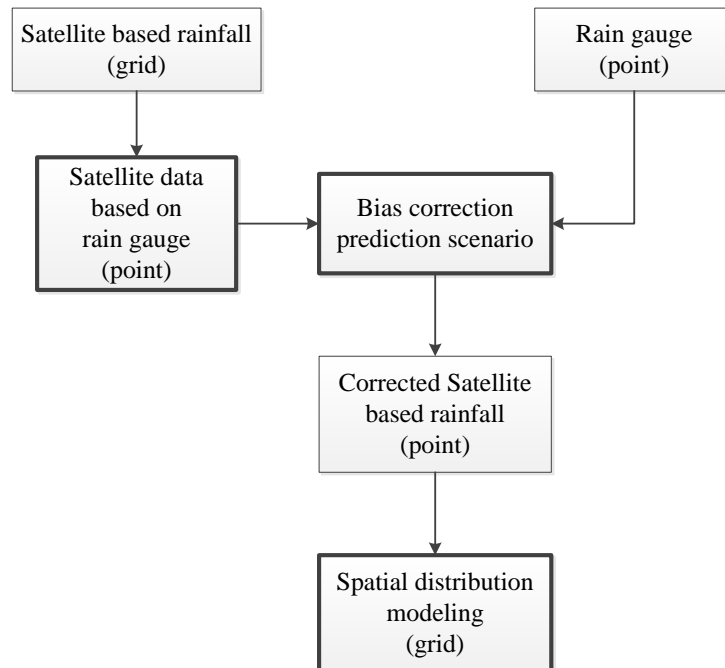
Figure 5-3 Point to point (Time variation) bias correction scheme concept

b) Grid to grid bias scenario

This scheme is analysis based on the grid approach between rain gauge and satellite data. **Figure 5-4** presents the stream line of this scheme. The rain gauge as point data sets is interpolated to grid as a spatial data set as same as a resolution of satellite data by using the best algorithm that is identified in the section 5.3 at first. The satellite data is corrected by using the observed grid rainfall with the different five techniques as mentioned above. Finally, the five bias satellite grid products are evaluated the best for runoff estimation in section 5.5.
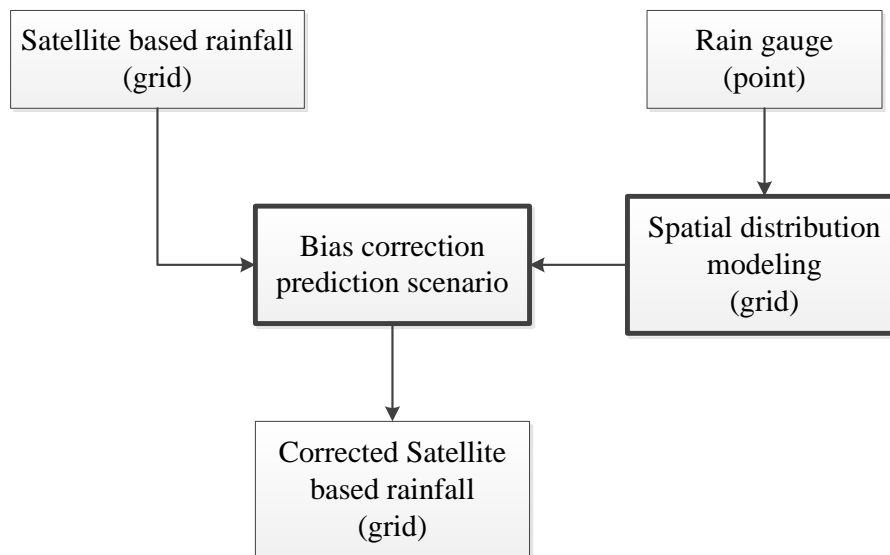
Figure 5-4 Grid to grid (Spatial variation) bias correction scheme concept

5.2.4 Performance statistics

The estimation results driven by the several methods based on the hourly and daily rain gauge data were evaluated to analysis bias of volume (V_{bias}), bias of peak (P_{bias}), root mean square error ($RMSE$), square of the Pearson correlation coefficient (r), and mean error(ME). The following formulas (see **Table 5-2**) were applied to evaluate simulation performance. The volume bias and peak bias estimate the systematic bias of modelled runoff in percentage (%). The correlation index is quantification in correlation of two data sets, simulated and observed runoff, which 0 is no correlation while 1 is perfect correlation. The $RMSE$ is a different measure of difference magnitude between two data sets, while the ME is the bias between two data sets.

Table 5-2 Description of performance statistical

Statistical index	Description
Volume bias (%)	$V_{bias} = \dfrac{\|Q_{vo} - Q_{vs}\|}{Q_{vo}} \times 100$
Peak bias (%)	$P_{bias} = \dfrac{\|Q_{po} - Q_{ps}\|}{Q_{po}} \times 100$
Root mean square error	$RMSE = \sqrt{\dfrac{\sum_{i=1}^{n}(Q_{o(i)} - Q_{s(i)})^2}{n}}$
Correlation	$R^2 = \dfrac{\sum_{i=1}^{n}((Q_{o(i)} - \overline{Q_o}) \cdot (Q_{s(i)} - \overline{Q_s}))}{\sqrt{\sum_{i=1}^{n}(Q_{o(i)} - \overline{Q_o})^2 \cdot \sum_{i=1}^{n}(Q_{s(i)} - \overline{Q_s})^2}}$
Mean bias	$ME = \dfrac{\sum_{i=1}^{n}(Q_{o(i)} - Q_{s(i)})}{n}$

where

Q_{vo} is observation volume

Q_{vs} is simulation volume

Q_{po} is observation peak

Q_{ps} is simulation peak

Q_o is observation data

Q_s is simulation data

n is total number of sample

5.2.5 Hydrological simulation

Input data sets of the RRI model are four data types; rainfall product, topography, land cover and soil type. On the definition of the distributed hydrologic model with the RRI model, the used hydrologic parameters were mentioned in the **Chapter 2** such as Manning's roughness of land cover type and Green-Amp parameter of soil type. The spatially pixel of DEM in this study it has been scaled to 500 m of pixel size (about 15 x 15 arc-second). Addition to the numbers of pixel, row and column numbers are 457 and 292 respectively to present the watershed area as 13,000 km^2 for the Nan river basin. For the Shikoku Island, row and column numbers are 401 and 650 respectively for the area about 18,000 km^2. The estimation of width and depth were recommended in the equation (4) and (5) in the **Chapter 2**. Rainfall data was collected from the rain gauges, covering the study area. For the Nan river basin, June 2011 and August 2014 storm events are implemented to evaluate different

rinfall products that are used to run the RRI model over the basin. The rainy season during July to October in 2014 is used to evaluate the runoff in different DEM source for the Shikoku Island.

The simulated results driven by the different rainfall sources were evaluated to analysis bias of volume (V_{bias}), bias of peak (P_{bias}), Root Mean Square Error ($RMSE$), square of the Pearson correlation coefficient (r), and Mean Error (ME). The following formulas in **Table 5-2** were applied to evaluate simulation performance.

5.3 Evaluation of spatial interpolation algorithms of rain gauge

The July to October 2014 during typhoon season were applied to evaluate different rainfall products that are used to run the RRI model over the Shikoku Island, Japan. In the 2014, the Shikoku Island was attracted from the huge storms about 5 typhoons. The first typhoon was typhoon number 8 during July 2 – 11, attracting on July 10. Typhoon number 11 came on August 9, and number 16 was small effect on September 24. At the end of typhoon season, typhoon number 18 attracted on October 5, and number 19 was October 13.

The June 2011 and the August 2014 storm events were implemented to evaluate different rainfall products that are used to run the RRI model over the Nan river basin, Thailand. In addition to Tropical storm and Thunderstorm, causing of a huge rainfall obtains from the storm that are originates from Pacific Ocean to travel westward cross this area in June to August. From 24th to 30th June 2011, tropical storm the Haima hit the northern part Thailand to bring precipitation as 200 mm in the upstream of study area over two days. Normally, the northern part of Thailand is affected by the Inter-Tropical Convergence Zone (ITCZ) (Schneider et al., 2014) during May to August. Monsoon during 28-30 August 2014 across the northern part of Thailand brought a heavy rainfall about 100 to 150 mm. The heavy rainfall caused severe flooding and river bank over flow.

5.3.1 Accuracy assessment of spatial interpolation algorithms: Shikoku Island, Japan

All of rainfall spatial products applied in the study from different spatial interpolation algorithms, Inverse distance weighting (IDW), Thiessen polygon (TSP), Surface Polynomial (SPL), Simple kriging (SKG), and Ordinary kriging (OKG). The difference data had same spatial and temporal resolution with 0.05 degree (5 km) and hourly, respectively. **Figure 5-5** show the watershed average rainfall comparison for the July to October in 2014. All interpolated products closed to the rainfall pattern observed by the rain station. On the peak, all of products could capture as the same time, which OKG could capture the biggest peak. SPL were differences from the four products on the peak that the difference was underestimation, and its pattern was also small different.

Figure 5-6 shows the average spatial of interpolation products for July to October 2014. The period 123 days, there are differences rainfall values of 3 to 40 mm over space of 250 km. The SPL method indicated most spatial variability, followed by the TSP, OKG, SKG and IDW (see **Figure 5-6**). The largest amount of rainfall fell in the central part for the five interpolation methods, which the SPL method produced the maximum rainfall intensities (about 38.397 mm/hour). Their smallest amount of rainfall spatial fell in the northern of the area.

The total rainfall amount for five interpolation methods for typhoon season (July to October 2014) was presented in **Table 5-3**, which was estimated by accumulating the hourly rainfall input over the area. The OKG was the largest amount of rainfall volume followed by the IDW, while the SPL was smallest. The largest amount of rainfall volume was the OKG that was about 136,248.7 MCM.
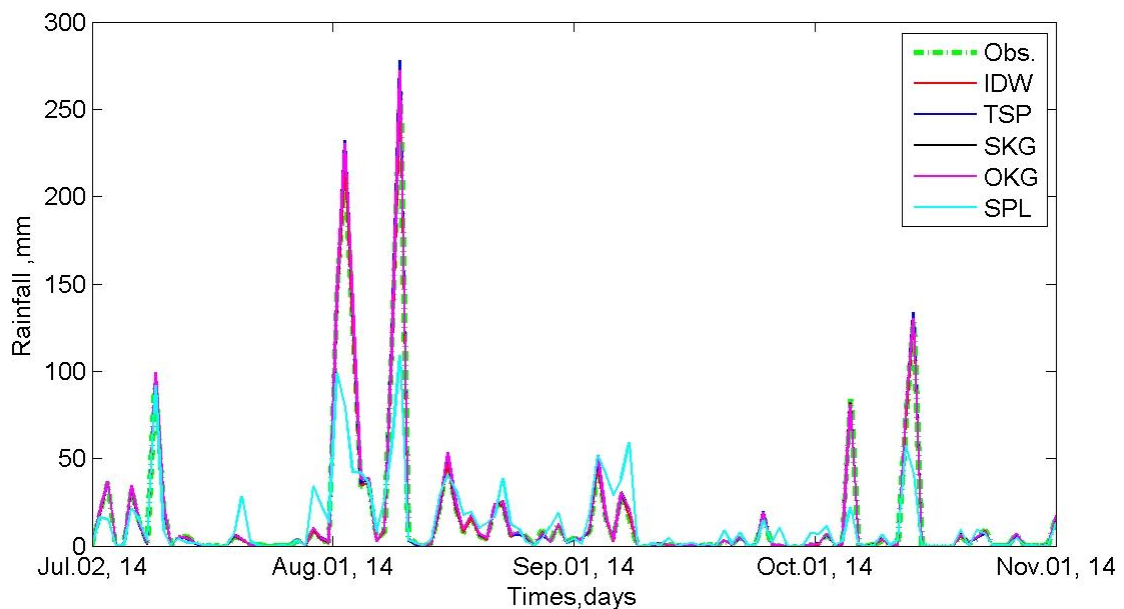
Figure 5-5 Average time series rainfall over the Shikoku area in each product in typhoon season 2014

Table 5-3 Volume of rainfall products amounts over the study watershed

Rainfall products	Rainfall volume, MCM
IDW	135,895.31
TSP	131,905.17
SKG	134,475.59
OKG	136,248.69
SPL	122,225.14
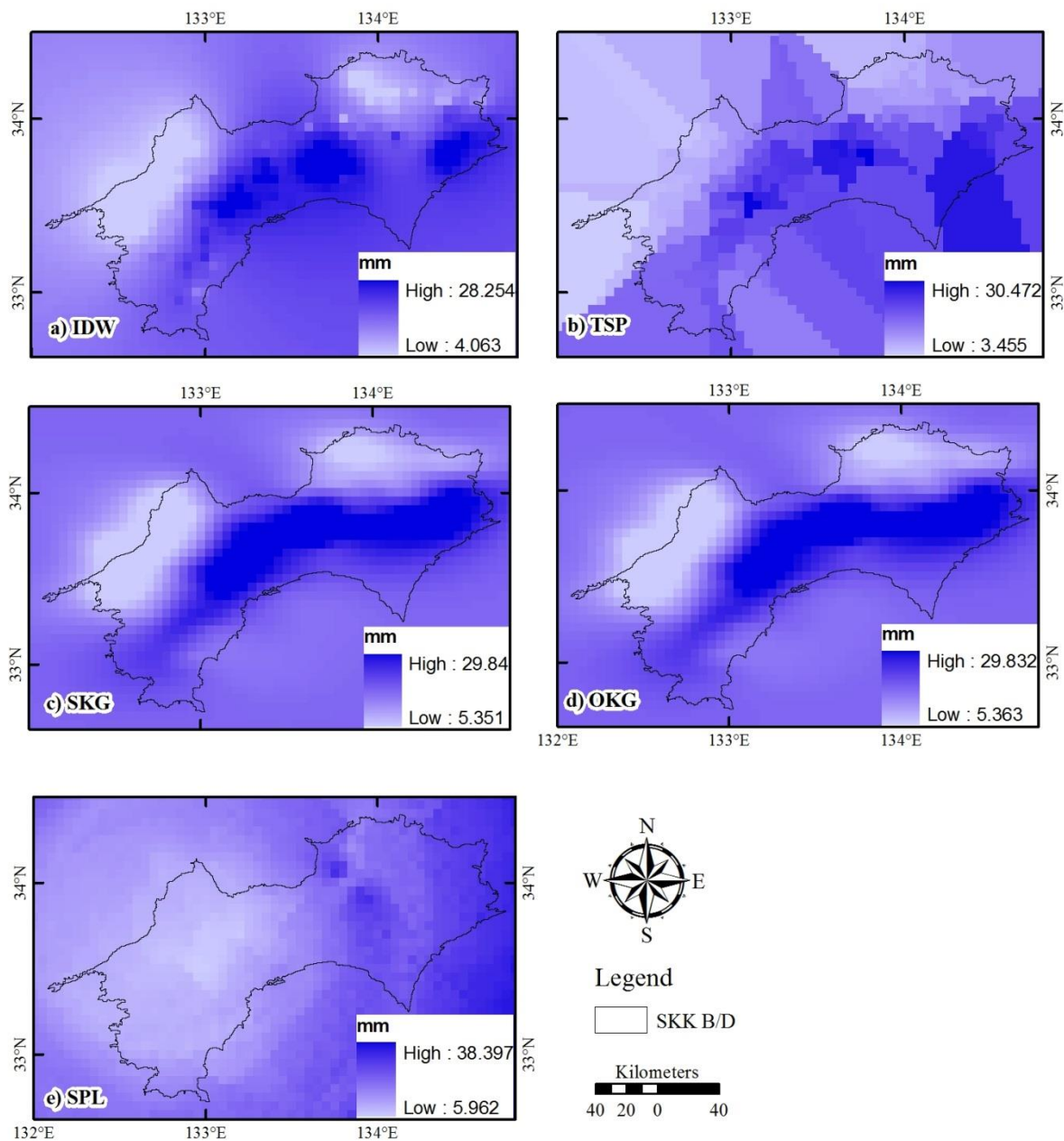
Figure 5-6 Average ground based rainfall in the Shikoku Island Japan (Jul-Nov, 2014)

All interpolated rainfall products demonstrated medium accuracy on daily rainfall, as presented by significant differences among observation and interpolation based on the performance statistical (see **Table 5-4**). Interpolated by IDW presented the best linear correlation with observed data ($r = 0.982$) and were followed by OKG, SKG, TSP, and SPL. Also, the IDW showed the lowest RMSE, following similar with the ranking of R^2. For the Shikoku area, the density of rain gauge can be presented as the dense network of rain gauge that the IDW was enough for estimation the highest performance of rainfall spatial. By the contrast, the best performance of the kriging was expected, as this had been demonstrated in previous studies (Tabios and Salas, 1985; Ly et al., 2011; Ly et al., 2013).

All of interpolation products for underestimated with two products comparing with observed hourly rainfall on the Peak bias. With negative volume bias and mean bias values, SPL underestimated observed data. By contract, the other four interpolation products overestimated the observed rain gauge data. By lowest negative Volume bias and Mean bias values, SPL underestimated observed rainfall by 16.47% and 2.54%, respectively. In the converse, the poorest performance of the TSP was reported by Goovaerts (2000) and Ly et al. (2013), which this method is not suitable for the complex topography such as mountain area because of the orographic rain. However, the elevation of the study area has a ranging from 0 to1,900 m.MSL over the short distance about 250 km.

The estimation accuracy of evaluated interpolation rainfall products over the Shikoku Island of Japan for hourly data with information was based on the spatial distribution of RMSE from July to October 2014. **Figure 5-7** showed the RMSE of the event, which the IDW method was the best agreement with the observed rainfall. Interestingly, the lowest RMSE value for all methods was found in the middle and southern part of area boundary. The northern part is represented by the high mountainous area, where the IDW was the best performance for interpolation products. The fact that the IDW could achieve a good performance over the mountainous area might be due to the high dense rain gauge network.

Table 5-4 Performance statistical of rainfall spatial products comparing with rain gauge

Rainfall products	Volume bias, %	Peak bias, %	RMSE, mm	Correlation	Mean bias, mm
IDW	**0.01**	**-0.43**	**9.57**	**0.982**	**0.01**
TSP	5.691	7.14	15.51	0.955	0.87
SKG	6.491	4.75	14.65	0.955	1.00
OKG	6.631	4.91	14.67	0.955	1.02
SPL	-16.471	-58.05	40.67	0.566	-2.54
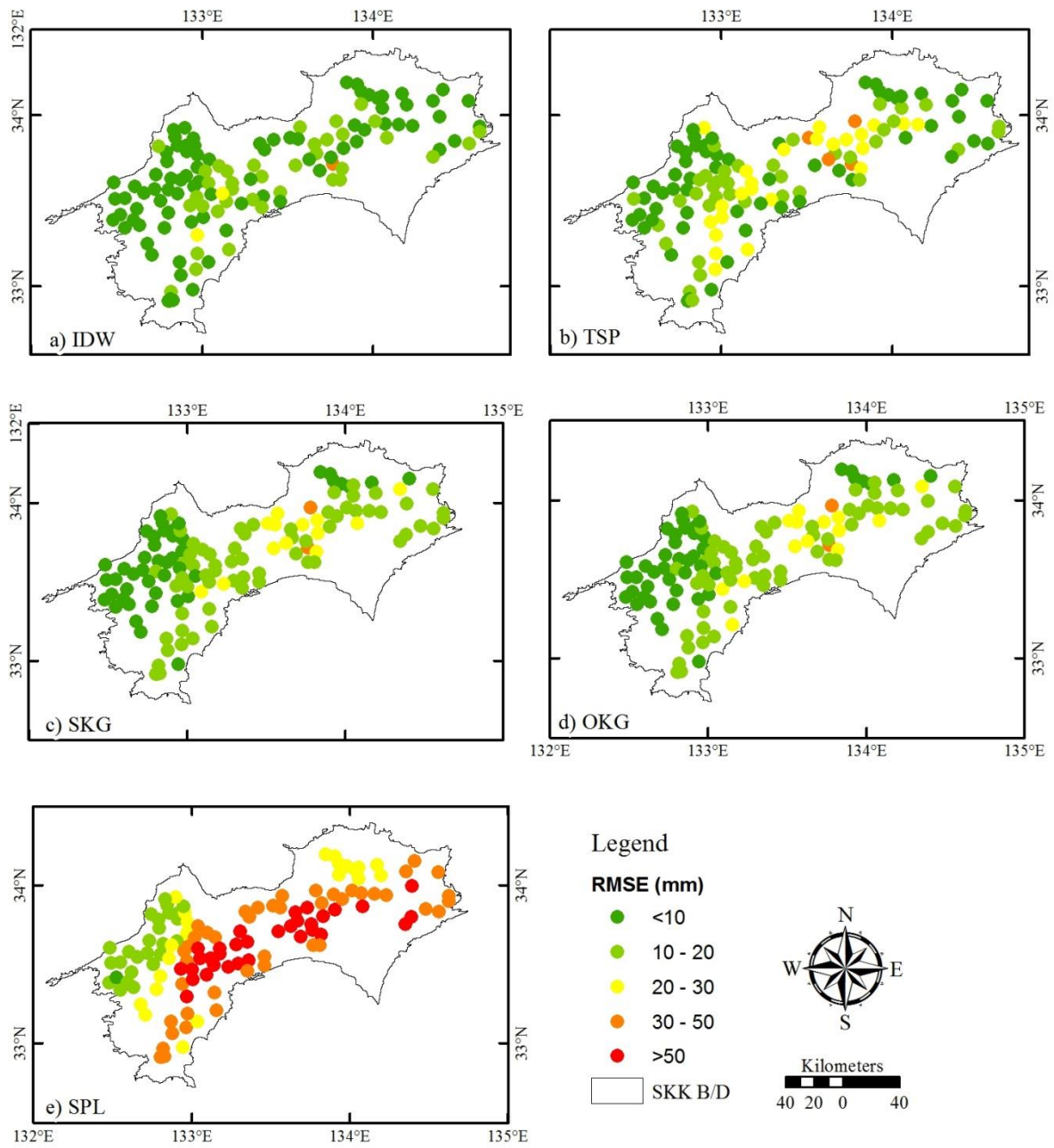
Figure 5-7 Root mean square error (RMSE) between rain gauge and spatial distribution products in the Shikoku Island Japan

5.3.2 Accuracy assessment of spatial interpolation algorithms: Nan river basin, Thailand

All of rainfall spatial products applied in the study from different spatial interpolation algorithms, Inverse distance weighting (IDW), Thiessen polygon (TSP), Surface Polynomial (SPL), Simple kriging (SKG), and Ordinary kriging (OKG). The difference data had same spatial and temporal resolution with 0.1 degree (10 km) and daily (24 h), respectively. **Figure 5-8** show the watershed average rainfall comparison for the June 2011. All interpolated products closed to the rainfall pattern observed by the rain station. On the first peak, all of products were underestimation, which IDW could capture the biggest peak. TSP and IDW were little differences from the three products on the second peak that the SPL was difference in overestimation, but the different pattern was occurred in the IDW. For the August 2014 in **Figure 5-9**, the average rainfall of the five interpolation products was compared with the observed rainfall. Their pattern is similar to the observation data with variability in overall. The OKG was small differences with overestimation on the first peak, while the TSP was underestimation to be similar to the June 2011 event. At the peak second, all of them were underestimation, after that the OKG was overestimation until the end of event.

Figure 5-10 shows the average spatial of interpolation products for the June 2011 storm event. The period 30 days, there are differences rainfall values of 0 to 15 mm over space of 200 km. The SPL method indicated most spatial variability, followed by the TSP, OKG, SKG and IDW (see **Figure 5-10**). The largest amount of rainfall fell in the north-eastern part for the five interpolation methods, which the SPL method produced the maximum rainfall intensities (about 19.5 mm/day). Their smallest amount of rainfall spatial fell in the middle of the watershed area. The spatial distribution rainfall of the August 2014 was shown in **Figure 5-11**, which all of method computed the spatial pattern similar with the event one in overall. In detail, the maximum intensity of four methods (IDW, TSP, OKG and SPL) was located in the north-eastern part along with the border of watershed (inside and outside), while the maximum intensity of the SKG was located in the northern part inside the boundary of the watershed area. The difference of the spatial interpolation on the SKG was depended on effect of rain gauge amount in the area and the poor semi-variogram model.

The total rainfall amount for five interpolation methods for two events (June 2011 and August 2014) was presented in **Table 5-5**, which was estimated by accumulating the daily rainfall input over the catchment area. In overall, the volume of rainfall in August 2014 was greater than the June 2011, while the peak of June 2011 was greater than the August 2014 as shown in **Figure 5-8** and **5-9**. On the first event, The IDW was the largest amount of rainfall volume followed by the SPL, while the TSP was smallest. The largest amount of rainfall volume on the second event was the OKG that was about 10,454 MCM. This event revealed that the TSP was the smallest rainfall amount.
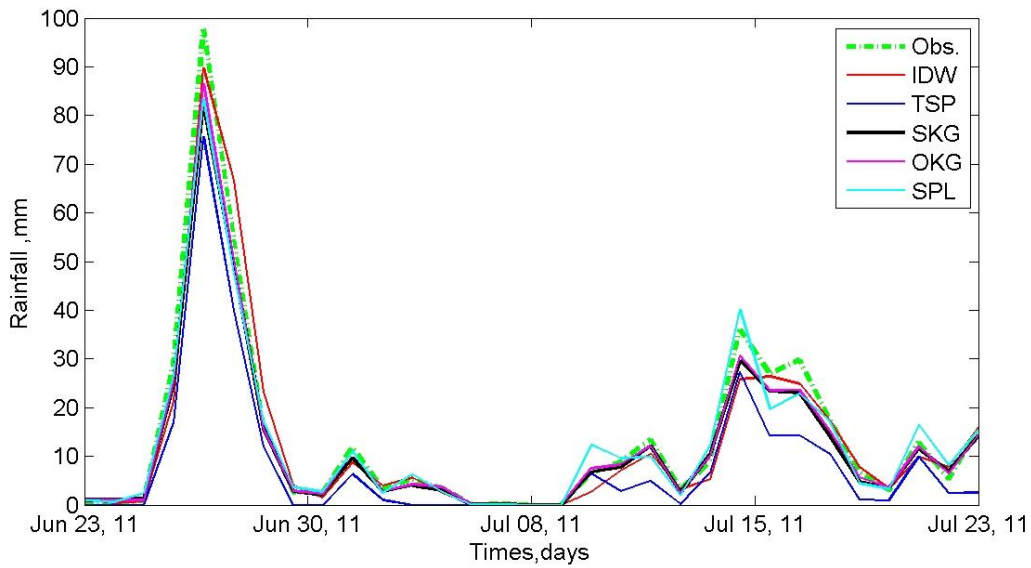
Figure 5-8 Average time series rainfall over the study area in each product of Event 1st (June 2011)
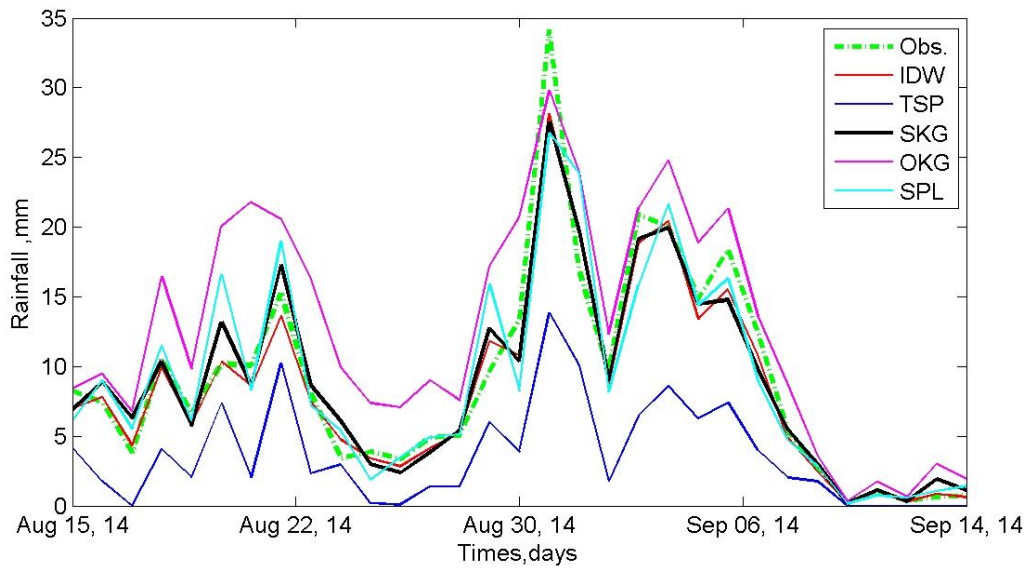
Figure 5-9 Average time series rainfall over the study area in each product of Event 2nd (August 2014)

Table 5-5 Volume of rainfall products amounts over the study watershed, Rainfall volume, MCM

Rainfall products	Event 1st (Jun2011)	Event 2nd (Aug2014)
IDW	6,663.13	6,944.61
TSP	4,096.80	2,916.00
SKG	5,960.52	7,288.34
OKG	6,151.46	10,454.04
SPL	6,269.39	7,379.26

143
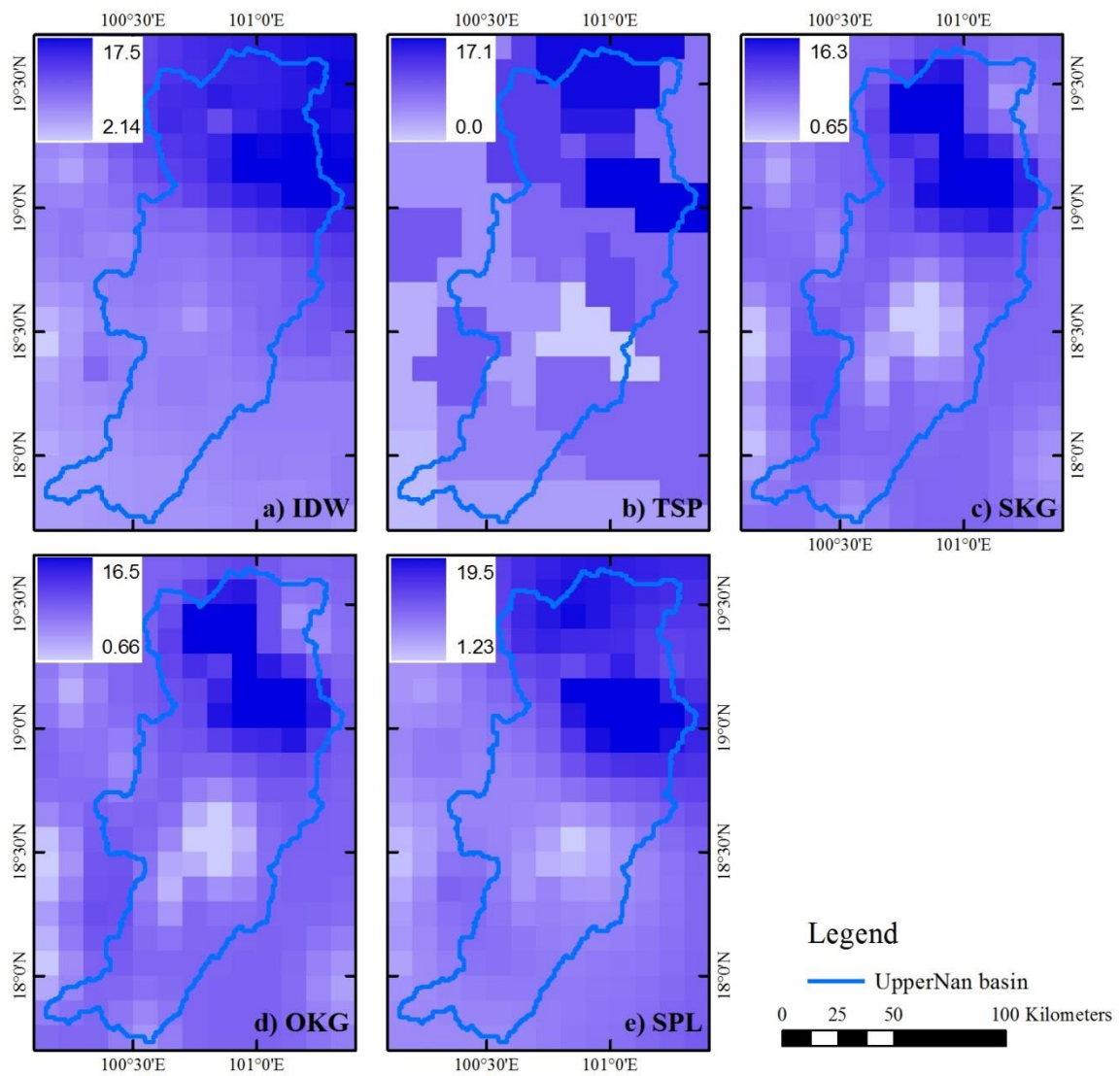
Figure 5-10 Average ground based rainfall spatial products during event 1st (June 2011)
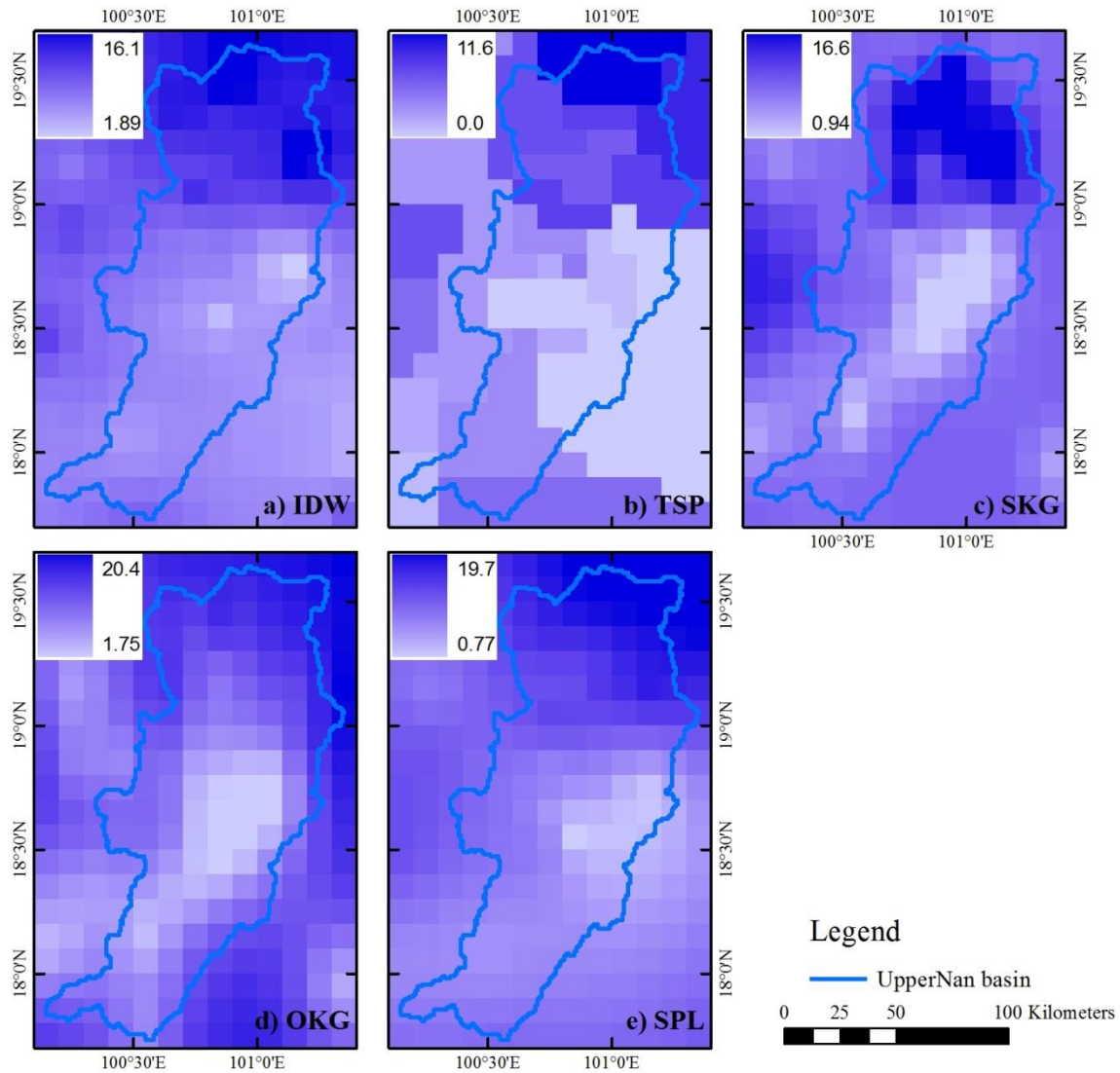
Figure 5-11 Average ground based rainfall spatial products during event 2nd (August 2014)

All interpolated rainfall products demonstrated medium accuracy on daily rainfall, as presented by significant differences among observation and interpolation based on the performance statistical (see **Table 5-6**). For the June 2011 event, interpolation by SKG and OKG presented the best linear correlation with observed data ($R^2 = 0.93$) and were followed by SPL, TSP, and IDW. Also, the SKG and OKG showed the lowest RMSE, following similar with the ranking of R^2. The SKG revealed the best R^2 with observed data ($R^2 = 0.95$) and was followed by OKG, SPL, IDW, and TSP for the August 2014. For the RMSE of the second event, the SKG also presented the best performance RMSE, followed by similar with above. By similarity, both kriging interpolation methods had the largest RMSE and lowest r value. The best performance of the kriging was expected, as this had been demonstrated in previous studies (Tabios and Salas, 1985; Ly et al., 2011; Ly et al., 2013).

All of interpolation products for both events underestimated observed daily rainfall on the Peak bias. With negative Volume bias and Mean bias values, OKG, SKG, and TSP underestimated observed

data for the first event. By contract, the other two interpolation products overestimated the observed rain gauge data. For second event based on the Volume bias and Mean bias values, the SPL and OKG were positive value, while the other three products were negative value. By lowest negative Volume bias and Mean bias values, TSP underestimated observed rainfall by 27.89% and 58.37% for the June 2011 and August 2014 respectively. The poorest performance of the TSP was reported by Goovaerts, 1999 and Ly et al., 2013, which this method is not suitable for the complex topography such as mountain area because of the orographic rain. The elevation of the study area has a ranging from 100 to 2000 m.MSL over the short distance about 200 km.; this point could donate to low underestimation of the TSP algorithm.

The estimation accuracy of evaluated interpolation rainfall products over the Nan river basin of Thailand for daily data with information was based on the spatial distribution of RMSE from two storm events, June 2011 and August 2014. **Figure 5-12** showed the RMSE of the June 2011, which the SKG and OKG method were the best agreement with the observed rainfall. For the August 2014 in **Figure 5-13**, the best agreement with the rain gauge was the SKG product. Interestingly, the lowest RMSE value for all methods was found in the middle and southern part of watershed boundary. The northern part is represented by the high mountainous area, where the SKG was the best performance for interpolation of the both events. The fact that the SKG could achieve a good performance over the mountainous area might be due to the semi-variogram fit to the complex terrain on the mountain represented by the orographic rain (Goovaerts, 1999; Ly et al., 2013).

Table 5-6 Performance statistical of rainfall spatial products

Rainfall products		Volume bias, %	Peak bias, %	RMSE, mm	Correlation	Mean bias, mm
Event 1st (Jun2011)	IDW	3.06	**-8.13**	14.71	0.84	0.73
	TSP	-27.89	**-22.49**	13.61	0.86	-1.96
	SKG	-0.89	-15.48	9.68	**0.93**	-0.07
	OKG	**-0.59**	-11.31	**9.67**	**0.93**	**-0.05**
	SPL	1.37	-14.53	10.94	0.91	0.25
Event 2nd (Aug2014)	IDW	-1.54	-17.45	7.26	0.89	-0.14
	TSP	-58.37	**-59.43**	10.42	0.82	-5.31
	SKG	**-0.17**	-19.22	**4.78**	**0.95**	**-0.01**
	OKG	3.99	**-12.64**	5.96	0.92	0.36
	SPL	0.28	-21.56	6.01	0.92	0.03
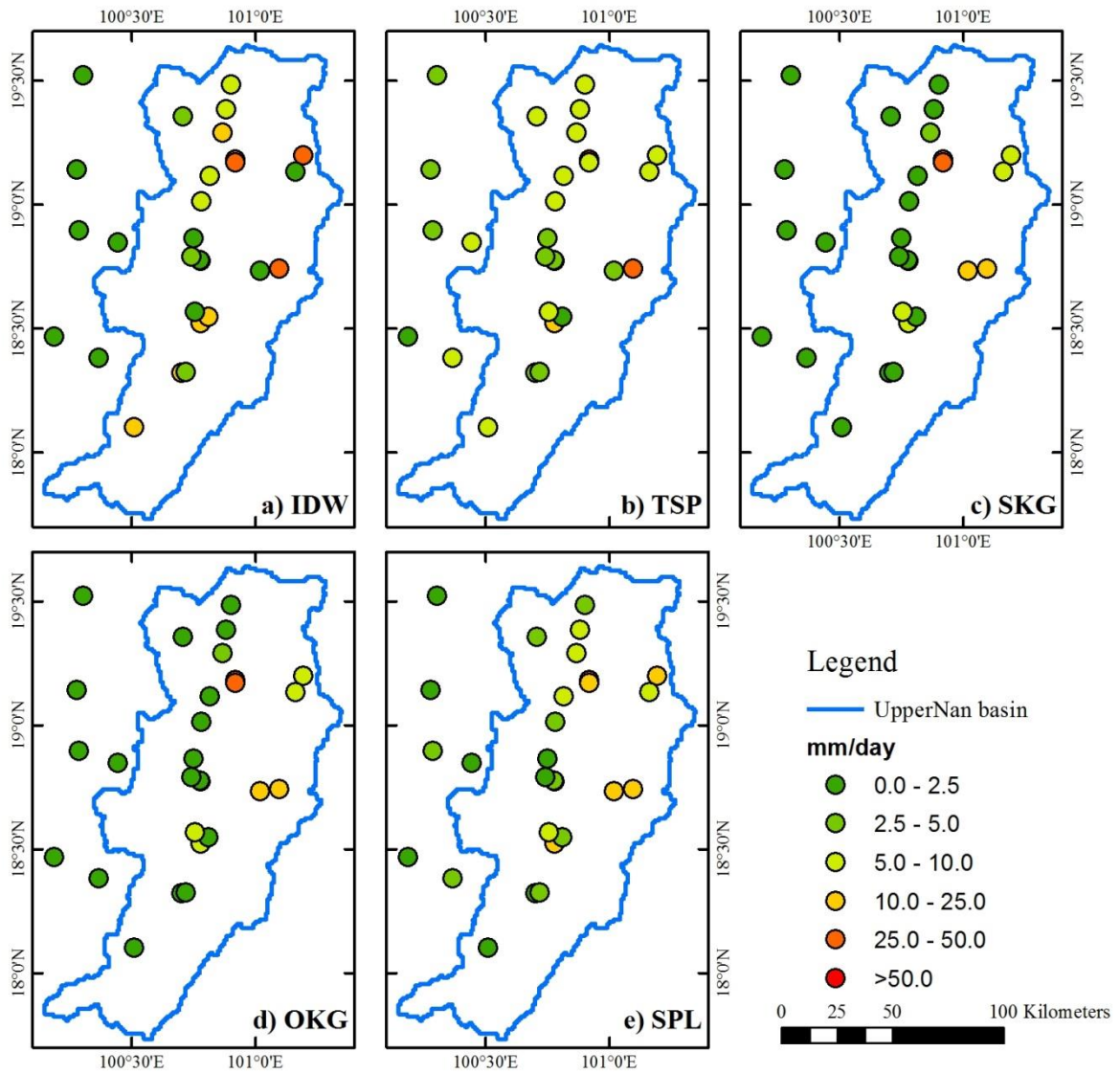
Figure 5-12 Root mean square error (RMSE) daily rainfall between rain gauge and spatial distribution products during event 1st (June 2011)
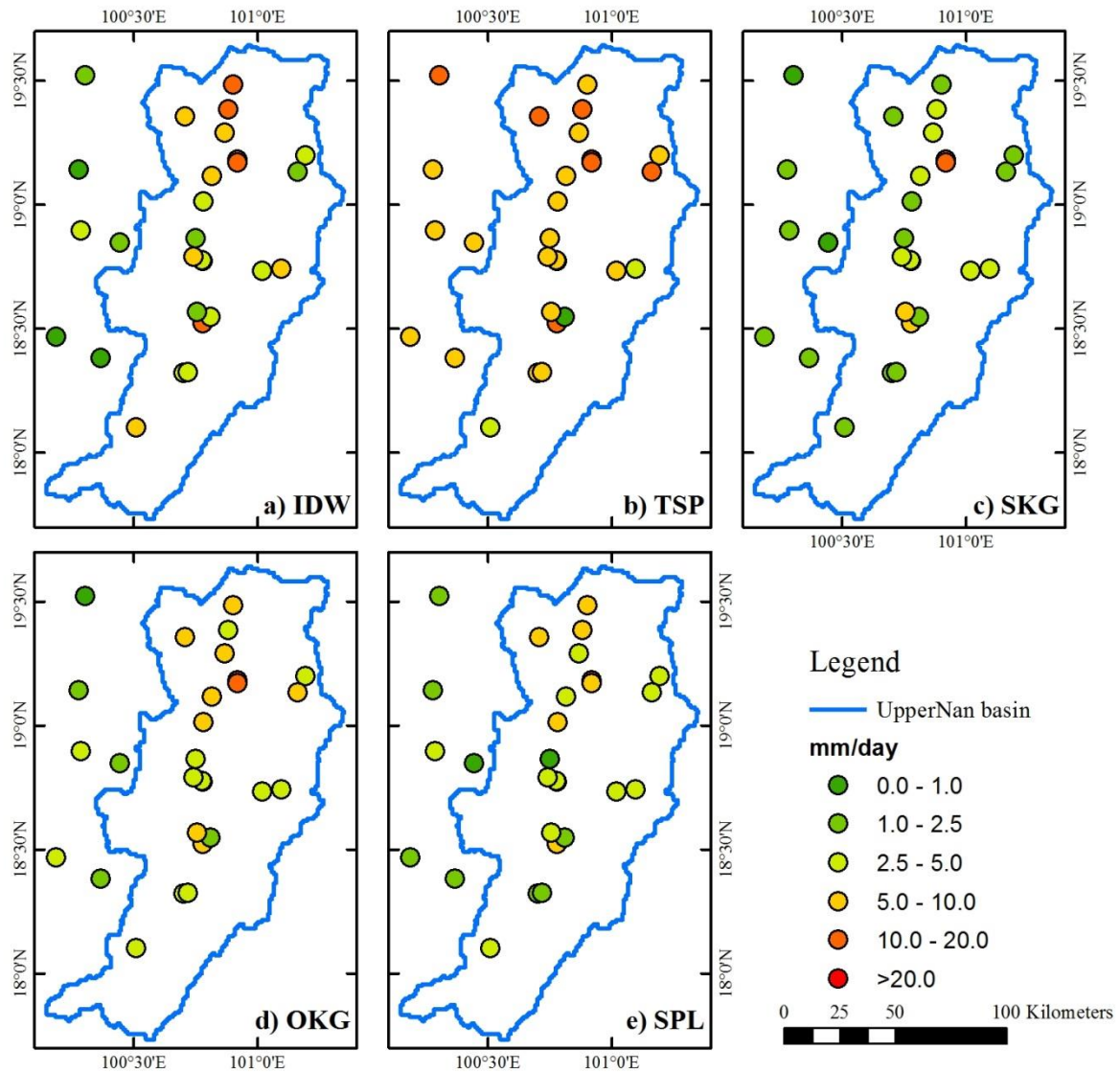
Figure 5-13 Root mean square error (RMSE) daily rainfall between rain gauge and spatial distribution products during event 2nd (August 2014)

5.3.3 Runoff simulation based on different spatial interpolation products: Shikoku Island, Japan

The hydrological model (RRI model) was driven for flood events in 2014. The five rainfall products were simulated at hourly on a temporal scale to match the observed streamflow data. Seven runoff stations were selected in the Shikoku Island (see **Figure 3-24**), the first (Ikeda dam) and second (Chuobashi) belong to the Yoshino River. The third (Furushou) is in the Naka River and the fourth (Fukabuchi) in the downstream area of the Monobe River. The fifth is located in the Ino, belonging to the Niyodo River; the sixth located in the Shimanto River is the Gudoudaini station. The seventh station is the Deai located in the Shigenobu River. All of stations showed in the hourly hydrograph

that results from the different topography source. **Figure 5-14** presents the hydrographs for all sources with the seven runoff stations.

All simulated runoff driven by different products was to provide the temporal pattern similar to the observed hydrograph for the flood event. Over view of all the runoff station, all products symmetrically captured the peak at the same time with the observation with the underestimation at the largest peak. IDW systematically underestimated observed runoff, while the other four products were overestimation.

All of seven runoff stations on hourly hydrograph were analysed and calculated for evaluation by the performance statistical. The results are given in **Table 5-7** that is concluded by five indexes. IDW simulated discharge was the best matched by observed runoff with a highest Correlation of 0.942 and lowest RMSE of 307.60 cms. This simulated runoff underestimated the runoff volume, peak flow and mean runoff by 2.55%, 31.4% and 7.26 cms, respectively. SKG and OKG simulated runoff were high Correlation and low RMSE, however, its simulated runoff was overestimation of Volume bias and Mean bias. The peak flow of the both products underestimated about 22%. The two products (TSP and SPL) significantly overestimated the runoff volume, and mean runoff with high RMSE and low correlation value, while their peak were underestimation.

In summary performance on estimating the streamflow, the best of the spatial interpolation products was IDW that statistical presented some value better than the other interpolated product.

Table 5-7 Performance statistical of runoff from the rainfall spatial prediction products in the Shikoku Island Japan

Rainfall products	Volume bias, %	Peak bias, %	RMSE, cms	Correlation	Mean bias, cms
IDW	**-2.55**	-31.41	**307.60**	**0.942**	**-7.26**
TSP	13.76	**-2.45**	664.45	0.760	39.21
SKG	9.66	-22.40	330.23	0.933	27.55
OKG	9.82	-22.10	330.51	0.933	27.97
SPL	58.18	-19.41	917.12	0.539	165.81
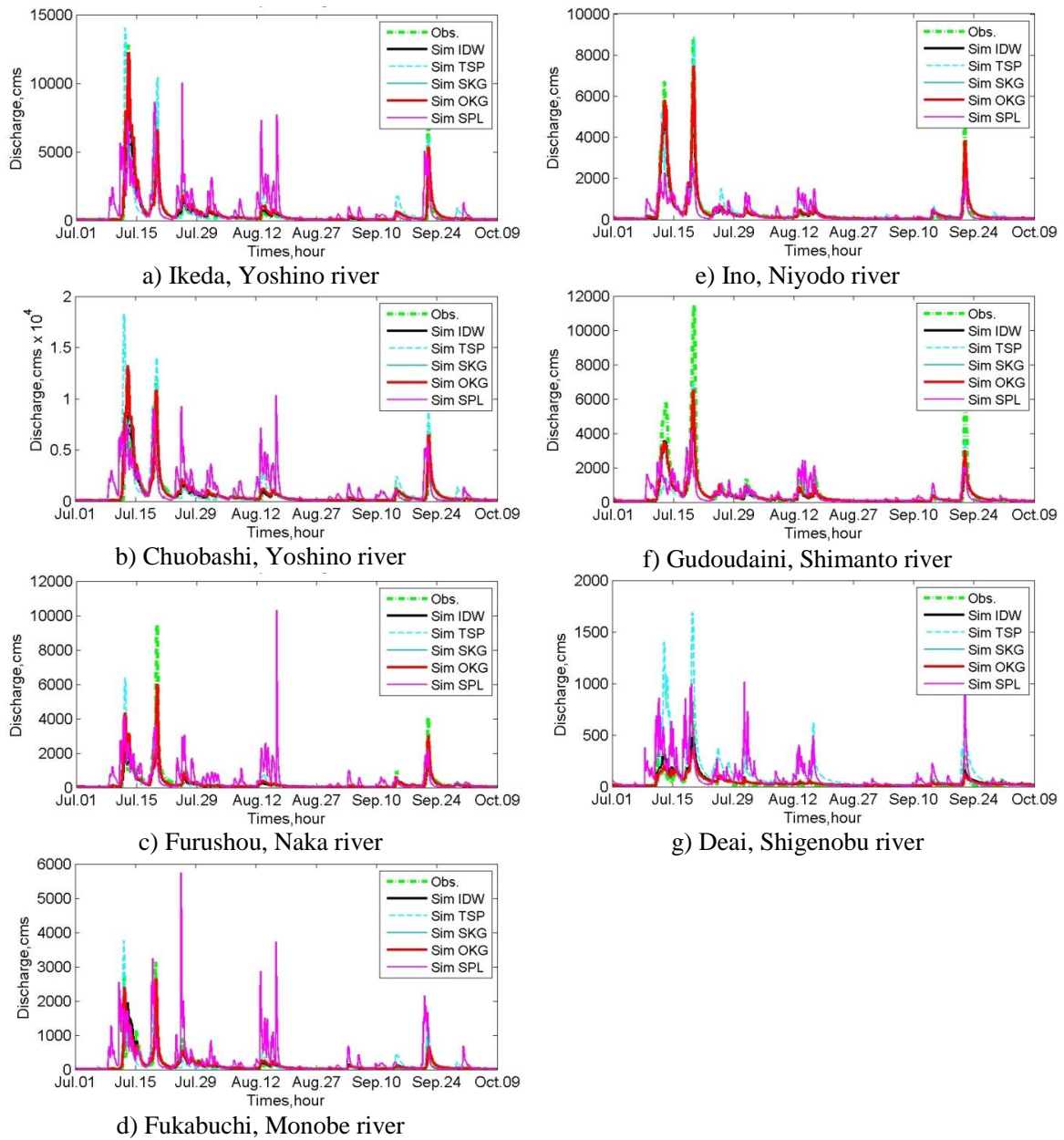
Figure 5-14 Hourly discharge hydrograph at runoff observation station of flood event based on different interpolation scenarios in the Shikoku Island Japan

5.3.4 Runoff simulation based on different spatial interpolation products: Nan river basin, Thailand

The hydrological model (RRI model) was driven for July 2011 and August 2014 storm events, using the similar hydrologic parameters set. The five rainfall scenario was estimated at daily on a temporal scale to match the Royal Irrigation Department Thailand observed streamflow data. Three runoff stations were selected in the Nan river basin (see **Figure 3-26**), the first one belonging to the upstream sub-catchment (N.64), the second one belonging to the middle area (N.1) and the third one belonging

to the downstream area (N.13A), to show the daily hydrograph that results from the different interpolation scenario. **Figure 5-15** and **5-16** present the hydrographs for all rainfall interpolation scenarios and storm event of respectively runoff station N64, N.1 and N.13A.

All the modeled runoff driven by different interpolation methods was to provide the temporal pattern similar to the observed hydrograph for the June 2011 event. Over view all the runoff station, TSP, SKG and OKG symmetrically captured the peak at the same time with the observation, while the other two products symmetrically lagged about 1 day. By contract, IDW and SPL systematically overestimated observed runoff in station N.64 and N.1, while the other three scenarios was underestimation. For N.13A, all of interpolation products were underestimation to compare with the observed hydrograph. The simulated streamflow in the August 2014 provided the similar temporal pattern with observed hydrograph. OKG was significantly overestimated of peak and runoff volume, while TSP was significantly underestimation. With the first peak, SKG was the best fit with observed hydrograph, while three products, IDW, OKG and SPL were overestimation. The IDW and OKG were difference pattern at the second peak; all of products on this peak at N.13A were underestimation.

All of three runoff station on the daily hydrograph were analyzed and calculated for evaluation by the performance statistical. The results are given in **Table 5-8** that is concluded by five indexes. The SKG simulated discharge best matched the observed runoff with the highest R^2 of 0.917 and lowest RMSE of 173.30 cms for the first event (June 2011). This simulated runoff underestimated the runoff volume, peak flow and mean runoff by 3.72%, 49.4% and 19.4 cms, respectively. The OKG simulated runoff was high r and low RMSE, however, its simulated runoff was lowest of Volume bias of 2.13% and Mean bias of 11.63%. The peak flow of the OKG underestimated about 49.3%. The SPL significantly overestimated the runoff volume and mean runoff, but peak flow was lowest about 10.57% on underestimation, with high RMSE and strong correlation value. The TSP runoff was high RMSE value with a good correlation value, this simulated results underestimated the runoff volume, peak and mean runoff. By contract, the IDW discharge overestimated the runoff volume and mean runoff, but its peak flow was underestimation, with high RMSE and lowest correlation value.

For the August 2014 storm event, The SKG simulated flow matched perfectly with overestimation based on the lowest of Volume bias, RMSE and Mean bias by 6.4%, 163.88 cms and 27% respectively and highest correlation of 0.821, with underestimation of peak flow. The OKG runoff overestimated with high runoff volume and mean runoff value, on the lowest bias of the peak about 1.05%. Its result presented the highest RMSE and good correlation value. The IDW and SPL results showed the overestimation of runoff volume and mean runoff, however, their peak flow were underestimation. The TSP was resulted on the highest underestimation of runoff volume, peak and mean runoff.

Table 5-8 Performance statistical of runoff from the rainfall spatial prediction products

Rainfall products		Volume bias, %	Peak bias, %	RMSE, cms	Correlation	Mean bias, cms
Event 1st (Jun2011)	IDW	9.04	-13.59	284.79	0.739	44.47
	TSP	-19.03	-49.47	226.75	0.876	-98.01
	SKG	-3.72	-49.43	**173.30**	**0.917**	-19.42
	OKG	**-2.13**	-49.29	190.96	0.889	**-11.63**
	SPL	26.78	**-10.57**	264.69	0.816	135.43
Event 2nd (Aug2014)	IDW	15.08	-28.40	183.02	0.795	63.49
	TSP	-39.49	-58.86	271.25	0.711	-166.22
	SKG	**6.40**	-34.60	**163.88**	**0.821**	**26.94**
	OKG	43.04	**1.05**	274.87	0.722	181.18
	SPL	31.55	-15.43	238.43	0.724	132.79

a) N.64

b) N.1

c) N.13A
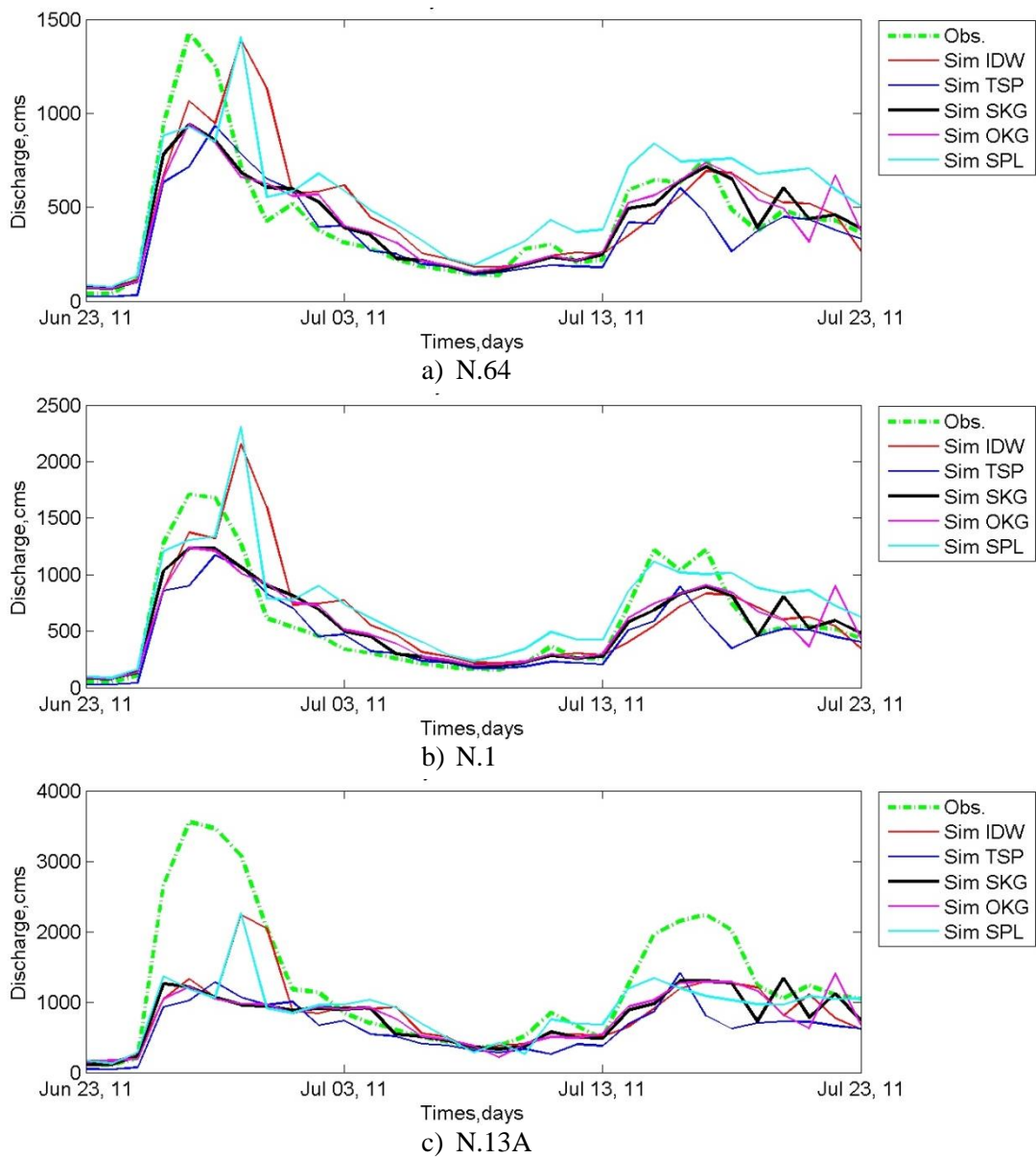
Figure 5-15 Daily discharge hydrograph at runoff observation station of flood event 1st (June 2011)

a) N.64

b) N.1

c) N.13A
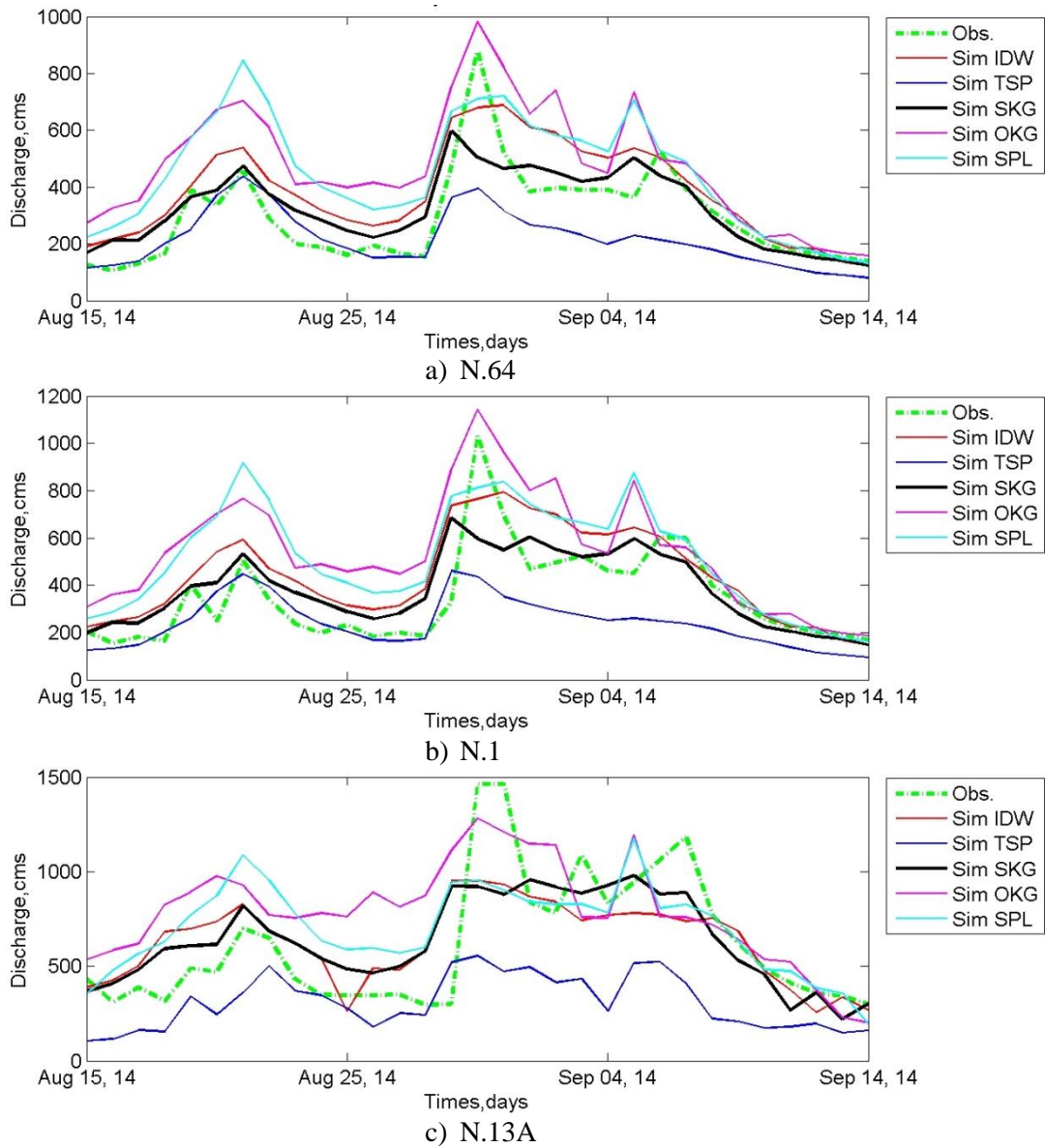
Figure 5-16 Daily discharge hydrograph at runoff observation station of flood event 2^{nd}(August 2014)

5.4 Evaluation of satellite rainfall products

The availability of different satellite products is presented in the **Table 5-1** with GPM only available from April 2014 and TRMM available to June 2015. Hence, the simulated storm event is selected from April 2014 to June 2015. According to the aim of this study is specific to the flood event that the storm event on the selected period occurs in the study area from monsoon during July to October. Large monsoon during 28-30 August 2014 across the northern part of Thailand brought a heavy rainfall about 100 to 150 mm. The heavy rainfall caused severe flooding and river bank over flow. Thus, the five satellite-based rainfall products were collected from August, 15 to September, 14 covering the flood event of the Nan area.

5.4.1 Accuracy assessment of satellite rainfall products: Shikoku Island, Japan

All of the satellite-based rainfall products were implemented in this study with different resolution of spatial and temporal. GPM, GSMaP and GPV have the high resolution of spatial scale about 0.1 degree and different temporal scale of 0.5 h and 1.0 h, respectively. TRMM 3B42V7, CMORPH, and PERSIANN have the course resolution about 0.25 degree of spatial and 3.0 h of temporal. **Figure 5-17** show the watershed average rainfall comparison during the flood event on 2014 (July to October). All satellite products were quite different from the observed rainfall pattern at some peak. On the peak, all products were different from the observed data on magnitude and time. The satellite products showed underestimation with the similar pattern.

Figure 5-18 shows the average spatial distribution of satellite-based rainfall and ground observation products during the typhoon season. The period 123 days, there are differences rainfall values of 3 to 15 mm over space of 250 km. The GPM rainfall products presented that maximum rainfall intensities were located in the eastern part along the border of area and also the other three products (TRMM, CMORPH, and PERSIANN). The GSMaP was different from the four products that the maximum intensity was located in the central part. This distribution was similar to the observed spatial interpolation product. GPV rainfall distribution was also similar with the GSMaP and rain gauge interpolation data.

The total rainfall amount for five satellite-based rainfall and ground observation products for flood events in 2014 were presented in **Table 5-9**, which was estimated by accumulating the rainfall input over the catchment area. In overall, TRMM was the largest amount of rainfall volume followed by GPM, while PERSIANN was smallest. The GPM and TRMM presented the total volume close to the rainfall volume of rain gauge. However, the both products were underestimation with the observation rainfall, for international satellite rainfall data. GPV outperform among the five satellite rainfall data that volume difference is about 10% for the Shikoku area.
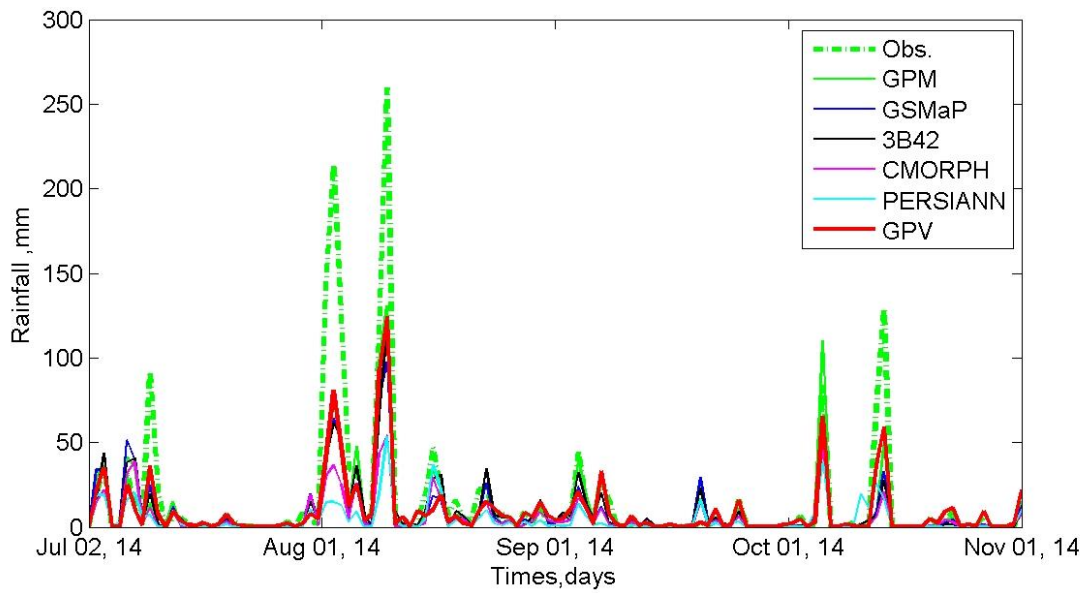
Figure 5-17 Average satellite based rainfall product over the Shikoku Island in temporal scale

Table 5-9 Volume of rainfall products amounts over the Shikoku Island

Rainfall products	Rainfall volume, MCM
Rain gauge	135,895.31
GPM	61,925.11
GSMaP	52,859.57
GPV	123,482.38
TRMM	64,465.38
CMORPH	41,430.34
PERSIANN	32,900.91
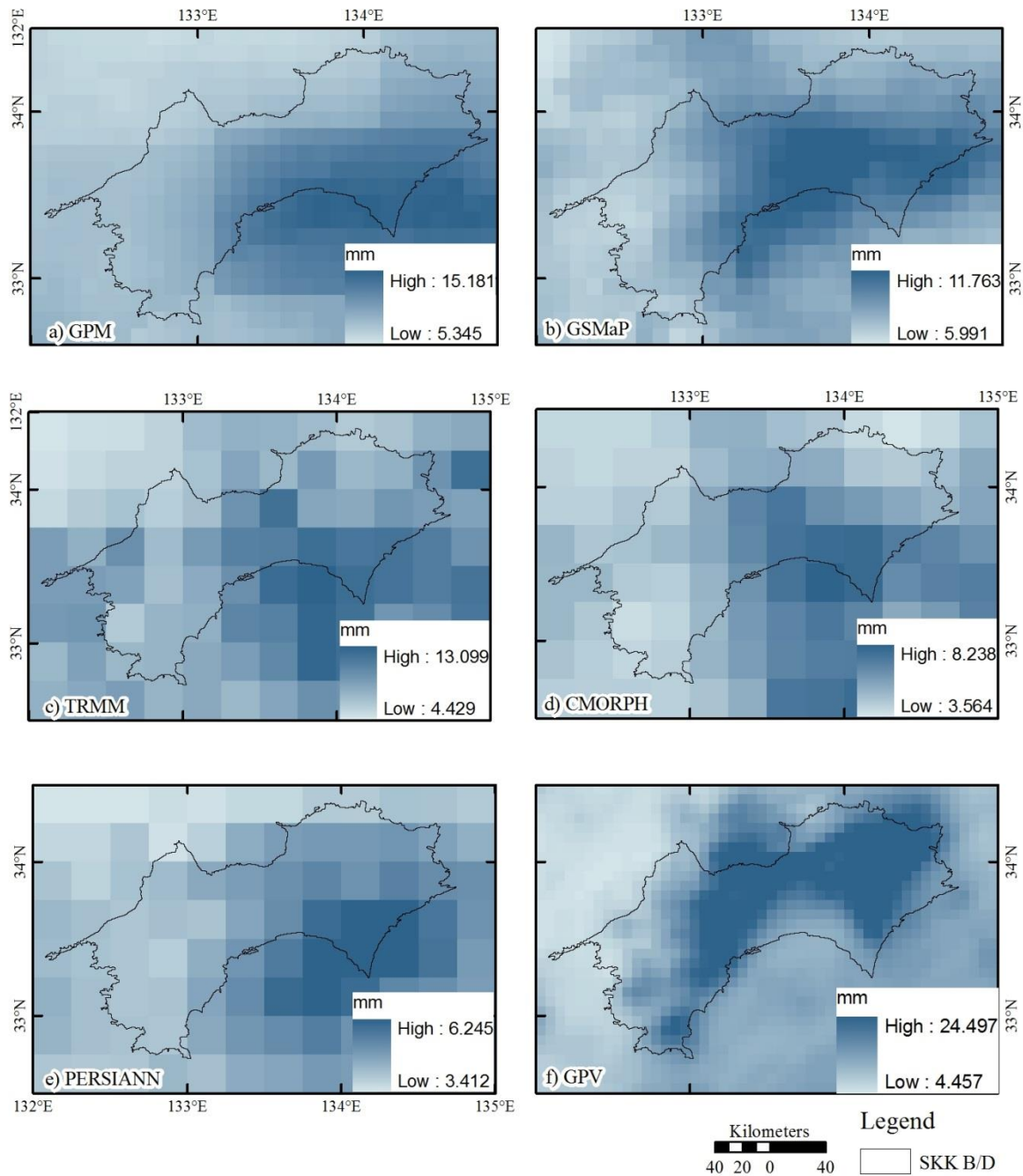
Figure 5-18 Average satellite-based rainfall in the Shikoku Island, Japan (Jul-Nov, 2014)

All satellite-based rainfall products revealed low accuracies by significant differences among comparing with rain gauges based on the performance statistical (see **Table 5-10**). The five products underestimated rainfall based on Volume bias and Mean bias. The satellite-based rainfall products were also underestimation reported by the other studies (Kidd et al., 2012; Tian et al., 2010; Qin et al., 2014; Sohn et al., 2009; Asadullah et al., 2010). The fact that most satellite-based rainfall products have been represented by underestimation rainfall might be due to the algorithm of estimation (Tian et al., 2010). The GSMaP underestimate rainfall represented by the mean bias in China about 0.53 mm/day and also in Columbia about 2.3 mm/day (Qin et al., 2014; Dinku et al., 2010). By the contrast,

157

TRMM and GPM represented by the Volume bias overestimated rainfall about 49.2% and 19.9%, respectively. The Mean bias of both products was about 4.5 mm/day and 1.54 mm/day, respectively. Overestimation of the TRMM has been reported by the previous studies that bias is about 30.5% in the USA and 4.5% in the China (Behrangi et al., 2011; Chen et al., 2015). The GPM has overestimated about 4.0% in Iran (Sharifi et al., 2016). Volume bias and Mean bias of CMORPH on underestimation were 11.06% and 1.01 mm/day, respectively. The CMORPH has underestimated rainfall reported by the other studies (Tan et al., 2015; Qin et al., 2014; Asadullah et al., 2010). In this study, the GPM was the best performance compared with the other products for international data set.

The Underestimation of peak rainfall had occurred in all, five products. In overall, the GPM performed the best match of peak bias. The highest accuracies on comparison, GSMaP presented the best linear correlation with observed data ($R^2 = 0.769$) and were followed by GPM, TRMM, CMORPH, and PERSIANN. All satellite products had range of RMSE about 36 to 47 mm/hour. The GSMaP was the best performance with lowest RMSE value, and the PERSIANN was the highest value with low performance. The low performance of the PERSIANN based on the RMSE value could be referred by the previous study (Chintalapudi et al., 2014). The mention on above was the evaluation for the international satellite data, while GPV was the best performance to specific to the Shikoku area and also underestimation to compare to the rain gauge data.

The estimation accuracy of evaluated satellite-based rainfall products over the Shikoku Island with information was based on the spatial distribution of RMSE from flood events in 2014. **Figure 5-19** showed the RMSE of satellite-based rainfall products on the flood event, which GSMaP was the best agreement with the observed rainfall, for worldwide data set. Interestingly, the lowest RMSE value for all methods was found in the northern part and north-western part of the area boundary. The central part is represented by the high mountain area, where all products have estimated on the high RMSE value. This indicated that the satellite-based rainfall could not explore to obtain a good performance covering the mountain area because of classification of warm clouds from the IR sensors and numerical modelling of microwave signal (Yilmaz et al., 2005; Huffman et al., 2007). For specification to combine only Japan and international data, GPV showed the highest performance that high error was located only the central part of the area.

Table 5-10 Performance statistical of rainfall spatial products of the Shikoku Island

Rainfall products	Volume bias, %	Peak bias, %	RMSE, mm	Correlation	Mean bias, mm
GPM	**-37.33**	**-54.94**	37.36	0.682	**-5.76**
GSMaP	-43.63	-60.91	**36.17**	**0.769**	-6.73
GPV	<u>**-8.39**</u>	<u>**-11.39**</u>	<u>**30.52**</u>	<u>**0.785**</u>	<u>**-1.29**</u>
TRMM	-45.11	-70.55	41.67	0.570	-6.96
CMORPH	-64.96	-79.03	44.59	0.527	-10.02
PERSIANN	-71.52	-76.55	47.05	0.436	-11.03

5.4.2 Accuracy assessment of satellite rainfall products: Nan river basin, Thailand

All of the satellite-based rainfall products were implemented in this study with different resolution of spatial and temporal. GPM and GSMaP have the high resolution of spatial scale about 0.1 degree and different temporal scale of 0.5 h and 1.0 h, respectively. TRMM 3B42V7, CMORPH, and PERSIANN have the course resolution about 0.25 degree of spatial and 3.0 h of temporal. **Figure 5-20** show the watershed average rainfall comparison during the flood event on 2014 (August, 15 to September, 14). All satellite products were quite different from the observed rainfall pattern at some peak. On the first peak, all products were different from the observed data on magnitude and time. The TRMM showed highest overestimation, while GSMaP and PERSIANN revealed the similar magnitude. At the third peak, the TRMM and GPM presented the best fit on magnitude; however, the GPM was different on time scale about 1 day. The other three products were difference value at this peak. The fourth and fifth peak was quite different on overestimation.

Figure 5-21 shows the average spatial distribution of satellite-based rainfall and ground observation products during the storm event. The period 30 days, there are differences rainfall values of 1 to 18 mm over space of 200 km. The TRMM 3B42V7 rainfall products presented that maximum rainfall intensities were located in the western part along the border of watershed and also the other three products (GSMaP, CMORPH, and PERSIANN). This distribution was similar to the observed spatial interpolation product, but it was different in the norther part. By the contract, the high intensities of GPM were in the northern part inside the boundary of the watershed, that the spatial pattern was similar to the observed rainfall spatial. However, the GPM was different in the western part.

The total rainfall amount for five satellite-based rainfall and ground observation products for flood events in 2014 were presented in **Table 5-11**, which was estimated by accumulating the rainfall input over the catchment area. In overall, TRMM was the largest amount of rainfall volume followed by

GPM, while PERSIANN was smallest. The GPM and CMORPH presented the total volume close to the rainfall volume of rain gauge. However, the GPM was overestimation and the CMORPH underestimation the observation rainfall.
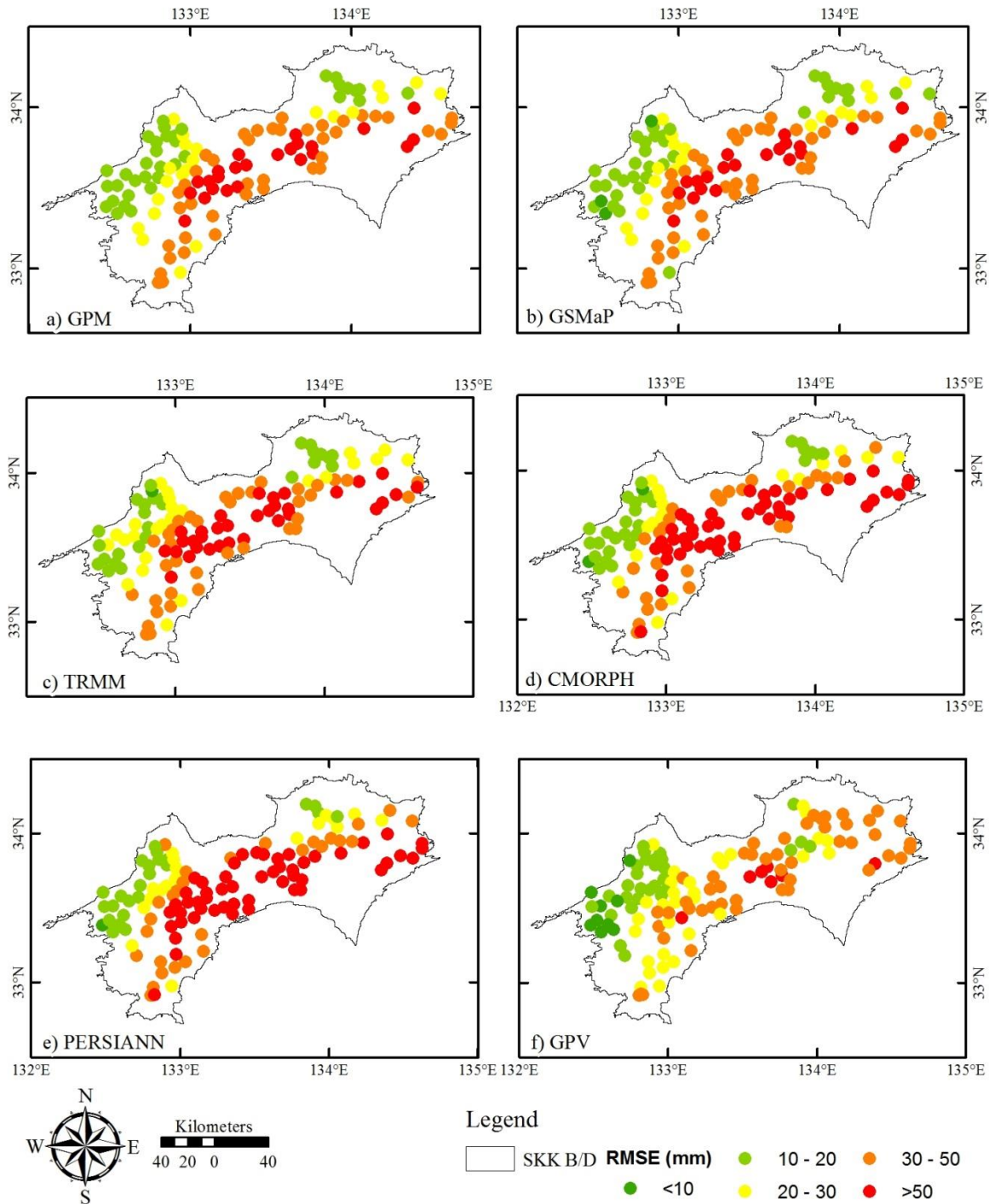
Figure 5-19 Root mean square error (RMSE) daily rainfall between rain gauge and satellite based rainfall products in the Shikoku Island
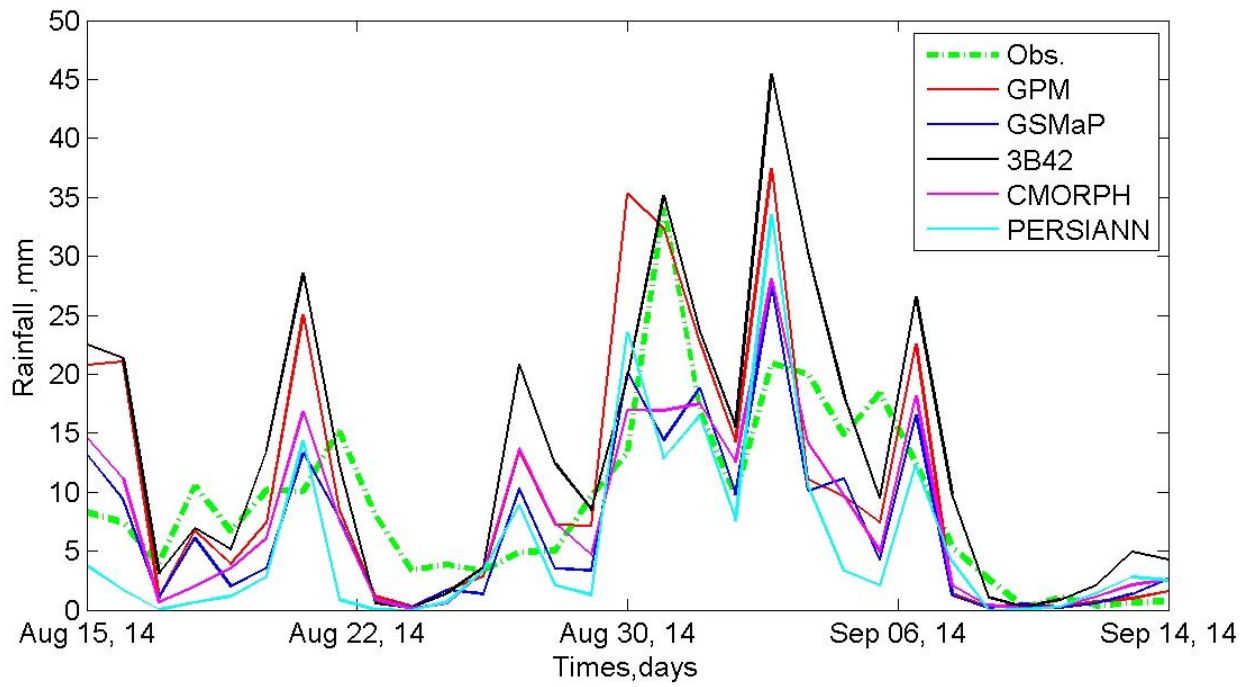
Figure 5-20 Average satellite based rainfall product over the study area in temporal scale

Table 5-11 Volume of rainfall products amounts over the study watershed

Rainfall products	Rainfall volume, MCM
Rain gauge	7,899.97
GPM	8,495.00
GSMaP	5,639.10
TRMM	12,254.51
CMORPH	7,223.27
PERSIANN	5,252.20
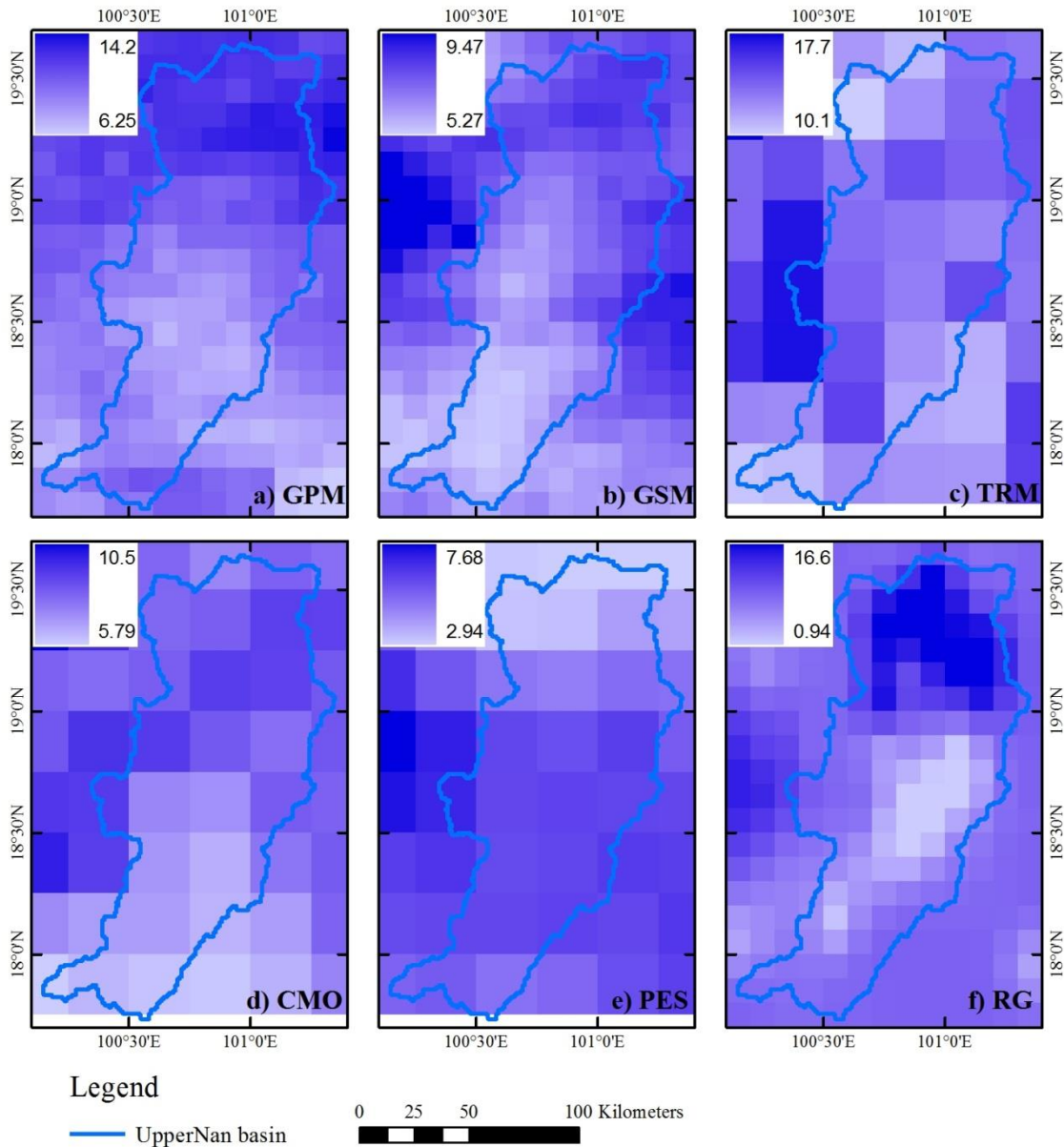
Figure 5-21 Average satellite based rainfall spatial products (August 2014)

All satellite-based rainfall products revealed low accuracies by significant differences among comparing with rain gauges based on the performance statistical (see **Table 5-12**). GSMaP and PERSIANN underestimated rainfall based on Volume bias by about 23.6% and 38.3%, respectively. Mean bias revealed that the both products underestimated rainfall about 2.15 mm/day and 3.5 mm/day, respectively. The satellite-based rainfall products were also underestimation reported by the other studies (Kidd et al., 2012; Tian et al., 2010; Qin et al., 2014; Sohn et al., 2009; Asadullah et al., 2010). The fact that most satellite-based rainfall products have been represented by underestimation rainfall might be due to the algorithm of estimation (Tian et al., 2010). The GSMaP underestimate rainfall represented by the mean bias in China about 0.53 mm/day and also in Columbia about 2.3 mm/day (Qin et al., 2014; Dinku et al., 2010). TRMM and GPM represented by the Volume bias overestimated rainfall about 49.2% and 19.9%, respectively. The Mean bias of both products was about 4.5 mm/day

and 1.54 mm/day, respectively. Overestimation of the TRMM has been reported by the previous studies that bias is about 30.5% in the USA and 4.5% in the China (Behrangi et al., 2011; Chen et al., 2015). The GPM has overestimated about 4.0% in Iran (Sharifi et al., 2016). Volume bias and Mean bias of CMORPH on underestimation were 11.06% and 1.01 mm/day, respectively. The CMORPH has underestimated rainfall reported by the other studies (Tan et al., 2015; Qin et al., 2014; Asadullah et al., 2010). In this study, the CMORPH was the best performance compared with the other products.

The Underestimation of peak rainfall had occurred in four products, GPM, GSMaP, CMORPH, and PERSIANN, while TRMM overestimated peak rainfall. In overall, the TRMM performed the best match of peak bias, but the GPM was the best among the underestimation products. The low accuracies on comparison, GPM presented the best linear correlation with observed data ($R^2 = 0.327$) and were followed by TRMM, GSMaP, CMORPH, and PERSIANN. All satellite products had range of RMSE about 16 to 20 mm/day. The GSMaP was the best performance with lowest RMSE value, and the TRMM was the highest value with low performance. The low performance of the TRMM based on the RMSE value could be referred by the previous study (Qin et al., 2014).

The estimation accuracy of evaluated satellite-based rainfall products over the Nan river basin of Thailand with information was based on the spatial distribution of RMSE from flood events in 2014. **Figure 5-22** showed the RMSE of satellite-based rainfall products on the flood event, which GSMaP was the best agreement with the observed rainfall. Interestingly, the lowest RMSE value for all methods was found in the middle part of watershed boundary. The northern part and north-eastern part is represented by the high mountainous area, where all products have estimated on the high RMSE value. This indicated that the satellite-based rainfall could not explore to obtain a good performance covering the mountain area because of classification of warm clouds from the IR sensors and numerical modelling of microwave signal (Yilmaz et al., 2005 and Huffman et al., 2007).
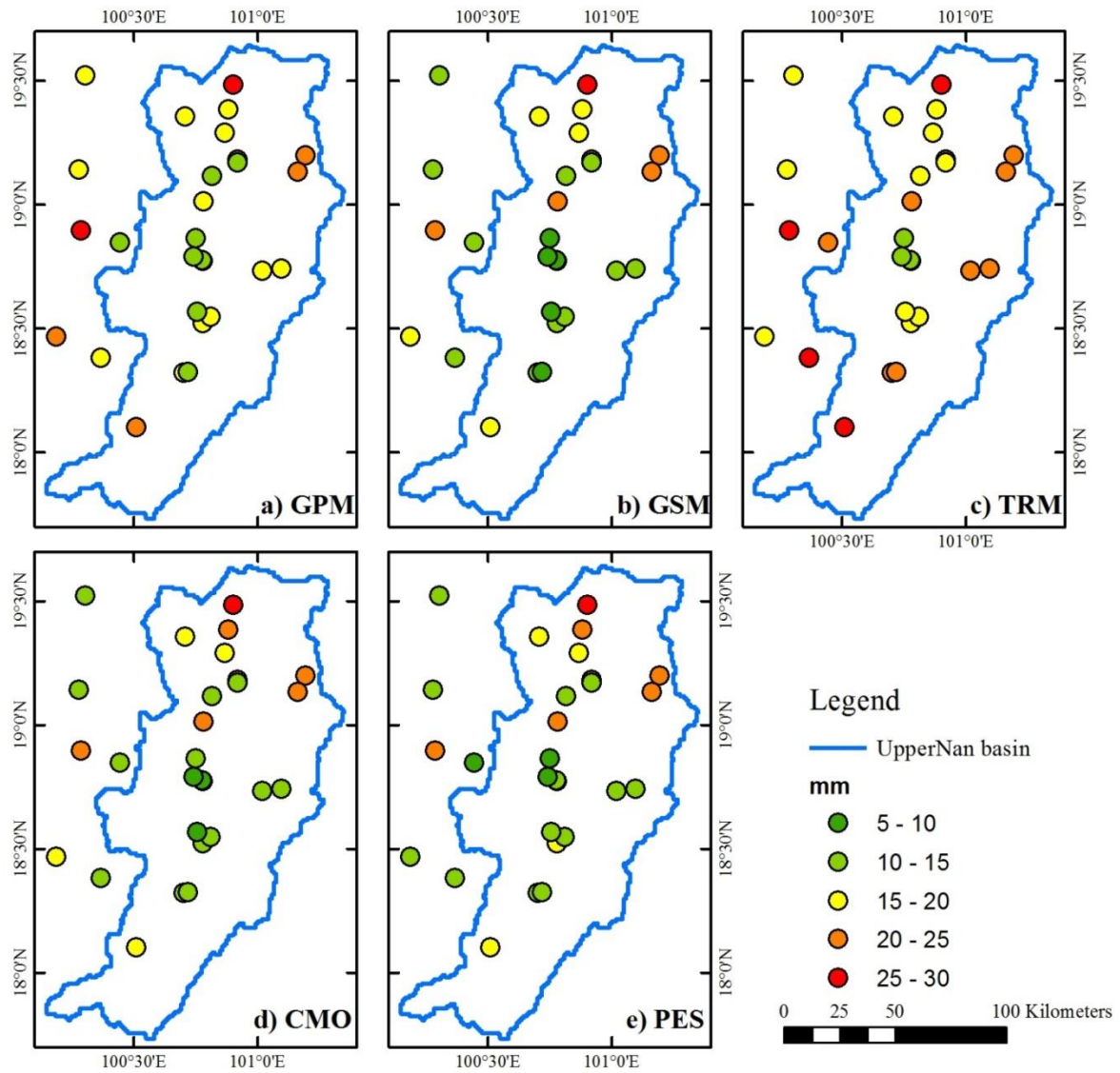
Figure 5-22 Root mean square error (RMSE) daily rainfall between rain gauge and satellite based rainfall products

Table 5-12 Performance statistical of rainfall spatial products

Rainfall products	Volume bias, %	Peak bias, %	RMSE, mm	Correlation	Mean bias, mm
GPM	16.94	-5.33	18.15	**0.327**	1.54
GSMaP	-23.66	-57.87	**16.08**	0.270	-2.15
TRMM	49.21	**2.89**	20.22	0.285	4.48
CMORPH	**-11.06**	-50.44	16.46	0.258	**-1.01**
PERSIANN	-38.35	-62.47	16.77	0.233	-3.49

5.4.3 Runoff simulation based on satellite rainfall products: Shikoku Island, Japan

The hydrological model (RRI model) was driven for flood events in 2014. The seven rainfall products were simulated at hourly on a temporal scale to match the observed streamflow data. Seven runoff stations were selected in the Shikoku Island (see **Figure 3-24**), the first (Ikeda dam) and second (Chuobashi) belong to the Yoshino River. The third (Furushou) is in the Naka River and the fourth (Fukabuchi) in the downstream area of the Monobe River. The fifth is located in the Ino, belonging to the Noyodo River; the sixth located in the Shimanto River is the Gudoudaini station. The seventh station is the Deai located in the Shigenobu River. All of stations showed in the hourly hydrograph that results from the different topography source. **Figure 5-23** presents the hydrographs for all sources with the seven runoff stations.

All simulated runoff driven by different products was to provide the temporal pattern similar to the observed hydrograph for the flood event. Over view of all the runoff station, six products symmetrically captured the peak at the same time with the observation. The products systematically underestimated observed runoff with a similar pattern.

All of seven runoff station on the hourly hydrograph were analysed and calculated for evaluation by the performance statistical. The results are given in **Table 5-13** that is concluded by five indexes. Simulated discharge of GPM and GSMaP was the best matched by observed runoff with a high Correlation and lowest RMSE, for the worldwide data set in the Shikoku. These simulated runoff data underestimated the runoff volume, peak flow and mean runoff. TRMM simulated runoff was high Correlation and low RMSE among the coarse resolution, however, its simulated runoff was underestimation of Volume bias and Mean bias. The peak flow of the TRMM also underestimated. The two products (CMORPH and PERSIANN) significantly underestimated the runoff volume, mean runoff, and peak flow, with high RMSE and low correlation value. Rain gauge simulated runoff was low RMSE value with strong correlation value of 0.75, this simulated results also underestimated the runoff volume, and mean runoff. The peak flow of the Rain gauge underestimated about 2.62%. For comparing the worldwide and only provided in Japan, GPV result was the highest performance to close to the observed data in every evaluated statistics, but it also underestimated in smallest.

In summary performance on estimating the streamflow, the best of the satellite-based rainfall products was GPM and GSMaP that statistical presented some value better than the Rain gauge interpolated product. The GSMaP product was represented on the high resolution products, while TRMM product was the best performance among the coarse resolution products. For provided in worldwide and Japan, GPV was the highest performance based on the remote sensing data sets.

Table 5-13 Performance statistical of runoff from the rainfall spatial prediction products in the Shikoku Island Japan

Rainfall products	Volume bias, %	Peak bias, %	RMSE, cms	Correlation	Mean bias, cms
Rain gauge	<u>-3.76</u>	<u>-2.62</u>	<u>32.58</u>	0.750	<u>-0.58</u>
GPM	**-43.87**	-75.34	672.94	0.802	**-125.02**
GSMaP	-51.22	**-72.84**	**667.59**	**0.839**	-145.98
GPV	<u>**-12.29**</u>	<u>**-35.76**</u>	<u>**440.05**</u>	<u>**0.883**</u>	<u>**-35.00**</u>
TRMM	-56.24	-82.70	747.70	0.700	-160.27
CMORPH	-70.23	-90.60	821.67	0.656	-200.14
PERSIANN	-81.27	-90.94	904.68	0.262	-231.62
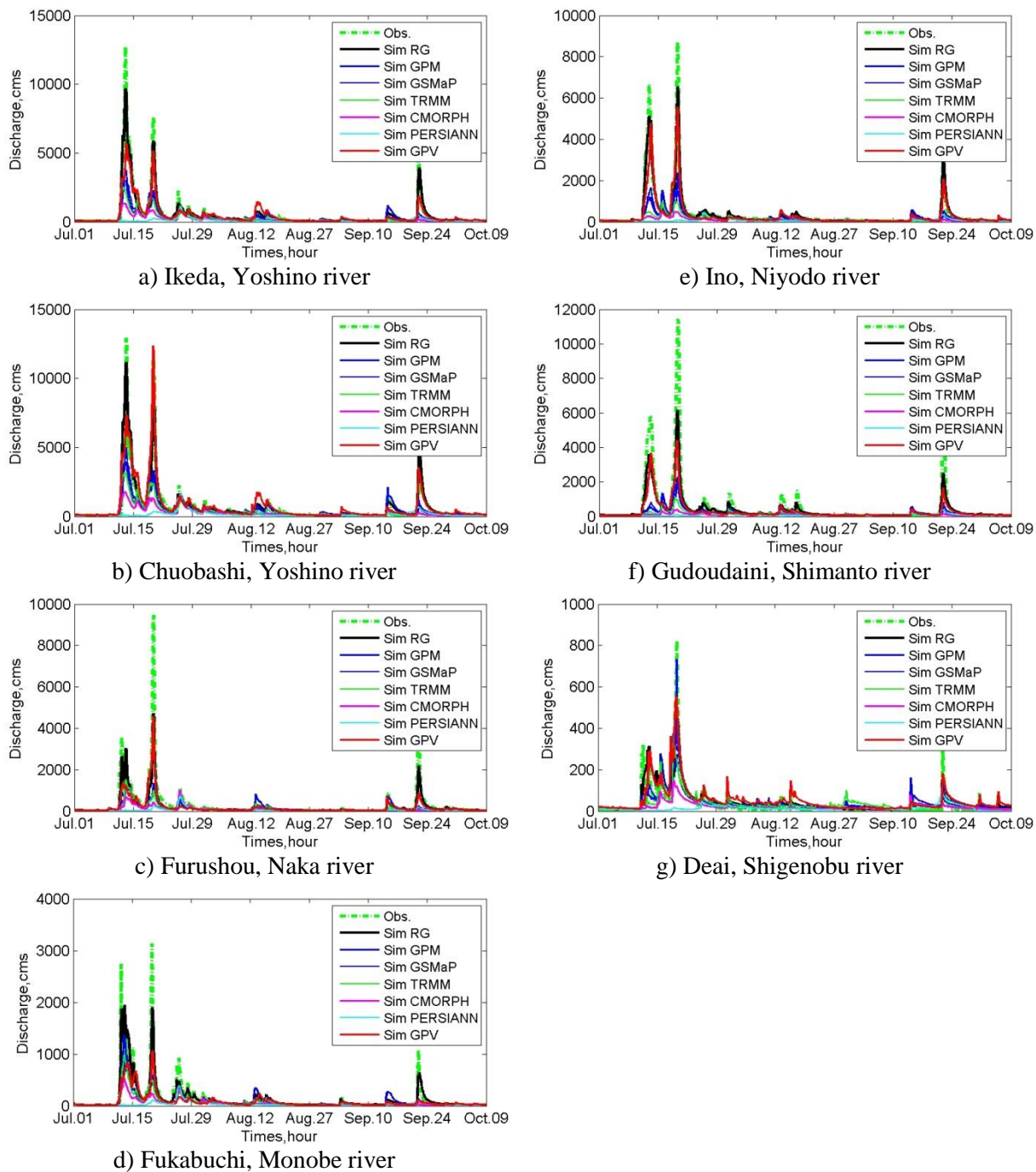
Figure 5-23 Hourly discharge hydrograph at runoff observation station of flood event based on different satellite products in the Shikoku Island Japan

167

5.4.4 Runoff simulation based on satellite rainfall products: Nan river basin, Thailand

The hydrological model (RRI model) was driven for flood events in 2014. The six rainfall products was simulated at daily on a temporal scale to match the Royal Irrigation Department Thailand observed streamflow data. Three runoff stations were selected in the Nan river basin (see **Figure 3-26**), the first one belonging to the upstream sub-catchment (N.64), the second one belonging to the middle area (N.1) and the third one belonging to the downstream area (N.13A), to show the daily hydrograph that results from the different interpolation scenario. **Figure 5-24** present the hydrographs for all rainfall products with the three runoff station, N64, N.1 and N.13A.

All simulated runoff driven by different products was to provide the temporal pattern similar to the observed hydrograph for the flood event. Over view of all the runoff station, GPM symmetrically captured the peak at the same time with the observation, while the other five products symmetrically lagged about 1 day. PERSIANN, GSMaP and CMORPH systematically underestimated observed runoff, while the other three products were underestimation. For N.13A, all patterns of rainfall products were underestimation to compare with the observed hydrograph.

All of three runoff station on the daily hydrograph were analysed and calculated for evaluation by the performance statistical. The results are given in **Table 5-14** that is concluded by five statistical. GPM simulated discharge was the best matched by observed runoff with a highest Correlation of 0.885 and lowest RMSE of 141.77 cms. This simulated runoff overestimated the runoff volume, peak flow and mean runoff by 10.6%, 3.55% and 44.6 cms, respectively. TRMM simulated runoff was high Correlation and low RMSE, however, its simulated runoff was overestimation of Volume bias of 13.27% and Mean bias of 55.84%. The peak flow of the TRMM underestimated about 17.8%. The three products (GSMaP, CMORPH and PERSIANN) significantly underestimated the runoff volume, mean runoff, and peak flow, with high RMSE and low correlation value. Rain gauge simulated runoff was low RMSE value of 163.88 cms with strong correlation value of 0.821, this simulated results overestimated the runoff volume, and mean runoff by 6.4%, 27 cms, respectively. The peak flow of the Rain gauge underestimated about 34.6%.

In summary performance on estimating the streamflow, the best of the satellite-based rainfall products was GPM that statistical presented some value better than the Rain gauge interpolated product. The GPM product was represented on the high resolution products, while TRMM product was the best performance among the coarse resolution products.

a) N.64

b) N.1

c) N.13A
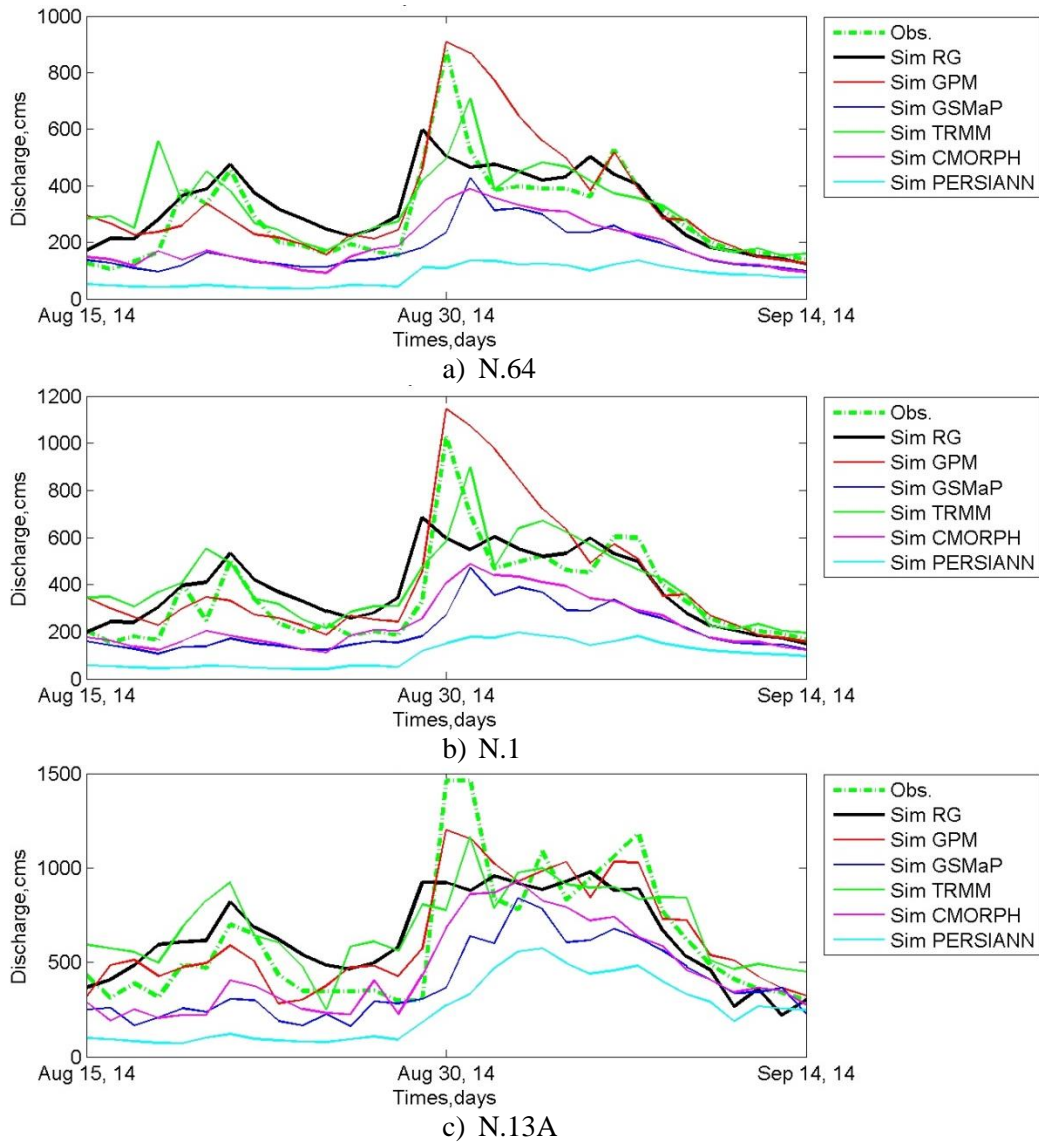
Figure 5-24 Daily discharge hydrograph at runoff observation station of flood event based on satellite base rainfall products

Table 5-14 Performance statistical of runoff from the rainfall spatial prediction products

Rainfall products	Volume bias, %	Peak bias, %	RMSE, cms	Correlation	Mean bias, cms
Rain gauge	<u>6.40</u>	-34.60	163.88	0.821	<u>26.94</u>
GPM	**10.60**	**3.55**	**141.77**	**0.885**	**44.61**
GSMaP	-39.05	-54.02	266.06	0.681	-164.39
TRMM	13.27	-17.86	192.35	0.761	55.84
CMORPH	-30.35	-48.51	222.88	0.767	-127.73
PERSIANN	-66.43	-73.86	348.26	0.742	-279.60

5.5 Evaluation of bias correction results of satellite rainfall data sets

The availability of different satellite products is presented in the **Table 5-1** with GPM only available from April 2014 and TRMM available to June 2015. Hence, the simulated storm event is selected from April 2014 to June 2015. According to the aim of this study is specific to the flood event that the storm event on the selected period occurs in the study area from monsoon during July to October. For the evaluation of satellite rainfall sources, the GPM was the best performance for the high resolution, and the TRMM was the highest performance among the coarse resolution. Then, the both satellite data are used to increase the accuracy by using bias correction methodology with five techniques and two schemes. The ten products of bias correction are used to simulate the runoff on hydrological modeling to reveal its effect.

5.5.1 Accuracy of bias correction in GPM product

GPM rainfall products applied in the study from different bias correction techniques, Mean ratio, Geometrics transformation, Linear transformation, Data assimilation and Quantile mapping, and different scheme, temporal and spatial. The difference data had same spatial and temporal resolution. **Figure 5-25** show the watershed average rainfall comparison for the temporal scheme. The data assimilation bias products closed to the rainfall pattern observed by the rain station. On the peak, the linear and Geometrics products were overestimation, while the three products were underestimation. The Mean ratio, Data assimilation and Quantile mapping showed the pattern similar with the observation, but the Quantile mapping was underestimation along the time scale. For the spatial scheme in **Figure 5-26**, the average rainfall of the five interpolation products was compared with the observed rainfall. Their pattern is similar to the observation data with variability on three products, Geometrics, Linear and Data assimilation. All products with underestimation on the peak, that the Mean ratio and Quantile mapping were underestimation data along the time scale.

Figure 5-27 shows the average spatial of bias products for the temporal scheme. The period 30 days, there are differences rainfall values of 1 to 27 mm over space of 200 km. The Geometrics technique indicated most spatial variability, followed by the Mean ratio, Linear, Data assimilation and Quantile mapping. The largest amount of rainfall fell in the north-eastern part for the five interpolation methods, which the Geometrics technique produced the maximum rainfall intensities (about 27.3 mm/day). Their smallest amount of rainfall spatial fell in the middle of the watershed area. The spatial distribution rainfall of the spatial scheme was shown in **Figure 5-28**, which all of method computed the spatial pattern similar with the event one in overall. The period time as same as the above scheme, and the Linear technique produced the maximum rainfall intensities about 17.2 mm/day. In detail, the maximum intensity of this scheme was located in the north-eastern part along with the border of watershed

The total rainfall amount for five techniques for two schemes (temporal and spatial) was presented in **Table 5-15**, which was estimated by accumulating the daily rainfall input over the catchment area. In overall, the volume of rainfall in temporal scheme was greater than the spatial scheme, and the peak of temporal scheme was also greater than the spatial scheme as shown in **Figure 5-25** and **5-26**. On the temporal scheme, The Linear technique was the largest amount of rainfall volume followed by the Mean ratio, while the Quantile mapping was smallest. The largest amount of rainfall volume on the spatial scheme was the Geometrics transformation technique that was about 7,268 MCM. This event also revealed that the Quantile mapping was the smallest rainfall amount.
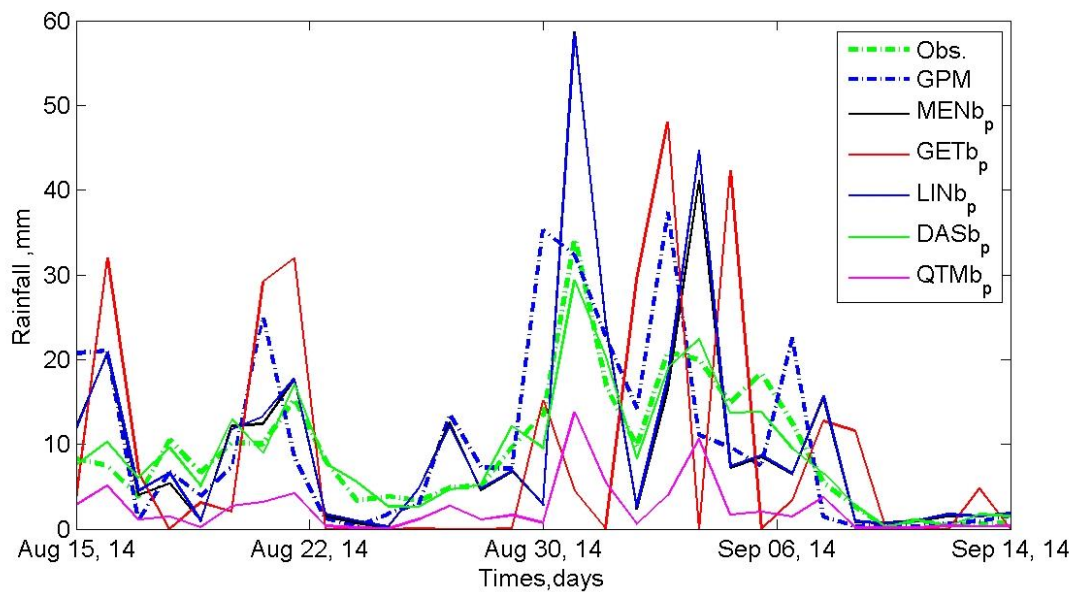
Figure 5-25 Average time series of GPM satellite based rainfall over the study area on the time series scheme
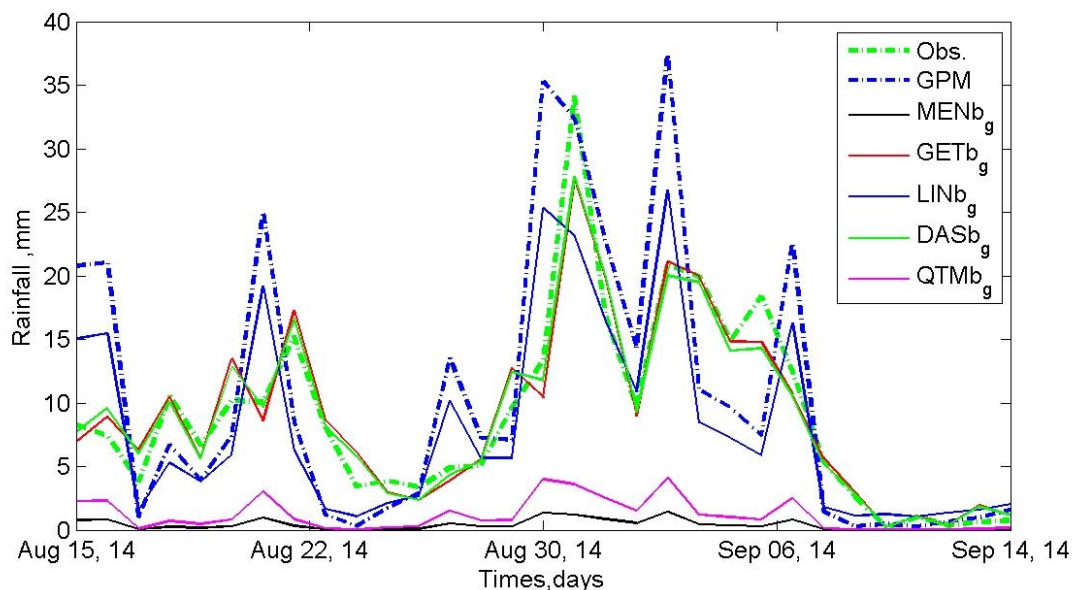
Figure 5-26 Average time series of GPM satellite based rainfall over the study area on the spatial scheme

171
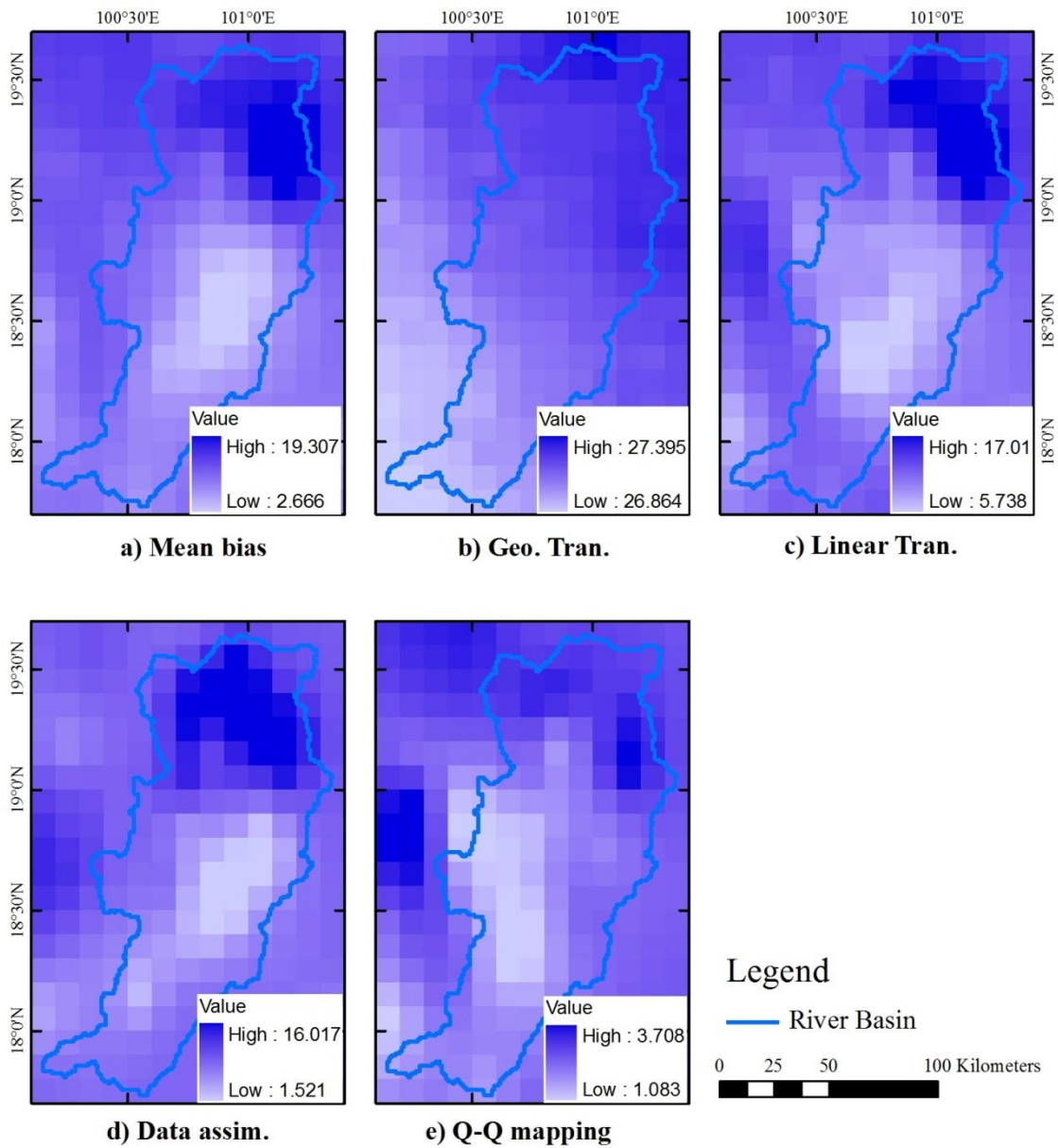
Figure 5-27 GPM bias correction spatial products based on the time series scheme
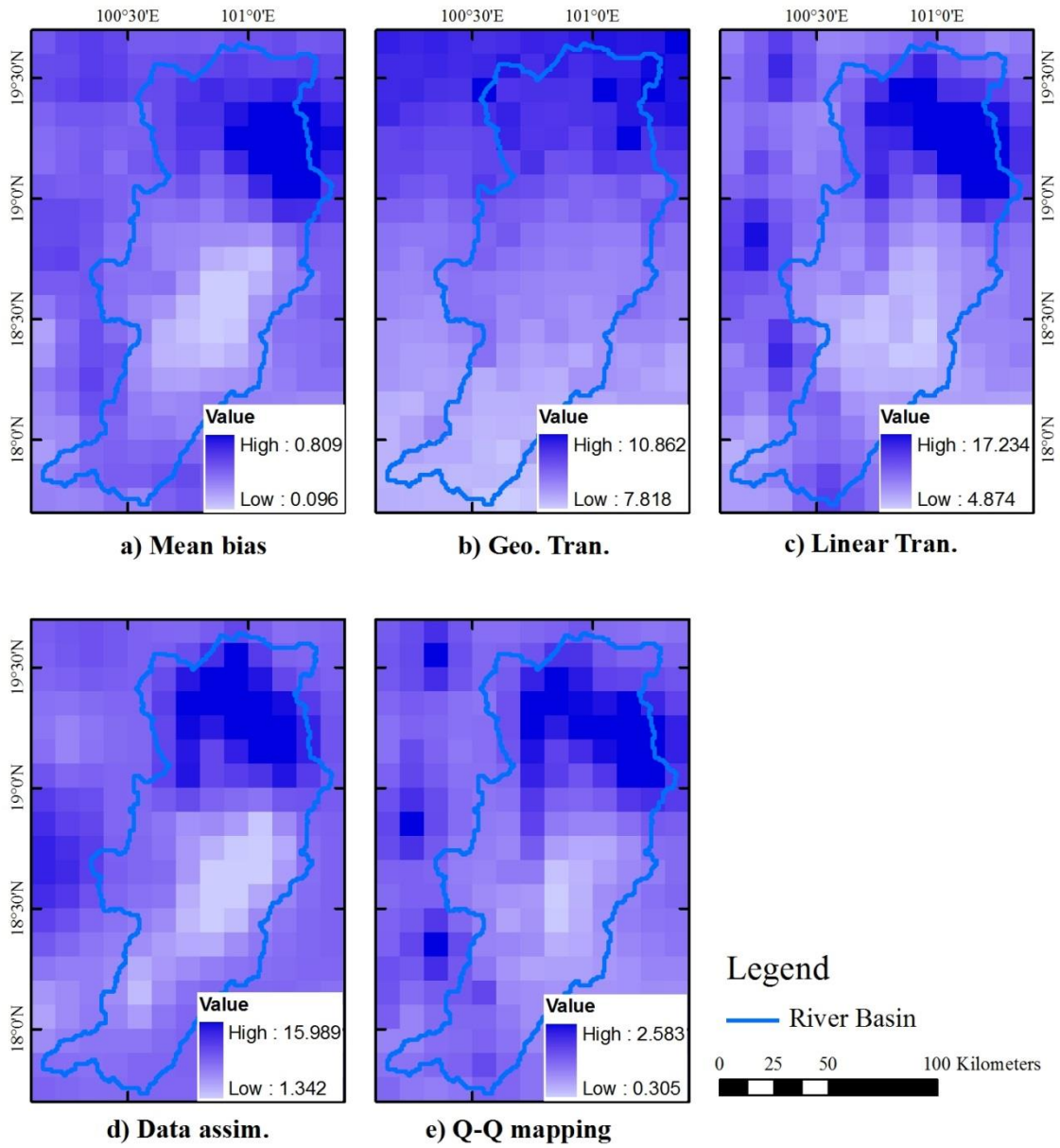
Figure 5-28 GPM bias correction spatial products based on the spatial scheme

Table 5-15 Volume of rainfall products amounts over the study watershed

Rainfall products		Rainfall volume, MCM
Rain gauge		7,899.97
GPM		8,495.00
Time series	Mean ratio	7,964.04
	Geometrics	7,293.13
	Linear	8,215.74
	Data assimilation	7,235.28
	QQ mapping	1,913.67
Spatial	Mean ratio	3,024.52
	Geometrics	7,314.12
	Linear	6,553.54
	Data assimilation	7,268.40
	QQ mapping	1,940.96

All biased rainfall products demonstrated medium accuracy on daily rainfall, as presented by significant differences among observation and correction based on the performance statistical (see **Table 5-6**). For the temporal scheme, biased by Mean ratio, Linear and Quantile mapping presented the best linear correlation with observed data ($R^2 = 0.4$) and were followed by Data assimilation, and Geometrics. Also, the Quantile mapping showed the lowest RMSE, following similar with the ranking of R^2. In overall, the Geometrics revealed the best R^2 with observed data ($R^2 = 0.56$) and was followed by Mean ratio, Linear, Quantile mapping, and Data assimilation for the spatial scheme. For the RMSE of the spatial scheme, the Geometrics also presented the best performance RMSE, followed by similar with above. On the both scheme, the Data assimilation showed the best performance among the four techniques to evaluate with the five statistics value.

The Data assimilation product as the best performance of both scheme underestimated observed daily rainfall on the Peak bias and overestimation on the Volume bias and Mean bias. With negative Volume bias and Mean bias values, Quantile mapping underestimated observed data for the temporal scheme. By contract, the other four correction products overestimated the observed rain gauge data. For spatial scheme based on the Volume bias and Mean bias values, the Geometrics, Linear and Data assimilation were positive value, while the other two products were negative value. By lowest

negative Volume bias and Mean bias values, Quantile mapping underestimated observed rainfall for the both scheme.

The estimation accuracy of evaluated correction rainfall products over the Nan river basin of Thailand for daily data with information was based on the spatial distribution of RMSE from two schemes, temporal and spatial. **Figure 5-29** showed the RMSE of the temporal scheme, which the Data assimilation and Linear technique were the best agreement with the observed rainfall. For the spatial in **Figure 5-30**, the best agreement with the rain gauge was the Geometrics product. Interestingly, the lowest RMSE value for all methods was found in the middle and southern part of watershed boundary. The northern part is represented by the high mountainous area, where the Geometrics technique was the best performance for correction of the spatial scheme.

Table 5-16 Performance statistical of rainfall spatial products

Rainfall products		Volume bias, %	Peak bias, %	RMSE, mm	Correlation	Mean bias, mm
GPM		16.94	-5.33	18.15	0.327	1.54
Time series	Mean ratio	5.86	71.87	16.63	0.497	0.53
	Geometrics	0.85	-60.66	45.91	0.146	8.02
	Linear	9.71	70.79	16.64	**0.481**	0.88
	Data assimilation	**0.65**	**-13.98**	17.32	0.291	**0.06**
	QQ mapping	-75.82	-59.56	**15.88**	0.454	-6.90
Spatial	Mean ratio	-95.60	-96.43	17.72	0.361	-8.70
	Geometrics	1.24	-19.22	**13.02**	**0.563**	0.11
	Linear	3.85	-32.37	16.96	0.349	0.35
	Data assimilation	**0.79**	**-18.56**	17.37	0.279	**0.07**
	QQ mapping	-84.22	-89.40	16.87	0.319	-7.67
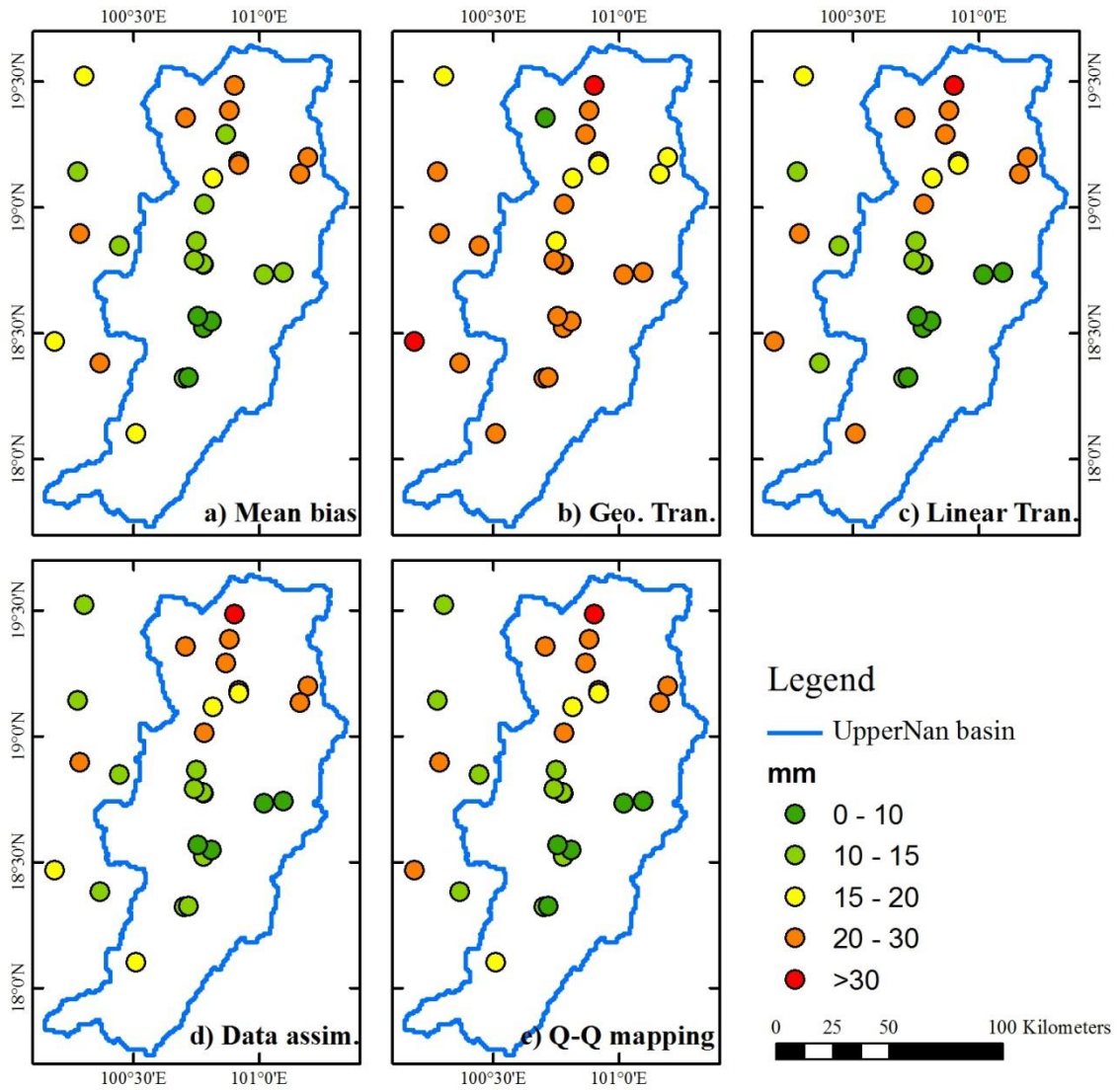
Figure 5-29 Root mean square error (RMSE) daily rainfall between rain gauge and GPM bias correction spatial distribution products on the time series scheme
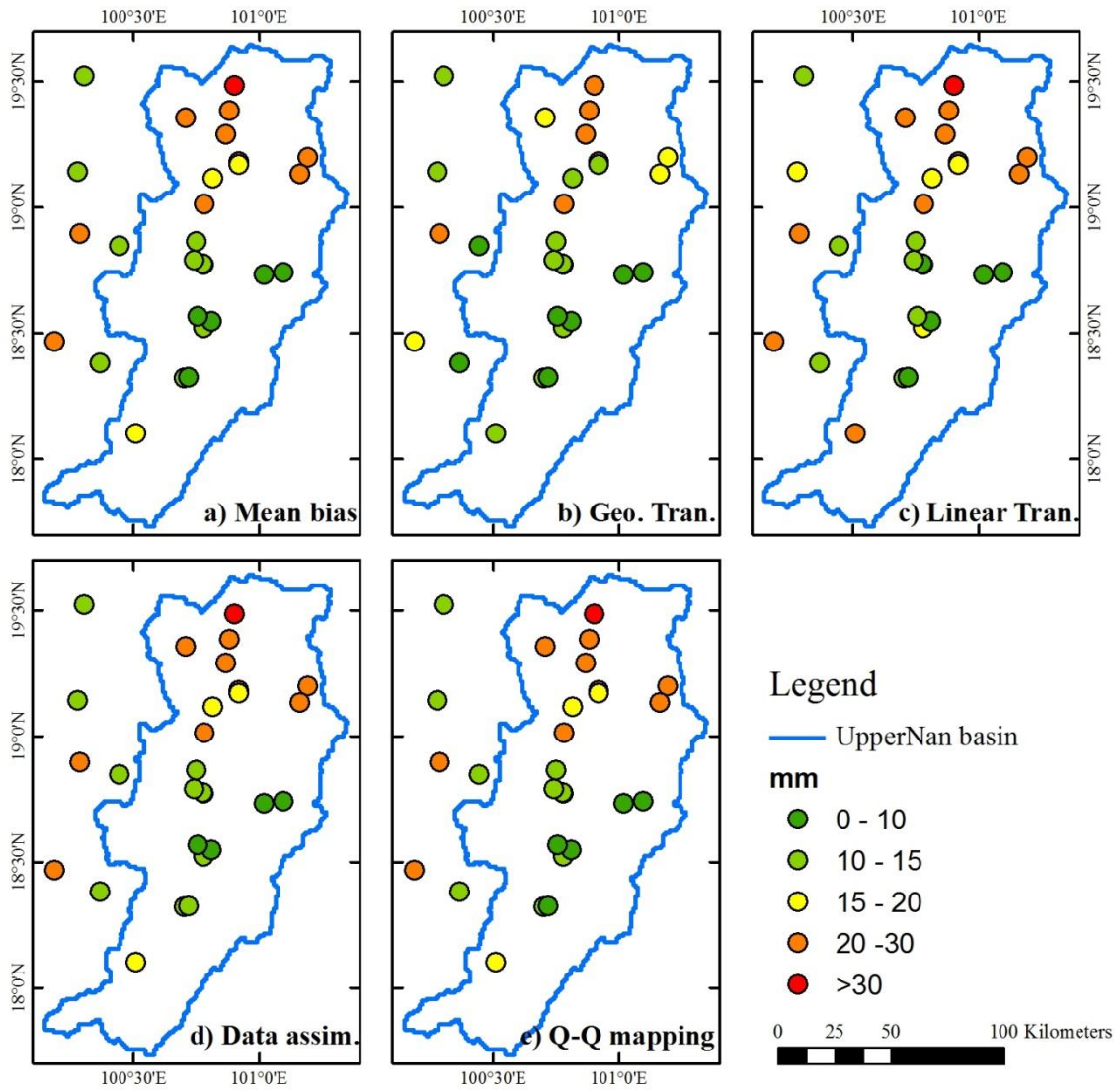
Figure 5-30 Root mean square error (RMSE) daily rainfall between rain gauge and GPM bias correction spatial distribution products on spatial scheme

5.5.2 Accuracy of bias correction in TRMM product

TRMM rainfall products applied in the study from different five bias correction techniques as mention in above, and two schemes, temporal and spatial. The difference data had same spatial and temporal resolution. **Figure 5-31** show the watershed average rainfall comparison for the temporal scheme. Data assimilation bias products closed to the rainfall pattern observed by the rain station, but three products, Mean ratio, Linear, and Quantile mapping, were underestimation with the same pattern. On the peak, Geometrics product was overestimation. For the spatial scheme in **Figure 5-32**, the average rainfall of the five interpolation products was compared with the observed rainfall. Their pattern is similar to the observation data with variability on three products, Geometrics, Linear and Data assimilation. All products with underestimation on the peak, that the Mean ratio and Quantile mapping were underestimation data along the time scale.

Figure 5-33 shows the average spatial of bias products for the temporal scheme. The period 30 days, there are differences rainfall values of 2 to 15 mm over space of 200 km. Data assimilation technique indicated most spatial variability, followed by the Mean ratio, Linear, Data assimilation and Quantile mapping. The largest amount of rainfall fell in the north-eastern part for the five interpolation methods, which the Data assimilation technique produced the maximum rainfall intensities (about 14.9 mm/day). Their smallest amount of rainfall spatial fell in the middle of the watershed area. The spatial distribution rainfall of the spatial scheme was shown in **Figure 5-34**, which all of method computed the spatial pattern similar with the event one in overall. The period time as same as the above scheme, and the Linear technique produced the maximum rainfall intensities about 17.5 mm/day. In detail, the maximum intensity of this scheme was located in the north-eastern part along with the border of watershed

The total rainfall amount for five techniques of TRMM for two schemes (temporal and spatial) was presented in **Table 5-17**, which was estimated by accumulating the daily rainfall input over the catchment area. In overall, the volume of rainfall in spatial scheme was greater than the temporal scheme that was different from GPM data, but the peak of temporal scheme was also greater than the spatial scheme as shown in **Figure 5-31** and **5-32**. On the temporal scheme, The Data assimilation technique was the largest amount of rainfall volume followed by the Geometrics, while the Mean ratio was smallest. The largest amount of rainfall volume on the spatial scheme was also the Data assimilation technique that was about 8,506 MCM. This event also revealed that the Mean ratio was the smallest rainfall amount.
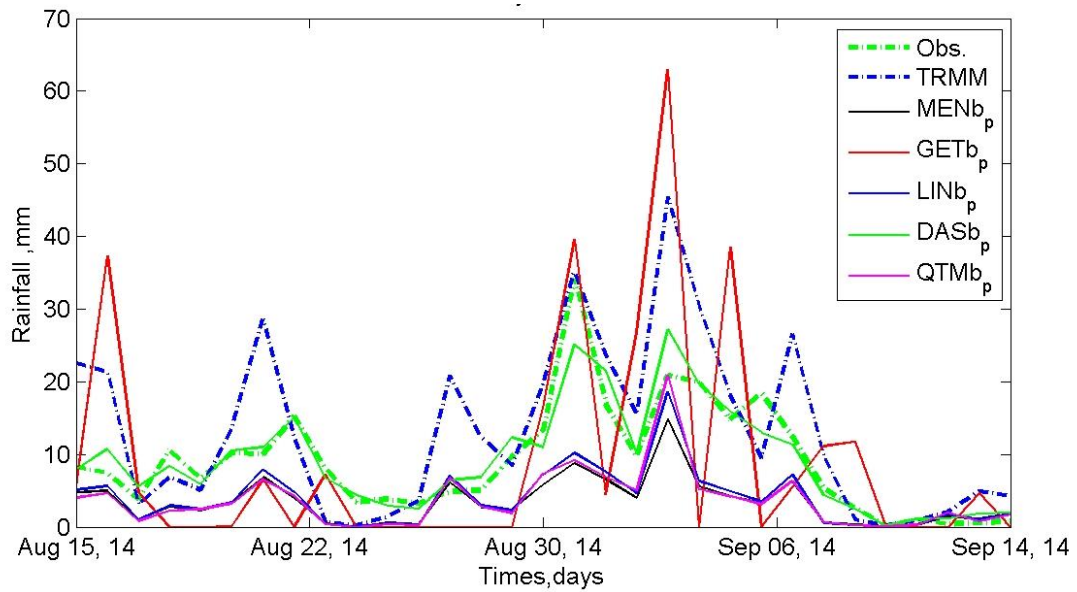
Figure 5-31 Average time series of TRMM satellite based rainfall over the study area on the time series scheme
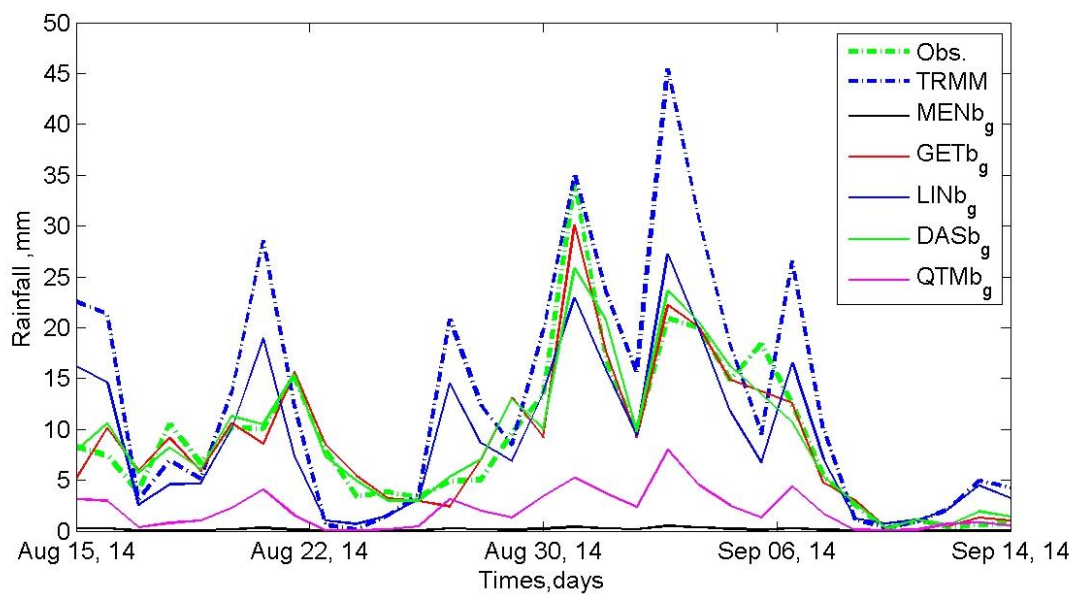
Figure 5-32 Average time series of TRMM satellite based rainfall over the study area on the spatial scheme

Table 5-17 Volume of rainfall products amounts over the study watershed

Rainfall products		Rainfall volume, MCM
Rain gauge		7,899.97
TRMM		12,254.51
Time series	Mean ratio	3,235.31
	Geometrics	8,490.38
	Linear	3,675.71
	Data assimilation	8,562.72
	QQ mapping	3,431.65
Spatial	Mean ratio	1,400.11
	Geometrics	8,253.47
	Linear	8,376.40
	Data assimilation	8,506.68
	QQ mapping	1,883.84

a) Mean bias   **b) Geo. Tran.**   **c) Linear Tran.**

d) Data assim.   **e) Q-Q mapping**
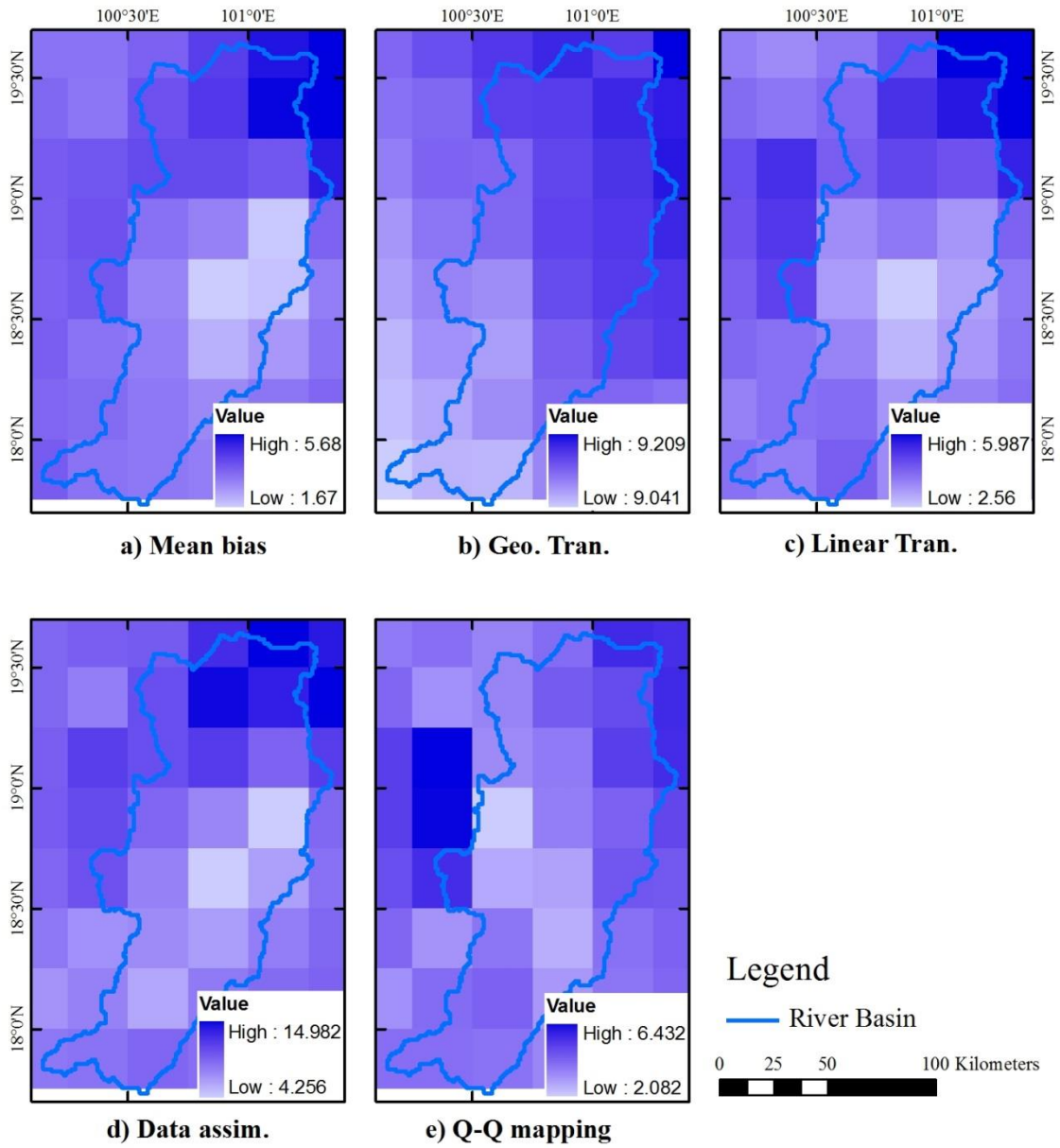
Figure 5-33 TRMM bias correction spatial products based on the time series scheme
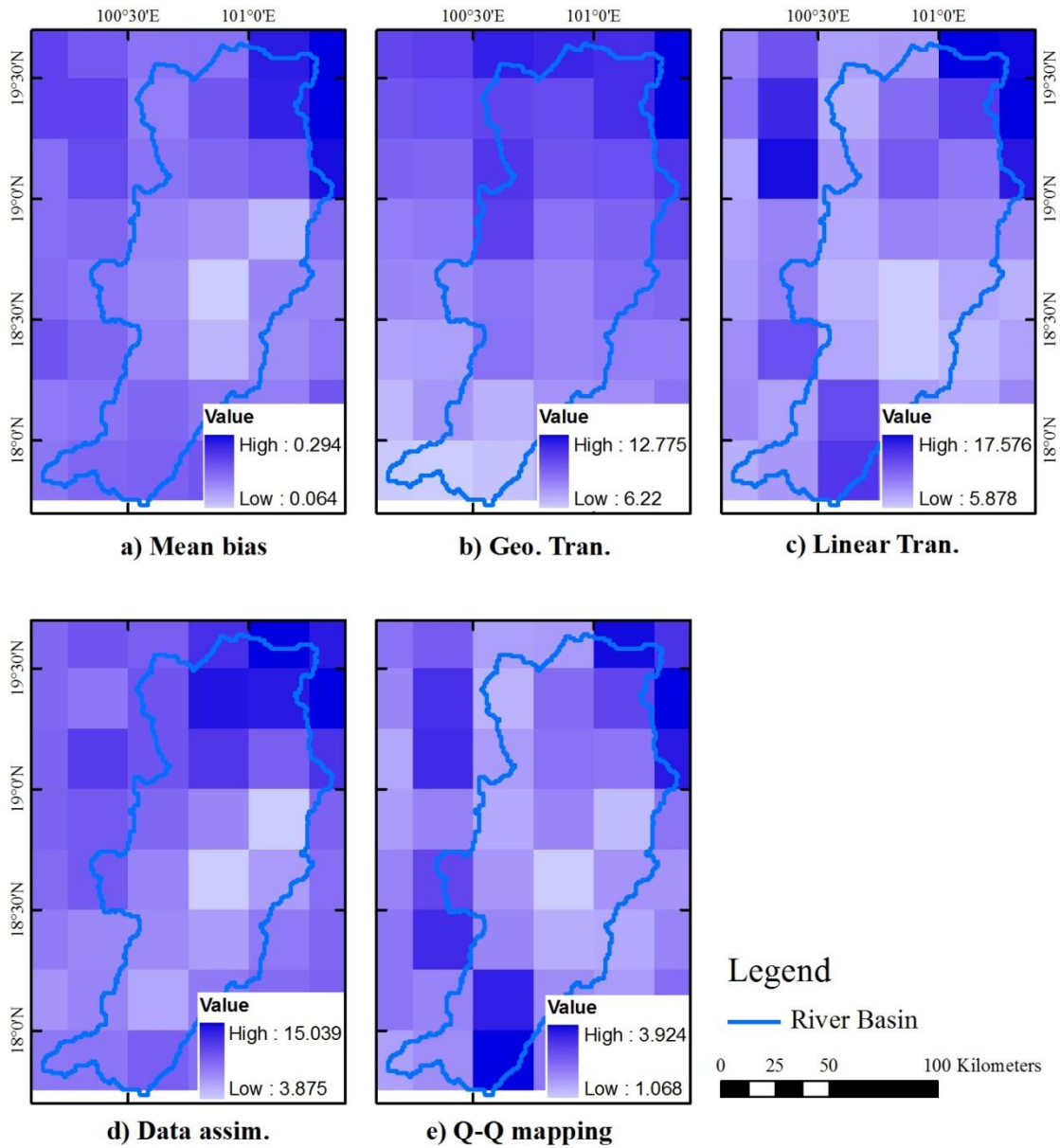
Figure 5-34 TRMM bias correction spatial products based on the spatial scheme

All biased rainfall products demonstrated medium accuracy on daily rainfall, as presented by significant differences among observation and correction based on the performance statistical (see **Table 5-6**). For the temporal scheme, biased by Mean ratio, Linear and Quantile mapping presented the best linear correlation with observed data ($r = 0.35$) and were followed by Geometrics, and Data assimilation. Also, the Linear showed the lowest RMSE, following similar with the ranking of R^2. In overall, the Geometrics revealed the best R^2 with observed data ($r = 0.53$) and was followed by Mean ratio, Linear, Quantile mapping, and Data assimilation for the spatial scheme as same as the GPM assessment. For the RMSE of the spatial scheme, the Geometrics also presented the best performance RMSE. On the both scheme, the Geometrics showed the best performance among the four techniques to evaluate with the five statistics value.

The Geometrics product as the best performance of both scheme, which overestimated observed daily rainfall on the Peak bias for first scheme but underestimated for the second scheme. The evaluation value of the product on the Volume bias and Mean bias that same the peak evaluation. With negative Volume bias and Mean bias values, four products, Quantile mapping, Mean ratio, Linear, and Data assimilation, underestimated observed data for the temporal scheme. By contract, the Geometrics correction products overestimated the observed rain gauge data. For spatial scheme based on the Volume bias and Mean bias value, all products were underestimation. By lowest negative Volume bias and Mean bias value that was the Quantile mapping and Mean ratio for the both scheme.

The estimation accuracy of evaluated TRMM correction rainfall products over the Nan river basin of Thailand for daily data with information was based on the spatial distribution of RMSE from two schemes, temporal and spatial. **Figure 5-35** showed the RMSE of the temporal scheme, which the Geometrics and Linear technique were the best agreement with the observed rainfall. For the spatial in **Figure 5-36**, the best agreement with the rain gauge was the Data assimilation and Linear product. Interestingly, the lowest RMSE value for all methods was found in the middle and southern part of watershed boundary. The northern part is represented by the high mountainous area, where the Linear technique was the high performance.

Table 5-18 Performance statistical of rainfall spatial products

	Rainfall products	Volume bias, %	Peak bias, %	RMSE, mm	Correlation	Mean bias, mm
	TRMM	49.21	2.89	20.22	0.285	4.48
Time series	Mean ratio	-63.89	-74.18	15.69	**0.394**	-5.81
	Geometrics	**0.30**	**16.19**	18.99	0.249	**0.03**
	Linear	-57.45	-70.10	**15.50**	0.369	-5.23
	Data assimilation	-1.12	-26.37	16.15	0.290	-0.10
	QQ mapping	-60.34	-73.03	15.87	0.308	-5.49
Spatial	Mean ratio	-98.51	-98.82	17.99	0.336	-8.97
	Geometrics	**-1.65**	**-11.69**	**13.25**	**0.535**	**-0.15**
	Linear	-3.36	-32.76	16.09	0.311	-0.31
	Data assimilation	-2.27	-24.29	16.24	0.288	-0.21
	QQ mapping	-79.13	-84.67	16.77	0.261	-7.20
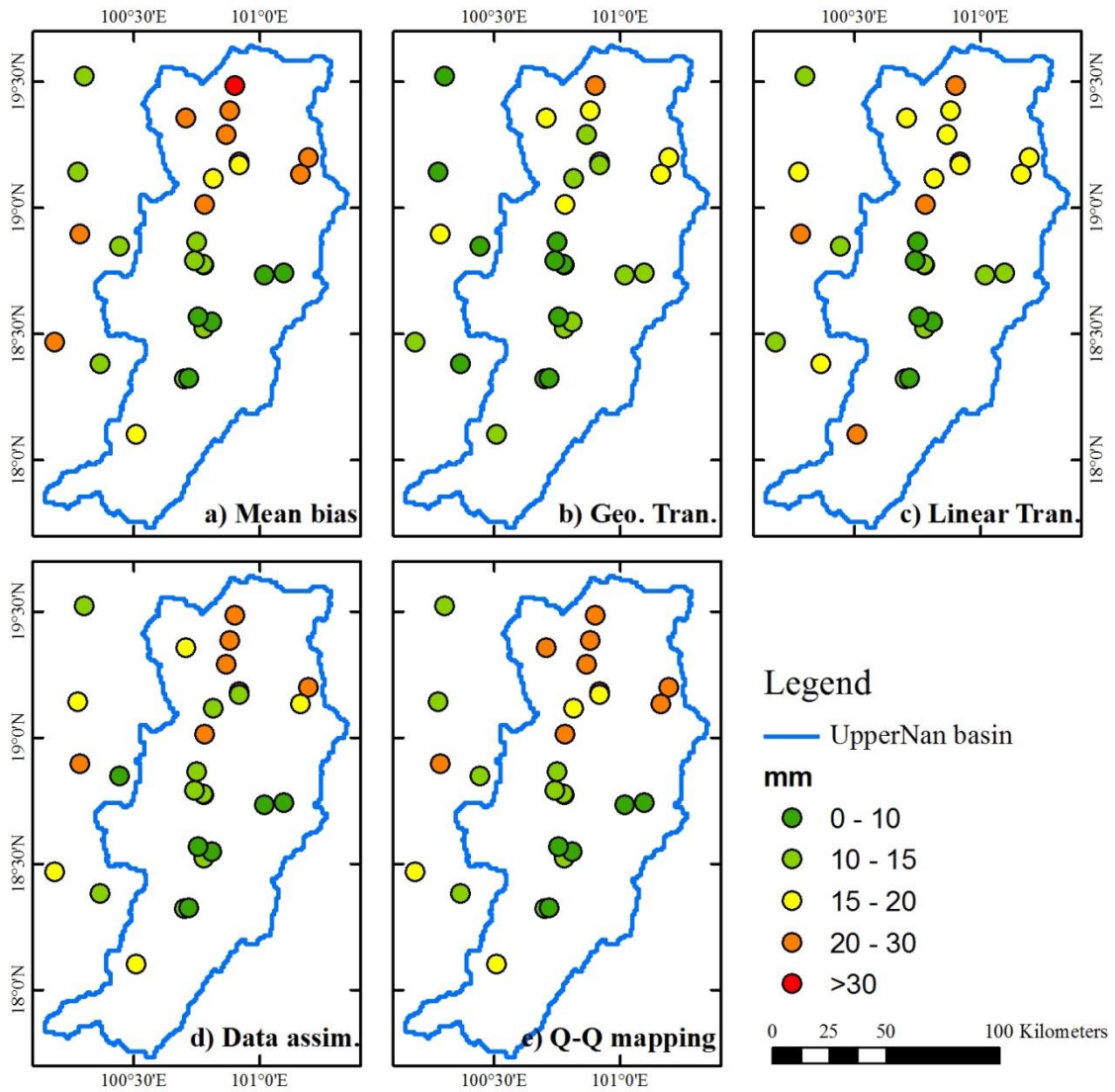
Figure 5-35 Root mean square error (RMSE) daily rainfall between rain gauge and TRMM bias correction spatial distribution products on the time series scheme
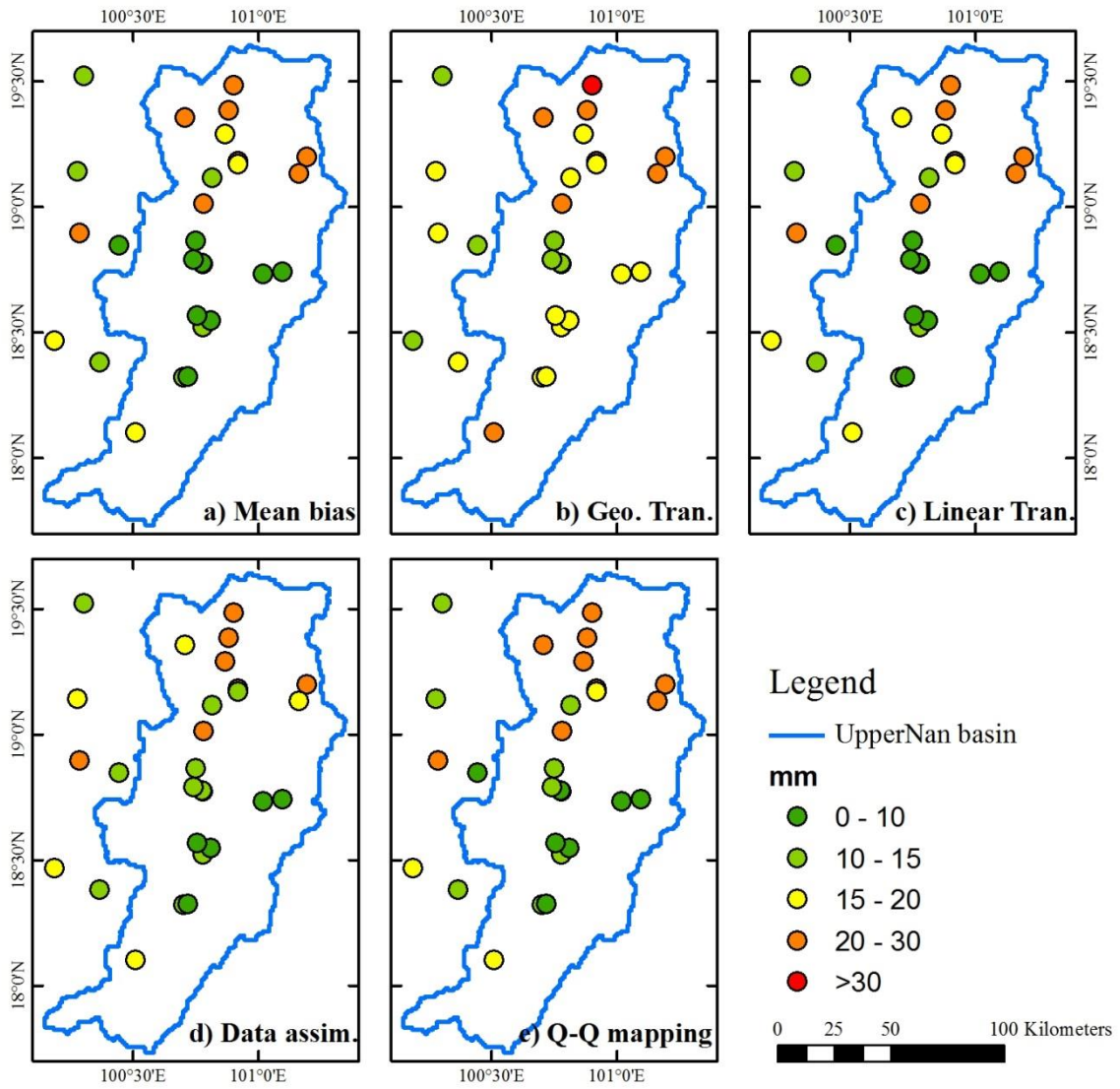
Figure 5-36 Root mean square error (RMSE) daily rainfall between rain gauge and TRMM bias correction spatial distribution products on spatial scheme

5.5.3 Simulated runoff based on different bias correction products of the GPM product

The hydrological model (RRI model) was driven by GPM correction products of two schemes and five techniques, using the similar hydrologic parameters, topography and land cover. The GPM bias corrected simulation was modeled at daily on a temporal scale to match the Royal Irrigation Department Thailand observed streamflow data. Three runoff stations were selected in the Nan river basin (see **Figure 3-26**), the first one belonging to the upstream sub-catchment (N.64), the second one belonging to the middle area (N.1) and the third one belonging to the downstream area (N.13A), to show the daily hydrograph that results from the different techniques and schemes . **Figure 5-37** and **5-38** present the hydrographs for all bias techniques and scheme of respectively runoff station N64, N.1 and N.13A.

All the modeled runoff driven by different technique and scheme was to provide the temporal pattern similar to the observed hydrograph. Overview all the runoff station for the temporal scheme, Mean ratio, Geometrics, Linear and Data assimilation symmetrically captured the peak and pattern to same with the observation, while the Quantile mapping products symmetrically stilled underestimation with different. By contract, the Mean ratio and Linear systematically overestimated observed runoff in station N.64 and N.1, while the other three scenarios was underestimation. For N.13A, all of correction products were underestimation to compare with the observed hydrograph. The simulated streamflow of the spatial scheme provided the similar temporal pattern with observed hydrograph. All products were significantly underestimation, and two products, Mean ratio and Quantile mapping, were stilled more underestimation. The Linear and Data assimilation could capture the peak with underestimation.

All of three runoff station on the daily hydrograph were analyzed and calculated for evaluation by the performance statistical. The results are given in **Table 5-19** that is concluded by five indexes. The Linear simulated discharge on best matched the observed runoff with the high r of 0.749 and lowest RMSE of 157.2 cms for the temporal scheme. This simulated runoff overestimated the runoff volume, peak flow and mean runoff. Data assimilation simulated runoff was highest r and lowest RMSE, however, its simulated runoff was over estimation of Volume bias and Mean bias. The peak flow of the Data assimilation was underestimation. Geometrics runoff significantly underestimated the runoff volume, mean runoff, and peak flow, with high RMSE and weak correlation value. Mean ratio runoff was high RMSE value with a good correlation value; this simulated results overestimated the runoff volume, peak and mean runoff. By contract, Quantile mapping discharge stilled more underestimated runoff volume, mean runoff, and peak flow, with high RMSE and low correlation value.

For the spatial scheme based on the **Table 5-19**, flow simulated from Linear technique matched perfectly with underestimation based on the lowest of Volume bias, Peak bias and Mean bias. The

technique provided the low RMSE about 109.86 cms and high correction about 0.821. Data assimilation runoff overestimated with low runoff volume and mean runoff value, on the underestimation bias of the peak about 34.2%. Its result presented the lowest RMSE and highest correlation value. Geometrics results showed the underestimation of runoff volume, mean runoff, and peak flow. Mean ratio and Quantile mapping resulted on the highest underestimation of runoff volume, peak and mean runoff.

Table 5-19 Performance statistical of runoff from the bias correction scenario products

	Rainfall products	Volume bias, %	Peak bias, %	RMSE, cms	Correlation	Mean bias, cms
	GPM	**10.60**	**-3.55**	**141.77**	**0.885**	**44.61**
Time series	Mean ratio	20.24	9.70	174.99	0.741	65.40
	Geometrics	-16.24	-37.82	238.81	0.594	-68.36
	Linear	<u>13.53</u>	<u>1.68</u>	157.16	0.749	<u>43.70</u>
	Data assimilation	14.48	-32.51	<u>111.01</u>	<u>0.835</u>	46.78
	QQ mapping	-83.58	-91.25	319.89	0.685	-269.99
Spatial	Mean ratio	-99.06	-99.38	368.36	0.472	-320.00
	Geometrics	-8.72	-46.66	134.87	0.698	-28.18
	Linear	**-6.87**	**-1.33**	109.87	0.821	**-22.19**
	Data assimilation	12.24	-34.23	**105.61**	**0.846**	39.53
	QQ mapping	-93.46	-96.11	350.41	0.736	-301.90

a) N.64

b) N.1

c) N.13A
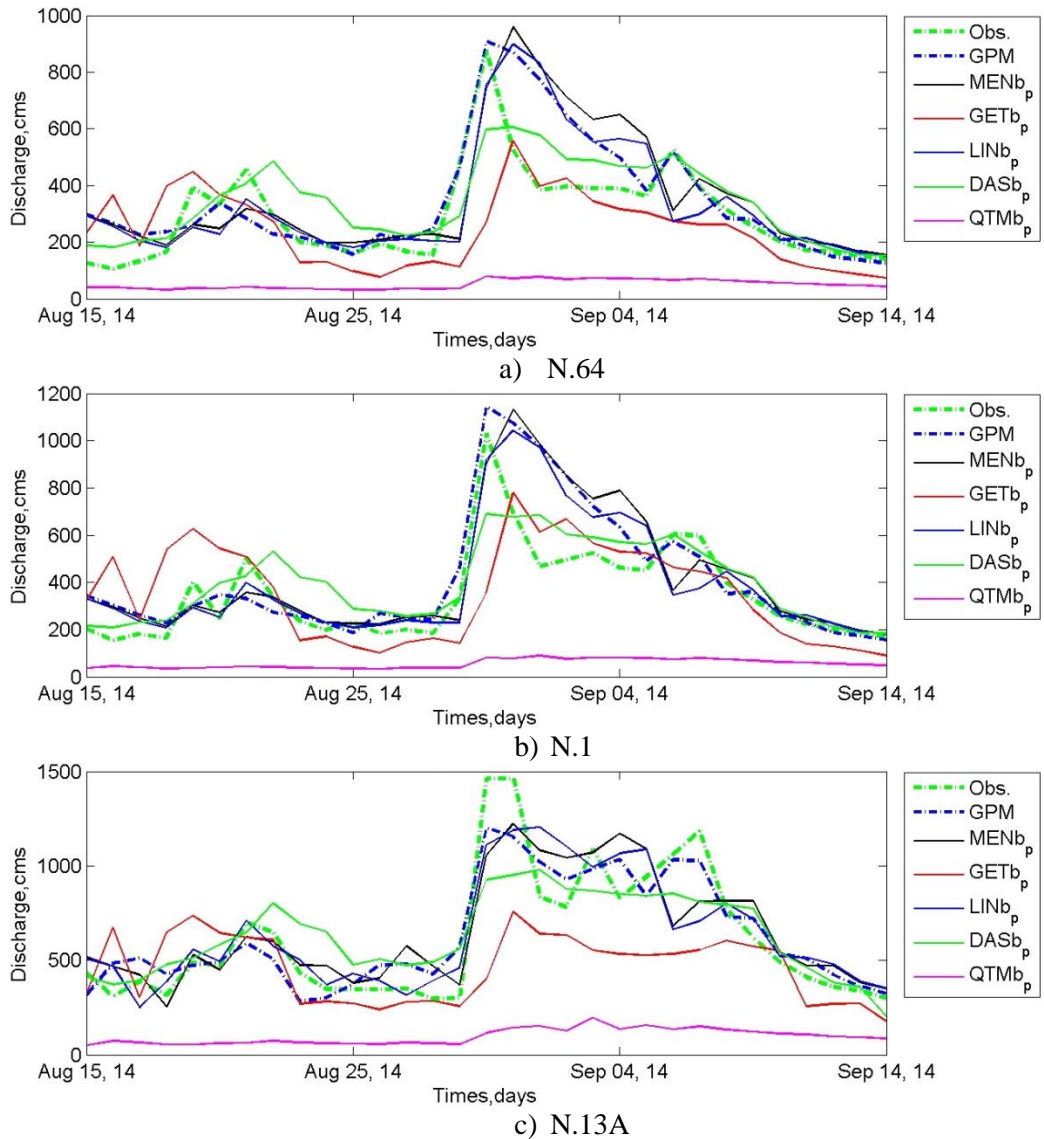
Figure 5-37 Daily discharge hydrograph at runoff observation station of flood event of GPM based on time series scheme in each method of bias correction

a) N.64

b) N.1

c) N.13A
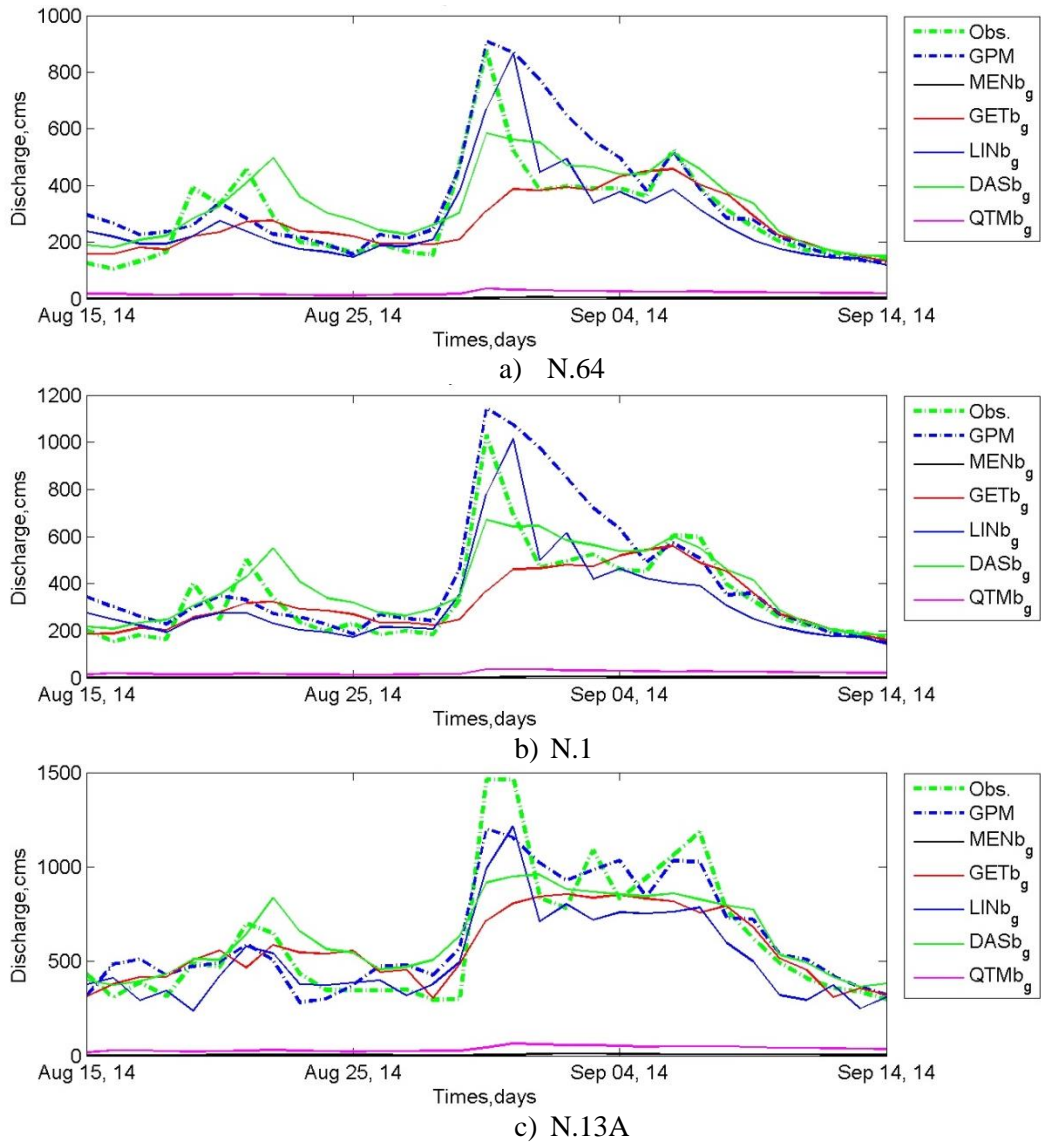
Figure 5-38 Daily discharge hydrograph at runoff observation station of flood event of GPM based on spatial scheme in each method of bias correction

5.5.4 Simulated runoff based on different bias correction products of the TRMM product

The hydrological model (RRI model) was driven by TRMM correction products of two schemes and five techniques, using the similar hydrologic parameters, topography and land cover. The TRMM bias corrected simulation was modeled at daily on a temporal scale to match the Royal Irrigation Department Thailand observed streamflow data. Three runoff stations were selected in the Nan river basin (see **Figure 3-26**), the first one belonging to the upstream sub-catchment (N.64), the second one belonging to the middle area (N.1) and the third one belonging to the downstream area (N.13A), to show the daily hydrograph that results from the different techniques and schemes. **Figure 5-39** and **5-40** present the hydrographs for all bias techniques and scheme of respectively runoff station N64, N.1 and N.13A.

All the modeled runoff driven by different technique and scheme was to provide the temporal pattern similar to the observed hydrograph. Over view all the runoff station for the temporal scheme, Data assimilation symmetrically captured the peak and pattern to same with the observation, while the four products, Mean ratio, Geometrics, Linear, and Quantile mapping, symmetrically stilled underestimation with a different. All products systematically underestimated observed runoff in three stations. The simulated streamflow of the spatial scheme provided the similar temporal pattern with observed hydrograph on the Geometrics, Linear, and Data assimilation. All products were significantly underestimation, and two products, Mean ratio and Quantile mapping, were stilled more underestimation along the time scale. The Data assimilation could capture the peak with underestimation.

All of three runoff station on the daily hydrograph were analyzed and calculated for evaluation by the performance statistical. The results are given in **Table 5-20** that is concluded by five indexes. Data assimilation simulated discharge on best matched the observed runoff with the highest r of 0.855 and lowest RMSE of 148.3 cms for the temporal scheme. This simulated runoff underestimated the lowest runoff volume, peak flow and mean runoff. Geometrics simulated runoff was high r and low RMSE, however, its simulated runoff was also underestimation of Volume bias, Mean bias, and peak flow. Geometrics, Mean ratio, and Quantile mapping runoff significantly underestimated the runoff volume, mean runoff, and peak flow, with high RMSE and weak correlation value.

For the spatial scheme based on the **Table 5-20**, flow simulated from Data assimilation technique matched perfectly with underestimation based on the lowest of Volume bias, Peak bias and Mean bias. The technique provided the low RMSE about 140.69 cms and highest correction about 0.876. Geometrics runoff underestimated with low runoff volume and mean runoff value, on the underestimation bias of the peak about 37%. Linear results showed the underestimation of runoff

volume, mean runoff, and peak flow. Mean ratio and Quantile mapping resulted on the highest underestimation of runoff volume, peak and mean runoff.

Table 5-20 Performance statistical of runoff from the bias correction scenario products

	Rainfall products	Volume bias, %	Peak bias, %	RMSE, cms	Correlation	Mean bias, cms
	TRMM	**13.27**	**-17.86**	**192.35**	**0.761**	**55.84**
Time series	Mean ratio	-74.45	-83.81	404.80	0.704	-313.39
	Geometrics	-21.70	-34.16	248.60	0.614	-91.32
	Linear	-70.37	-78.97	384.66	0.719	-296.22
	Data assimilation	<u>2.09</u>	**-20.79**	<u>148.29</u>	<u>0.855</u>	<u>8.79</u>
	QQ mapping	-76.00	-84.69	402.61	0.770	-319.91
Spatial	Mean ratio	-99.78	-99.87	506.14	0.542	-419.98
	Geometrics	-6.77	-37.02	163.68	0.829	-28.50
	Linear	-16.48	-45.91	174.82	0.858	-69.36
	Data assimilation	**-0.25**	<u>-23.06</u>	**140.69**	**0.876**	**-1.07**
	QQ mapping	-89.65	-94.32	463.70	0.812	-377.34
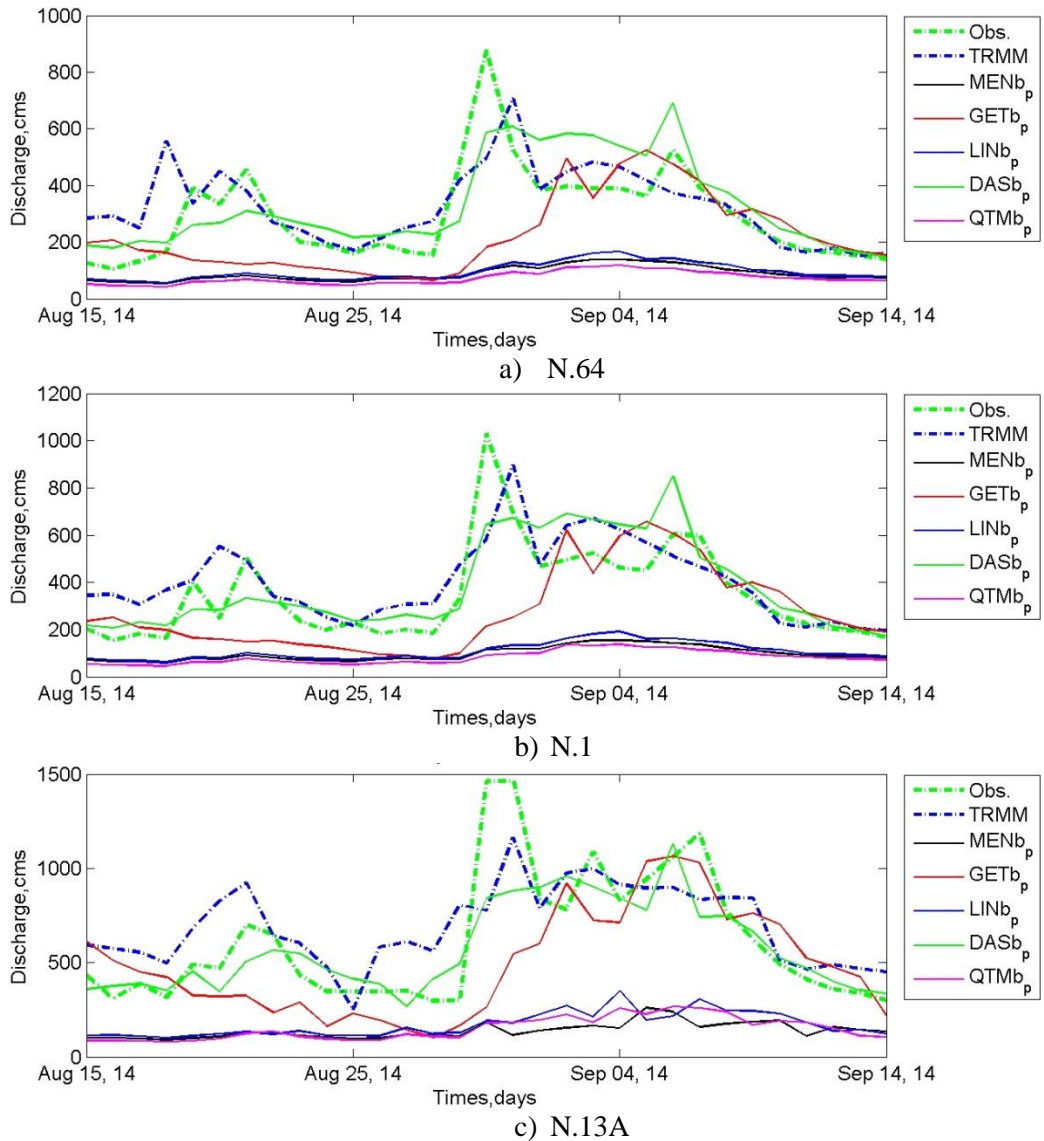
Figure 5-39 Daily discharge hydrograph at runoff observation station of flood event of TRMM based on time series scheme in each method of bias correction

a) N.64

b) N.1

c) N.13A
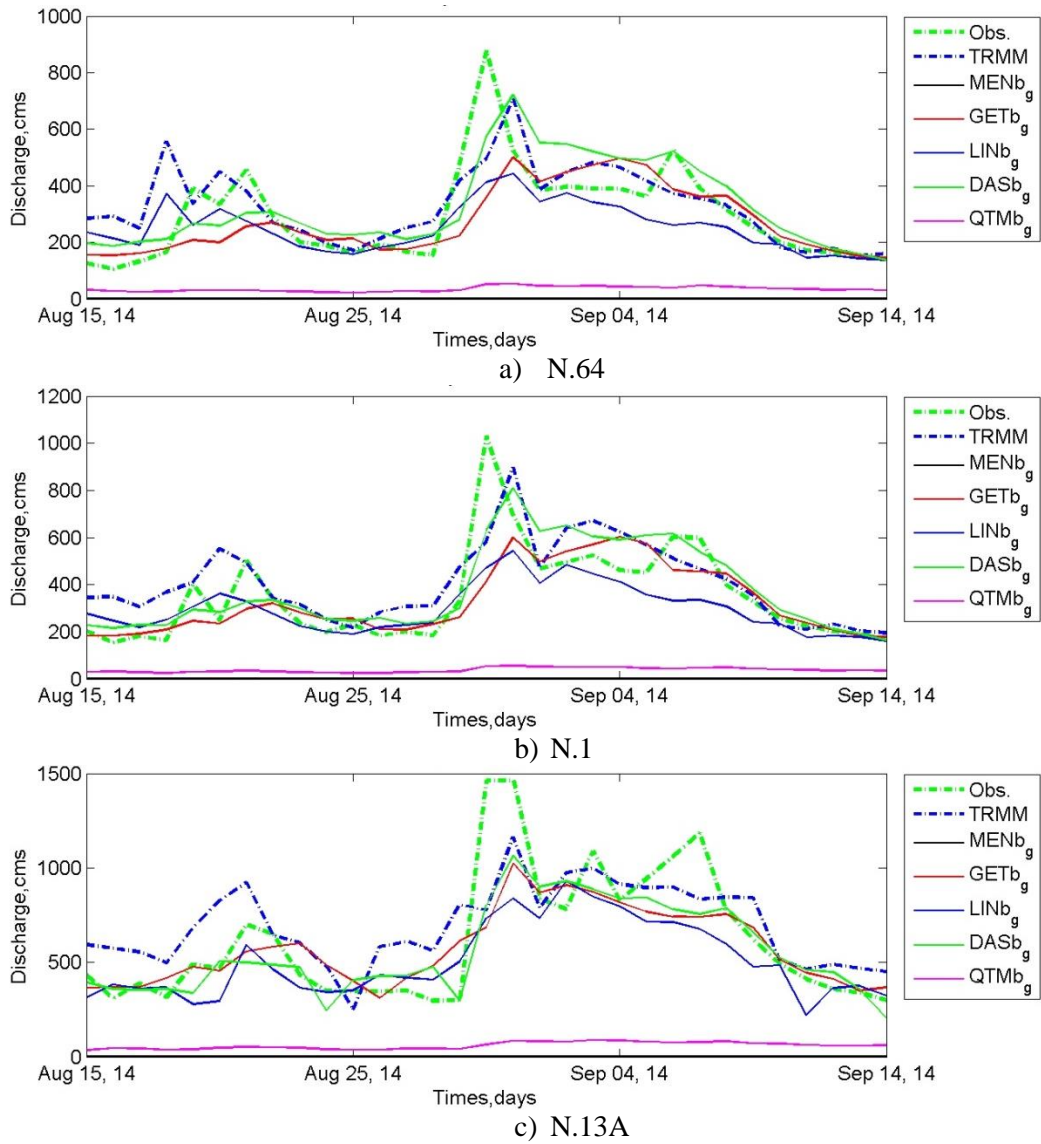
Figure 5-40 Daily discharge hydrograph at runoff observation station of flood event of TRMM based on spatial scheme in each method of bias correction

5.6 Conclusion

The chapter was done by three objectives. Firstly, evaluating effect of spatial interpolation method of rain gauges on runoff estimation is considered. Secondly, validating effect of satellite rainfall is investigated on runoff simulation using hydrological modeling. Thirdly, investigating effect of satellite rainfall bias correction is evaluated in five algorithms and two schemes.

The first study present that at specific storm events the spatial variability of rainfall has a main effect on discharge of the river basin area. The spatial distribution of rainfall is important parameter to improve the water budget volume in the river basin supporting a dynamic interaction for generating flow processes that is generally hydrological behavior reported by Obled et al. (1994).

The evaluation of five rainfall interpolation methods (IDW, TSP, SKG, OKG and SPL) was input to the physical-based hydrological model (RRI model) over the Shikoku Island Japan and the Nan river basin Thailand. According to the aim of this study used the typhoon season in 2010 for the Shikoku and the June 2011 and August 2014 storm event from the Nan River to estimate the streamflow for evaluating the performance of each interpolation methods. The simulation of the streamflow was done by using without a calibration of the hydrologic parameter to specific interpolation product. The streamflow were simulated and reported at hourly and daily to match with the observed runoff.

The total average rainfall in the Shikoku comparison results presented that the IDW products was the best fit to the observed rainfall, however, it underestimation the peak flow. TSP, SKG and OKG were overestimation based on runoff volume, mean runoff and peak, with low RMSE and strong correlation value. By contract, SPL was high underestimation on runoff volume, peak and mean runoff. The both peak events of IDW was underestimation, however it was overestimation for the first event and underestimation for the second event. Among all the spatial interpolation rainfall products, the IDW model presented the best matching with the observed average rainfall. The fact that the IDW could achieve a good performance over the mountainous area might be due to the high dense rain gauge network.

The Nan basin average rainfall comparison results presented that the both kriging, SKG and OKG, products were the best fit to the observed rainfall for both events, however, there underestimation the peak flow. SPL on both events was overestimation based on runoff volume and mean runoff, while its peak was underestimation, with low RMSE and strong correlation value. By contract, TSP was high underestimation on runoff volume, peak and mean runoff. The both peak events of IDW was underestimation, however it was overestimation for the first event and underestimation for the second event. Among all the spatial interpolation rainfall products, the kriging method estimated with the semi-variogram model presented the best matching with the observed basin average rainfall. The

investigation agrees with results from other researches (Tabios and Salas, 1985; Ly et al., 2011; Ly et al., 2013).

IDW demonstrated to be the best algorithm interpolating a spatial of rain gauge to model a streamflow for typhoon season in 2014 on the Shikoku. The simulated runoff of SKG and OKG also closed to the observed data sets; however, it overestimated the runoff volume and mean runoff during the event. TSP and SPL overestimation the runoff volumes and mean runoff, while their peak were underestimation. TSP was the highest overestimation of runoff volume and mean runoff, with high performance of peak flow. In conclusion, the IDW model was the best interpolation method for hydrological modeling to estimate the runoff on the Shikoku area that represented with the high density rain gauge area.

SKG demonstrated to be the best algorithm interpolating a spatial of rain gauge to model a streamflow for June 2011 and August 2014 of the Nan river basin. The simulated runoff of OKG also closed to the observed data sets; however, it overestimated the runoff volume and mean runoff during the second event. SPL and IDW overestimation the runoff volumes and mean runoff, while their peak were underestimation. TSP was the highest underestimation of runoff volume, peak and mean runoff, with high RMSE and weak correlation value. In conclusion, the SKG simulated by the semi-variogram was the best interpolation method for hydrological modeling to estimate the runoff on the Nan river basin with sparse rain gauge network.

This study applies a hydrological model to analyze the spatial variable rainfall on river basin response. It can be done when the model reproduces the true watershed response. As mentioned for this study, the effects are depended on the rainfall spatio-temporal variation and the hydrological characteristics of the river basin. Actually, their space and time correlate in rainfall variability. According to the space-time correlation on the basin response, the temporal distribution is higher sensibility than the spatial distribution of the rainfall data (Krajewski et al., 1991). This study presents the spatial rainfall variability that is one objective to predict runoff on the hydrological modeling of the river basin watershed.

On the second objective, the evaluation of seven rainfall products (Rain gauge, GPM, GSMaP, GPV, TRMM, CMORPH and PERSIANN) was input to the physical-based hydrological model (RRI model) over the study areas. According to the aim of this study used the flood event for estimating the streamflow to evaluate the performance of each product. The simulation of the streamflow was done by using without a calibration of the hydrologic parameter to specific product. The streamflow were simulated and reported at hourly and daily to match with the observed runoff.

Satellite-based rainfall product average whole in the Shikoku area a comparison results in worldwide data sets presented that the GPM, products were the best fit with Volume, peak and Mean bias to the observed rainfall, however, there were underestimation. The results of well performance are not agreement with the other studies (Dinku et al., 2008, Vera et al., 2012, and Zeweldi et al., 2011). GSMaP presented the lowest value of the RMSE and highest correction value that indicated the best degree of estimates different from the observation. TRMM, CMORPH and PERSIANN were underestimation on the peak, volume and mean bias. For combining the Japan data sets, GPV showed the highest performance.

The average satellite-based rainfall product whole watershed (the Nan river basin) a comparison results presented that the CMORPH products were the best fit with Volume and Mean bias to the observed rainfall, however, there underestimation the peak flow. The results of well performance on the CMORPH agree with the other studies (Dinku et al., 2008, Vera et al., 2012, and Zeweldi et al., 2011). TRMM was overestimation the peak bias; however, it was the best performance of peak flow. GSMaP presented the lowest value of the RMSE that indicated the best degree of estimates different from the observation. GPM indicated the best degree of the linear relationship between estimation and observation with the Correlation measures.

GPM verified to be the best satellite rainfall product to simulate a streamflow for flood event on 2014 in the Shikoku Island with lowest volume and mean bias that results agrees with the previous study (Tang et al., 2016). The simulated runoff of GSMaP also closed to the observed dataset to validate with peak, RMSE and correlation; however, it was underestimated on the runoff volume and mean runoff. The peak flow of the GSMaP was underestimation. TRMM was also underestimation the runoff volumes, mean runoff, and peak flow. CMORPH and PERSIANN were the highest underestimation of runoff volume, peak and mean runoff, with high RMSE and weak correlation value. In conclusion, the GPM and GSMaP simulated was the best performance satellite product for hydrological modeling to estimate the runoff on the river basin scale, representing with the high resolution products. However, the TRMM was the best among the course resolution products. GPV was the highest performance to consider in the worldwide and Japan data.

GPM demonstrated to be the best satellite-based rainfall product to model a streamflow for flood event on 2014 in the Nan river basin. The result of the GPM agrees with the previous study (Tang et al., 2016). The simulated runoff of TRMM also closed to the observed dataset; however, it overestimated the runoff volume and mean runoff. The peak flow of the TRMM was underestimation. GSMaP and CMORPH underestimation the runoff volumes, mean runoff, and peak flow. PERSIANN was the highest underestimation of runoff volume, peak and mean runoff, with high RMSE and weak correlation value. In conclusion, the GPM simulated was the best performance satellite product for hydrological modeling to estimate the runoff on the river basin scale, representing with the high

resolution products. However, the TRMM was the best among the course resolution products, for the Nan river basin.

Satellite-based rainfall products, can capture the overall rainfall pattern, are alternative for implementation in the remote area such as the ungauged basins. Among five satellite-based rainfall products, GPM and TRMM have potential to produce a simulated streamflow on the hydrological modeling. The satellite-based rainfall products might be needed correction methods before application as input to the hydrological modeling. More studies on the correction of the satellite-based rainfall products are in the other researches (Habib et al., 2014; Muller and Thompson, 2013; Vernimmen et al, 2012).

Different researches have investigated that satellite rainfall products are contained by systematic and random error. Therefore, the challenge is how the products can be make more accuracy for previous propose. This third objective of the study assessed the effect of precipitation bias correction in GPM and TRMM represented by high and coarse resolution, respectively, on the performance of distributed hydrological model (RRI model). In this study, the point is assessed in the temporal and spatial aspects of both satellite data, GPM and TRMM, bias for the hydrological modeling in watersheds. The finding of this study can contribute to affect that key of increasing the application of satellite rainfall products in the real world. The study in Nan river basin Thailand can benefit from satellite rainfall products for monitoring and assessing resource. Conclusions of bias correction study are summarized below.

GPM has rainfall bias in overestimation about 1.54 mm in average over the watershed area, while TRMM overestimate about 4.5 mm. The bias could be affected to precipitation generation processes, sampling and error of satellite data (Gebremichael and Krajewski, 2004). A cross variation is presented from combination application of rain gauge and satellite data.

The evaluation of five correction techniques (Mean ratio, Geometrics transformation, Linear transformation, Data assimilation and Quantile mapping) combined with two schemes (temporal and spatial) was input to the physical-based hydrological model (RRI model) over the study areas. According to the aim of this study used the flood event for estimating the streamflow to evaluate the performance of each product. The simulation of the streamflow was done by using without a calibration of the hydrologic parameter to specific product. The streamflow were simulated and reported at daily to match with the observed runoff.

Data assimilation technique in the temporal scheme could reduce the bias of GPM about -96% on the mean bias, while TRMM bias correction with Geometrics transformation on the temporal scheme increased an accuracy about 97% on the mean bias. The significant achievement of results presented

that the key aspect of the GPM and TRMM bias is their temporal scale as accounting for it substantially increased the accuracy of rainfall bias. It had some instances that were not possible to increase the accuracy on the watershed average bias. The rain gauge specifically in the northern parts of the watershed is not to match between the satellite bias correction and rain gauge data.

RRI model could capture a better runoff hydrograph in volume and pattern when satellite bias correction data sets were utilized instead of the exiting satellite data. The analysis of simulation results indicated that small rainfall error generated a larger error effect on runoff simulation in average. The satellite bias correction results outperformed the existing satellite on magnitudes of error evaluated from five statistical indexes. From the performance analysis, +16.94% bias of GPM rainfall data is generated to +10.6% of runoff bias, while TRMM rainfall bias about +13.27% is simulated to runoff bias about +49.21%. For the bias correction products, the bias error was reduced that from -3.85% rainfall biases transferred to -6.87% runoff biases in the GPM data, and TRMM data rainfall bias about 2.77% generated runoff bias about -0.25%. The recommendation of bias correction technique is Data assimilation technique for merging data when their have a rain gauge data sets to supervise the data product, while an unsupervised method is Geometrics and Linear transformation. The unsupervised have a limitation due to its parameter can be used in some specific time. When comparing on temporal and spatial scheme bias corrections were used to the GPM and TRMM rainfall input, accounting for the spatial scheme of both satellite bias have the largest effect on hydrological model simulation and should be taken into account. The error of modeling is not depended only on the rainfall input, but also on the effect of topography and land cover data sets. Future studies should assess comparative advantage of complex algorithm in mathematics of bias correction techniques, and application in a radar rainfall study.

Chapter 6 Application of flood simulation[.]

This chapter contains an objective with two main approaches: flood forecasting and flood risk assessment. The flood forecasting implements in river basin scale as coarse resolution result and related to small area as high resolution result. For the flood risk assessment, economic data sets related to land cover data are collected to estimate the vulnerability of the simulated small area that are overlaid with the flood simulation results of the small area as well as the flood hard map.

6.1 Flood forecasting

6.1.1 Introduction

Floods are one kind of natural disasters causing human life and economic losses. Approximately about 66% of water related disasters in the world are floods (WWC, 2000). Nowadays, impacts of floods have been increased because of population growth, decreasing of floods plain, and climate change. Mitigation impacts of floods are implementation of structural and non-structural scheme (Bedient et al., 2008; USEOP, 1994). The major tools firstly used for planning and developing structural and non-structural flood mitigation and management approaches are Hydrologic and hydraulic models (Jin and Fread, 1997; Hokr et al., 2003). Mathematic models of floods have been established from peak flow estimation schemes with multi dimension, multi-scale distributed simulations able of demonstrating the spatial and temporal variation of floods runoff over a river basin surface (Singh and Woolhiser, 2002).

Mathematics model of flood based on hydrological processes have been used for more than thirty years ago and it is a powerful tool for water resources management (Crawford and Linslay 1966; Liang and Smith 2015). The model is developed on accuracy with a complexity of the hydrological mechanism on the computational using a governing equation with continuity and momentum (Zhang and Cundy 1989; Tayfur et al. 1993; Lamb et al. 2009; Kalyanapu et al. 2011). It has 2 tasks in a traditional for flood simulation, Rainfall-Runoff model on a terrain and flow routing model in a river channel. Most of the modern mathematics model of Rainfall-Runoff model is based on a physical-based of hydrological processes represented by using the spatial heterogeneity on a continuous grid cell system.

Physical hydrologic models are well known in the distributed hydrologic modeling as a 2D model, their mathematical intensity and complexity remain point of limitation factor for modeling specialists. The 2D hydrologic models involve time to complete in a limitation of computer technology that potentially prevents their implementation to meet simulating time constraints. Different flood simulation objectives demand different principal time, time period of flood area scale simulation, as shown in **Figure 6-1**. Normally, the significant estimation intensity of a flood model accrues with level of detail and differentiation time need for a specific flood management scale. From the Figure 6-1, flood risk assessment modeling time that results must be an hourly, which might be applied as bottom-up scheme of water resources management. For the flood plain management, the average simulation time is resulted as daily data, which the activity is a top-down scheme. However, the current trend towards the integrate management in of river basin, the linkage between basin area and local area is key point in sustainable development.

The objective of this topic in the dissertation is to assess flood forecasting in the small area related to the river basin scale. The study area is the case of the Nan river basin and Yoshino river basin. The specific objective for the Nan uses the natural flood event, while the Yoshino uses the scenario based on the breaking dike.
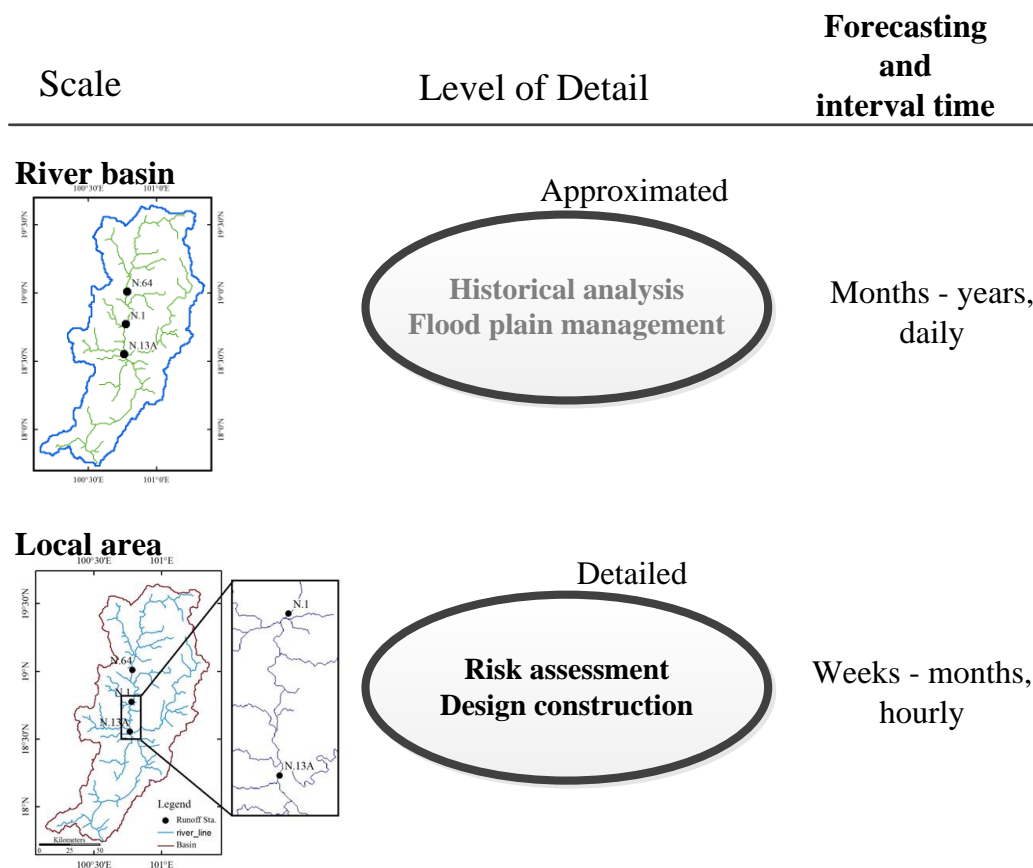
Figure 6-1 Forecasting duration and interval time step for different flood simulation tasks
(adopt from Kalyanapu, 2011)

6.1.2 Methodology

Flood simulation on the basin area is first run, which is identified as boundary condition of small area. The steam flow as shown in **Figure 6-2** that is the flow chart of the linkage between basin area and small area. As the first run, watersheds and rainfall data is input into the RRI model, their outputs have performed an accuracy assessment with observation discharge at runoff station, using five performance statistical coefficients. Based on the performance of river basin modeling, the results are captured by boundary of small area. In this study, the boundary is identified as point in the main and tributary river. For inputting the boundary data set, upstream condition is the flow data, while the downstream is the water level data to control the flood mechanism in the small area simulation. The performance of small area results is assumed as same as the large area model.
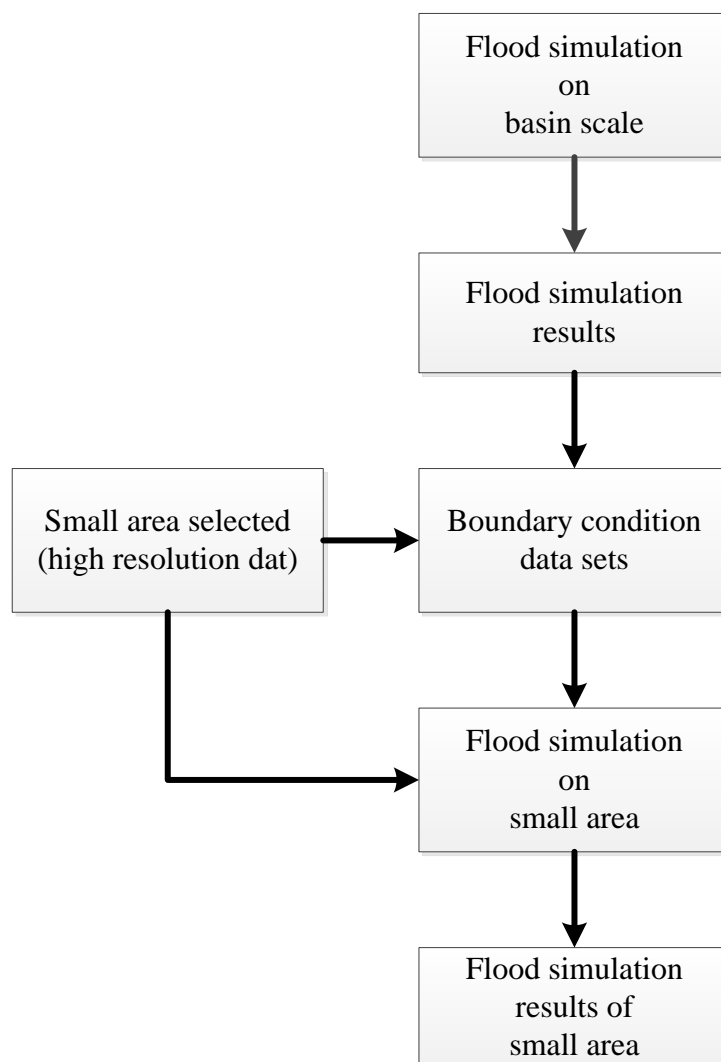
Figure 6-2 Stream flow of flood forecasting in a small area, using boundary condition data sets from basin simulation results

6.1.3 Case study on small area flood forecasting using boundary condition from basin flood simulation data on natural extreme flood in the Nan river basin, Thailand

Upper part of Nan River Basin or upper part of SIRIKIT dam is important area because release of the SIRIKIT dam have been supplied for the central plain of Thailand, including Bangkok area. The selected area for small area simulation shows in **Figure 6-4**, is in the middle of the Nan river basin, the area cover the urban area in the Nan province. For first run in basin area, the June 2011 storm events were implemented that are used to run the RRI model over the basin as a demonstration. From 24th to 30th June 2011, tropical storm the Haima hit the northern part Thailand to bring precipitation as 200 mm in the upstream of study area over two days. From the rain gauge station, there are 28 stations as shown in **Figure 6-5b**, were used to construct the rainfall spatial distribution by using inverse distance weight. Input data sets of the RRI model are four data types; rainfall data, topography (see **Figure 6-5a**), land cover and soil type (see **Figure 6-5c and 6-5d**). On the definition of the distributed hydrologic model with the RRI model, the used hydrologic parameters in this study are recommended by previous study. **Table 6-1** show the Manning's roughness of the land covers type based on the MODIS data set. Soil parameters represented by the Green-Amp parameter is shown in **Table 6-2**. The hydrologic parameters as shown were utilized to simulate on the RRI model for boundary condition of a small area.
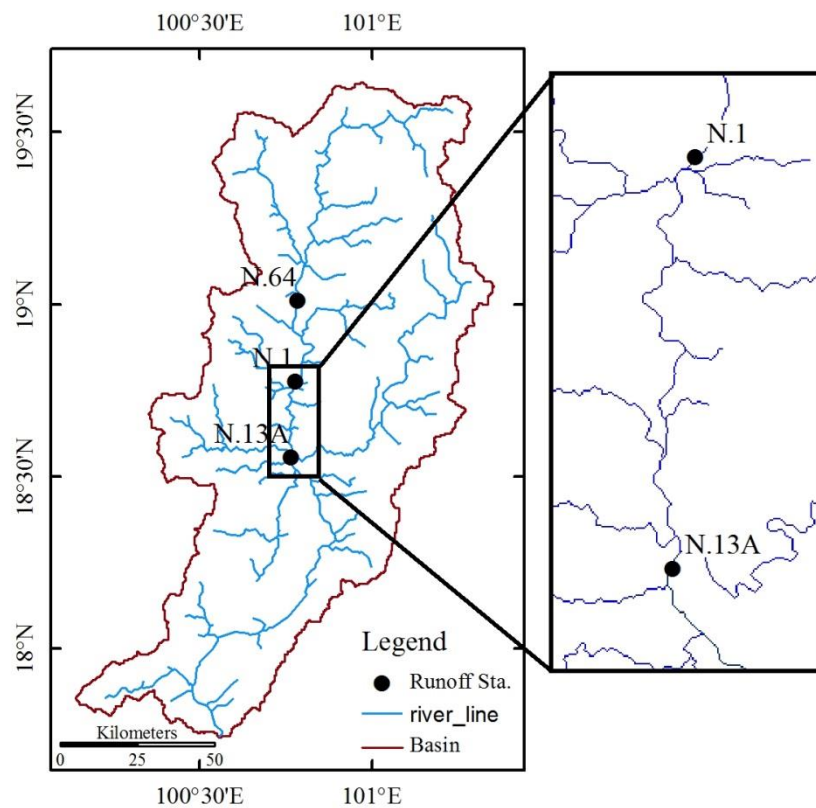
Figure 6-3 Nan river basin and target area for forecasting flood as a high resolution of flood map

a) Topography

b) Rain gauge and Runoff sta.

c) Land cover type

d) Soil textural
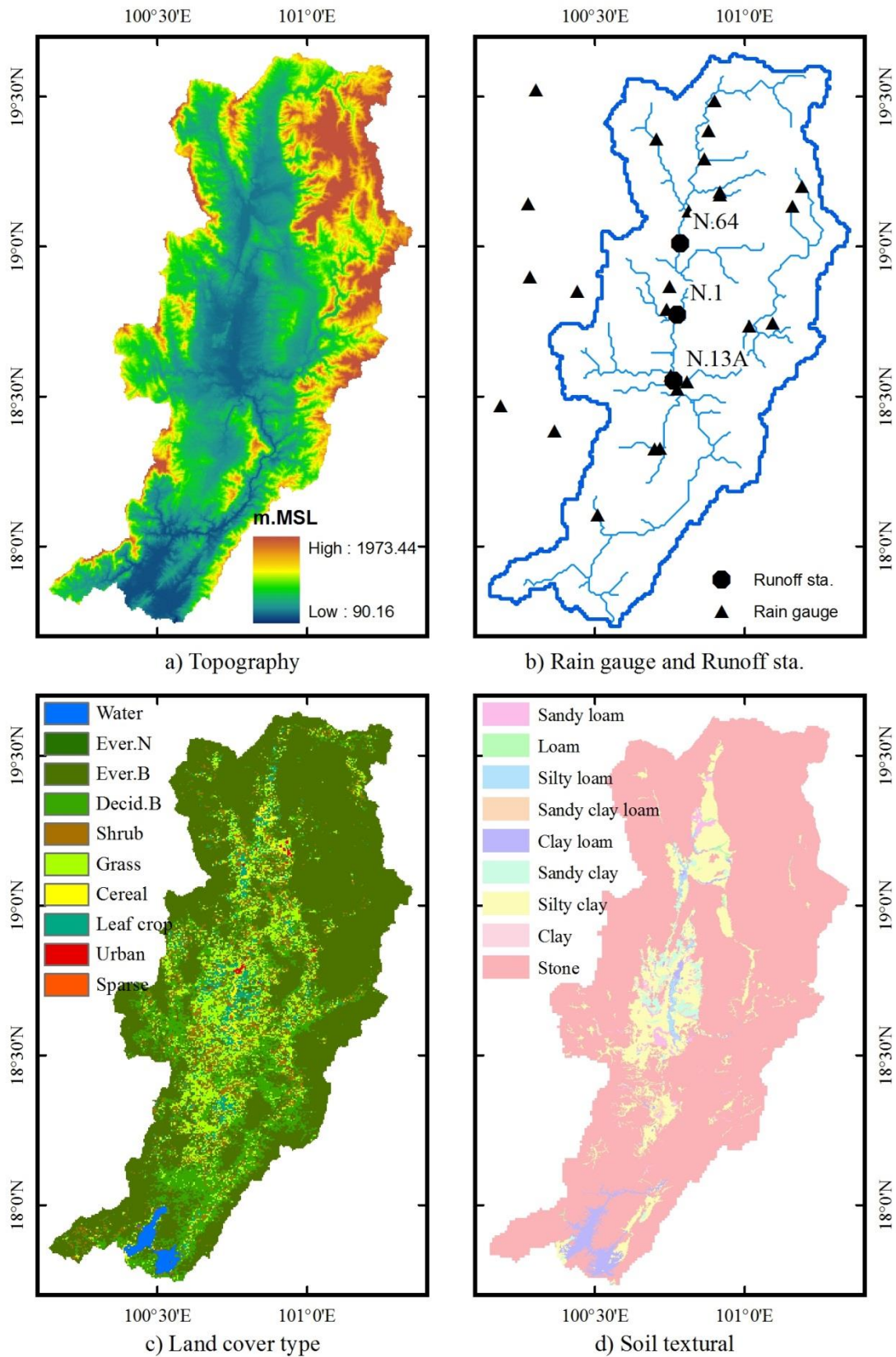
Figure 6-4 Watershed datasets in the Nan river basin, Thailand

Table 6-1 Land cover parameter represented by the n manning coefficient

No	Land cover	Manning's n coefficient
1	Evergreen Needle leaf forest	0.40
2	Evergreen Broadleaf forest	0.60
3	Deciduous Broadleaf forest	0.80
4	Shrub	0.40
5	Grass	0.30
6	Croplands	0.35
7	Broad-left crops	0.30
8	Urban and build-up	0.05
9	sparsely vegetation	0.10
10	Water bodies	0.05

Table 6-2 Soil type parameter represented by the Green-Amp coefficient

Soil textural	Soil depth, m	Saturated hydraulic conductivity (ka), cm/h	Green-Ampt parameter		
			K_{sv}, cm/h	Porosity	Capillary head, cm
Clay	1.0	0.462	0.06	0.475	31.63
Clay loam	1.0	0.882	0.20	0.464	20.88
Loam	1.0	2.500	1.32	0.463	8.89
Sandy clay	2.0	0.781	0.12	0.430	23.90
Sandy clay loam	1.5	2.272	0.30	0.398	21.85
Sandy loam	1.5	12.443	2.18	0.453	11.01
Silty clay	1.0	0.366	0.10	0.430	29.22
Silty loam	1.0	2.591	0.68	0.501	16.68
Stone	1.5	-	-	-	-

The hydrological model (RRI model) was driven for June 2011 storm events. The results were estimated at hourly and accumulating as daily on a temporal scale to match the Royal Irrigation Department Thailand observed streamflow data. Three runoff stations were selected in the Nan river basin (**Figure 6-5b**), **Figure 6-6** present the hydrographs for the first run on the basin area. All of three runoff station on the daily hydrograph were analyzed and calculated for evaluation by the performance statistical. The results are given in **Table 6-3** that is concluded by five indexes. The discharge matched the observed runoff with the r of 0.881 and RMSE of 387.63 cms. This simulated runoff overestimated the runoff volume, peak flow and mean runoff by 19.26%, 22.22% and 139.04 cms, respectively.

Table 6-3 Performance statistics of large area simulation (River basin area) results

Performance statistics	Simulated runoff
Volume bias, %	19.26
Peak bias, %	2.22
RMSE, cms	387.63
Correlation	0.881
Mean bias, cms	139.04
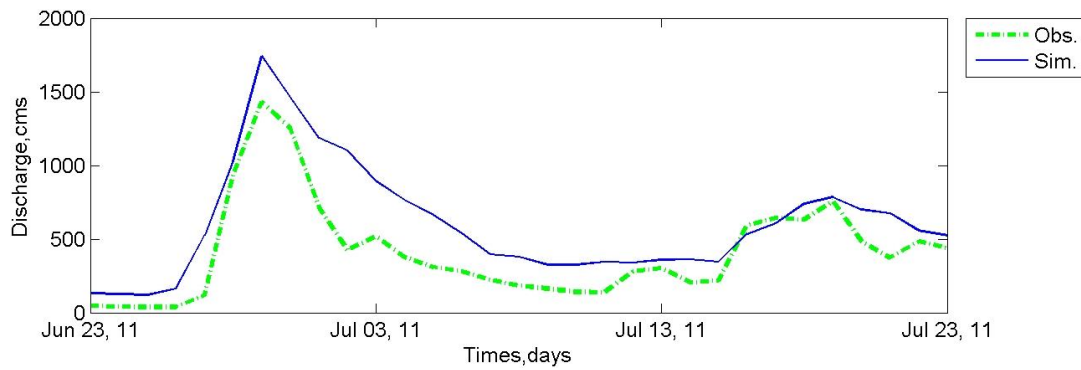
a) N.64
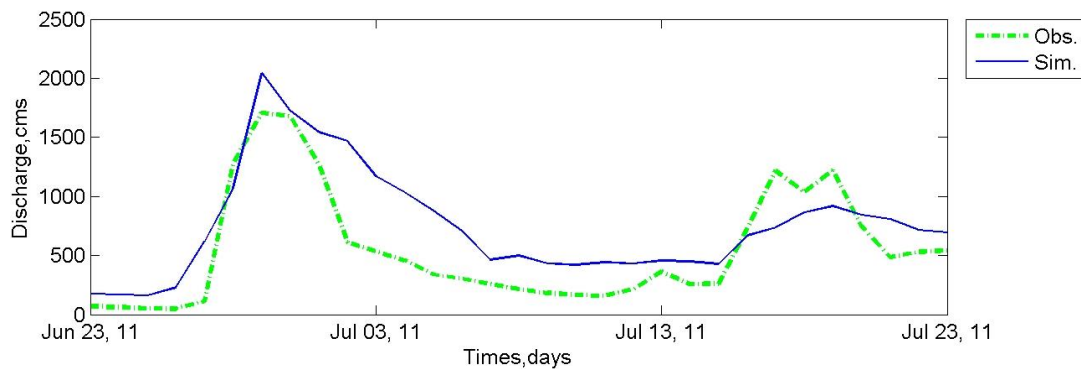
b) N.1
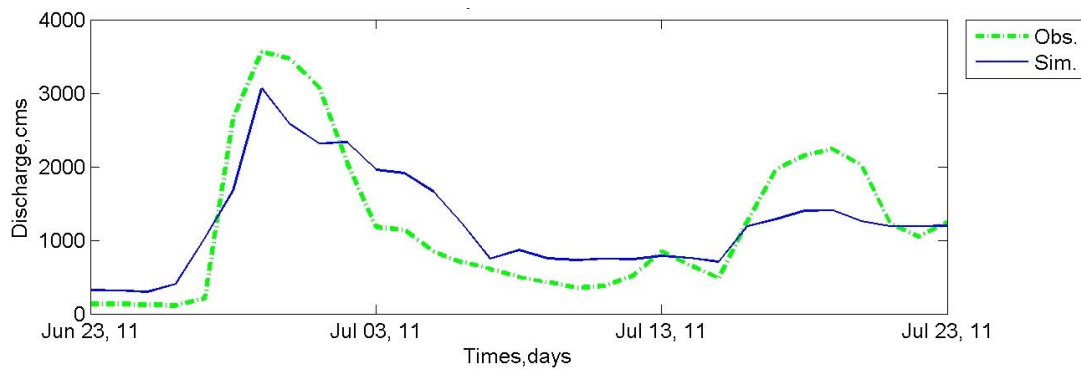
c) N.13A

Figure 6-5 Daily discharge hydrograph at runoff observation station of 2011 storm event

The small area was selected to run during 400 hours for the first peak in **Figure 6-6**, during 15 days beginning at 24 June. **Figure 6-7** presents boundary condition points of the small area that have 7 points. On the main Nan River have two point, inflow (M.In) and outflow (M.out) point, their boundary data of both points is shown in **Figure 6-8a** as inflow and **Figure 6-8b** as outlet water level, on the time series. The lateral inflow is presented by the five points that the temporal data is shown in **Figure 6-9**, Nam Smun (L.1), Nam Sa (L.2), Nam Sakorn (L.3), Nam Hang (L.4), and Nam Wa (L.5). The watershed data are topography (DEM) and land cover that the 90m resolution is used as SRTM DEM. All of data sets such as high resolution DEM and land cover, boundary data, and rainfall during modeling time, are input into the RRI model and resulted on hourly. **Figure 6-10** shows the flood simulation resulted on the inundation map at peak with high resolution product.
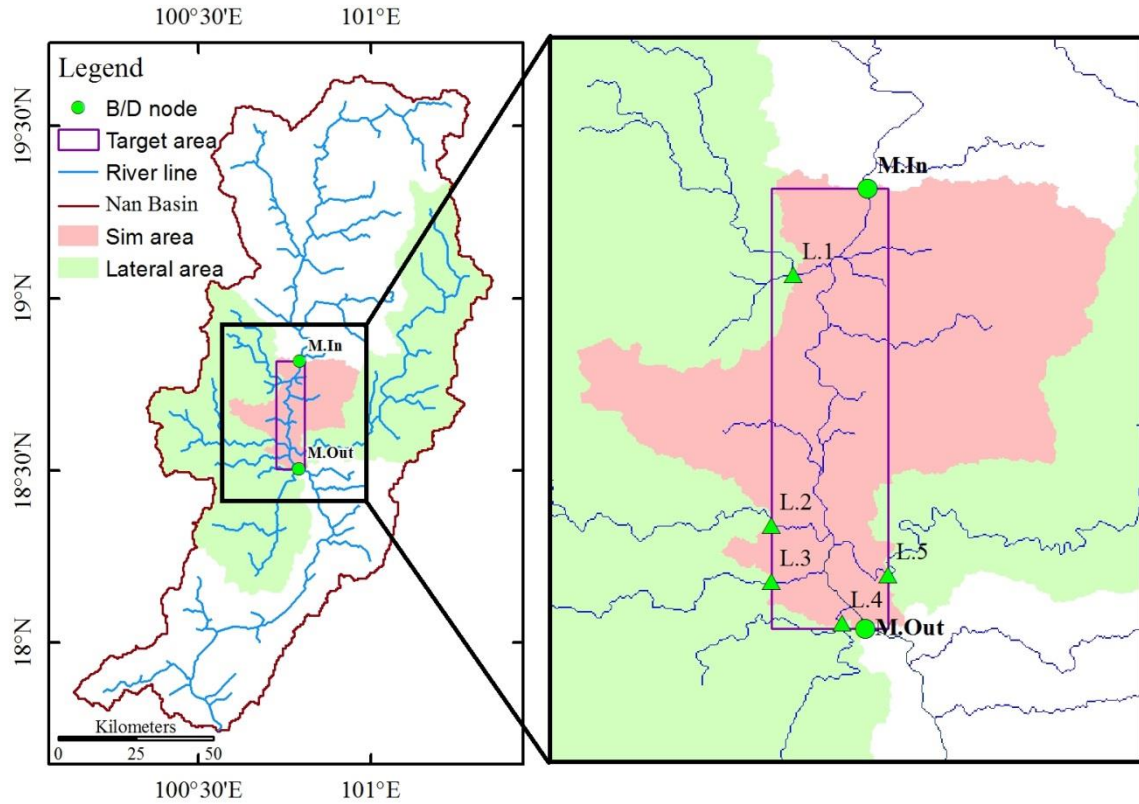
Figure 6-6 Boundary condition points of the simulation area for small target area
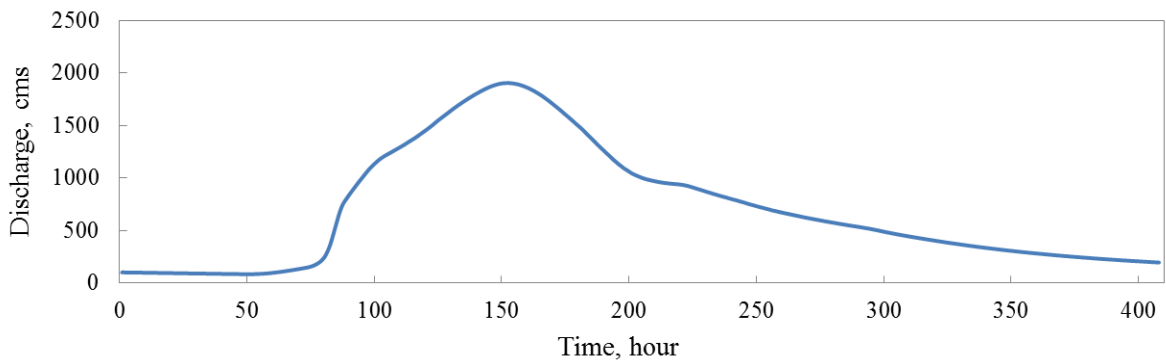
a) Inflow data at inlet point on the main stream (M.In)
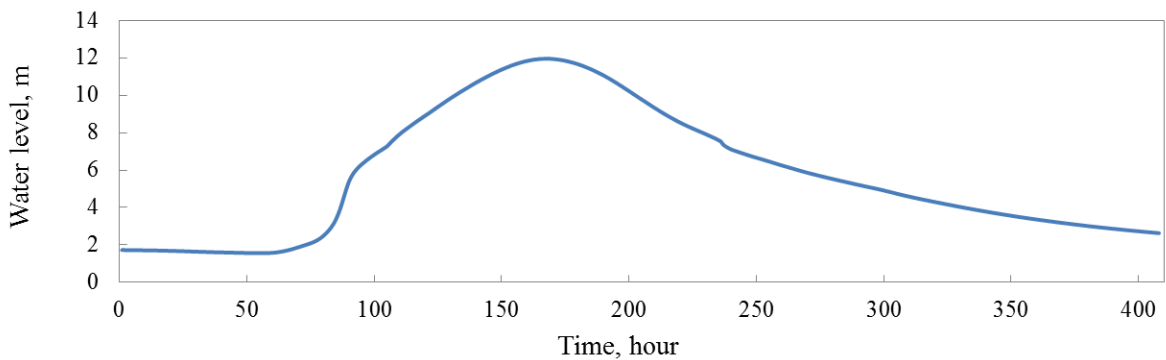
b) Water level data at outlet point on the main stream (M.Out)

Figure 6-7 Boundary condition data sets for the main river, a) Inflow data (M.In) and b) Water level at outlet (M.Out)

a) Inflow of Nam Samuun (L.1)

b) Inflow of Nam Sa (L.2)

c) Inflow of Nam Sakorn (L.3)

d) Inflow of Nam Hang (L.4)

e) Inflow of Nam Wa (L.5)
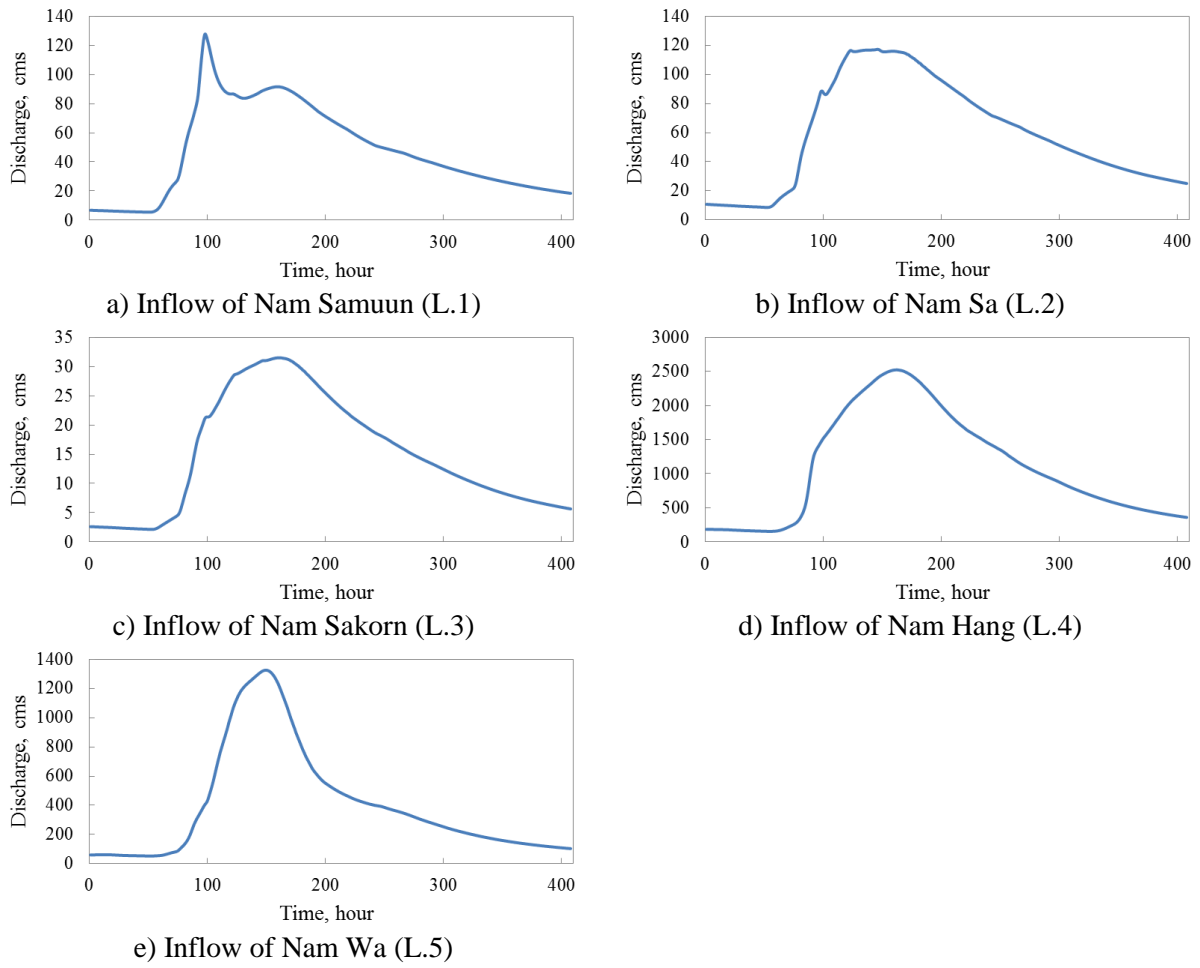
Figure 6-8 Boundary condition data sets for the lateral inflow each sub-basin
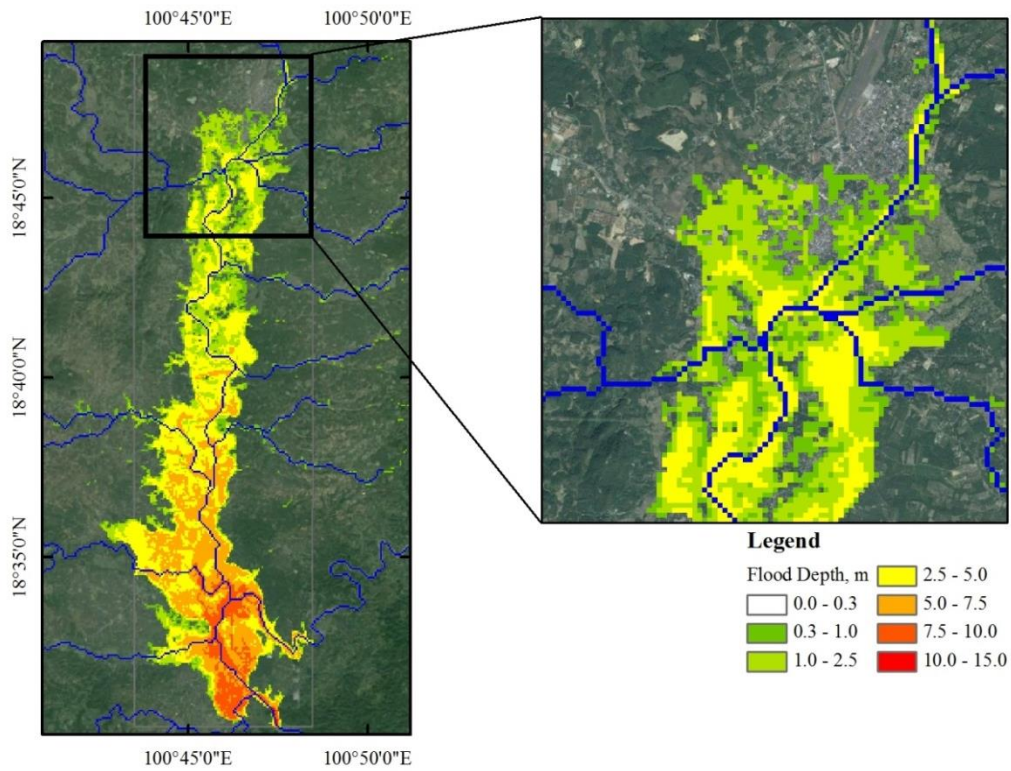
Figure 6-9 Flood depths from the simulations at maximum peak of the event

6.1.4 Case study on the Yoshino River in Shikoku Island, Japan, for flood forecasting with a dike breaking of polder area in Ishii town, Tokushima prefecture

The selected area for small area simulation shows in **Figure 6-11**, is in the eastern part of the Yoshino river basin, the area cover the urban area in the Ishii town in Tokushima prefecture in the Sikoku Island. In this case study, the upstream condition is identified as one point of breaking dike in a middle of simulation area for inputting represented by the water level to capture from the basin simulation. The outlet of small area is assumed by no condition data as well as free flow.

For first run in basin area, the July to October in 2014 rainfall data were implemented that are used to run the RRI model over the basin as a demonstration. Input data sets of the RRI model are four data types; rainfall, topography (see **Figure 6-12a**), land cover (see **Figure 6-12c**) and soil type (see **Figure 6-12d**). On the definition of the distributed hydrologic model with the RRI model, the used hydrologic parameters were mentioned in the chapter 2 such as Manning's roughness of land cover type and Green-Amp parameter of soil type. The spatially pixel of DEM is scaled to 500 m of pixel size (about 15 x 15 arc-second). Addition to the numbers of pixel, row and column numbers is 401 and 650 respectively for the area about 18,000 km^2. The estimation of width and depth were recommended in the equation (4) and (5) in the chapter 2. Rainfall data was collected from the rain gauges (location in **Figure 6-12b**), covering the study area. The rainy season during July to October in 2014 is used to evaluate the runoff for the Shikoku Island.

The estimated results driven by the different topography sources were evaluated to analysis bias of volume (V_{bias}), bias of peak (P_{bias}), Root Mean Square Error ($RMSE$), square of the Pearson correlation coefficient (r), and Mean Error (ME). The following formulas in **Table 2-10** were applied to evaluate simulation performance.

The RRI model was driven for rainy season from July to October in 2014 in the Shikoku Island. The results were estimated at hourly on a temporal scale to match the observed streamflow data. Seven runoff stations were selected in the Shikoku Island as mention in **Figure 6-12b**, the first (Ikeda dam) and second (Chuobashi) belong to the Yoshino River. The third (Furushou) is in the Naka River and the fourth (Fukabuchi) in the downstream area of the Monobe River. The fifth is located in the Ino, belonging to the Noyodo River; the sixth located in the Shimanto River is the Gudoudaini station. The seventh station is the Deai located in the Shigenobu River. All of stations showed in the hourly hydrograph that results from the basin scale modeling. **Figure 6-13** presents the hydrographs with the seven runoff stations.
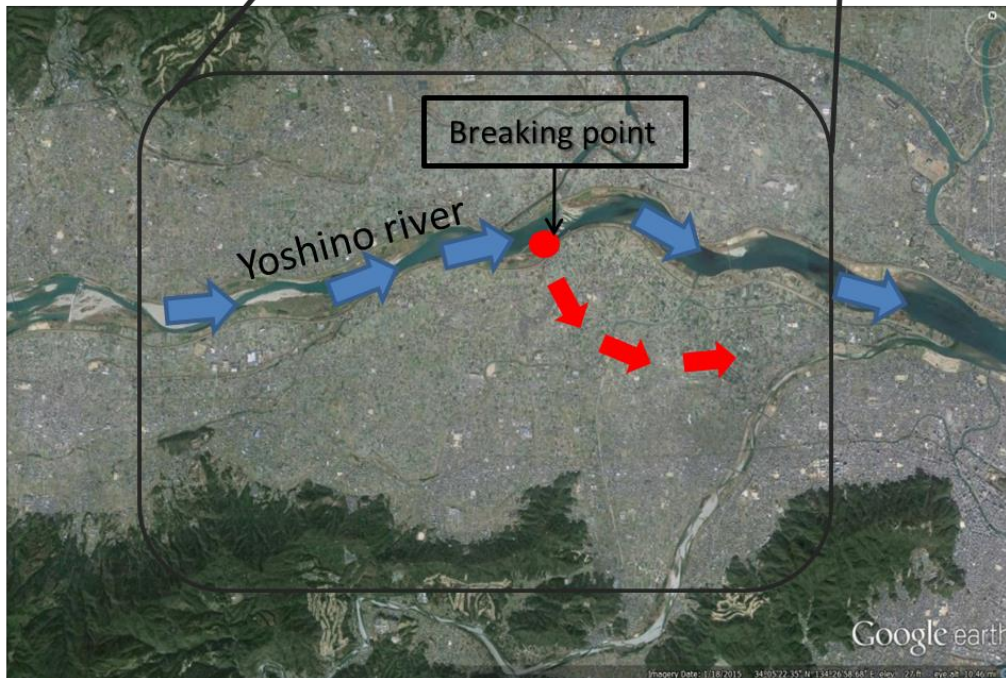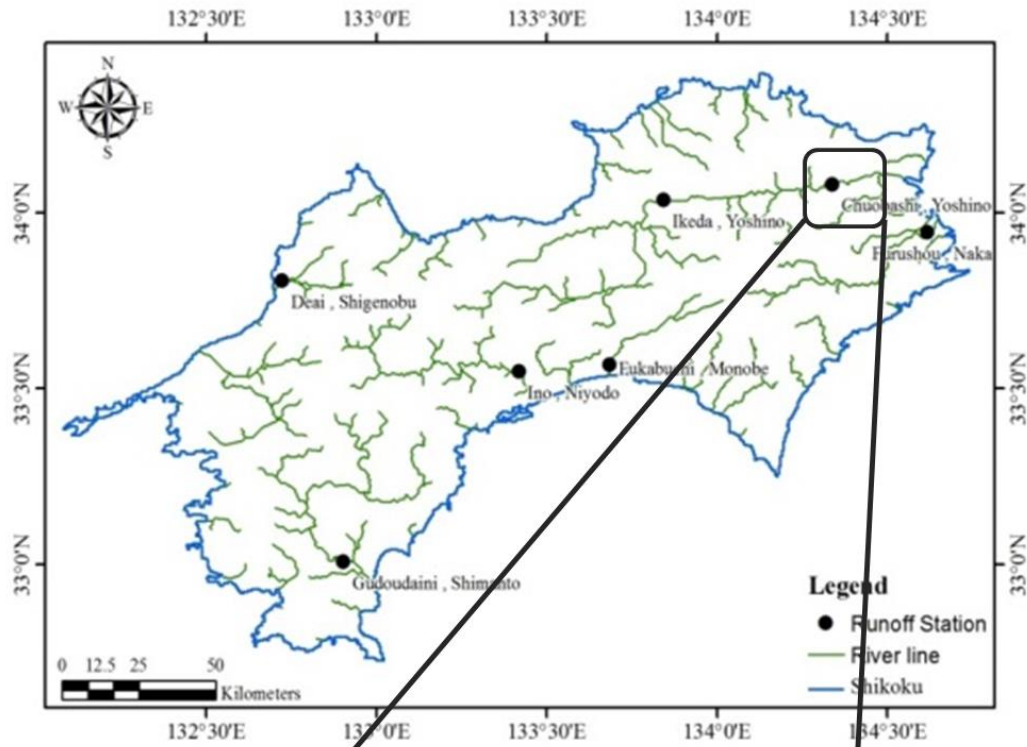
Figure 6-10 Shikoku Island Japan and target area for flood forecasting as a high resolution of flood map on the scenario based by a dike breaking of polder area in Ishii town, Tokushima prefecture, Japan

a) Topography

b) Rain gauge and Runoff sta.

c) Land cover type

d) Soil textural
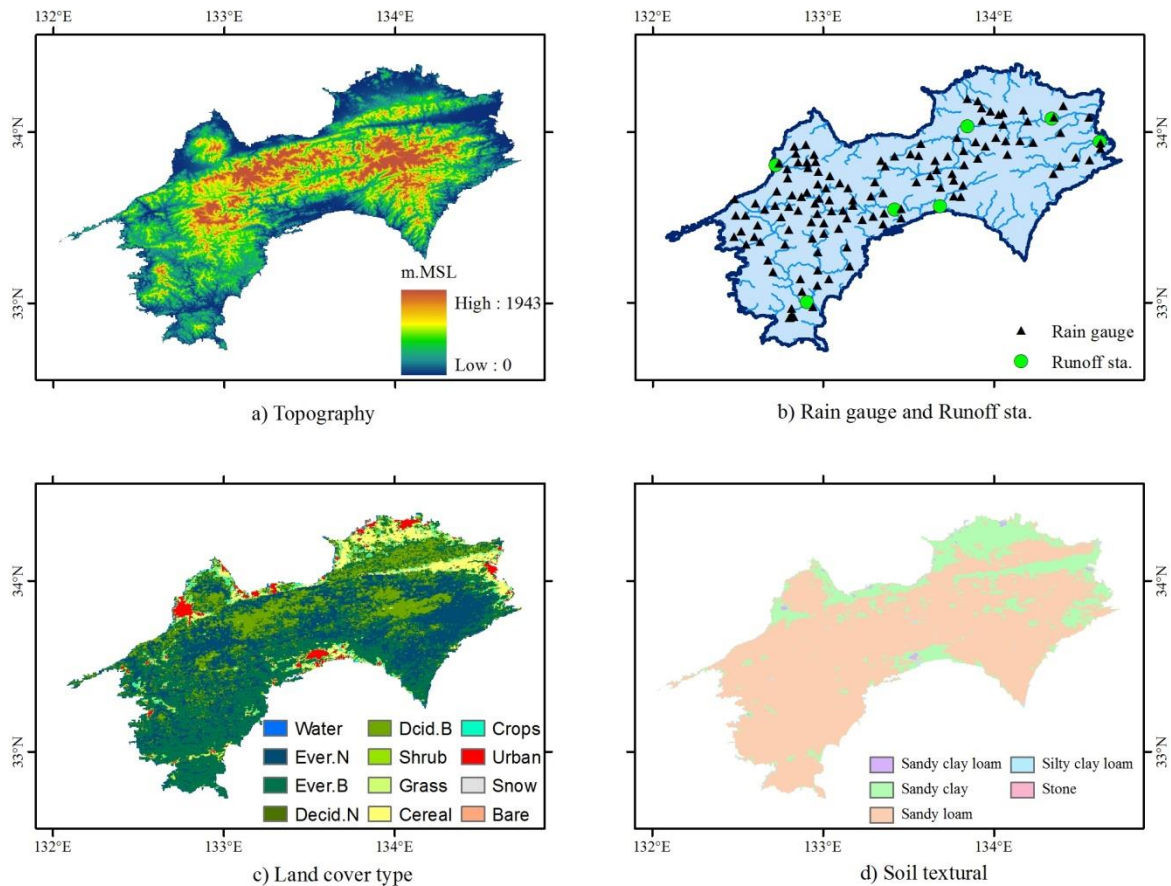
Figure 6-11 Watershed datasets in the Shikoku Island, Japan

All of seven runoff station on the hourly hydrograph were analyzed and calculated for evaluation by the performance statistical. The results are given in **Table 6-4** that is concluded by five indexes. The discharge matched the observed runoff with the r of 0.941 and RMSE of 312.05 cms. This simulated runoff underestimated the runoff volume, peak flow and mean runoff by 2.65%, 32.79% and 7.57 cms, respectively.

The small area was selected to run during 168 hours for the first peak in **Figure 6-3**, during 7 days beginning at 7 July. **Figure 6-14** presents boundary condition points of the small area, the breaking point of dike in polder area. On the simulation, it assumes with no lateral inflow. The watershed data are topography (DEM) and land cover that the 50m resolution is used as GSI-DEM. All of data sets such as high resolution DEM and land cover, boundary data, and rainfall during modeling time, are input into the RRI model and resulted on hourly. **Figure 6-15** shows the flood simulation resulted on the inundation map at 24 hours after breaking of dike with high resolution product.

a) Ikeda, Yoshino river

b) Chuobashi, Yoshino river

c) Furushou, Naka river

d) Fukabuchi, Monobe river

e) Ino, Niyodo river

f) Gudoudaini, Shimanto river

g) Deai, Shigenobu river
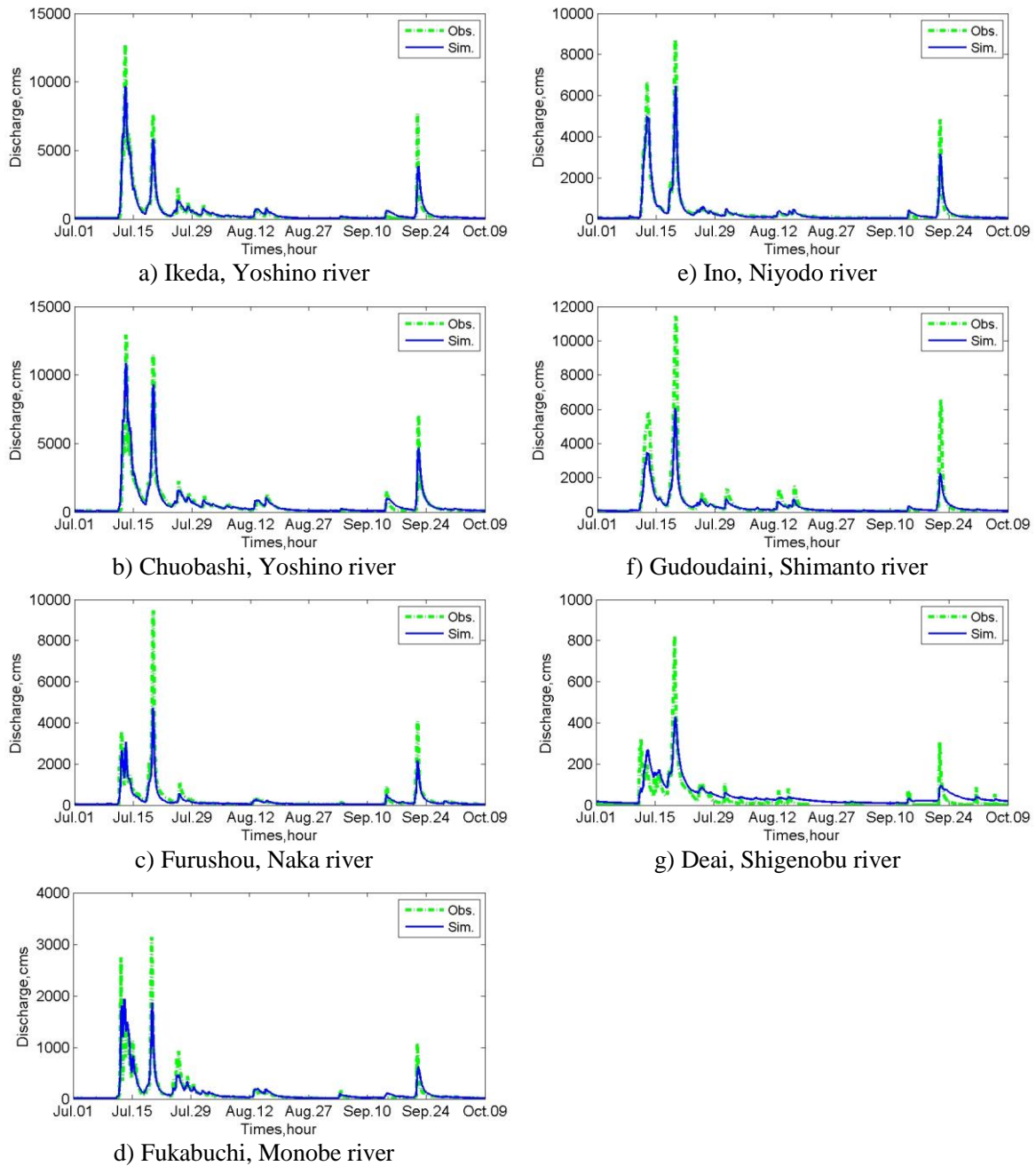
Figure 6-12 Hourly discharge hydrograph at runoff observation station of flood event based on different satellite products in the Shikoku Island Japan

Table 6-4 Performance statistics of large area simulation (River basin area) results

Performance statistics	Simulated runoff
Volume bias, %	-2.65
Peak bias, %	-32.79
RMSE, cms	312.05
Correlation	0.941
Mean bias, cms	-7.57
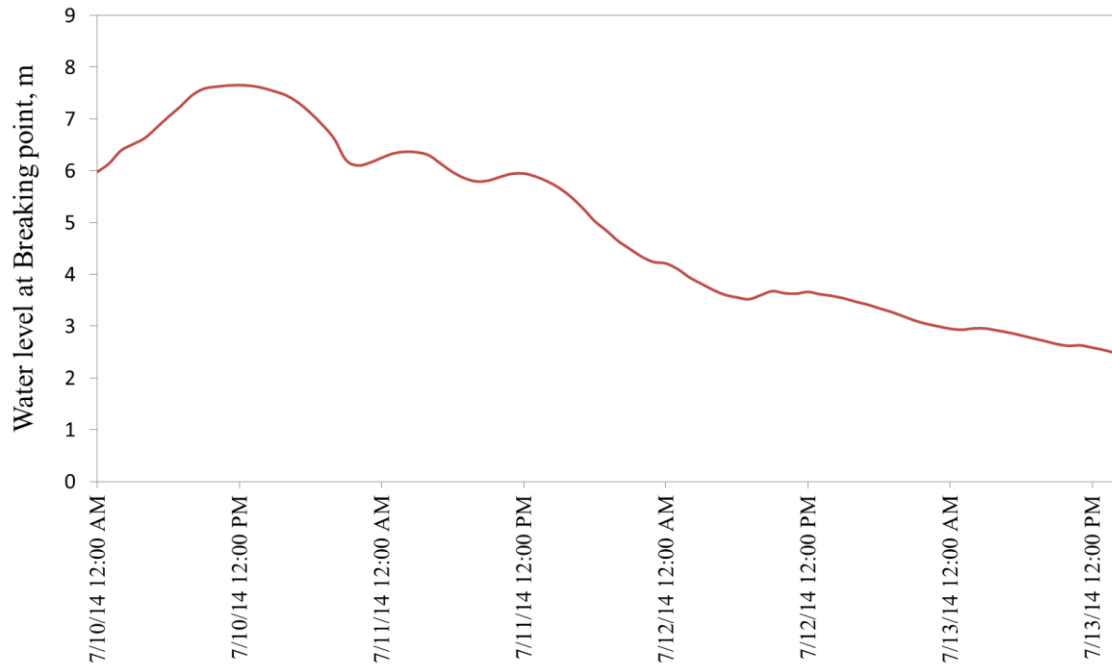
Figure 6-13 Boundary condition data sets for the main river as the water level at breaking point
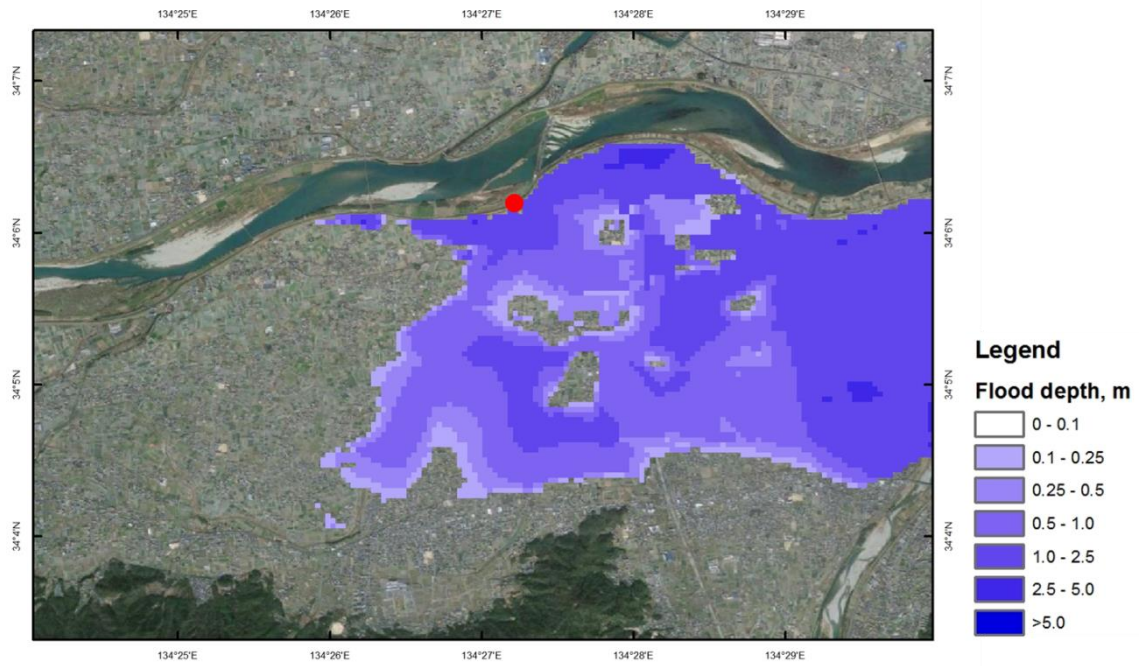
Figure 6-14 Flood depths from the simulations at 24 hours of the scenario, after breaking

212

6.1.5 Conclusion

Flood forecasting in the small area related to the river basin scale was assessed that referred to the linkage between basin area and local area for sustainable development in water resources management. The study area is the case of the Nan river basin and Yoshino river basin. The specific objective for the Nan uses the natural flood event, while the Yoshino uses the scenario based on the breaking dike.

The methodology was done by simulating in the river basin scale at first to identify as the boundary condition of small area to reveal a high resolution results. For the Nan river basin the small area is selected as a flood plain area in a middle of the river basin including the capital area of the Nan province. The event based of this forecasting was the June 2011 storm when Haima monsoon attracted to this area. For the Shikoku Island, the Ishii town in Tokushima prefecture of the Yoshino river basin is selected for demonstration the flood forecasting on a scenario based as a dike breaking. The event based was the storm in July 10th, 2014. The both simulation were resulted in hourly data sets of inundation map. The methodology of simulation in specific area to make more resolution of the results was the point for this approach. These results can be used to classify the hazard level and to identify the flood hazard map, using for flood risk assessment in the next approach.

6.2 Flood risk assessment

6.2.1 Introduction

Floods are ones of disaster causing significant losses of human life and economic. Approximately about 66% of water related disasters in the world are floods (WWC, 2000). In this study, an algorithm able of estimating the flood risk into the economic sector was developed that is the first step for flood management planning. Flood losses in rural areas are litter than those in urban, that their risk assessment is regularly estimated by an assumption approaches (Förster et al., 2008). However, in area of intensive service, manufacturing and agricultural sector, where the economy relies mainly on each sector production, a tool able of estimating risk because flooding is essential.

The suitable flood variable selection is the key point when developing an algorithm to identify the flood risk. The flood variables are significantly depended on the morphological of the modeled area such as topography, slope, or river network. In several studied, flood depths have often used to identify as the main parameter for estimating flood risk (Dutta et al., 2003; Thieken et al., 2008; Pistrika 2010). There are no typical methods to identify flood risk mapping, still, several responding in hazard map and total risk summary in the large region.

In this study, the flood risk map product due to a natural river flood and scenario flood event was assessed. Synthetic risk assessment model was created, relating flood depth as flood hazard level and economic cost as vulnerability classes. A rational method was adopted for the flood hazard level identification based on the characteristic of economic sector activity. For the vulnerability category, the intersection between land cover and economic data (GDP, sector of IO table, and Investment value) was done to estimate the unit cost of each candidate pixel. Risk level was modeled by using the degree of hazard and vulnerability level, a decision tree was used to make the risk assessment model for identifying the flood risk map and designed using Python programming language. This decision model was applied to the Nan river basin in Thailand and the Yoshino river basin in Japan. The proposed method could be useful for the flood mitigation policy in flood prone area.

6.2.2 Flood risk assessment methodology

The steam flow as shown in **Figure 6-15** that is flow chart for flood risk assessment. The flow chart is consisted by two main modules, hazard and vulnerability classification. A hazard category was represented by degree of hazard to correspond with different inundation depths. In several researches, flood hazard categories base on identification classes to represent the hazard level (Chowdhury and Karim, 1997; Tingsanchili and Karim, 2010). The five categories devise a scale for flood area, which the hazard level is based on three critical inundation depths such as 0.3, 0.8, 1.0 and 3.5 m. The critical inundation depths were selected from adaptation of guidelines in the flood-plain development manual (NSWG, 1986). The first class is about 0.3 m that the floor of factory is normally about 0 −

0.5 above the ground level, causing the damage in this sector. For the second class of critical depth, floor height is normally about 0.8 m above ground level in residential, school and building. The adults would have difficulty to ford, and the damage potential would be low. For a little depth increasing about 0.2 m on a ford, the damage of flood can be high and more difficult for fording. The flood depth is greater than 1.0 m, human life's property is under the threat. When the flood level increase greater than 3.5 m, the top of single floor building cannot take refuge for safety of life, and also damage in the vegetation area. The property damage comes to its maximum at this situation (ESCAP, 1991; NSWG, 1986; UNDRO, 1991). Based on these four critical values among inundation depth, hazard levels were categorized as No hazard (0 m ≤ depth < 0.3 m), Low hazard (0.3 m ≤ depth < 0.8 m), Medium hazard (0.8 m ≤ depth < 1.0 m), High hazard (1.0 m ≤ depth < 3.5 m), and Very high hazard (≥ 3.5 m).

The vulnerability of component at risk causing from the natural disaster is the estimated degree of loss to that component (UNDRO,1991). A land cover map was firstly grouped into four categories, factory, agriculture (paddy, farm land, agriculture area), urban, and other (forest, grassland, and water), that the categorization is similar to those defined for flood-plain classification (NSWG 1986; Dutta and Herath 2003). Related to the hazard level, a vulnerability level was represented by the economic land cover types. The vulnerability level based on economic cost was developed as pixel based model in the Python programming, using the same pixel size with the RRI model. The algorithm estimated economic cost in every pixel ($V_{i,j}$), using data from IO table results and land cover grid. The total economic cost of ever pixel was described in equation (1), and unit cost of each land cover type was written in equation (2).

$$V(i,j) = \sum_{k=1}^{m} C(k) \cdot A(i,j,k) \tag{1}$$

$$C(k) = TC(k)/TA(k) \tag{2}$$

where, i, j is coordinate of pixel (row and column), m is total number of land cover type, k is number of land cover type, C is unit cost of land cover type, A is area of land cover type in a pixel, TC is the total cost of land cover type in the region that can capture from the total final demand value in the IO table of the study area, TA is the total area of each land cover type in the region.

```
┌─────────────────┐          ┌─────────────────┐          ┌─────────────────┐
│ Flood map       │          │                 │          │ Economic data   │
│ simulation on   │          │ Land cover map  │          │ -Input-Output   │
│ specific area   │          │                 │          │  Table          │
│                 │          │                 │          │ -GPP, Investment│
└────────┬────────┘          └────────┬────────┘          └────────┬────────┘
         │                            │                            │
         ▼                            ▼                            ▼
┌─────────────────┐          ┌─────────────────┐          ┌─────────────────┐
│                 │          │                 │          │                 │
│ Flood hazard    │          │ Land cover      │ ──────►  │ Unit pixel cost │
│ map             │          │ types           │          │                 │
└────────┬────────┘          └─────────────────┘          └────────┬────────┘
         │                                                         │
         │                                                         ▼
         │                                                ┌─────────────────┐
         │                                                │                 │
         │                                                │ Vulnerability   │
         │                                                │ map             │
         │                                                └────────┬────────┘
         │                                                         │
         ▼                                                         ▼
┌─────────────────┐                                       ┌─────────────────┐
│ Hazard level    │                                       │ Vulnerability   │
│ of              │                                       │ classes         │
│ flood           │                                       │                 │
└────────┬────────┘                                       └────────┬────────┘
         │                   ┌─────────────────┐                   │
         └─────────────────► │ Flood risk      │ ◄─────────────────┘
                             │ analysis        │
                             └────────┬────────┘
┌─────────────────┐                   │
│ Flood hazard    │ ───┐              │
│ map             │    │              ▼
└─────────────────┘    │     ┌─────────────────┐     ┌─────────────────┐
┌─────────────────┐    ├───► │ Decision tree   │ ──► │ Flood risk map  │
│ Vulnerability   │ ───┘     └─────────────────┘     └─────────────────┘
│ map             │
└─────────────────┘
```
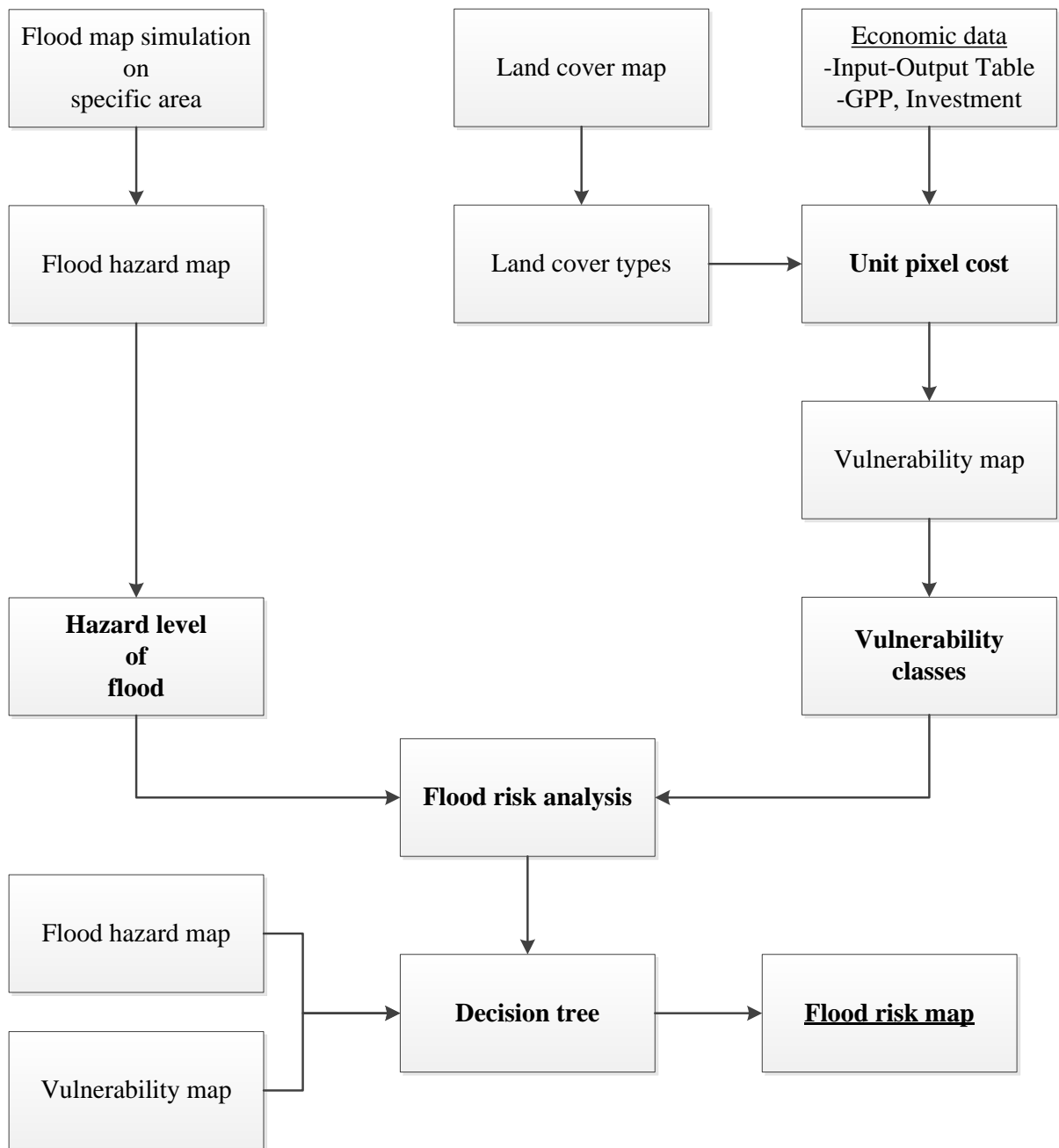
Figure 6-15 Stream flow of flood risk mapping concept

6.2.3 Flood risk assessment in the Nan river basin, Thailand, of the small selected area

The methodology was implemented to the Nan province, located in the northern part of Nan river basin in Thailand. The area represents on the flood plain area and covers a total area of 700 km². In this study, the methodology for the risk estimation was caused by the flood event of June 24-30, 2011.

The RRI model was done to simulate the flood event of June 24th and 30th, 2011. The model was able to estimate the maximum inundation depth at pixel size about 90 m x 90 m. The simulated flood event was illustrated in **Figure 6-16** by using the hazard level. The spatial distribution of the maximum inundation depth values based on the hazard level category was summarized in **Table 6-5** that the maximum hazard was about 49.3% of very high hazard. The minimum was Medium hazard level about 2.8% of total inundation area.

The economic data for vulnerability estimation were computed in Python programming language, interacting with the land cover in raster format via QGIS. The data at every 90 m x 90 m pixel size of the model was estimated by equation (1) and (2). The parameter values for the cost per each land cover type and total area of land cover were obtained from the Department of Industrial Works, Office of the National Economics and Social Development Board and Land Development Department official data in Thailand (DIW, 2011; NESDB, 2010; LDD, 2010). The C values for Factory, Paddy, Agriculture and Urban type are $42 - 0.05 \times 10^6$ Baths/point, 4,373.07 Baths/rai, 2,042.22 Baths/rai, and 50,067 Baths/capita, respectively. The density of population was collected from the Gridded Population of the World (GPW), v3 provided from NASA. The population density in this study area were 82 persons/pixel for urban area in the northern, 73 persons/pixel for urban area in the southern, and 38 persons/pixel for urban area in rural, capturing with resident area of land cover map for estimating cost.

The unit cost was evaluated for the entire pixel by summing up the price values on a pixel by pixel basis, based on the **Figure 6-17a**. **Table 6-6** shows the vulnerability assessment caused to the aforementioned land cover and the ranking price. The simulated area covered 710 km² (**Table 6-6**), of which 34% were No vulnerability, 46% Low vulnerability, 13% Middle vulnerability, 3% High vulnerability, and 5% Very high vulnerability. **Figure 6-17b** depicts the spatial distribution of the vulnerability category caused in every pixel.

The computation of risk based on the degree of hazard level and vulnerability class could be represented by the 5 x 5 matrix as shown in **Figure 6-18** that had assessed into 25 types. The several type of risk in the matrix was grouped into four risk level based on the reason as motion in the methodology that the risk level is described by No risk, Low risk, Mid risk, and High risk. The risk matrix was modeled by the decision tree model as presented in **Figure 6-19** to estimate the flood risk map with flood hazard and vulnerability map. **Figure 6-20** depicts the spatial distribution of the risk

category caused in every pixel as the flood risk map. **Table 6-7** shows the risk assessment caused to the aforementioned the ranking of risk. The flood risk area covered 161.36 km^2 (**Table 6-6**), of which 31% were No risk, 15% Low risk, 47% Mid risk, and 7% high risk.
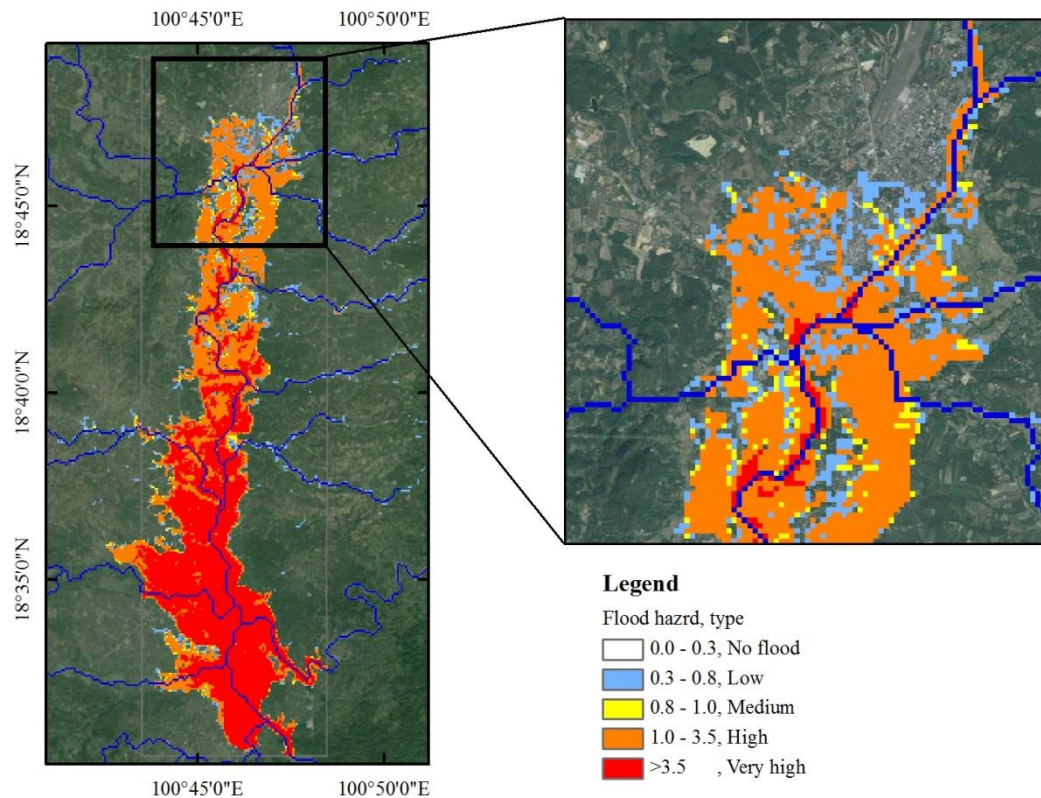
Figure 6-16 Flood hazard map in the small of the Nan river basin, based on the 5 categories

Table 6-5 Flood assessment for the 2011 flood event

Hazard category	Flood area, sq.km
No hazard	589.11
Low hazard	15.29
Medium hazard	3.35
High hazard	42.99
Very high hazard	59.86

Table 6-6 Vulnerability cost assessment for the selected area of Nan river basin, Thailand

Vulnerability category cost, Bath/pixel	Area, sq.km
No econ. price	239.68
0 – 15,000	323.32
15,000 – 25,000	90.25
25,000 – 2,000,000	18.47
>2,000,000	38.87

| | a) Land cover type | b) Land cover cost / pixel |
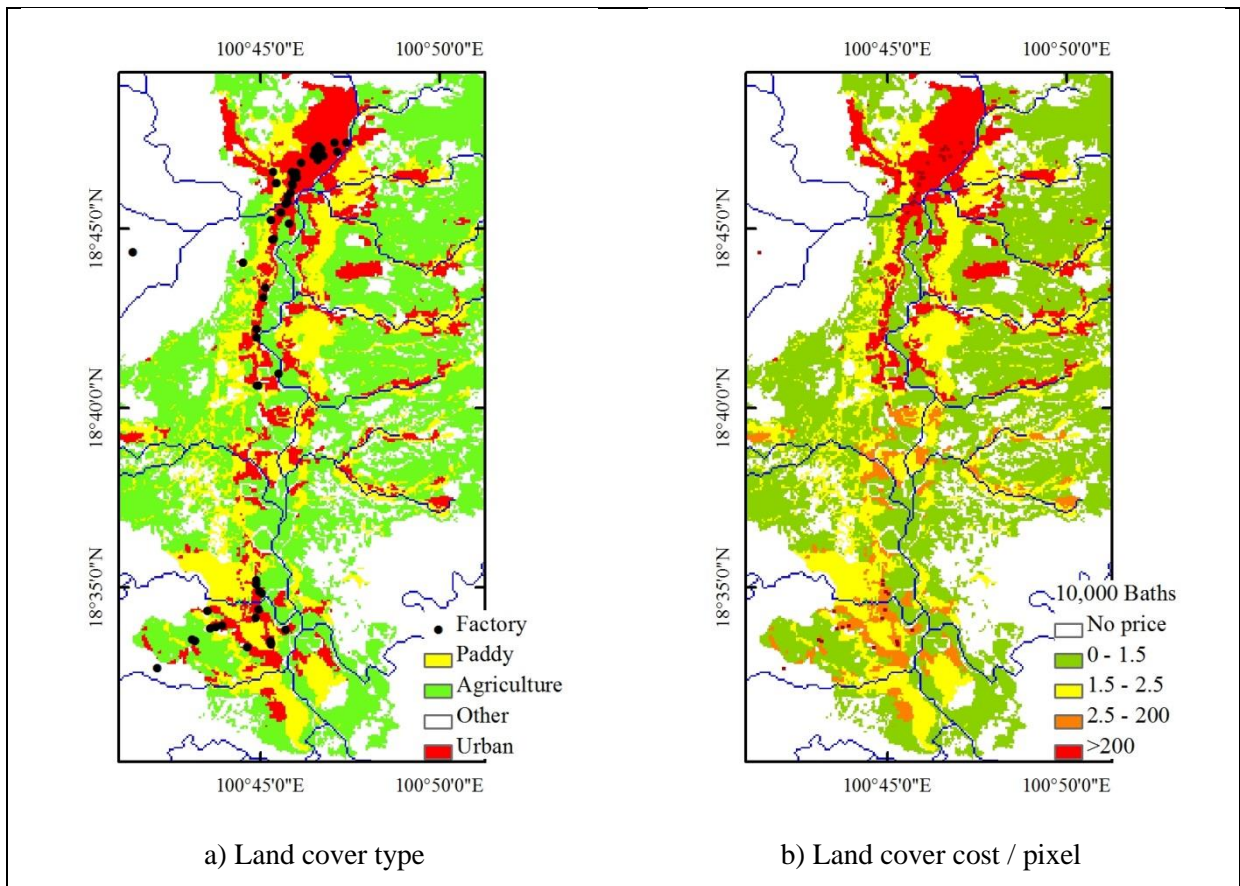
Figure 6-17 Vulnerability map in the small of the Nan river basin, based on the cost per pixel
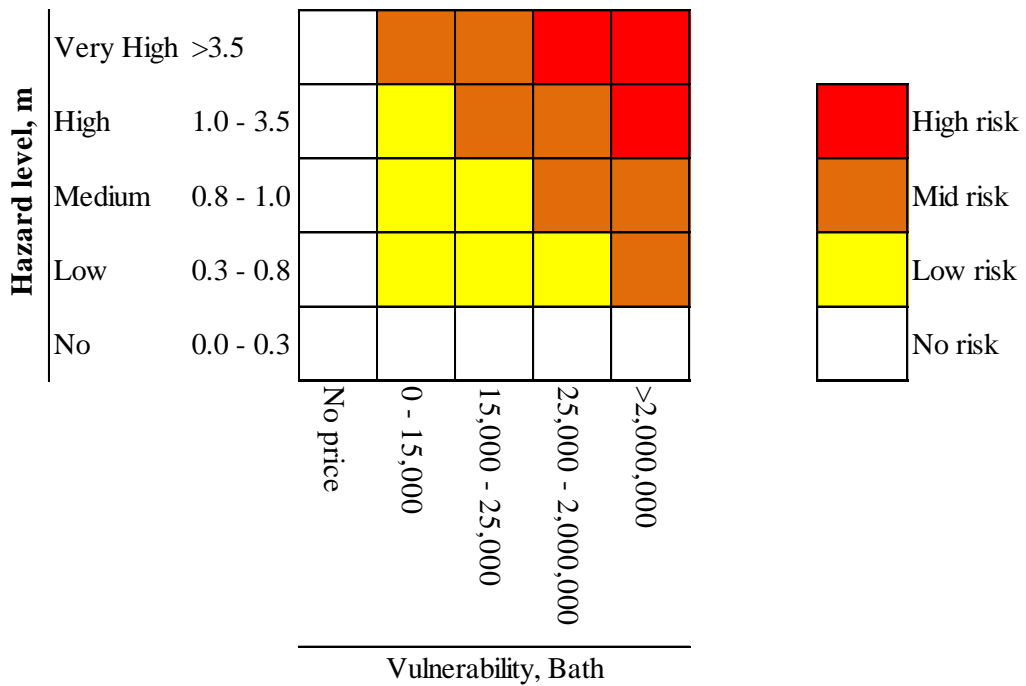
Figure 6-18 Risk category assessment based on the hazard and vulnerability situation
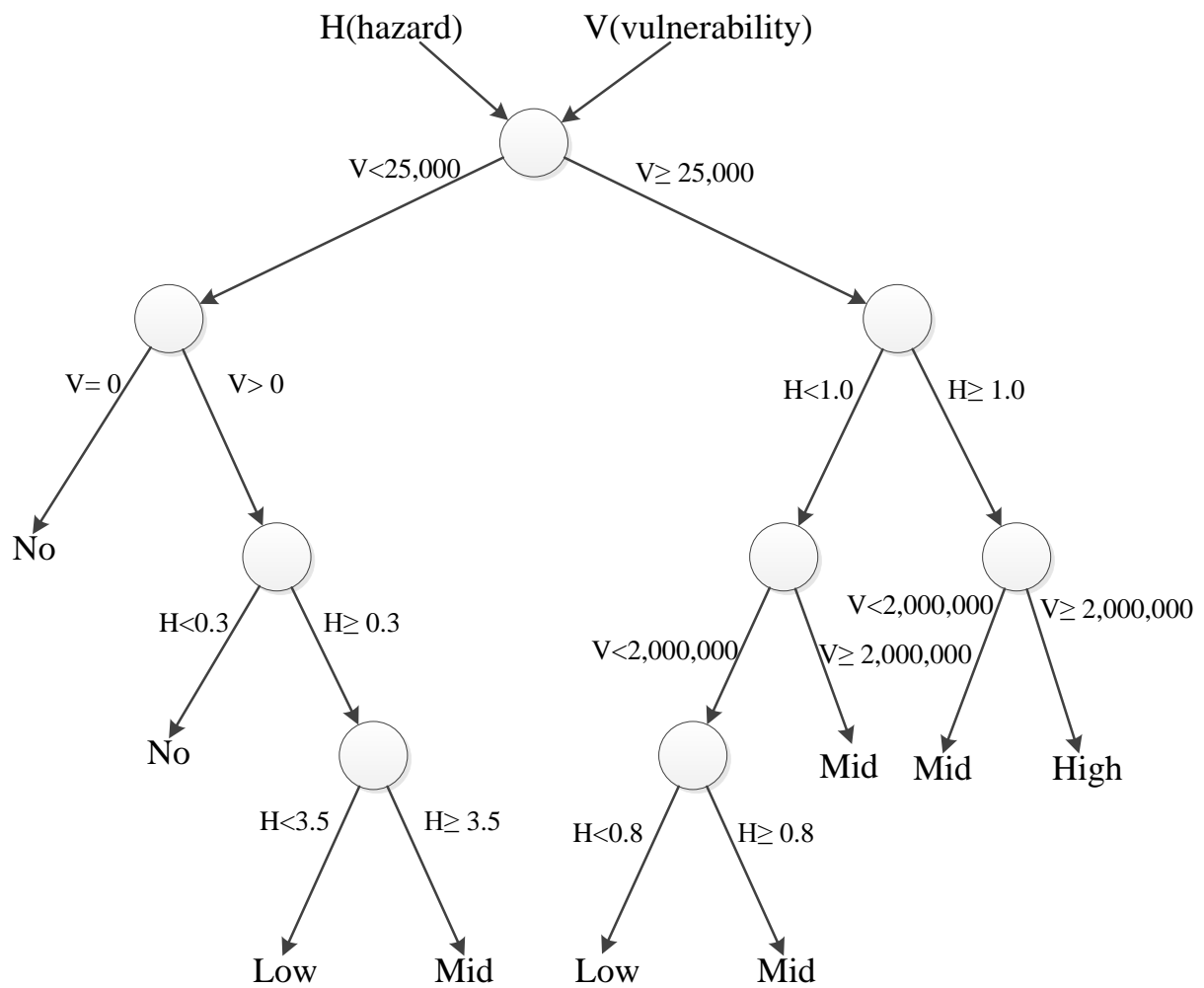
Figure 6-19 Decision tree of the risk assessment on each pixel

Table 6-7 Flood risk assessment for the selected area of Nan river basin, Thailand

Risk category	Area, sq.km	Area(%)*
No risk	50.34	31.2
Low risk	23.82	14.8
Mid risk	75.16	46.6
High risk	12.04	7.5

* Total of inundation area = 161.36 sq.km
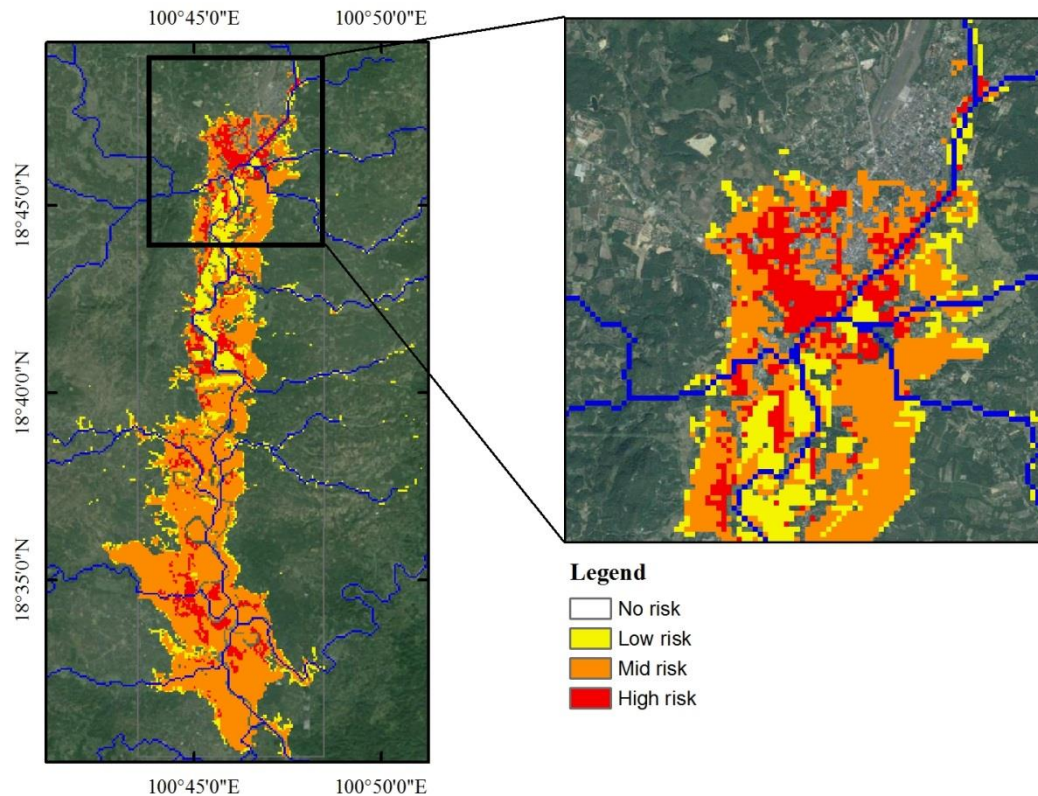
Figure 6-20 Flood risk map for the selected area of Nan river basin, Thailand

6.2.4 Flood risk assessment in the Yoshino River on the Shikoku Island, Japan: case study of Dike breaking

The methodology was implemented to the Ishii town, located in the Tokushima prefecture in Japan. The area represents on the flood plain area of the Yoshino River and covers a total area of 43 km^2. In this study, the methodology for the risk estimation was caused by the flood event of July 10-13, 2014.

The RRI model was done to simulate the flood event of July 10th and 13th, 2014. The model was able to estimate the maximum inundation depth at pixel size about 50 m x 50 m. The simulated flood event was illustrated in **Figure 6-21** by using the hazard level. The spatial distribution of the maximum inundation depth values based on the hazard level category was summarized in **Table 6-8** that the maximum hazard was about 44% of High hazard. The minimum was Low hazard level about 8% of total inundation area.

The economic data for vulnerability estimation were computed in Python programming language, interacting with the land cover in raster format via QGIS. The data at every 50 m x 50 m pixel size of the model was estimated by equation (1) and (2). The parameter values for the cost per each land cover type and total area of land cover were obtained from the Ministry of Economy, Trade and Industry and Ministry of Land, Infrastructure, Transport and Tourism official data in Japan (METI, 2005; MLIT, 2010). The C values for Factory, Agriculture and Urban type are 683,541 Yens/point,

195.26 x 10^6 Yens/km^2, and 300,458 Yens/capita, respectively. The density of population was collected from the Gridded Population of the World (GPW), v3 provided from NASA. The population density in this study area was 910 persons per km^2 for urban area, capturing with resident area of land cover map for estimating cost.

The unit cost was evaluated for the entire pixel by summing up the price values on a pixel by pixel basis, based on the **Figure 6-22**. **Table 6-9** shows the vulnerability assessment caused to the aforementioned land cover and the ranking price. The simulated area covered 43 km^2 (**Table 6-9**), of which 15.9% were No vulnerability, 48.5% Low vulnerability, 35.1% Middle vulnerability, and 0.5% High vulnerability. **Figure 6-23** depicts the spatial distribution of the vulnerability category caused in every pixel.

The computation of risk based on the degree of hazard level and vulnerability class could be represented by the 5 x 4 matrix as shown in **Figure 6-24** that had assessed into 20 types. The several type of risk in the matrix was grouped into four risk level based on the reason as motion in the methodology that the risk level is described by No risk, Low risk, Mid risk, and High risk. The risk matrix was modeled by the decision tree model as presented in **Figure 6-25** to estimate the flood risk map with flood hazard and vulnerability map. **Figure 6-26** depicts the spatial distribution of the risk category caused in every pixel as the flood risk map. **Table 6-10** shows the risk assessment caused to the aforementioned the ranking of risk. The flood risk area covered 12.68 km^2 (see **Table 6-10**), of which 16% were No risk, 32% Low risk, 27% Mid risk, and 25% high risk.

Table 6-8 Flood assessment for the breaking dike scenario

Hazard category	Flood area, sq.km
No hazard	32.60
Low hazard	3.66
Medium hazard	0.94
High hazard	4.86
Very high hazard	1.60

Table 6-9 Vulnerability cost assessment for the selected area of the Shikoku Island, Japan

Vulnerability category, 1,000,000 Yens/pixel	Area, sq.km
No econ. price	6.95
0 – 0.5	21.18
0.5 – 1.0	15.31
>1.0	0.21
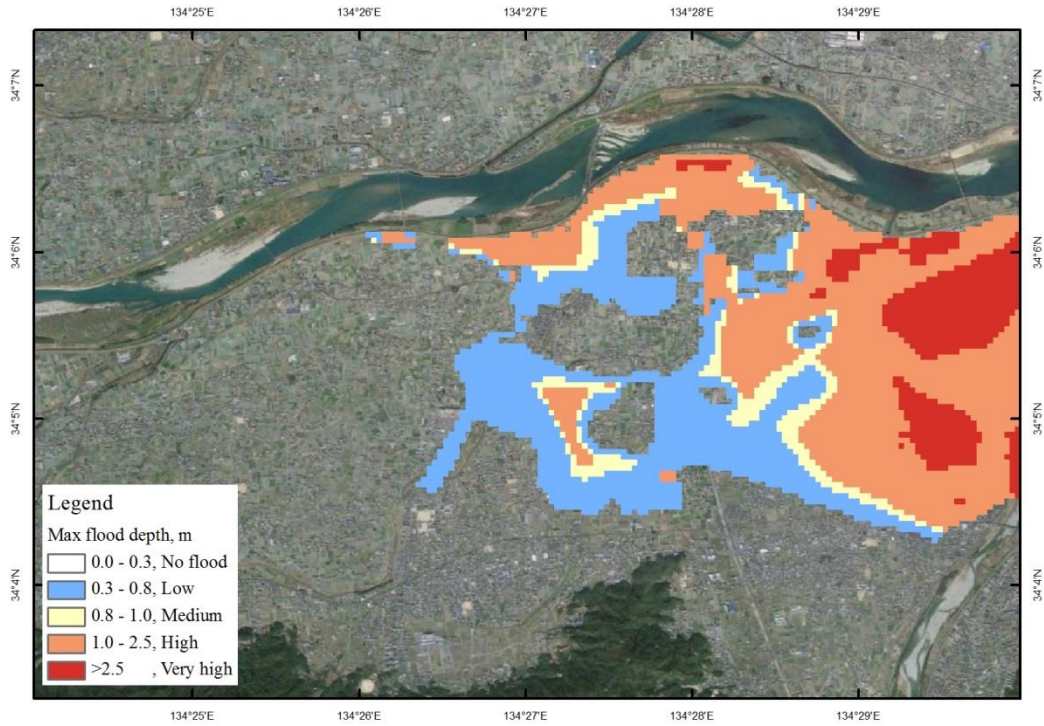
Figure 6-21 Flood hazard map in the small area of the Yoshino river basin in Ishii town Tokushima prefecture, Japan, based on the 5 categories
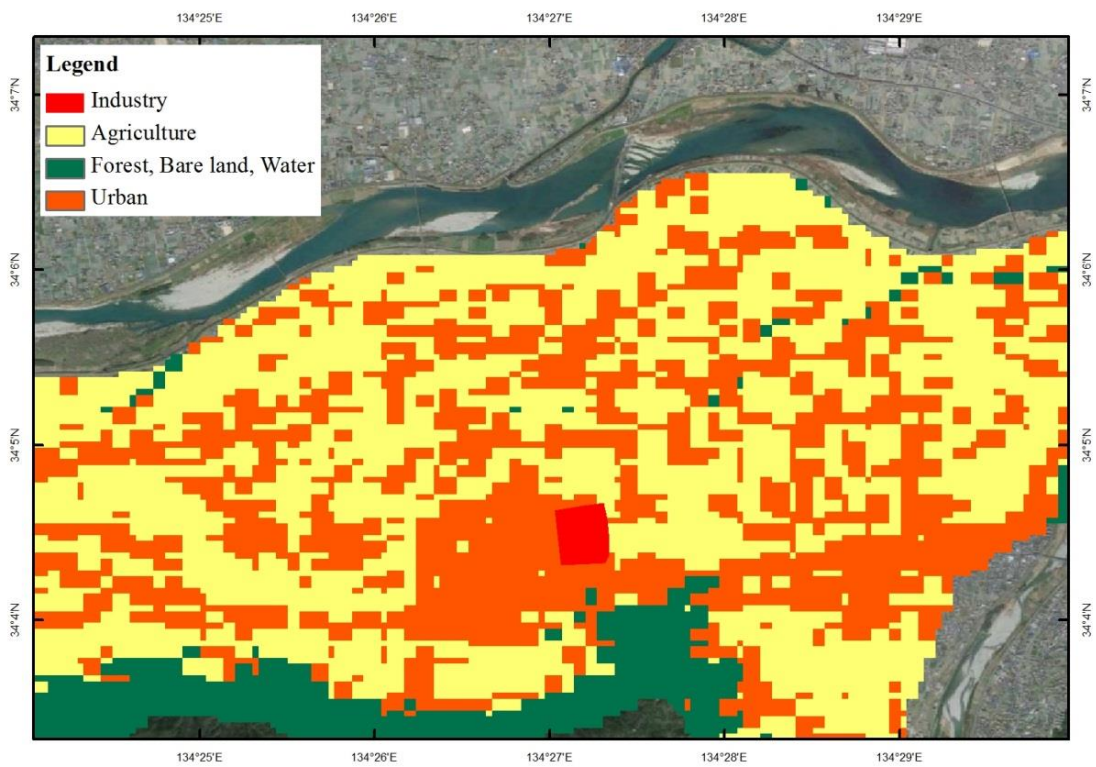
Figure 6-22 Economic land cover map in the small area of the Yoshino river basin in Ishii town Tokushima prefecture, Japan
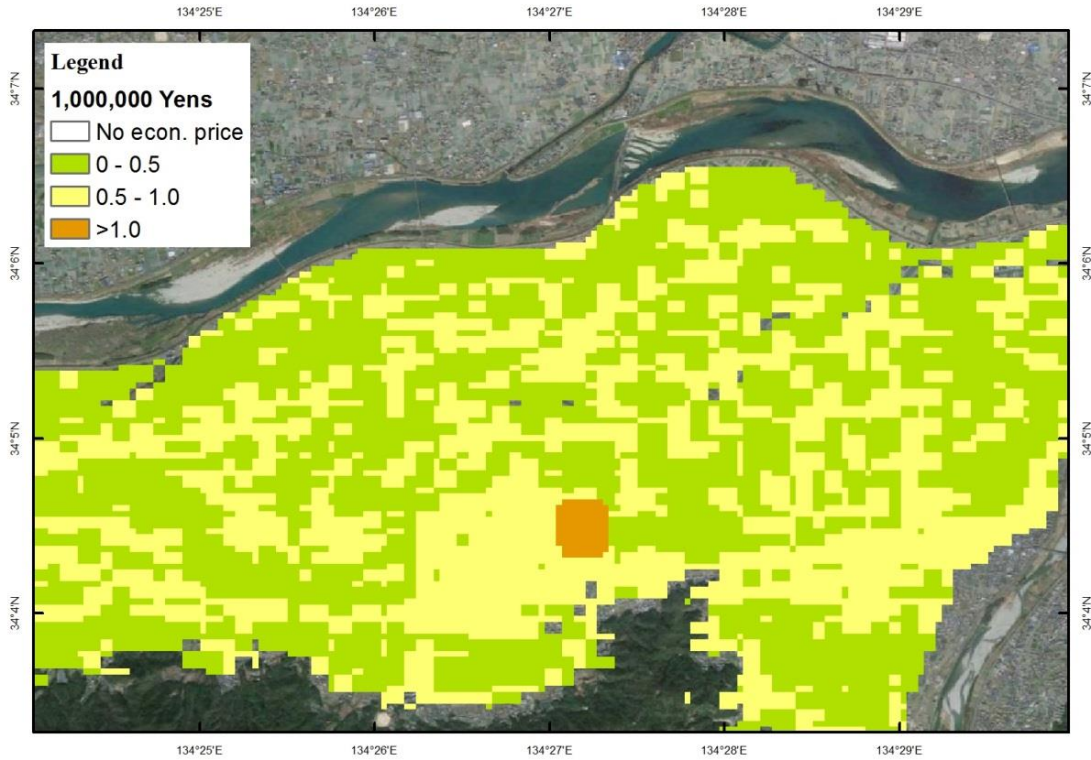
Figure 6-23 Vulnerability map in the small area of the Yoshino river basin in Ishii town Tokushima prefecture, Japan, based on the cost per pixel
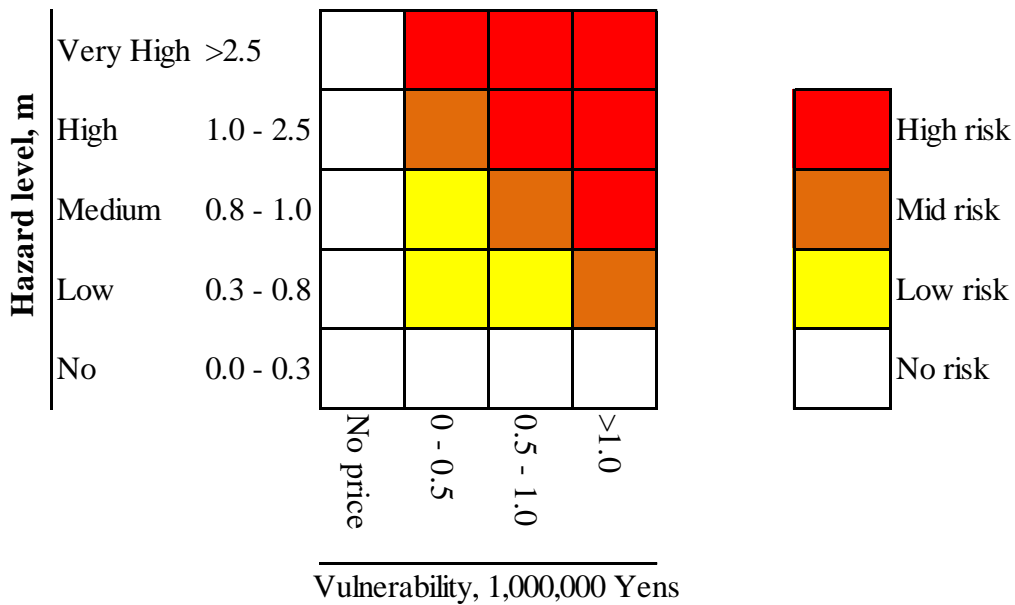
Figure 6-24 Risk category assessment based on the hazard and vulnerability situation
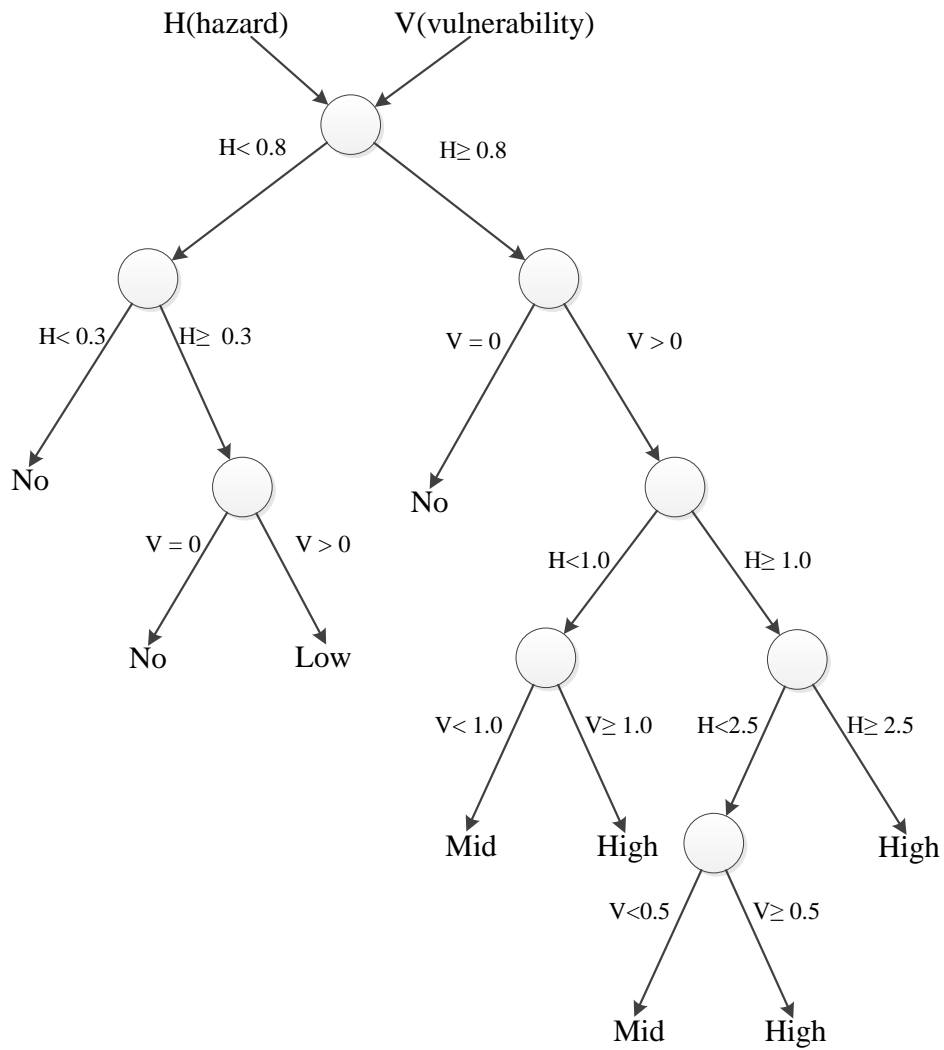
Figure 6-25 Decision tree of the risk assessment on each pixel

Table 6-10 Flood risk assessment for the Ishii town of Tokushima prefecture, Shikoku Island, Japan, based on the scenario of breaking dike

Risk category	Area, sq.km	Area(%)*
No risk	2.02	15.7
Low risk	4.15	32.3
Mid risk	3.41	26.5
High risk	3.30	25.5

* Total of inundation area = 12.68 sq.km
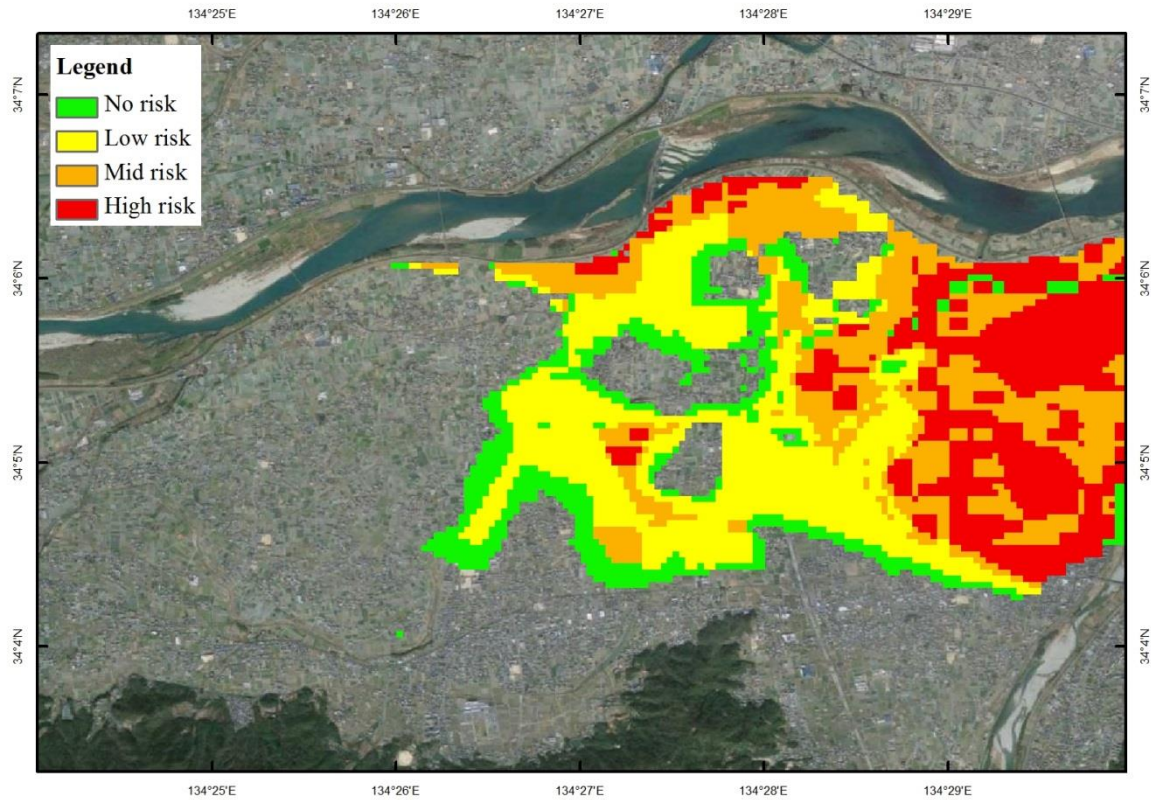
Figure 6-26 Flood risk map in the small area of the Yoshino river basin in Ishii town Tokushima prefecture, Japan

6.2.5 Conclusion

This approach based on small area of both study areas, Thailand and Japan, the flood risk assessment consist with two main data sets, hazard and vulnerability data. The simulated flood map presented as spatial of inundation depth is firstly categorized into five hazard levels, No, Low, Medium, High, and Very high hazard, as the hazard data. For the vulnerability data, economic data as IO table, GPP, and investment are collected to relate with land cover type that its unit cost on the pixel is estimated from there data sets. Based on both estimated data sets, hazard and vulnerability, the risk ranking is run by magnitude of both data sets. The high risk is identified as maximum hazard and vulnerability, but minimum on both data is low risk. The classification of risk level is modeled by the decision tree model to create the flood risk map.

Chapter 7 Conclusion and recommendation for further studies

This dissertation research is contribution of correction and evaluation of remote sensing sources for flood assessment through basin scales, and application of the flood model to demonstrate the approach of flood loss estimation method on small area. It can be summarized by (1) application of the distributed hydrological model as the Rainfall-Runoff-Inundation model that is a combination of rainfall-runoff processes and flood modeling, (2) investigation of the accuracy, bias correction of DEM data set and evaluating flood simulation results from different topography sources, (3) investigation of the accuracy of both approaches, satellite land cover data sources and surface roughness coefficient, and evaluating flood modeling results from different surface roughness data sets, (4) evaluation of the accuracy of rainfall sources, rain gauge spatial, satellite, and simulated products, investigating bias correction of the satellite rainfall product as a demonstration, and evaluating runoff simulation results from different rainfall sources, (5) application of the flood simulation model for water resource management in flood hazard mapping for flood damage cost estimation. Intend to answer the research question was described in the first chapter.

The five research questions were replied in core chapters of this thesis (2, 3, 4, 5, and 6). This summary chapter begins with a summarizing of the core chapters, and follows with answers of each research questions. Finally, contribution and recommendation of this dissertation are explained for the future direction.

7.1 Summary and conclusion

(1) Applying the distributed hydrological model as the Rainfall-Runoff-Inundation model is a combination of rainfall-runoff processes and flood modeling

The hydrological modeling was introduced for flood event in the Chapter 2 that used the RRI model for simulating the runoff. For integrating component of flood model based on its mechanism with topography, rainfall, and land cover, the VOXEL model was used to collect the data set. In acceleration of the RRI model, GPUs was applied on the CUDA coding that implemented on the natural and simple terrain, including comparison with other researches.

Input dataset were simulated by the RRI model that the results of the flood simulation were analyzed as spatial runoff and inundation depth every temporal scale. The VOXEL model of the daily runoff was implemented into the RRI model. Accuracy of the RRI model on was assessed on simulating in the Nan river basin. The model was driven for 2011 rainfall events that scenario case was estimated at daily on a temporal scale to match the Royal Irrigation Department Thailand observed stream flow data. Three runoff stations were selected in the Nan river basin, the first one belonging to the upstream sub-catchment (N.64), the second one belonging to the middle area (N.1) and the third one

belonging to the downstream area (N.13A), to show the daily hydrograph that results from the different scenario. Over all of the runoff station, the simulation captured the peak at the same time with the observation. The three runoff station on the daily hydrograph were analyzed and calculated for evaluation by the performance statistical. The results are that is concluded by five indexes. The N.64 simulated discharge best matched the observed runoff with the highest R^2 of 0.906 and lowest RMSE of 67.07 cms. This simulated runoff overestimated the runoff volume, peak flow and mean runoff by 3.09%, 8.16% and 4.46 cms, respectively. The N.1 simulated runoff was lowest R^2 and low RMSE, however, its simulated runoff was the lowest difference of Volume bias of 2.13% and Mean bias of -4.09%. The peak flow of N.1 overestimated about 39.3%. The N.13A significantly underestimated the runoff volume, peak and mean runoff, with high RMSE and low correlation value. This study has presented a task for application of VOXEL model on the RRI model. The VOXEL model application has convenient to present and input to the numerical model.

RRI model applied by the GPU used NVIDIA's CUDA coding is presented as introduction. The RRI-GPU model is simulated and validated by using a simple terrain and natural terrain model in Thailand. The computational have the advantage to use the GPU that outperform the CPU. This is presented in the two different scenarios. The RRI-GPU model is done by using the complex terrain to represent the implementation of natural effect. The natural river basin (the Nan river basin, Thailand) has tested on the two scenarios based on the resolution size (500 m and 1,000 m). The GPU speedup is about 2.6x, with high accuracy of the simulated runoff.

Second, the RRI model accelerated of using the parallel programming technology is shown with analysis speedups ranging between 1.5x to 4.4x compared to a CPU model computing the same mathematical scheme. For the simple terrain scenario, the RRI-GPU model executed on the NVIDIA GeForce GTX 780 Ti is done by simulating amount cell ranging between 144 to 129,600 pixels and iteration times between 2,160 to 52,560 time steps, contained with single slope, soil type and uniform rainfall. The GPU model have only affected with the spatial resolution scale, which the 2,304 pixels is a responding value of GPU performance.

Overall, the RRI-GPU model offer faster hydrological simulation on flood event results that are obtained from parallelization method implementing the diffusive wave routing. The next generation of GPU implementation in hydrological modeling has more potential development in high level computer language and new hardware technology.

(2) Investigating the accuracy, bias correction of DEM data set and evaluating flood simulation results from different topography sources

The vertical accuracy of six DEMs (GSI DEM, ASTER GDEM, SRTM, GMTED2010, HydroSHEDS, and GTOPO30) on the Shikoku Island in Japan, all of which are open source data was implemented in the Chapter 3. The validation was operated by the GCPs with matching coordinate to compare the elevation value. The impacts of terrain morphology and land cover properties were analyzed. The river networks estimated from six DEMs were evaluated.

First, the DEMs characteristics were described on basically. Then, the six DEMs were presented with vertical accuracy estimated from the difference elevation. Finally, DEM accuracy was analyzed on the statistical approach. For the accuracy assessment, the statistical approach was based on the four performance parameters, scatter plot, and histogram of error that were investigated. The investigation revealed that the GSI DEM provided the highest accuracy, followed by ASTER GDEM, SRTM, GMTED2010, GTOPO30, and HydroSHEDS, in overall. Interestingly, the GTOPO30 provided higher accuracy than the HydroSHEDS, with lower definition.

Effect of terrain morphology in the vertical accuracy of the DEMs was assessed by using altitudinal range and slope range. The altitudinal have affect to the vertical accuracy presented by the RMSE value. The DEM was more error until altitudinal zone in range about 500 – 750 m, after that the error was drop down among the fine resolution. For the coarse resolution, the HydroSHED have error drop down at range about 700 – 1,000 m, while the GTOPO30 presented the drop down of error at the highest range. The slope effect was revealed by the relationship between RMSE value and slope range. The fine resolution DEMs was more error in the higher slope range. By the contrast, the coarse resolution provided the slope effect on the 0 – 15 degree, after that the error was drop down in the steepest slope.

In this study, land cover was divided into 6 types and the DEMs in each type were evaluated on the vertical accuracy. All the DEM data had the lowest accuracy in the forest area because of the top of canopy affected to the sensor. This result presented the key of validation DEM on the statistical approach. It also described the spatial information of DEM accuracy for various terrain morphology and land cover.

According to DEM differences were discussed from the statistical assessment. For the evaluation of the accuracy, statistical approaches based on histograms and Q-Q plots were presented and the error characteristics in six sources of DEM were investigated. After bias correction using a linear transformation, the validation statistics were recomputed for each DEM. The results for RMSE of terrain elevation are 5.87 m for GSI-DEM with GCPs on high definition resolution. For the fine

resolution, the RMSE is 9.08 m for the ASTER, 9.31 for the SRTM and 16.53 m for GMTED2010. The RMSE of coarse resolution DEM is 53.37 m for HydroSHEDS and 45.94 m for GTOPO30. For all DEM sources, the transformed results suggest to unbias altitudes based on the mean error value. The top of the canopy has an effect to the sensors, ASTER, and SRTM. That is the reason of negative bias that occurs in ASTER and SRTM, including other test DEM. In conclusion, this study has revealed the importance point of computing validation statistics for DEM before and after bias correction.

The evaluation of six DEM products (GSI, ASTER, SRTM, GMTED2010, HydroSHEDS and GTOPO30) was input to the physical-based hydrological model (RRI model) over the Shikoku Island Japan and the Nan river basin Thailand. According to the aim of this study used the flood event for estimating the streamflow to evaluate the performance of each product. The simulation of the streamflow was done by using without a calibration of the hydrologic parameter to specific product. The streamflow were simulated and reported at hourly to match with the MLIT observed runoff and daily to match with the RID observed runoff.

For the Shikoku Island, GSI DEM demonstrated to be the best product to model a streamflow for flood event on 2014. The simulated runoff of ASTER also closed to the observed dataset; however, it underestimated the runoff volume, mean runoff, and peak flow. The four DEM (SRTM, GMTED2010, HydroSHEDS and GTOPO30 also underestimation the runoff volumes, mean runoff, and peak flow. In conclusion, the GSI DEM simulation was the best performance DEM product for hydrological modeling to estimate the runoff, representing with the high resolution products. However, the ASTER was the best among the international products.

The Nan river basin in Thailand used only the international DEM sources for evaluation on runoff simulation in 2011. GMTED2010 DEM demonstrated to be the best product to model a streamflow for flood event with underestimation on the runoff volume and mean runoff. The simulated runoff of SRTM also closed to the observed dataset; however, it overestimated the peak flow. The three DEM (ASTER, HydroSHEDS and GTOPO30 also underestimation the runoff volumes and mean runoff. In conclusion, the GMTED2010 DEM simulation was the best performance DEM product for hydrological modeling to estimate the runoff on the river basin scale. However, the SRTM was the second performance among the international products. For the simulated inundation map comparison, the SRTM presented the highest accuracy among the five DEM products. The evaluation accuracy of inundation map used the MODIS data for referent data.

Based on the DEM data and simulation results, Shikoku is the mountain complex terrain to contain with a steep slope, while Nan river basin is the mountain area where represent with the mild slope. In the Shikoku Island, ASTER DEM is suitable to apply for runoff simulation using distributed

hydrologic modeling, have estimated from stereo matching. SRTM presented a performance for runoff and inundation simulation in the Nan river basin, have explored from radar laser scan with Shuttle.

(3) Investigating the accuracy of both approaches, satellite land cover data sources and surface roughness coefficient, and evaluating flood modeling results from different surface roughness data sets

The error presented into hydrologic modeling results when using the satellite based land cover data sets for estimating Manning's coefficient for surface roughness in the river basin scale as presented in the Chapter 4. The impact of generating a Manning's coefficient map from the satellite sources are presented from comparison to the referent land cover map that is lack of the study to archive from the literature. This study presented a comparison of Manning's coefficient maps to estimate the uncertainty created in distributed hydrologic modeling simulation.

The uncertainty affected in approximating the Manning's coefficients of surface roughness and the effect it has on distributed hydrologic modeling outputs. A land cover based approach to approximate Manning's coefficient on a satellite based was compared to referent observed land cover (aerial based) for two study areas, the Shikoku Island Japan and the Nan river basin Thailand. The two satellite sources Manning's coefficient maps produced by the look-up table method were compared and significant differences in the aerial based Manning's coefficient values were observed. The relationship between land cover classes and Manning's coefficient values were collected from the previous as a literature review. The based referent map generated "smoother" surfaces than the MODIS, while the AVHRR generated "rougher" surfaces than those the based referent map, in the Shikoku Island, Japan. For the Nan river basin, Thailand, The based referent map generated "smoother" surfaces than the MODIS, while the AVHRR also generated "smoother" surfaces than those the based referent map. These variations are attributed to the unsupervised classification algorithm used in the development of both satellite data sources (MODIS and AVHRR). It is also observed that the significant variation of Manning's coefficient between the three sources does not translate into significant runoff response differences on both hydrograph magnitude and shape, for the distributed hydrological model (RRI model). This is confirmed by three storm events on two study areas, although small differences in runoff response were observed at the observed runoff station. This observation suggests the use of MODIS, AVHRR or other Manning's coefficient estimation approaches for large watersheds provide a reasonable estimate of Manning's coefficient for simulating runoff hydrographs. Further studies are needed to confirm this observation for different watersheds and different method for estimating Manning's coefficient.

(4) Evaluating accuracy of rainfall sources, rain gauge spatial, satellite, and simulated products, investigating bias correction of the satellite rainfall product as a demonstration, and evaluating runoff simulation results from different rainfall sources

The rainfall study in the Chapter 5 is consisted by three objectives. Firstly, evaluation effect of spatial interpolation method of rain gauges on runoff estimation is considered. Secondly, evaluation effect of satellite rainfall is investigated on runoff simulation using hydrological modeling. Thirdly, effect of satellite rainfall bias correction is evaluated in five algorithms and two schemes.

Firstly, the evaluation of five rainfall interpolation methods (IDW, TSP, SKG, OKG and SPL) was input to the physical-based hydrological model (RRI model) over the Shikoku Island Japan and the Nan river basin Thailand. According to the aim of this study used the typhoon season in 2014 for the Shikoku and the June 2011 and August 2014 storm event from the Nan to estimate the streamflow for evaluating the performance of each interpolation methods. The simulation of the streamflow was done by using without a calibration of the hydrologic parameter to specific interpolation product. The streamflow were simulated and reported at hourly and daily to match with the observed runoff.

IDW demonstrated to be the best algorithm interpolating a spatial of rain gauge to model a streamflow for typhoon season in 2014 on the Shikoku. The simulated runoff of SKG and OKG also closed to the observed data sets; however, it overestimated the runoff volume and mean runoff during the event. TSP and SPL overestimation the runoff volumes and mean runoff, while their peak were underestimation. TSP was the highest overestimation of runoff volume and mean runoff, with high performance of peak flow. In conclusion, the IDW model was the best interpolation method for hydrological modeling to estimate the runoff on the Shikoku area that represented with the high density rain gauge area.

SKG demonstrated to be the best algorithm interpolating a spatial of rain gauge to model a streamflow for June 2011 and August 2014 of the Nan river basin. The simulated runoff of OKG also closed to the observed data sets; however, it overestimated the runoff volume and mean runoff during the second event. SPL and IDW overestimation the runoff volumes and mean runoff, while their peak were underestimation. TSP was the highest underestimation of runoff volume, peak and mean runoff, with high RMSE and weak correlation value. In conclusion, the SKG simulated by the semi-variogram was the best interpolation method for hydrological modeling to estimate the runoff on the Nan river basin with sparse rain gauge network.

Secondly, the evaluation of six rainfall products (Rain gauge, GPM, GSMaP, TRMM, CMORPH and PERSIANN) was input to the physical-based hydrological model (RRI model) over the study areas. According to the aim of this study used the flood event for estimating the streamflow to evaluate the

performance of each product. The simulation of the streamflow was done by using without a calibration of the hydrologic parameter to specific product. The streamflow were simulated and reported at hourly and daily to match with the observed runoff.

GPM in the Shikoku verified to be the best satellite rainfall product to simulate a streamflow for flood event on 2014 with lowest volume and mean bias. The simulated runoff of GSMaP also closed to the observed dataset to validate with peak, RMSE and correlation; however, it was underestimated on the runoff volume and mean runoff. The peak flow of the GSMaP was underestimation. TRMM was also underestimation the runoff volumes, mean runoff, and peak flow. CMORPH and PERSIANN were the highest underestimation of runoff volume, peak and mean runoff, with high RMSE and weak correlation value. In conclusion, the GPM and GSMaP simulated was the best performance satellite product for hydrological modeling to estimate the runoff on the river basin scale, representing with the high resolution products. However, the TRMM was the best among the course resolution products.

GPM demonstrated to be the best satellite-based rainfall product to model a streamflow for flood event on 2014 for the Nan river basin. The simulated runoff of TRMM also closed to the observed dataset; however, it overestimated the runoff volume and mean runoff. The peak flow of the TRMM was underestimation. GSMaP and CMORPH underestimation the runoff volumes, mean runoff, and peak flow. PERSIANN was the highest underestimation of runoff volume, peak and mean runoff, with high RMSE and weak correlation value. In conclusion, the GPM simulated was the best performance satellite product for hydrological modeling to estimate the runoff on the river basin scale, representing with the high resolution products. However, the TRMM was the best among the course resolution products.

Satellite-based rainfall products, can capture the overall rainfall pattern, are alternative for implementation in the remote area such as the ungauged basins. Among five satellite-based rainfall products, GPM and TRMM have potential to produce a simulated streamflow on the hydrological modeling. The satellite-based rainfall products might be needed correction methods before application as input to the hydrological modeling.

Different researches have investigated that satellite rainfall products are contained by systematic and random error. Therefore, the challenge is how the products can be make more accuracy for previous propose. This study assessed the effect of precipitation bias correction in GPM and TRMM represented by high and coarse resolution, respectively, on the performance of distributed hydrological model (RRI model). In this study, the point is assessed in the temporal and spatial aspects of both satellite data, GPM and TRMM, bias for the hydrological modeling in watersheds. The finding of this study can contribute to affect that key of increasing the application of satellite rainfall products in the real world. The study in Nan river basin Thailand can benefit from satellite

rainfall products for monitoring and assessing resource. Conclusions of bias correction study are summarized below.

The evaluation of five correction techniques (Mean ratio, Geometrics transformation, Linear transformation, Data assimilation and Quantile mapping) combined with two schemes (temporal and spatial) was input to the physical-based hydrological model (RRI model) over the study areas. According to the aim of this study used the flood event for estimating the streamflow to evaluate the performance of each product. The simulation of the streamflow was done by using without a calibration of the hydrologic parameter to specific product. The streamflow were simulated and reported at daily to match with the observed runoff.

Data assimilation technique in the temporal scheme could reduce the bias of GPM about -96% on the mean bias, while TRMM bias correction with Geometrics transformation on the temporal scheme increased an accuracy about 97% on the mean bias. The significant achievement of results presented that the key aspect of the GPM and TRMM bias is their temporal scale as accounting for it substantially increased the accuracy of rainfall bias. It had some instances that were not possible to increase the accuracy on the watershed average bias. The rain gauge specifically in the northern parts of the watershed is not to match between the satellite bias correction and rain gauge data.

RRI model could capture a better runoff hydrograph in volume and pattern when satellite bias correction data sets were utilized instead of the exiting satellite data. The analysis of simulation results indicated that small rainfall error generated a larger error effect on runoff simulation in average. The satellite bias correction results outperformed the existing satellite on magnitudes of error evaluated from five statistical indexes. From the performance analysis, +16.94% bias of GPM rainfall data is generated to +10.6% of runoff bias, while TRMM rainfall bias about +13.27% is simulated to runoff bias about +49.21%. For the bias correction products, the bias error was reduced that from -3.85% rainfall biases transferred to -6.87% runoff biases in the GPM data, and TRMM data rainfall bias about 2.77% generated runoff bias about -0.25%. The recommendation of bias correction technique is Data assimilation technique for merging data when their have a rain gauge data sets to supervise the data product, while an unsupervised method is Geometrics and Linear transformation. The unsupervised have a limitation due to its parameter can be used in some specific time. When comparing on temporal and spatial scheme bias corrections were used to the GPM and TRMM rainfall input, accounting for the spatial scheme of both satellite bias have the largest effect on hydrological model simulation and should be taken into account. The error of modeling is not depended only on the rainfall input, but also on the effect of topography and land cover data sets. Future studies should assess comparative advantage of complex algorithm in mathematics of bias correction techniques, and application in a radar rainfall study.

(5) Applying the flood simulation model for water resource management in flood hazard mapping for flood damage cost estimation

The application of flood modeling in the Chapter 6 has two main approaches: flood forecasting and flood risk assessment. The flood forecasting implements in river basin scale as coarse resolution result and related to small area as high resolution result. For the flood risk assessment, economic data sets related to land cover data are collected to estimate the vulnerability of the simulated small area that are overlaid with the flood simulation results of the small area as flood hard map.

According to the first approach, the river basin scale simulation is run as firstly that is uses to identify as the boundary condition of small area to reveal a high resolution results. For the Nan river basin the small area is selected as a flood plain area in a middle of the river basin including the capital area of the Nan province. The event based of this forecasting is the June 2011 storm when Haima monsoon attracted to this area. For the Shikoku Island, the Ishii town in Tokushima prefecture of the Yoshino river basin is selected for demonstration the flood forecasting on a scenario based as a dike breaking.

The second approach based on small area of both study areas, Thailand and Japan, the flood risk assessment consist with two main data sets, hazard and vulnerability data. The simulated flood map presented as spatial of inundation depth is firstly categorized into five hazard levels, No, Low, Medium, High, and Very high hazard, as the hazard data. For the vulnerability data, economic data as IO table, GPP, and investment are collected to relate with land cover type that its unit cost on the pixel is estimated from there data sets. Based on both estimated data sets, hazard and vulnerability, the risk ranking is run by magnitude of both data sets. The high risk is identified as maximum hazard and vulnerability, but minimum on both data is low risk. The classification of risk level is modeled by the decision tree model to create the flood risk map.

7.2 Answers to the research question

Research question 1: How do flood simulation based on hydrological modeling, using satellite remote sensing datasets?

In Chapter 2, developing a distributed hydrologic model (RRI model) in modification and implementation formwork was studied. The framework consisted with three modules: (i) VOXEL model assisted the RRI model such as input and output data sets; (ii) GPU coding based on the NVIDIA CUDA was applied into the RRI model to accelerate the computed time, and (iii) the satellite data sets were implemented in flood simulation by using the RRI model. The VOXEL model as a 3D array was used to integrate the data sets in two groups, watershed data (DEM and Land cover) and rainfall data (spatial and temporal), for the input data, and the output data were runoff and inundation depth in spatial and temporal scale. Second, the GPU on NVIDIA CUDA coding could

made a speedup is about 2.6x on the complex terrain represented by the Nan river basin area, with two resolution size (500 m and 1,000 m). Finally, the RRI model was demonstrated by using the satellite data sets such as SRTM DEM (topography), GLCC (land cover), and TRMM (rainfall). This module presented the method for setup model parameter as Manning's coefficient of land cover surface, Green-Amp parameter of soil type, and dimension of river.

Research question 2: What are the effects of DEM sources on flood estimation?

Chapter 3 explored the investigation of DEM affect to accuracy, bias correction, and flood estimation, was assessed. The accuracy assessment was done by using the field observation data sets, referent elevation points, referent land cover map, and rain gauges. The accuracy of three variables evaluated a performance with statistical approach. The DEM data validated the accuracy only the Shikoku area where the GCPs points have been surveyed by the GPS. From six candidate DEMs were GSI-DEM, ASTER GDEM, SRTM, GMTED2010, HydroSHEDS, and GTOPO30, that the GSI-DEM was a high accuracy among the five DEMs. However, the high accuracy DEM was only provided in Japan, for the international open sources, the ASTER GDEM was the high accuracy. For DEM data sources, a spatial linear transformation was implemented to correct the elevation of the DEMs. The correction algorithm could improve the accuracy responding with the coarse resolution DEMs (HydroSHEDS and GTOPO30), while the high resolution (GSI-DEM, ASTER GDEM, SRTM, and GMTED2010) had a small sensitivity. The bias correction DEMs was investigated on the effect to estimate runoff and inundation area. Based on the DEM data and simulation results, Shikoku is the mountain complex terrain to contain with a steep slope, while Nan river basin is the mountain area where represent with the mild slope. In the Shikoku Island, ASTER DEM is suitable to apply for runoff simulation using distributed hydrologic modeling, have estimated from stereo matching. SRTM presented a performance for runoff and inundation simulation in the Nan river basin, have explored from radar laser scan with Shuttle.

Research question 3: What are the impacts of surface roughness based on different land cover sources on flood simulation results?

Chapter 4 investigated in the second variable of hydrologic model as the land cover data, MODIS and AVHRR land cover products were collected and evaluated for the both study areas. MODIS with MCD12Q1 outperformed the AVHRR products on the both sites. The satellite based land cover data sets were used to represent a surface roughness based on the Manning's coefficient that is the important parameter for runoff estimation. The Manning's coefficient produced from the MODIS data also showed higher performance than the AVHRR roughness products. The significant performance of satellite remote sensing data run by the GPU-RRI model is implemented in investigating the impact of corrected and estimated on satellite products sources. The evaluation of the different in runoff

results when using the three Manning's coefficient map from satellite and aerial observation in distributed hydrologic model as RRI model is involved. This investigation recommends the use of MODIS, AVHRR or other Manning's coefficient estimation approaches for large watersheds provide a reasonable estimate of Manning's coefficient for simulating runoff hydrographs. Manning's n coefficient based on the MODIS presented higher performance than the AVHRR that was evaluated by using runoff data estimated from the hydrological modeling.

Research question 4: What are the results from different rainfall sources driven by the Distributed Hydrological modeling?

Chapter 5 showed investigation of significant performances done by accuracy assessment of rainfall sources were assessed by three modules, (i) evaluating the best spatial interpolation algorithm for rain gauges, (ii) investigation the high performance of satellite rainfall products and (iii) correcting methodology of satellite rainfall. The rain gauge data sets as a point data were interpolated into grid data sets with five algorithms, Inverse Distance Weight (IDW), Thiessen Polygon (TSP), Simple Kriging (SKG), Ordinary Kriging (OKG), and Surface Polynomial (SPL). The IDW outperformed as high performance algorithm in the Shikoku area that represented with the dense rain gauge network area, while the sparse rain gauge network area was the Nan river basin that the SKG was suitable algorithm. According to considering in the situation of rain gauge network, the Shikoku Island is dense area of rain gauge data, while Nan river basin is a sparse rain gauge data. The IDW was also suitable method for interpolating from point to grid and simulating runoff on flood event, for the Shikoku area. In the Nan river basin, The SKG interpolated with semi-variogram model had performance to establish a rain gauge spatial distribution and estimate runoff with the GPU-RRI model. Satellite and simulation based rainfall data sets as GPV, GPM, GSMaP, TRMM, CMORPH and PERSIANN, evaluated the accuracy using the rain gauges data sets as point data. For the high resolution data, GSMaP showed the high accuracy for the Shikoku in Japan, while CMORPH outperformed among other sources in the Nan area in Thailand, on the international sources. According to specify in the Shikoku area, the GPV outperformed among the five remote sensing data, but it has been only provided in Japan. The hydrological model (RRI model) was driven for flood events that the different five rainfall spatial interpolation products were simulated on a temporal scale to match the observed streamflow data. For satellite based rainfall products, GPV and GSMaP in Japan and GPM in Thailand as the high resolution data showed a performance to simulate runoff on the hydrological modeling. For low resolution of satellite rainfall, TRMM presented high performance. Developing a bias correction method of satellite data sets to make more their accuracy was investigated. The bias correction method evaluated with five algorithms (Mean ratio, Geometrics transformation, Linear transformation, Data assimilation, and Quantile mapping) and two schemes (Temporal and Spatial), only GPM and TRMM in the Nan river basin, Thailand as the demonstration.

The temporal scheme had better suitable method than the spatial scheme in small different to compare with rain gauge data. The three algorithms (Linear, Geometrics, Data assimilation) showed the high performance among ten candidate algorithms, resulting in runoff products. The bias correction module has only demonstrated in the Nan river basin, spatial bias correction scheme is higher performance than Time series scheme. Bias correction with Data assimilation algorithm is suitable for supervised method, while an unsupervised method is Linear and Geometrics transformation algorithm.

Research question 5: What are the applications of flood modeling approaches for estimating floods to map flood hazard to analyze flood damage?

Chapter 6 presented the application of flood simulation have two main approaches: flood forecasting and flood risk assessment. The first approach, the river basin scale simulation is run as firstly that is uses to identify as the boundary condition of small area to reveal a high resolution results. The methodology of simulation in specific area to make more resolution of the results was the point for this approach to present a flood hazard map. The second approach based on small area results, the flood risk assessment consist hazard and vulnerability data. The high risk is identified as maximum hazard and vulnerability, but minimum on both data is low risk. The classification of risk level is modeled by the decision tree model to create the flood risk map. The streamflow for estimating the flood risk map was the main point of this approach.

7.3 Significant contributions and recommendations for future direction of this dissertation

The objectives of this dissertation research is to contribute the correction and evaluation of remote sensing sources for flood assessment through basin scales, and application of the model to demonstrate the approach of flood loss estimation method on small area. The dissertation is accomplished by (1) applying the distributed hydrological model as the Rainfall-Runoff-Inundation model that is a combination of rainfall-runoff processes and flood modeling, (2) exploring the accuracy, bias correction of DEM data set and evaluating flood simulation results from different topography sources, (3) exploring the accuracy of both approaches, satellite land cover data sources and surface roughness coefficient, and evaluating flood modeling results from different surface roughness data sets, (4) exploring the accuracy of rainfall sources, rain gauge spatial, satellite, and simulated products, investigating bias correction of the satellite rainfall product as a demonstration, and evaluating runoff simulation results from different rainfall sources, (5) applying of flood simulation model for water resource management in flood hazard mapping for flood damage cost estimation.

Summary finding of this dissertation from correcting satellite remote sensing data sets by providing increased accuracy performance on flood simulation, evaluating quantification of flood uncertainty,

and a understanding of flood forecasting and risk assessment. Significant contribution proposed in this thesis should contain in below.

The first contribution is VOXEL model and GPUs have the potential to assist the hydrological modeling for input and output data. The VOXEL model represented by the 3D array framework was used to contain the watershed and rainfall data sets for spatial and temporal scales. However, the VOXEL model of data sets cannot be directly input to the original RRI model. Therefore, this study developed the tool as linkage between VOXEL model of raw data sets and input format of the RRI model, with the Python language script. In the RRI model, the GPU parallel programing on the Compute Unified Data Architecture (CUDA) with NVIDIA ® Corporation was setup to develop new engine of RRI model. The new engine can help the CPU to reduce the computation time and increate a decision time of policy maker for flood forecasting.

The second contribution is that the accuracy of satellite data sets were revealed by using the field observation data based on statistical approach. DEM was evaluated by the referent elevation points based on the GCPs data. Their accuracy revealed that the high resolution have high accuracy while the low resolution have conversely. The DEM can be used to present the terrain morphology such as the slope and drainage network, based on the 8D algorithm. Satellite land cover data sets have been validated on accuracy by using the observed land cover map. The validation methodology used the pixel to pixel base comparison method. Finally, rainfall analysis has two approach, rain gauge spatial distribution and satellite rainfall evaluation. For the rain gauge spatial distribution, IDW have high performance on the Shikoku Island in Japan during the rainy season at 2014 where the terrain has been represented by the complex terrain and high slope zone, with high dense rain gauge network. In the Nan river basin in Thailand, the rain gauge network have been represented by the sparse points that the kriging algorithm based on the semi-variogram model showed the high performance in the mild slope terrain. On the satellite rainfall evaluation, GPM data set, high resolution data, showed the best accuracy on the both study area to evaluate among the international data sets. For the low resolution data sets, TRMM was the high performance.

The third contribution is bias corrections with transformation methods have efficiency to make more accurate precision values. This contribution is the main originality of this dissertation that the developed tools were proposed to modify the satellite data sets to close to the real data, for input to the flood modeling. DEMs were collected in several resolutions in range 10m to 1,000m and corrected by using spatial linear transformation algorithm. The bias correction algorithm can increase their accuracy in higher than the existing, which was more effect on the low resolution while the high resolution was conversely. In the correction approach on the land cover data, transformation methodology from the land cover type to surface roughness coefficient represented by the manning's n value was proposed. The transform algorithm used the lookup table linkage to the GIS technique for

making the surface roughness map based on each satellite source that the AVHRR have smoother than the MODIS. Finally, satellite rainfall bias correction, the two schemes, time series and spatial, combined with five algorithms, Mean ratio, Linear transformation, Geometrics transformation, Data assimilation, and Quantile mapping, were proposed for generating the new rainfall data sets, in the hypothesis as containing more accuracy.

The fourth contribution is satellite data sets applied to simulate and evaluated for flood estimation by using hydrologic model. This contribution presented the uncertainty of satellite data based on the runoff value estimation and evaluated the best source for simulating the flood model. For the Shikoku Island that have represented with the complex terrain; ASTER DEM, have been established from the stereo matching to make a point could, can be the high performance for estimation the runoff. SRTM DEM was observed from the radar laser scan with Shuttle, was the high performance in the Nan river basin represented by the mild slope area, evaluating with runoff and inundation area. MODIS land cover outperformed AVHRR land cover on the both study area, the two data sets of satellite land cover and observed land cover were used to simulate runoff in uncertainty. The uncertainty of runoff in the land cover was small effect in sensitivity. In the contrast to land cover accuracy assessment, the AVHRR showed higher performance than the MODIS. Rain gauge interpolations to spatial such as grid systematic have a several methodology that this thesis evaluated the five algorithms to find the best algorithm for estimating the runoff on the distributed hydrological modeling. The results revealed that IDW interpolation algorithm had suitable to the Shikoku Island to contain the high dense rain gauge networks. For the Nan river basin, the Kriging on simple systematic showed the high performance on the sparse rain gauge networks area. On the satellite sources evaluation, GPM presented the high performance on the both area in overall of international data, while the TRMM showed the high performance among the low resolution data sets. In case of the Shikoku Island, GPV have only provided in Japan on the highest resolution, presented its runoff to close to the observation. In bias correction of satellite data, the GPM and TRMM were selected for evaluation on the two schemes and five algorithms. Spatial scheme of bias correction presented higher performance than time series scheme to evaluate on estimated runoff. Geometrics and Linear transformation were represented by the one side bias correction methodology, can estimated the runoff to closed to the observation data on a pattern in temporal scale. However, Data assimilation also capture the runoff pattern as same as the observed data, was represented by the two side methodology of bias correction (supervise method).

The fifth contribution is hydrologic flood model with satellite data sets were implemented for flood forecasting and risk assessment as demonstration. The Nan river basin used the flood event in 2011 to simulate the results in high resolution data, while the Yoshino River in the Shikoku Island applied on a scenario based on the breaking dike. For the flood forecasting, the inundation modeling couple

rainfall-runoff (IMCR) was implemented for create a linkage between large area data and local area data such as a boundary condition to run on high resolution model in specific area. According to high resolution inundation map, the results from the flood forecasting were identified as water level classes to establish the flood hazard map. To reveal the flood risk map, the impotent point is the vulnerability that has been created by the economic data combined with the land cover types to represent in a spatial map. Next, the assessment of risk category can be estimated by the hazard and vulnerability level that has been represented in a matrix format. From the matrix of risk level, the risk map can be estimated by using the overlay between the hazard and vulnerability map. The methodology as mention in above that is one method for estimating the flood risk map.

Outcomes of this research are improved satellite remote sensing data sets by providing increased accuracy performance on flood simulation, improved quantification of flood uncertainty, and a understanding of flood forecasting and risk assessment. Future work covering this study should contain in a following.

In this study, the RRI model has recommended as distributed hydrological modeling and has modified to setup the GPU coding to accelerate the computation time. From the profiling of the RRI model coding, the slope subroutine has often called for computation and used a lot of time for simulation. Therefore, the key of GPU implementation has been done to specific in the slope routing mechanism based on the diffusive wave routing to solve with Range-Kutta method for mathematic modeling. The implementation of GPU can accelerated the computing time faster than the CPU about 2.6x in the complex terrain. Based on the limitation of GPU applied on the RRI model, the second subroutine has often called for computation is river routing module. To make more efficiency of the RRI model in computation time, the implementation of GPU in each module is the next generation of new RRI model. On GPU technology, the next generation of GPU implementation in hydrological modeling has more potential development in high level computer language and new hardware technology.

The land cover data sets, are the key point of hydrological modeling, have been used to input to the RRI model based on the Manning's coefficient. The effect of land cover sources was the key finding of the topic. However, the transforming from the land cover type to surface roughness based on the Manning's coefficient has only used a mean value to reveal as limitation of this study. By contract, the relationship between land cover type and the Manning's coefficient from the previous study have provided in range about maximum and minimum values. Therefore, the future direction of the topic will be done by using the other index such as vegetation index or backscatter to make more a precision of the Manning's coefficient values. In the other hand, the land cover evaluation is needed to confirm this observation for different watersheds and different method for estimating Manning's coefficient.

The original point of this dissertation has been specified in the bias correction with the transformation methodology. Finding a suitable correction tool, that was the key of this article. DEM bias correction has been done by the spatial linear transformation with the hypothesis in normal distribution based on the distortion in elevation axis. Also, the satellite rainfall bias correction with five algorithms has been based on the normal distribution but difference in the systematic. However, the rainfall corrections have suggested in the spatial scheme. Therefore, the future direction of bias correction studies should assess comparative advantage of complex algorithm in mathematics of bias correction techniques, and application in several sources.

The flood modeling as a simulation systematic has been represented about the first task before flood disaster mitigation is designed. The final objective of this dissertation has been presented about how to create the high resolution of inundation map in specific area and risk assessment as demonstration. The limitation of this approach was that the RRI model can be modeled as the natural flow and input some countermeasures such as dike along the river and boundary condition only in river channel. Therefore, the future direction for model the flood near to real situation, the RRI model need to establish the countermeasures modules such as dike in terrain (polder system), pumping station, and etc. For the risk assessment used two dimensions for validation, it is needed to include the frequency and temporal magnitude for assessing the flood risk map to make more accuracy of flood management.

References

Abbott, M. B., Bathurst, J. C., Cunge, J. A., O'Connell, P. E., Rasmussen, J., 1986. An introduction to the European Hydrological System – Systeme Hydrologique Europeen, 'SHE,' 2: Structure of a physically-based, distributed modeling system, Journal of Hydrology, 87(1-2), 61-77.

Abood, M. M., Yusuf, B., Mohammed, T. A., Ghazali, A. H., 2006. Manning roughness coefficient for grass-lined channel, Journal of Science and Technology, 13(4), 317-330.

Acharya, N., Chattopadhyay, S., Mohanty, U. C., Dasha, S. K., Sahooc, L. N., 2013. On the bias correction of general circulation model output for Indian summer Monsoon, J Meteorol Appl 20(3), 349–356.

Ajaaj, A. A., Mishra, A. K., Khan, A. A., 2015. Comparison of BIAS correction techniques for GPCC rainfall data in semi-arid climate, Stoch Environ Res Risk Assess 1, 1-17.

Akhtar, M. K., Corzo, G. A., Andel, S. J. van, Jonoski , A., 2009. River flow forecasting with artificial neural networks using satellite observed precipitation pre-processed with flow length and travel time information: case study of the Ganges river basin, Hydrol. Earth Syst. Sci. 13, 1607–1618.

Arcement, G. Schneider, V., 1990. Guide for selecting Manning's roughness coefficients for natural channels and flood plains, U. S. Geological Survey Water-Supply Paper 2339.

Arnaud, P., Bouvier, C., Cisner, L., Dominguez, R., 2002. Influence of rainfall spatial variability on flood prediction, J. Hydrol., 260, 216-230.

Artan, G., Gadain, H., Smith, J. L., Asante, K., Bandaragoda, C. J., Verdin, J. P., 2007. Adequacy of satellite derived rainfall data for stream flow modeling. Nat. Hazards 43, 167–185.

Asadullah, A, Mcintyre, N. E. I. L., Kigobe, M. A. X., 2010. Evaluation of five satellite products for estimation of rainfall over Uganda, Hydrolg. Sci. J., 53, 1137-1150.

ASTER GDEM Validation Team, 2012. ASTER Global DEM Validation Summary Report. Available online http://www.ersdac.or.jp. Accessed on 19 October 2012.

Azziz, A., 2014. Rainfall-Runoff Modeling of the Trans-Boundary Kabul River Basin Using Integrated Flood Analysis System (IFAS), Pakistan Journal of Meteorology 10 (20), 75-81.

Bedient, P. B., Huber, W. C., and Vieux, B. E., 2008. Hydrology and floodplain analysis, Prentice-Hall, New Jersey.

Behrangi, A., Khakbaz, B., Jaw, T. C., AghaKouchak, A., Hsu, K., Sorooshian, S., 2011. Hydrologic evaluation of satellite precipitation products over a mid-size basin. J. Hydrol. 397, 225–237.

Bell, V. A., Moore, R. J., 2000. The sensitivity of catchment runoff models to rainfall data at different spatial scales, Hydrol. Earth Syst. Sci., 4, 653-667.

Bindlish, R., Crow, W. T., Jackson, T. J., 2009. Role of Passive Microwave Remote Sensing in Improving Flood Forecasts, IEEE Geoscience and Remote Sensing Letters, 6, 112–116.

Bitew, M. M., Gebremichael, M., 2011. Assessment of satellite rainfall products for streamflow simulation in medium watersheds of the Ethiopian highlands. Hydrol. Earth Syst. Sci. 15, 1147–1155.

Blanco, P. D., Colditz, R. R., López Saldaña, G., Hardtke, L. A., Llamas, R. M., Mari, N. A., Fischer, A., Caride, C., Aceñolaza, P. G., del Valle, H. F., Lillo-Saavedra, M., Coronato, F., Opazo, S. A., Morelli, F., Anaya, J. A., Sione, W. F., Zamboni, P., Arroyo, V. B., 2013. A land cover map of Latin America and the Caribbean in the framework of the SERENA project, Remote Sens. Environ. 132, 13–31.

Boushaki, F. I., Hsu, K.-L., Sorooshian, S., Park, G.-H., Mahani, S., Shi, W., 2009. Bias adjustment of satellite precipitation estimation using ground-based measurement: A case study evaluation over the southwestern United States. J. Hydrometeorol. 10, 1231–1242.

References (continued)

Burian, S. J., Brown, M. J., McPherson, T. N., 2002. Evaluation of land use/land cover datasets for urban watershed modeling, Water Science and Technology, 45(9), 269-276.

Burnash, Robert J. C., Ferral, R. Larry, McGuire, Richard A., 1973. A generalized streamflow simulation system, conceptual modeling fordigital computers, National Weather Service and California Department of Water Resources.

Cai, Z., Roussas, G. G., 1998. Kaplan-Meier Estimator under Association, Journal of Multivariate Analysis 67, 318–348.

Carabajal, C. C., Harding, D. J., Jean-Paul, B., Danielson, J. J., Gesch, D. B.,Suchdeo, V. P., 2011. Evaluation of the Global Multi-Resolution Terrain Elevation Data 2010 (GMTED2010) using ICESat geodetic control, In Proceedings of SPIE-The international society for optical engineering, Nanjing, China.

Chang, K. T., 2006. Introduction to Geographic Information Systems, 3rd ed., New York, USA, McGrow-Hill, ch. 15, 295-317.

Chavoshian, A., Ishidaira, H., Takeuchi, K., Yoshitani, J., 2007. Hydrological Modeling of Large-scale Ungauged Basin Case Study: Ayeyarwady (Irrawaddy) Basin, Myanmar, Paper presented at the HRSD 2007 conference in conjunction with the 15th Regional Steering Committee for UNESCO-IHE Southeast Asia and The Pacific.

Chen, C., Yu, Z., Li, L., and Yang, C., 2011. Adaptability Evaluation of TRMM Satellite Rainfall and Its Application in the Dongjiang River Basin, Proced. Environ. Sci. 10, 396–402.

Chiang, Y. M., Hsu, K. L., Chang, F. J., Hong, Y., Sorooshian, S., 2007. Merging multiple precipitation sources for flash flood forecasting, J. Hydrol. 340, 183–196.

Chiles, J. P., Delfiner, P., 1999. Geostatistics: Modeling Spatial Uncertainty, 1st ed., New York, Wiley Interscience.

Chintalapudi, S., Sharif, H. O., Yeggina, S., Elhassan, A., 2012. Physically-based, hydrologic model results based on three precipitation products, J. Am. Water Resour. Assoc. JAWRA, 48, 1191-1203.

Chintalapudi, S., Sharif, H. O., Yeggina, S., Elhassan, A., 2012. Physically-based, hydrologic model results based on three precipitation products, J. Am. Water Resour. Assoc. JAWRA, 48, 1191-1203.

Chowdhury, J. U. & Karim, M. F. (1997) A risk based zoning of storm surge prone area of the Ganges tidal plain. UNCRD Proceeding Series 17(2), 171–185.

Clark, M. L., Aide, T. M., Grau, H. R., Riner, G., 2010. A scalable approach to mapping annual land cover at 250m using MODIS time series data: A case study in the Dry Chaco ecoregion of South America, Remote Sens. Environ., 114, 2816–2832.

Conesa-Garcia, C., Caselles-Miralles, V., Sanchez Tomas, J.M., Garcia-Lorenzo, R., 2010. Hydraulic Geometry, GIS and Remote Sensing, Techniques against Rainfall-Runoff Models for Estimating Flood Magnitude in Ephemeral Fluvial Systems, Remote Sensing 2, 2607–2628.

Cosgrove, W. J., Rijsberman, F. R., 2000. World Water vision, Earthscan Publication Ltd, London, UK.

Crawford, N. H., Linsley, Jr., R. K., 1966. Digital simulation in hydrology: Stanford watershed model IV. Technical Report No. 39, Department of Civil Engineering, Stanford University, Stanford, California, USA.

Cressie, N., 1991. Statistics for spatial data, Wiley, New York, pp. 900.

References (continued)

Danielson, J. J., Gesch, D. B., 2011. Global Multi-Resolution Terrain Elevation Data 2010 (GMTED2010), U.S. Geological Survey Open-File Report, U.S. Geological Survey: Sioux Falls, SD, USA.

Das, A., 2004. Parameter estimation in flow in open-channel networks, Journal of Irrigation and Drainage Engineering, 130(2), 160-165.

De Roo, A. P. J., Van Der Knijff, J. Schmuck, G., Bates, P., 2000. A simple floodplain inundation model to assist in floodplain management, Journal of Hydrology, 236, 54-77.

Dickinson, R. E., Henderson-Sellers, A., Kennedy, P. J., 1993. Biosphere Atmosphere Transfer Scheme (BATS), Version le as Coupled to the NCAR Community Climate Model, NCAR Technical Note, NCAR, Boulder, Colorado.

Dinku, T., Ruiz, F., Connor, S. J., Ceccato, P., 2010. Validation and intercomparison of satellite rainfall estimates over Colombia, J. Appl. Meteorol. Climatol., 49, 1004-1014.

Djamel, A., Achour, H., 2014. External validation of the ASTER GDEM2, GMTED2010 and CGIAR-CSI-SRTM v4.1 free access digital elevation models (DEMs) in Tunisia and Algeria, Remote sens, 6, 4600-4620.

Dutta, D., Herath, S., Musiake, K., 2003. A mathematical model for flood loss estimation. Journal of Hydrology 277, 24-49.

Dutta, D., Herath, S., 2003. Urban flood risk analysis using distributed mathematical model: a case study in Yom River basin, Thailand. J. Inst. Indust. Sci., Univ. Tokyo 55(2), 88–91.

ESCAP (Economic and Social Commission for Asia and the Pacific), 1991. Manual and Guidelines for Comprehensive Flood Loss Prevention and Management. ST/ESCAP/933, ESCAP,Bangkok, Thailand.

Feldman, A. D., 1981. HEC models for water resources system simulation: Theory and experience, Advances in Hydrosciences, 12, 297-423.

Ferguson, B. K., 1998. Introduction to Stormwater, Concept, Purpose and Design, 111, John Wiley & Sons, Inc. USA.

Finn, M. P., Usery E, L. , Scheidt, D. J. , Beard, T., Ruhl, S., Bearden, M., 2002. AGNPS Watershed Modeling with GIS Databases, Proceedings of 2nd Federal Interagency Hydrologic Modeling Conference, Las Vegas, NV.

Fisher, P. F., Tate, N. J., 2006. Causes and consequences of error in digital elevation models, Prog. Phys. Geogr., 30, 467-489.

Forkuor, G., Maathuis, B., 2012. Comparison of SRTM and ASTER Derived Digital Elevation Models over Two Regions in Ghana Implications for Hydrological and Environmental Modeling, In Studies on Environmental and Applied Geomorphology, Piacentini, T., Ed., InTech: Rijeka, Croatia, pp. 219-240.

Förster, S., Kuhlmann, B., Lindenschmidt, K.-E., and Bronstert, A., 2008. Assessing flood risk for a rural detention area. Nat. Hazards Earth Syst. Sci. 8, 311-322.

Fraser, C. S., Baltsavias, E., Gruen, A., 2002. Processing of IKONOS imagery for submeter 3D positioning and building extraction, ISPRS Journal of Photogrammetry & Remote Sensing, 56, 177-194.

Freund, Y., Schapire, R. E.,1997. A decision-theoretic generalization of on-line learning and an application to boosting. Journal of Computer and System Sciences, 55, pp. 119–139.

References (continued)

Friedl, M. A., Sulla-Menashe, D., Tan, B., Schneider, A., Ramankutty, N., Sibley, A., and Huang, X., 2010. MODIS Collection 5 global land cover: Algorithm refinements and characterization of new datasets, Remote Sens. Environ. 114, 168–182.

Garcia, M. J. L., Camarasa, A. M., 1999. Use of Geomorphological units to Improve drainage Network Extraction from a DEM, JAG Journal, 1 (3/4), 187-195.

Gebremichael, M., Krajewski, W., 2004. Characterization of the temporal sampling error in space-time averaged rainfall estimates from satellites, JOURNAL OF GEOPHYSICAL RESEARCH 109, 1-16.

Gervin, J. C., Kerber, A. G., Witt, R. G., Lu, Y. C., Sekhon, R., 1985. Comparison of level I land cover classification accuracy for MSS and AVHRR data, International Journal of Remote Sensing 6, 47-57.

Gioia, G., Bombardelli, F. A., 2002. Scaling and similarity in rough channel flows, Physics Review Letters, 88(1), 014501/1-4.

Gonga-Saholiariliva, N., Gunnell, Y., Petit, C., Mering, C., 2011. Techniques for quantifying the accuracy of gridded elevation models and for mapping uncertainty in digital terrain analysis, Prog. Phys. Geogr., 35, 739–764.

Goodrich, D. C., Faures, J. M., Woolhiser, D. A., Lane, L. J., Sorooshain, 1995. Measurements and analysis of small-scale convective storm rainfall variability, J. Hydrol., 173, 283-308.

Goovaerts, P., 2000. Geostatistical approaches for incorporating elevation into the spatial interpolation of rainfall, J. Hydrol., 228, 113-129.

Guth, P. L., 2006. Geomorphometry from SRTM-comparison to NED, Photogrammetric Engineering & Remote Sensing, 72 (3), 269-277.

Haan, C. T., 1982. Hydrological Modelling of Small Watersheds, 211, Published by American Society of Agricultural Engineers, USA.

Habib, E, Haile, A. T., Sazib, N., Zhang, Y., Rientjes, T., 2014. Effect of bias correction of satellite-rainfall estimates on runoff simulation as the source of the Upper Blue Nile, remote sensing, 6(7), 6688-6708.

Hagen, T. R., Hjelmervik, J. M., Lie, K. A., Natvig, J. R., Henriksen, M. O., 2005. Visual simulation of shallow-water waves, Simulation Modelling and Practice and Theory, 13, 716-726.

Harris, A., Rahman, S., Hossain, F., Yarborough, L., Bagtzoglou, A. C., Easson, G., 2007. Satellite-based Flood Modeling Using TRMM-based Rainfall Products, sensors 7(12), 3416-3427.

Harris, M. J., Coombe, G., Scheuermann, T., Lastra, A., 2002. Physically-based visual simulation on graphics hardware, Proceedings of the SIGGRAPH/Eurographics Workshop on Graphics Hardware, 109-118.

Hirabayashi, Y., Mahendran, R., Koirala, S., Konoshima, L., Yamazaki, D., Watanabe, S., Kim, H., Kanae, S., 2013. Global flood risk under climate change, NATURE CLIMATE CHANGE LETTER 3, 816-821.

Hokr, M., Marysk, J., Sotner, O., 2003. Problems and modeling in forecasting of floods, Proceedings of SIMONA, Hokr, M., and Sembera, J., Ed., Technical University of Libercec, 37-46.

Holmes, K. W., Chadwick, O. A., Kyriankidis, P. C., 2000. Error in USGS 30-meter digital elevation model and its impact on terrain modeling, Journal of Hydrology, 233, 154-173.

Hong, Y., Hsu, K., Moradkhani, H., Sorooshian, S., 2006. Uncertainty quantification of satellite precipitation estimation and Monte Carlo assessment of the error propagation into hydrologic response, Water Resour. Res. 42.

References (continued)

Hong, Y., Hsu, K. L., Sorooshian, S., Gao, X. G., Precipitation estimation from remotely sensed imagery using an artificial neural network cloud classification system, J. Appl. Meteorol., 43, 1834-1852.

Hornberger, G. M., Boyer, E. W., 1995. Recent advances in watershed modeling, In Pielke, R. A. Sr., and Vogel, R. M., (eds) U.S. National Report to International Union of Geodesy and Geophysics 1991-1994: Contributions in Hydrology, Washington DC. American Geophysical Union, 949-957.

Horritt, M. S., Bates, P. D., 2001. Predicting floodplain inundation: raster-based modelling versus the finite-element approach, Hydrological Processes 15 (5), 825–842.

Huber, W. C., Dickinson, R. E., 1988. Storm Water Management Model User's Manual Version IV, EPA-600/3-88-001a (NTIS-PB88-236641/AS), Environmental Protection Agency, Athens, Georgia.

Huber, W. C., 1995. Chapter 22: EPA storm water management model SWMM, Computer models of watershed hydrology, Singh, V. P., ed., Water Resources Publications, Littleton, CO.

Huffman, G. J., Adler, R. F., Bolvin, D. T., Gu, G. J., Nelkin, E. J., Bowman, K. P., Hong, Y., Stocker, E. F., Wolff, D. B., 2007. The TRMM multisatellite precipitation analysis (TMPA).Quasi-global, multiyear, combined-sensor precipitation estimates at fine scales, J. Hydrometeorol. 8, 38–55.

Ines, A. V. M. , Hansen, J. W., 2006. Bias correction of daily GCM rainfall for crop simulation studies, J Agric For Meteorol 138, 44–53.

Ishida, K., Takagi, M., 2010. Change detection of surface elevation by ALOS/PRISM for disaster monitoring, In Proceedings of ISPRS 38th, Kyoto, Japan.

Jain, M. K., Kothyari, U. C., Raju, K. G. R., 2004. A GIS based distributed rainfall-runoff model, Journal of Hydrology, 299, 107-135.

Jarvis, A., Reuter, H. I., Nelson, A., Guevara. E., 2012. Hole-Filled SRTM for the Globe Version 4. CGIAR-CSI SRTM 90 m Database 2008, Available online http://srtm.csi.cgiar.org, Accessed on 1 July 2012.

Jason, S., Edward, B., 2006. Influence of Vegetation, Slope, and Lidar Sampling Angle on DEM Accuracy, Photogrammetric Engineering & Remote Sensing 72 (11), 1265–1274.

Jenson, S .K., Domingue, J. O., 1988. Extracting topographic structures from digital elevation data from geographic information system analysis, Photogrammetric Engineering and Remote Sensing 54, 1593-1600.

Jiang, S., Ren, L., Yong, B., Yang, X., Shi, L., 2010. Evaluation of high-resolution satellite precipitation products with surface rain gauge observations from Laohahe Basin in northern China, Water Science and Engineering, 3 (4), 405-417.

Jin, M., Fread, D. L., 1997. Dynamic flood routing with explicit and implicit numerical solution schemes, Journal of Hydraulic Engineering 123(3), 166-173.

Joyce, R. L., Janowiak, J. E., Arkin, P. A., Xie, P., 2004. CMORPH: A method that produces global preipitaion estimates from passive microwave and infrared data at high spatial and temporal resolution, J. Hydrometeorol., 5, 487-503.

Justice, C. O., Townshend, J. R. G., Vermote, E. F., Masuoka, E., Wolfe, R. E., Saleous, N., Roy, D. P., & Morisette, J. T., 2002. An overview of MODIS land data processing and product status, Remote Sensing of Environment, 83, 244 – 262.

Kalyanapu, A. J., Burian, S. J., McPherson, T. N., 2009. Effect of land use-based surface roughness on hydrologic model output, Journal of Spatial Hydrology 9(2), 51-71.

References (continued)

Kayanapu, A. J., Shankar, S., Pardyjak, E. R., Judi, D. R., Burian, S. J., 2011. Assessment of GPU computational enhancement to a 2D flood model, Environmental Modelling & Software 26(8), 1009-1016.

Khan, S. I., Hong, Y., Wang, J., Yilmaz, K. K., Gourley, J. J., Adler, R. F., Brakenridge, G. R., Policelli, F. P., Habbib, S., Irwin, D., 2011. Satellite Remote Sensing and Hydrologic Modeling for Flood Inundation Mapping in Lake Victoria Basin: Implications for Hydrologic Prediction in Ungauged Basins, IEEE TRANSACTIONS ON GEOSCIENCE AND REMOTE SENSING 49, 85-95.

Kharin, V. V., Zwiers, F. W., 2002. Notes and correspondence climate predictions with multimodel ensembles. J Clim 15, 793–799.

Kidd, C., Bauer, P., Turk, J., Huffman, G. J., Joyce, R., Hsu, K. L., Braithwaite, D., 2012. Intercomparison of high-resolution precipitation products over northern Europe, J. Hydrometeol., 13, 67-83.

Kidson, R. L., Richards, K. S., Carling, P. A., 2006. Hydraulic model calibration for extreme floods in bedrock-confined channels: case study from northern Thailand, Hydrological Processes 20(2), 329-344.

Kimaro, T. A., Tachikawa, Y., Takara, K., 2005. Distributed hydrologic simulations to analyze the impacts of land use changes on flood characteristics in the Yasu River basin in Japan, Journa; of Natural Disaster Science 27(2), 85-94.

Klein, I., Gessner, U., Kuenzer, C., 2012. Regional land cover mapping and change detection in Central Asia using MODIS time-series, Appl. Geogr., 35, 219–234.

Kolecka, N., Kozak, J., 2013. Assessment of the accuracy of SRTM C- and X-Band high mountain elevation data: A case study of the Polish Tatra Mountains, Pure Appl. Geophys., 171, 897-912.

Krakauer, N. Y., Pradhanang, S. M., Lakhankar, T., Jha, A. K., 2013. Evaluating satellite products for precipitation estimation in mountain regions: A case study for Nepal. Remote Sens. 5,4107–4123.

Krishnamurti, T. N., Kishtawal, C. M., Shin, D. W., Williford, C. E., 2000. Multi-model superensemble forecasts for weather and seasonal climate. J Climat 13, 4196–4216.

Kubota, T., Ushio, T., Shige, S., Kida, S., Kachi, M., Okamoto, K., 2009. Verification of high resolution satellite-based rainfall estimates around Japan using a gauge calibrated ground radar data set, Journal of the Meteorological Society of Japan, 87A, 203-222.

Kuriakose, E., Viswan, A., 2013. Remote sensing image matching using sift and a transformation, International Journal of Computer Applications, 80, 22-27.

Kuriakose, E., Viswan, A., 2013. Remote Sensing Image Matching using Sift And Affine Transformation, IJCA Journal 80(14), 22-27.

Lakshmi, V., 2004. The role of satellite remote sensing in the Prediction of Ungauged Basins, Hydrol Process 18, 1029–1034.

Lamb, R., Crossley, A., Waller, S., 2009. A fast two-dimensional flood inundation model. Proceedings of the Institute of Civil Engineers – Water Management 162(6), 363-370.

Lee, G. , Kim, S., Jung, K., Tachikawa, Y., 2011. Development of a large basin rainfall-runoff modeling system using the object-oriented hydrologic modeling system (OHyMoS), KSCE Journal of Civil Engineering 15 (3), 595-606.

Lee, S. J., Komatitsch, D., Huang, B., Tromp, J., 2009. Effect of topography on seismic-wave propagation: an example from north Taiwan, Bull. Seismol. Soc. Am., 99, 314-325.

References (continued)

Lee, S., Park, S, 2008. A Vegetated Urban Canopy Model for Meteorological and Environmental Modelling, Boundary-Layer Meteorol 126, 73–102.

Lehner, B., 2013. Quality assessment In HydroSHEDS Technical documentation, 1st ed. World Wildlife Fund US: Washington DC, USA, pp 1314.

Li, J., Chapman, M. A., Sun, X., 2006. Validation of satellite-derived digital elevation model from in-track IKONOS stereo imagery, Toronto, Ontario Ministry of Transportation.

Li, S., Sun, D., Golgberg, M., Stefanidis, A., 2013. Derivation of 30-m-resolution water maps from TERRA/MODIS and SRTM, Remote Sensing of Environment 134, 417-430.

Liang Q, Smith L, 2015. A high-performance integrated hydrodynamic modelling system for urban flood simulation, J Hydroin-formatic 17, 518-533.

Limerinos, J. T., 1970. Determination of the Manning coefficient from measured bed roughness in natural channels, U. S. Geological Survey Water-Supply Paper, 1898-B, 47.

Lloyd, C. D., 2005. Assessing the effect of integrating elevation data into the estimation of monthly precipitation in Great Britain, J. Hydrol., 308, 128-150.

Lohmann, D., Mitchell, K., Houser, P., Wood, E.F., Schaake, J., Robock, A., Cosgrove, B., Sheffield, J., Duan, Q., Luo, L., Higgins, R., Pinker, R., Tarpley, J., 2004. Streamflow and water balance intercomparisons of four land surface models in the North American Land Data Assimilation System project, Journal of Geophysical Research-Atmosphere 109, D07S9.

Lull, H. W., 1964. Ecological and silvicultural aspects, Handbook of applied hydrology, ed., Ven Te Chow, 6.1-6.30, McGraw-Hill, New York.

Ly, S., Charles, D., Degre, A., 2011. Geostatistical interporation of daily rainfall at catchment scale: the use of several variogram models in the Ourthe and Ambleve catchments, Belgium, Hydrol. Earth Syst. Sci., 15, 2259-2274.

Makino, S., 2012. Verification of the accuracy of rainfall data by global satellite mapping of precipitation (GSMaP) product, Yamaguchi University Thesis.

Manning, R., 1891. On the flow of water in open channels and pipes, Transactions on the Institution of Civil Engineers of Ireland.

Manz, B., Buytaert, W., Zulkafli, Z., Lavado, W., Willems, B., Robles, L. A., Rodriguez-Sanchez, J., 2016. High-resolution satellite-gauge merged precipitation climatologies of the Tropical Andes, JGR 121(3), 1190-1207.

Marcus, A. W., Roberts, K., Harvey, L., Tackman, G., 1992. An evaluation of methods for estimating Manning's n in small mountain streams, Mountain Research and Development, 12(3), 227-239.

Martz, L. W., Jong, D. E., 1988. CATCH: a FORTRAN program for measuring catchment area from digital elevation models, Computer & Geosciences, 14, 627-640.

Mason, D. C., Horrit, M. S., Dall'Amico, J. T., Scott, T. R., and Bates, P. D., 2007. Improving River Flood Extent Delineation From Synthetic Aperture Radar Using Airborne Laser Altimetry, IEEE T. Geosci. Remote, 45, 3932–3943.

Metcalf and Eddy, Inc., University of Florida, and Water Resources Engineers Inc., 1971. Storm Water Management Model, Version I, EPA-1102DOC07/71, Environmental Protection Agency, Washington, District of Columbia.

MetEd, 2015. In. https://www.meted.ucar.edu/training_module.php?id=207#.V1jlwvmLRhE.

Mohamad, A. M., Kavian, A., 2015. Effects of rainfall patterns on runoff and soil erosion in field plots, International Soil and Water Conservation Research 3, 273–281.

References (continued)

Mukherjee, S., Joshi, P. K., Mukherjee, S., Ghosh, A., Garg, R. D., Mukhopadhyay, A., 2013. Evaluation of vertical accuracy of open source Digital Elevation Model (DEM). International Journal of Applied Earth Observation and Geoinformation, 21, 205-217.

Muller, M. F., Thompson, S. E., 2013. Bias adjustment of satellite rainfall data through stochastic modeling: Methods development and application to Nepal, Advances in Water Resources 60, 121-134.

Nalder, I. A., Wein, R. W., 1998. Spatial interpolation of climatic Normals: test of a new method in the Canadian boreal forest, Agric. For. Meteorol., 92, 211-225.

Nawaratha, N. B., Ao, T., Kazama, S., Sawamoto, M., Takeuchi, K., 2000. Influence of human activities on the BTOPMC runoff simulations in large-scale, XXIX IAHR Congress Proceeding, Theme a, 93-99.

Nikolakopoulos, K. G., Kamaratakis, E. K., Chrysoulakis, N., 2006. SRTM vs. ASTER elevation products comparison for two regions in Crete, Greece, Int. J. Remote Sens., 27, 4819-4838.

NSWG (New South Wales Government), 1986. Flood plain development manual. PWD 86010, NSWG, Australia.

O'Callaghan, J., D. Mark, The extraction of drainage networks from digital elevation data, Comput. Vision Graphics Process., 28, 323-344.

Pakoksung, K., Takagi, M., 2015. Remote sensing data application for flood mideling, JAST 26, 115-122.

Pakoksung, K., Takagi, M., 2015. Digital elevation models on accuracy validation and bias correction in vertical, Modeling Earth Systems and Environmant 2(11), 1-13.

Paniconi, C., Kleinfeldt, S., Deckmyn, J., Giacomelli, A., 1999. Integrating GIS and data visualization tools for distributed hydrologic modeling, Transactions in GIS, 3(2), 97-118.

Philips, J. V., Tadayon, S., 2006. Selection of Manning's roughness coefficient for natural and constructed vegetated and non-vegetated channels, and vegetation maintenance plan guidelines for vegetated channels in central Arizona, U. S. Geological Survey, Science Investigations Report, 5108.

Piani, C., Haerter, J., Coppola, E., 2010. Statistical bias correction for daily precipitation in regional climate models over Europe. Theor Appl Climatol 99, 187–192.

Picado, A., Lopes, C.L., Mendes, R., Vas, N., Dias, J.M., 2013. Storm surge impact in the hydrodynamics of tidal lagoon: the case of Ria de Aveiro, Journal of Coastal Research, Special Issue, 796–801.

Pistrika, A., 2010. Flood Damage Estimation based on Flood Simulation Scenarios and a GIS Platform. European Water; 30: 3-11.

Pulighe, G., Fava, F., 2013. DEM extraction from archive aerial photos: Accuracy assessment in areas of complex topography, Eur., J. Remote Sens, 46, 363-378.

Qin, Y., Chen, Z., Shen, Y., Zhang, S., Shi, R., 2014. Evaluation of satellite rainfall estimates over the Chinese mainland, remote sensing, 6, 11649-11672.

Reichle, R. H., 2008. Data assimilation methods in the Earth sciences, Advances in Water Resources 31, 1411–1418.

Rexer, M., Hirt, C., 2014. Comparison of free high resolution digital elevation data sets (ASTER GDEM2, SRTM v2.1/v4.1) and validation against accurate heights from the Australian National Gravity Database, Aust. J. Earth Sci., 61, 213-226.

Rowe, L.K., 1983. Rainfall interception by an evergreen beech forest, J. Hydrol 66, 143-158.

References (continued)

Saito, K., Fujita, T., Yamada, Y., Ishida, J., Kumagai, Y., Aranami, K., Ohmori, S., Nagasawa, R., Kumagai, S., Muroi, C., Kato, T., Eito, H., Yamazaki, Y., 2006. He operational JMA nonhydrostatic mesoscale model, MONTHLY WEATHER REVIEW 134, 1266-1298.

Sayama, T., Tatebe, Y., Iwami, Y., Tanaka, S., 2015. Hydrologic sensitivity of flood runoff and inundation: 2011 Thailand floods in the Chao Phraya River basin, Nat. Hazards Earth Syst. Sci. 15, 1617-1630.

Sayama, T., Ozawa, G., Kawakami, K., Nabesaka, S., Fukami, K., 2012. Rainfall-Runoff-Inundation Analysis of Pakistan Flood 2010 at the Kabul River Basin, Hydrological Sciences Journal, Hydrological Sciences Journal 57(2), 298-312.

Schneider, T., Bischoff, T., Hang, G.H., 2014. Migrations and dynamics of the intertropical convergence zone, NATURE 513, 45–53.

Schultz, G., 1996. Remote sensing applications to hydrology: runoff, Hydrological Sciences Journal/Journal des Sciences 41 (4).

Schuurmans, J. M., Bierkens, M. F. P., 2007. Effect of spatial distribution of daily rainfall on interior catchment reponse of a distributed hydrological model, Hydrol. Earth Syst. Sci., 11, 677-693.

Sellin, R. H. J., Bryant, T. B., Loveless, J. H., 2003. An improved method for roughening floodplains on physical river models, Journal of Hydraulic Research, 41(1), 3-14.

Seo, D. J., Breidenbach, J., 2002. Real-time correction of spatially nonuniform bias in radar rainfall data using rain gauge measurements. J. Hydrometeorol. 3, 93–111.

Seo, D. J., Briedenbach, J.P., Johnson, E.R., 1999. Real-time estimation of mean field bias in radar rainfall data. J. Hydrol. 223, 131–147.

Seto, S., 2009. An evaluation of overland rain rate estimates by the GSMaP and GPROF Algorithm: the role of lower frequency channels, Journal of the Meteorological Society of Japan, 87A, 183-202

Shao, Y., Lunetta, R. S., 2012. Comparison of support vector machine, neural network, and CART algorithms for the land-cover classification using limited training data points, ISPRS J. Photogramm. Remote Sens., 70, 78–87.

Sharifi, E., Steinacker, R., Saghafian, B., 2016. Assessment of GPM-IMERG and Other Precipitation Products against Gauge Data under Different Topographic and Climatic Conditions in Iran: Preliminary Results, remote sensing 8(2), 1-24.

Shretha, V., Takara, K., Kubota, T., Bajracharya, S. R., 2011. Verification of GSmaP rainfall estimates over the central Himalayas, Hydraulic Engineering, 67(4), 137-142.

Singh, V. P., Woolhiser, D. A., 2002. Mathematical modeling of watershed hydrology, Journal of Hydrologic Engineering, 7(4), 270-292.

Sohn, B. J., Han, H. J., Seo, E. K., 2009. Validation of satellite-based high-resolution rainfall products over the Korean Peninsula using data from a dense rain gauge network, J. Appl. Meteorol. Climatol., 49, 701-714.

Sorooshian, S., Hau, K., Braithwaite, D., Ashouri, H., 2014. NOAA Climate Data Record (CDR) of Precipitation Estimation from Remotely Sensed Information Using Artificial Neural Networks (PERSIANN-CDR), Version 1 Revision 1, NOAA National Climatic Data Center, Asheville, NC, USA.

Sriariyawat, A., Pakoksung, P., Sayama, T., Koomtanakulvong, S., 2013. Approach to Estimate the Flood Damage in Sukhothai Province Using Flood Simulation, Journal of Disaster Research 8(3), 406-414.

<center>**References (continued)**</center>

Stevens, G. T., Mueller, D. S., Strauser, C. N., 1983. A new approach to the elusive Manning's n., Proceedings of the Conference on Rivers: River Meandering, New Orleans, 586-597.

Sulla-Menashe, D., Friedl, M. A., Krankina, O. N., Baccini, A., Woodcock, C. E., Sibley, A., Sun, G., Kharuk, V., Elsakov, V., 2011. Hierarchical mapping of Northern Eurasian land cover using MODIS data, Remote Sens. Environ., 115, 392–403.

Suwandana, E., Kawamura, K., Sakuno; Y., Kustiyanto, E., Raharjo, B., 2010. Evaluation of ASTER GDEM2 in comparison with GDEM1, SRTM DEM and topographic-map-derived DEM using inundation area analysis and RTK-dGPS data, Remote Sens., 4, 2419-2431.

Tabios, G. Q., Salas, J. D., 1985. A comparative analysis of techniques for spatial interpolation of precipitation, Water Resour. Bull., 21, 265-380.

Tachikawa, T., Kaku, M., Iwasaki, A., 2011. In ASTER GDEM Version 2 Validation Report, pp. A1A24. 2nd ed, Japan.

Tan, M .L., Ibrahim, A. L., Duan, Z., Cracknell, A. P., Chaplot, V., 2015. Evaluation of six high-resolution satellite and ground-based precipitation products over malayia, Remote Sensing, 7, 1504-1528.

Tang, G., Ma, Y., Long, D., Zhong, L., Hong, Y., 2016. Evaluation of GPM Day-1 IMERG and TMPA Version-7 legacy products over Mainland China at multiple spatiotemporal scales. J. Hydrol. 533, 152–167.

Tayfur, G., Kavvas, M. L., Govidaraju, R. S., Storm, D. E., 1993. Applicability of St. Venant equations for two-dimensional overland flows over rough infiltrating surfaces. Journal of Hydraulic Engineering 119(1), 51-63.

Teegavarapu, R., Chandramouli, V., 2005. Improved weighting methods, deterministic and stochastic data-driven models for estimation of missing precipitation records, J. Hydrol., 312, 191-206.

Thieken, A. H., Ackermann, V., Elmer, F., Kreibich, H., Kuhlmann, B., Kunert, U., Maidwald, H., Merz, B., Muller, M., Piroth, K., Schwarz, J., Schwarze, R., Seifert, I., Seifert, J., 2008. Methods for the evaluation of direct and indirect flood losses. 4th International Symposium on Flood Defence, Toronto, Ontario, Canada, May 6-8.

Tian, Y., Peters-Lidard, C. D., Eylander, J. B., 2010. Real-time bias reduction for satellite-based precipitation estimates, J. Hydrometeorol. 11, 1275–1285.

Tingsanchali, T., Karim, F., 2010. Flood-hazard assessment and risk-based zoning of a tropical flood plain: case study of the Yom River, Thailand, Hydrological Sciences Journal 55(2), 145-161.

Tobin, K. J., Bennett, M. E., 2010. Adjusting satellite precipitation data to facilitate hydrologic modeling. J. Hydrometeorol. 11, 966–978.

Townshend, J. R. G., Justice, C.O., 1988. Selecting the spatial resolution of satellite sensors required for global monitoring of land transformations, International Journal of Remote Sensing, 9, 187-236.

Townshend, J. R. G., Justice, C. O., 2002. Towards operational monitoring of terrestrial systems by moderate-resolution remote sensing. Remote Sensing of Environment, 83, 352-360.

Tsihrintzis, V. A., 2001. Discussion on Variation of roughness coefficients for unsubmerged and submerged vegetation, Journal of Hydraulic Engineering, 127(3), 241-244.

Tsintikidis, D., Georgakakos, K. P., Sperfslage, J. A., Smith, D. E., Carpenter, T. M., 2002. Precipitation uncertainty and rain gauge network design within Folsom Lake watershed, J. Hydrol. Eng., 7, 175-184.

References (continued)

U. S. Executive Office of the President (USEOP), Interagency Floodplain Management Review Committee. 1994. Sharing the Challenge: Floodplain management ino the 21st Century. Washington D.C.: GPO.

Uda, K., Takagi, M., 2010. Suitable type of GCP for accuracy registration of high resolution satellite data, In Proceedings of the 31th Asian Conference on Remote Sensing, Hanoi, Vietnam.

Ugarte, A., Madrid, M., 1994. Roughness coefficient in mountain rivers, Proceedings of the National Conference of Hydraulic Engineering, Buffalo, NY, pp. 652-656.

UNDRO, 1991. Mitigating Natural Disasters; Phenomena, Effects and Options, United Nations Publication, UNDRO/MND/1990 Manual, Geneva, Switzerland.

USGS Data sources of HydroSHEDS, 2008. Available online http://hydrodheds.cr.usgs.gov/datasource, Accessed on 31 January 2008.

USGS GTOPO30, 2008. Available online http://lta.cr.usgs.gov/GTOPO30, Accessed on January 2015.

Ven T. Chow, David R. Maidment, Larry W. Mays, 1988. Applied Hydrology, McGraw Hill International Editions, New York. 6th ed.

Vera, T., Rojas, R., Zambrano-Bigiarini, M., Levizzani, V., de Roo, A., 2012. Validation of satellite-based precipitation products over sparsely gauged frican river basins, J. Hydrometeor. 13, 1760-1783.

Vernimmen, R. R. E., Hooijer, A., Mamenun, Aldrian, E., van Dijk, A. I. J., 2012. Evaluation and bias correction of satellite rainfall data for drought monitoring in Indonesia, Hydrol. Earth Syst. Sci., 16, 133-146.

Vieux, B. E., 2001. Distributed hydrologic modeling using GIS, Kluwer Academic Publishers, Dordrecht, The Netherlands.

Vila, D.A., de Goncalves, L.G.G., Toll, D.L., Rozante, J., 2009. Statistical evaluation of combined daily gauge observations and rainfall satellite estimates over continental South America. J. Hydrometeorol. 10, 533–543.

Vozinaki, A.-E., Kourgialas, N., Karatzas, G., 2012. Estimation of agricultural flood loss in the Koiliaris river basin in Crete, Greece. European Water; 39: 53-63.

Webster, R., Oliver, M. A., 2007. Geostatistics for Environmental Scientists, Statistics in Practice Series, John Wiley & Son Ltd.

Weibel, R., Heller, M., 1990. A framework for digital terrain modeling, In: Forth International Symposium on Spatial Data Handling, Zurich, Switzerland, 219-229.

Wilson, M., Bates, P., Alsdorf, D., Forsberg, B., Horritt, M., Melack, J., Frappart, F., Famiglietti, J., 2007. Modeling large-scale inundation of Amazonian seasonally flooded wetlands, GEOPHYSICAL RESEARCH LETTERS 34, 1-6.

WMO, 2014. Atlas of mortality and economic losses from weather, climate and water extreames (1970-2012). World Meteorological Organization (WMO) Publication: WMO-No. 1123.

Wood, A. W., Maurer, E. P., Kumar, A., Lettenmaier, D. P., 2002. Long-range experimental hydrologic forecasting for the eastern United States. J Geophys Res (Atmos) 107, 4429.

Wu, H., Adler, R. F., Tian, Y., Huffman, G. J., Li, H., Wang, J., 2014. Real-time global flood estimation using satellite-based precipitation and a coupled land surface and routing model, Water Resources Research 50 (3), 2693-2717.

Wu, F., Shen, H. W., Chou, Y., 1999. Variation of roughness coefficients for unsubmerged and submerged conditions, Journal of Hydraulic Engineering, 125(9), 934-942.

References (continued)

Xia, Y., Mitchell, K., Ek, M., Sheffield, J., Cosgrove, B., Wood, E., Luo, L., Alonge, C., Wei, H., MENG, J., Livneh, B., Lettenmaier, D., Koren, V., Duan, Q., Mo, K., Fan, Y., Mocko, D., 2012. Continental-scale water and energy flux analysis and validation for the North American Land Data Assimilation System project phase 2 (NLDAS-2): 1. Intercomparison and application of model products, Journal of Geophysical Research 117, D03109.

Yen, B. C., 1992. Channel Flow Resistance: centennial of Manning's Formula, 43, Water Resources Publications, USA.

Yilmaz, K. K., Hogue, T. S., Hsu, K. L., Sorooshian, S., Gupta, H. V., Wagener, T., 2005. Intercomparison of rain gauge, radar, and satellite-based precipitation estimates with emphasis on hydrologic forecasting, J. Hydrometeorol., 6, 497-517.

Yong, B., Ren, L. L., Hong, Y., Wang, J.-H., Gourley, J. J., Jiang, S. H., Chen, X., Wang, W., 2010. Hydrologic evaluation of Multisatellite Precipitation Analysis standard precipitation products in basins beyond its inclined latitude band: A case study in Laohahe basin, China. Water Resour. Res. 46.

Zandbergen, P. A., 2008. Positional accuracy of spatial data: Non-normal distributions and a critique of the national standard for spatial data accuracy, Trans. GIS, 12, 103-130.

Zeweldi, D. A., Gebremichael, M., Downer, C. W., 2011. On CMORPH rainfall for stream flow simulation in a small, Hortonian watershed. J. Hydrometeorol. 12, 456–466.

Zhang, J., Zhang, Z., 2011. Strict geometric model based on a transformation for remote sensing image with high resolution, In Proceedings of ISPRS 34th, Sydney, Australia.

Zhang, W., Cundy, T. W., 1989. Modeling of two-dimensional overland flow. Water Resources Research 25(9), 2019-2035.

Zhang, J., NOAA/NSSL, Norman, O. K., Howard, K., Vasiloff, S., Langston, C., Kaney, B., Arthur, A., van Cooten, S., Kelleher, K., National Mosaic and QPE (NMQ) system—Description, results and future plan. In Proceedings of the 34th Conference on Radar Meteor, Williamsburg, VA, USA, 6 October 2009.

Zhao, G., Xue, H., Ling, F., 2010. Assessment of ASTER GDEM Performance by Comparing with SRTM and ICESat/GLAS Data in Central China, In Proceedings of the 18th International Conference on Geoinformatics, Beijing, China.

Zinke, P. J., 1967. Forest interception studies in the United States, International Symposium on Forest Hydrology, eds., W.E. Sopper & H.W. Hull, 137-161, Pergamon Press, Oxford.

Appendices

A. GPU setup for RRI model based on CUDA Fortran language

B. Inundation mapping from MODIS data

C. Rain gauge data in this study

D. Probability distribution modeling of rainfall data

E. Input-Output table

G. Python programing in this study

A. GPU setup for RRI model based on CUDA Fortran language

A.1 Setup CPU code for sending variables to GPU device

```
! RRI_Slope_GPU
!Variable definition (Slope)
subroutine funcs_gpu( hs_idx, qp_t_idx, fs_idx, qs_idx )
use cudafor
use globals
use gpu_sub
implicit none

! Subroutine vector
real(4) :: hs_idx(slo_count), qp_t_idx(slo_count)
real(4) :: qs_idx(i4,slo_count), fs_idx(slo_count)
integer :: k, l, kk

! Device input vectors from module
real(4), allocatable, device :: zb_slo_idx_d(:), ns_slo_idx_d(:)
real(4), allocatable, device :: ka_idx_d(:), da_idx_d(:), dm_idx_d(:)
real(4), allocatable, device :: beta_idx_d(:), soildepth_idx_d(:)
real(4), allocatable, device :: dis_slo_idx_d(:,:), len_slo_idx_d(:,:)
real(4), allocatable, device :: dis_slo_1d_idx_d(:), len_slo_1d_idx_d(:)
integer, allocatable, device :: dif_slo_idx_d(:)
integer, allocatable, device :: down_slo_idx_d(:,:), down_slo_1d_idx_d(:)!, kkk_dev(:)

! Device input vectors from subroutine
real(4), allocatable, device :: hs_idx_d(:), qs_idx_d(:,:)
real(4), allocatable, device :: qp_t_idx_d(:), fs_idx_d(:)
!real(4), allocatable, device :: qp_t_idx_d(:)

! GPU variable
integer block_dim, block_no

! Allocate memory for each vector on GPU
!  Device input vectors from module
allocate (zb_slo_idx_d(slo_count), ns_slo_idx_d(slo_count))
allocate (ka_idx_d(slo_count), da_idx_d(slo_count), dm_idx_d(slo_count))
allocate (beta_idx_d(slo_count), soildepth_idx_d(slo_count))
allocate (dis_slo_idx_d(i4,slo_count), len_slo_idx_d(i4,slo_count))
allocate (dis_slo_1d_idx_d(slo_count), len_slo_1d_idx_d(slo_count))
allocate (dif_slo_idx_d(slo_count))
allocate (down_slo_idx_d(i4,slo_count), down_slo_1d_idx_d(slo_count))

!  Device input vectors from subroutine
allocate (hs_idx_d(slo_count), qs_idx_d(i4,slo_count))
allocate (qp_t_idx_d(slo_count), fs_idx_d(slo_count) )
!allocate (qp_t_idx_d(slo_count))

!GPU variable initilization
block_dim = 512
block_no  = ceiling(real(slo_count,4)/real(block_dim,4))

! Implicit copy of Host vectors to Device
hs_idx_d   = hs_idx
qp_t_idx_d = qp_t_idx

qs_idx_d   = qs_idx
fs_idx_d   = fs_idx

zb_slo_idx_d    = zb_slo_idx
ns_slo_idx_d    = ns_slo_idx
ka_idx_d        = ka_idx
da_idx_d        = da_idx
dm_idx_d        = dm_idx
beta_idx_d      = beta_idx
```

```
dif_slo_idx_d   = dif_slo_idx
down_slo_idx_d  = down_slo_idx
down_slo_1d_idx_d= down_slo_1d_idx
dis_slo_idx_d   = dis_slo_idx
dis_slo_1d_idx_d = dis_slo_1d_idx
len_slo_idx_d   = len_slo_idx
len_slo_1d_idx_d = len_slo_1d_idx
soildepth_idx_d = soildepth_idx

! call funcs_gpu from 1-slo_count
call funcs_gpu<<<block_no, block_dim>>>( slo_count, area, lmax, &
                        hs_idx_d, qs_idx_d, qp_t_idx_d,&
                        zb_slo_idx_d, ns_slo_idx_d, ka_idx_d, da_idx_d, &
                        dm_idx_d, beta_idx_d, dif_slo_idx_d, &
                        down_slo_idx_d, down_slo_1d_idx_d, &
                        dis_slo_idx_d, dis_slo_1d_idx_d, len_slo_idx_d, &
                        len_slo_1d_idx_d, soildepth_idx_d )

qs_idx(1:lmax,1:slo_count)   = qs_idx_d

do k = 1, slo_count
        fs_idx(k) = qp_t_idx(k) - (qs_idx(1,k) + qs_idx(2,k) + qs_idx(3,k) + qs_idx(4,k))
enddo

do k = 1, slo_count
        do l = 1, lmax
                if( dif_slo_idx(k) .eq. 0 .and. l .eq. 2 ) exit ! kinematic -> 1-direction
                kk = down_slo_idx(l, k)
                if( dif_slo_idx(k) .eq. 0 ) kk = down_slo_1d_idx(k)
                if( kk .eq. -1 ) cycle
                fs_idx(kk) = fs_idx(kk) + qs_idx(l, k)
        enddo
enddo

end subroutine funcs_gpu
```

A.2 CUDA Fortran code to start the GPU

```
module gpu_sub
        contains
        ! CUDA kernal
        attributes(global) subroutine funcs_gpu( slo_count, area, lmax, &
                        hs_idx, qs_idx, qp_t_idx, &
                        zb_slo_idx, ns_slo_idx, ka_idx, da_idx, dm_idx, beta_idx, &
                        dif_slo_idx, down_slo_idx, down_slo_1d_idx, dis_slo_idx, &
                        dis_slo_1d_idx, len_slo_idx, len_slo_1d_idx, soildepth_idx )
                ! Variable device only
                real(4) :: zb_p, hs_p, ns_p, ka_p, da_p, dm_p, b_p
                real(4) :: zb_n, hs_n, ns_n, ka_n, da_n, dm_n, b_n
                real(4) :: lev_p, lev_n
                integer :: dif_p, dif_n

                integer :: tid
                integer :: kk, l
                real(4) :: distance, len, dh, hw, q

                !GPU memory by value
                integer, value :: slo_count, lmax
                real(4), value :: area

                !GPU memory allocation
                real(4), device :: hs_idx(slo_count), qs_idx(lmax,slo_count), qp_t_idx(slo_count)
                real(4), device :: zb_slo_idx(slo_count), ns_slo_idx(slo_count), ka_idx(slo_count),
da_idx(slo_count)
                real(4), device :: dm_idx(slo_count), beta_idx(slo_count), soildepth_idx(slo_count)
```

257

```fortran
real(4), device :: dis_slo_idx(lmax,slo_count), dis_slo_1d_idx(slo_count)
real(4), device :: len_slo_idx(lmax,slo_count), len_slo_1d_idx(slo_count)
integer, device :: down_slo_idx(lmax,slo_count), down_slo_1d_idx(slo_count)
integer, device :: dif_slo_idx(slo_count)

! Get global thread ID
tid = threadIdx%x + (blockIdx%x - 1)*blockDim%x

! Make sure do not go out of bounds
if (tid .le. slo_count) then

        zb_p = zb_slo_idx(tid)
        ns_p = ns_slo_idx(tid)
        ka_p = ka_idx(tid)
        da_p = da_idx(tid)
        dm_p = dm_idx(tid)
        b_p  = beta_idx(tid)
        hs_p = hs_idx(tid)
        dif_p=dif_slo_idx(tid)

        do l = 1, lmax ! lmax for 8 direction
        kk = down_slo_idx(l, tid)
        if( dif_p .eq. 0 ) kk = down_slo_1d_idx(tid)
                if( kk .eq. -1 ) cycle

                        distance = dis_slo_idx(l, tid)
                        len = len_slo_idx(l, tid)
                        if( dif_p .eq. 0 ) distance = dis_slo_1d_idx(tid)
                        if( dif_p .eq. 0 ) len = len_slo_1d_idx(tid)

                        ! information of the destination cell
                        zb_n = zb_slo_idx(kk)
                        hs_n = hs_idx(kk)
                        ns_n = ns_slo_idx(kk)
                        ka_n = ka_idx(kk)
                        da_n = da_idx(kk)
                        dm_n = dm_idx(kk)
                        b_n = beta_idx(kk)
                        dif_n = dif_slo_idx(kk)

                        call h2lev_gpu(hs_p, lev_p, soildepth_idx(tid), da_idx(tid))
                        call h2lev_gpu(hs_n, lev_n, soildepth_idx(kk), da_idx(kk))

                        ! diffusion wave
                        dh = ((zb_p + lev_p) - (zb_n + lev_n)) / distance

                        ! 1-direction : kinematic wave
                        if( dif_p .eq. 0 ) dh = max( (zb_p - zb_n) / distance, 0.001 )

                        ! water coming in or going out?
                        if( dh .ge. 0.0 ) then
                        ! going out
                        hw = hs_p
                        !if(emb .gt. 0.d0) hw = max(hs_p - emb, 0.d0)
                        if( zb_p .lt. zb_n ) hw = max(0.0, zb_p + hs_p - zb_n)
                        call hq_gpu(ns_p, ka_p, da_p, dm_p, b_p, hw, dh, len, q, area)
                        qs_idx(l,tid) = q
                        else
                        ! coming in
                        hw = hs_n
                        !if(emb .gt. 0.d0) hw = max(hs_n - emb, 0.d0)
                        dh = abs(dh)
                        if( zb_n .lt. zb_p ) hw = max(0.0, zb_n + hs_n - zb_p)
                        call hq_gpu(ns_n, ka_n, da_n, dm_n, b_n, hw, dh, len, q, area)
                        qs_idx(l,tid) = -q
                        endif
        enddo
```

```fortran
            endif

    end subroutine funcs_gpu

  ! water depth (h) to actual water level (lev)
   attributes(device) subroutine h2lev_gpu(h, lev, soildepth, da)
            implicit none

            real(4), value :: soildepth, da
            real(4), value :: h
            real(4) :: rho, lev

            if ( soildepth .eq. 0.0 ) then
             lev = h
            elseif ( h .ge. da ) then ! including da = 0
             lev = soildepth + (h - da) ! surface water
            else
             if (soildepth .gt. 0.0 ) rho = da/ soildepth
             lev = h / rho
            endif

        end subroutine h2lev_gpu

        ! water depth and discharge relationship
        attributes(device) subroutine hq_gpu(ns_p, ka_p, da_p, dm_p, b_p, h, dh, len, q, area)
            implicit none

            real(4) ns_p, da_p, dm_p, ka_p, b_p, h, dh, len, q, area
            real(4) km, vm, va, al, m

            if( b_p .gt. 0.0 )then
             km = ka_p / b_p
            else
             km = 0.0
            endif
            vm = km * dh

            if( da_p .gt. 0.0 ) then
             va = ka_p * dh
            else
             va = 0.0
            endif

            if( dh .lt. 0 ) dh = 0.0
            al = sqrt(dh) / ns_p
            m = 5.0 / 3.0

            if( h .lt. dm_p ) then
             q = vm * dm_p * (h / dm_p) ** b_p
            elseif( h .lt. da_p ) then
             q = vm * dm_p + va * (h - dm_p)
            else
             q = vm * dm_p + va * (h - dm_p) + al * (h - da_p) ** m
            endif

            ! discharge per unit area
            ! (q multiply by width and divide by area)
            q = q * len / area

            ! water depth limitter (1 mm)
            ! note: it can be set to zero
            !if( h.le.0.001 ) q = 0.d0

        end subroutine hq_gpu

  end module gpu_sub
```

B. Inundation mapping from MODIS data

B.1 Satellite imagery

The data format to submit should be Microsoft word file or PDF. Terra/MODIS surface-reflectance 8-day composite data on MOD09A1 v005 at 500-m resolution was provided from the Earth Observing System Data and Information System (EOSDIS 2012), during 2000 to 2011. For Thailand area with MODIS grid dataset were formed a MODIS grid number, covering H27V06, H27V07, H27V08, H28V08, and H28V07.

The EVI in equation (1) and LSWI in equation (2) (Kotera et al. 2015) were used for the flood mapping estimation.

$$EVI = G \times \frac{NIR - RED}{NIR + C_1 \cdot RED - C_2 \cdot BLUE + L} \tag{1}$$

$$LSWI = \frac{NIR - SWIR}{NIR + SWIR} \tag{2}$$

where **RED**, **NIR**, **BLUE**, and **SWIR** are the surface reflectance at 500 resolution in the red band (band 1), near-infrared band (band 2), blue band (band 3), and short-wave infrared band (band 6), respectively. **G** is the gain factor (**G** = 2.5). **C₁** and **C₂** are the coefficients of the aerosol resistance term, on the 500-m blue band of MODIS to correct aerosol influences on the red band (**C₁** = 6.0 and **C₂** = 7.5). **L** is the canopy background adjustment (**L** = 1) (Kotera et al. 2015).

MODIS 8-day composite-reflectance data have an absence of clouds or cloud shadow pixels that are affected by monsoon clouds (Islam A. S. et al. 2009). To remove noise and interpolate missing data, we applied the cubic spline interpolation algorithm to fill the abnormal data (Li et al. 2014) implemented by using python language v. 2.7.9 to EVI and LSWI time series data.

B.2 Detection of inundation area

To detect the inundation on spatial distribution and time series change, the artificial data was created by using filter for smoothing. The inundation is a differential between LSWI and EVI when LSWI is above EVI and based on a condition described by equation (3) or (4).

$$DVEL \leq 0.05 \text{ and } EVI \leq 0.1 \tag{3}$$

$$LSWI \leq 0 \text{ and } EVI \leq 0.05 \tag{4}$$

Flood pixels occur more than 120 days that are the water bodies. For example of EVI, LSWI and DVEL in temporal that is shown in **Figure B1** over two years with noise removed. The flood pixels are present from 289-305 (DOY), 2009 and from 289-361 (DOY), 2011.
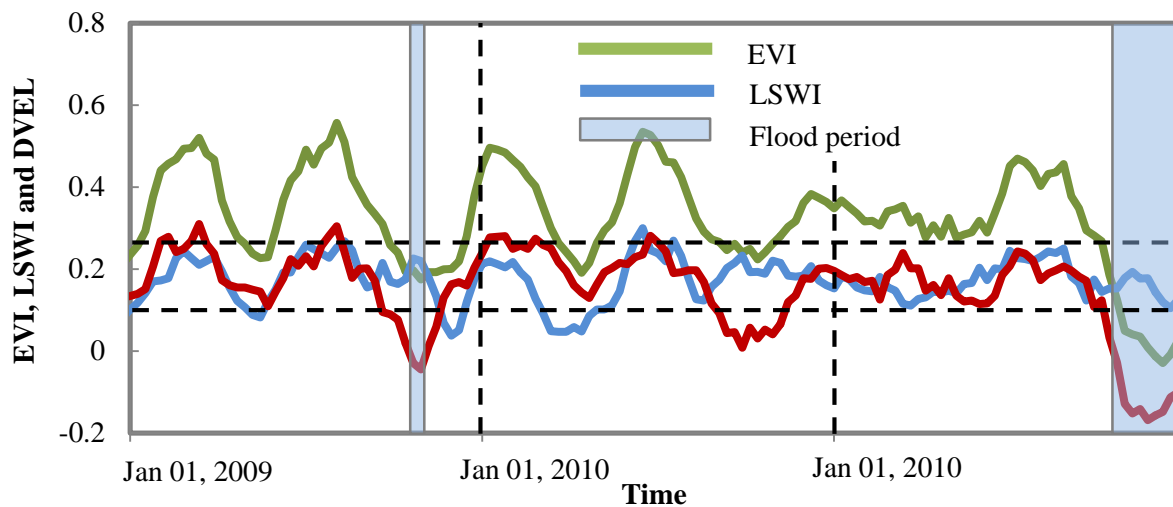
Figure B1 Temporal of EVI, LSWI and DVEL with noise removed at 14d01'N, 100d30'E

B.3 Validation inundation data

In order to validate of inundation map estimated from MODIS datasets, RADASAT-1 satellite images datasets were used for the validation, which flood map are produced by the Geo-Informatics and Space Technology Development Agency, Thailand (GISTDA). The RADASAT-1 is investigated using a C-band at 50 meters resolution (Kotera et al. 2015).

B.4 Comparison of inundation areas by MOSID and RADASAT products

The proposed technique applied to identify the inundation map from MODIS temporal data and validated it with RADARSAT product. **Figure B2** shows a comparison of MODIS resulting annual inundation map on 2005 with the following available RADARSAT derived annual inundation map at the same time. From two satellite products, most of the area in both images displays quite a good matching. In south west and middle region, MODIS displays more flooding areas than RADARSAT while in the northern are the RADARSAT shows more inundation area than the MODIS. **Figure B3** shows a scattered plot of the crossing inundation area of the MODIS and RADARSAT products between 2005 and 2010. The flood area estimated by MODIS inclined to be about 20 % larger than the RADARSAT products. This overestimation was generally from the difference in spatial resolution of the data source. MODIS pixel about 500 meters is calculated as inundated but RADARSAT represented as fine pixel size about 50 meters. For the overestimation in the MODIS data, the high resolution RADASAT can interpret non-inundated area such as roads and building (Kotera et al.

2015). In spite of the overestimation resulting from inundation pixels, MODIS product would still have useful advantages for investigating inundations area in time-series.
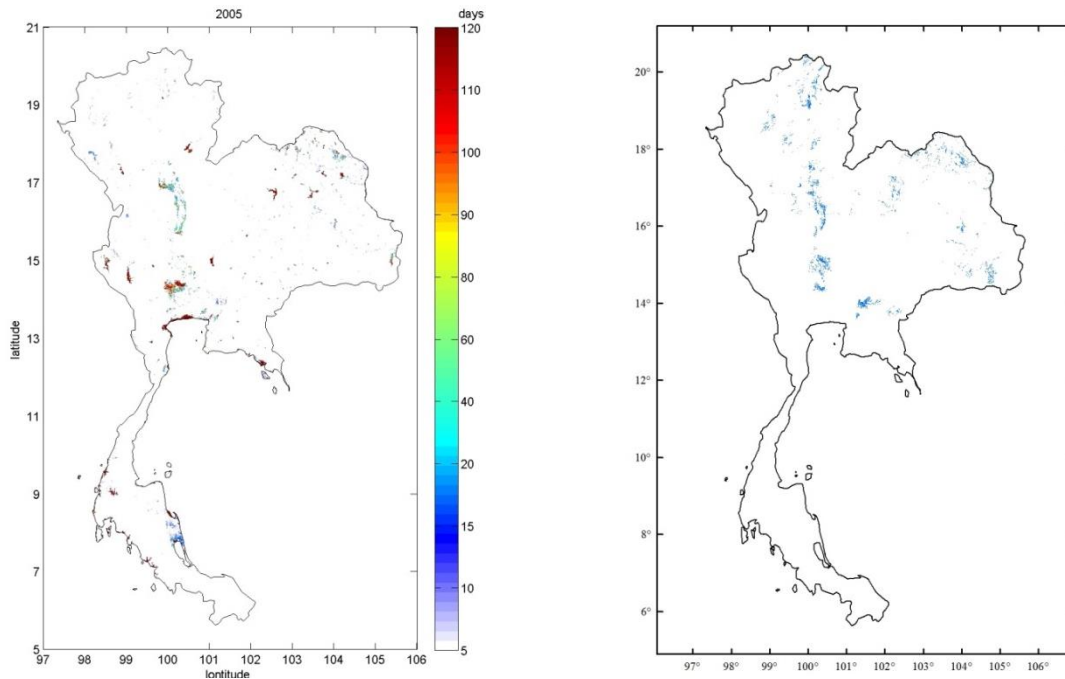
a) MODIS 2005   b) RADASAT 2005
Figure B2 Comparison between MODIS and RADASAT product in 2005

B.5 Flood damage from 2000 to 2011

Figure B4 shows the inundation area that its damage area is a paddy field region from 2000 to 2011. The mean and the standard deviation of damaged areas over 12 years were 9,830 square kilometers and 3,581 square kilometers, respectively. The flood damage in 2011 occurred over area about 19,717 square kilometers that was approximately twice of the average damaged area in 12 years. The second largest damage occurred in 2006, and the least damage was in 2004. When the results in 12 years were overlaid at the same location by using GIS technique, **Figure B5** displays the frequency of the estimated spatial inundation area during the 12-year period from 2000 to 2011.

B.6 References

EOSDIS, 2012. NASA's earth observing system data and information system, URL: http://earthdata.nasa.gov/.

Islam, A. S., Bala, S. K., Haque, A., 2009. Flood inundation map of Bangladesh using MODIS surface reflectance data, *ICWFM* , Brazil, 1 – 10.

Kotera, A., Nagano, T., Hanittinan, P., Koontanakulvong, S., 2015. Assessing the degree of flood damage to rice crops in the Chao Phraya delta, Thailand, *using MODIS satellite imaging*, *Paddy water Environ*, CrossMark.

Li, H., Wan, X., Gao, S., 2014. Dynamic time waping based on cubic spline interpolation for time series data mining, *IEEE international Conference*, China, 19 – 26.
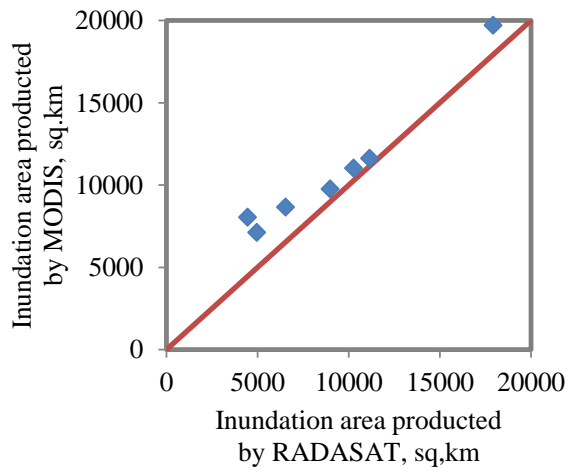
Figure B3 Comparison annual data between MODIS and RADASAT product from 2000 to 2011
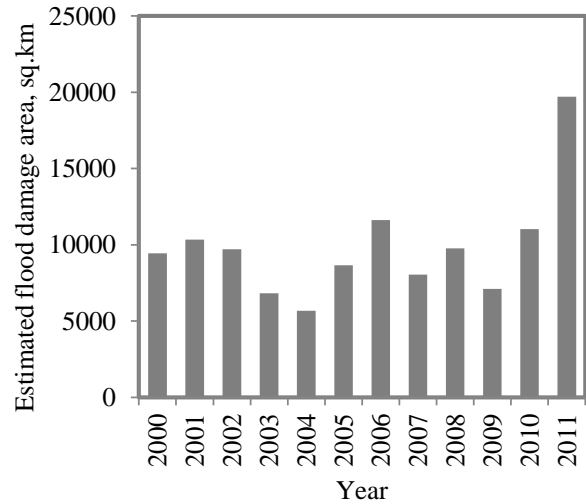
Figure B4 Change of annual flood damage area from 2000 to 2011
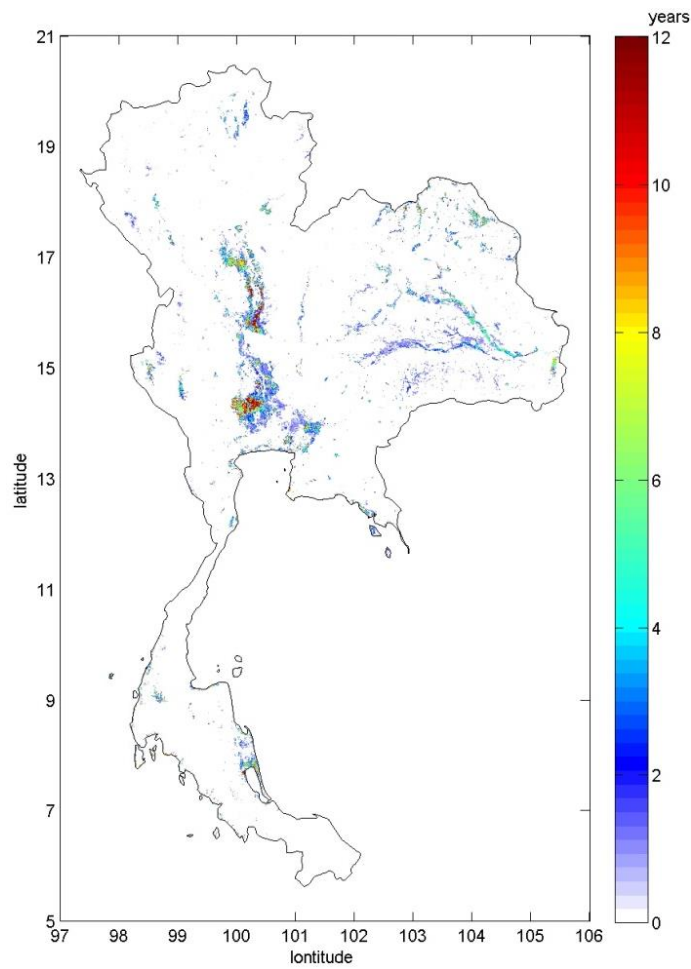
Figure B5 Flood frequency period in 12-year from 2000 to 2011

C. rain gauge data in this study

C.1 Rain gauge in the Shikoku Island, Japan

Table C1 Rain gauges across Shikoku Island, Japan, from MLIT Japan

No.	Prefecture	Code	Latitude(d)	Longitude (d)	Height (m)	Annual Rainfall, mm
1	Kagawa	108081288804002	34.195	133.845	87.0	1,282
2	Kagawa	108081288804003	34.183	133.905	206.0	1,419
3	Kagawa	108081288804004	34.140	133.928	286.0	1,547
4	Kagawa	108081288804005	34.120	133.978	498.0	1,648
5	Kagawa	108081288804006	34.102	134.028	531.0	1,769
6	Tokushima	108061288803001	33.934	134.624	21.0	4,015
7	Tokushima	108061288803002	33.852	134.479	96.0	4,196
8	Tokushima	108061288803004	33.799	134.387	175.0	4,640
9	Tokushima	108061288803008	33.903	134.622	12.0	3,694
10	Tokushima	108061288803010	33.836	134.561	67.0	3,985
11	Tokushima	108061288803011	33.757	134.348	297.0	5,074
12	Tokushima	108071288801003	34.153	134.406	390.0	2,082
13	Tokushima	108071288801005	34.086	134.557	1.0	2,005
14	Tokushima	108071288801008	34.129	134.170	420.0	1,776
15	Tokushima	108071288801009	34.087	134.351	23.0	1,547
16	Tokushima	108071288801010	33.995	134.389	400.0	3,172
17	Tokushima	108071288801016	34.063	134.196	35.0	2,014
18	Tokushima	108071288801017	33.939	134.229	700.0	2,593
19	Tokushima	108071288801018	33.948	134.151	620.0	2,209
20	Tokushima	108071288801019	33.949	134.068	305.0	2,161
21	Tokushima	108071288801020	34.044	134.053	58.0	1,627
22	Tokushima	108071288801021	34.113	134.052	1,034.0	1,446
23	Tokushima	108071288801022	33.968	134.011	500.0	2,443
24	Tokushima	108071288801023	34.066	133.930	465.0	1,808
25	Tokushima	108071288801025	33.847	133.904	800.0	3,328
26	Tokushima	108071288811001	33.968	133.783	120.0	2,043
27	Tokushima	108071288811002	33.941	133.893	1,200.0	2,480
28	Tokushima	108071288811003	33.890	133.821	430.0	2,777
29	Tokushima	108071288811004	33.915	133.950	1,515.0	2,883
30	Tokushima	108071288811005	33.868	134.079	1,460.0	3,567
31	Tokushima	108071288811010	33.860	133.731	530.0	3,641
32	Ehime	108011288805001	33.731	132.791	113.0	1,486
33	Ehime	108011288805002	33.825	132.854	180.0	1,566
34	Ehime	108011288805003	33.823	132.904	183.0	1,733
35	Ehime	108011288805004	33.791	132.910	120.0	1,666
36	Ehime	108011288805005	33.770	132.972	365.0	2,389
37	Ehime	108011288805006	33.825	132.956	290.0	2,158
38	Ehime	108011288805007	33.867	132.946	370.0	2,247

Table C1 Rain gauges across Shikoku Island, Japan, from MLIT Japan (continuous)

No.	Prefecture	Code	Latitude(d)	Longitude (d)	Height (m)	Annual Rainfall, mm
39	Ehime	108011288805009	33.785	132.791	35.0	1,454
40	Ehime	108011288805011	33.875	132.841	214.0	1,700
41	Ehime	108011288805012	33.927	132.898	450.0	2,235
42	Ehime	108011288805013	33.818	132.742	10.0	1,368
43	Ehime	108011288805015	33.915	132.832	440.0	1,762
44	Ehime	108021288806001	33.653	132.729	609.0	1,882
45	Ehime	108021288806001	33.653	132.729	609.0	1,882
46	Ehime	108021288806003	33.630	132.818	414.0	1,874
47	Ehime	108021288806004	33.607	132.482	3.0	1,486
48	Ehime	108021288806005	33.583	132.603	415.0	1,818
49	Ehime	108021288806006	33.571	132.720	110.0	1,749
50	Ehime	108021288806007	33.565	132.800	217.0	1,843
51	Ehime	108021288806008	33.547	132.658	51.0	1,699
52	Ehime	108021288806009	33.514	132.547	15.0	1,641
53	Ehime	108021288806010	33.511	132.488	340.0	1,890
54	Ehime	108021288806011	33.502	132.755	528.0	2,003
55	Ehime	108021288806012	33.454	132.617	241.0	1,971
56	Ehime	108021288806013	33.429	132.801	200.0	2,264
57	Ehime	108021288812001	33.357	132.631	178.0	2,074
58	Ehime	108021288812002	33.341	132.548	202.0	1,807
59	Ehime	108021288812003	33.386	132.478	220.0	1,199
60	Ehime	108021288812004	33.419	132.521	447.0	1,849
61	Ehime	108021288812005	33.388	132.596	226.0	2,039
62	Ehime	108031288809018	33.182	132.706	360.0	3,465
63	Ehime	108031288809021	33.249	132.677	168.0	2,570
64	Ehime	108031288809022	33.342	132.777	420.0	2,732
65	Ehime	108041288813010	33.742	133.040	745.0	2,404
66	Ehime	108041288813020	33.703	133.098	720.0	3,304
67	Ehime	108041288813030	33.696	132.969	571.0	2,287
68	Ehime	108041288813040	33.672	133.018	475.0	2,502
69	Ehime	108041288813050	33.648	132.906	480.0	2,140
70	Ehime	108041288813060	33.622	132.874	508.0	2,254
71	Ehime	108041288813070	33.613	132.977	380.0	2,595
72	Ehime	108041288813080	33.603	133.037	650.0	3,403
73	Ehime	108041288813090	33.584	132.952	998.0	2,995
74	Ehime	108041288813110	33.541	132.854	932.0	2,950
75	Ehime	108041288813120	33.538	133.050	233.0	3,744
76	Ehime	108041288813130	33.521	132.967	560.0	3,324
77	Ehime	108041288813140	33.474	132.930	970.0	3,876
78	Ehime	108071288811006	33.933	133.572	320.0	2,646
79	Ehime	108071288811007	33.870	133.512	650.0	3,377
80	Ehime	108071288811008	33.859	133.419	545.0	3,184
81	Ehime	108071288811009	33.834	133.338	1,100.0	3,214

Table C1 Rain gauges across Shikoku Island, Japan, from MLIT Japan (continuous)

No.	Prefecture	Code	Latitude(d)	Longitude (d)	Height (m)	Annual Rainfall, mm
82	Kochi	108031288809002	32.978	132.942	23.0	3,300
83	Kochi	108031288809006	32.968	132.816	7.0	3,705
84	Kochi	108031288809009	33.066	132.875	160.0	3,912
85	Kochi	108031288809010	33.101	132.964	70.0	3,693
86	Kochi	108031288809011	33.140	133.035	360.0	3,150
87	Kochi	108031288809012	33.141	132.868	714.0	3,872
88	Kochi	108031288809014	33.191	132.970	128.0	3,952
89	Kochi	108031288809016	33.213	133.154	476.0	4,130
90	Kochi	108031288809019	33.298	132.969	260.0	3,965
91	Kochi	108031288809020	33.325	133.141	420.0	3,831
92	Kochi	108031288809024	33.376	132.937	780.0	3,353
93	Kochi	108031288809025	33.405	133.005	580.0	3,856
94	Kochi	108031288809026	33.437	133.091	660.0	5,219
95	Kochi	108031288809028	33.468	133.003	1,170.0	4,494
96	Kochi	108031288809913	32.914	132.802	110.0	3,699
97	Kochi	108031288810101	32.924	132.814	100.0	3,771
98	Kochi	108031288810102	32.915	132.808	92.0	3,680
99	Kochi	108031288810103	32.918	132.828	104.0	4,089
100	Kochi	108041288808010	33.672	133.145	580.0	3,665
101	Kochi	108041288808040	33.644	133.349	130.0	4,081
102	Kochi	108041288808060	33.626	133.281	120.0	3,935
103	Kochi	108041288808080	33.603	133.175	170.0	3,891
104	Kochi	108041288808090	33.570	133.175	110.0	3,954
105	Kochi	108041288808100	33.550	133.457	50.0	3,829
106	Kochi	108041288808110	33.526	133.357	20.0	3,947
107	Kochi	108041288808120	33.506	133.294	70.0	3,908
108	Kochi	108041288808130	33.496	133.456	9.4	3,809
109	Kochi	108041288808140	33.497	133.139	360.0	4,614
110	Kochi	108041288808150	33.486	133.229	180.0	4,447
111	Kochi	108041288808160	33.461	133.349	28.0	3,898
112	Kochi	108041288813100	33.541	133.117	241.0	4,241
113	Kochi	108051288808020	33.716	133.763	190.0	5,128
114	Kochi	108051288808030	33.689	133.818	398.0	4,262
115	Kochi	108051288808040	33.623	133.764	118.0	3,557
116	Kochi	108051288808050	33.623	133.807	170.0	3,661
117	Kochi	108071288811011	33.807	133.827	710.0	3,622
118	Kochi	108071288811012	33.756	133.754	1,390.0	4,383
119	Kochi	108071288811013	33.676	133.688	350.0	4,743
120	Kochi	108071288811014	33.777	133.666	210.0	4,095
121	Kochi	108071288811015	33.832	133.656	440.0	3,970
122	Kochi	108071288811016	33.743	133.626	400.0	4,749
123	Kochi	108071288811017	33.709	133.546	570.0	4,781
124	Kochi	108071288811018	33.861	133.558	1,005.0	3,822

Table C1 Rain gauges across Shikoku Island, Japan, from MLIT Japan (continuous)

No.	Prefecture	Code	Latitude(d)	Longitude (d)	Height (m)	Annual Rainfall, mm
125	Kochi	108071288811019	33.801	133.364	715.0	3,401
126	Kochi	1411180701080	33.709	133.303	830.0	4,279

C.2 Rain gauge in Thailand

Table C2 The summary statistic in average annual of rain gauges.

No	station	code	Mean, mm	SD, mm	CV, %	Skewness	Wet days
1	Mae Hong Son*	300201	1304.6	210.28	16.12	-0.169	139
2	Mae Sariang*	300202	1183.4	213.11	18.01	-0.047	142
3	Chiang Rai*	303201	1744.8	259.04	14.85	0.439	136
4	Chiang Rai Agromet	303301	1696.5	249.92	14.73	0.494	136
5	Phayao*	310201	1219.4	245.31	20.12	0.095	140
6	Mae Jo	327301	1135.2	213.25	18.78	0.100	121
7	Chiang Mai	327501	1174.4	218.09	18.57	0.008	117
8	Lampang*	328201	1091.5	250.27	22.93	0.730	113
9	Lampang Agromet	328301	1161.4	213.10	18.35	0.517	134
10	Lamphun*	329201	1085.3	245.66	22.63	0.424	123
11	Phrae*	330201	1130.2	205.06	18.14	0.007	114
12	Nan*	331201	1270.6	221.27	17.41	0.469	120
13	Nan Agromet	331301	1345.5	264.62	19.67	0.782	125
14	Tha Wang Pha*	331401	1437.2	266.24	18.52	0.215	128
15	Thung Chang	331402	1484.4	300.52	20.25	0.343	147
16	Uttaradit*	351201	1438.5	284.34	19.77	0.925	117
17	Nong Khai*	352201	1630.7	357.46	21.92	0.365	127
18	Loei*	353201	1270.9	213.66	16.81	0.868	127
19	Loei Agromet	353301	1255.2	186.13	14.83	-0.140	117
20	Udon Thani*	354201	1446.4	304.28	21.04	0.563	121
21	Sakon Nakhon*	356201	1633.8	272.24	16.66	-0.297	129
22	Sakon Nakhon Agromet	356301	1566.5	245.36	15.66	0.002	123
23	Nakhon Phanom*	357201	2333.4	364.55	15.62	-0.003	138
24	Nakhon Phanom Agromet	357301	2057.8	382.41	18.58	0.145	128
25	Nongbualumphu	360201	1384.3	221.58	16.01	0.465	182
26	Sukhothai	373201	1255.6	240.06	19.12	0.838	156
27	Si Samrong Agromet	373301	1234.1	233.53	18.92	0.673	109
28	Tak*	376201	1074.0	212.32	19.77	0.057	105
29	Mae Sot*	376202	1470.0	317.52	21.60	-0.068	141
30	Bhumibol Dam*	376203	1077.8	251.63	23.35	0.487	108
31	Doi Muser Agromet Stn.	376301	1346.2	296.24	22.01	1.228	173
32	Umphang*	376401	1448.9	231.88	16.00	0.683	164
33	Phitsanulok*	378201	1359.7	245.12	18.03	-0.066	118
34	Phetchabun*	379201	1124.9	236.09	20.99	0.322	119
35	Lom Sak*	379401	1045.0	190.17	18.20	0.272	118

Table C2 The summary statistic in average annual of rain gauges (continues).

No	station	code	Mean, mm	SD, mm	CV, %	Skewness	Wet days
36	Wichian Buri*	379402	1229.5	217.89	17.72	1.031	112
37	Kamphaeng Phet*	380201	1286.8	217.56	16.91	-0.162	142
38	Khon Kaen*	381201	1239.5	212.29	17.13	0.143	107
39	Tha Phra Agromet	381301	1187.2	222.53	18.74	0.574	102
40	Mukdahan*	383201	1512.0	201.23	13.31	0.326	116
41	Pichit Agromet	386301	1284.1	257.02	20.02	0.325	149
42	Kosum Phisai*	387401	1249.7	185.42	14.84	0.708	103
43	Kamalasai	388401	1350.1	155.97	11.55	0.428	154
44	Nakhon Sawan*	400201	1141.2	233.06	20.42	-0.048	109
45	Tak Fa Agromet	400301	1199.5	232.59	19.39	0.376	109
46	Chai Nat*	402301	1060.6	246.74	23.26	0.532	101
47	Chaiyaphum*	403201	1146.8	259.65	22.64	0.532	102
48	Roi Et*	405201	1362.1	182.94	13.43	0.160	110
49	Roi Et Agromet	405301	1348.5	160.68	11.91	0.325	115
50	Ubon Ratchathani Agromet	407301	1611.9	253.43	15.72	-0.266	120
51	Ubon Ratchathani*	407501	1604.9	240.75	15.00	0.108	120
52	Si Sa Ket Agromet	409301	1458.7	267.13	18.31	1.243	129
53	Ayuttaya Agromet	415301	1156.7	189.37	16.37	-0.204	165
54	Pathumthani Agromet	419301	1251.5	372.18	29.74	-1.697	172
55	Chacherngsao Agromet	423301	1419.2	224.21	15.80	0.425	168
56	Ratchaburi	424301	1158.6	182.58	15.76	0.200	162
57	Suphan Buri*	425201	1040.6	253.31	24.34	0.357	102
58	U Thong Agromet	425301	1032.9	243.20	23.55	0.408	100
59	Lop Buri*	426201	1136.8	182.33	16.04	-0.084	101
60	Bua Chum*	426401	1106.7	167.74	15.16	-0.034	106
61	Pilot Station*	429201	1070.8	248.52	23.21	0.148	123
62	Suwanabhum Airport	429601	1410.0	206.35	14.63	0.141	200
63	Prachin Buri*	430201	1878.3	296.75	15.80	-0.059	135
64	Kabin Buri*	430401	1629.9	270.12	16.57	-0.172	135
65	Nakhon Ratchasima*	431201	1062.2	215.61	20.30	-0.220	110
66	Pak Chong Agromet	431301	1132.4	183.39	16.20	0.499	122
67	Chok Chai*	431401	1098.9	164.63	14.98	0.292	114
68	Surin*	432201	1398.2	214.20	15.32	0.198	117
69	Surin Agromet	432301	1429.0	242.58	16.98	0.067	114
70	Tha Tum*	432401	1384.0	230.44	16.65	0.311	112
71	Burirum*	436201	1371.8	185.45	13.52	0.465	168
72	Nang Rong*	436401	1208.5	213.94	17.70	0.428	117
73	Aranyaprathet*	440201	1373.3	169.02	12.31	-0.535	130
74	Sa Kaew	440401	1531.3	225.16	14.70	-0.143	177
75	Kanchanaburi*	450201	1078.9	209.59	19.43	0.164	110
76	Thong Pha Phum*	450401	1735.0	397.88	22.93	-1.841	152

Table C2 The summary statistic in average annual of rain gauges (continues).

No	station	code	Mean, mm	SD, mm	CV, %	Skewness	Wet days
77	Kamphaeng Saen Agromet	451301	1053.5	214.74	20.38	-0.154	112
78	Bangkok Metropolis*	455201	1589.4	322.88	20.31	0.288	129
79	Klong Toey*	455203	1569.5	290.06	18.48	0.168	142
80	Bang Na*	455301	1516.4	290.98	19.19	0.475	123
81	Bang Khen*	455302	1444.6	287.02	19.87	0.049	149
82	Donmuang	455601	1330.3	327.07	24.59	0.212	113
83	Chon Buri*	459201	1294.7	223.89	17.29	-0.056	119
84	Ko Sichang*	459202	1217.1	311.89	25.62	0.955	103
85	Phatthaya*	459203	1172.5	246.60	21.03	0.362	131
86	Sattahip*	459204	1308.9	288.40	22.03	0.840	110
87	Lam Chabang*	459205	1207.8	243.35	20.15	0.720	152
88	Phetchaburi*	465201	1046.1	203.63	19.47	0.330	131
89	Rayong*	478201	1418.2	275.84	19.45	0.225	141
90	Huai Pong Agromet	478301	1420.3	302.38	21.29	0.681	122
91	Chanthaburi*	480201	2932.5	473.47	16.15	0.252	167
92	Phriu Agromet	480301	3199.0	518.58	16.21	0.086	175
93	Prachuap Khiri Khan*	500201	1140.0	312.49	27.41	0.326	123
94	Hua Hin*	500202	984.6	265.67	26.98	0.391	109
95	Nong Phlup Agromet	500301	1076.8	266.28	24.73	0.766	126
96	Khlong Yai*	501201	4635.1	1027.88	22.18	-2.172	188
97	Chumphon*	517201	1923.6	337.27	17.53	0.257	166
98	Sawi Agromet	517301	1931.4	283.00	14.65	-0.074	168
99	Ranong*	532201	4114.7	571.92	13.90	0.622	195
100	Surat Thani*	551201	1639.8	309.70	18.89	0.546	157
101	Phunphin Airport	551202	1587.0	315.93	19.91	0.628	156
102	Ko Samui*	551203	2001.4	487.87	24.38	0.581	157
103	Surat Thani Agromet	551301	1951.9	439.51	22.52	0.650	199
104	Phra Sang	551401	1839.6	348.40	18.94	0.391	212
105	Nakhon Si Thammarat*	552201	2504.5	523.41	20.90	0.899	170
106	Khanom*	552202	2037.2	467.20	22.93	0.599	227
107	Nakhorn Sri Thammarat Agromet	552301	2361.4	534.10	22.62	1.117	184
108	Chawang	552401	2081.9	350.67	16.84	0.531	231
109	Phatthalung Agromet	560301	2087.8	421.61	20.19	0.937	184
110	Takua Pa*	561201	3304.4	712.54	21.56	-0.270	202
111	Phuket*	564201	2261.9	396.05	17.51	0.083	172
112	Phuket Airport*	564202	2525.1	420.32	16.65	-0.045	183
113	Ko Lanta*	566201	2202.4	323.06	14.67	0.073	180
114	Krabi*	566202	2267.4	343.18	15.14	0.422	227

Table C2 The summary statistic in average annual of rain gauges (continues).

No	station	code	Mean, mm	SD, mm	CV, %	Skewness	Wet days
115	Trang Airport*	567201	2166.6	329.87	15.23	0.332	172
116	Kho Hong Agromet	568301	2047.6	439.33	21.46	0.357	163
117	Sa Dao	568401	1735.0	379.45	21.87	0.176	213
118	Songkhla*	568501	2100.2	489.36	23.30	0.515	156
119	Hat Yai Airport*	568502	1753.7	336.59	19.19	0.586	164
120	Satun*	570201	2239.1	343.37	15.34	-0.544	190
121	Pattani Airport*	580201	1868.0	374.13	20.03	0.449	147
122	Yala Agromet	581301	2181.8	463.21	21.23	0.339	187
123	Narathiwat*	583201	2518.6	607.81	24.13	0.685	172

D. Demonstration of rainfall modeling on probability distribution; case study in Thailand

D.1 Modeling daily rainfall data

Daily observation rainfall data were controlled on a quality by using the null values. In this section, the continuous daily data are analyzed and resulted in the cumulative distribution function (CDF). These data were modeled by using 9 statistical distributions.

We used the Kaplan-Meier method to estimate the ECDF represented by the observed data. The Kaplan-Meier (K-M) method, proposed by E. L. Kaplan and Paul Meier in 1958 (Kaplan 1958), is normally used for survival analysis in medical science, but is also applicable for time series data (Picado *et al*. 2013, Cai and Roussas 1998) and rainfall data (Atencia *et al*. 2011, Oriani *et al*. 2014). This method is used to summarize censored data and not assume the value for constructing data distributions. The K-M method calculates the relative of data rank and statistical distribution based on right-censoring of the survival probability function.

Count variables, which have zero values for underlying probability distribution of counts, can be modeled using the zero-Inflated method. The zero-inflated method, proposed by J. Mullahy in 1986 and Diane Lambert in 1992 has been applied in economics, medical, public health and hydrology (Mullahy 1986, Lambert 1992, Ngatchou-Wandji 2011, Suhaila *et al*. 2013). The method can be divided into two sub-models, probability distributions of zero data and positive data. The general formula of the zero-inflated is.

$$P(Y = y) = \omega + (1 - \omega) \cdot f(y) \tag{1}$$

where Y is the count data; ω is the zero-inflation probability, and $f(y)$ is the density of the count distribution.

The nine Candidate statistical distributions were Generalize Pareto, Exponential, Beta, Gamma, Generalize extreme value, Extreme value, Log Normal, Weibull and Rayleigh distribution. **Table D1**

shows the 9 candidate distributions represented in a CDF form. We applied these 9 distributions with the zero-inflection value into equation (1). The resulted distributions could be used to fit continuous daily rainfall data. In this study, these distributions had shape parameter (a), scale parameter (b), location parameter (c), and zero probability value (w). The parameters were estimated by using maximum likelihood estimation method (MLE) that is occasionally used to optimize coefficient in statistical method (Myung 2003). The MLE is done by selecting a set of values of distribution parameters for underlying statistical distributions, where the selection parameter set maximizes the likelihood function (Geman and Hwang 1982, Uhler 2012, Huang *et al*. 2015). The distribution parameters were searched to obtain results from the multi-dimension parameter sets (Fienberg and Rinaldo 2012).

The goodness-of-fit (GOF) test reveals how well a statistical distribution fits an observed data. The 9 distributions were resulted by CDF using the parameters from MLE. The GOF test measures discrepancy between simulated and observed values (Maydeu-Olivares 2013). This test can be applied in statistical hypothesis testing as a null hypothesis, H_0 and H_1 (Shama and Singh 2010, Morey 2014). The H_0 is that the ECDF conform to the specific CDF, and the H_1 is that ECDF does not conform to the specific CDF. In this study, we used 3 GOF tests (Kolmogorov-Smirnov, Anderson-Darling, and Chi-Square test) that were qualitatively controlled by significance level of 5% to screen out unsuitable distributions.

Kolmogorov-Smirnov (K-S) test is a nonparametric test used to measure applicable continuous variable. The K-S test can be applied to evaluate the compatibility between empirical CDF (F(x)) and theoretical CDF (G(x)). The K-S statistic value is based on a maximum vertical difference of the both function (Frank 1951, Justel *et al*. 1997). Comparing F(x) and G(x), the K-S statistic is

$$D_{KS} = \max |F(X) - G(X)| \tag{3}$$

Critical values of K-S test regarding the tested statistical distribution is rejected when the P-value of tested statistic is greater than the significance level of 5% that was mentioned in the previous paragraph. The P-value of the K-S test is

$$Z_{KS} = D_{KS} \cdot \sqrt{n} \tag{4}$$

$$P(Z_{KS}) = 2 \cdot \sum_{k=1}^{\infty} (-1^{K-1} \cdot exp^{-2k^2 Z_{KS}^2}) \tag{5}$$

where n is a sample size of the CDF, Z_{KS} is the integral probability distribution.

Anderson-Darling (A-D) test, proposed by T. W. Anderson and D. A. Daring in 1952 (Anderson and Darling 1954), is normally used for testing a specified statistical distribution. The A-D test is modified to give more weight for the tail of the K-S test. This test statistic is defined as

$$A^2 = -n - \frac{1}{n}\sum_{i=1}^{n}(2i-1).[\ln F(X_i) + \ln(1 - F(X_{n-i+1}))] \tag{6}$$

The A-D test is screened out an unsuitable distribution based on the significance level of 5% to mention on above. P-value of the A-D test is used to reject when it is less than the critical values at 5%. The P-value of the A-D test is

$$P(A^2) = [1 + exp^{(-1+1.25 \cdot \log(A^2 + 4.48 \cdot A^2))}]^{-1} \tag{7}$$

Chi-Square (C-S) test, developed by Pearson in the 1900s is used to compare the statistical distribution and hypothesis test (Plackett 1983). The C-S test is also a nonparametric statistical test, used like the K-S test to determine whether two or more classified data are independent or dependent (Bolboaca *et al.* 2011). This test is normally used to evaluate the fit model between simulated and observed value, statistic of the test is defined as

$$\chi^2 = \sum_{i=1}^{k} \frac{(O_i - E_i)^2}{E_i} \tag{8}$$

where O_i is the observed frequency for bin i, E_i is expected frequency for bin i The expected frequency is estimated by

$$E_i = N[F(Y_u) - F(Y_l)] \tag{8}$$

where F is the CDF of tested distribution, Y_u is the upper limit for i, Y_l is the lower limit for i, and N is the sample size. A P-value of C-S test is depended on two variables, C-S statistic and degree of freedom (df), and estimated by using the Gamma function. This test can reject the tested distribution based on the critical value at 5% also on above test. The P-value of the C-S test is

$$df = n - 1 \tag{9}$$

$$P(C-S) = \frac{1}{\Gamma(\frac{\chi^2}{2})}\int_{0}^{\frac{df}{2}} e^{-t}t^{\frac{\chi^2}{2}-1}dt \tag{10}$$

where n is a sample size of the observation data.

The three GOF tests, which were set for a critical value at a 5% significance level, selected some conformity distribution to model the daily rainfall as mentioned above. The CDF of the conformity

distributions was generated and evaluated to find the best distribution. An evaluation index, two coefficients (residual (R) and correlation (Cor)), which was calculated as the difference between observed CDF represented by ECDF and simulated CDF, was used to assess the best fit simulation distribution (Sharma and Singh 2010, Prosser *et al.* 2011). The R and Cor coefficient are defined as

$$R = \frac{\sum_{i=1}^{n}|O_i - E_i|}{n} \tag{11}$$

$$Cor = \frac{\sum_{i=1}^{n}(O_i - \overline{O}) \cdot \sum_{i=1}^{n}(E_i - \overline{E})}{\sqrt{\sum_{i=1}^{n}(O_i - \overline{O})^2} \cdot \sqrt{\sum_{i=1}^{n}(E_i - \overline{E})^2}} \tag{12}$$

where O_i is observed data, E_i is estimated data and n is a total number of sampling data.

The ranking method for finding the best fit distribution used a ranking number that represents among the 9 distributions to create an order number between 1 and 9. The order number is marked on each distribution by using the R and Cor coefficient. To identify the order number, the distribution contain the lowest R and the highest Cor, is rank number 1, while the rank number 9 is the highest R, and lowest Cor. The best fit coefficient was calculated by an average of the ranking based on the R, and Cor coefficient. The best fit probability distribution was identified as the minimum of the best fit coefficient.

Table D1 Description of asymmetric statistical distribution functions.

Distribution	CDF	Parameter
GP (2P)	$F(x\|a,b) = 1 - e^{\left(-\frac{x-a}{b}\right)}$	$a = shape\ parameter$ $b = scale\ parameter$
Exp	$F(x\|a) = 1 - e^{-ax}$	$a = mean$
Beta	$F(x\|a,b) = I_x(a,b)$ $I_x(a,b) = \frac{\int_0^x t^{a-1} \cdot (1-t)^{b-1}\, dt}{B(a,b)}$	$\left.\begin{array}{l} a \\ b \end{array}\right\} = shape\ parameter$ $B = Beta\ function$ $I = Indicator\ function$
Gamma (2P)	$F(x\|a,b) = \frac{b^{-a} \cdot x^{a-1} \cdot e^{\frac{-x}{b}}}{\Gamma(a)}$	$a = shape\ parameter$ $b = scale\ parameter$ $\Gamma = Gamma\ function$
Gev	$F(x\|a,b,c) = e^{\left\{-\left[1+c\left(\frac{x-a}{b}\right)\right]^{\frac{-1}{c}}\right\}}$	$a = shape\ parameter$ $b = scale\ parameter$ $c = location\ parameter$
Ev (Type I)	$F(x\|a,b) = 1 - e^{-e^{\left(\frac{x-a}{b}\right)}}$	$a = shape\ parameter$ $b = scale\ parameter$
Log Normal	$F(x\|a,b) = \Phi\left(\frac{\log(x) - a}{b}\right)$	$a = mean$ $b = standard\ Deviation$ $(b > 0)$
Weibull (2P)	$F(x\|a,b) = 1 - e^{-\left(\frac{x}{b}\right)^a}$	$a = shape\ parameter$ $b = scale\ parameter$
Rayleigh	$F(x\|a) = 1 - e^{\frac{-x^2}{2a^2}}$	$a = shape\ parameter$

D.2 RESULTS AND DISCUSSION

The methodology mentioned above was applied to 123 rain gauges Thailand, covered 37 years of daily data for the continuous temporal data. According to a results, the cumulative distribution function (CDF) and the probability in the different distributions have shown in the first. Analysis of the results in the middle, a goodness-of-fit test, and a ranking test result were presented. Finally, the best-fit distribution of each rain gauge was shown.

On fitting distribution result, the 123 rain gauges data were fitted by using the 9 distributions resulted in CDF. The 9 simulated CDFs were compared to ECDF by 95% confidence interval of the ECDF for evaluation. For the example, **Figure D1** presented the simulated and observed CDF on rain gauge number 300201. **Figure D2** presented a probability difference between observation and theoretical from this station.

Kolmogorov-Smirnov (K-S), Anderson-Darling (A-D) and Chi-Square (C-S) test was used and analyzed on the 9 distributions in each rain gauge to screen an incompatible distribution base on the level of significance. The incompatible distribution was identified by P-value on the significance level at 0.05. **Table D2** shows the P-value of each distribution and conformable distribution. Selecting the compatible distribution based on the hypothesis test, when the two-thirds of 3 hypothesis tests were acceptable, the tested distribution was selected. On the other hand, unselected distribution was identified in the two-thirds of 3 hypothesis tests are rejected. For the station No. 300201, seven distributions were accepted that were used to identify the best model by using the ranking method.

The best-fit distribution was based on residual (R) and correlation (Cor) coefficient between simulation and observation CDF. **Table D3** shows these both coefficient values of each selected distribution on the station No. 300201. For the best model, the minimum value of the R and the maximum value of the Cor were selected. Summary ranking could be calculated by the average of both coefficients, was used to identify the best-fit distribution. Weibull distribution among the eight distributions was the best model on the station No. 300201 for the example. The 123 rain gauges have gotten the results in the same processes as the example.

The best probability distribution of all rain gauges (**Figure D3**) was plotted by using its coordinate based on latitude and longitude. The rain gauge coordinate was used to distribute presented on the spatial map by using the Kriging algorithm. The poorly fitted parameters of the spherical semi-variogram model were the nugget variance (C_0) is 0.01, the partial sill (C) is 0.04 and the range (a) is 5.0 degree, are used to analyze.

Weibull distribution conforms to 118 stations while 5 rain gauge stations fit to the Gamma distribution. Most of the stations, which are located in the continental area, fitted to the Weibull distribution. The 5 rain gauges accepted with the Gamma distribution are the highest annual rainfall zone that has been influenced by the monsoon and typhoon. Ranong station fitted to the Gamma that is located at the foot of the mountain and affected by the southwest monsoon and the Bengol Cyclone. Also, Phriu Agr and Khlong Yai same as the Ranong station where the location have influenced from the northeast monsoon and typhoon. While the both Nakhon Phanom station located far from the mountain are influenced by the typhoon to get the high annual rainfall and fitted to the Gamma distribution.

The study results can be compared to the several researches that the comparison is only relative as fitted distribution name, while the other components are different such as temporal scale, rainfall event, and location domain. Based on the location in the Phrae province, The 9 rain gauges of the study was fitted by the Weibull distribution, while the previous study these 9 rain gauges was fitted by the Extreme value distribution (T. Tingsanchali and F. Karin, 2010). Also, by the contrast, the fitted distribution on the previous study on the north-eastern part was presented by the Leakage distribution that was different to this study (Phien et al., 1980). This study results showed the Weibull distribution that fitted to the rain gauge data on the north-eastern part. The results on the southern part was indirectly compared to neighbor area as Malesia that the fitted distribution of the neighbor country was Lognormal (Suhaila et al., 2011). The fitted distribution of this study was the Weibull that contrasted to the previous study.

Generally, the modeling distribution results have gotten an effect from the difference of elevation and location of rain gauges, including monsoon and typhoon. Also, the results will be influenced by terrain and climate change.

Table D2 The hypothesis test of 300201 rain gauge station.

Distribution	K-S test		A-D test		C-S test		Remark
	Null	P-Value	Null	P-Value	Null	P-Value	
GP (2P)	0	0.981	0	0.204	0	0.971	Accept
Exp	0	0.413	1	0.018	0	0.431	Accept
Beta	0	0.999	1	0.001	0	0.921	Accept
Gamma (2P)	0	1.000	0	0.454	0	1.000	Accept
Gev	0	0.988	1	0.024	0	0.961	Accept
Ev (2P)	1	0.001	0	0.001	1	0.002	Reject
Log Normal	0	0.998	1	0.049	0	0.997	Accept
Weibull (2P)	0	1.000	0	0.891	0	1.000	Accept
Rayleigh	1	0.001	1	0.001	1	0.001	Reject

Table D3 The ranking number of 300201 rain gauge station.

Distribution	Res		Cor		Rank
	Coef.	Rank	Coef.	Rank	
GP (2P)	3.150	3	0.9958	4	3
Exp	6.408	6	0.9941	5	5
Beta	4.640	4	0.9974	3	3
Gamma (2P)	1.623	2	0.9995	2	2
Gev	8.310	7	0.9869	7	7
Ev (2P)	-	-	-	-	-
Log Normal	5.982	5	0.9927	6	5
Weibull (2P)	0.866	1	0.9996	1	1
Rayleigh	-	-	-	-	-
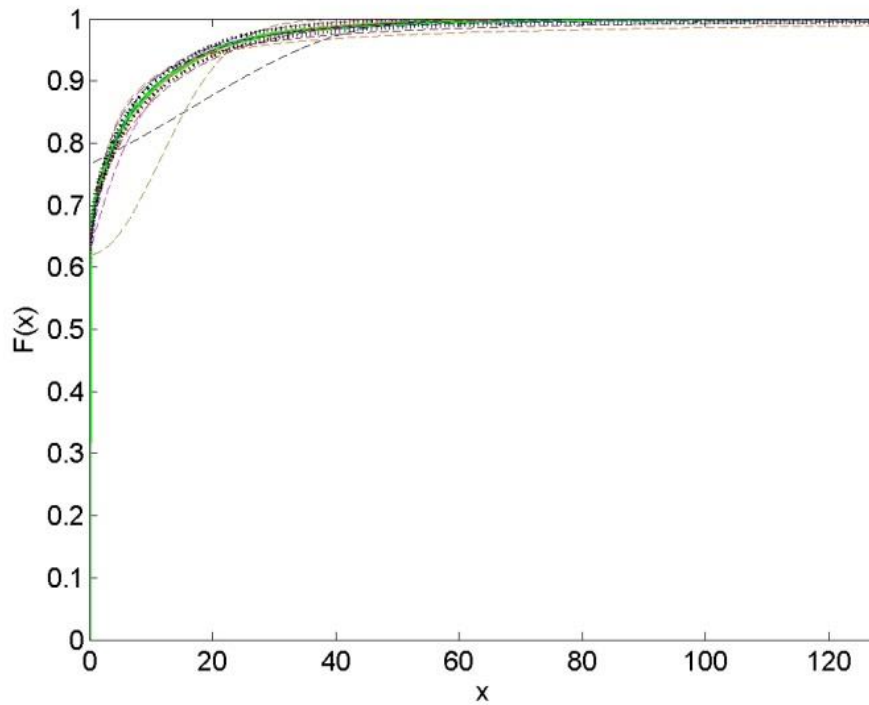
Figure D1 Cumulative distribution function (CDF) of each distribution was stretched by using the zero-inflated on rain gauge station No.300201
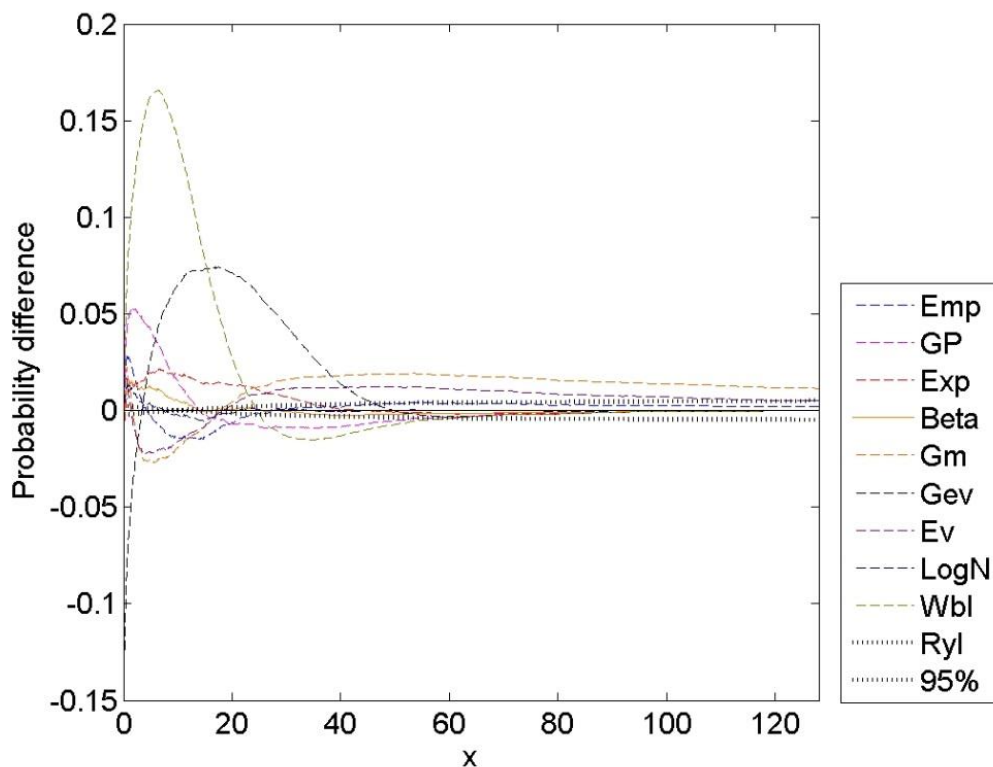
Figure D2 Probability difference between ECDF and modelled CDF on rain gauge No. 300201.

D.3 CONCLUSIONS

The goal was to consider compatible statistical distribution for daily rainfall data to simulate rainfall intensity. This research indicates that the continue data can be fitted by using probability distribution with a zero-inflated approach. The tested distributions are General Pareto, Exponential, Beta, Gamma, Generalize extreme value, Extreme value, Log-normal, Weibull, and Rayleigh distributions.

It found that a statistical distribution with zero-inflated on Weibull distribution was the most fitted distribution of daily rainfall intensity in Thailand with the goodness of fit score between observed and simulated value based on hypothesis test, maximum correlation (Cor) and minimum residual (R). In the second favorite distribution, the rain gauge stations were fitted by Gamma distribution, located in huge and orographic precipitation zone. In summary rainfall in Thailand, the rain gauge data are greatly influenced by their elevation, terrain and climate change to provide uncertainty on the rainfall distribution.

The scientific approach sufficiently established that the analytical methodology devised and test in this study may be utilized for the identification of the best fit statistical probability distribution of weather parameters. However, our statistical distributions can be used available to the scientific community through the hydrology modeling for use in the rainfall prediction application to water resources management.
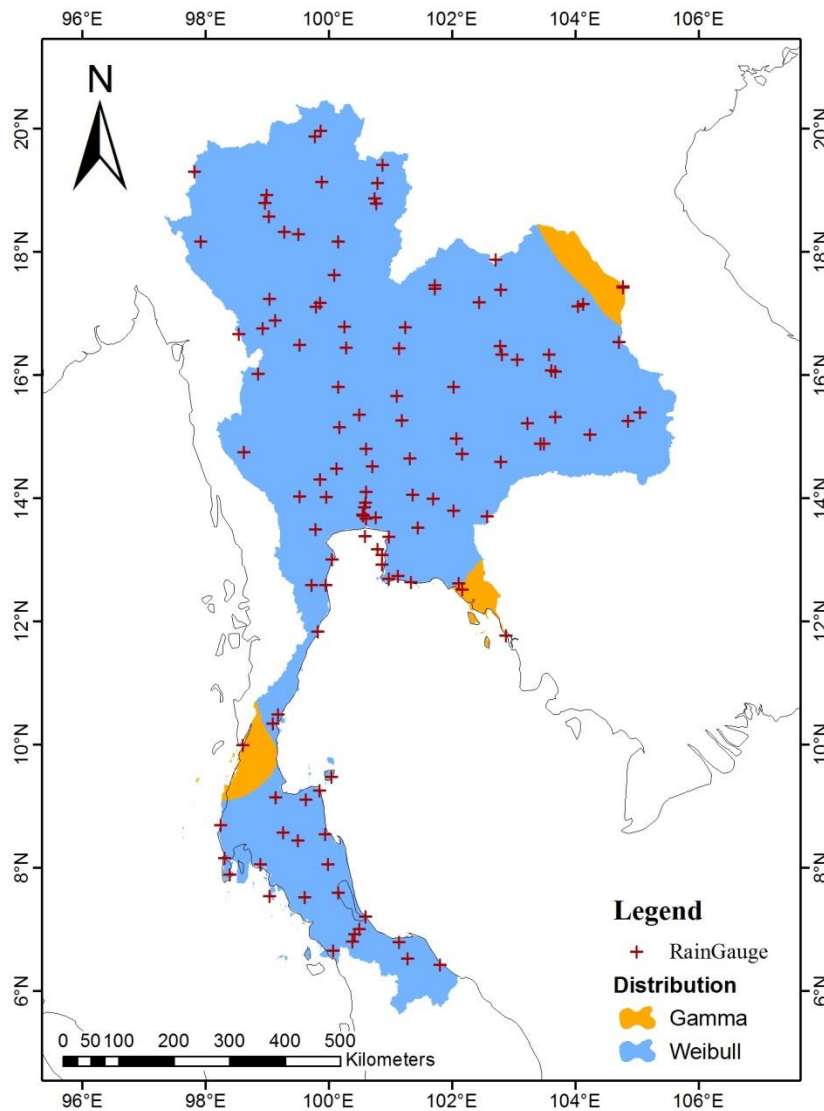
Figure D3 The best-fit probability distribution of rain gauges on daily rainfall in Thailand.

D.4 REFERENCES

Anderson, T. W., Darling, D. A., 1954. A Test of Goodness of Fit. Journal of the American Statistical Association, 49, 765–769.

Atencia, A., Mediero, L., Llasat, M. C., Garrote, L., 2011. Effect of radar rainfall time resolution on the predictive capability of a distributed hydrologic model. Hydrology and Earth System Sciences, 15, 3809–3827.

Bolboaca, S. D., Jantschi, L., Sestras, A. F., Sestras, R. E., Pamfil, D. C., 2011. Pearson-Fisher Chi-Square Statistic Revisited. Information, 2, 528–545.

Cai, Z., Roussas, G. G., 1998. Kaplan-Meier Estimator under Association. Journal of Multivariate Analysis, 67, 318–348.

Danʻazami, S., Shamsudin, S., Aris, A., 2010. Modeling of Rainfall Intensity using Hourly Data. American Journal of Environmental Sciences, 6, 238-243.

Dan'azumi, S., Shamsudin, S., Rahman, A. A., 2010. Probability Distribution of Rainfall Depth at Hourly Time-Scale. International Journal of Environment, Earth Science and Engineering, 4, 1–5.

Famoye, F., Singh, K. P., 2006. Zero-Inflated Generalized Poisson Regression Model with an Application to Domestic Violence Data. Journal of Data Science, 4, 117–130.

Fienberg, S. E., Rinaldo, A., 2012. Maximum Likelihood Estimation in Log-Linear Models. The Annals of Statistics, 40, 996–1023.

Frank J. Massey, J., 1951. The Kolmogorov-Smirnov Test for Goodness of Fit. Journal of the American Statistical Association, 46, 68–78.

Geman, S., Hwang, C., 1982. Nonparametric Maximum Likelihood Estimation by the Method of Sieves. The Annals of Statistics, 10, 401–414.

Ha, E., Yoo, C., 2007. Use of Mixed bivariate distributions for deriving inter-station correlation coefficients of rain rate. HYDROLOGICAL PROCESSES, 21, 3078–3086.

Hanson, L. S., Vogel, R., 2008. The Probability Distribution of Daily Rainfall in the United States, World Environmental and Water Resources Congress 2008, Honolulu Hawaii, USA, May 12-16, 2008; Roger W. Babcock, Raymond Walton, Eds.

Huang, K., Guo, S. T., Shattuck, M. R., Chen, S. T., Qi, X. G., Zhang, P., Li, B.G., 2015. A maximum-likelihood estimation of pairwise relatedness for autopolyploids. Heredity, 114, 133–142.

Jiang, Q., 2003. Moist dynamics and orographic precipitation. Tellus, 55A, 301–316.

Justel, A., Pefia, D., Zamar, R., 1997. A multivariate Kolmogorov-Smirnov test of goodness of fit. Statistics and Probability Letters, 35, 251–259.

Kaplan, E. L., Meier, P., 1958. Nonparametric Estimation from Incomplete Observations. Journal of the American Statistical Association, 53, 457–481.

Lambert, D., 1992. Zero-Inflated Poisson Regression, with an Application to Defects in Manufacturing. Technometrics, 34, 1–14.

Maydeu-Olivares, A., 2013. Goodness-of-Fit Assessment of Item Response Theory Models. Measurement: Interdisciplinary Research and Perspectives, 11, 71–101.

Morey, R. D., Wagenmakers, E. J., 2014. Simple relation between Bayesian order-restricted and point-null hypothesis tests. Statistics and Probability Letters, 92, 121–124.

Mullahy, J., 1986. Specification and test of some modified count data models. Journal of Econometrics, 33, 341–365.

Myung, I. J., 2003. Tutorial on maximum likelihood estimation. Journal of Mathematical Psychology, 47, 90–100.

Ngatchou-Wandji, J., Chritophe., 2011. On the Zero-Inflated Count Models with Application to Modelling Annual Trends in Incidences of Some Occupational Allergic Diseases in France. Journal of Data Science, 9, 639–659.

Oriani, F., Straubhaar, J., Renard, P., Mariethoz, G., 2014. Simulation of rainfall time series from different climatic regions using the direct sampling technique. Hydrology and Earth System Sciences, 18, 3015–3031.

Phien, H. N., Arbhabhirama, A., Sunchindah, A., 1980. Rainfall distribution in northeastern Thailand. Hydrological Sciences-Bulletin, 25, 167–182.

Picado, A., Lopes, C. L., Mendes, R., Vas, N., Dias, J. M., 2013. Storm surge impact in the hydrodynamics of tidal lagoon: the case of Ria de Aveiro. Journal of Coastal Research, Special Issue, 796–801.

Plackett, R. L., 1983. Karl Pearson and the Chi-Squared Test. International Statistical Review, 51, 59–72.

Prosser, D. J., Wu, J., Ellis, E. C., Gale, F., Boeckel, T. P. V., Wint, W., Robinson, T., Xiao, X., Gilbert, M., 2011. Modelling the distribution of chickens, ducks, and geese in China. Agriculture, Ecosystems and Environment, 141, 381–389.

Sharma, M. A., Singh, J. B., 2010. Use of Probability Distribution in Rainfall Analysis. New York Science Journal, 3, 40–49.

Suhaila, J., Jmain, A. A., 2007. Fitting Daily Rainfall Amount in Malaysia Using the Normal Transform Distribution. Journal of Applied Sciences, 7, 1880-1886.

Suhaila, J., Ching-Yee, K., Fadhilah, T., Hui-Mean, F., 2011. Introduction the Mixed Distribution in Fitting Rainfall Data. Open Journal of Modern hydrology, 1, 11-22.

Suhaila, J., Ching-Yee, K., Yusof, F., Hui-Mean, F., 2013. Effect of Zero Measurements in Rainfall Data. Journal Teknologi, 63, 35–39.

Tawatchai Tingsanchili, Fazlul Karim, 2010. Flood-hazard assessment and risk-based zoning of a tropical flood plain: case study of the Yom River, Thailand. Hydrological Sciences Journal, 55:2, 154–161.

Uhler, C., 2012. Geometry of Maximum Likelihood Estimation in Gaussian Graphical Models. The Annals of Statistics, 40, 238–261.

E. Economic data sets

E.1 Input-Output table of the Shikoku Island, Japan

Table E1 Input-output (I-O) table of the Shikoku Island with 7 industrial sectors in summary on 2005.

million yen	Arg	Mining	Textile	Paper	Chemical	Househole	Service	Final demand	Total output
Arg	65,381	4	154,032	31,229	1,322	1,296	30,861	300,315	584,440
Mining	22	106	2	10,882	843,609	104	123,939	-936,909	41,755
Textile	40,135	-	84,584	20,008	1,579	1,343	99,018	517,029	763,696
Paper	14,967	265	20,860	251,229	18,872	10,356	188,114	556,549	1,061,212
Chemical	20,043	3,033	27,243	38,647	492,151	51,066	432,677	2,733,727	3,798,587
Househole	5,563	175	377	2,228	14,428	54,027	61,861	382,270	520,929
Service	65,326	15,220	94,750	176,383	527,752	130,255	2,888,649	10,308,214	14,206,549
Value added	373,003	22,952	381,848	530,606	1,898,874	272,482	10,381,430		
Total input	584,440	41,755	763,696	1,061,212	3,798,587	520,929	14,206,549		

E.2 Input-Output table of the Thailand

Table E2 Inter-regional input-output (IRIO) table of the Thailand with 2 industrial sectors and other country in summary on 2005.

Part I: IRIO table (2005)
Unit: 1,000 million US

	Indonesia (AI)	Malasia (AM)	Philippines (AP)	Singapore (AS)	Thailand (paddy) (ATP)	Thailand (Non paddy) (ATN)	China (AC)	Taiwan (AN)	Korea (AK)	Japan (AJ)	USA (AU)	Final Demand (F)	Exports (E)	Imports (I)	Total output (XX)
Indonesia (AI)	231.27	2.79	0.87	6.61	0.03	1.82	6.94	3.64	7.68	17.70	3.69	267.60	65.63	-30.12	586.14
Malasia (AM)	2.18	194.22	1.51	6.31	0.06	5.22	15.67	3.83	4.80	10.19	16.12	108.53	89.57	-34.44	423.77
Philippines (AP)	0.20	0.90	95.44	1.55	0.00	1.16	4.11	1.46	1.43	3.71	3.86	109.64	38.03	-21.75	239.74
Singapore (AS)	4.40	9.15	2.75	90.45	0.00	3.17	12.99	3.57	7.94	7.61	8.41	72.82	156.42	-65.03	314.65
Thailand (paddy) (ATP)	-	-	0.00014	-	0.18	4.41	-	0.00007	-	0.00002	-	0.477	0.3401	-0.8403	4.57
Thailand (Non paddy) (ATN)	2.86	5.05	1.13	2.75	0.75	180.03	9.21	2.16	2.12	10.16	10.33	190.186	193.26	-140.89	469.09
China (AC)	5.83	10.03	2.35	7.08	0.06	8.26	3,853.32	13.44	23.71	41.64	72.44	2,140.833	809.93	-316.42	6,672.50
Taiwan (AN)	1.07	5.02	2.34	4.67	0.00	3.02	33.61	295.17	6.67	14.02	17.11	322.918	172.43	-72.18	805.85
Korea (AK)	2.35	3.69	1.67	1.98	0.01	3.82	52.24	10.06	891.57	19.48	20.46	803.680	309.55	-138.65	1,981.89
Japan (AJ)	6.60	12.86	5.98	6.89	0.01	16.29	65.69	29.95	39.64	3,719.27	60.03	4,387.361	534.45	-268.99	8,616.02
USA (AU)	2.83	9.26	3.15	16.57	0.03	9.23	29.32	14.52	25.78	47.89	9,838.29	12,362.596	1,851.99	-900.00	23,311.46
Value added (V)	326.56	170.78	122.56	169.80	3.43	232.67	2,589.41	428.05	970.56	4,724.35	13,260.74				
Total input (XX)	586.14	423.77	239.74	314.65	4.57	469.09	6,672.50	805.85	1,981.89	8,616.02	23,311.46				

282

G. Python programming in this study

G.1 Loading satellite rainfall data from FTP

G.1.1 GPM

```
# GPM ftp
# downloading file from ftp by folder of monthly
# Jun 18, 2015
# for GPM data @ 30 min

from ftplib import FTP
import os, sys, os.path

Name = 'arthurhou.pps.eosdis.nasa.gov' # main FTP downloading
ftp = FTP(Name)

print 'Logging in. :' + Name
ftp.login('178011e@gs.kochi-tech.ac.jp','178011e@gs.kochi-tech.ac.jp') # user ID and password

yy = 2014 # year

for mm in range(3,4): # month
    if mm in (1,3,5,7,8,10,12):
        days = 31
    elif mm in (4,6,9,11):
        days = 30
    else:
        days = 28
    for dd in range(1,days+1): # day
            directory = '/gpmdata/'+ str(yy) + '/' + str("{:0>2d}".format(mm)) + '/' \
                + str("{:0>2d}".format(dd)) + '/imerg/'
            print 'Changing to ' + directory
            ftp.cwd(directory)
            ftp.retrlines('LIST')
            filenames = ftp.nlst() # get filenames within the directory
            print 'Accessing files'
        for filename in filenames:
            local_filename = os.path.join('../loadedData/2014GPM', filename)
            file = open(local_filename, 'wb')
            ftp.retrbinary('RETR '+ filename, file.write)
            print '.'+filename
            file.close()
ftp.close()
```

G.1.2 GSMaP

```
# GSmap ftp
# Download GSmap data v.6 from ftp of JAXA in hourly data
# v.0.0.1 by kwanchai at june 12. 2015

from ftplib import FTP
import os, sys, os.path

Name = 'hokusai.eorc.jaxa.jp'
ftp = FTP(Name)

print 'Logging in. :' + Name
ftp.login('rainmap','Niskur+1404') # user ID and password

yy = 2015 # year

for mm in range(3,4): # month
    if mm in (1,3,5,7,8,10,12):
        days = 31
```

```
    elif mm in (4,6,9,11):
      days = 30
    else:
      days = 28
    for dd in range(8,days+1): # day
      directory = '/standard/v6/hourly/'+ str(yy) + '/' + str("{:0>2d}".format(mm)) + \
            '/' + str("{:0>2d}".format(dd)) + '/'
      print 'Changing to ' + directory
          ftp.cwd(directory)
          #ftp.retrlines('LIST')
      filenames = ftp.nlst() # get filenames within the directory
      filenames.sort()
      print 'Accessing files'
      for filename in filenames:
        local_filename = os.path.join('../loadedData/2014GSmap', filename)
        file = open(local_filename, 'wb')
        ftp.retrbinary('RETR '+ filename, file.write)
        print '.'+filename
        file.close()
ftp.close()
```

G.1.3 TRMM

```
#!/usr/bin/python
# TRMM ftp
# Download TRMM data v.7 from ftp of NASA in 3-hourly data
# v.0.0.1 by kwanchai at june 10. 2015

from ftplib import FTP
import os, sys, os.path

Name = 'trmmopen.gsfc.nasa.gov' # main FTP downloading
ftp = FTP(Name)
print 'Logging in. :' + Name
ftp.login() # user ID and password

yy = 2015 # year
directory = '/pub/merged/3B42RT/' + str(yy) + '/'
print 'Changing to ' + directory
ftp.cwd(directory)
#ftp.retrlines('LIST')
filenames = ftp.nlst() # get filenames within the directory
filenames.sort()
#filenames = filenames[1738::]
print 'Accessing files'
for filename in filenames:
  local_filename = os.path.join('../loadedData/2014TRMM', filename)
  file = open(local_filename, 'wb')
  ftp.retrbinary('RETR '+ filename, file.write)
  print '.'+filename
  file.close()
ftp.close()
```

G.1.4 CMORPH

```
# CMORPH ftp
# downloading file from ftp by folder of monthly
# Jun 18, 2015

from ftplib import FTP
import os, sys, os.path

Name = 'ftp.cpc.ncep.noaa.gov'
ftp = FTP(Name)

print 'Logging in. :' + Name
ftp.login()
```

```
yy = 2014

for m in range(2,4): # by month
    directory = '/precip/CMORPH_V1.0/RAW/0.25deg-3HLY/'+ str("{:0>2d}".format(yy)) \
            +'/'+ str("{:0>2d}".format(yy)) +str("{:0>2d}".format(m))
    print 'Changing to ' + directory
    ftp.cwd(directory)
    ftp.retrlines('LIST')
    filenames = ftp.nlst() # get filenames within the directory
    print 'Accessing files'
    for filename in filenames:
        local_filename = os.path.join('../loadedData/2014CMORPH', filename)
        file = open(local_filename, 'wb')
        ftp.retrbinary('RETR '+ filename, file.write)
        print '.'+filename
    file.close()

ftp.close()
```

G.1.5 PERSIANN

```
#!/usr/bin/python
# PERSIANN ftp
# Download PERSIANN data from ftp of JAXA in daily data
# v.0.0.1 by kwanchai at june 12. 2015

from ftplib import FTP
import os, sys, os.path

Name = 'persiann.eng.uci.edu' # main FTP downloading
ftp = FTP(Name)
print 'Logging in. :' + Name
ftp.login() # user ID and password

directory = '/pub/PERSIANN/daily/'
print 'Changing to ' + directory
ftp.cwd(directory)
#ftp.retrlines('LIST')
filenames = ftp.nlst() # get filenames within the directory
filenames.sort()
ftp.close()

with open('new_file.txt', 'w') as out_file:
    out_file.write('\n'.join(filenames))
```

G.2 Capturing grid data of satellite data to rain gauge points

G.2.1 GPM

```
# -*- coding: utf-8 -*-
#!/usr/local/bin/python

import glob, os
import pandas as pd
import numpy as np
import h5py as h5

# GPM char.
ulLat = 89.95
llLon = -179.95
rainfallN = 'precipitationCal'

# read rain gauge coor.
RG = pd.read_csv('./raingaugeNaN2014_coor.csv')
RG['R']=((ulLat-RG['N'])/0.1)
```

```
RG['C']=((RG['E']-llLon)/0.1)
RG[list("RC")]=RG[list("RC")].apply(np.round)

# read GPM files
os.chdir('../../GPM2_2014')
#os.chdir('./temp_GPM/test')
fileN = glob.glob('*.HDF5')
fileN.sort()
RGn = len(RG) # num. of rain gauge
GPM = np.array([np.arange(1, RGn+1, dtype=float)]).T
print len(fileN)
n = 1 # counter

# to capture with RG coor
for fname in fileN:
    print n, fname
    n+=1
    fid = h5.File(fname,'r')
    grp = fid['Grid']
    prec= grp[rainfallN].value
    fid.close()
    precT = np.fliplr(prec) # mirror matrix
    Rain = precT.T
    temp = np.array([Rain[RG['R'],RG['C']]]).T
    GPM  = np.hstack((GPM, temp))

# save txt file
GPM = np.array([GPM]).T
np.savetxt("../scrip_analysis/RG_capture_rev01/SPP2RG_data/A_GPM2RG_Nan.csv",    GPM,    delimiter=",",
fmt='%-7.3f')
```

G.2.2 GSMaP

```
# -*- coding: utf-8 -*-
#!/usr/local/bin/python

import glob, os
import gzip
import pandas as pd
import numpy as np

# GSMaP parameter
num_lon = 1200
num_lat = 3600

ulLat = 59.95
llLon = 0.05

# reading gz file
def read_bin(gz, num_lon, num_lat):
    arr = np.fromstring(gz.read(), dtype='f').reshape(num_lon, num_lat)
    return arr

# read rain gauge coor.
#RG = pd.read_csv('./tempRG/tempRG.csv')
RG = pd.read_csv('./raingauge2014_coor.csv')
RG['R']=((ulLat-RG['N'])/0.1)
RG['C']=((RG['E']-llLon)/0.1)
RG[list("RC")]=RG[list("RC")].apply(np.round)

# read GSMaP files
path = '../../../download_data/loadedData/2014GSmap/*.gz'
fileN = glob.glob(path)
fileN.sort()
```

```
RGn = len(RG) # num. of rain gauge
GSM = np.array([np.arange(1, RGn+1, dtype=float)]).T
print len(fileN)
n = 1 # counter

# to capture with RG coor
for fname in fileN:
    gz = gzip.open(fname)
    Rain = read_bin(gz, num_lon, num_lat)
    n+=1
    print n, fname
    temp = np.array([Rain[RG['R'],RG['C']]]).T
    GSM  = np.hstack((GSM, temp))

# save txt file
GSM = np.array([GSM]).T
np.savetxt("../../../analysis/scrip_analysis/RG_capture_rev01/SPP2RG_data/B_GSMaP2RG.csv",          GSM,
delimiter=",", fmt='%-7.3f')
```

G.2.3 TRMM

```
import glob, os
import pandas as pd
import numpy as np
import matplotlib.pyplot as plt
from mpl_toolkits.basemap import Basemap

# TRMM parameter
precip_scale_factor = 100.0
rows = 480
cols = 1440

# identify lat lon
# create one rwo of N-S coordinates
# coordinate locates the centre of the cell
lat=np.arange(59.875,-60.125,-0.25, dtype=float)
lat=lat[:, None]
lng=np.arange(0.125,360.125,+0.25, dtype=float)
# ones metrix
la1=np.ones(cols)
ln1=np.ones((rows,1))
# lat,lon
lat=la1*lat
lng=ln1*lng
ulLat = lat.max() # upper left conner
llLon = lng.min() # lower left coner

# read rain gauge coor.
RG = pd.read_csv('./raingauge2014_coor.csv')
RG['R']=((ulLat-RG['N'])/0.25)
RG['C']=((RG['E']-llLon)/0.25)
RG[list("RC")]=RG[list("RC")].apply(np.round)

# read TRMM file
os.chdir("../../TRMM2_2014")
fileN = glob.glob('*.bin')
fileN.sort()
RGn = len(RG) # num. of rain gauge
TRMM = np.array([np.arange(1, RGn+1, dtype=float)]).T
n = 1

# to read TRMM file
for fname in fileN:
```

```
        print n,fname
        n+=1
        fp = open(fname, 'rb')
        data_string = fp.read()
        fp.close()
        precip = np.fromstring(data_string[2880:1385280], np.int16)
        precip = precip.byteswap()
        precip = np.asarray(precip, np.float32)
        precip /= precip_scale_factor
        precip = precip.reshape(rows, cols)
        temp = np.array([precip[RG['R'],RG['C']]]).T
        TRMM = np.hstack((TRMM, temp))

# save txt file
TRMM = np.array([TRMM]).T
np.savetxt("../scrip_analysis/RG_capture_rev01/SPP2RG_data/C_TRMM2RG.csv", TRMM, delimiter=",", fmt='%-
7.3f')
```

G.2.4 CMORPH

```
# -*- coding: utf-8 -*-
#!/usr/local/bin/python

import bz2
import glob, os
import pandas as pd
import numpy as np

# CMORPH parameter
Nrows = 480
Ncols = 1440

ulLat = 59.875
llLon = 0.125

# read rain gauge coor.
RG = pd.read_csv('./raingauge2014_coor.csv')
RG['R']=((ulLat-RG['N'])/0.25)
RG['C']=((RG['E']-llLon)/0.25)
RG[list("RC")]=RG[list("RC")].apply(np.round)

# CMORPH data folder
path = '../../../download_data/loadedData/2014CMORPH/*.bz2'
fileN = glob.glob(path)
fileN.sort()

RGn = len(RG) # num. of rain gauge
CMH = np.array([np.arange(1, RGn+1, dtype=float)]).T
print len(fileN)

n = 1
# to capture with RG coor.
for fname in fileN:
    print n, fname
    n+=1
    bzFile = bz2.BZ2File(fname).read()
    data_type = np.dtype ('f32').newbyteorder ('<f')
    data = np.frombuffer(bzFile, data_type).reshape(8,Nrows,Ncols)
    print data.shape
    for t in range(0,8):
        temp0 = data[t,:,:]
        temp1 = temp0.T
        temp2 = np.fliplr(temp1)
        Rain = temp2.T
```

```
        print t, Rain.shape
        temp = np.array([Rain[RG['R'],RG['C']]]).T
        CMH  = np.hstack((CMH, temp))

# save txt file
CMH = np.array([CMH]).T
np.savetxt("../../../analysis/scrip_analysis/RG_capture_rev01/SPP2RG_data/D_CMORPH2RG.csv",          CMH,
delimiter=",", fmt='%-7.3f')
```

G.2.5 PERSIANN

```
# -*- coding: utf-8 -*-
#!/usr/local/bin/python

import glob, os
import numpy as np
import pandas as pd
import gzip

# PERSIANN parameter
rows = 480
cols = 1440

ulLat = 59.875
llLon = 0.125

# read rain gauge coor.
RG = pd.read_csv('./raingauge2014_coor.csv')
RG['R']=((ulLat-RG['N'])/0.25)
RG['C']=((RG['E']-llLon)/0.25)
RG[list("RC")]=RG[list("RC")].apply(np.round)

# read PERSIANN files
path = ('../../PERSIANN2_2014/data_2014/*.gz')
fileN = glob.glob(path)
fileN.sort()

RGn = len(RG) # num. of rain gauge
PRS = np.array([np.arange(1, RGn+1, dtype=float)]).T

n = 1
# to capture with RG coor
for fname in fileN:
    print n, fname
    n+=1
    gz = gzip.open(fname)
    data_type = np.dtype('float32').newbyteorder ('>')
    data = np.fromstring(gz.read(), data_type).reshape(rows,cols)
    temp = np.array([data[RG['R'],RG['C']]]).T
    PRS  = np.hstack((PRS, temp))

# save txt file
PRS = np.array([PRS]).T
np.savetxt("../../scrip_analysis/RG_capture_rev01/SPP2RG_data/E_PRS2RG.csv",  PRS,  delimiter=",",  fmt='%-
7.3f')
```

G.3 Rain gauge spatial

G.3.1 IDW, TSP, SPL

```python
import numpy as np
import pandas as pd
import itertools

# This is the actual nearest neighbor function
def nearest_neighbor(x,y,v,grid):
    for i in xrange(grid.shape[0]):
        for j in xrange(grid.shape[1]):
            distance = np.sqrt((x-i)**2+(y-j)**2)
            grid[i,j] = v[distance.argmin()] # argmin gives us the index of the minimum value.
    return grid

# This is the IDW function
def idw(x, y, z, xi, yi):
    dist = distance_matrix(x,y, xi,yi)

    # In IDW, weights are 1 / distance
    weights = 1.0 / dist

    # Make weights sum to one
    weights /= weights.sum(axis=0)

    # Multiply the weights for each interpolated point by all observed Z-values
    zi = np.dot(weights.T, z)
    return zi

def distance_matrix(x0, y0, x1, y1):
    obs = np.vstack((x0, y0)).T
    interp = np.vstack((x1, y1)).T

    # Make a distance matrix between pairwise observations
    # Note: from <http://stackoverflow.com/questions/1871536>
    # (Yay for ufuncs!)
    d0 = np.subtract.outer(obs[:,0], interp[:,0])
    d1 = np.subtract.outer(obs[:,1], interp[:,1])

    return np.hypot(d0, d1)

# to fit polynomial parameter
def Fit2Dpoly(x, y, z, k1, k2):
    p   = (k1+1)*(k2+1)
    M   = np.zeros((x.size, p))
    ij  = itertools.product(range(k1+1), range(k2+1))
    for g, (i,j) in enumerate(ij):
            M[:,g] = x**i*y**j
    c,_,_,_ = np.linalg.lstsq(M,z)
    return c

# to model polynomial model
def Sim2Dpoly(x,y,c,k1,k2):
    ij = itertools.product(range(k1+1), range(k2+1))
    z  = np.zeros_like(x)
    for p, (i,j) in zip(c, ij):
            z += p*x**i*y**j
    return z

# Error of simulation
def rmse(predictions, targets):
    return np.sqrt(((predictions - targets) ** 2).mean())
```

G.3.2 Simple and Ordinary kriging

```
import numpy as np
import pandas as pd
from sklearn.gaussian_process import GaussianProcess
import scipy.interpolate as interpolate

# Main program
# load rain gauge data
RG = pd.read_csv('./raingauge_gridMerge2011.csv', sep=',',header=None)
RG = RG.values
print RG.shape

# load coor.
coor = pd.read_csv('./gridMerge_coor.csv', sep=',',header=None)

# grid char.
ulLat = 19.65
llLon = 100.15
coor['R'] = ((ulLat-coor[1])/0.1)
coor['C'] = ((coor[0]-llLon)/0.1)
coor[list("RC")]=coor[list("RC")].apply(np.round)

# grid spatial
SP = np.nan*np.ones(shape=(20,13))
r = np.linspace(0, 1.9, SP.shape[0])
c = np.linspace(0, 1.2, SP.shape[1])
rr, cc = np.meshgrid(c, r)
beta0 = [0]

# temp prediction
pRG = np.zeros((1,13))
n = 1 # counter
t_temp = np.zeros((1,13))

for k in range(1,3)
        for t in range(len(RG)):
                #t = 3
                v = RG[t,:]
                print v
                SP[coor['R'],coor['C']] = v/24
                #print SP
                vals = ~np.isnan(SP)
                # identification parameter
                If k==1
                        gp = GaussianProcess(theta0=len(RG), thetaL=1, thetaU=10, nugget=0.1)
                else:
                        gp = GaussianProcess(theta0=len(RG), beta0=beta0, thetaL=1, \
                                thetaU=10, nugget=0.1)

                gp.fit(X=np.column_stack([rr[vals],cc[vals]]), y=SP[vals])
                rr_cc_as_cols = np.column_stack([rr.flatten(), cc.flatten()])
                grid = gp.predict(rr_cc_as_cols).reshape(SP.shape)
                grid = np.where(grid[:] < 0.005, 0, grid) # filtering
                # merge to RRI format
                t_temp[0, 0] = (n-1)*86400 # temporal @ 24h => 86400 sec
                t_temp[0, 1] = 13
                t_temp[0, 2] = 20
                pRG2 = np.concatenate((t_temp,grid), axis=0)
                pRG = np.concatenate((pRG,pRG2), axis=0)
                n = n + 1
                print t,np.mean(SP[vals]),np.mean(grid)

                # save txt file
                If k==1
                        np.savetxt("./A_SK2RRI2011.txt", pRG, delimiter=" ", fmt='%-7.3f')
                else:
                        np.savetxt("./A_OK2RRI2011.txt", pRG, delimiter=" ", fmt='%-7.3f')
```

G.4 Example of input GPM data into VOXEL model for RRI model

```
import glob, os
import pandas as pd
import numpy as np
import h5py as h5

# GPM char.
rainfallN = 'precipitationCal'

# read GPM files
os.chdir('../../GPM2_2014')
#os.chdir('./temp_GPM/test')
fileN = glob.glob('*.HDF5')
fileN.sort()
GPM = np.zeros((1,13))
n = 1 # counter
# for the Nan prov. region
t_temp = np.zeros((1,13))

# to capture with RG coor
for fname in fileN:
    print n, fname
    fid = h5.File(fname,'r')
    grp = fid['Grid']
    prec= grp[rainfallN].value
    fid.close()
    precT = np.fliplr(prec) # mirror matrix
    Rain = precT.T
    #print Rain.shape
    GPM1 = Rain[702: 722, 2800: 2813]
    t_temp[0, 0] = (n-1)*1800 # temporal @ 0.5h => 1800 sec
    t_temp[0, 1] = 13
    t_temp[0, 2] = 20
    GPM2 = np.concatenate((t_temp,GPM1), axis=0)
    GPM = np.concatenate((GPM,GPM2), axis=0)
    n = n + 1

# save txt file
np.savetxt("../scrip_analysis/RRI_input/A_GPM2RRI.txt", GPM, delimiter=" ", fmt='%-7.3f')
```


G.5 Linearly Geometric Transformation program

```
# -*- coding: utf-8 -*
import sys
import numpy as np
import pandas as pd
from scipy import stats

# defind function
import numpy as np
def rmse(predictions, targets):
    return np.sqrt(((predictions - targets) ** 2).mean())

# Start program
# load data from file
if len(sys.argv) < 2:
        print 'Usage:  ' + sys.argv[0] + ' [data file]'
        sys.exit()

# input data to metrix
dataGSI = pd.read_csv(sys.argv[1])

# add field
# GSI data
```

```python
dataGSI['UU']=dataGSI['X']*dataGSI['X']
dataGSI['UV']=dataGSI['X']*dataGSI['Y']
dataGSI['UW']=dataGSI['X']*dataGSI['W']
dataGSI['VV']=dataGSI['Y']*dataGSI['Y']
dataGSI['VW']=dataGSI['Y']*dataGSI['W']
dataGSI['WW']=dataGSI['W']*dataGSI['W']
dataGSI['ZU']=dataGSI['Z']*dataGSI['X']
dataGSI['ZV']=dataGSI['Z']*dataGSI['Y']
dataGSI['ZW']=dataGSI['Z']*dataGSI['W']

# to create matrix
PGSI = np.matrix([[dataGSI.sum().UU,dataGSI.sum().UV,dataGSI.sum().UW,dataGSI.sum().X],
                  [dataGSI.sum().UV,dataGSI.sum().VV,dataGSI.sum().VW,dataGSI.sum().Y],
                  [dataGSI.sum().UW,dataGSI.sum().VW,dataGSI.sum().WW,dataGSI.sum().W],
                  [dataGSI.sum().X,dataGSI.sum().Y,dataGSI.sum().W,len(dataGSI)]])

YGSI = np.matrix([[dataGSI.sum().ZU],[dataGSI.sum().ZV],[dataGSI.sum().ZW],[dataGSI.sum().Z]])

# estimated parameter by inverse matrix
PaGSI = PGSI.I*YGSI
print PaGSI

# to transform data
zt=PaGSI[0]*np.array(dataGSI['X'])+PaGSI[1]*np.array(dataGSI['Y'])+PaGSI[2]*np.array(dataGSI['W'])+PaGSI[3]
ZT = zt.transpose()
dataGSI['ZT'] = pd.DataFrame(ZT)

# evaluated error
# mean error
dataGSI['DZE']=dataGSI['W']-dataGSI['Z']
dataGSI['DZT']=dataGSI['ZT']-dataGSI['Z']

# absolute mean error
dataGSI['ADZE']=abs(dataGSI['W']-dataGSI['Z'])
dataGSI['ADZT']=abs(dataGSI['ZT']-dataGSI['Z'])

MEGSI = dataGSI.mean()

# RMSE
rmseGSIT = rmse(np.array(dataGSI['ZT']), np.array(dataGSI['Z']))
rmseGSIE = rmse(np.array(dataGSI['W']), np.array(dataGSI['Z']))

# R^2
slope, intercept, r_E, p_value, std_err = stats.linregress(np.array(dataGSI['W']), np.array(dataGSI['Z']))
slope, intercept, r_T, p_value, std_err = stats.linregress(np.array(dataGSI['ZT']), np.array(dataGSI['Z']))

print
print "Existing,Transform"
print "ME   :",MEGSI.DZE,MEGSI.DZT
print "MAE  :",MEGSI.ADZE,MEGSI.ADZT
print "RMSE :",rmseGSIE,rmseGSIT
print "R^2  :",r_E,r_T
```

LIST OF PUBLICCATION

Peer reviewed papers:

1. Pakoksung, Takagi, 2015, Remote Sensing Data Application for Flood Modeling: JAST, 26, 115-122.
2. Pakoksung, Takagi, 2015, Digital Elevation Models on Accuracy Validation and Bias Correction in Vertical: Modeling Earth Systems and Environment, 2(1), 1-13. DOI :10.1007/s40808-015-0069-3
3. Pakoksung, Takagi, 2016, Effect of Satellite Based Rainfall Products on River Basin Responses of Runoff Simulation on Flood Event: Modeling Earth Systems and Environment, 2(143), 1-14. DOI :10.1007/s40808-015-0200-0
4. Pakoksung, Takagi, 2016, Assessing Flood Losses in Thailand, using Remote Sensing Data and Input-Output Table: Journal of Society for Social Management Systems, (**accepted**).
5. Pakoksung, Takagi, 2016, Efficient River Basin Scale Runoff Simulation using GPUs-accelerated Rainfall-Runoff-Inundation Model: *Environmental Earth Sciences journal* (**submitted**).
6. Pakoksung, Takagi, 2016, Assessment and Comparison of Digital Elevation Model (DEM) Products in Varying Topographic, Land Cover Region and Its Attribute: *Journal of the Indian Society of Remote Sensing* (**submitted**).
7. Pakoksung, Takagi, 2016, Effect of Spatial Distribution of Ground Rainfall Products on River Basin Responses of a Distributed Hydrological Model: *Journal of Spatial Hydrology* (**submitted**).
8. Pakoksung, Takagi, 2016, Modeling the Distribution of Rainfall Intensity using Daily Data: *Engineering Journal* (**submitted**).
9. Pakoksung, Takagi, 2016, Effect of DEM sources on Distributed Hydrologic model outputs of Runoff and Inundation data : (in **preparing**)
10. Pakoksung, Takagi, 2016, Effect of Land Cover based Surface Roughness on Runoff estimation : (in **preparing**)
11. Pakoksung, Takagi, 2016, Effect of Bias Correction Methodologies on Runoff estimation : (in **preparing**)
12. Pakoksung, Takagi, 2016, Flood simulation in small area based on the condition data from river basin area : (in **preparing**)
13. Pakoksung, Takagi, 2016, Flood hazard and risk assessment in small area based on the macro economic data : (in **preparing**)

Oral presentation on conference:

14. Pakoksung, Takagi, 2014, Satellite Based Application for Flood Simulation, Asian Association on Remote Sensing 2014, Oct 2014, Nay Pyi Taw, Myanmar.
15. Pakoksung, Takagi, 2015, Vertical Accuracy Validation of Digital Elevation Models (DEMs) in Shikoku Island, Japan, Asian Association on Remote Sensing 2015, Oct 2015, Manila, Philippines.

Poster presentation:

16. Pakoksung, Takagi, 2015, Remote Sensing Data Application for Flood Modeling, 23-IIS-forum, Tokyo, Japan.
17. Pakoksung, Takagi, 2016, VOXEL Model Assisted Distributed hydrological Modeling, 24-IIS-forum, Tokyo, Japan.

CURRICULUM VITAE

Home address: Thailand
Current address: Japan, Kochi, Kami-city, Tosayamada, Takaramachi 3-1-12.

Name: **Pakosung Kwanchai**
Date of birth: 06/02/1978

<u>Educational background</u>

Feb, 1997   **Vocational Certificate in Civil Construction**, Chaiyaphum Technical College, Thailand (graduated).

Jun, 1997   **Bachelor's degree, Department of Civil Engineering**, Faculty of Engineering, Rajamangala Institute of Technology, Thailand (enrolled).

Feb, 2001   -same as above- (graduated).

Jun, 2001   **Master's degree, Department of Water Resources Engineering**, Faculty of Engineering, Chulalongkorn University, Thailand (enrolled).

Apr, 2005   -same as above- (graduated).

Oct, 2013   **Doctoral Program in Special Scholarship Program (SSP), Infrastructure Systems Engineering**, School of Engineering, Kochi University of Technology (enrolled).

Sep, 2016   -same as above- (graduated).

<u>Professional background</u>

Jun, 2002   **Researcher assistant** in Hydraulic and Coastal engineering lab., Department of Water Resources Engineering, Faculty of Engineering, Chulalongkorn University, Thailand (jointed).

Aug, 2005   **Civil and Water resources Engineer in Consultant Company**, Thailand (jointed).

Jun, 2009   -same as above- (resigned).

Aug, 2009   **Researcher**, Water Resources System Research Unit, Department of Water Resources Engineering, Faculty of Engineering, Chulalongkorn University, Thailand (jointed).

Sep, 2013   -same as above- (resigned).

<u>Research background</u>

Jun, 2001 – Apr, 2005

Department of Water Resources Engineering, Faculty of Engineering, Chulalongkorn University, Thailand, "Hydraulics Behavior of Flow Through an Outlet Work: Case Study of Nong Kho Reservoir" involved in during Master's program.

Oct, 2013 – Sep, 2016

Special Scholarship Program (SSP), Infrastructure Systems Engineering, School of Engineering, Kochi University of Technology, "Runoff Analysis using Satellite Data for Flood Reginal Assessment: Spatial and Time-series Bias Correction of Satellite Data" involved in during Doctoral program.